Alaska Department of Transportation & Public Facilities

Alaska University Transportation Center

The Effect of Load History on Reinforced Concrete Bridge Column Behavior

Prepared By:

Jason Goodnight, Yuhao Feng
Dr. Mervyn Kowalsky, Dr. James Nau

August 2012

Prepared By:

Alaska University Transportation Center
Duckering Building Room 245
P.O. Box 755900
Fairbanks, AK 99775-5900

Alaska Department of Transportation
Research, Development, and Technology Transfer
2301 Peger Road
Fairbanks, AK 99709-5399

INE # 12.15

FHWA-AK-RD-12-09

REPORT DOCUMENTATION PAGE

Form approved OMB No.

1. AGENCY USE ONLY (LEAVE BLANK)	2. REPORT DATE	3. REPORT TYPE AND DATES COVERED
FHWA-AK-RD-12-09	August 2012	Final Report (7/2012-8/15/2012)

4. TITLE AND SUBTITLE
The Effect of Load History on Reinforced Concrete Bridge Column Behavior

5. FUNDING NUMBERS
AUTC #410002
DTRT06-G-0011
AKDOT&PF T2-10-06

6. AUTHOR(S)
Jason Goodnight, Yuhao Feng, Dr. Mervyn Kowalsky, Dr. James Nau

7. PERFORMING ORGANIZATION NAME(S) AND ADDRESS(ES)
Alaska University Transportation Center
P.O. Box 755900
Fairbanks, AK 99775-5900

8. PERFORMING ORGANIZATION REPORT NUMBER
INE/AUTC 12.15

9. SPONSORING/MONITORING AGENCY NAME(S) AND ADDRESS(ES)
Alaska Department of Transportation Research, Development, and Technology Transfer
2301 Peger Road
Fairbanks, AK 99709-5399

10. SPONSORING/MONITORING AGENCY REPORT NUMBER
FHWA-AK-RD-12-09

11. SUPPLENMENTARY NOTES
Performed in cooperation with the U.S. Department of Transportation, Federal Highway Administration.

12a. DISTRIBUTION / AVAILABILITY STATEMENT
No restrictions
This document is available to the public through NTIS: National Technical Information Service Alexandria, Virginia http://www.ntis.gov

12b. DISTRIBUTION CODE

13. ABSTRACT (Maximum 200 words)

To satisfy the aims of performance based design, levels of damage which interrupt the serviceability of the structure or require more invasive repair techniques must be related to engineering criteria. In this report, the influence of displacement history on performance limit states, the relationship between strain and displacement, and the spread of plasticity in reinforced concrete structures is explored. An experimental study is underway to assess the performance of thirty circular, well-confined, bridge columns with varying lateral displacement history, transverse reinforcement detailing, axial load, aspect ratio, and longitudinal steel content. Eight of these columns, with similar geometry and detailing, were subjected to various unidirectional displacement histories including standardized laboratory cyclic loading and recreations of the displacement responses obtained from non-linear time history analysis of multiple earthquakes with distinct characteristics. Longitudinal reinforcing bars were instrumented to obtain strain hysteresis, vertical strain profiles, cross section curvatures, curvature distributions, and fixed-end rotations attributable to strain penetration. Results indicate that bar buckling was influenced by load history, but the relationship between strain and displacement along the envelope curve was not. The main impact of load history on bar buckling is its influence on accumulated strains within the longitudinal reinforcement and transverse steel.

14- KEYWORDS:
Bridge design (Esusb), Concrete structures (Pbcc), Earthquake resistant structures (Pbce), Columns (Pbpbvvd), Earthquake resistant design (Esdc), Earthquake resistant structures (Pbce), Dynamic structural analysis (Geb), Finite element method (Gej), Yield stress (Smvy),Strain gages (Gumppv), Instruments for measuring loads or pressure (Gumpp)

15. NUMBER OF PAGES
367

16. PRICE CODE
N/A

17. SECURITY CLASSIFICATION OF REPORT	18. SECURITY CLASSIFICATION OF THIS PAGE	19. SECURITY CLASSIFICATION OF ABSTRACT	20. LIMITATION OF ABSTRACT
Unclassified	Unclassified	Unclassified	N/A

SI* (MODERN METRIC) CONVERSION FACTORS

APPROXIMATE CONVERSIONS TO SI UNITS

Symbol	When You Know	Multiply By	To Find	Symbol
		LENGTH		
in	inches	25.4	millimeters	mm
ft	feet	0.305	meters	m
yd	yards	0.914	meters	m
mi	miles	1.61	kilometers	km
		AREA		
in^2	square inches	645.2	square millimeters	mm^2
ft^2	square feet	0.093	square meters	m^2
yd^2	square yard	0.836	square meters	m^2
ac	acres	0.405	hectares	ha
mi^2	square miles	2.59	square kilometers	km^2
		VOLUME		
fl oz	fluid ounces	29.57	milliliters	mL
gal	gallons	3.785	liters	L
ft^3	cubic feet	0.028	cubic meters	m^3
yd^3	cubic yards	0.765	cubic meters	m^3
		NOTE: volumes greater than 1000 L shall be shown in m^3		
		MASS		
oz	ounces	28.35	grams	g
lb	pounds	0.454	kilograms	kg
T	short tons (2000 lb)	0.907	megagrams (or "metric ton")	Mg (or "t")
		TEMPERATURE (exact degrees)		
^oF	Fahrenheit	5 (F-32)/9 or (F-32)/1.8	Celsius	^oC
		ILLUMINATION		
fc	foot-candles	10.76	lux	lx
fl	foot-Lamberts	3.426	$candela/m^2$	cd/m^2
		FORCE and PRESSURE or STRESS		
lbf	poundforce	4.45	newtons	N
lbf/in^2	poundforce per square inch	6.89	kilopascals	kPa

APPROXIMATE CONVERSIONS FROM SI UNITS

Symbol	When You Know	Multiply By	To Find	Symbol
		LENGTH		
mm	millimeters	0.039	inches	in
m	meters	3.28	feet	ft
m	meters	1.09	yards	yd
km	kilometers	0.621	miles	mi
		AREA		
mm^2	square millimeters	0.0016	square inches	in^2
m^2	square meters	10.764	square feet	ft^2
m^2	square meters	1.195	square yards	yd^2
ha	hectares	2.47	acres	ac
km^2	square kilometers	0.386	square miles	mi^2
		VOLUME		
mL	milliliters	0.034	fluid ounces	fl oz
L	liters	0.264	gallons	gal
m^3	cubic meters	35.314	cubic feet	ft^3
m^3	cubic meters	1.307	cubic yards	yd^3
		MASS		
g	grams	0.035	ounces	oz
kg	kilograms	2.202	pounds	lb
Mg (or "t")	megagrams (or "metric ton")	1.103	short tons (2000 lb)	T
		TEMPERATURE (exact degrees)		
^oC	Celsius	1.8C+32	Fahrenheit	^oF
		ILLUMINATION		
lx	lux	0.0929	foot-candles	fc
cd/m^2	$candela/m^2$	0.2919	foot-Lamberts	fl
		FORCE and PRESSURE or STRESS		
N	newtons	0.225	poundforce	lbf
kPa	kilopascals	0.145	poundforce per square inch	lbf/in^2

*SI is the symbol for the International System of Units. Appropriate rounding should be made to comply with Section 4 of ASTM E380.
(Revised March 2003)

Table of Contents

List of Figures

List of Tables

Acknowledgements

The authors wish to acknowledge Alaska DOT&PF and Alaska University Transportation Center (AUTC) who supported this research through a series of grants. Special acknowledgement goes to Elmer Marx of Alaska DOT&PF who was closely involved in this research as the primary technical contact. Lastly, the assistance of the entire staff of the Constructed Facilities Laboratory is greatly appreciated.

Abstract

The goal of performance based seismic engineering is to design structures to achieve a specific level of performance under a specific earthquake hazard within definable levels of reliability. To satisfy the aims of performance based design, levels of damage which interrupt the serviceability of the structure or require more invasive repair techniques must be related to engineering criteria. For reinforced concrete structures, concrete compressive and steel tensile strain limits are the best indicators of damage. In this paper, the importance of displacement history and its effects on performance limit states, the relationship between strain and displacement, and the spread of plasticity in reinforced concrete structures is explored. An experimental study is currently underway to assess the performance of thirty large-scale circular, well-confined, bridge columns subjected to various unidirectional displacement histories including monotonic, reversed cyclic, and earthquake time-history response. The test variables include load history, transverse reinforcement detailing, axial load ratio, and aspect ratio. This report focuses on specimens 8-18 which included load history and transverse steel detailing as primary variables. Longitudinal reinforcing bars were instrumented to obtain strain hysteresis, vertical strain profiles, cross section curvatures, curvature distributions, and fixed-end rotations attributable to strain penetration.

Summary of Findings

Results have shown that the damage control steel tensile strain limit was influenced by load history, but the relationship between strain and displacement was not. Specific earthquake time-history response characteristics were evaluated including: the number and amplitude of cycles prior to the peak, degree of symmetry, and the peak displacement in each direction of loading. The symmetric three cycle set load history is more severe than the displacement history produced by real earthquakes, when evaluated to the same peak displacement, because of the high number of inelastic reversals of loading of increasing magnitude. The earthquake load histories needed to be scaled to larger displacements to produce bar buckling. Large inelastic strains, caused by large concrete compressive demand, decreased the effectiveness of the transverse steel in restraining buckling of the longitudinal bars. Plastic curvatures followed a linear distribution and as curvature ductility increased, the extent of plasticity stretched higher above the footing. Improvements to the moment curvature prediction for the relationship between strain and displacement can be made by taking into account the curvature ductility dependent linear distribution of plastic curvatures.

Improvements to the plastic hinge method for member deformation are necessary to produce accurate limit state target displacements at levels of response other than the ultimate condition which the constant plastic hinge length was intended for. The Optotrak instrumentation system allows for measurement of cross section curvature profiles and fixed-end rotations due to strain penetration of longitudinal reinforcement into the footing. The use of a constant plastic hinge length does not take into account the response level dependent, linear distribution of plastic curvatures within the hinge regions. As the base section curvature increase, the height at which the linear plastic curvature distribution intersects the elastic curvature profile extends further above the footing. The spread of plasticity in bridge columns is primarily due to the effects of tension shift and hardening within the hinge region. Due to the effects of tension shift, compressive strains are concentrated near the column base and tensile strains are fanned out to a greater height following inclined crack distribution. The tensile strains at the beginning of an inclined flexural shear crack do not coincide with the perceived moment demand at that location based on its height above the footing and the applied lateral load.

This report focused on specimens 8-18 which included load history and transverse steel detailing as primary variables. The remaining specimens 19-30 in the research program will focus on aspect ratio, axial load ratio, and longitudinal steel content. Conclusions in the form of design recommendations for performance strain limits require inspection and comparison of the entire experimental dataset. For the purposes of this report, the influence of load history and transverse steel on column behavior was presented in the form of experimental observations. Similarly, improvements to the plastic hinge method for member deformations can only be made once additional design variables are explored in the remaining tests.

Analysis with fiber-based model showed that the relationship between strain and displacement was not influenced by load history. It is concluded based on considering a number of load histories and important structural variables which includes axial load ratio, transverse steel detailing, aspect ratio and longitudinal steel content. Analysis with other load histories will be conducted to confirm this statement.

A finite element model was developed to capture the longitudinal reinforcement bucking under cyclic loading. Results from analysis has shown that the model was able to capture the bar buckling and the load history effect on bar buckling. The bar buckling model will be implemented in the parametric study of the load history effect on the steel tensile strain limit.

CHAPTER 1 - INTRODUCTION AND RESEARCH APPROACH

1.1. Problem Statement and Research Objective

"The goal of performance based seismic engineering is to design structures to achieve a specific level of performance under a specific earthquake hazard within definable levels of reliability," as defined by the SEAOC (1999). To satisfy the aims of performance based design, levels of damage which interrupt the serviceability of the structure or require more invasive repair techniques must be related to engineering criteria. For reinforced concrete flexural member such as bridge columns, concrete compressive and steel tensile strain limits are the best indicators of damage. Closely spaced transverse steel hoops or spirals provide adequate confinement and shear resistance to produce a flexural mode of failure for columns with modern detailing. An understanding of the spread of plasticity in reinforced concrete structures is required to determine the deformation at damage limit states.

Serviceability limit states such as concrete cover crushing or residual crack widths exceeding 1mm may occur during smaller, more frequent earthquakes, (Priestley, Seible, and Calvi (1996)). While the serviceability limit states do not pose a safety concern, the hinge regions must be repaired to prevent corrosion of internal reinforcing steel. At higher ductility demands produced by larger less frequent earthquakes, reinforcing bar buckling may lead to permanent elongation in the transverse steel, which diminishes its effectiveness in confining the concrete core. Bar buckling and significant damage to the core concrete represent the damage control limit states, which when exceeded lead to significant repair or replacement costs. Rupture of previously buckled bars during subsequent cycles of loading may lead to significant strength loss. The life safety or collapse prevention limit state is characterized by fracture of previously buckled bars under displacements at or exceeding those required to initiate bar buckling.

Previous experimental studies on circular bridge columns have shown that reinforcing bar buckling is influenced by displacement history: (Moyer and Kowalsky (2003)), (Kunnath et al. (1997)), and (Freytag (2006)). According to (Kunnath et al. (1997)), random displacement cycles provide a better means for understanding the effects of cumulative damage and assessing the performance of structures subjected to low-cycle fatigue. Analytical studies by (Syntzirma, Pantazopoulou, and Aschheim (2010)) concluded that when flexural members are controlled by bar buckling, the deformation capacity cannot be defined uniquely since it is a function of the applied cyclic deformation history.

1.2. Scope of Study

For the design of a new structural component subjected to earthquake loading, an engineer may develop a suite of performance objectives for each of the following damage levels: (1) serviceability, (2) damage control, and (3) collapse prevention. A given performance objective is represented by a single damage limit state, a specific earthquake hazard, and an associated repair or replacement cost and strategy. This information may be expressed to an owner in terms of probability for each damage limit state occurring to facilitate the decision making process for new construction. Under this design methodology, the controlling limit state may not be collapse prevention, but rather a serviceability consideration for a piece of critical infrastructure which must remain operational after a seismic event.

To satisfy the aims of performance based design, each of the damage levels must be related to engineering demand parameters to successfully design the component for the seismic hazard. Typical engineering demand parameters include: strain, curvature, rotation, displacement, drift, and ductility. While the progression of damage in flexural bridge columns has been thoroughly investigated in the past, to the author's knowledge, none of the previous studies had the ability to measure strains at the level of the reinforcement throughout the entire range of response. The goal of the experimental program presented in this paper is to investigate the impact of load history and other design variables on the relationship between strain and displacement, performance strain limits, and the spread of plasticity. The current performance strain limits, summarized in Table 1-1 from (Kowalsky (2000)), have little experimental basis due to the coarse strain measurements utilized in previous experimental studies. Furthermore, they do not account for the effects load history on accumulated strains in the longitudinal and transverse steel.

Accurate limit state target displacements are required to appropriately design a structural component for a specific level of damage and seismic hazard. In a design scenario, this is accomplished utilizing moment curvature analysis and an equivalent distribution of curvature. Moment curvature analysis is an accepted design technique which can be used to determine the base-section curvature at the performance strain limit in question. The target displacement may then be calculated using the plastic hinge method for member deformations. While there are many versions of this method, such as the method shown in Figure 1-1 from (Priestley, Calvi, and Kowalsky (2007)), they all operate by integrating an equivalent distribution of curvature with the moment area method. The elastic and plastic curvature distributions are separated into simplified shapes facilitate design. The elastic flexural displacement is determined using a triangular curvature distribution. The plastic flexural displacement is obtained using a rectangular curvature distribution with a constant height called the plastic hinge length. The width of the rectangle is equal to the plastic curvature at the base section. Due to the effects of strain penetration of longitudinal reinforcement into the footing, the curvature distribution extends into the footing by a depth termed the strain penetration length. The constant plastic hinge length is not physical parameter; it is simply a numerical convenience to obtain the correct top column displacement.

The use of a constant plastic hinge length to describe the equivalent plastic curvature distribution for the whole range of displacements in which a performance limit state may lie is inconsistent with the derivation of the method. The plastic hinge length expression is only appropriate for the ultimate displacement level. Improvements to the moment curvature prediction for the relationship between strain and displacement can be made by taking into account the curvature ductility dependent linear distribution of plastic curvatures observed by (Hines, Restrepo, and Seible (2004)). The instrumentation system utilized within the research program presented in this paper allows for further improvements to the equivalent curvature distributions used to determine the limit state target displacements at various levels of response. The limit state target displacements may be incorporated into a displacement-based design procedure to achieve a specific level of performance under a specific seismic hazard, (Priestley, Calvi, and Kowalsky (2007)).

Table 1-1. Performance Strain Limits from (Kowalsky (2000))

Limit State	**Concrete Compressive Strain Limit**	**Steel Tensile Strain Limit**
Serviceability	0.004 Cover Concrete Crushing	0.015 Residual Crack Widths Exceed 1mm
Damage Control	0.018 (Mander ε_{cu}) Limit of Economical Concrete Repair	0.060 Tension Based Bar Buckling

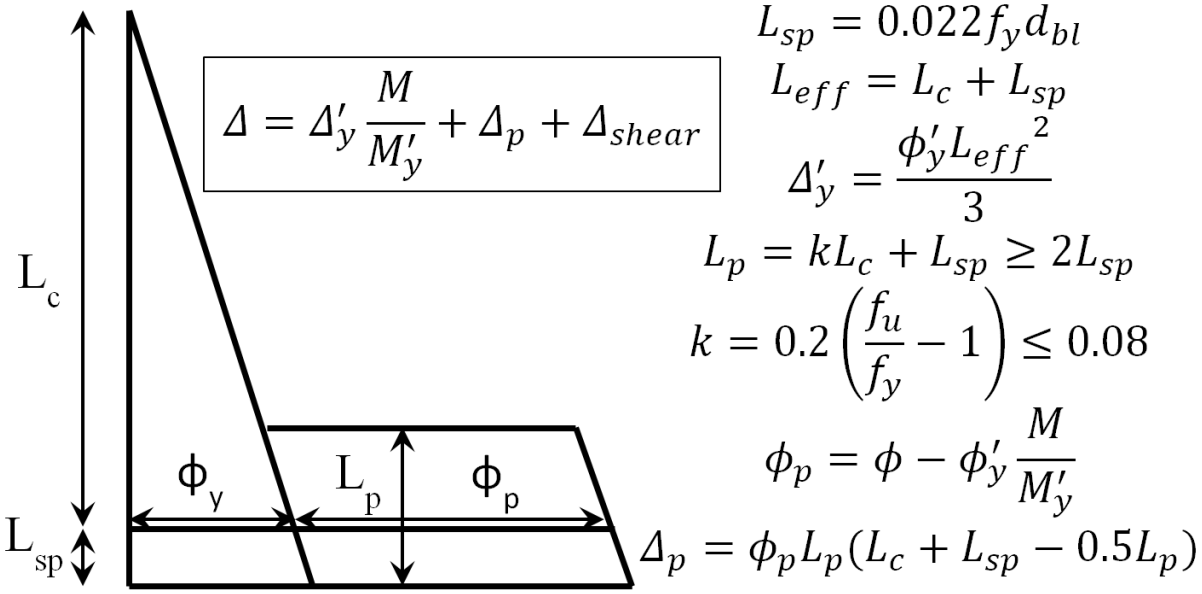

Figure 1-1. Plastic Hinge Method for Member Deformations (Priestley, Calvi, and Kowalsky (2007))

1.3. Research Approach

The research program employs both experimental and analytical methods. The experimental methods consist of thirty bridge column subjected to lateral and axial loads. The test results are utilized to validate and improve the analytical methods. These methods include moment curvature analysis of sections, fiber-based analysis of members, and finite element analysis of sub-assemblies. The numerical simulation is necessary to define the top-column displacement histories for earthquakes records recreated in the experimental tests with a displacement controlled quasi-static loading procedure. Experimentally validated numerical simulation methods may be then be used to explore column arrangements outside of the scope of the experimental program.

1.3.1. Experimental Methods

The specimen was designed to represent a single degree of freedom bridge column subjected to lateral and axial load, see Figure 1-2. The test specimen consists of a footing, column, and loading cap. The footing is a capacity protected member which secures the specimen to the lab strong floor using post tensioned bars. A 220kip hydraulic actuator, with a 40" stroke capacity, applies lateral load to the loading cap of the specimen. A spreader beam, two hydraulic jacks, and a load cell are placed above the loading cap to apply a constant axial compressive load.

The first twelve specimens contained identical geometry and reinforcement and were subjected to different quasi-static top-column displacement histories. The 2ft diameter bridge columns contained 16 #6 ASTM A706 bars for longitudinal reinforcement ($A_{st}/A_g = 1.6\%$) and a #3 A706 spiral at 2" on center ($4A_{sp}/(D's) = 1\%$). The discussion in this paper is limited to Tests 8-18 which utilized an improved instrumentation technique. The test matrix in Figure 1-6 shows the specific load histories and scaling utilized in Tests 8-12. Specific earthquake time-history response characteristics were

evaluated including: the number and amplitude of cycles prior to the peak, degree of symmetry, and peak displacement in each direction of loading.

The effect of transverse steel detailing on restraint of longitudinal bars was the main variable for Tests 13-18. The same column geometry and longitudinal reinforcement were utilized with variable spiral detailing as shown in Figure 1-7. Load history was maintained as a variable for Tests 16-18 which had the same transverse steel detailing. To this point, all of the columns tested were subjected to a constant axial load of 170kips ($P/(f_c'A_g) \approx 5\%$) and had a cantilever aspect ratio of four.

Aspect ratio and axial load ratio are the main variables for the current phase of specimens in progress, 19-24 in Figure 1-8. The 18" diameter bridge column contains 10 #6 ASTM A706 bars for longitudinal reinforcement ($A_{st}/A_g = 1.7\%$) and a #3 A706 spiral at 2" on center ($4A_{sp}/(D's) = 1.3\%$). Future tests in the research program, 25-30, will focus on longitudinal steel content and axial load ratio. Upon completion of the experimental program, all of the variables found to be statistically significant towards describing bar buckling in an experimental column dataset by (Berry and Eberhard (2005)) will have appeared within the test matrix.

1.3.1.1. Instrumentation

The experimental program utilized an innovative instrumentation method to measure large strains at the level of the reinforcement with multiple Optotrak Certus HD 3D position monitors. The Optotrak system can read the location of target markers placed on the specimen in three dimensional space during a test. By calculating the change in three dimensional distances between target markers, strains can be determined with respect to the original unloaded gage lengths. The longitudinal reinforcement in extreme fiber regions was instrumented to obtain strain hysteresis, vertical strain profiles, cross section curvatures, curvature distributions, and fixed-end rotations attributable to strain penetration. Strain gages were applied to layers of transverse steel overlaying the extreme fiber longitudinal reinforcement to observe the interaction between compressive demand, transverse steel strain, and anti-buckling restraint. The discussion in this paper is related to the instrumentation method utilizing two Optotrak position monitors, Tests 8-18, with target markers directly applied to six longitudinal reinforcing bars as shown in Figure 1-4.

A comparison of the accuracy of the strains obtained from the Optotrak system and traditional instrumentation methods such as a strain gage and an extensometer appears in Figure 1-5 for a uniaxial tensile test on a reinforcing bar. The three instrumentation methods agree well before the strain gage debonds from the surface of the bar at low inelastic strain levels.

Traditional instrumentation was also utilized within the test setup. The top column displacement was obtained through a string potentiometer placed at the center of the lateral load. The lateral load and stroke of the 220kip hydraulic actuator were measured through an integrated load cell and LVDT. An axial load cell measured the contribution of one hydraulic jack to the total axial load of the column. A self-regulating axial load system was utilized with a third hydraulic jack in a force controlled MTS machine to regulate the pressure, and thus the load, of two jacks on top of the specimen to maintain a constant axial load throughout testing.

Figure 1-2. Experimental Specimen and Test Setup

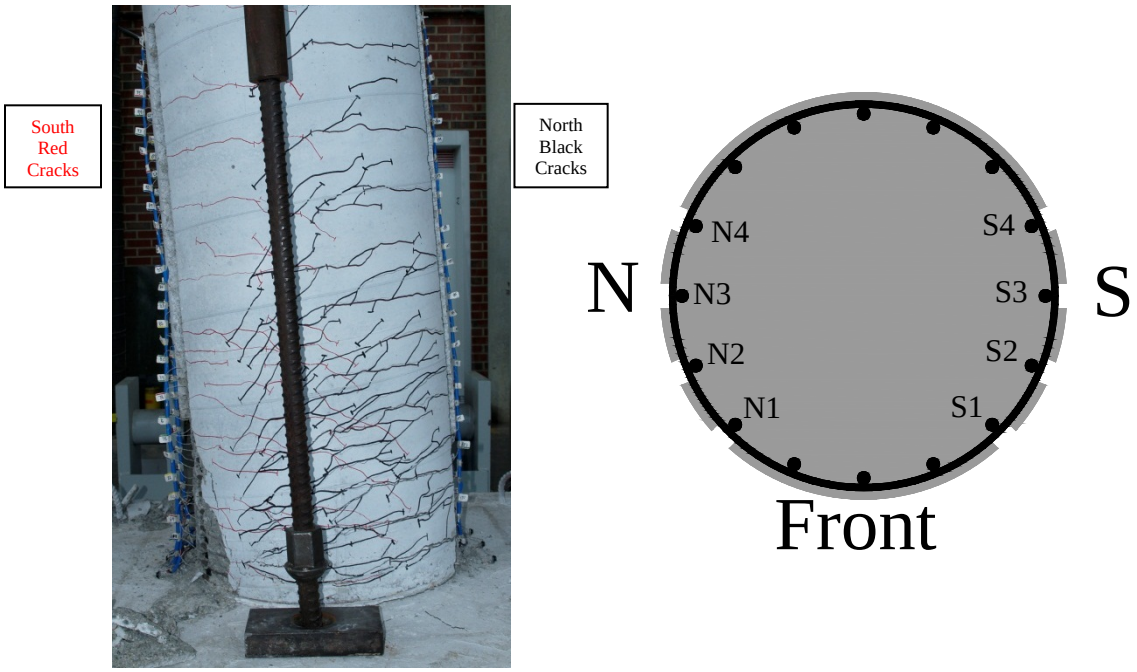

Figure 1-3. Cross Section Bar Designations – North Reinforcement is Placed into Tension during Push Cycles while South Reinforcement is placed into Tension during Pull Cycles (Photo Taken from the Back Side of the Specimen)

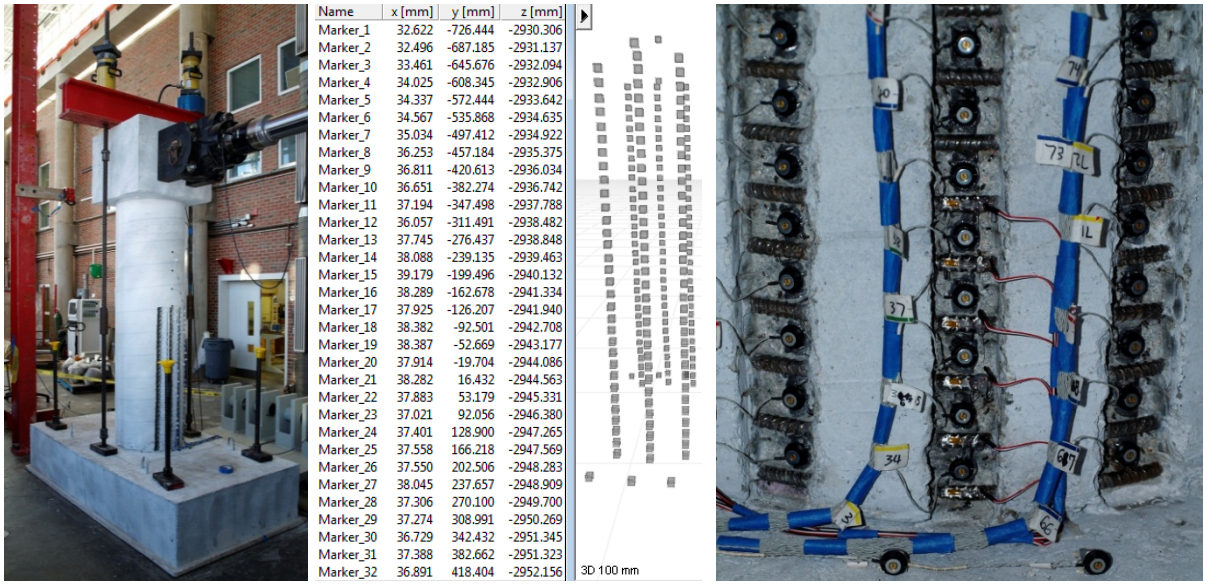

Name	x [mm]	y [mm]	z [mm]
Marker_1	32.622	-726.444	-2930.306
Marker_2	32.496	-687.185	-2931.137
Marker_3	33.461	-645.676	-2932.094
Marker_4	34.025	-608.345	-2932.906
Marker_5	34.337	-572.444	-2933.642
Marker_6	34.567	-535.868	-2934.635
Marker_7	35.034	-497.412	-2934.922
Marker_8	36.253	-457.184	-2935.375
Marker_9	36.811	-420.613	-2936.034
Marker_10	36.651	-382.274	-2936.742
Marker_11	37.194	-347.498	-2937.788
Marker_12	36.057	-311.491	-2938.482
Marker_13	37.745	-276.437	-2938.848
Marker_14	38.088	-239.135	-2939.463
Marker_15	39.179	-199.496	-2940.132
Marker_16	38.289	-162.678	-2941.334
Marker_17	37.925	-126.207	-2941.940
Marker_18	38.382	-92.501	-2942.708
Marker_19	38.387	-52.669	-2943.177
Marker_20	37.914	-19.704	-2944.086
Marker_21	38.282	16.432	-2944.563
Marker_22	37.883	53.179	-2945.331
Marker_23	37.021	92.056	-2946.380
Marker_24	37.401	128.900	-2947.265
Marker_25	37.558	166.218	-2947.569
Marker_26	37.550	202.506	-2948.283
Marker_27	38.045	237.657	-2948.909
Marker_28	37.306	270.100	-2949.700
Marker_29	37.274	308.991	-2950.269
Marker_30	36.729	342.432	-2951.345
Marker_31	37.388	382.662	-2951.323
Marker_32	36.891	418.404	-2952.156

Figure 1-4. Dual Optotrak Position Sensors with Direct Application of Target Markers to Reinforcement

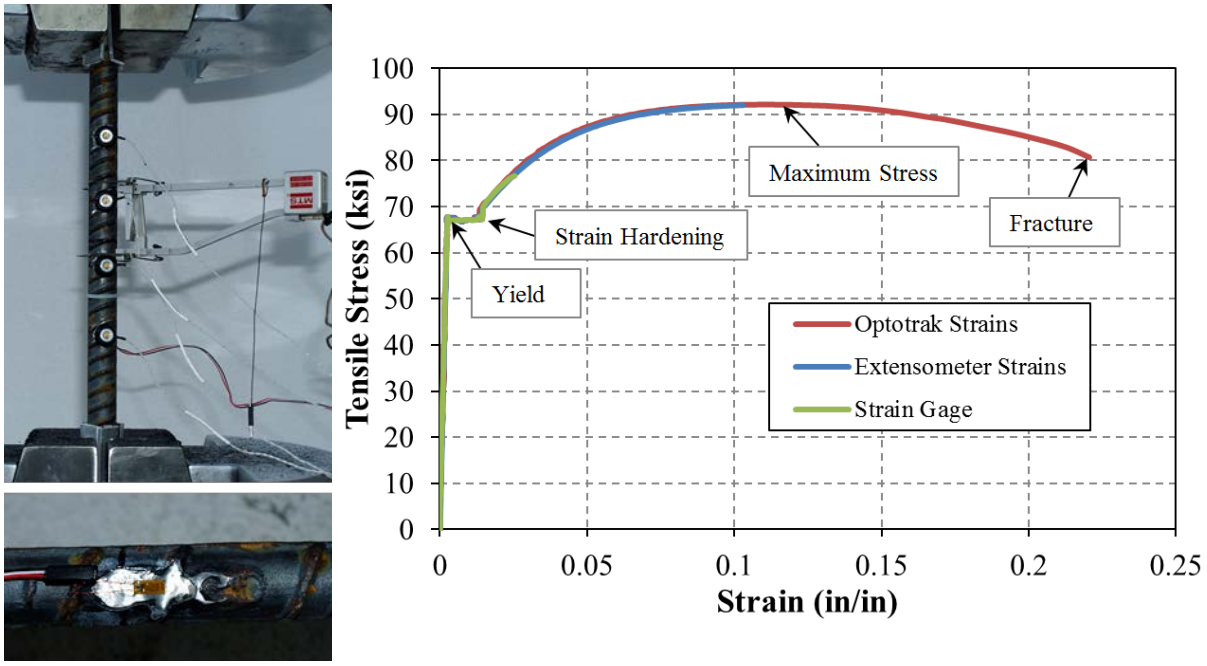

Figure 1-5. Strain Measurement Comparison to Traditional Instrumentation for a Sample Tensile Reinforcing Bar Test

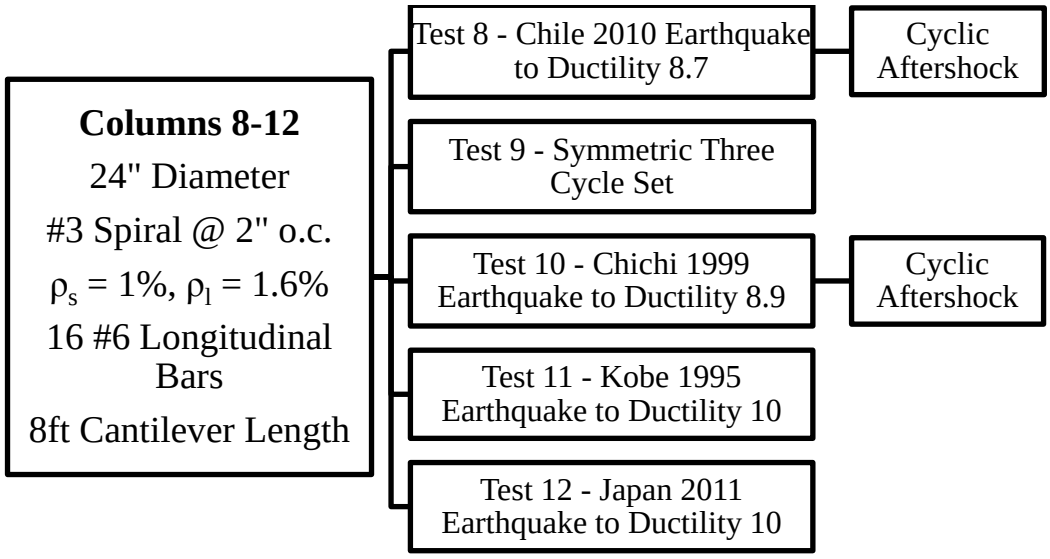

Figure 1-6. Test Matrix for Specimens 8-12 (Load History Variable)

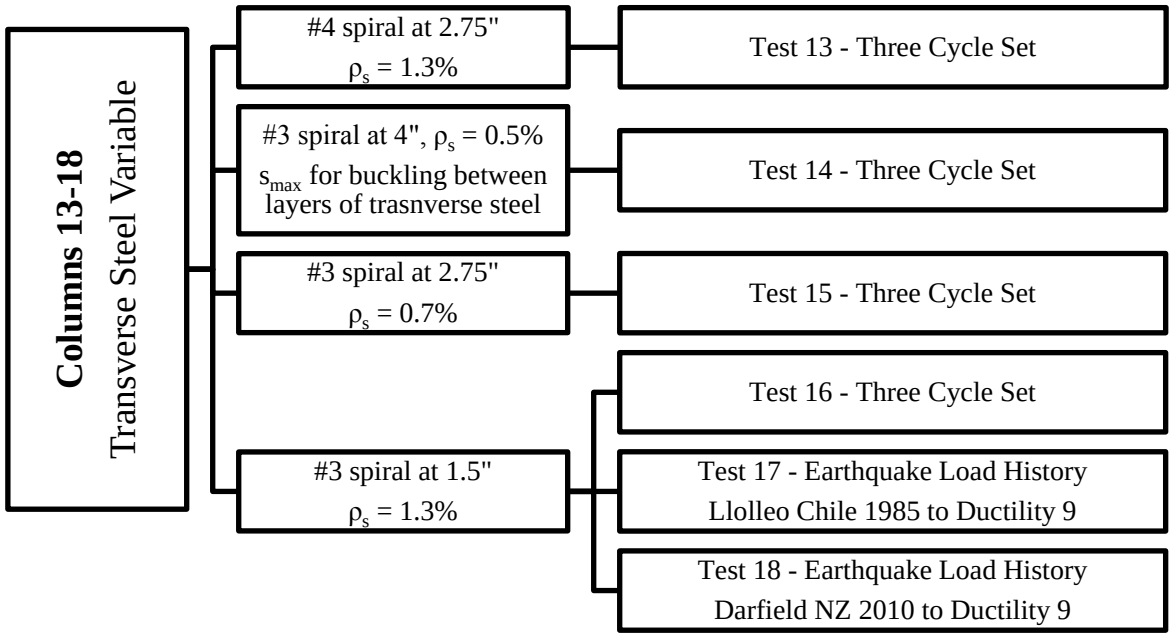

Figure 1-7. Test Matrix for Specimens 13-18 (Transverse Steel Variable)

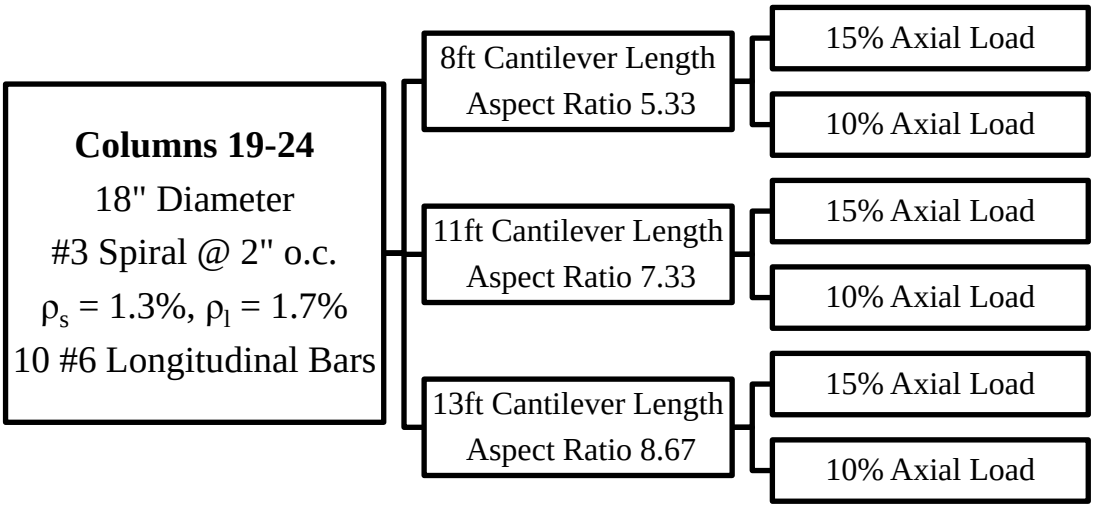

Figure 1-8. Test Matrix for Specimens 19-24 (Axial Load and Aspect Ratio Variables)

1.3.2. Analytical Methods:

The goal of the analytical study is to investigate the effect of seismic load history on the (1) relationship between strain and displacement and (2) the strain limits themselves. It requires two different analytical methods to approach each aspect.

1.3.2.1.Introduction of Fiber-based Model

The fiber-based modeling is a low computational cost technique which is able to conduct both static and dynamic analyses and provide sectional information including strain, stress and curvature. With these features, fiber-based modeling is adequate for investigating the effect of load history on the relationship between strain and displacement. The fiber-based model and the associated analyses are conducted within the framework of the Open System for Earthquake Engineering Simulations (OpenSees). OpenSees is an open source program which allows researchers to update its features, including material and element types. Therefore, a number of advanced elements and recently developed material models are available in this program.

In the parametric study, a series time history analyses will be conducted with the fiber-based model and a variety of earthquakes. The impact of load history on strain and displacement relationship will be investigated with the results from the analyses.

1.3.2.2.Introduction of Finite Element Bar Buckling Model

A common ultimate limit state in well-detailed reinforced concrete section is the buckling of reinforcement. The goal of numerical bar buckling model is to capture the bar buckling and the impact of load history and other structural variables on it. Bar buckling occurs under cyclic loading which leads to high nonlinearity in local areas. This multi-dimensional behavior requires a modeling technique which is able to simulate change of geometry at the local area. Therefore, a finite element method is utilized to accomplish this goal. The software Abaqus is selected to generate the finite element model.

CHAPTER 2 - EXPERIMENTAL FINDINGS

2.1. Load History Variable Tests 8-12 Experimental Results

Specimens 8-12 all contained the same geometry and reinforcement, but were subjected to different displacement histories. The test specimen was designed to represent a single degree of freedom bridge column subjected to lateral and axial load. The 2' diameter columns contained 16 #6 (A706) bars for longitudinal reinforcement ($A_{st}/A_g = 1.6\%$) and a #3 (A706) spiral at 2" pitch for transverse reinforcement ($4A_{sp}/(D's) = 1\%$). The columns had a cantilever length of 8ft and were subjected to a constant axial load of 170 kips which produced an axial load ratio of approximately($P/(f_c'A_g) \approx 5\%$) depending on the concrete strength.

The specimens were subjected to various unidirectional displacement histories including monotonic, reversed cyclic, and earthquake time-history response. Specific earthquake time-history response characteristics were evaluated including: the number and amplitude of cycles prior to the peak, degree of symmetry, and peak displacement in each direction of loading. All of the tests utilized a quasi-static displacement controlled loading procedure. The monotonic load history included a single push cycle to failure which occurred when extreme tensile reinforcement ruptured without prior buckling on the compression side. The symmetric three cycle set laboratory load history is used to evaluate the seismic performance of structural components. The load history begins with elastic cycles to the following increments of the analytically predicted first yield force: ¼ Fy', ½ Fy', ¾ Fy', and Fy'. The experimental first yield displacement is the average of the recorded displacements during the first yield push and pulls cycles. The equivalent yield displacement, used to determine the displacement ductility levels ($\mu_{\Delta 1} = 1 * \Delta_y$), is then calculated as $\Delta_y = \Delta_y'(M_n/M_y')$. The symmetric three cycle set load history resumes with three balanced cycles at each of the following ductility levels: 1, 1.5, 2, 3, 4, 6, 8, 10, 12, etc.

For earthquake time-history tests, the analytical top column displacement history is determined using numerical analysis in OpenSees with a force-based fiber element (Scott and Fenves (2006)) to model the column and a zero-length strain penetration element (Zhao and Sritharan (2007)). For more information on the numerical simulation of the bridge columns, refer to Chapter 3. The original acceleration input is multiplied by a constant scale factor to produce a peak displacement response suitable for the experimental test. Specific earthquake time-history response characteristics were chosen including: the number and amplitude of cycles prior to the peak, degree of symmetry, and peak displacement in each direction of loading. A separate symmetric three cycle set load history was conducted prior to earthquake time-history tests to establish the displacement ductility levels which were later verified by measured strains at the first yield displacement.

Past research by (Moyer and Kowalsky (2003)) suggests that reinforcement buckling occurs after reversal from a peak tensile strain, while the bar is still under net elongation but compressive stress. After reversal from the peak displacement, the cracks on the tensile side begin to close, and before the column reaches zero displacement the reinforcement enters a state of compressive stress but net elongation. It is during this time, while the cracks are still open, that the reinforcement is the sole source of compression zone stability and the bars are prone to buckling. Once the cracks have closed and the concrete is reengaged, the reinforcement is unlikely to buckle.

The deformation capacity of all of the cyclically loaded specimens was limited by reinforcement bar buckling and subsequent rupture during later cycles of the load history. The following sequence of damage was observed for all of the cyclically loaded specimens: cracking, longitudinal reinforcement

yield, cover concrete crushing, yielding of transverse steel, bar buckling, and then reinforcement rupture. Rupture of transverse steel was never observed. The first significant loss of strength occurred when previously buckled reinforcement ruptured in tension.

Table 2-1. Column Property Summary for Load History Variable Tests 8-12

Test	Load History	D (in)	L/D	Long. Steel (ρ_l)	Spiral Detailing (ρ_s)	f'c (psi)	P/f'c*Ag
8	Chile 2010	24	4	16 #6 bars (1.6%)	#3 at 2" (1%)	6988	5.4%
8b	Cyclic Aftershock	24	4	16 #6 bars (1.6%)	#3 at 2" (1%)	6988	5.4%
9	Three Cycle Set	24	4	16 #6 bars (1.6%)	#3 at 2" (1%)	6813	5.5%
10	Chichi 1999	24	4	16 #6 bars (1.6%)	#3 at 2" (1%)	5263	7.1%
10b	Cyclic Aftershock	24	4	16 #6 bars (1.6%)	#3 at 2" (1%)	5263	7.1%
11	Kobe 1995	24	4	16 #6 bars (1.6%)	#3 at 2" (1%)	6070	6.2%
12	Japan 2011	24	4	16 #6 bars (1.6%)	#3 at 2" (1%)	6100	6.2%

Table 2-2. Material Property Summary for Longitudinal and Transverse Reinforcement

Longitudinal Reinforcement	ε_y	f_y (ksi)	ε_h	f_h (ksi)	ε_u	f_u (ksi)
Tests 8-12	0.00235	68.1	0.0131	68.2	0.1189	92.8
Tests 13-18	0.00235	68.1	0.0146	68.2	0.1331	94.8

Transverse Steel	Yield Stress, f_y (ksi)
Tests 8-12 (#3 Spiral)	74.1
Tests 13-18 (#3 Spiral)	64.6
Tests 13-18 (#4 Spiral)	69.9

2.1.1.Test 9 – Symmetric Three Cycle Set Load History

Table 2-3. Results Summary for Test 9 – Symmetric Three Cycle Set Load History

LOAD HISTORY: Symmetric Three Cycle Set Load History

VALUES OF INTEREST:

Concrete Compressive Strength:	$f_c' = 6814psi$
Axial Load:	$P = 170kips$
Analytical First Yield Force:	$F_y' = 46.9kips$
Experimental First Yield Displacement:	$\Delta_y' = 0.63"$
Analytical Nominal Moment Capacity:	$M_n = 503.6kip * ft$
Equivalent Yield Displacement:	$\Delta_y = 0.84"$
Maximum Lateral Force:	$70.3kips$
Failure Mode:	Fracture of Previously Buckled Reinforcement

DAMAGE OBSERVATIONS: (Drift %) [Displacement Ductility, μ_Δ]

First Cracking North:	$3/4Fy' = 0.40"$
First Cracking South:	$-3/4Fy' = -0.38"$
Cover Concrete Crushing North:	$\mu_2^{-2} = -1.67"$
Cover Concrete Crushing South:	$\mu_2^{+2} = 1.69"$
Transverse Steel Yield North:	At $-0.22"$ during pull to $\mu_8^{-1} = -6.78"$
Transverse Steel Yield South:	At $-3.69"$ during push to $\mu_8^{+2} = 6.71"$
Longitudinal Bar Buckling North:	Reversal from $\mu_8^{+1} = 6.72"$
Longitudinal Bar Buckling South:	Reversal from $\mu_8^{-2} = -6.70"$
Longitudinal Bar Fracture North:	At $5.18"$ during push to $\mu_{10}^{+1} = 8.38"$
Longitudinal Bar Fracture South:	At $-4.56"$ during pull to $\mu_{10}^{-2} = -8.42"$

*$\mu_{10}^{-2} = -8.42"$ represents the second pull cycle of displacement ductility ten which reached a peak displacement of 8.42 inches

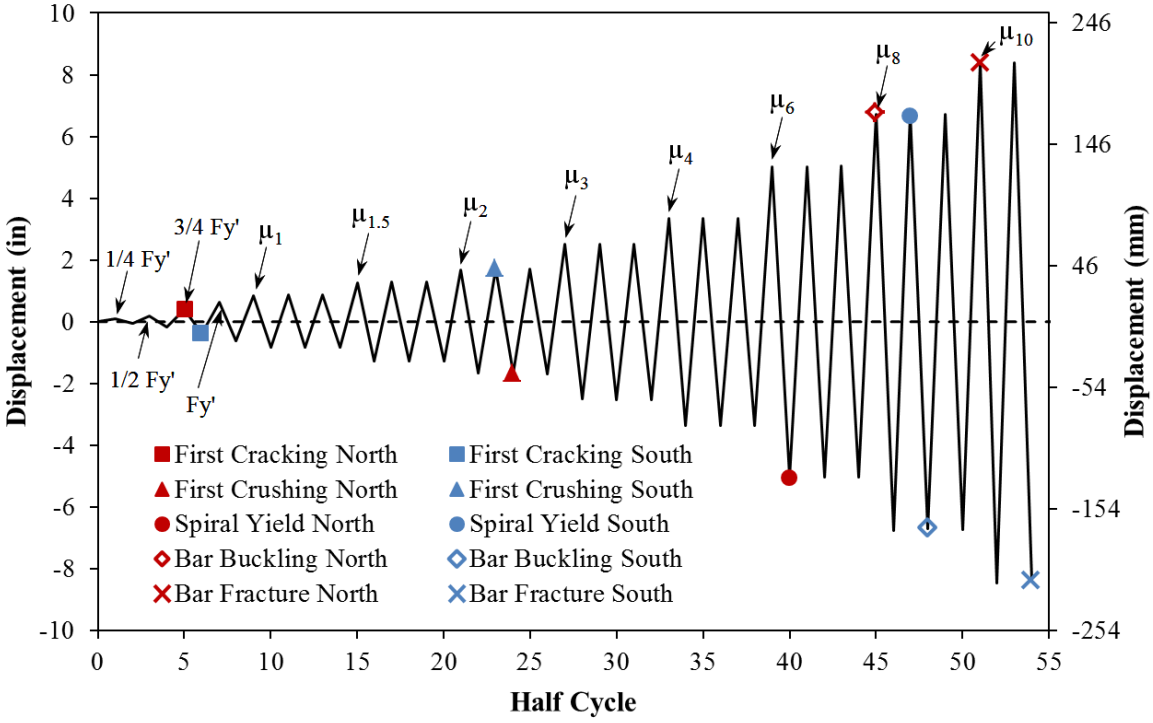

Figure 2-1. Test 9 – Symmetric Three Cycle Set Load History

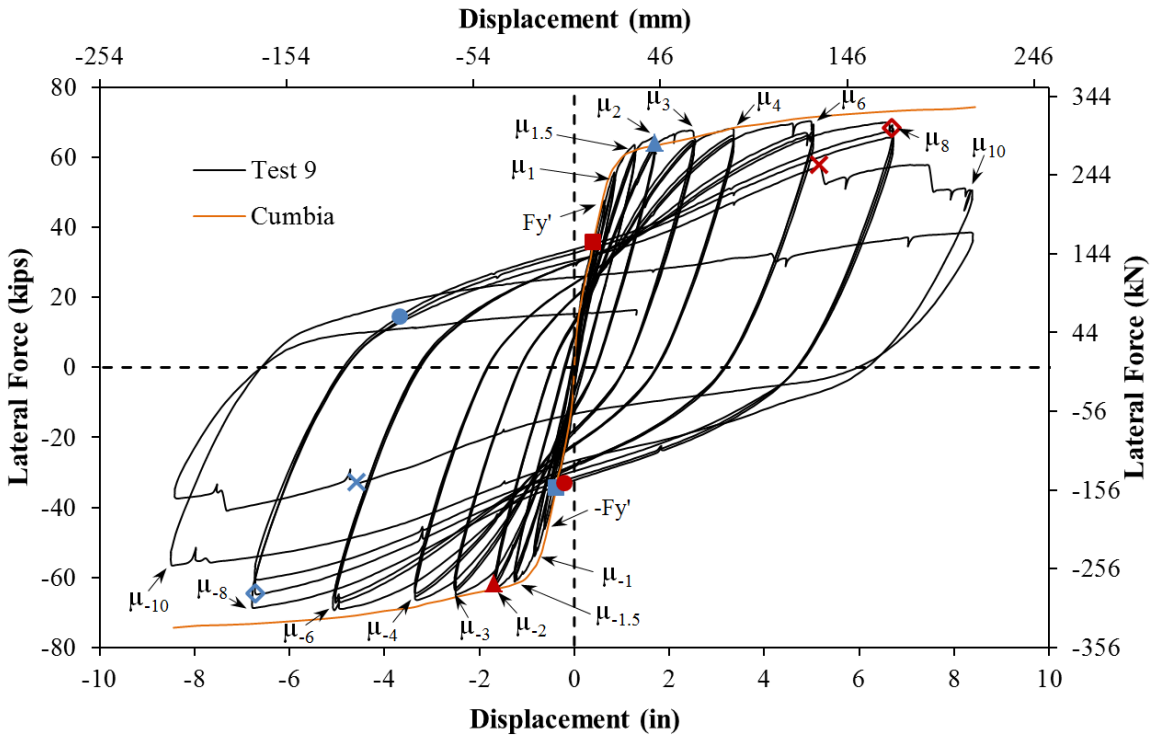

Figure 2-2. Test 9 - Lateral Force vs. Top Column Displacement Hysteretic Response

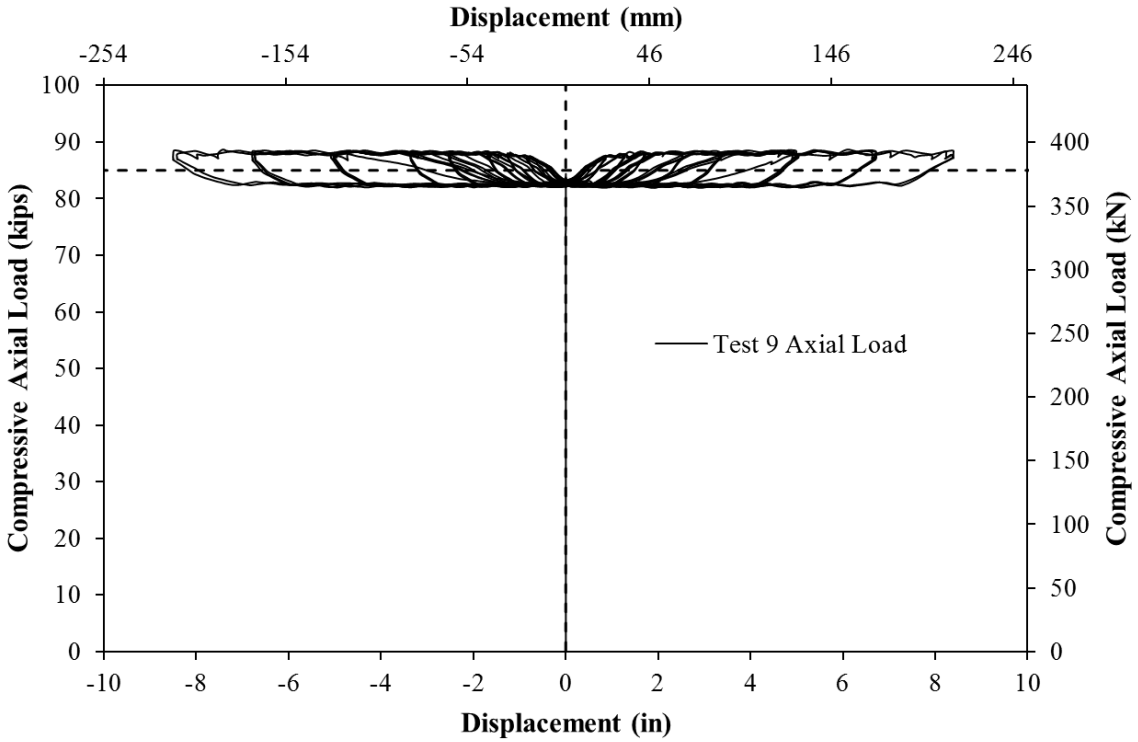

Figure 2-3. Test 9 – Compressive Axial Load from One Jack (Total = 2*Value)

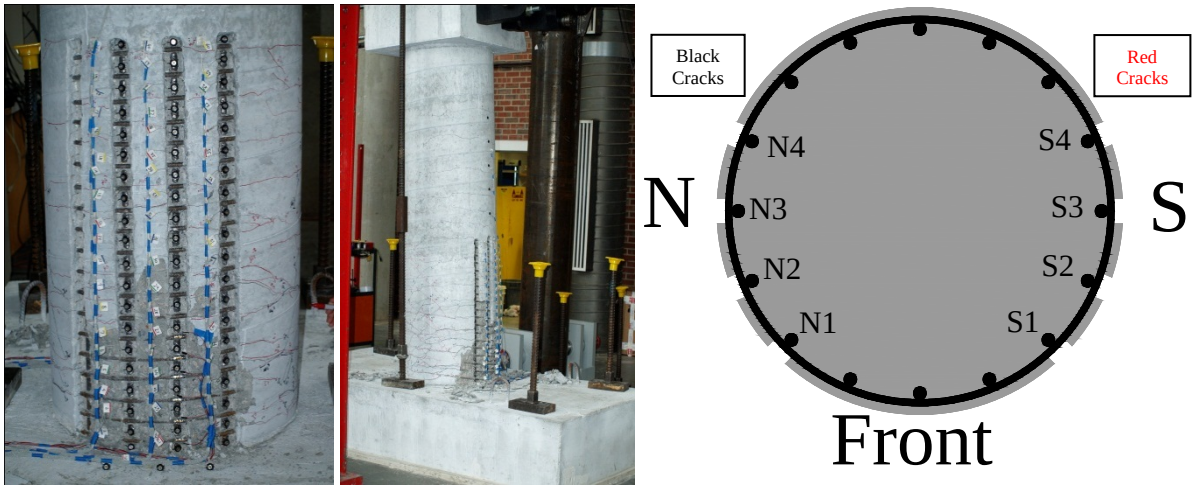

Figure 2-4. Cross Section Bar Designation – North reinforcement is placed into tension during push cycles while South reinforcement is placed into tension during pull cycles

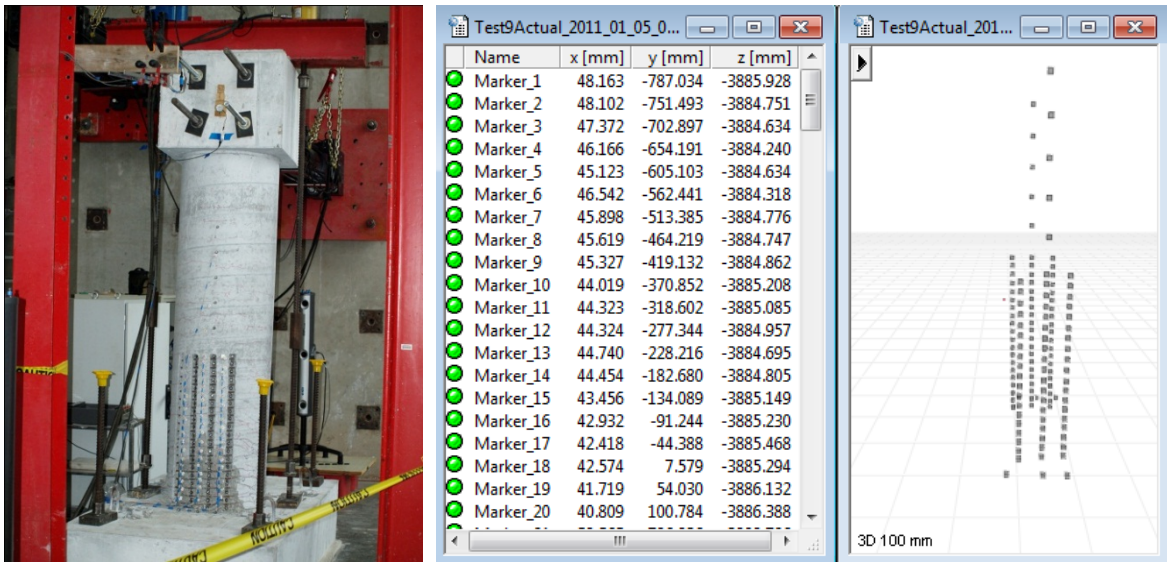

Figure 2-5. Test 9 – Dual Optotrak Position Sensors with Direct Application of Target Markers to Reinforcement

2.1.1.1. Test 9 Symmetric Three Cycle Set Experimental Observations:

The first yield force for the tested material and geometric properties was determined using moment curvature analysis (Cumbia $F_y' = 46.9kips$ with $f_c' = 6814psi$). The initial elastic portion of the symmetric three cycle set load history contains reversals of loading at ¼ Fy', ½ Fy', ¾ Fy', and Fy'. After the specimen has reached the first yield force in each direction, the first yield displacement is obtained as an average ($\Delta_y' = 0.63$"). The equivalent yield displacement, used to determine the displacement ductility levels ($\mu_{\Delta n} = \mathrm{n} * \Delta_y$), is then calculated as $\Delta_y = \Delta_y'(M_n/M_y') = 0.84$". The symmetric three cycle set load history continues with three complete cycles at each ductility level, as shown in Figure 2-1. The resulting lateral force vs. top column displacement response appears in Figure 2-2. The compressive axial load applied by one of the two self-regulating hydraulic jacks placed above the loading cap is shown in Figure 2-3. Since the pressure in the two jacks is equal, the total axial load ($170kips$) is obtained by multiplying the recorded value by two. The extreme fiber vertical strain profiles for the initial elastic cycles appear in Figure 2-6.

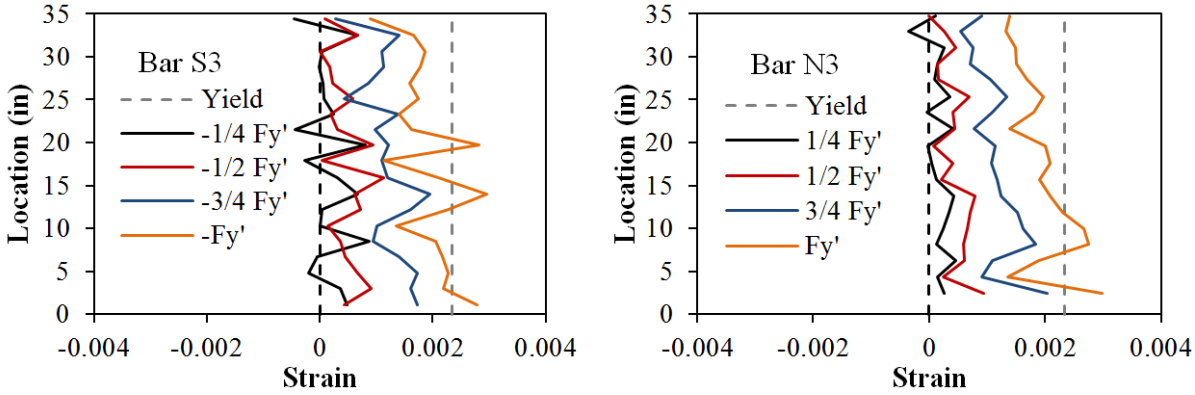

Figure 2-6. Test 9 - Vertical Strain Profiles to First Yield

The first cracks on the North side of the specimen appeared during the ($3/4Fy' = 0.40$") push cycle had a measured crack width of 0.1mm and were spaced at approximately 7" as shown in Figure 2-7. The first cracks on the on the South side of the specimen measured 0.2mm at approximate 8" spacing during ($-3/4Fy' = -0.38$"). During the first yield cycles the cracks on the North side measured 0.3mm at 6" spacing and the cracks on the South side measured 0.35mm at 5". The vertical strain profiles in Figure 2-6 show that the yield strain, marked by the gray dashed line, was reached during the first yield push and pull cycles for each extreme fiber bar.

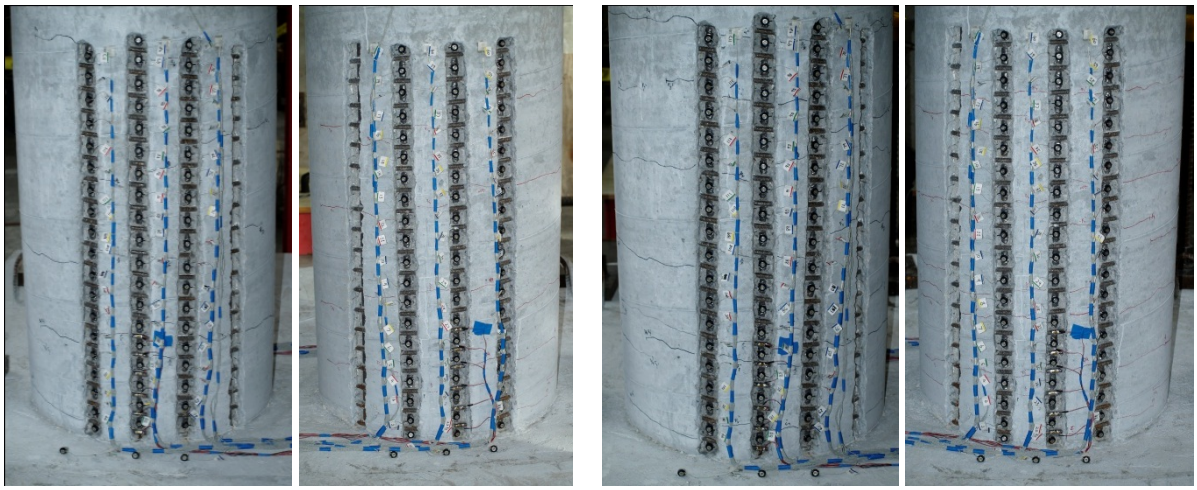

Figure 2-7. Test 9 – First Cracking during ¾ Fy' Cycles (North Black Push Cracks and South Red Pull Cracks) and (Right) Crack Pattern during First Yield Cycles

At ($\mu_1^{+1} = 0.84$") the cracks on the North side of the specimen measured 0.35mm at approximate 6" spacing. The cracks on the South side of the specimen extended to 0.4mm at 5" during ($\mu_1^{-1} = -0.84$"). During ($\mu_{1.5}^{+1} = 1.26$"), the cracks on the North measured 0.5mm at 6" spacing. The cracks on the South side of the specimen reached 0.75mm at 5" spacing during ($\mu_{1.5}^{-1} = -1.26$"). The North cracks extended to 1.6mm at 5" spacing during ($\mu_2^{+1} = 1.69$") as shown in Figure 2-9. The cracks on the South side of the specimen measured 1.7mm at 5" spacing during ($\mu_2^{-1} = -1.68$"). The cover concrete on both sides of the specimen showed signs of visible flaking, which precedes crushing, during ($\mu_2^{+2} = 1.69$") and ($\mu_2^{-2} = -1.67$") as shown in Figure 2-8. During ($\mu_3^{+1} = 2.51$"), the extent of crushing on the South side of the column reached 17" above the footing and 2.5mm crack widths were measured on the North side of the column. The extent of crushing on the North side of the specimen reached 13" above the footing during ($\mu_3^{-1} = -2.51$"), as shown in Figure 2-10.

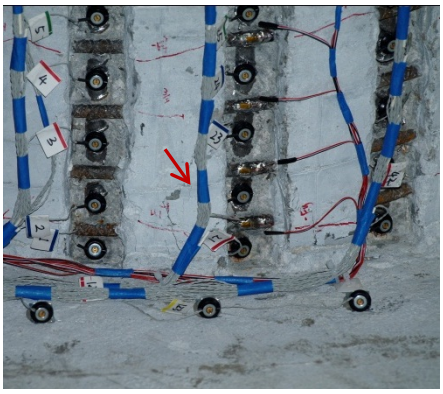
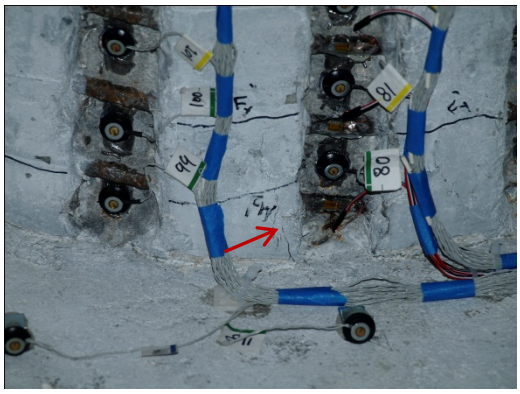

Figure 2-8. Test 9 – First Signs of Cover Concrete Flaking which Precedes Crushing (Left) South Side during ($\mu_2^{+2} = 1.69$") and (Right) North Side during ($\mu_2^{-2} = -1.67$")

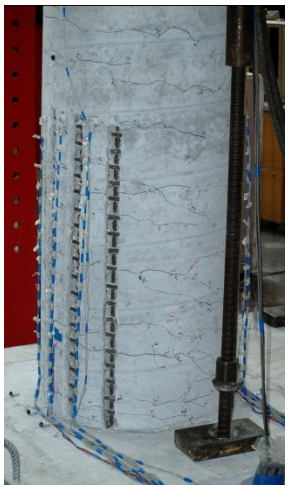
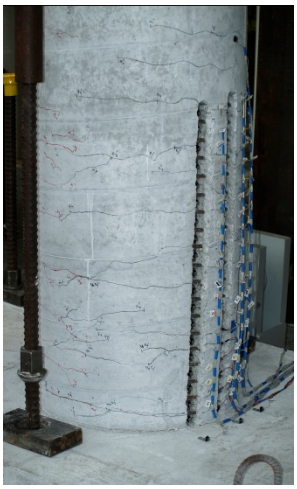


Figure 2-9. Test 9 – (Left) Front and Back of Specimen during ($\mu_2^{+1} = 1.69$") and (Right) South Crack Pattern during ($\mu_2^{-1} = -1.68$")


Figure 2-10. Test 9 – Cover Concrete Crushing (Left) South Side of the Specimen during ($\mu_3^{+1} = 2.51$") and (Right) North Side of the Specimen during ($\mu_3^{-1} = -2.51$")

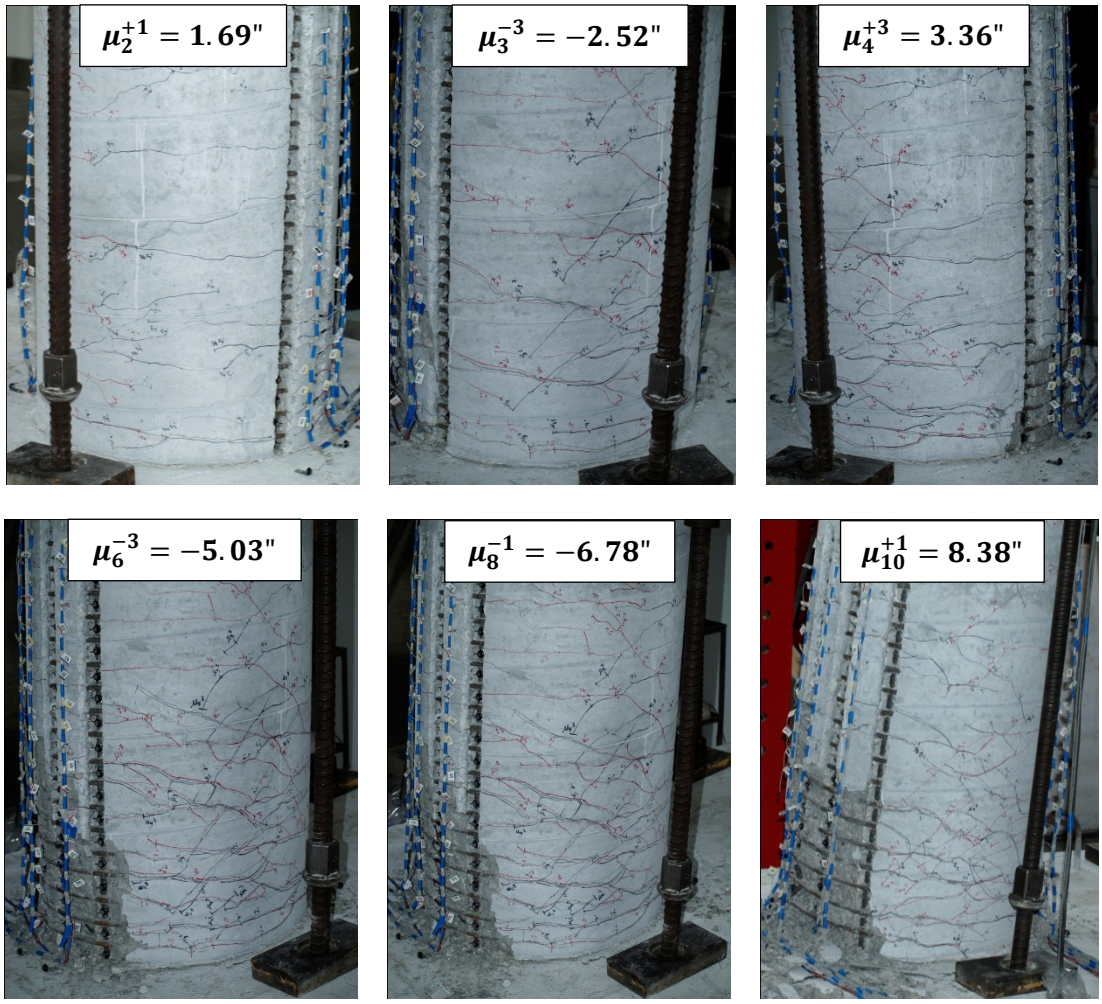

Figure 2-11. Test 9 – Crack Progression with Increasing Ductility Demands

The test progressed through ($\mu_8^{+1} = 6.72"$) without incident. The progression of cracking on the shear faces of the column appears in Figure 2-11. As the compression zone continued to shrink with increasing ductility, the cracks became more inclined and linked up with cracks formed during loading in the opposite direction. The North extreme fiber reinforcing bar buckled after reversal from ($\mu_8^{+1} = 6.72"$), as shown in Figure 2-12. Additional North reinfrocing bars N2 and N4 buckled after reversal from ($\mu_8^{+2} = 6.71"$). The extreme fiber South reinforcing bar S3 buckled after reversal from ($\mu_8^{-2} = -6.70"$), as shown in Figure 2-13. During ($\mu_{10}^{+1} = 8.38"$), prevously buckled bars N3 and N4 ruptured and bar S2 buckled as shown in Figure 2-13. Two additional North reinforcing bars outside of the instrumented region buckled during ($\mu_{10}^{-1} = -8.48"$). During ($\mu_{10}^{+2} = 8.39"$), previously buckled bar N2 ruptured and bars S1 and S4 buckled. The test was concluded after the pull cycle to ($\mu_{10}^{-2} = -8.42"$) when previously buckled bars S3 and S2 ruptured. Rupture of previously buckled reinfrocing bars limited the displacement capacity of the bridge column as shown in Figure 2-15.

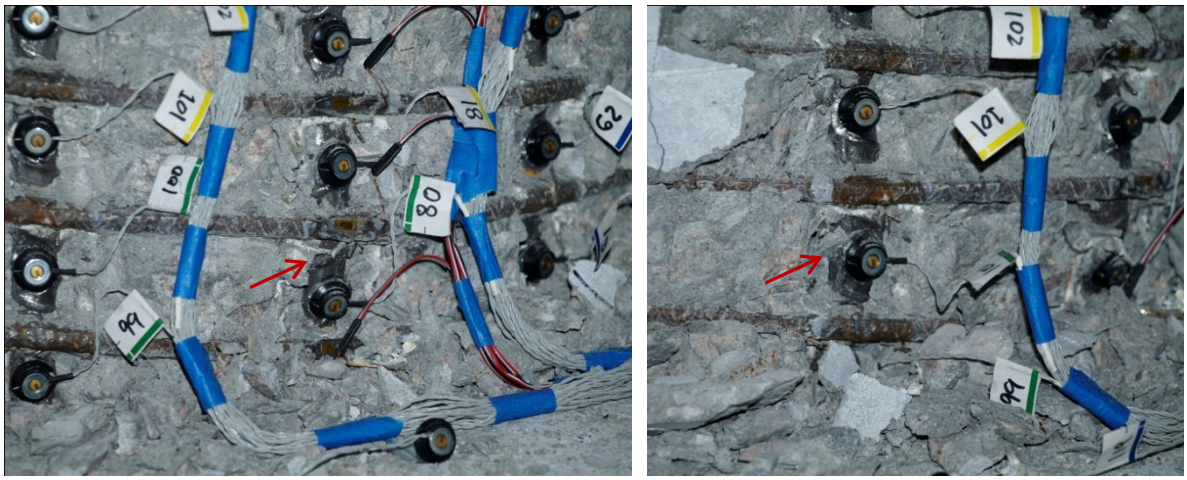

Figure 2-12. Test 9 – (Left) Buckling of Extreme Fiber Bar N3 during ($\mu_8^{-1} = 6.78$") and (Right) Additional Buckling of Bars N2 and N4 during ($\mu_8^{-2} = 6.70$") (Bar N4 Pictured)

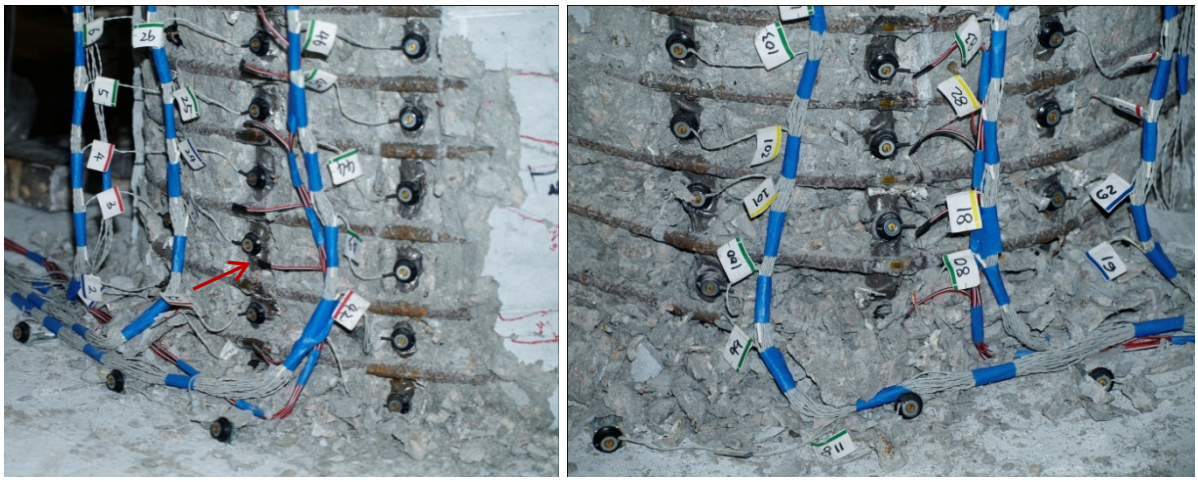

Figure 2-13. Test 9 – (Left) Buckling of Extreme Fiber Bar S3 after Reversal from ($\mu_8^{-2} = -6.70$") and (Right) Additional deformation in Bars N4, N3, and N2 during ($\mu_8^{-3} = 6.73$")

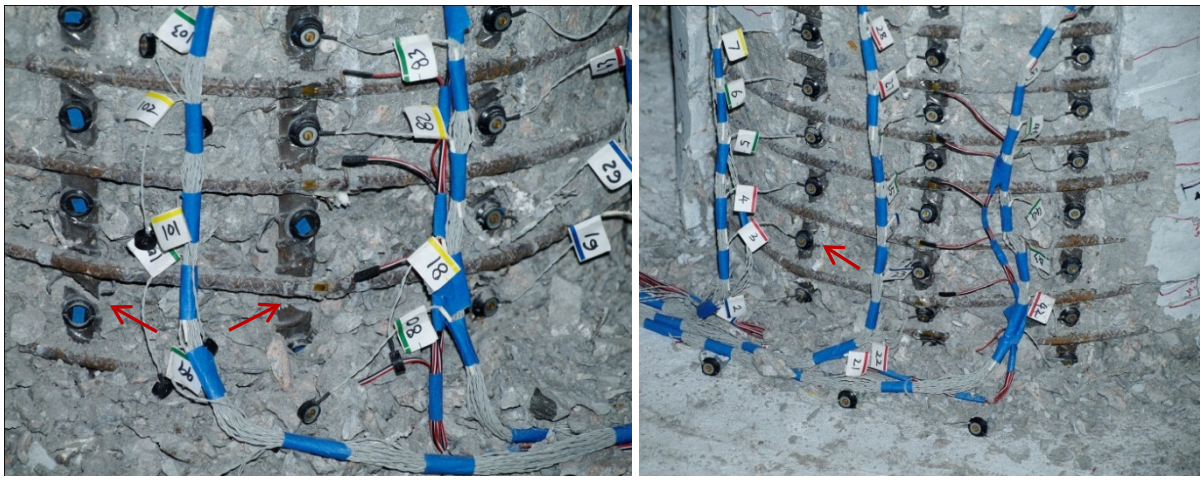

Figure 2-14. Test 9 – Photos during ($\mu_{10}^{+1} = 8.38$") (Left) Rupture of N4 and N3 and (Right) Buckling of S2 and Additional Deformation in Previously Buckled Bar S3

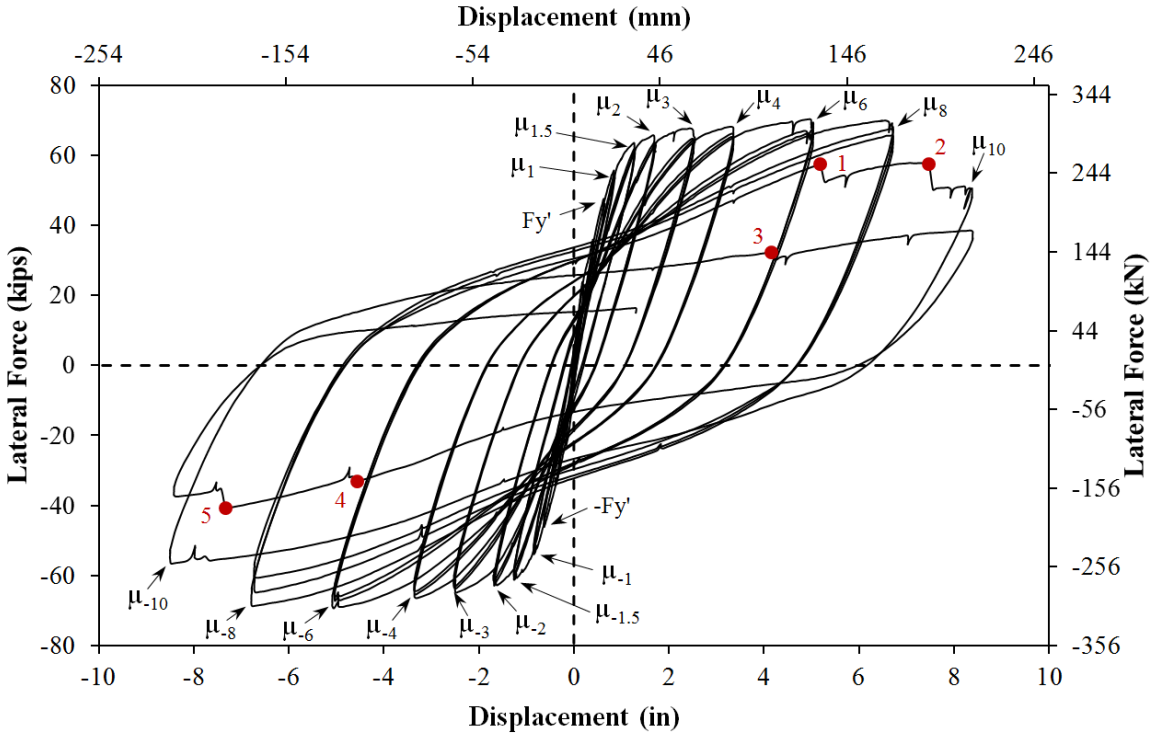

Figure 2-15. Test 9 – Reinforcement Rupture History and Corresponding Loss of Strength

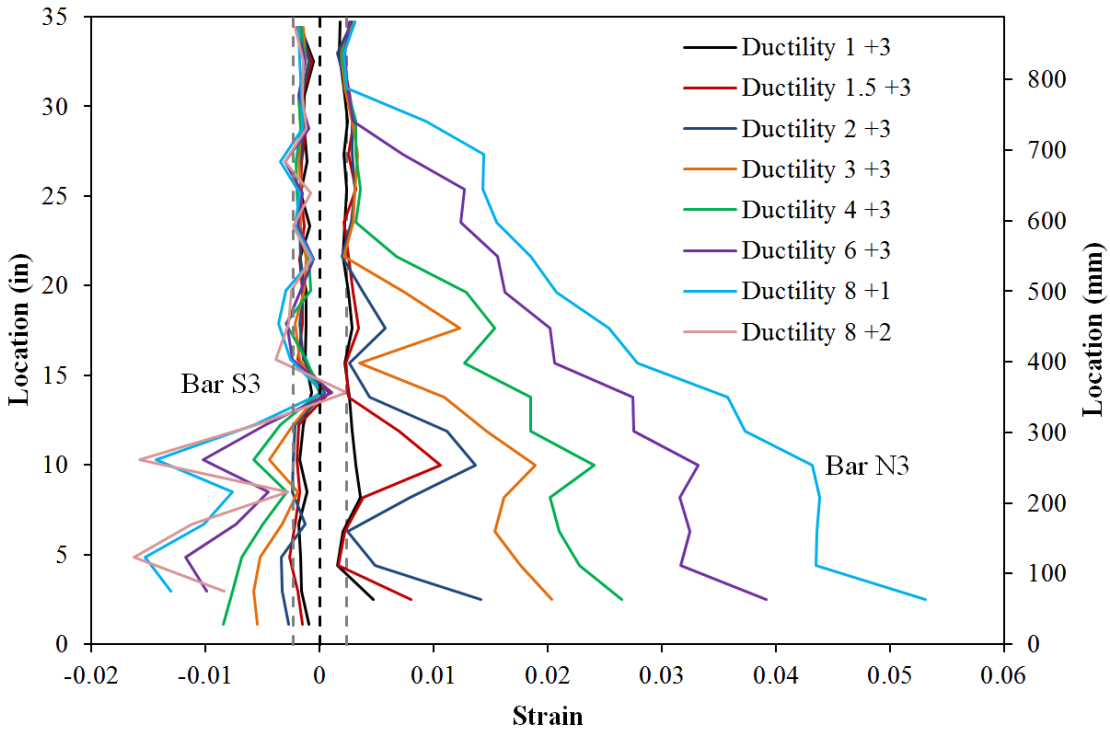

Figure 2-16. Test 9 – Extreme Fiber Vertical Strain Profiles During Push Cycles

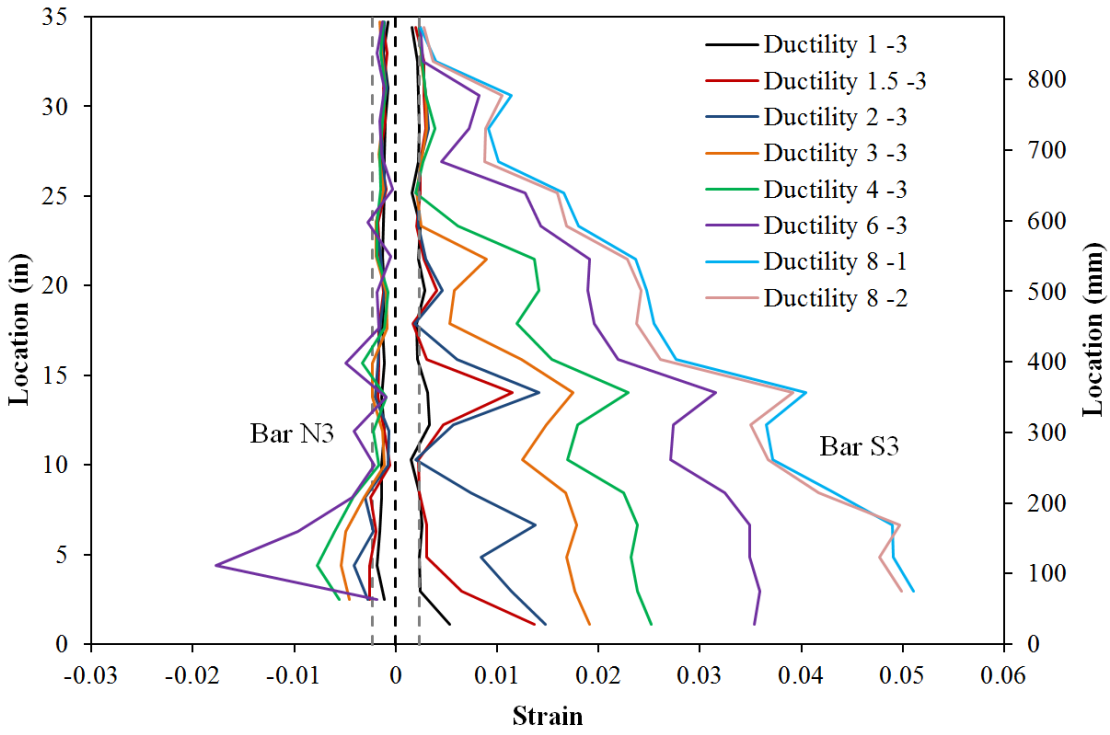

Figure 2-17. Test 9 – Extreme Fiber Vertical Strain Profiles during Pull Cycles

2.1.1.2. Test 9 Symmetric Three Cycle Set Strain Data:

North Reinforcement:

The vertical strain profile for North extreme fiber bar N3 placed into tension during push cycles appear in the right half of Figure 2-16. This figure shows both extreme fiber bars on the same graph to illustrate the effects of tension shift on strain profiles. As the hinge rotates about inclined flexural shear cracks, compressive strains are concentrated at the base and tensile strains are fanned out to a greater height following the crack distribution. Near the footing cracks remain effectively horizontal, but above this base section the flexural shear cracks are inclined as shown in Figure 2-11. The effects of tension shift increase as the cracks become more inclined at higher ductility levels. Due to the effects of tension shift, the tensile strains at the beginning of an inclined flexural shear crack do not coincide with the perceived moment demand at that location based on its height above the footing and the applied lateral load. Since the tensile strains are fanned out over a greater distance, the measured tensile strains above the base section and at the beginning of inclined flexural shear cracks are increased. The initial vertical tensile strain profiles are highly influenced by individual crack locations, but latter profiles past displacement ductility three appear much smoother. The compressive vertical strain profile for North extreme fiber bar N3 during pull cycles appears in the left half of Figure 2-17.

A peak tensile strain of 0.053 was measured 2.50” above the footing on North extreme fiber bar N3 before the bar buckled after reversal from ($\mu_8^{+1} = 6.72$"). The relationship between tension strain and displacement for this gage length during significant push cycles appears in Figure 2-18. Solid lines represent push cycles to the peak displacement while dashed lines correspond to the subsequent reversal of loading. The recorded relationship between strain and displacement matches the moment

curvature prediction well for cycles under displacement ductility three. As the displacement increases, moment curvature analysis begins to over predict the reinforcement tensile strains at an increasing rate. The intersection of the dashed unloading line with the vertical axis at zero displacement represents the residual growth strain measured over this gage length. The relationship between compression strain and displacement during significant push cycles for bar N3 centered 4.38" above the footing appears in Figure 2-19. The recorded strains match the Cumbia prediction well with the exception of the second and third pull cycles of ductility six.

The compressive strain profile for bar N3, in Figure 2-20, shows that the compressive strains measured 4.38" above the footing increased with each additional cycle during displacement ductility six. This observation, combined with lower strains measured over the first gage length during these cycles suggests measurable deformation occurred before bar buckling. Six spiral layers closest to the footing-column interface were instrumented with strain gages at the location where they overlaid the extreme fiber reinforcement on each side of the specimen. The spiral strains measured on the North side of the specimen appear in Figure 2-21. The spiral layer 3" above the footing entered the inelastic range during ($\mu_6^{-1} = -5.05"$). During the next two pull cycles of ductility six, the spiral strains continued to rise as the measurable deformation increased. The North extreme fiber bar N3 visibly buckled after reversal from ($\mu_8^{+1} = 6.72"$) at the location of the previously inelastic spiral layer, as shown in Figure 2-12. The inelastic spiral layer, alone, did not lead to bar buckling during ductility six. Instead, the peak tensile strain of 0.053 sustained during ($\mu_8^{+1} = 6.72"$), combined with inelastic transverse steel restraint were sufficient to produce bar buckling upon reversal of load.

The strain hysteresis centered 2.50" above the footing on extreme fiber bar N3 appears in Figure 2-22 with a color bar that represents elapsed time while testing. During the first pull cycle of ductility eight, bar N3 begins to buckle at the location of the data label (X- Displacement, Y-Strain, and Z-Time). During pull cycles the strain in bar N3 should decrease, but the recorded strain begins increasing after the data label due to the outward deformation over the buckled region shown in Figure 2-12. The stain hysteresis also shows a small amount of deformation during each successive pull cycle of ductility six prior to visible buckling. The deformation over the first gage length above the footing causes an increase in strain with each successive cycle while the second gage length contracts causing larger compression strains, as shown in Figure 2-12.

The transverse steel strain hysteresis over the North buckled region appears in Figure 2-23. The transverse steel strain sharply increases upon reversal from the first push cycle of ductility eight, which is marked by the data label. The increase in transverse steel strain occurred before the increase in deformation of longitudinal bar N3 which signified the beginning of visible bar buckling. The measurable deformation in bar N3 during ductility six also caused small increases in the transverse steel strain prior to bar buckling.

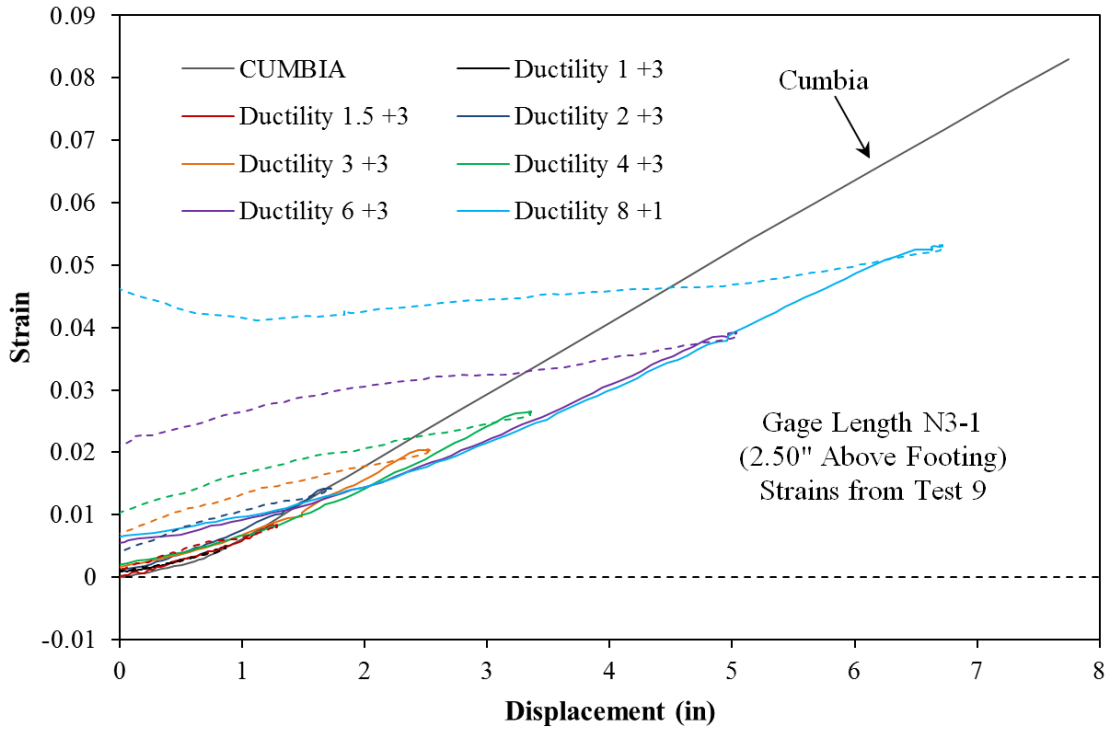

Figure 2-18. Test 9 – Strain and Displacement for Bar N3 during Push Cycles

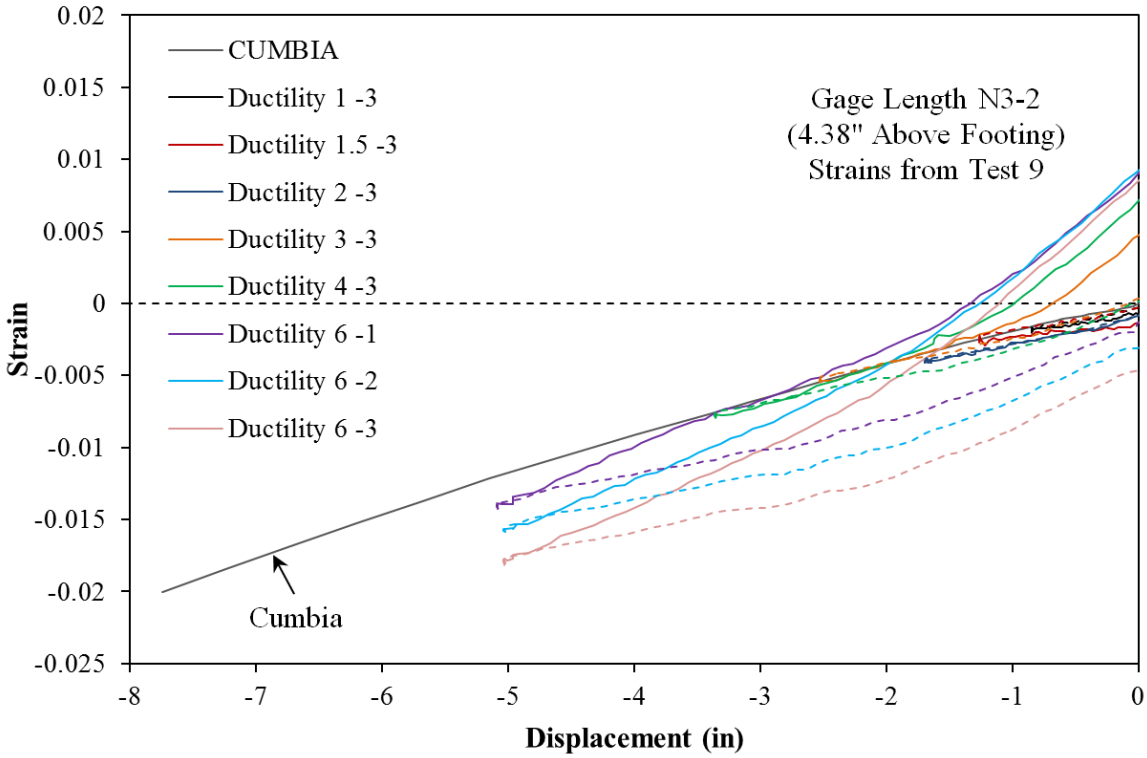

Figure 2-19. Test 9 – Strain and Displacement for bar N3 during Pull Cycles

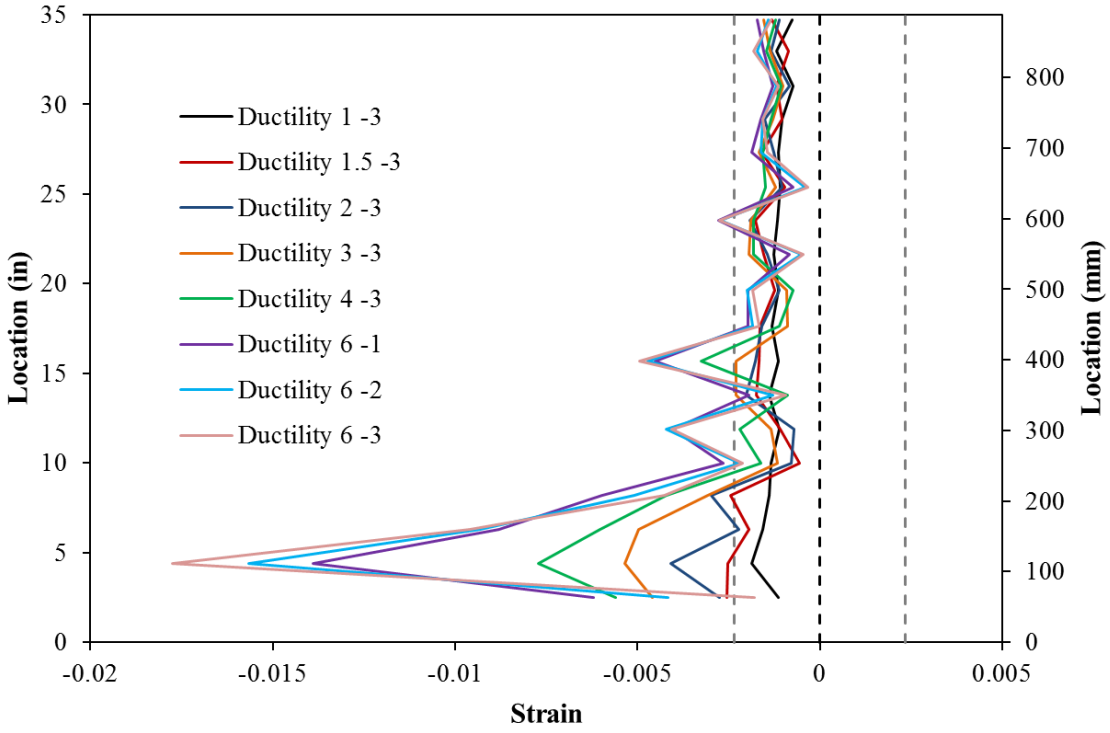

Figure 2-20. Test 9 – Vertical Strain Profile for North Extreme Fiber Bar N3 with All Cycles during Ductility Six

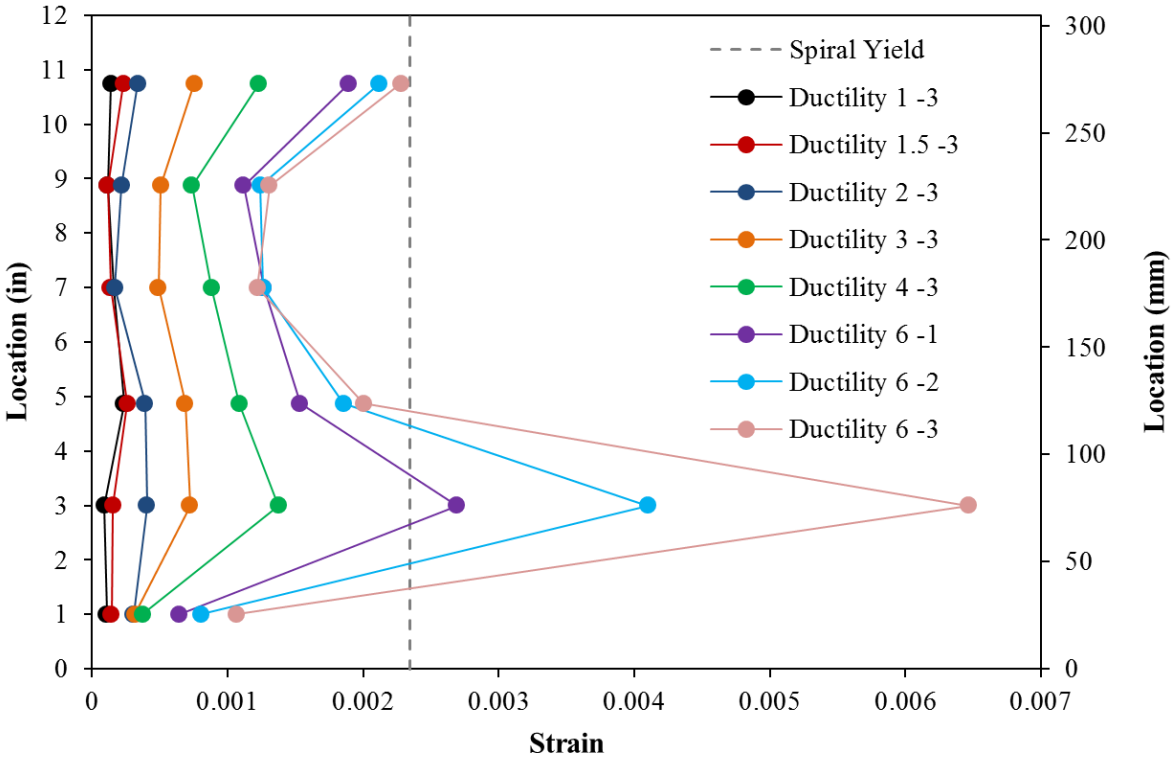

Figure 2-21. Test 9 – Transverse Steel Strain for the Lowest Six North Spiral Layers

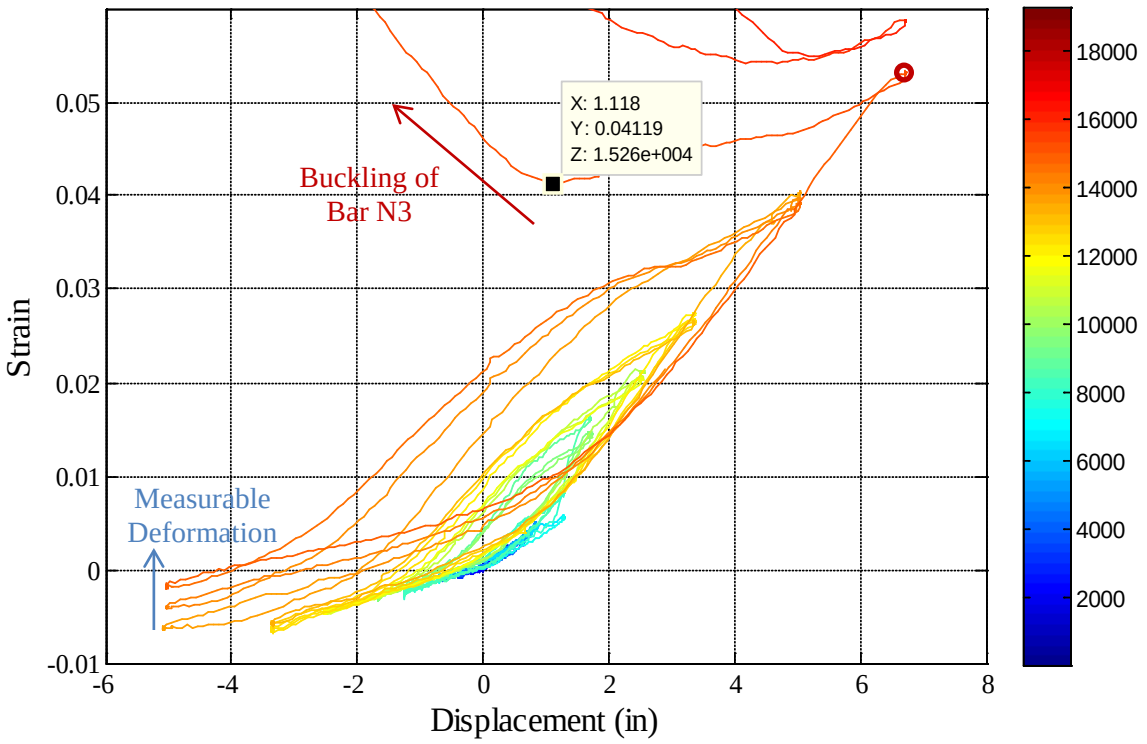

Figure 2-22. Test 9 – Bar N3 Strain Hysteresis, Gage Length Centered 2.50” above Footing

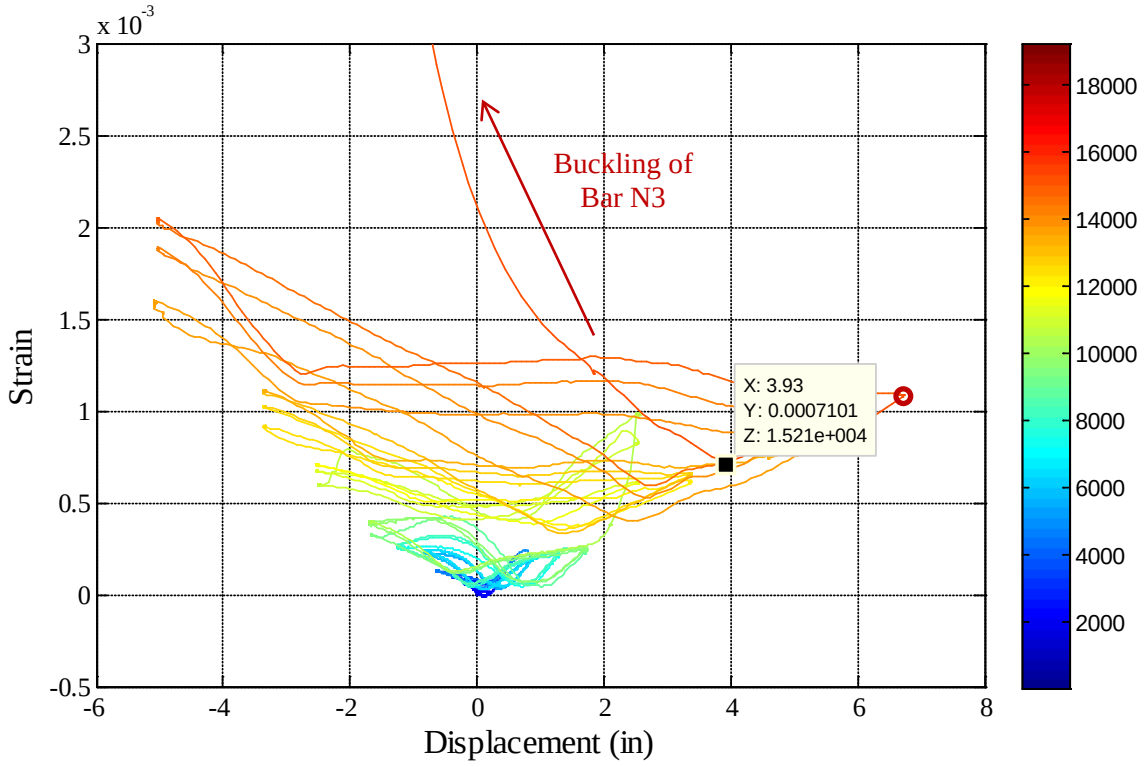

Figure 2-23. Test 9 – Transverse Steel Strain Hysteresis for North Spiral Layer 4.88” Above the Footing

South Reinforcement:

The vertical strain profile for South extreme fiber bar S3 which is placed into tension during pull cycles appears in the right half of Figure 2-17. The compressive strain profiles during push cycles are shown in the left half of Figure 2-16. The extreme fiber South reinforcing bar buckled during the third push cycle of ductility eight after sustaining a tension strain of 0.051 centered 2.95" above the footing at ($\mu_8^{-1} = -6.78"$). The tension strain over the same gage length during ($\mu_8^{-2} = -6.70"$) was 0.050. The compressive vertical strain profile for bar S3 during ($\mu_8^{+2} = 6.71"$) shows measurable deformation 2.95" and 8.47" above the footing before visible buckling occurred in the third push cycle. A peak compressive strain of -0.0177 was measured 4.38" above the footing on South extreme fiber bar S3 during ($\mu_6^{-3} = -5.03"$).

The relationship between tension strain and displacement from when the column was vertical to the peak of significant pull cycles for bar S3, 2.95" above the footing, appears in Figure 2-25. The relationship between compression strain and displacement for push cycles 4.84" above the footing on bar S3 appears in Figure 2-24. Moment curvature analysis does a good job of predicting the compressive strains, but the tensile strains are over predicted significantly at higher displacements.

The strain hysteresis 2.95" above the footing for extreme fiber South reinforcing bar S3 appears in Figure 2-27. The graph includes a color bar which represents elapsed time while testing to track the progression of the experiment. The strain hysteresis for bar S3 indicates that buckling occurred after reversal from ($\mu_8^{-2} = -6.70"$), which agrees with the test observations. While the South reinforcement should be in compression during the push cycle to ($\mu_8^{+3} = 6.71"$), the outward deformation of bar S3 during bar buckling causes elongation over the gage length. The transverse steel strain hysteresis for the spiral layer overlaying the outward buckled region of bar S3 appears in Figure 2-28. A data label shows when the transverse steel strain begins to sharply increase during bar buckling. A similar data label is shown in the strain hysteresis for bar S3 at the same displacement when the spiral strain began to increase. As extreme fiber bar S3 began to visibly buckle, it placed a larger strain demand on the transverse steel. The measurable deformation in bar S3 during ($\mu_8^{+2} = 6.71"$), prior to visible buckling, lead to an increase in the transverse steel strain.

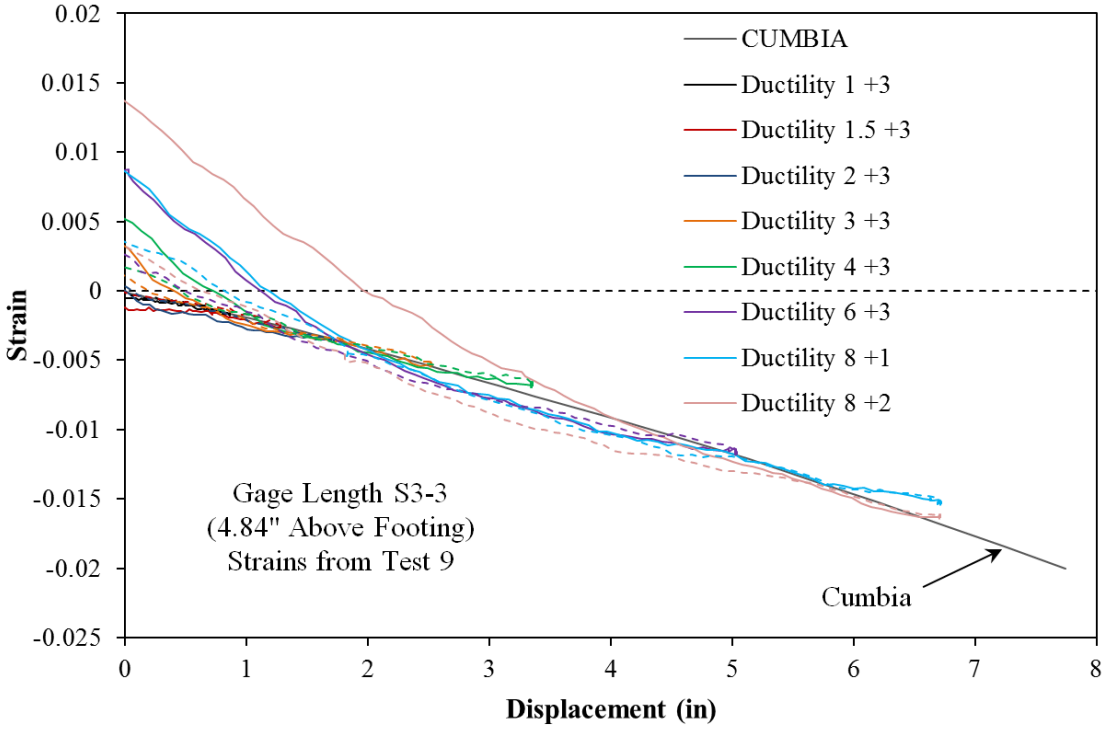

Figure 2-24. Test 9 – Strain and Displacement for Bar S3 during Push Cycles

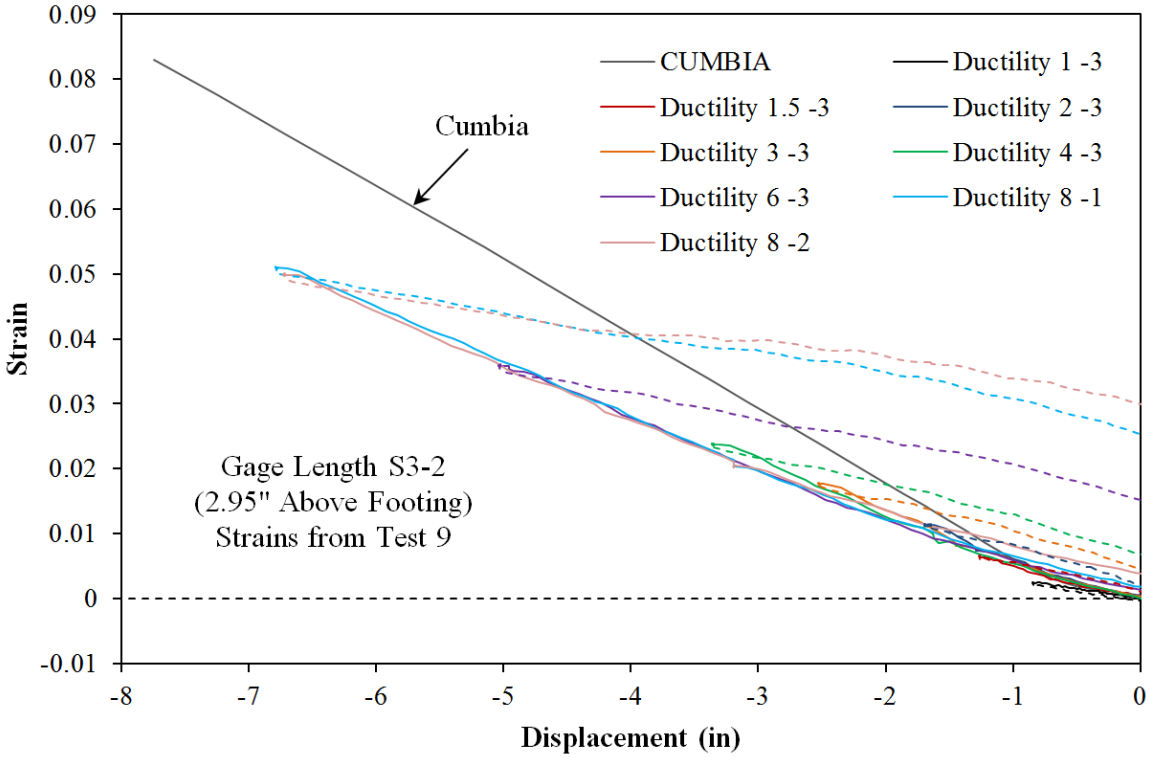

Figure 2-25. Test 9 – Strain and Displacement for Bar S3 during Pull Cycles

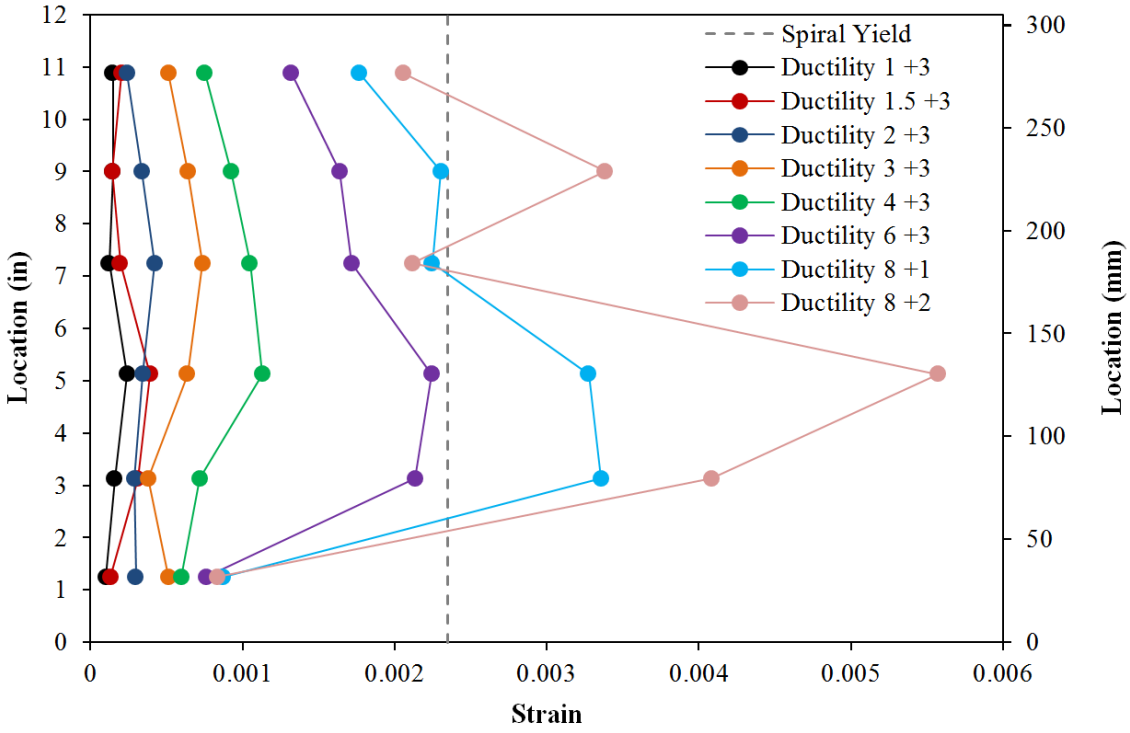

Figure 2-26. Test 9 – Transverse Steel Strain for the Lowest Six Spiral Layers Restraining South Reinforcing Bar S3

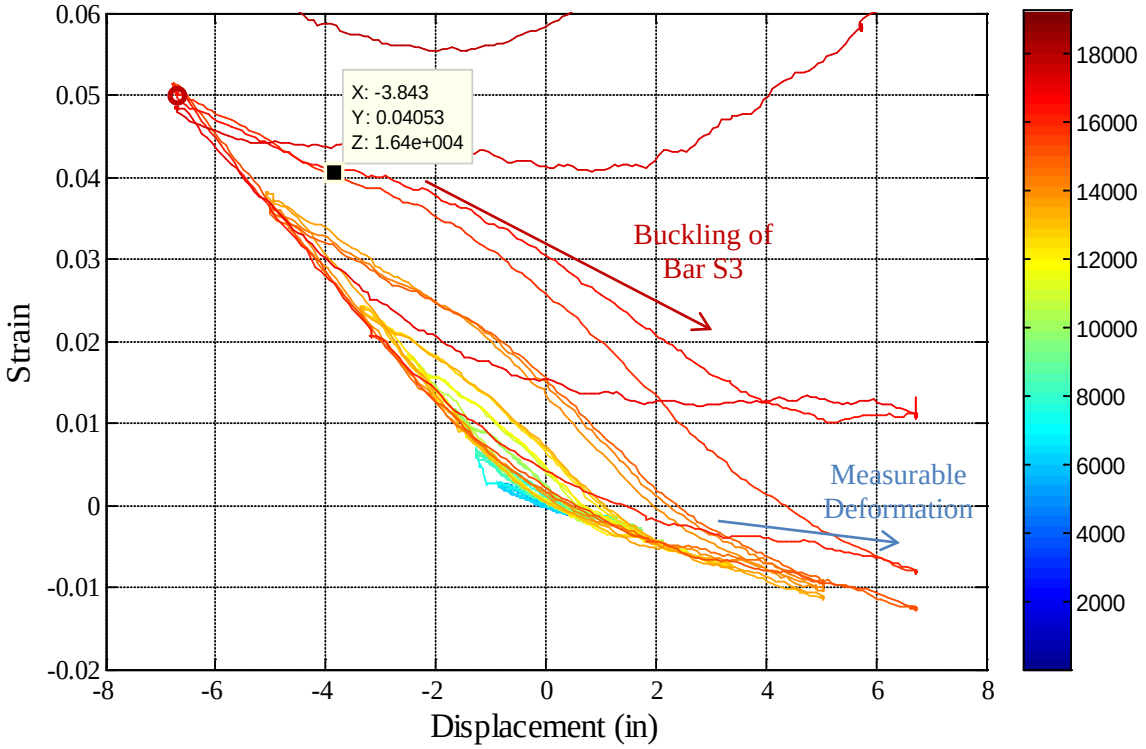

Figure 2-27. Test 9 – Bar S3 Strain Hysteresis, Gage Length Centered 2.95" above Footing

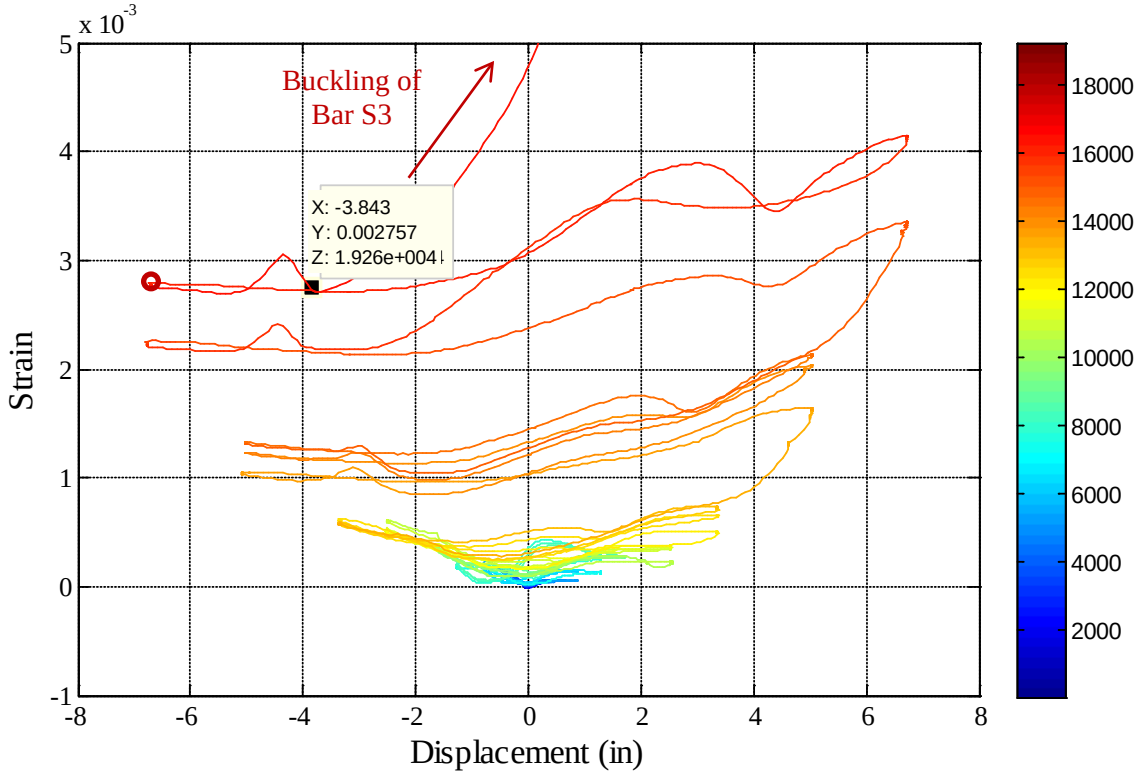

Figure 2-28. Test 9 – Transverse Steel Strain Hysteresis for South Spiral Layer 3.13" Above the Footing

2.1.1.3. Test 9 Curvature and Strain Penetration Data:

The cross section curvature profiles are plotted by connecting the measured strains from all six instrumented bars on a given horizontal cross section with a least squared error line. The curvature is then extracted from the slope of the least squared error line, see Figure 2-29. Vertical curvature profiles are plotted for push and pull cycles in Figure 2-30 and Figure 2-31 respectively. These figures show that plastic curvatures have a linear distribution at higher displacement ductility levels. The extent of plastic curvatures above the footing can be calculated by determining where the linear plastic curvature distribution intersects the triangular yield curvature distribution, shown as a grey dashed line. The dashed lines for each curvature distribution represent a least squared error linear fit to the plastic portion of the measured curvatures. The data points used to create the least squared error lines appear as circle data markers.

The target marker on each bar placed closest the footing-column interface can be used to create slip hysteresis and horizontal slip profiles attributable to strain penetration. The slip hysteresis for extreme fiber bars N3 and S3 appear in Figure 2-32 and Figure 2-33 respectively. The peak tensile slip of each bar exceeds 0.4in during ductility eight in each bar. If the measured slip of all of the instrumented bars is plotted along the cross section depth, the base rotation attributable to strain penetration may be calculated. The slip profiles for push and pull cycles appear in Figure 2-34 and Figure 2-35 respectively. The rotation of the base section can be extracted from the slope of the least squared error line connecting all six measured bar slips.

The displacement at the center of the lateral load may be calculated by combining the measured curvatures over the instrumented region (3ft above the footing), base rotation due to strain

penetration, and an elastic curvature assumption above the instrumented region. This process is shown graphically in Figure 2-36. This integrated displacement calculated from the Optotrak system is compared to the measured string potentiometer displacement at the center of loading in Figure 2-37. The calculated displacements match well over the entire range of response indicating that shear displacements are negligible in comparison to flexural displacements for these columns. A bar chart which plots the components of top column displacement for each displacement ductility level appears in Figure 2-38. Strain penetration accounts for between 25-35% of the top column displacement throughout the entire range of response.

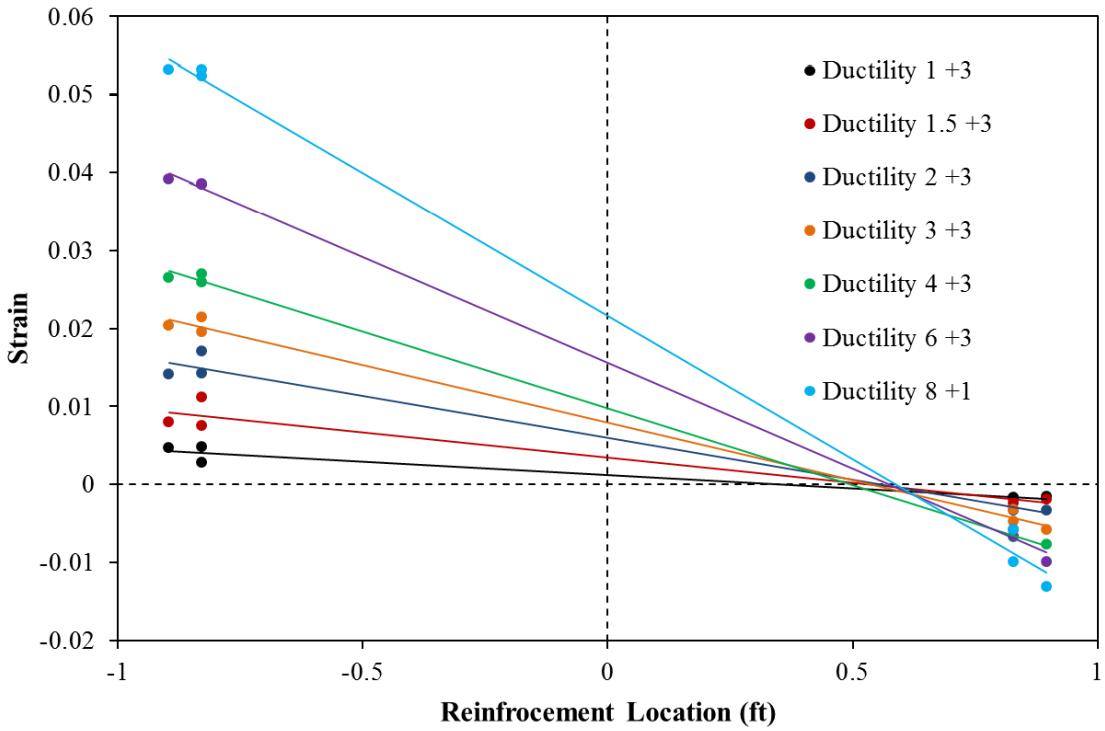

Figure 2-29. Test 9 – Base Section Curvature Profiles during Push Cycles

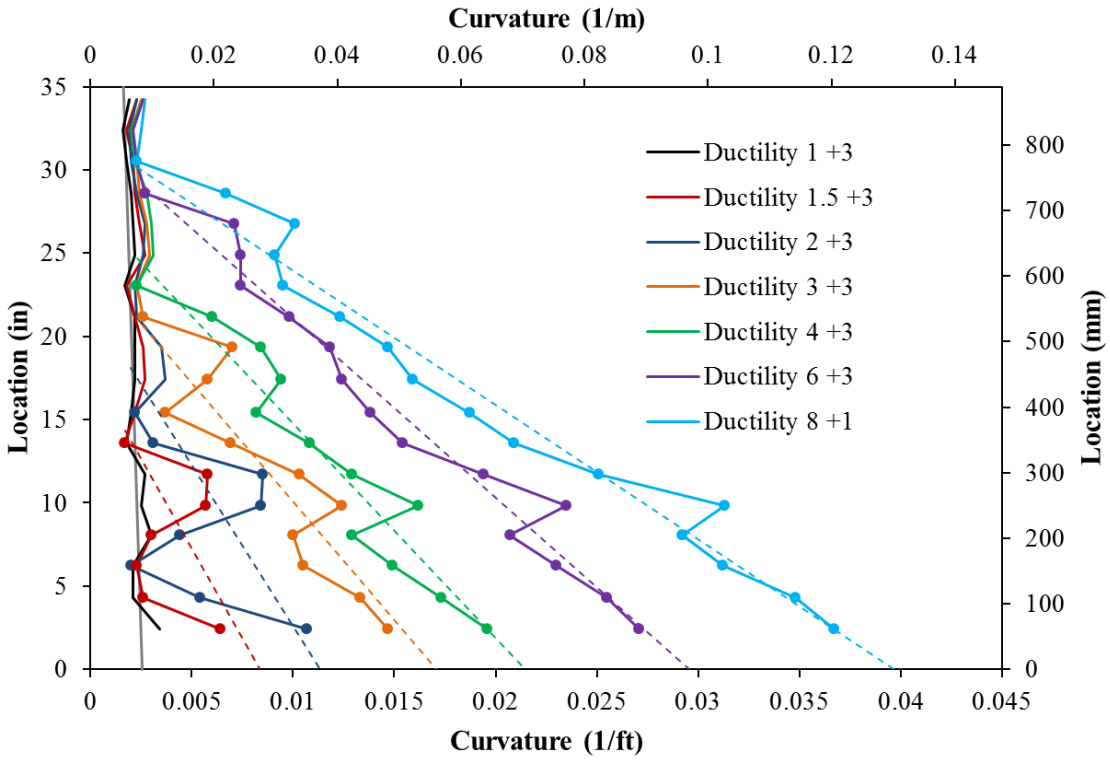

Figure 2-30. Test 9 – Curvature Profiles during Push Cycles with Linearized Least Squared Error Plastic Curvature Lines

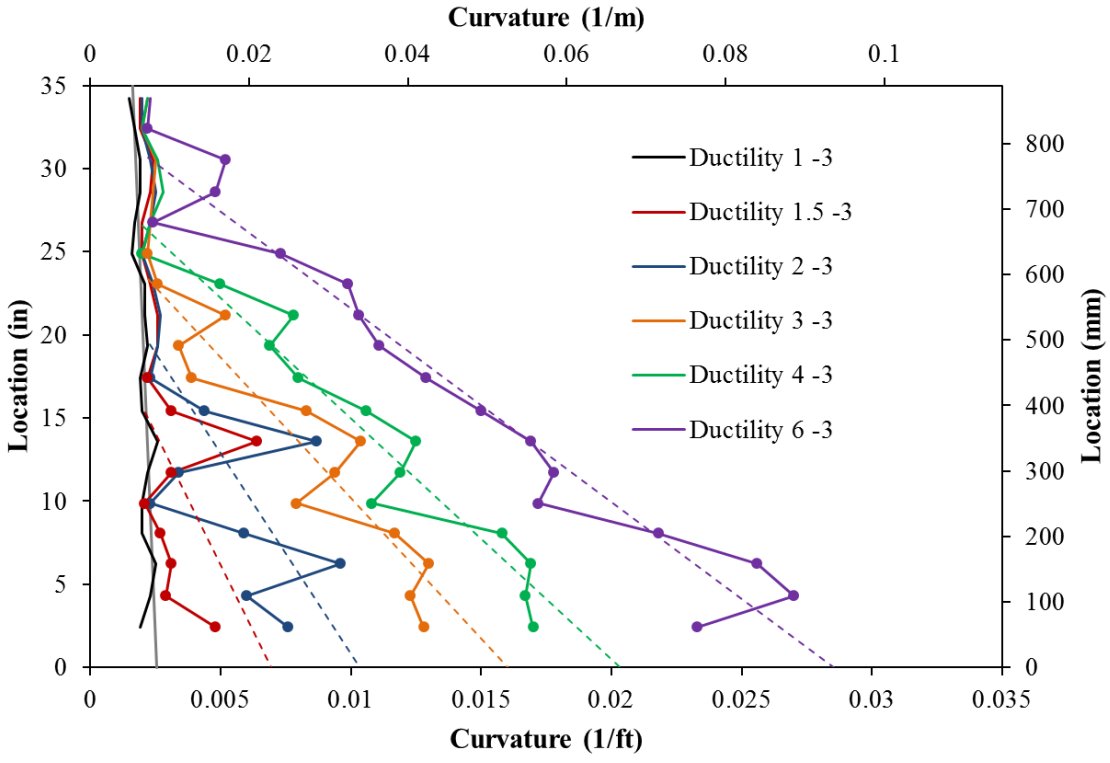

Figure 2-31. Test 9 – Curvature Profiles during Pull Cycles

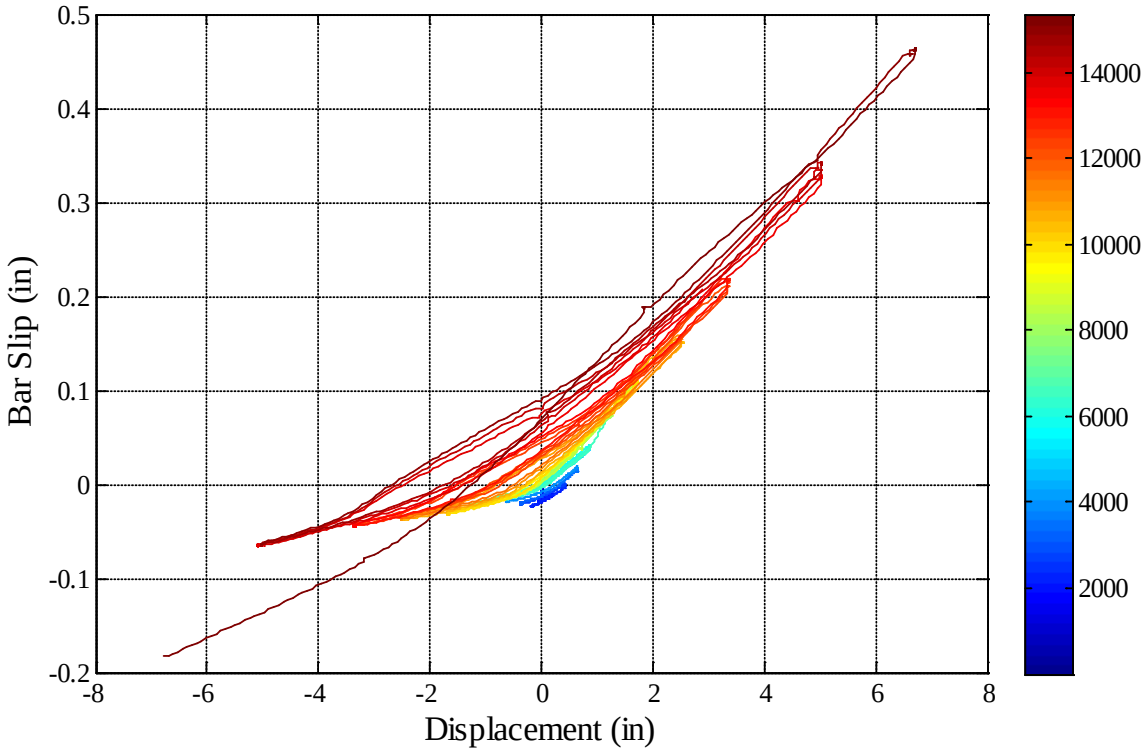

Figure 2-32. Test 9 – Bar N3 Base Section Slip Hysteresis due to Strain Penetration

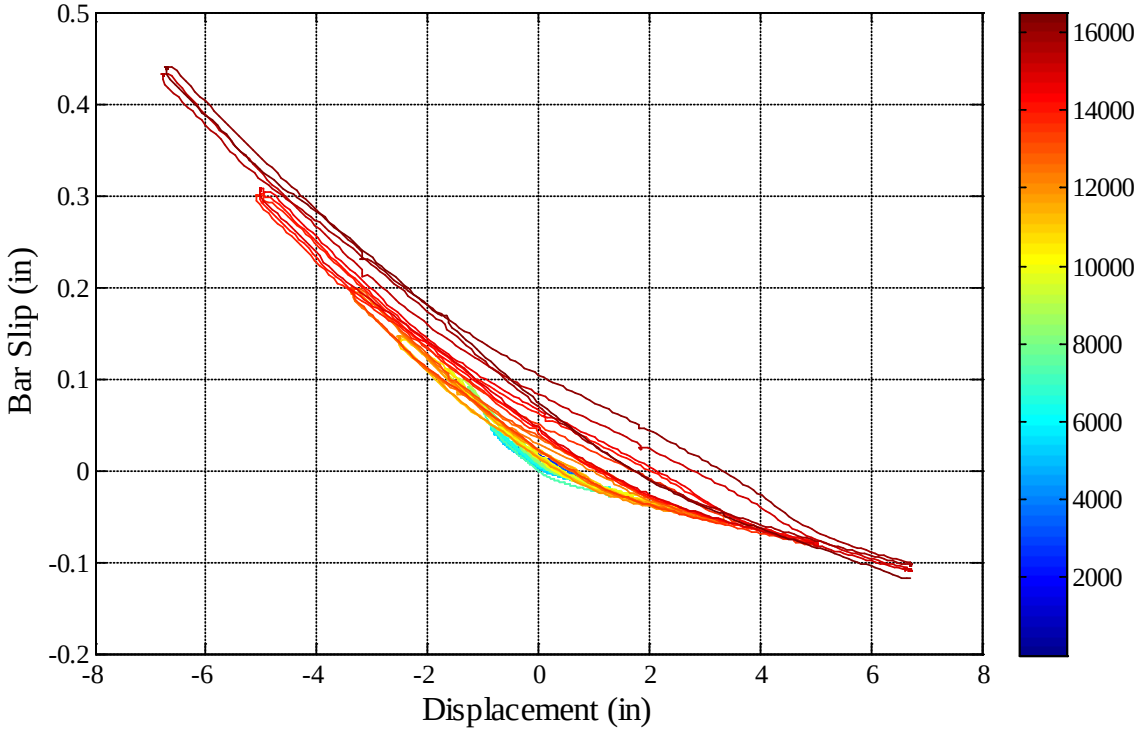

Figure 2-33. Test 9 – Bar S3 Base Section Slip Hysteresis due to Strain Penetration

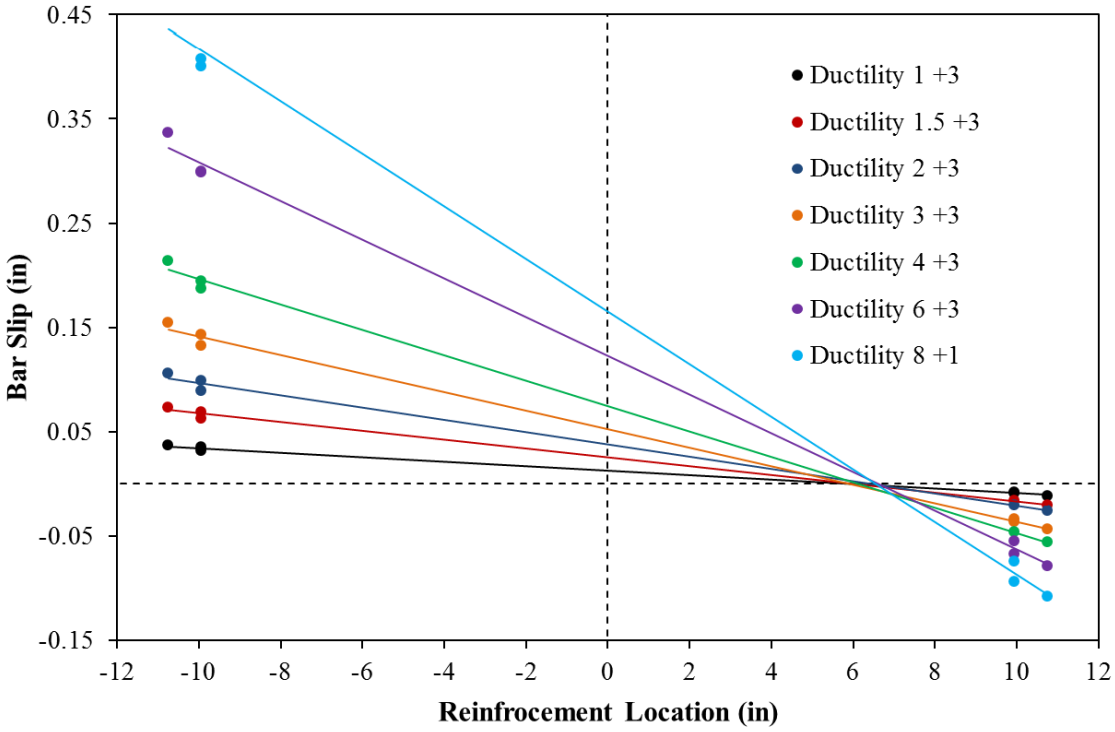

Figure 2-34. Test 9 – Base Section Rotation due to Strain Penetration during Push Cycles

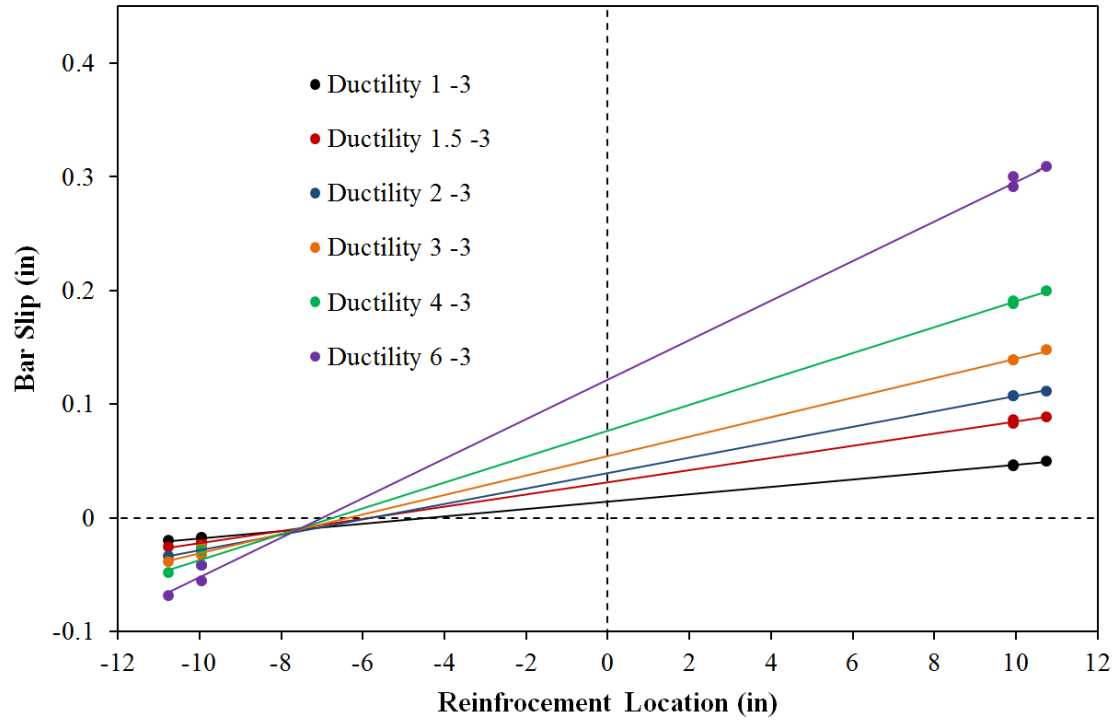

Figure 2-35. Test 9 – Base Section Rotation due to Strain Penetration during Pull Cycles

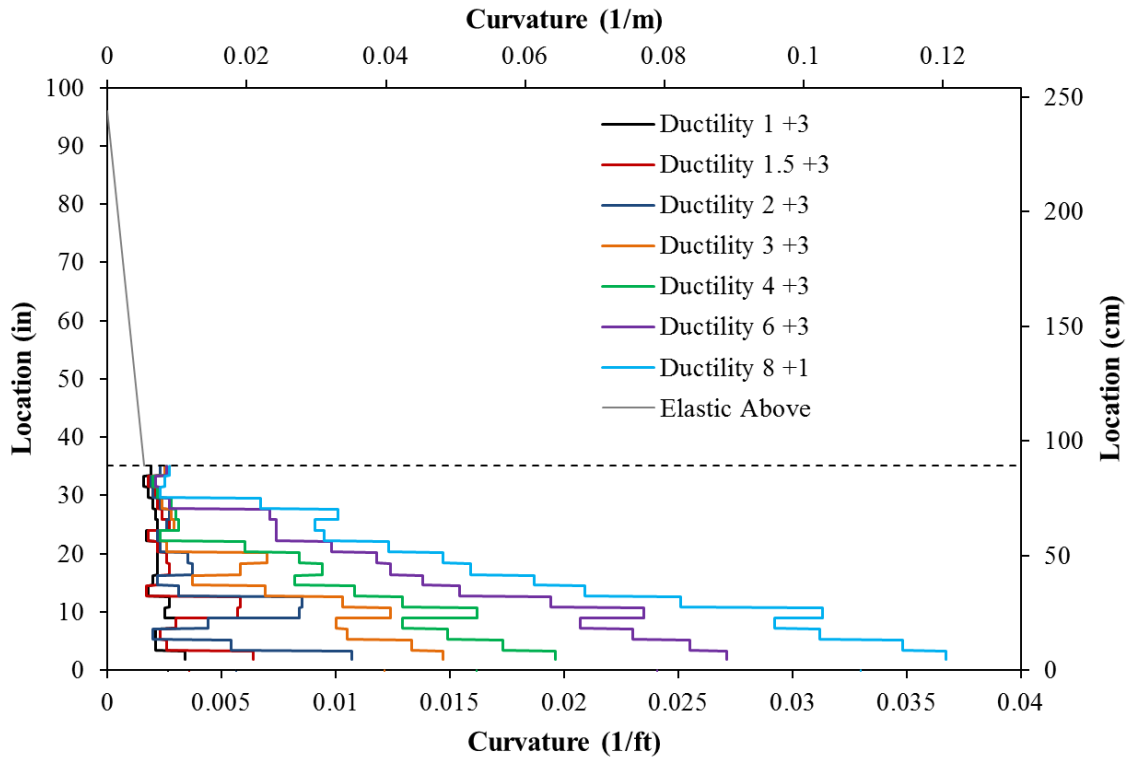

Figure 2-36. Test 9 – Integration Method for Flexural Displacements

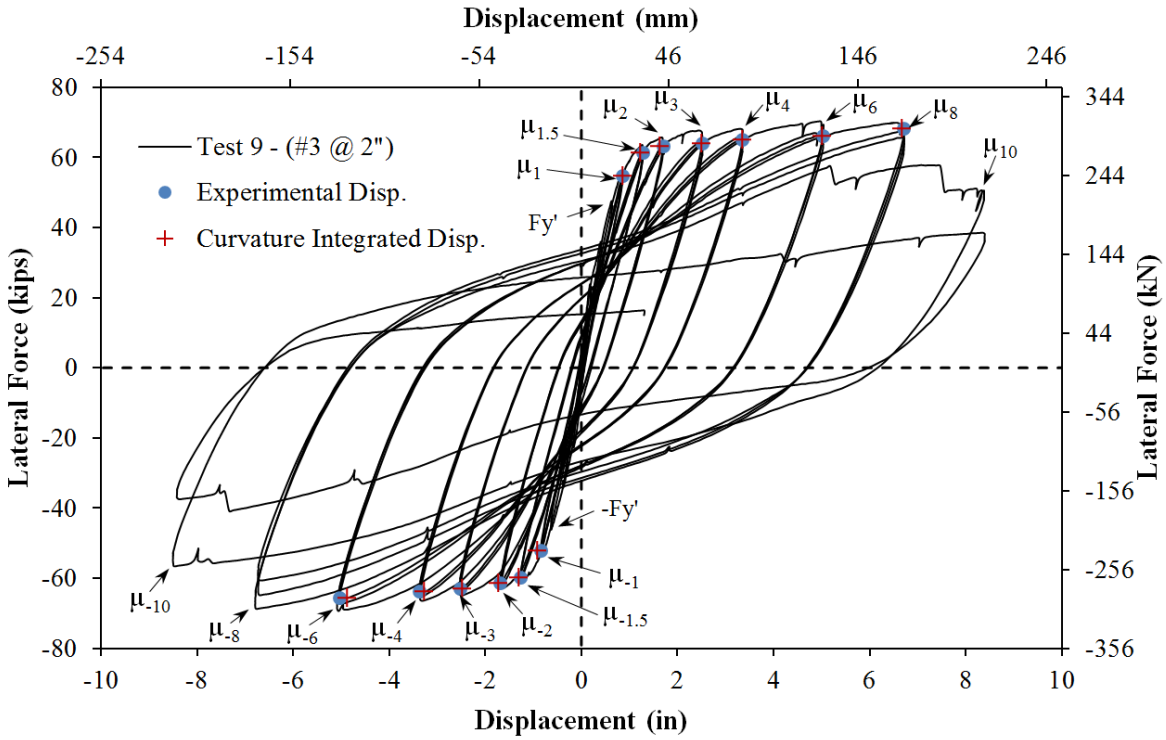

Figure 2-37. Test 9 – Comparison of String Potentiometer and Integrated Displacements

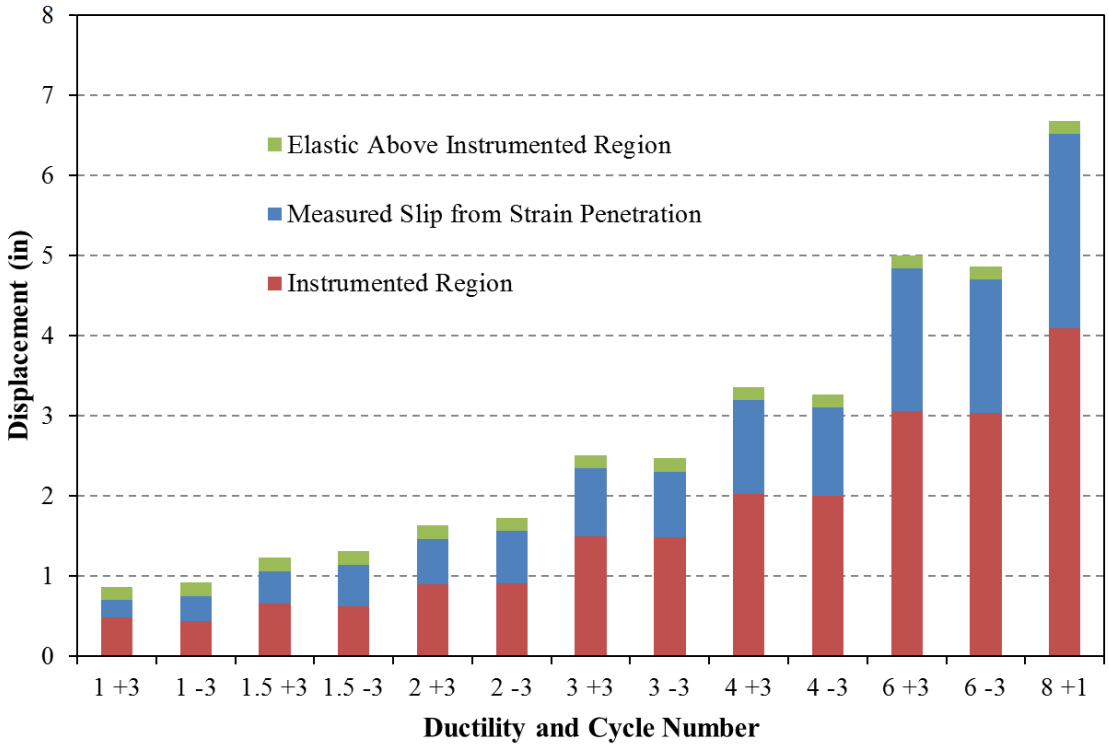

Figure 2-38. Test 9 – Components of Integrated Deformation

2.1.2. Test 8 and 8b – Chile 2010 Earthquake and Cyclic Aftershock Load History

Table 2-4. Results Summary for Test 8 – Chile 2010 Earthquake Load History

LOAD HISTORY: Chile 2010 Earthquake Load History

VALUES OF INTEREST:

Concrete Compressive Strength:	$f_c' = 6988psi$
Axial Load:	$P = 170kips$
Analytical First Yield Force:	$F_y' = 40.0kips$
Experimental First Yield Displacement:	$\Delta_y' = 0.63"$
Analytical Nominal Moment Capacity:	$M_n = 503.8kip * ft$
Equivalent Yield Displacement:	$\Delta_y = 0.84"$
Maximum Lateral Force:	$69.2kips$
Maximum Lateral Displacement:	$\mu_{8.7}^{26.34\,sec} = 7.25"$
Failure Mode:	No significant damage from earthquake.

DAMAGE OBSERVATIONS: [Displacement Ductility, μ_Δ]

First Cracking North:	$\mu_{0.3}^{6.95\,sec} = 0.21"$
First Cracking South:	$\mu_{-0.2}^{7.14\,sec} = -0.20"$
Cover Concrete Crushing North:	*During cycle to $\mu_{-4.0}^{9.69\,sec} = -4.03"$
Cover Concrete Crushing South:	$\mu_{2.92}^{9.17\,sec} = 2.42"$
Transverse Steel Yield North:	At $-0.34"$ otwt $\mu_{-3.2}^{26.90\,sec} = -2.65"$
Transverse Steel Yield South:	At $5.98"$ otwt 7.25 $\mu_{8.7}^{26.34\,sec} = 7.25"$

*$\mu_{8.7}^{26.34\,sec} = 7.25"$ represents a push cycle 26.34 seconds into the earthquake load history which reached a peak displacement of 7.25” and a displacement ductility of 8.7

Table 2-5. Results Summary for Test 8b – Cyclic Aftershock Load History

LOAD HISTORY: Symmetric Three Cycle Set Aftershock after Chile 2010

DAMAGE OBSERVATIONS: (Drift %) [Displacement Ductility, μ_Δ]

Longitudinal Bar Buckling North:	Reversal from $\mu_8^{+1} = 6.64"$
Longitudinal Bar Buckling South:	Reversal from $\mu_8^{-1} = -6.65"$
Failure Mode:	Specimen Saved as a Repair Candidate after Each Extreme Fiber Longitudinal Bar Buckled

*$\mu_8^{+1} = 6.64"$ represents the first push cycle of displacement ductility eight which reached a peak displacement of 6.64”

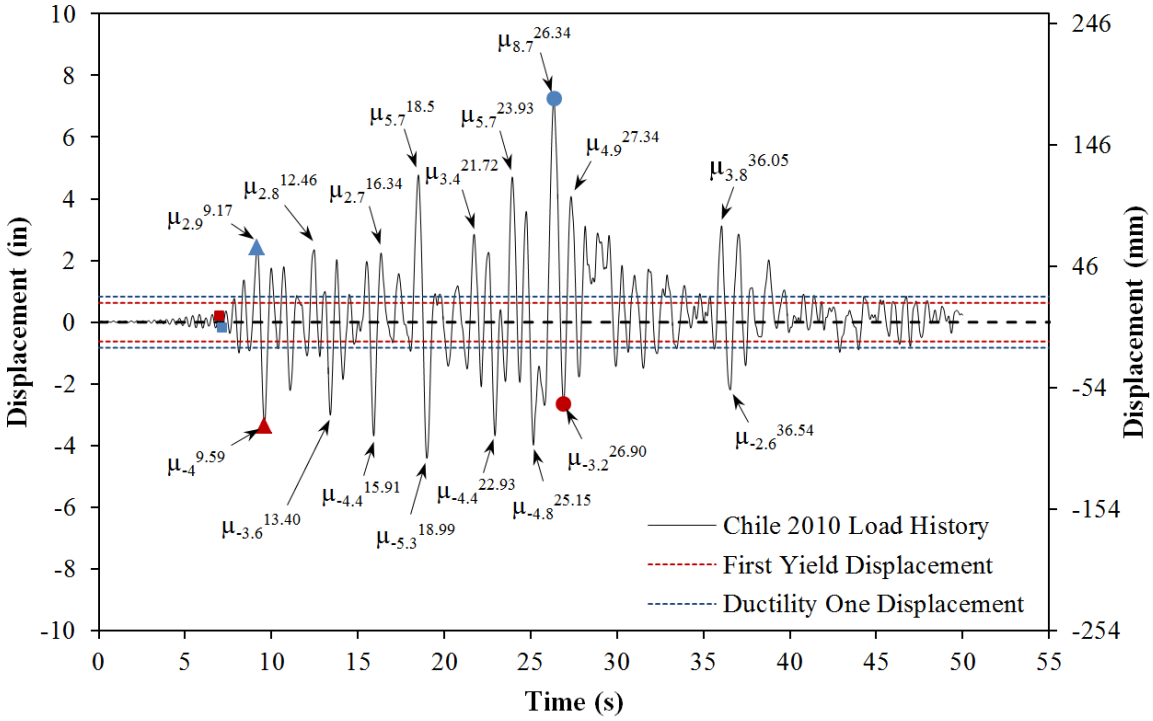

Figure 2-39. Test 8 – Chile 2010 Earthquake Load History

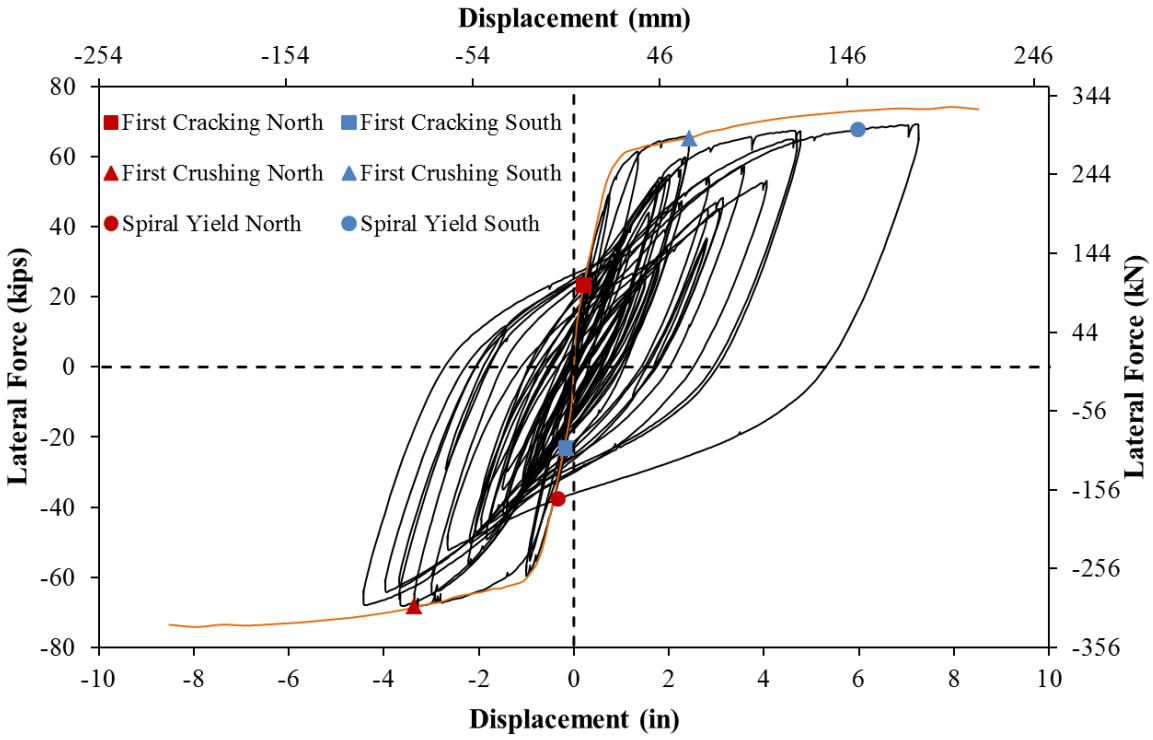

Figure 2-40. Test 8 – Chile 2010 Lateral Force vs. Top Column Displacement Response

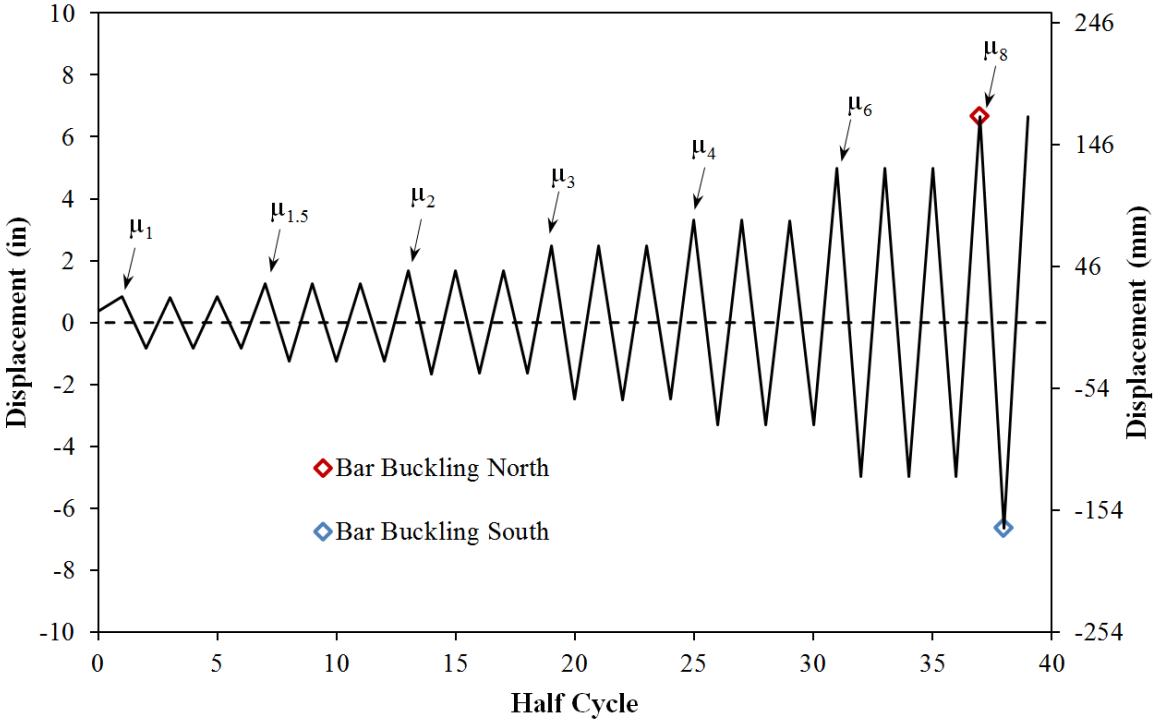

Figure 2-41. Test 8b – Symmetric Three Cycle Set Aftershock Load History

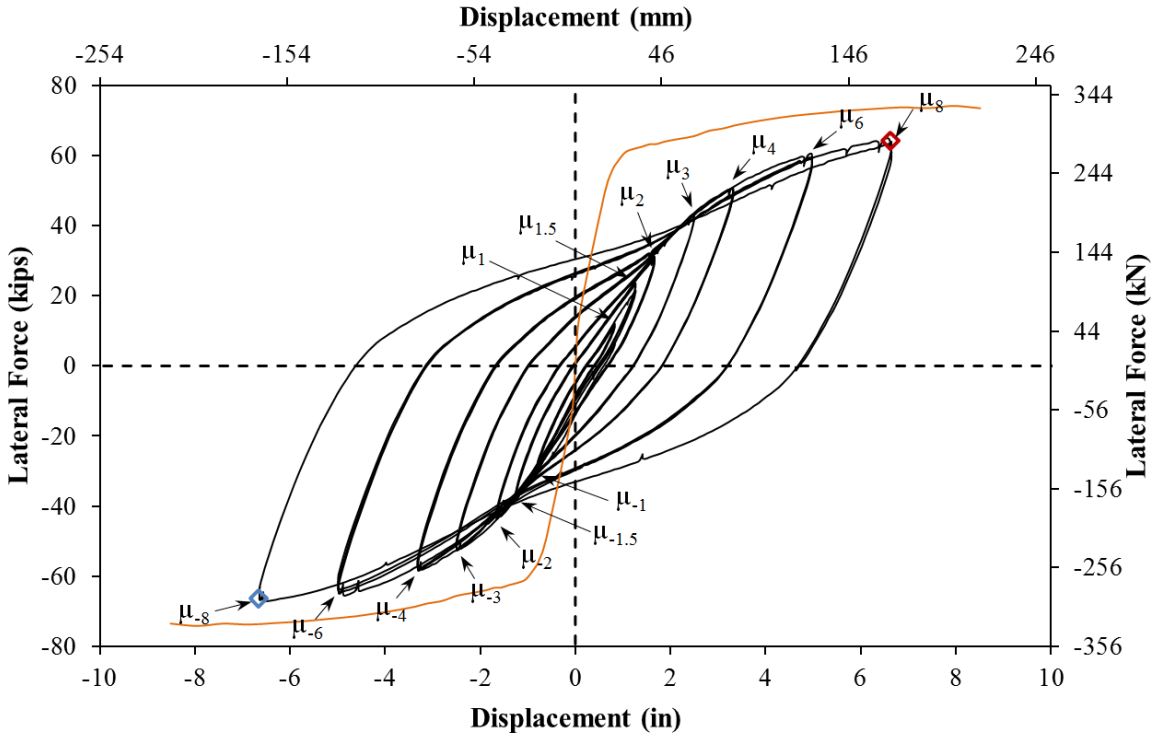

Figure 2-42. Test 8b – Cyclic Aftershock Lateral Force vs. Top Column Displacement Response

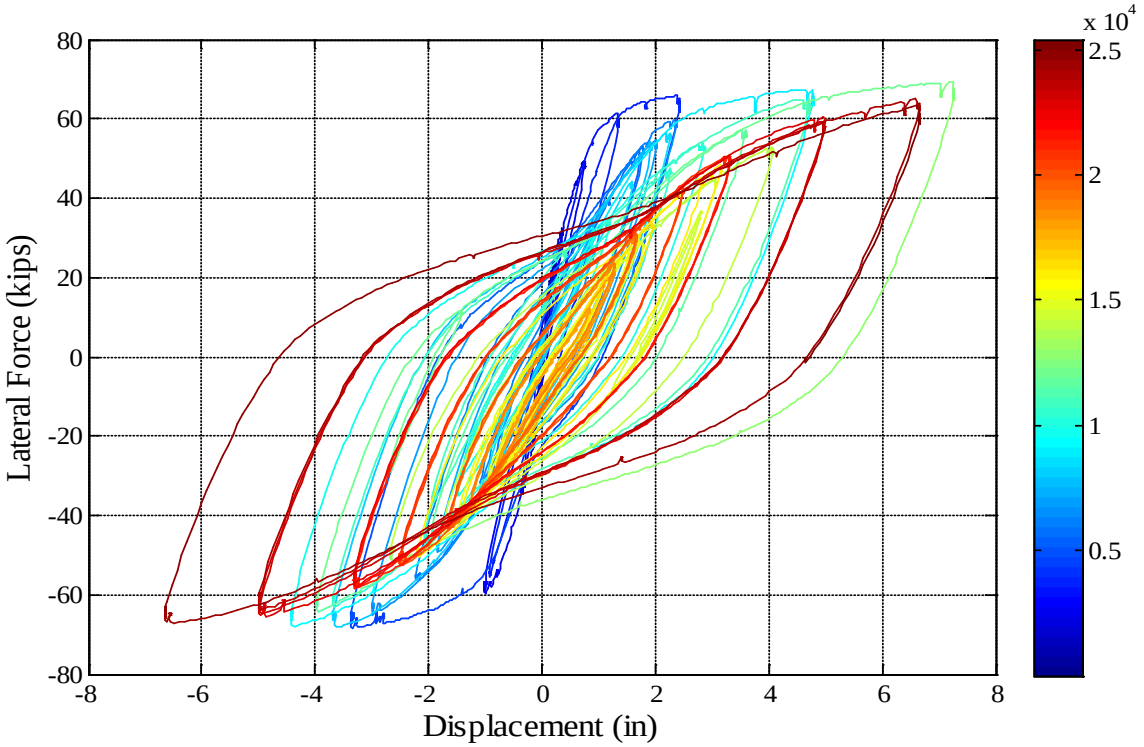

Figure 2-43. Complete Test 8 and 8b – Hysteretic Response with Elapsed Time Color Bar

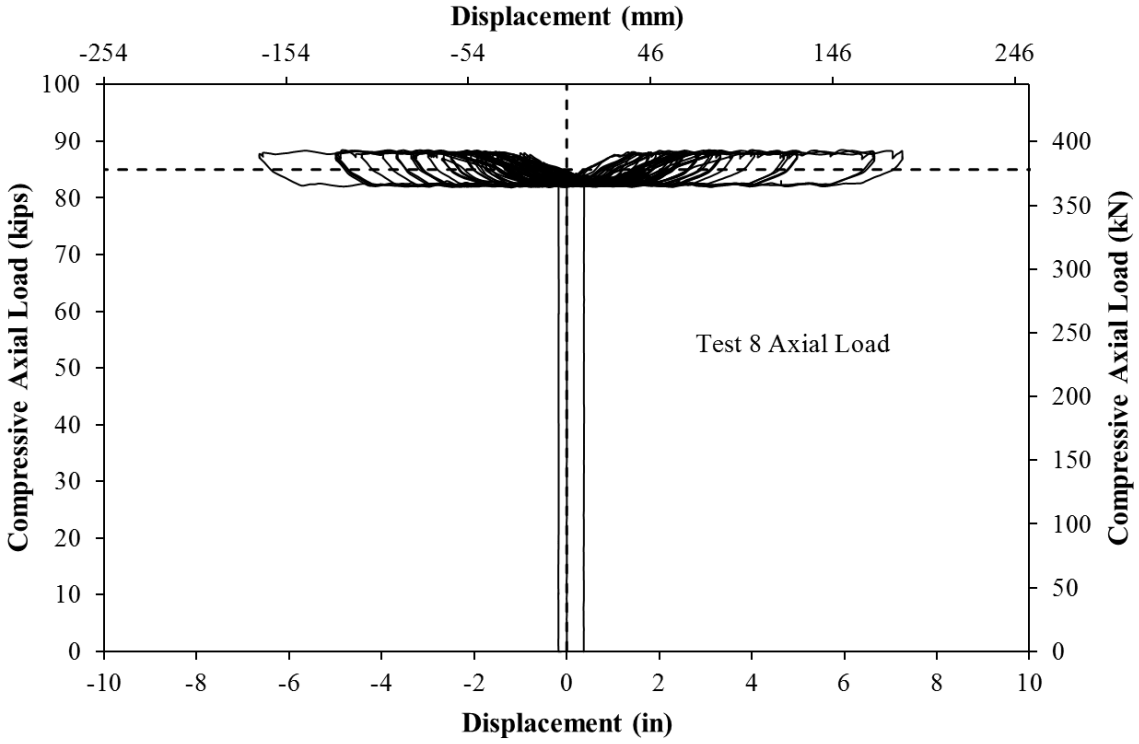

Figure 2-44. Test 8 and 8b – Compressive Axial Load from One Jack (Total = 2*Value)

2.1.2.1. Test 8 Chile Load History:

Fiber based analytical modeling in OpenSees was used to determine the top column displacement history using a scaled version of the 2010 Chile earthquake. The acceleration values from the Chile time history were scaled until the peak displacement was equal to 7.25" as shown in Figure 2-39. This peak displacement was chosen based on engineering judgment and the results of the first six specimens. For the first six tests, a displacement ductility of ten produced buckling for specimens with transverse steel spacing in the plastic hinge region closest to 2". The Chile displacement history includes a large amount of high ductility reversals before the peak cycle. With the exception of the peak displacement cycle, the load history is symmetric with similar ductility demands in each direction.

The analytical displacement history has a series of small cycles within the first eight seconds. The experimental load history began during the first cycle which exceeded the displacement at half yield from Test 7. Since the concrete begins to crack around half yield, leaving out smaller cycles at the beginning of the load history should not impact the response. Every intermediate cycle in the analytical displacement history was matched in the experimental test from 6.95sec to 39.24sec when the last meaningful cycle past ductility one was concluded. The displacement history was recreated in the lab using a displacement controlled quasi-static loading procedure with displacement rates below 6 in/min.

The resulting experimental lateral force vs. displacement response for the Chile 2010 earthquake record appears in Figure 2-40. The Chile load history scaled to a peak displacement of 7.25" was concluded without buckling of reinforcement on either side of the specimen and without any loss of strength. A symmetric three cycle set aftershock study was then conducted to determine when reinforcement buckling would occur in a column with degraded stiffness and strain accumulation, but without loss of strength. The cyclic aftershock load history and hysteretic response appear in Figure 2-41 and Figure 2-42 respectively.

2.1.2.2. Test 8 Chile Load History Experimental Observations:

The first cracks on the North side of the specimen were measured at 0.1mm during ($\mu_{0.3}^{6.95\,sec} = 0.21"$). The cycle annotation represents a push cycle 6.95 second into the Chile load history to 0.21", which is equivalent to displacement ductility 0.3. During the next cycle, the South side of the specimen had cracks measuring 0.1mm at ($\mu_{-0.2}^{7.14\,sec} = -0.17"$). Cracks on the South side of the specimen measured 0.75mm at approximate 6" spacing during ($\mu_{-1.2}^{8.12\,sec} = -1.00"$), see Figure 2-45. Cracks on the North side of the specimen were measured at 1mm at approximate 5" spacing during ($\mu_{1.6}^{8.40\,sec} = 1.35"$). The first signs of cover concrete crushing over the bottom 5" of the South side of the column occurred during ($\mu_{2.9}^{9.17\,sec} = 2.42"$), as shown in Figure 2-46, while cracks on the tension side of the column were measured at 1/8" at approximate 4" spacing. Crushing of the cover concrete on the North side of the specimen extended 15" above the top of the footing during ($\mu_{-4.0}^{9.59\,sec} = -3.35"$) while cracks on the tension side measured 1/8". The peak displacement of ($\mu_{8.7}^{26.34\,sec} = 7.25"$) from the scaled Chile 2010 load history was reached with a lateral force of 69.18 kips, see Figure 2-47. During subsequent reversals of loading the reinforcement did not visibly buckle. Bar buckling or rupture did not occur, therefore, the load history was completed with degraded stiffness but no large losses in strength.

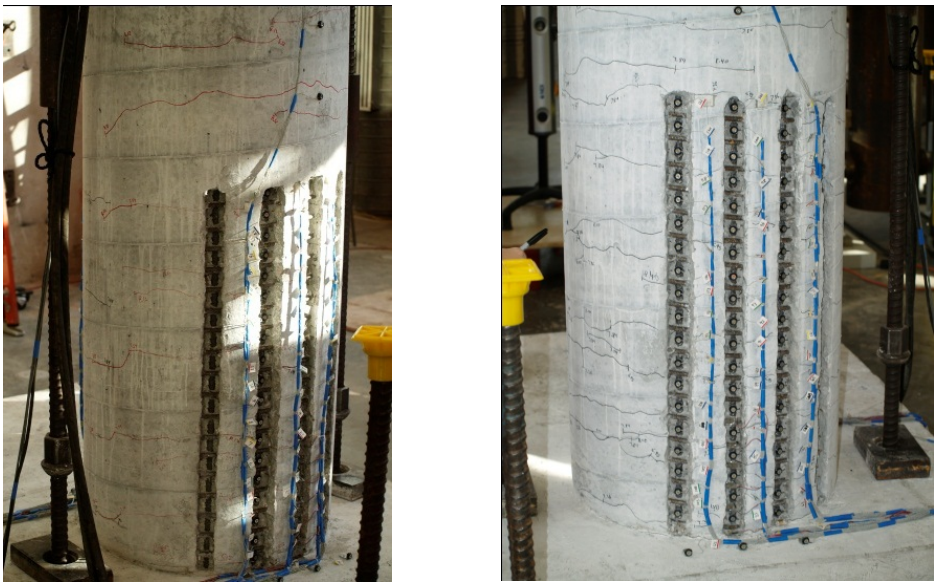

Figure 2-45. Test 8 – Crack Patterns on the (Left) South Side at ($\mu_{-1.2}^{8.12\,sec} = -1.00$") and (Right) North Side at ($\mu_{1.6}^{8.40\,sec} = 1.35$")

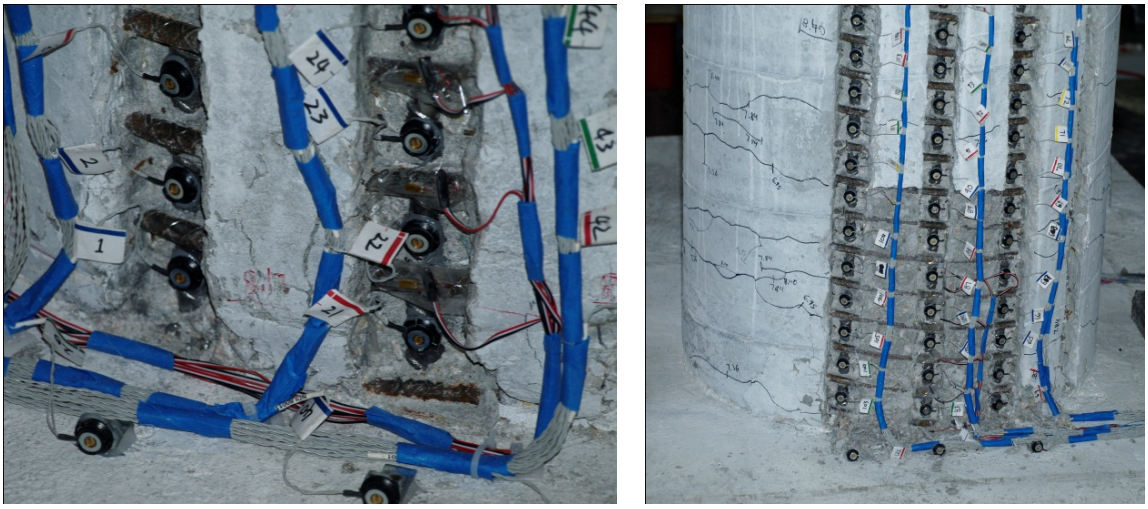

Figure 2-46. Test 8 – Crushing on the (Left) South Side at ($\mu_{2.9}^{9.17\,sec} = 2.42$") and (Right) North Side at ($\mu_{-4.0}^{9.59\,sec} = -3.35$")

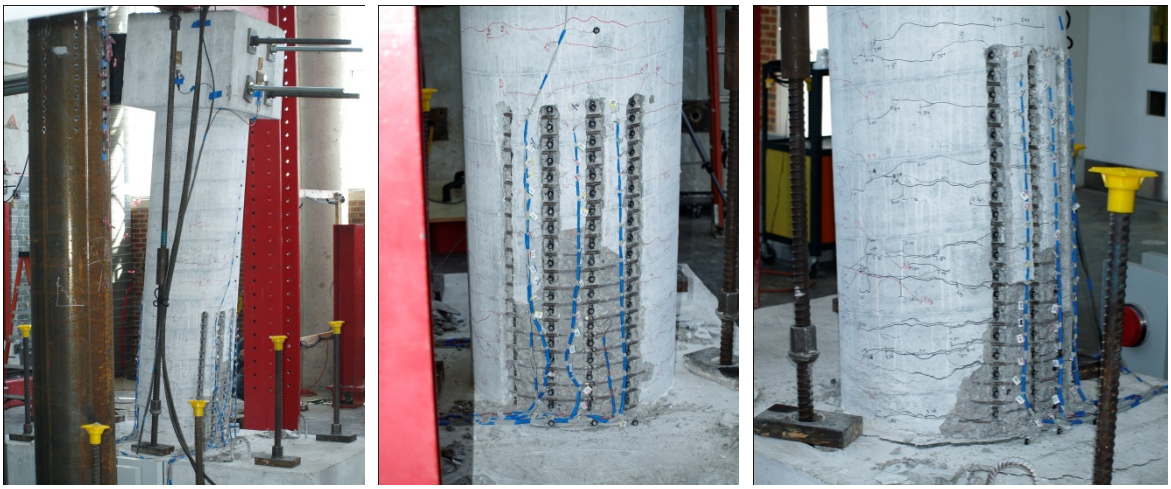

Figure 2-47. Test 8 – Peak Displacement from Test 8 ($\mu_{8.7}^{26.34\,sec} = 7.25"$) (Middle – South Side) and (Right – North Side)

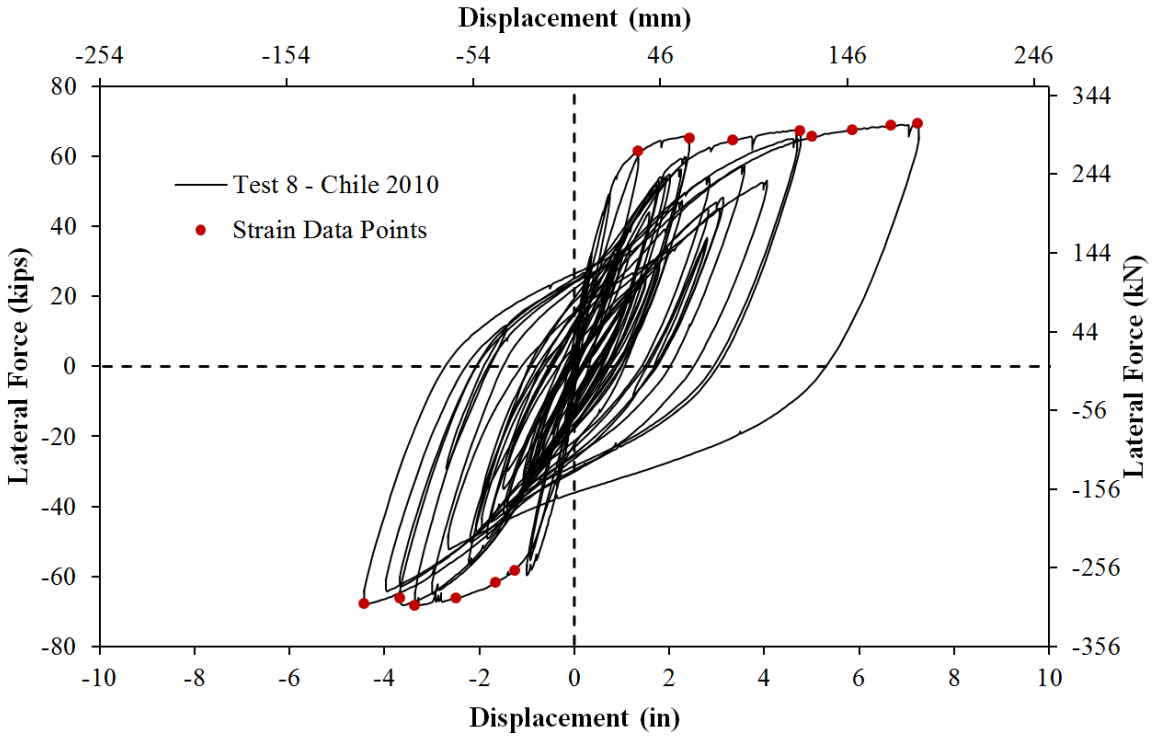

Figure 2-48. Test 8 – Strain Data Observation Points along the Envelope Curve

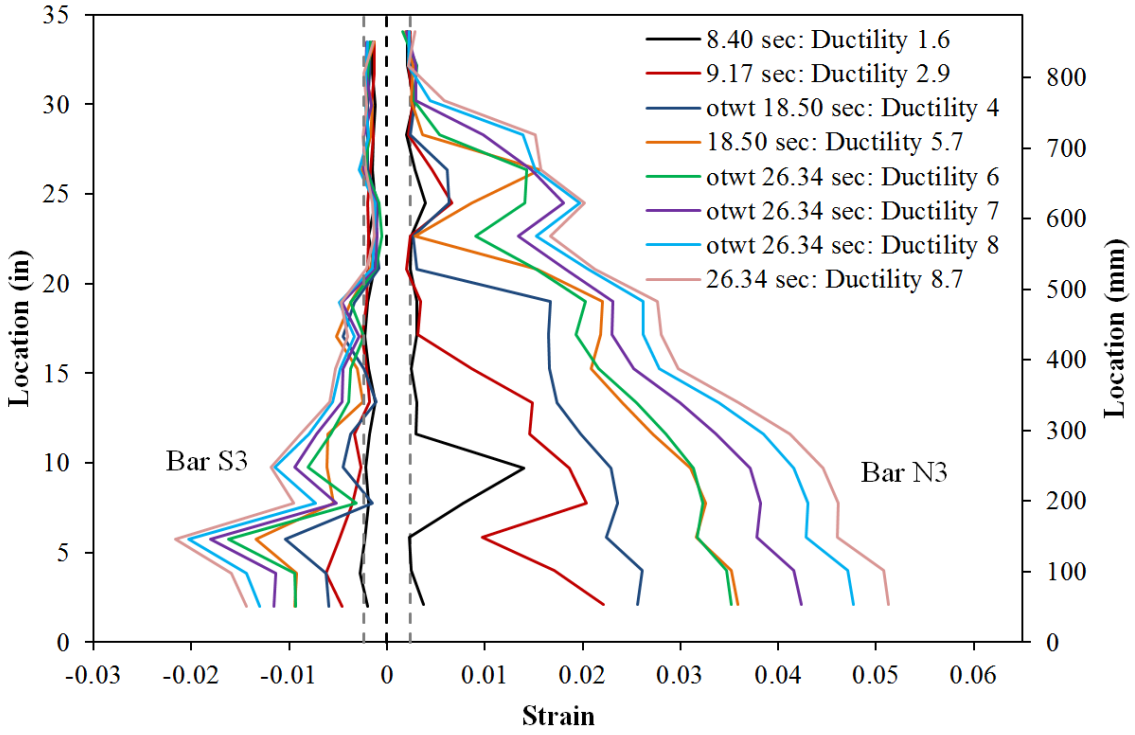

Figure 2-49. Test 8 – Extreme Fiber Vertical Strain Profiles during Push Cycles

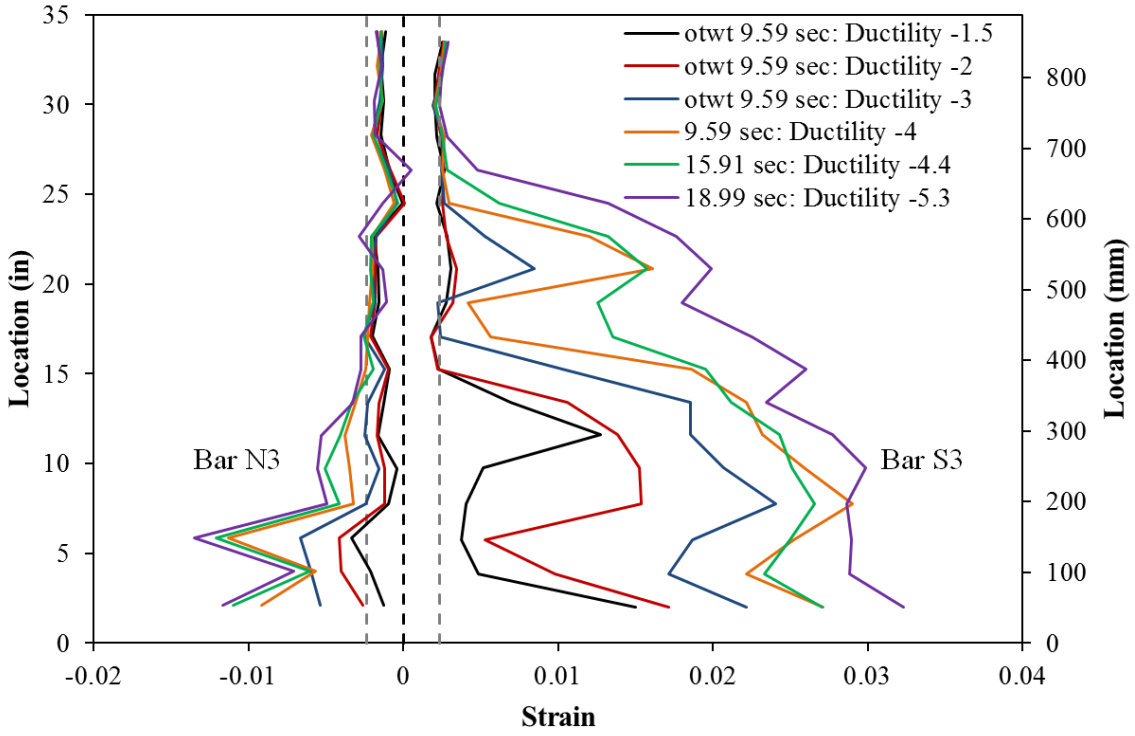

Figure 2-50. Test 8 – Extreme Fiber Vertical Strain Profiles during Pull Cycles

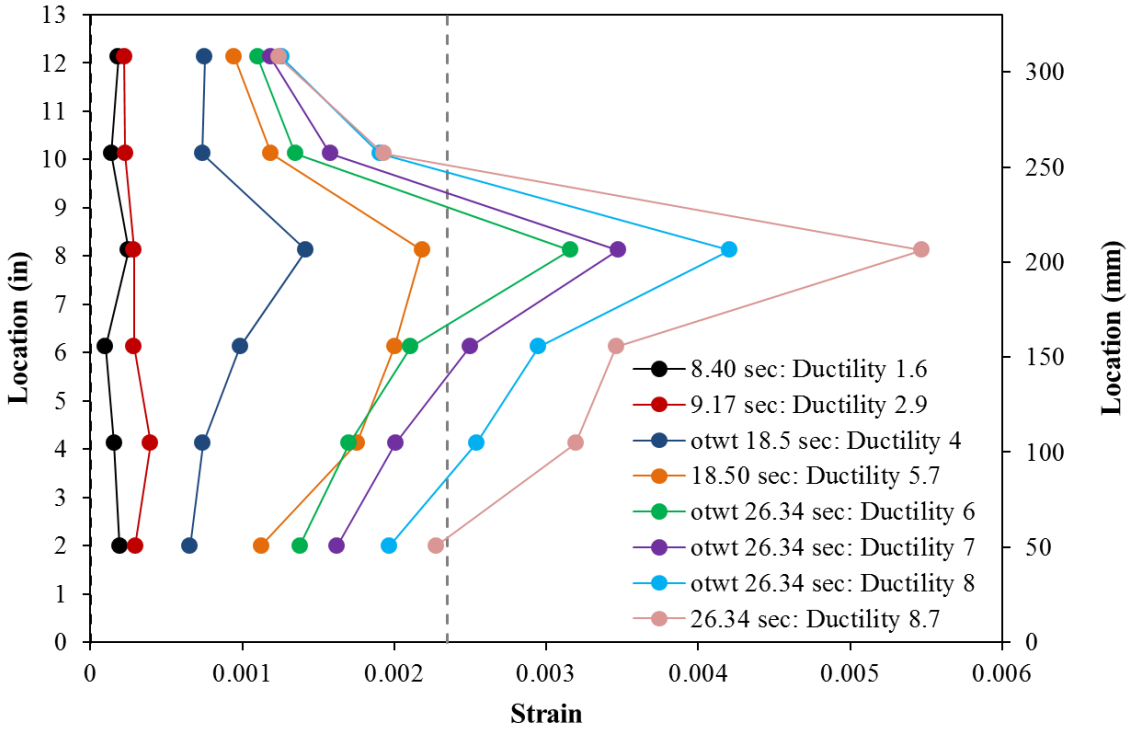

Figure 2-51. Test 8 – Transverse Steel Strains over the South Extreme Fiber Bar S3

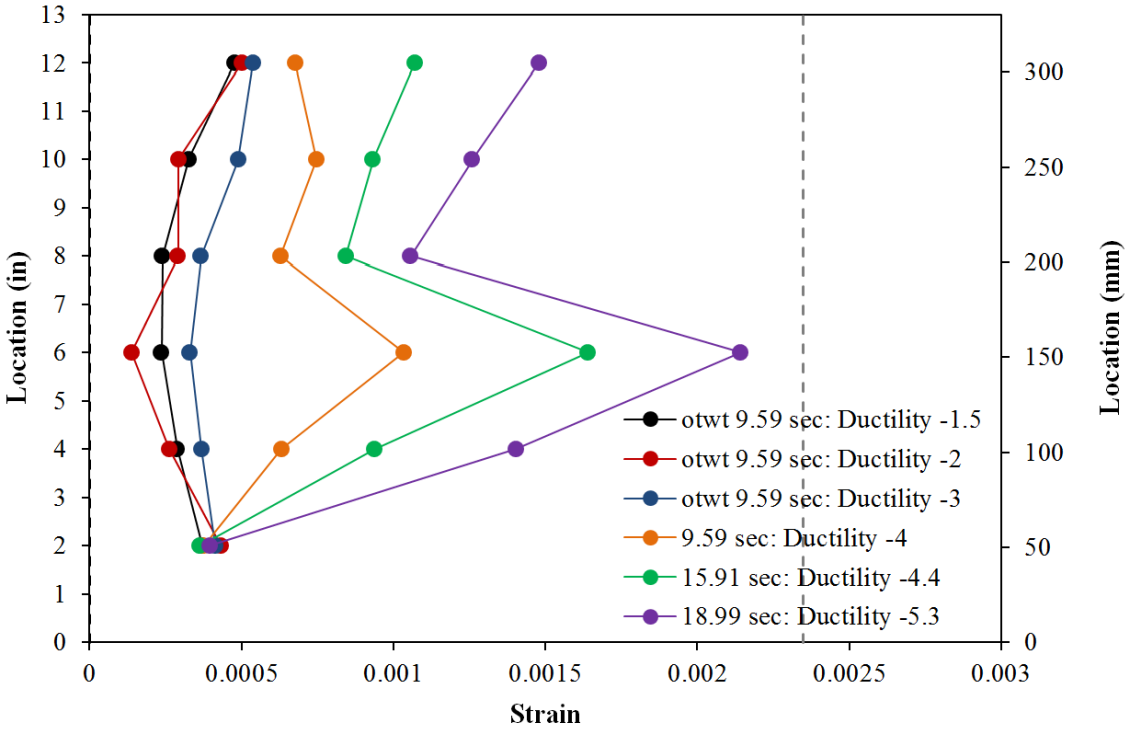

Figure 2-52. Test 8 – Transverse Steel Strains over the North Extreme Fiber Bar N3

2.1.2.3. Test 8 Chile Load History Strain Data:

Due to the random cyclic nature of the earthquake load histories, specific observation points along the backbone curve of cyclic response were chosen for data analysis in Figure 2-48. The tensile and compressive vertical strain profiles for bar S3 appear in the right half of Figure 2-50 and the left half of Figure 2-49 respectively. The transverse steel strains in the lowest six spiral layers for the South and North extreme fiber regions in compression appear in Figure 2-51 and Figure 2-52. A peak tension strain of 0.031 was measured 2.02" above the footing on bar S3 during ($\mu_{-5.3}^{18.99\,sec} = -4.42"$). The relationship between tensile strain and displacement for this gage length appears in Figure 2-55. The maximum compression strain of -0.02 in reinforcing bar S3 occurred 5.75" above the footing during ($\mu_{8.7}^{26.34\,sec} = 7.25"$). The relationship between compression strain and displacement for bar S3 for this gage length appears in Figure 2-56.

Vertical strain profiles for extreme fiber bar N3 appear in Figure 2-49 and Figure 2-50 for push tension strains and pull compression strains respectively. The largest tensile strain of 0.051, located 2.09" above the footing, was measured on bar N3 at ($\mu_{8.7}^{26.34\,sec} = 7.25"$). The relationship between tensile strain and displacement for this gage length appears in Figure 2-53. The error in strain prediction by moment curvature analysis becomes larger with increasing displacement. The largest compression strain value of -0.013 for extreme fiber bar N3 occurred 5.85" above the footing at ($\mu_{-5.3}^{18.99\,sec} = -4.42"$). The relationship between compression strain and displacement for significant pull cycles, 5.85" above the footing, for bar N3 appears in Figure 2-54.

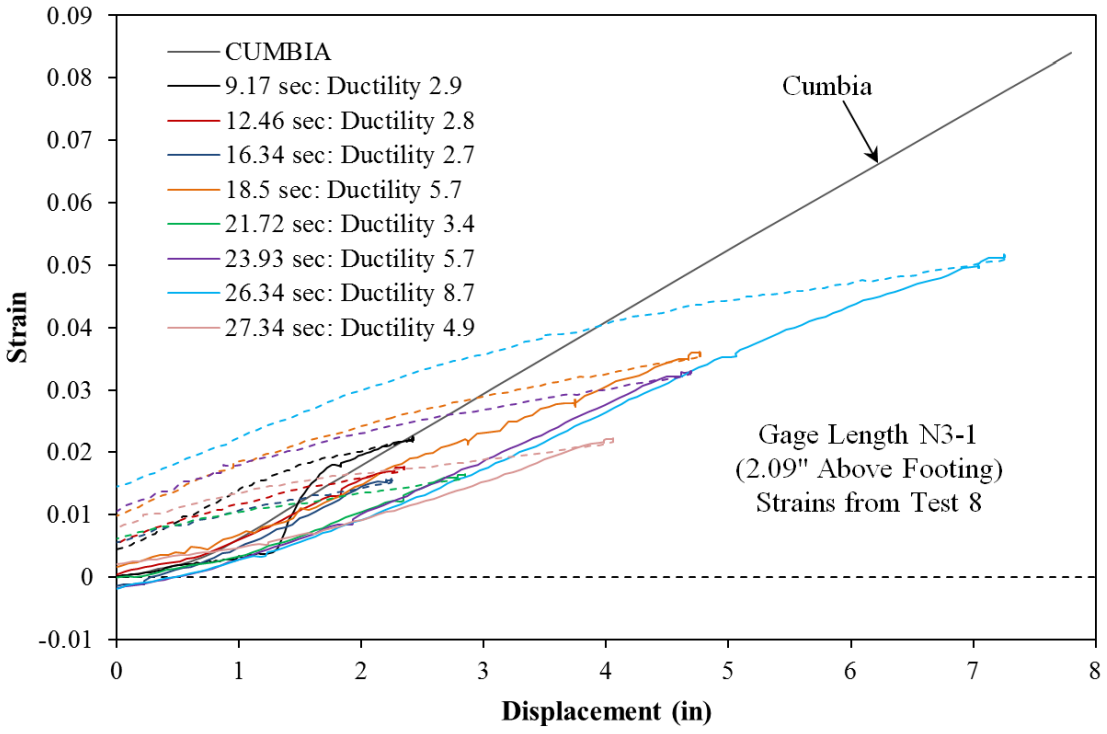

Figure 2-53. Test 8 – Strain and Displacement for Bar N3 during Push Cycles

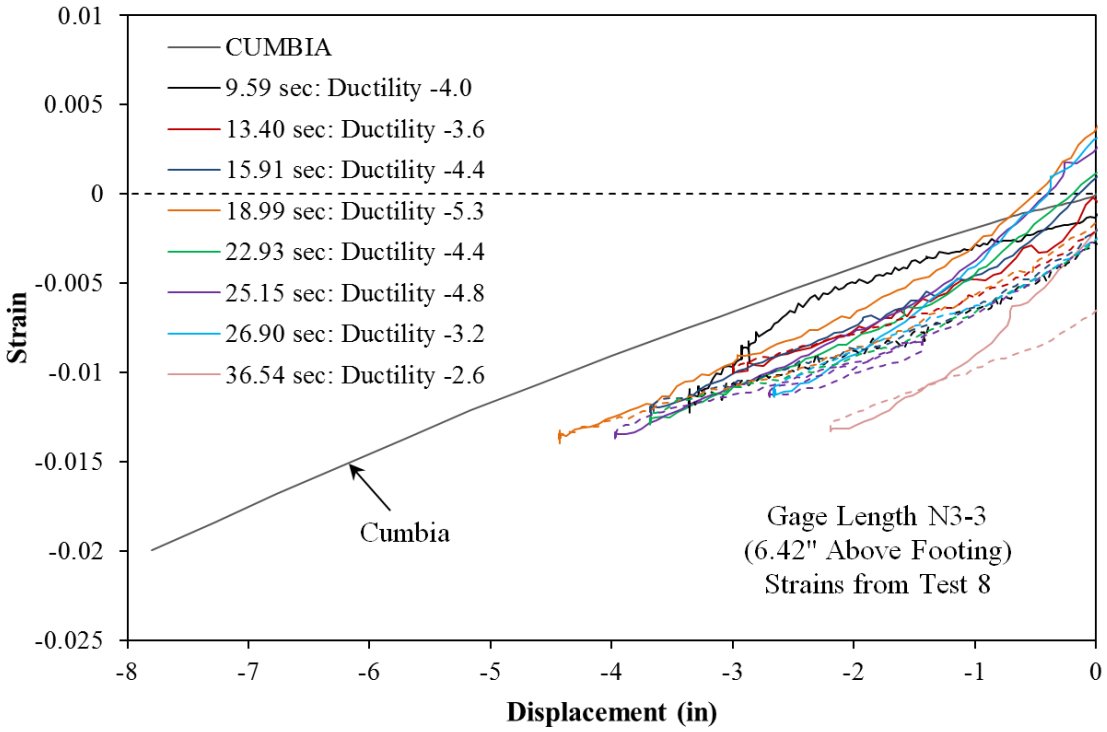

Figure 2-54. Test 8 – Strain and Displacement for Bar N3 during Pull Cycles

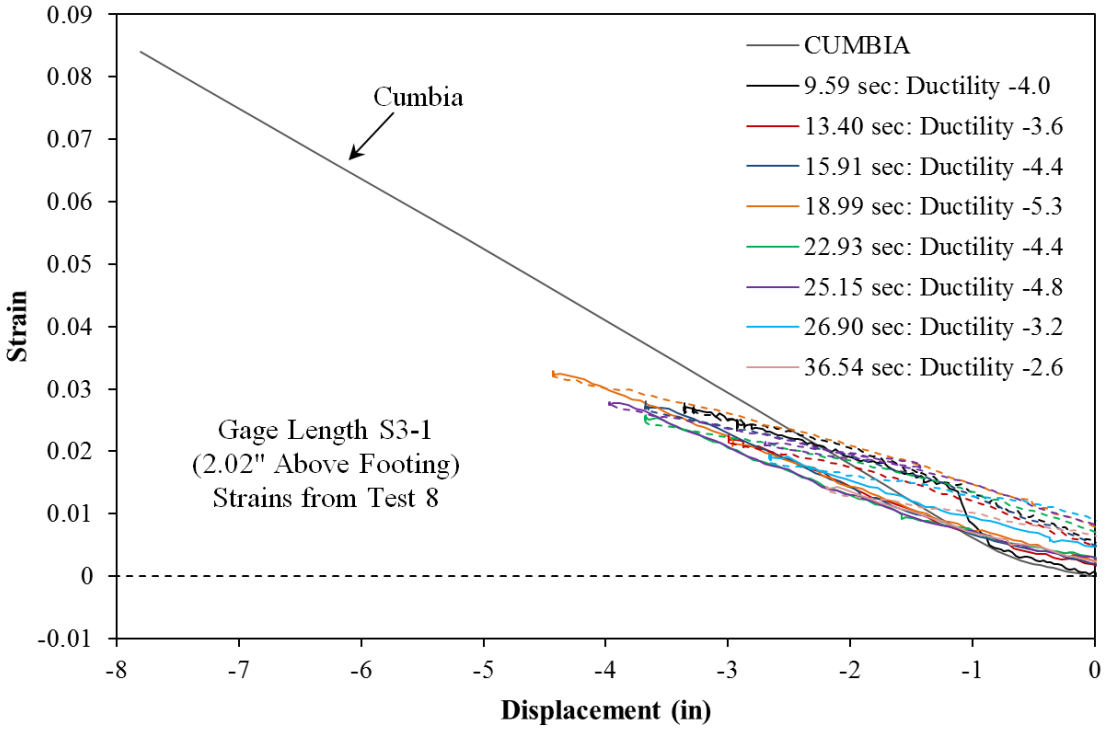

Figure 2-55. Test 8 – Strain and Displacement for Bar S3 during Pull Cycles

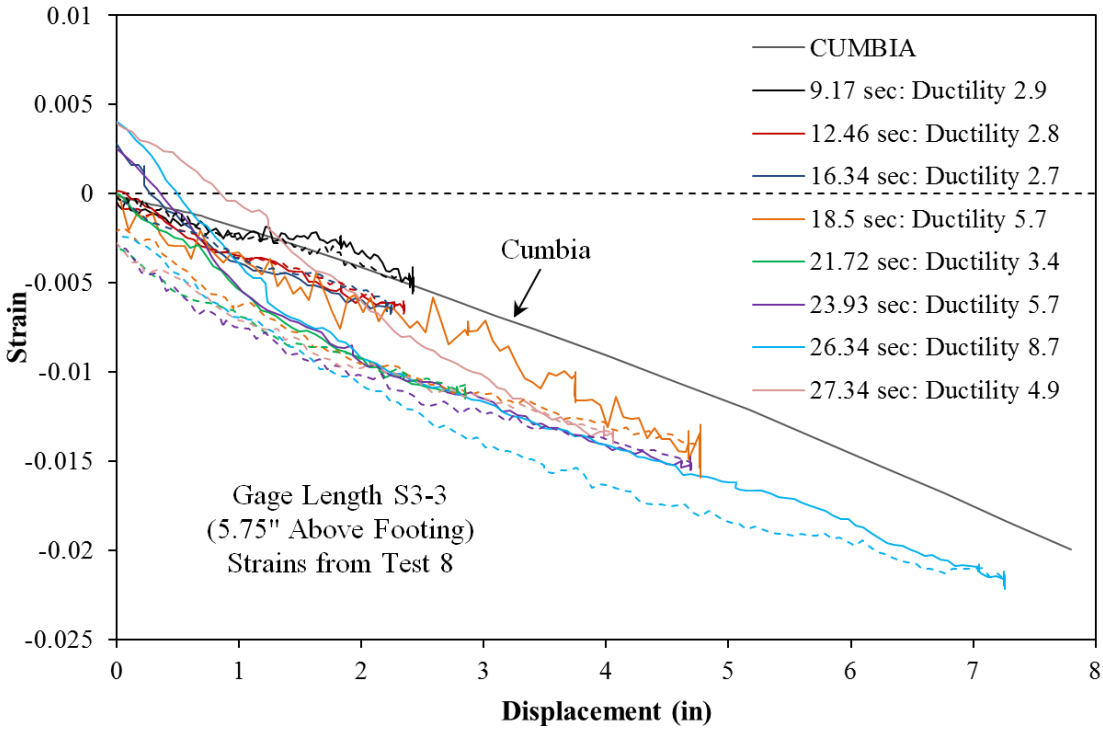

Figure 2-56. Test 8 – Strain and Displacement for Bar S3 during Push Cycles

2.1.2.4. Test 8 Chile Load History Slip and Curvature Data:

The vertical strain profiles for observation points along the backbone curve of cyclic response, see Figure 2-48, for push and pull cycles appear in Figure 2-57 and Figure 2-58. The slip hysteresis for extreme fiber bars N3 and S3 due to strain penetration of the reinforcement into the footing appear in Figure 2-70 and Figure 2-71 respectively. The slip hystereses contain data from the Chile and Cyclic Aftershock load histories up until each reinforcing bar buckled. The base section rotation attributable to strain penetration of reinforcing bars appears in Figure 2-59 and Figure 2-60 for push and pull cycles respectively. The total deformation calculated by integrating the measured curvature profiles and extrapolating the base section rotation to the center of loading appear in Figure 2-61. The integrated curvatures match well throughout the entire range of displacements.

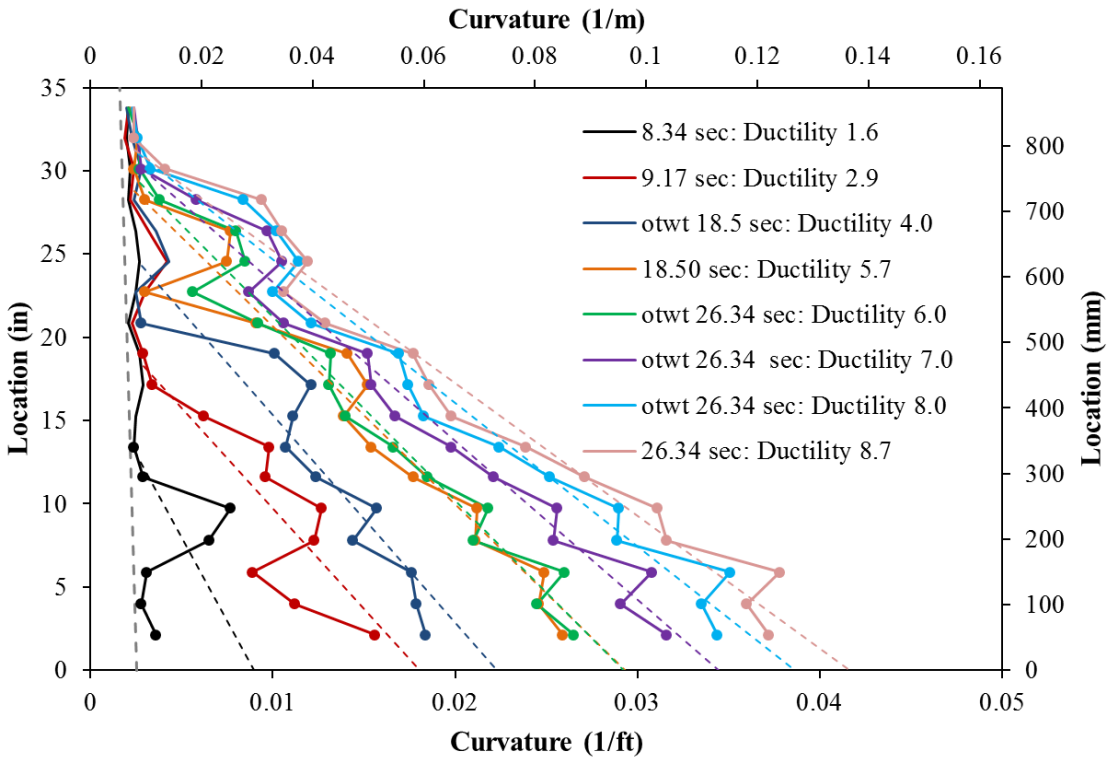

Figure 2-57. Test 8 – Curvature Profiles during Push Cycles with Linearized Least Squared Error Plastic Curvature Lines

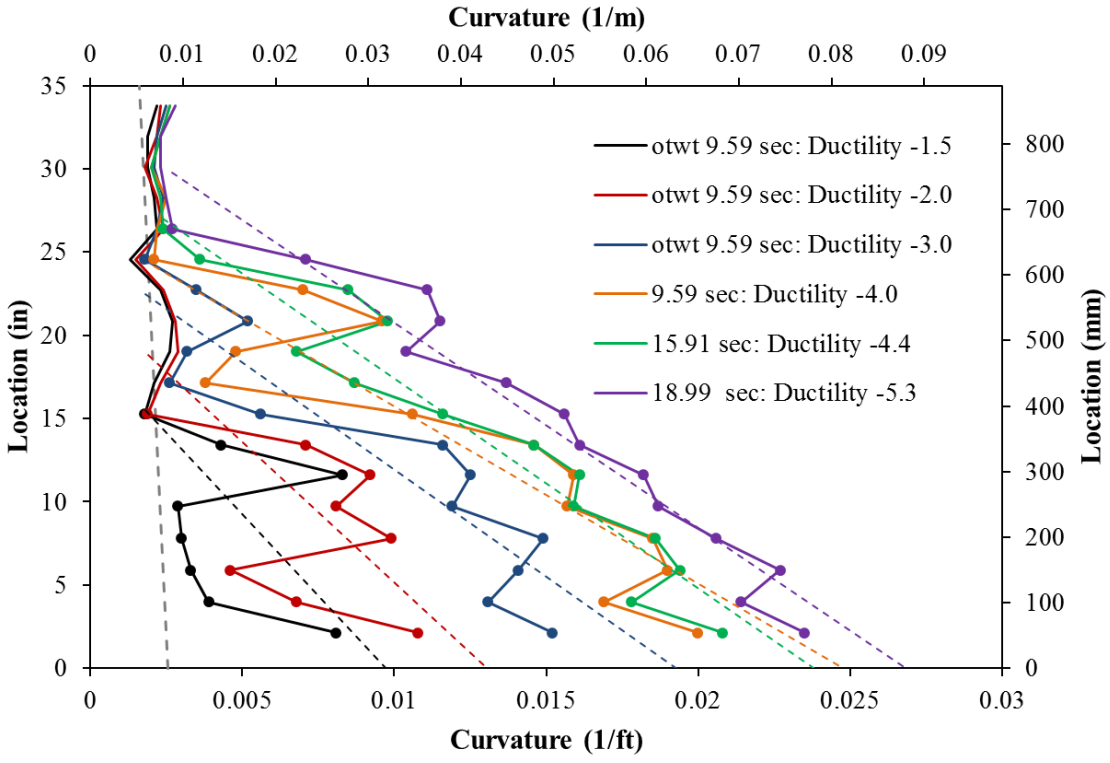

Figure 2-58. Test 8 – Curvature Profiles during Pull Cycles

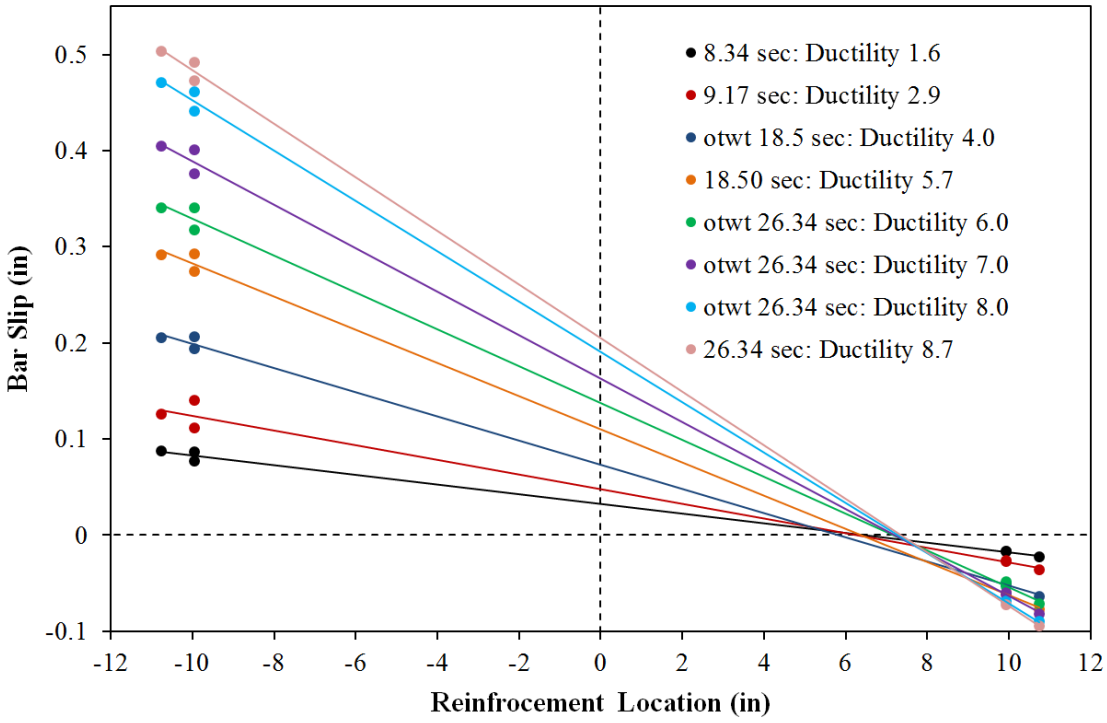

Figure 2-59. Test 8 – Base Section Rotation due to Strain Penetration during Push Cycles

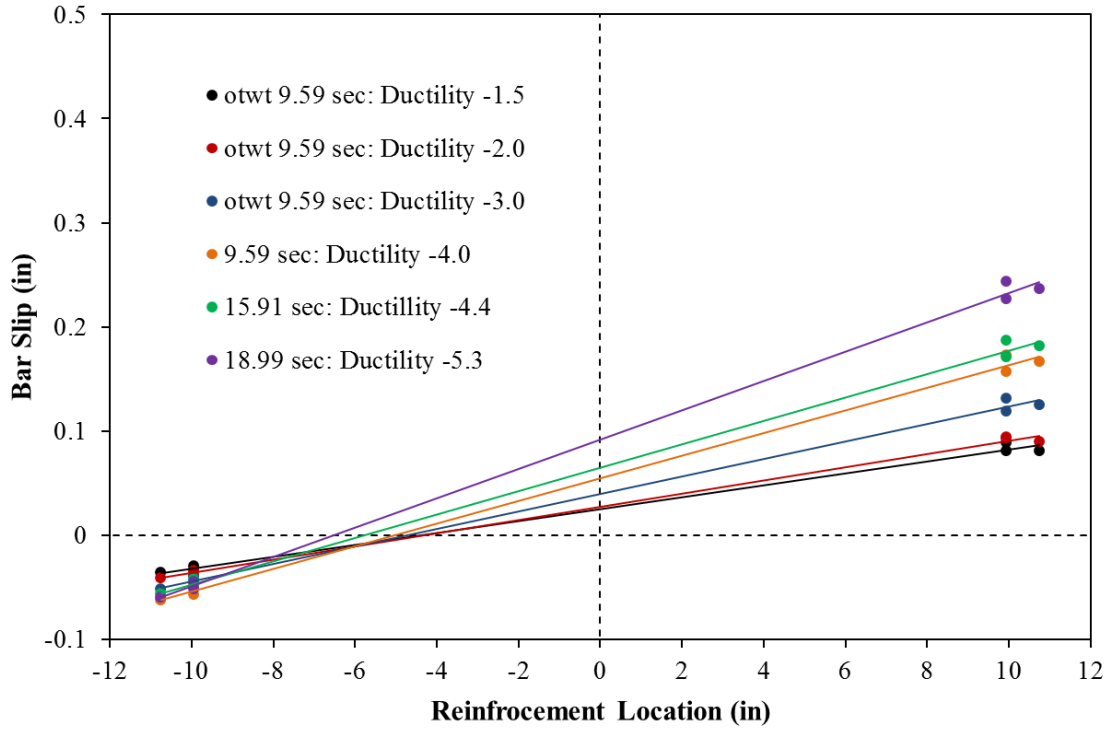

Figure 2-60. Test 8 – Base Section Rotation due to Strain Penetration during Pull Cycles

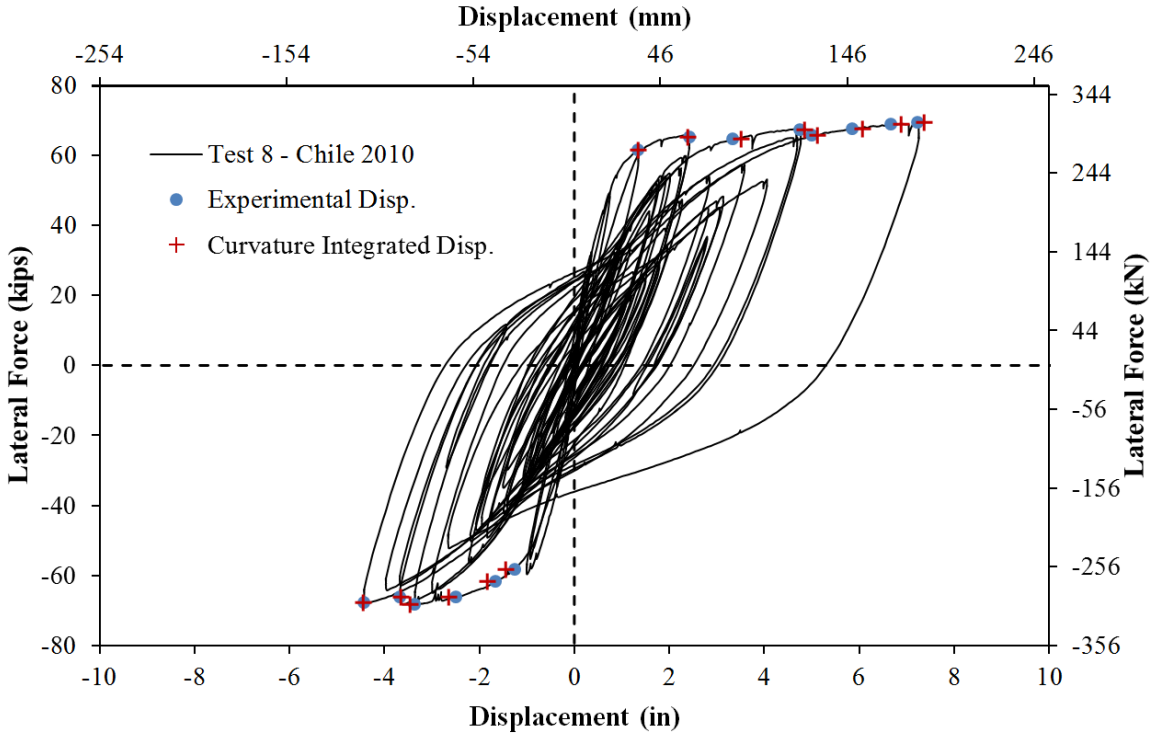

Figure 2-61. Test 8 – Comparison of Integrated and Measured Lateral Displacements

2.1.2.5. Test 8b Cyclic Aftershock Experimental Observations:

Since the Chile load history scaled to a peak displacement of 7.25" was concluded without buckling reinforcement on either side of the specimen, a symmetric three cycle set aftershock study was then conducted to determine when buckling would occur to the column with degraded stiffness and accumulated strains. The top column displacement history and resultant force vs. displacement response for the cyclic aftershock study appear in Figure 2-41 and Figure 2-42 respectively. The complete hysteretic response for Tests 8 and 8b appears in Figure 2-43 with a color bar which represents elapsed time during the experiment. Since the largest cycle in the Chile load history exceeded the peak displacement of the aftershock study in the push direction, there is more strength degradation in the push direction of loading.

The symmetric three cycle set load history progressed through ductility six without incident. After the North reinforcement was exposed to tension during ($\mu_8^{+1} = 6.64$"), the extreme fiber bar N3 buckled over the first and second gage lengths during the subsequent reversal, as shown in Figure 2-62. Remember that the North reinforcement had already been subjected to larger displacements placing the bars in tension during ($\mu_{8.7}^{26.34} = 7.25$") in the Chile load history. After being exposed to tension during ($\mu_8^{-1} = -6.65$"), extreme fiber bar S3 buckled over the first and fourth gage lengths as shown in Figure 2-62. The experiment was concluded with buckled reinforcement on each side of the specimen to save the column as a repair candidate for another project.

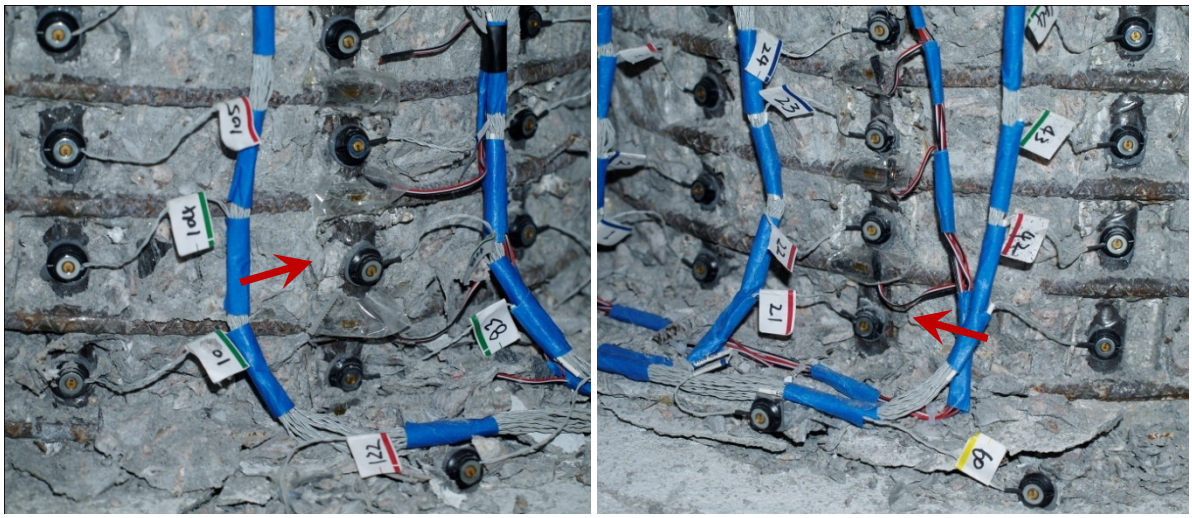

Figure 2-62. Test 8b – (Left) Buckling of Bar N3 after Reversal from ($\mu_8^{+1} = 6.64$") and (Right) Buckling of Bar S3 after Reversal from ($\mu_8^{-1} = 6.65$")

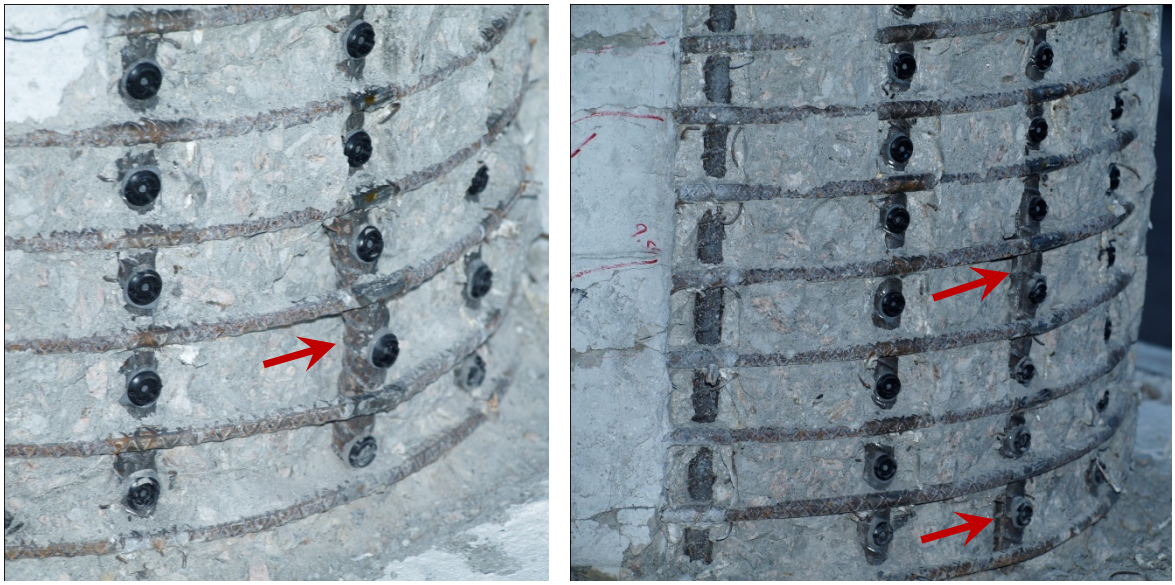

Figure 2-63. Test 8b – (Left) Buckling of N3 after Experiment and (Right) Buckling of S3

2.1.2.6. Test 8b Cyclic Aftershock Strain Data:

Extreme fiber vertical strain profiles for push and pull cycles of the symmetric three cycle set aftershock load history are shown in Figure 2-64 and Figure 2-65 respectively. The strain profiles shape is controlled by the crack distribution set in place during high ductility cycles of the original Chile load history. The compressive vertical strain profiles for each extreme fiber reinforcing bar show significant deformation prior to visible bar buckling. If the reinforcing bar where to outwardly deform, the gage length over the deformation would increase in tensile strain while the gage lengths above and below would further increase in compressive strain. The strain values measured when this deformation occurred do not represent engineering strains, but they are shown to highlight the progression of damage.

South Reinforcement:

Visible buckling of Bar S3 was not observed until the second push cycle of ductility eight. The South reinforcing bar buckled over the first and fourth gage lengths, see Figure 2-63, which matches the problematic areas of the vertical strain profile. The tension strain sustained by bar S3 prior to visible buckling during the aftershock study was 0.048, for the gage length 2.02" above the footing, during ($\mu_8^{-1} = 6.65"$). The largest strain sustained by bar S3 during the Chile load history was 0.032 located 2.02" above the footing at ($\mu_{-5.3}^{18.99\,sec} = -4.42"$).

The complete strain hysteresis for extreme fiber bar S3 appears in Figure 2-68 for the gage length 7.76" above footing in the upper buckled region. The strain hysteresis obtained from a strain gage located on the transverses steel overlaying the upper buckled region of bar S3 appears in Figure 2-69. The strains in bar S3 increase during each successive push cycle of ductility six during the aftershock study even though visible buckling was not noticeable. For the second and third push cycles of ductility six the peak strain increases with each successive cycle indicating measureable deformation prior to buckling. The trend continues as the first push cycle of ductility eight produces an even larger tensile strain in the South reinforcement even though this region should be in compression during push cycles. The tension strain during push cycles becomes much larger after reversal from ($\mu_8^{-1} = 6.65"$), which coincides with visible buckling of bar S3. When buckling occurs, the reinforcing bar places additional strain demand on the transverse steel, which can be seen in Figure 2-69. During each successive cycle of ductility six the strain demands on the transverse steel in the upper buckled region of bar S3become larger. During the first push cycle of ductility eight prior to visible buckling, the strain in the transverse steel sharply increases to the point where the strain gage goes off scale preventing further measurement. The longitudinal and transverse strain hystereses show that buckling may be a more gradual process with measurable deformation prior to visible buckling.

North Reinforcement:

The extreme fiber bar N3 was exposed to 0.043 during ($\mu_8^{+1} = 6.64"$) which is less than the strain which occurred during the largest cycle of the Chile load history 0.051 at ($\mu_{8.7}^{26.34\,sec} = 7.25"$). The compressive strain vertical profile in Figure 2-65 for bar N3 during pull cycles shows measurable deformation during ($\mu_6^{-3} = -4.99"$) before visible buckling. The complete strain hysteresis, for the same gage length 4.02" above the footing on bar N3 is shown in Figure 2-66. After each successive pull cycle of ductility six the deformation in the buckled region of bar N3 increases, as indicated by positive strain when the reinforcement should be in compression. Similarly, the strain rises sharply after reversal from ($\mu_8^{+1} = 6.64"$) when visible buckling was observed. The transverse steel strain hysteresis over the buckled region of bar N3 is shown in Figure 2-67. Again, each cycle of ductility six produces a greater strain demand on the transverse steel which is restraining the small amounts of deformation prior to visible buckling. After reversal from ($\mu_8^{+1} = 6.64"$), when the bar visibly buckled, the transverse steel strain gage goes off scale preventing further measurement.

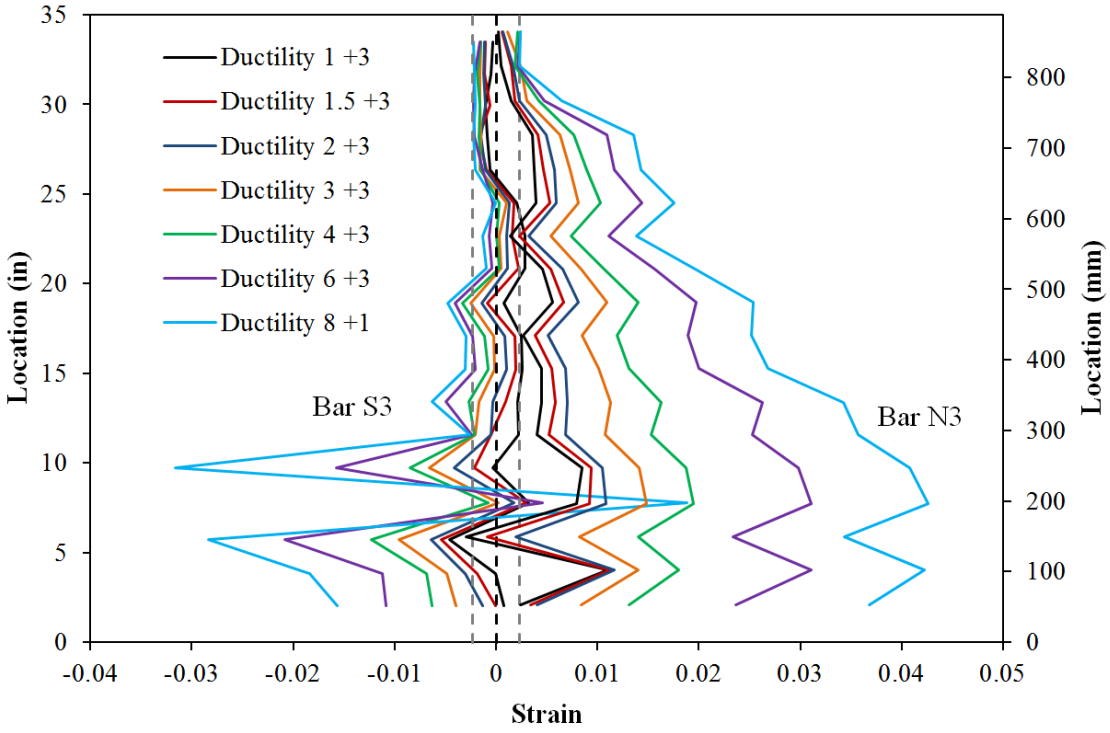

Figure 2-64. Test 8b – Aftershock Vertical Strain Profiles during Push Cycles (Significant Deformation Present before Visible Buckling)

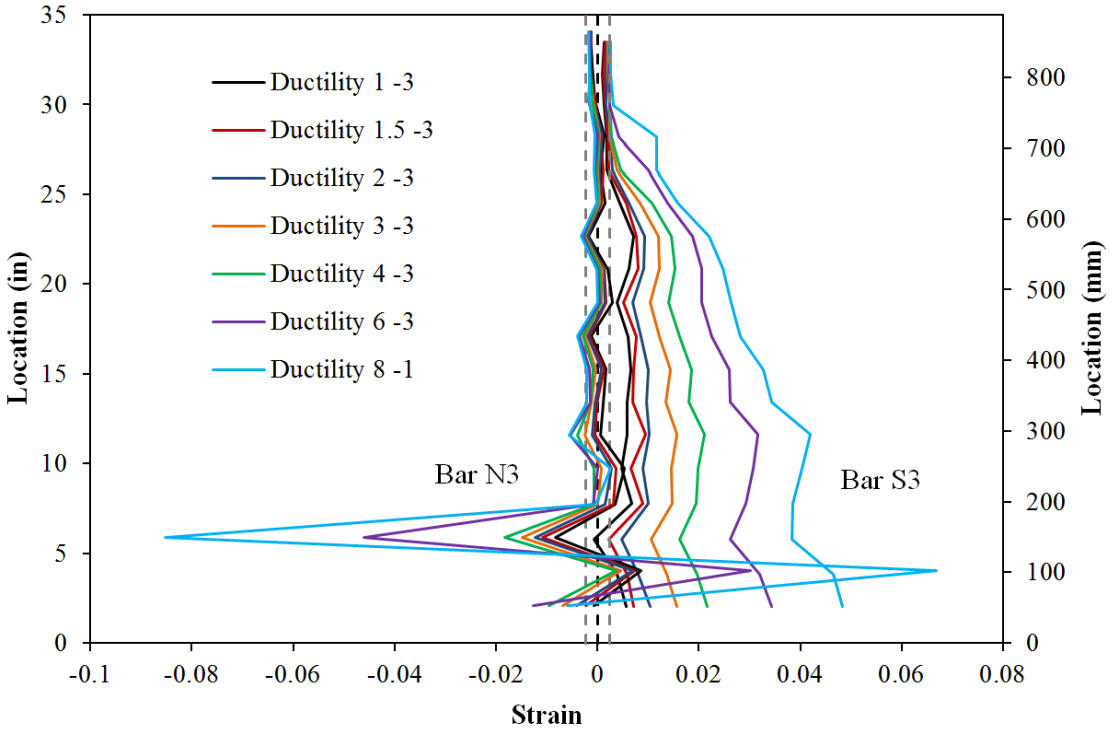

Figure 2-65. Test 8b – Aftershock Vertical Strain Profiles during Pull Cycles

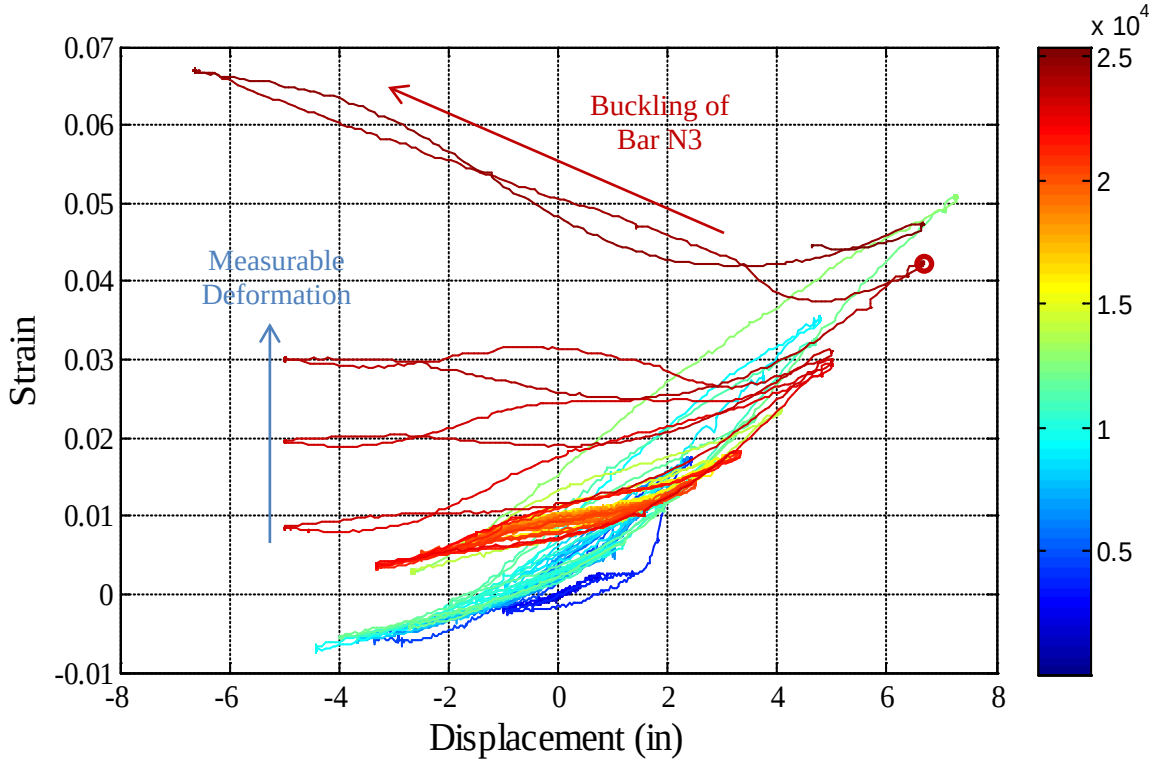

Figure 2-66. Test 8 and 8b – Extreme Fiber Bar N3 Strain Hysteresis (4.02" Above Footing) with Elapsed Time Color Bar

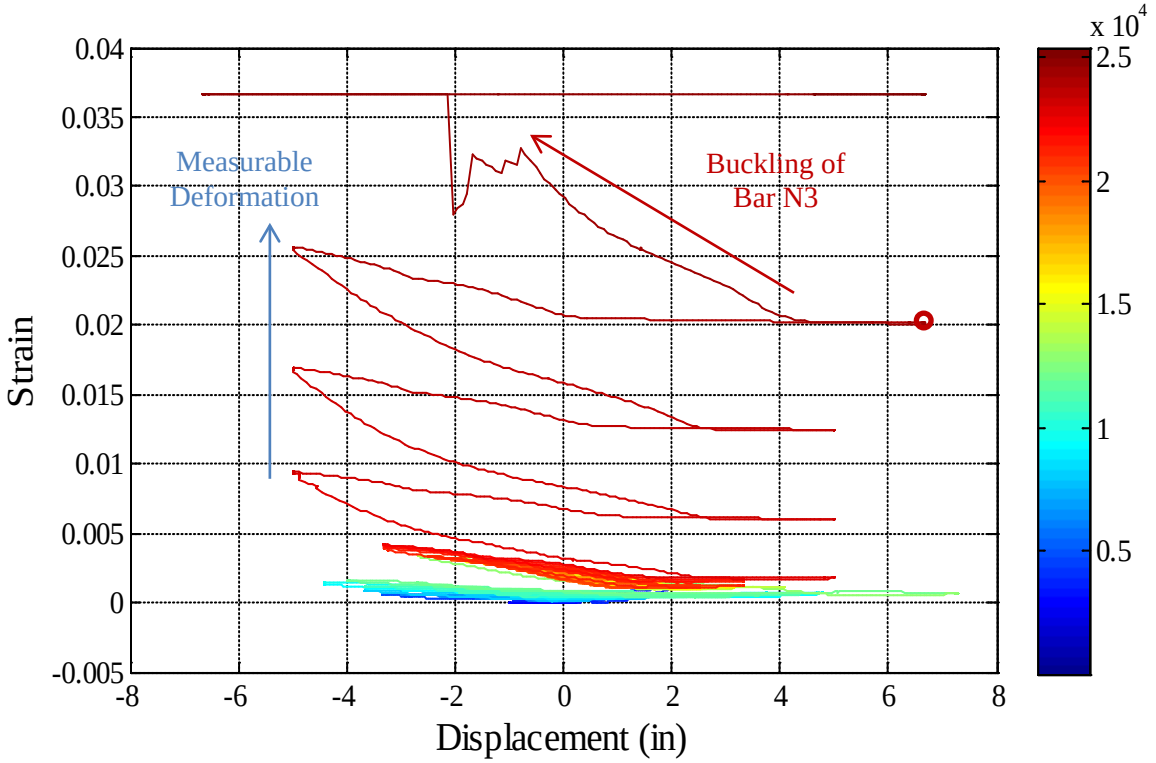

Figure 2-67. Test 8 and 8b – Transverse Steel Strain Hysteresis over Buckled North Region

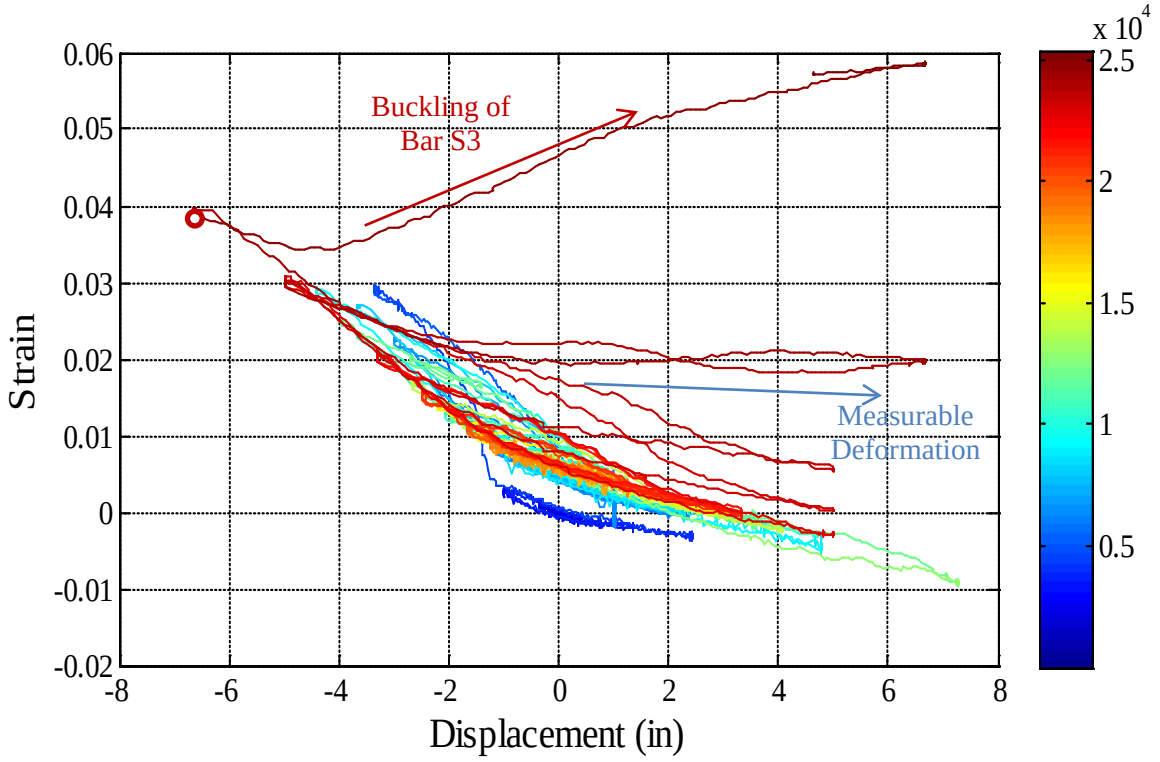

Figure 2-68. Test 8 and 8b – Extreme Fiber Bar S3-4 Strain Hysteresis (7.76" Above Footing)

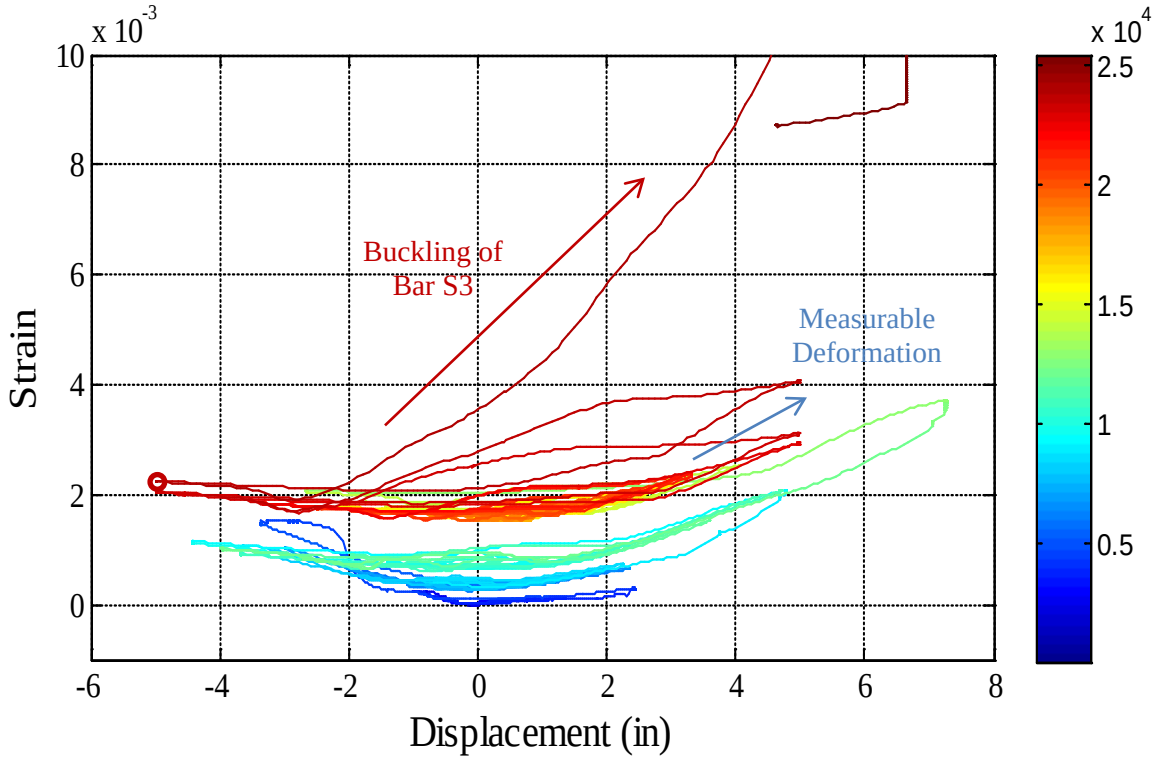

Figure 2-69. Test 8 and 8b – Transverse Steel Strain Hysteresis for Buckled South Region

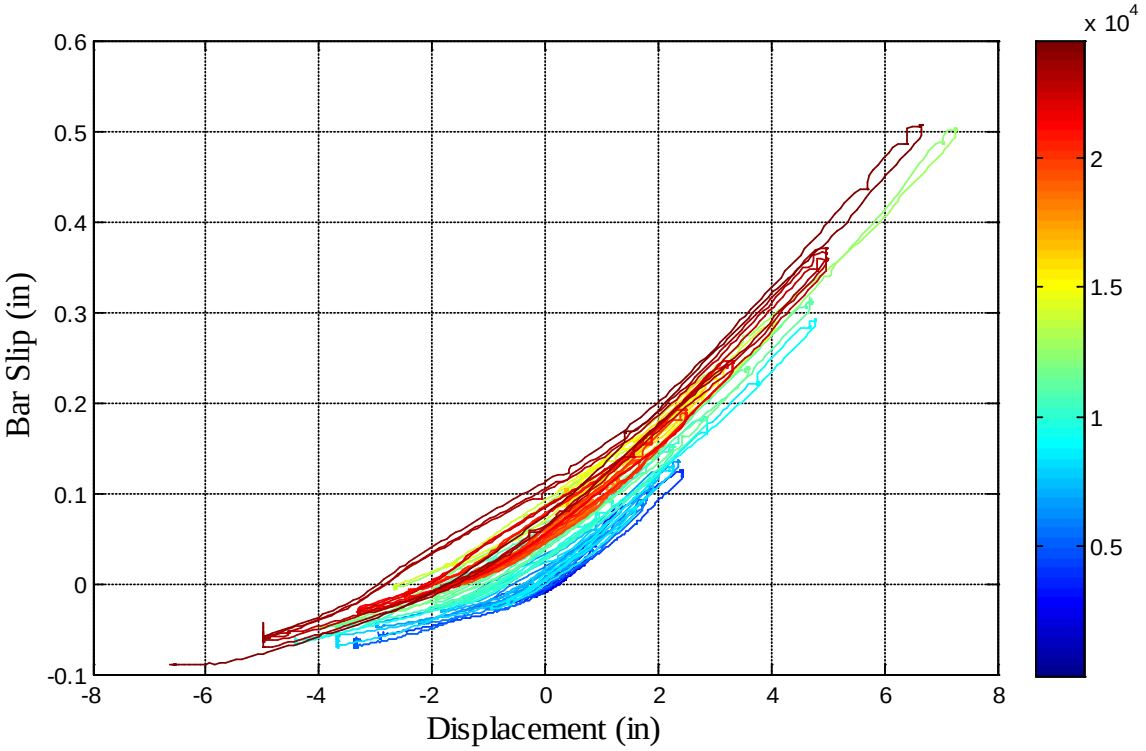

Figure 2-70. Test 8 and 8b – North Extreme Fiber Bar N3 Slip Hysteresis

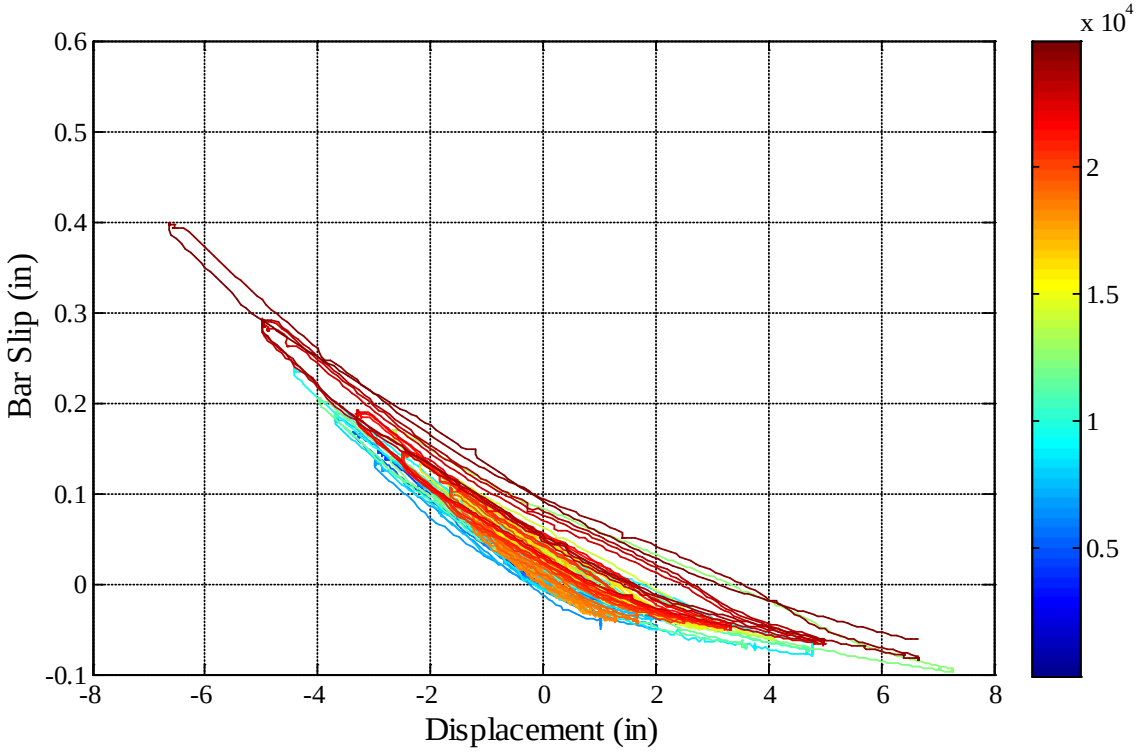

Figure 2-71. Test 8 and 8b – South Extreme Fiber Bar S3 Slip Hysteresis

2.1.3. Test 10 and 10b – Chichi Earthquake and Cyclic Aftershock Load History

Table 2-6. Results Summary for Test 10 – Chichi Earthquake Load History

LOAD HISTORY: Chichi Earthquake Load History

VALUES OF INTEREST:

Concrete Compressive Strength:	$f_c' = 5263psi$
Axial Load:	$P = 170kips$
Analytical First Yield Force:	$F_y' = kips$
Experimental First Yield Displacement:	$\Delta_y' = 0.62"$ (Same as Test 9)
Analytical Nominal Moment Capacity:	$M_n = 505.6kip * ft$
Equivalent Yield Displacement:	$\Delta_y = 0.84"$
Maximum Lateral Force:	$70.6kips$
Maximum Lateral Displacement:	$\mu_{8.9}^{17.31\,sec} = 7.40"$
Failure Mode:	No significant damage from earthquake.

DAMAGE OBSERVATIONS: (Drift %) [Displacement Ductility, μ_Δ]

First Cracking North:	$\mu_{0.3}^{7.02\,sec} = 0.25"$
First Cracking South:	$\mu_{-0.27}^{6.80\,sec} = -0.22"$
Cover Concrete Crushing North:	$\mu_{-1.7}^{13.72\,sec} = -1.39"$
Cover Concrete Crushing South:	$\mu_{2}^{13.40\,sec} = 1.70"$
Transverse Steel Yield South:	At 4.47" otwt $\mu_{8.9}^{17.31\,sec} = 7.40"$

*$\mu_{8.9}^{17.31\,sec} = 7.40"$represents a push cycle 17.31 seconds into the earthquake load history which reached a peak displacement of 7.40" and a displacement ductility of 8.9

Table 2-7. Results Summary for Test 10b – Cyclic Aftershock Load History

LOAD HISTORY: Symmetric Three Cycle Set Aftershock after Chichi Load History

DAMAGE OBSERVATIONS: (Drift %) [Displacement Ductility, μ_Δ]

Transverse Steel Yield North:	At $-4.57"$ otwt $\mu_6^{-3} = -4.98"$
Longitudinal Bar Buckling South:	Reversal from $\mu_6^{-1} = -5.01"$
Failure Mode:	Specimen Saved as a Repair Candidate after Each Extreme Fiber Longitudinal Bar Buckled

*$\mu_6^{-1} = -5.01"$ represents the first pull cycle of displacement ductility six which reached a peak displacement of -5.01"

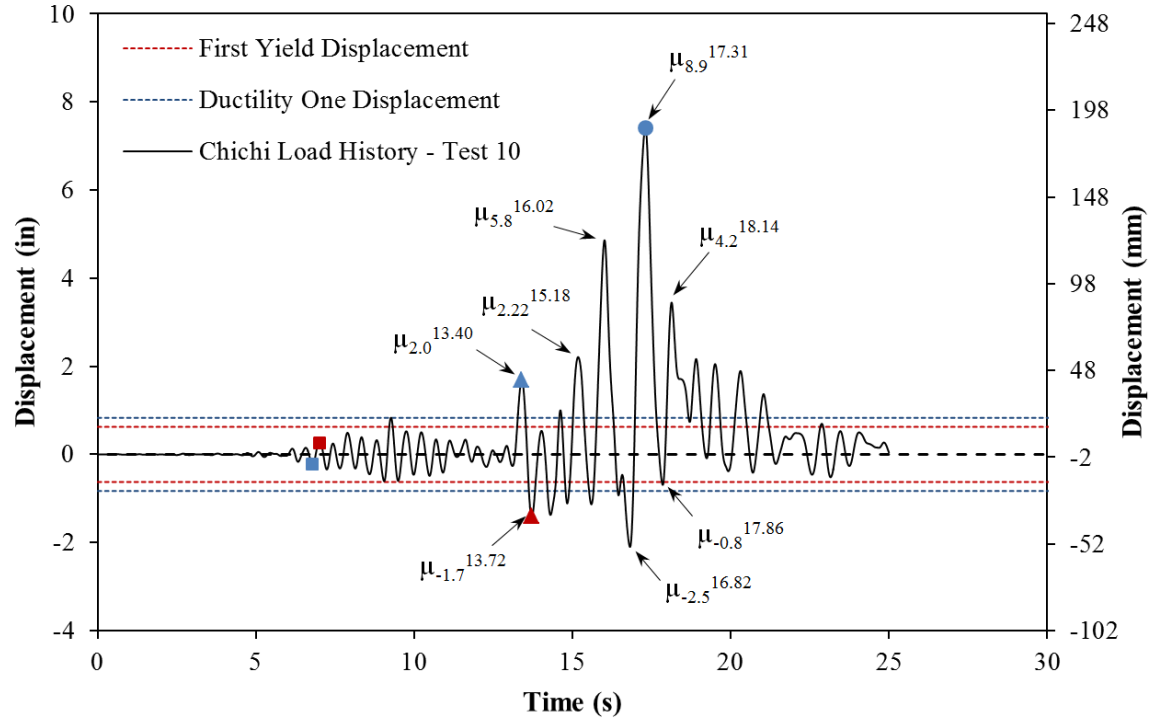

Figure 2-72. Test 10 – Chichi Earthquake Load History

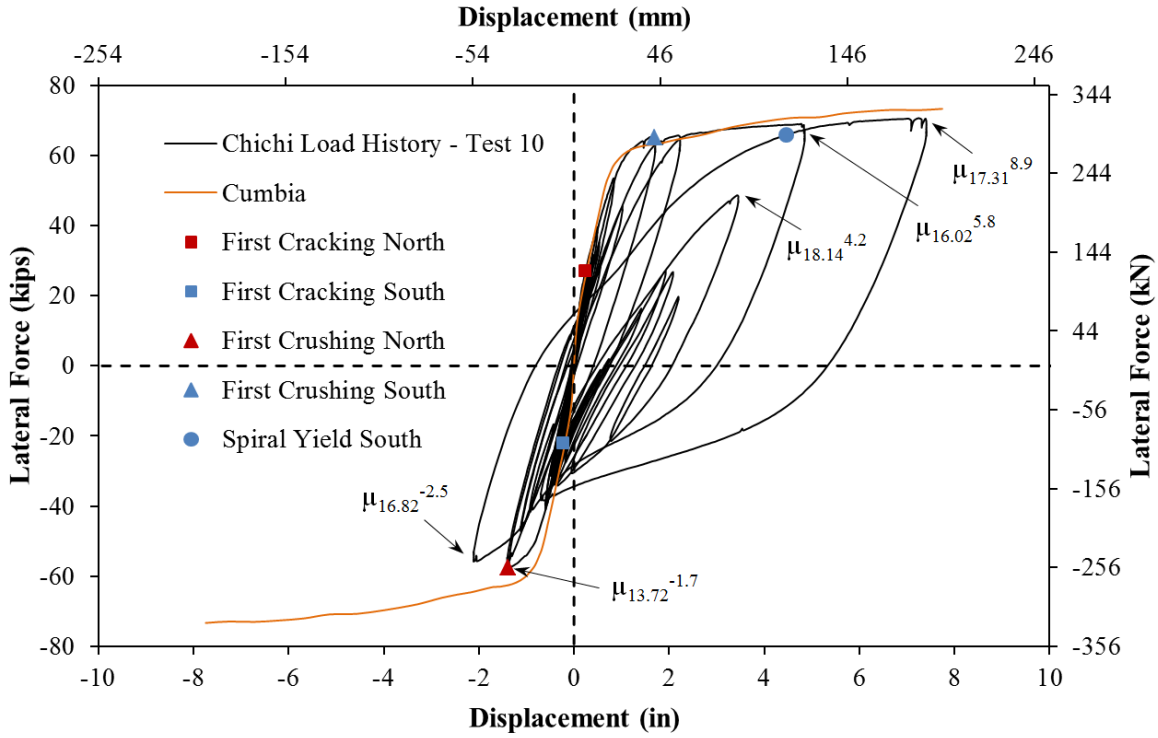

Figure 2-73. Test 10 – Chichi Lateral Force vs. Top Column Displacement Response

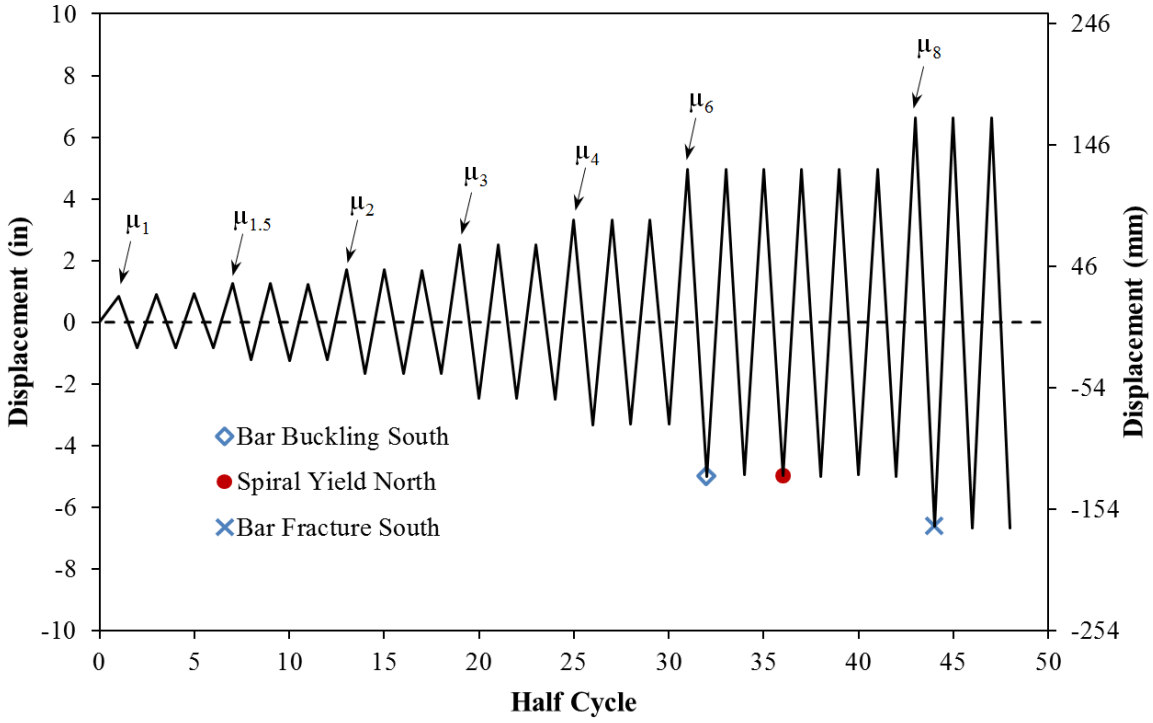

Figure 2-74. Test 10b – Symmetric Three Cycle Set Load History

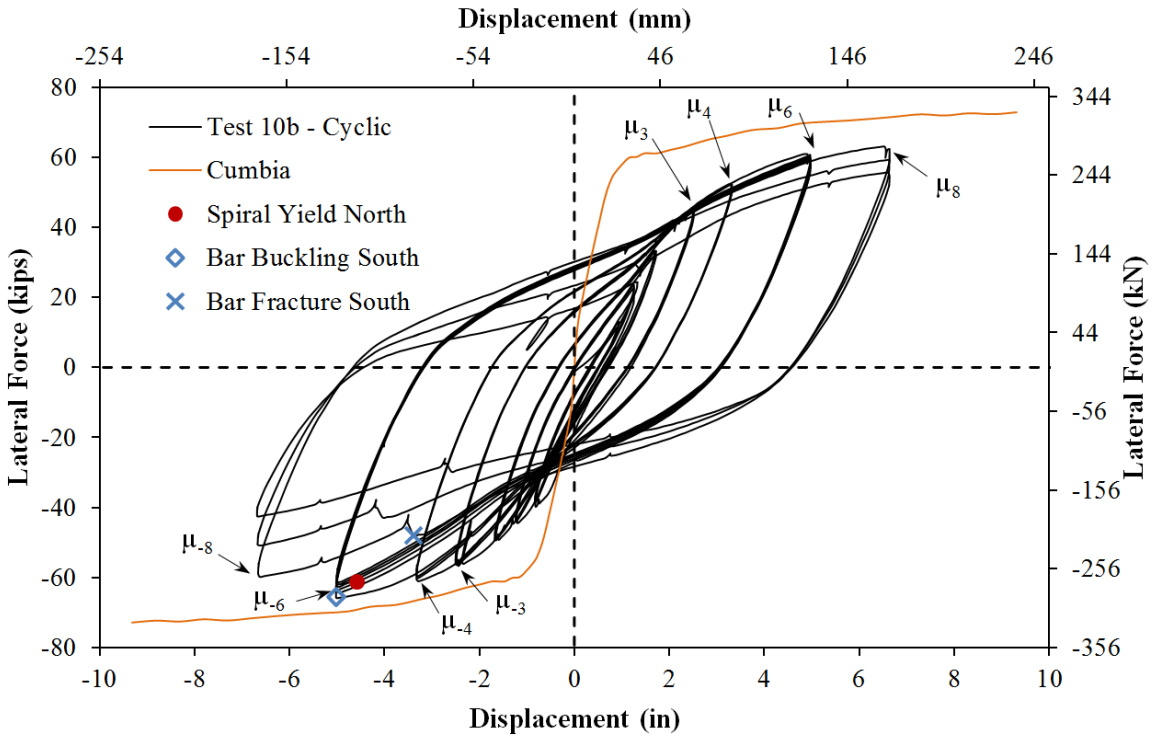

Figure 2-75. Test 10b – Symmetric Three Cycle Set Aftershock Hysteretic Response

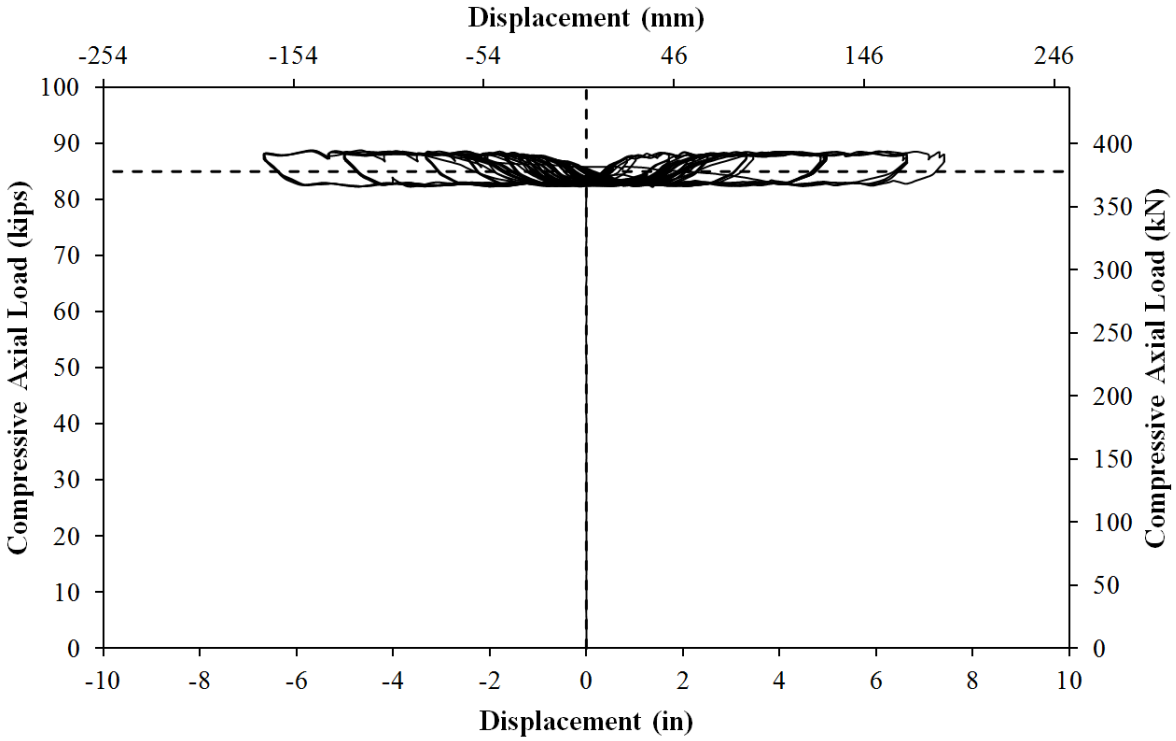

Figure 2-76. Test 10 and 10b – Compressive Axial Load from One Jack (Total = 2*Value)

2.1.3.1. Test 10 Chichi Earthquake Experimental Observations:

To determine possible effects of different load history characteristics on the relationship between strain and displacement, an asymmetric displacement history from the 1999 Chichi Earthquake in Taiwan was used. The Chichi record, see Figure 2-72, produced a one sided response with a displacement ductility demand of 8.9 in one direction of loading and a ductility demand of only 2.5 in the opposing direction. The resulting lateral force vs. top column displacement response appears in Figure 2-73. Buckling did not occur during the Chile or Chichi load histories even though the peak displacements exceeded ductility eight which produced buckling during the symmetric three cycle set load history of Test 9. The purpose of running the Chichi load history was to determine if the asymmetric load history characteristic had an impact on the relationship between strain and displacement. The asymmetric load history produces significantly different tensile demands on the North and South sides of the specimen.

Cracks measuring 0.1mm at approximate 6” spacing on the South side of the specimen first occurred at ($\mu_{-0.3}^{6.80\,sec} = -0.22$"). On the North side of the specimen cracks measuring 0.1mm at approximate 9” spacing where observed at ($\mu_{0.3}^{7.02\,sec} = 0.25$"). The cracks on the North side of the specimen increased to 0.3mm at approximate 8” spacing during ($\mu_{0.6}^{7.90\,sec} = 0.49$"). The cracks on the South side of the specimen increased to 0.3mm at approximate 5” spacing during ($\mu_{-0.7}^{9.06\,sec} = 0.60$"). Crushing of the cover concrete 8” above the footing on the South side of the specimen began during ($\mu_{2.0}^{13.40\,sec} = 1.70$") while cracks on the North side of the specimen measured 1.25mm at approximate 4” spacing. The cover concrete on the North side of the specimen crushed 5” above the footing during ($\mu_{-1.7}^{13.72\,sec} = -1.39$"), as shown in Figure 2-77. The extent of crushing on the South side of the specimen extended 15” above the footing during ($\mu_{2.6}^{15.18\,sec} = 2.20$"). The peak cycle of the load history at ($\mu_{8.9}^{17.31\,sec} = 7.40$"), with a lateral force of 69.98 kips, was completed without

additional visible damage. Subsequent reversals of loading of the Chichi load history failed to produce visible buckling of reinforcement on either side of the specimen. Photos of each side of the specimen after the Chichi record are shown in Figure 2-78.

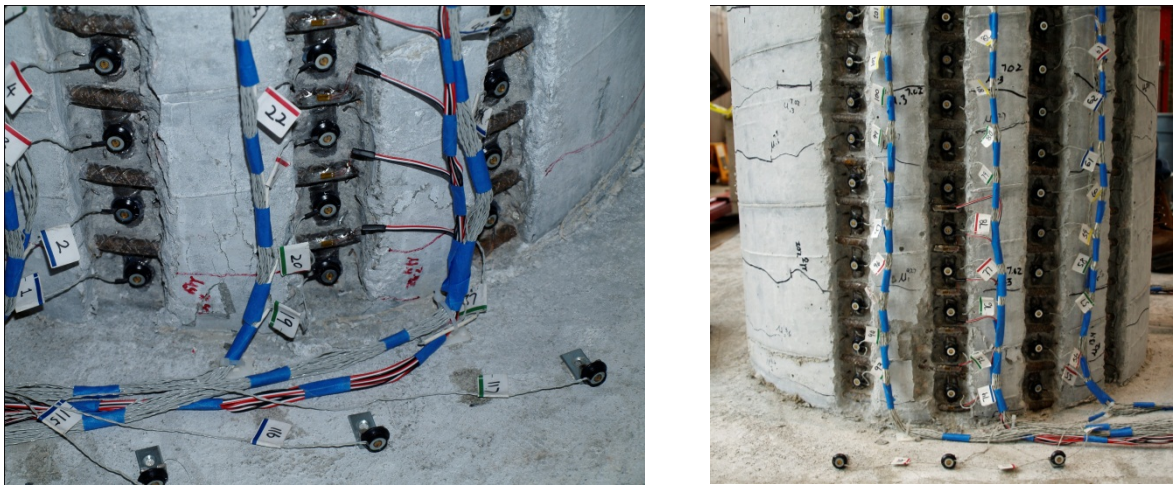

Figure 2-77. Test 10 – (Left) Concrete Crushing of South Side of the Column during ($\mu_{2.0}^{13.40\ sec} = 1.70$") and (Right) Crushing of North Side during ($\mu_{-1.7}^{13.72\ sec} = -1.39$")

Figure 2-78. Test 10 – (Left) South Side of the Specimen after Chichi Record and (Right) North Side of the Specimen Subjected to Low Ductility Demands

2.1.3.2. Test 10 Chichi Earthquake Strain Data:

Due to the random cyclic nature of the Chichi earthquake load history, specific data observation points along the backbone curve of cyclic response were chosen in Figure 2-79. The vertical strain profiles for each extreme fiber bar during push and pull cycles are shown in Figure 2-80 and Figure 2-81. The strain profiles for cycles exceeding displacement ductility three are smoother and are influenced less by individual crack locations. The maximum recorded compression strain in the extreme fiber bar S3 during ($\mu_{8.9}^{17.31\,sec} = 7.40"$) was 0.032 measured 7.64" above the footing. A peak tensile strain of 0.052, centered 4.33" above the footing, was measured on bar N3 during the push cycle to ($\mu_{8.9}^{17.3\,sec1} = 7.40"$). Tests 8, 9, and 10 (Chile 2010, Symmetric three cycle set, and Chichi) were subjected to similar values of peak tensile strain (0.051, 0.053, and 0.052 respectively) at different levels of displacement ductility (8.7, 8, and 8.9 respectively), but buckling only occurred during the symmetric three cycle set load history of Test 9.

The relationship between tensile strain and displacement for North extreme fiber bar N3, centered 4.33" above the footing, appears in Figure 2-82. The Cumbia moment curvature analysis prediction significantly over predicts the tensile strains at higher displacements. The relationship between compressive strain and displacement for extreme fiber bar N3 during significant pull cycles appears in Figure 2-83. The ductility demands in the pull direction after the peak cycle were not large enough to place the North reinforcement back into compression due to the large residual growth strains.

The relationship between compressive strain and displacement, for gage length centered 1.82" above the footing on extreme fiber bar S3, from when the column was vertical to the peak of significant push cycles appears in Figure 2-85. The moment curvature prediction for compressive strains matches the recorded strains well. The graph shows compressive strains over the first gage length above the footing, even though measured strains in the fourth gage length were larger. The recorded strains during the ($\mu_{8.9}^{17.31\,sec} = 7.40"$) push cycle exceed the moment curvature prediction. Strains recorded during later cycles of the load history are similarly under predicted by moment curvature analysis. The relationship between tensile strain and displacement for extreme fiber bar S3 placed into tension during pull cycles appears in Figure 2-84.

2.1.3.3. Test 10 Chichi Earthquake Curvature and Strain Penetration Data:

Vertical curvature profiles obtained for points along the backbone curve of cyclic response during push and pull cycles appear in Figure 2-86 and Figure 2-87 respectively. Linear plastic curvature least squared error lines show that the curvatures are linearly distributed after displacement ductility three when the profiles smooth out. Initial cycles below ductility three are highly influenced by individual crack locations. The base section rotation attributable to strain penetration of reinforcing bars appears in Figure 2-88 and Figure 2-89 for push and pull cycles respectively. The total deformation calculated by integrating the measured curvature profiles and extrapolating the base section rotation to the center of loading appear in Figure 2-90. The integrated curvatures match well throughout the entire range of displacements.

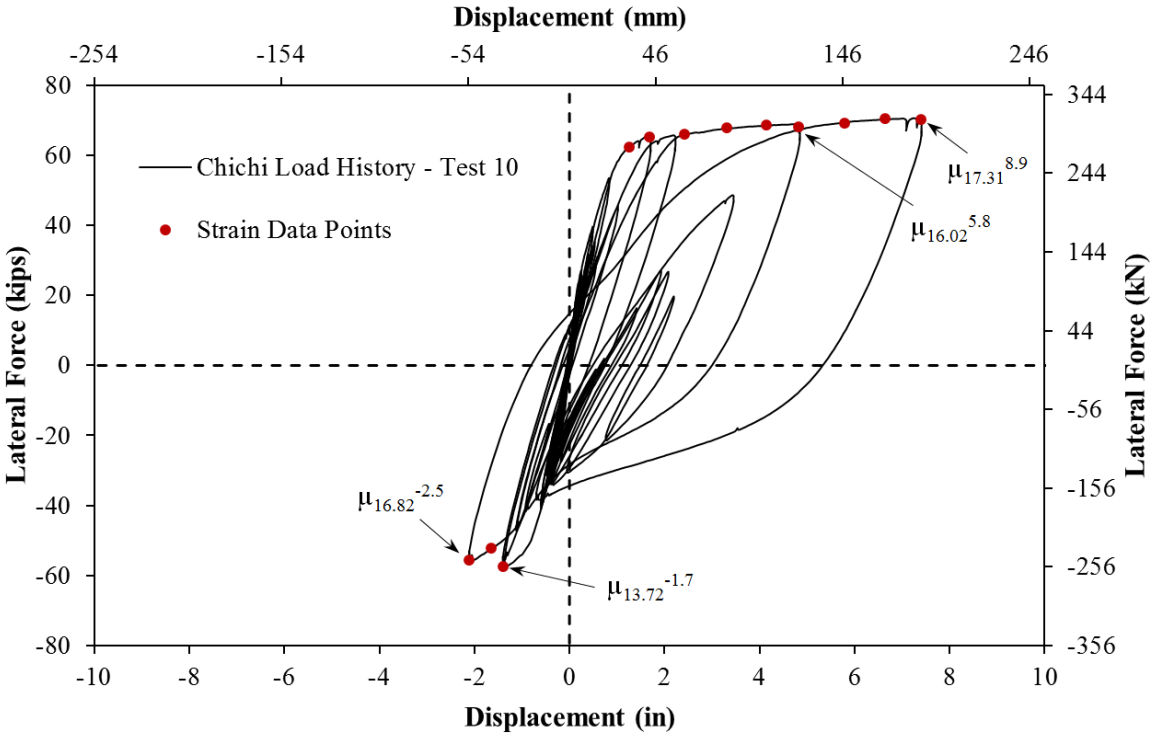

Figure 2-79. Test 10 – Strain Data Observation Points along the Backbone Curve

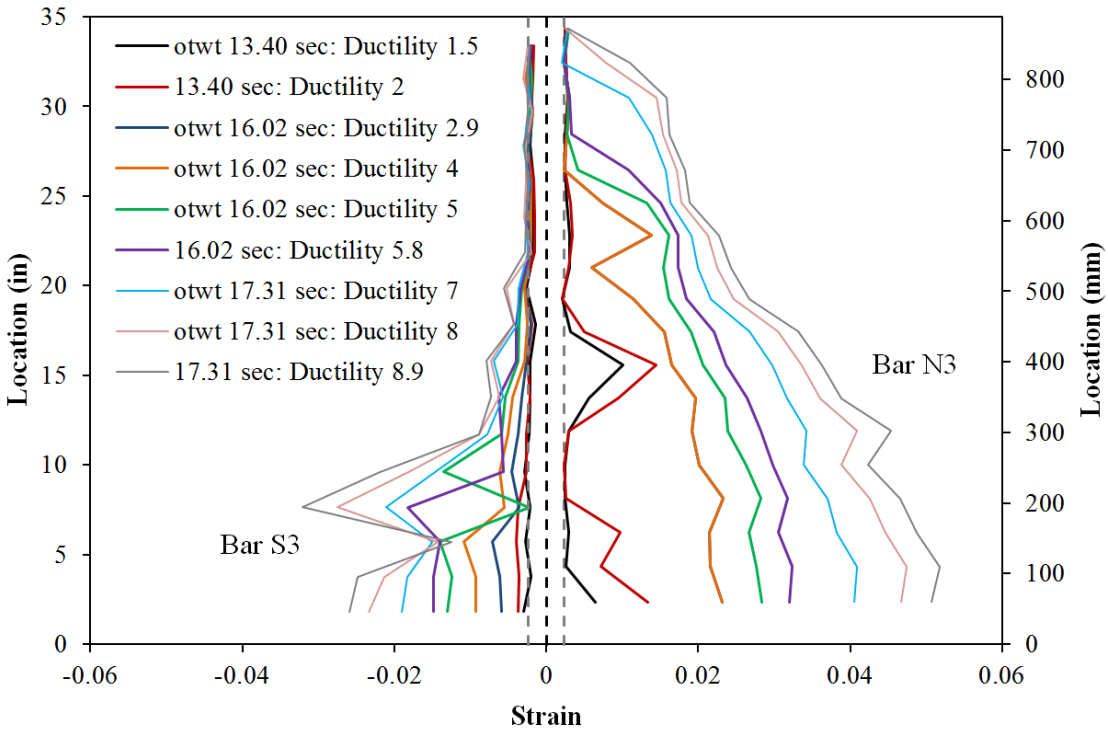

Figure 2-80. Test 10 – Extreme Fiber Vertical Strain Profiles During Push Cycles

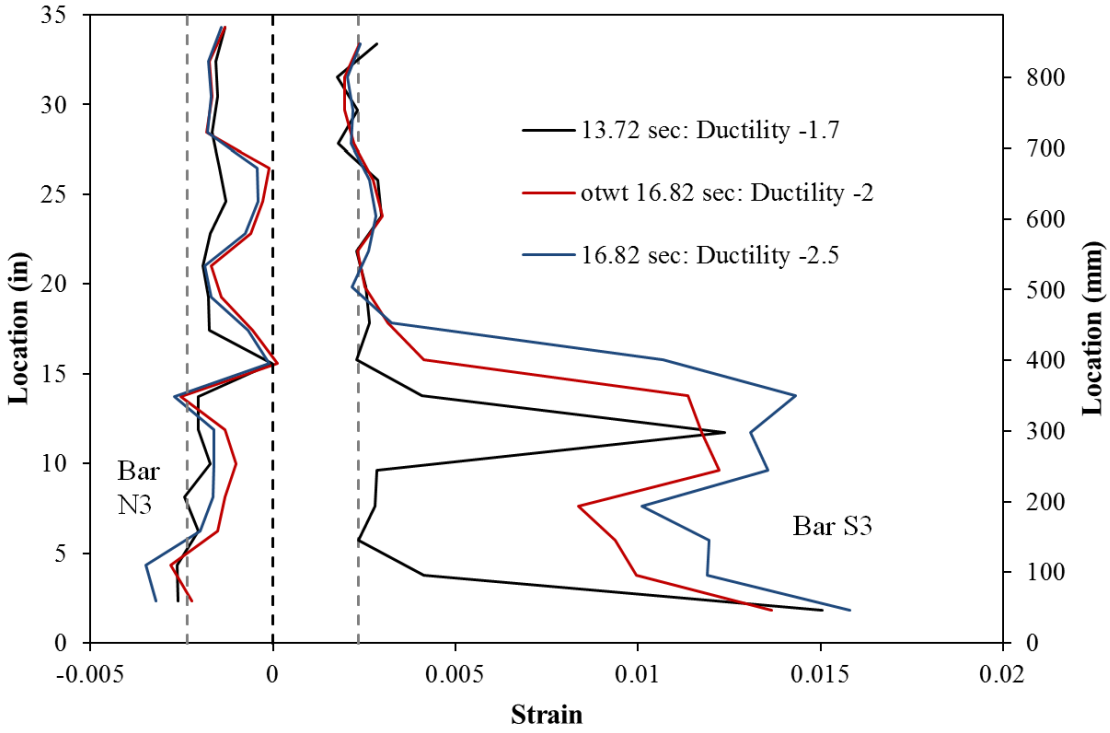

Figure 2-81. Test 10 – Extreme Fiber Vertical Strain Profiles During Pull Cycles

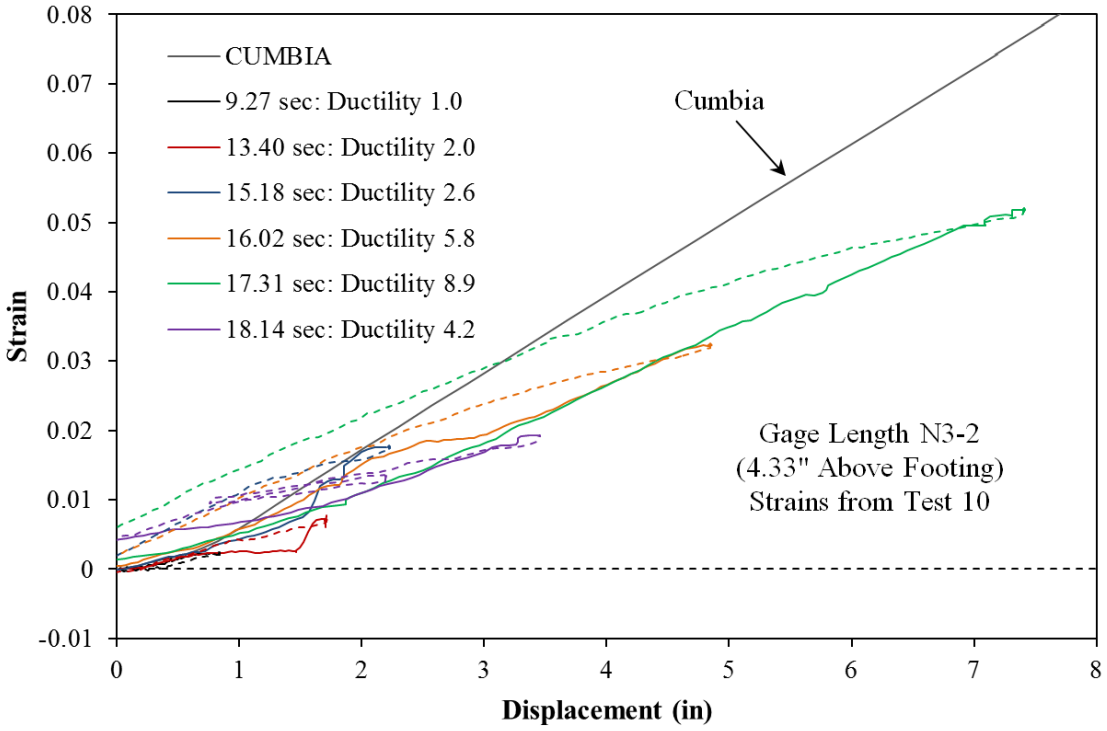

Figure 2-82. Test 10 – Strain and Displacement for Bar N3 during Push Cycles, with the Cumbia Moment Curvature Prediction

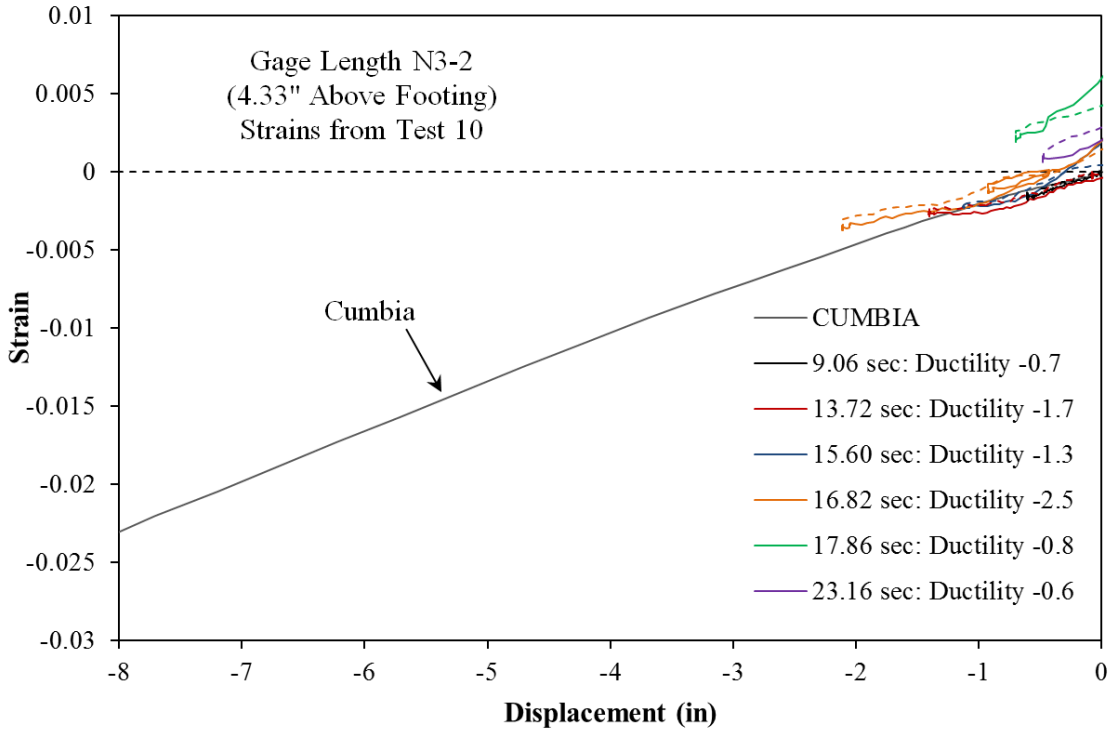

Figure 2-83. Test 10 – Strain and Displacement for Bar N3 during Pull Cycles

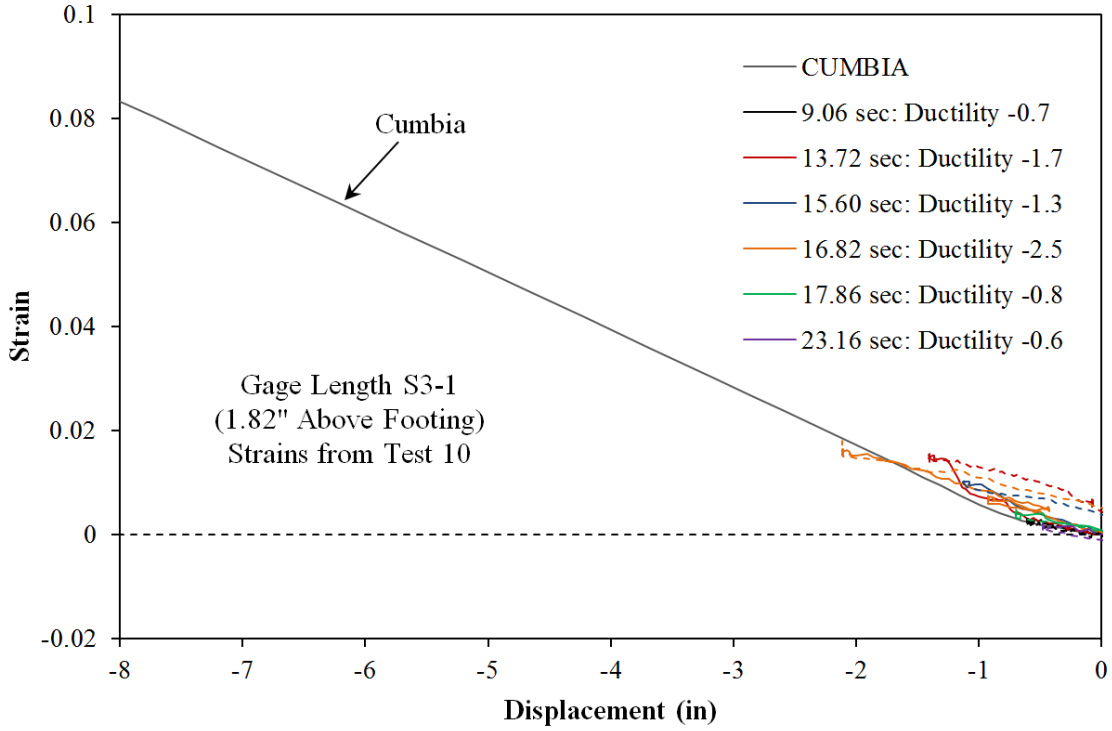

Figure 2-84. Test 10 – Strain and Displacement for Bar S3 during Pull Cycles

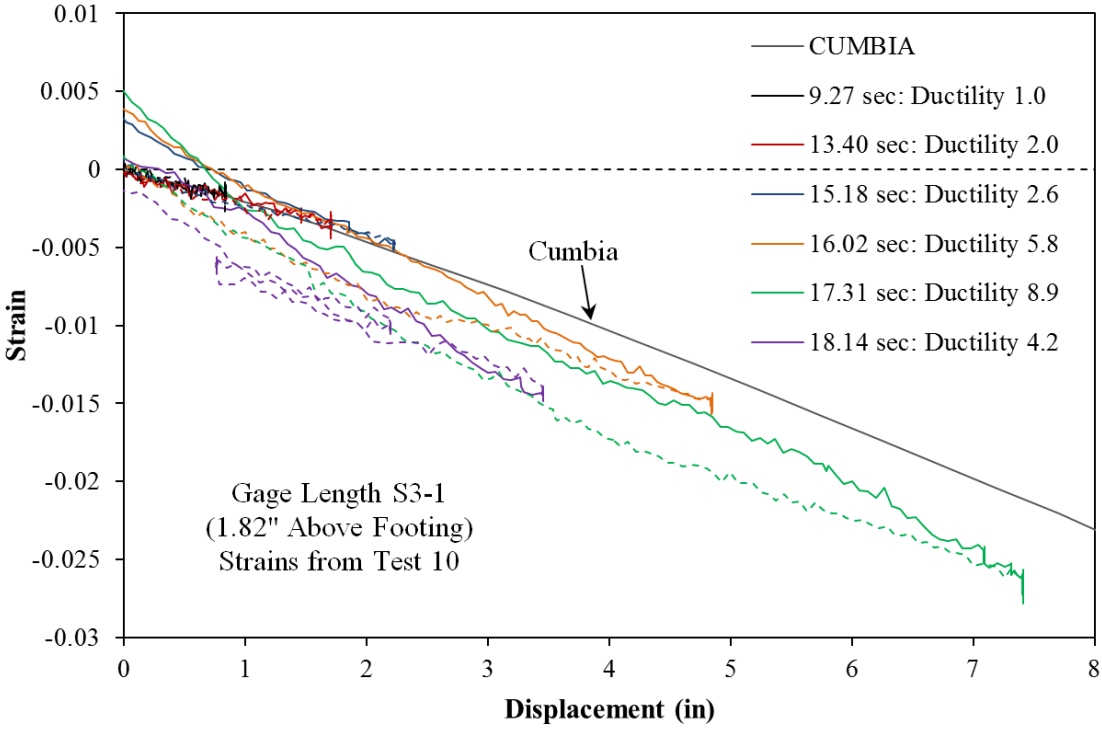

Figure 2-85. Test 10 – Strain and Displacement for Bar S3 during Push Cycles

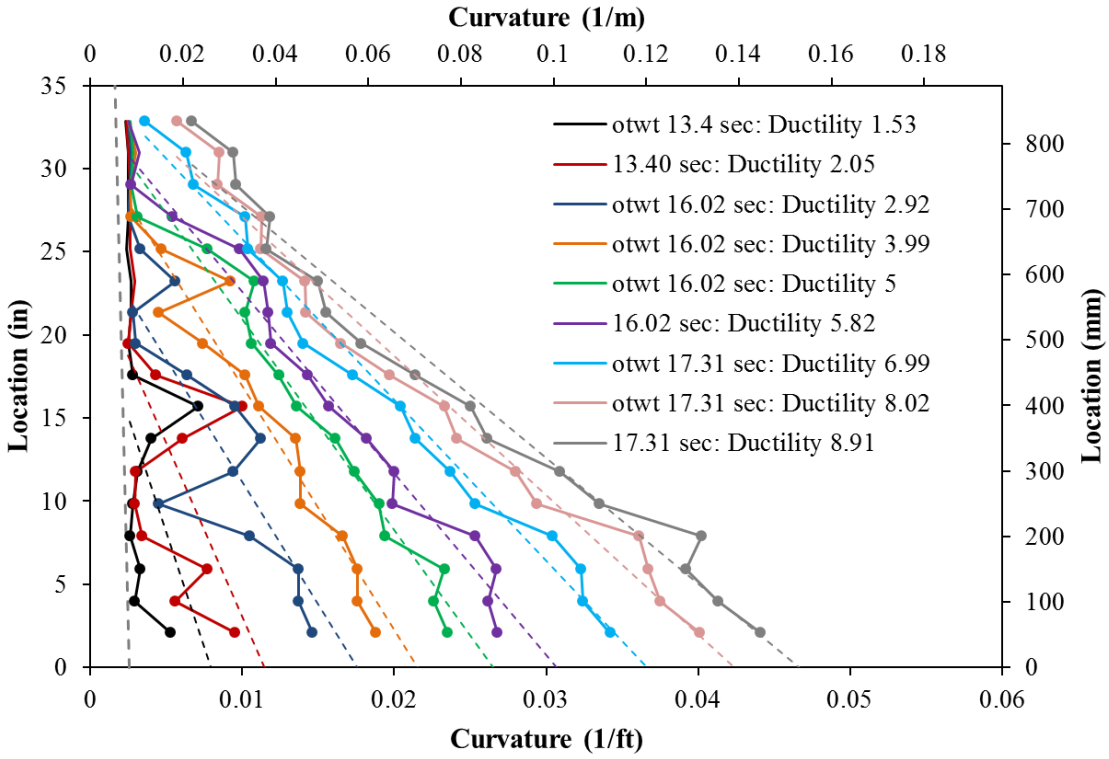

Figure 2-86. Test 10 – Vertical Curvature Profiles during Push Cycles

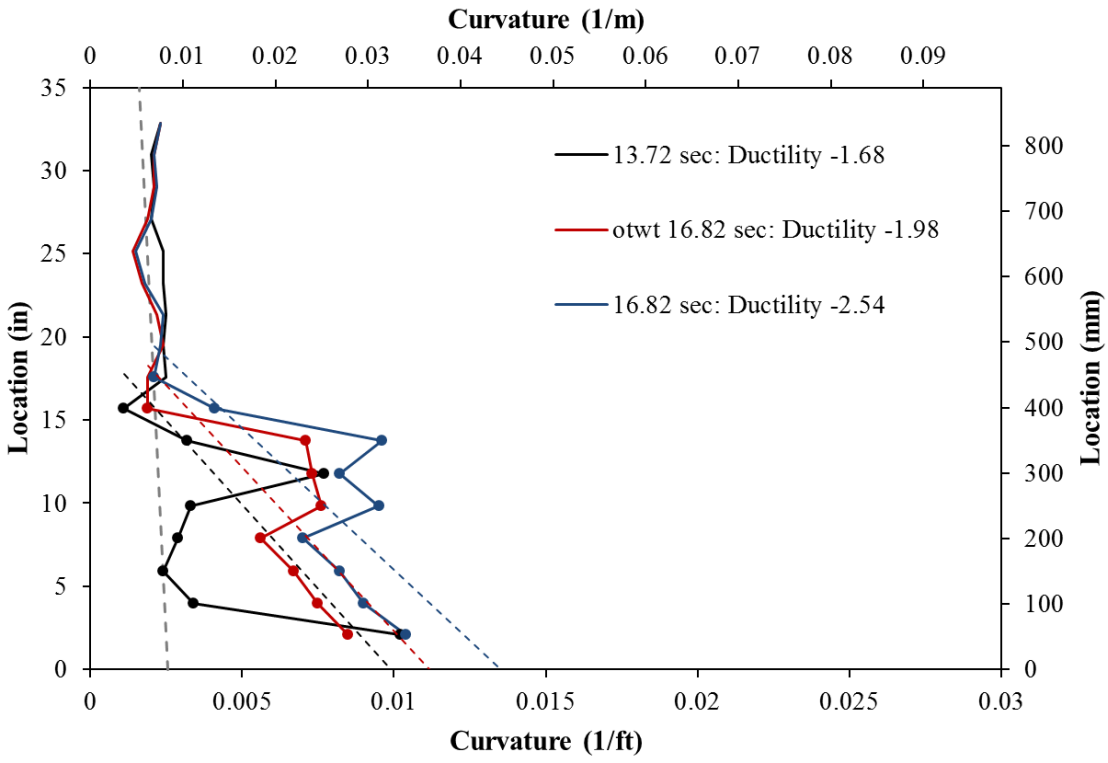

Figure 2-87. Test 10 – Vertical Curvature Profiles during Pull Cycles

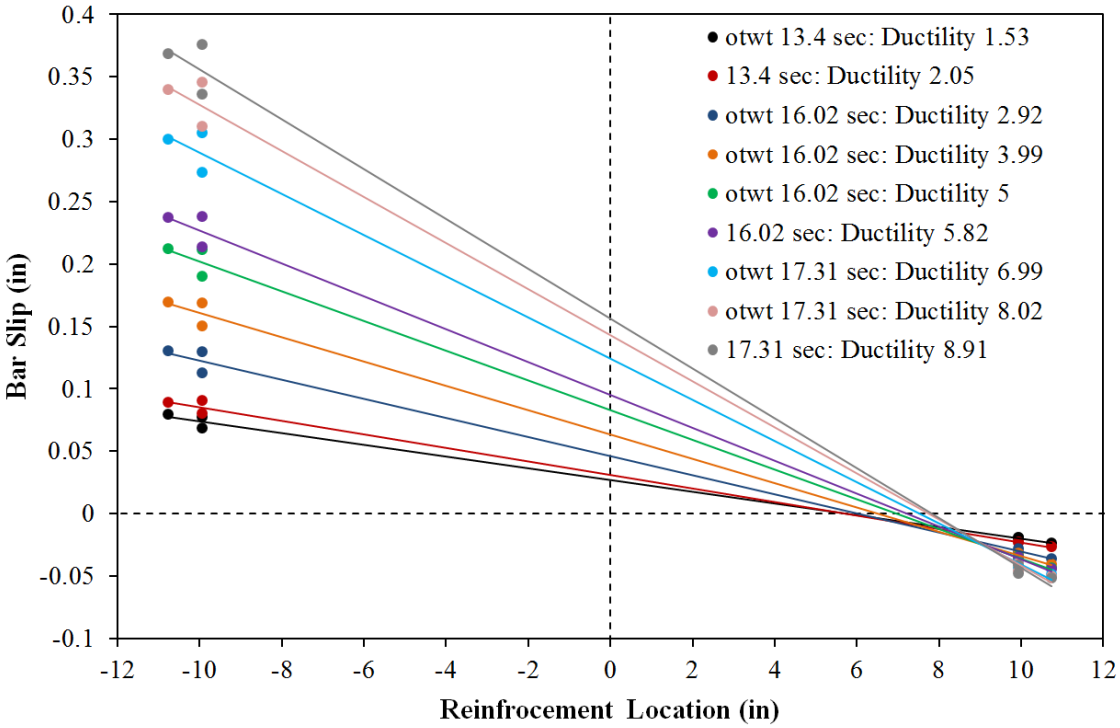

Figure 2-88. Test 10 – Base Section Rotation due to Strain Penetration during Push Cycles

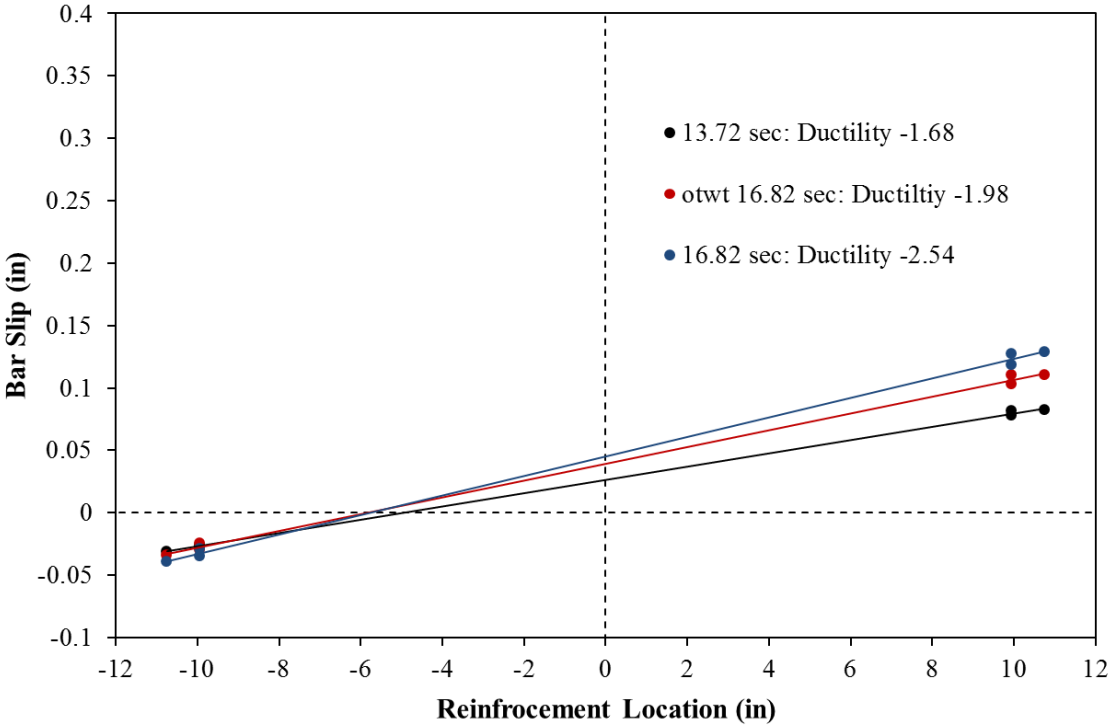

Figure 2-89. Test 10 – Base Section Rotation due to Strain Penetration during Pull Cycles

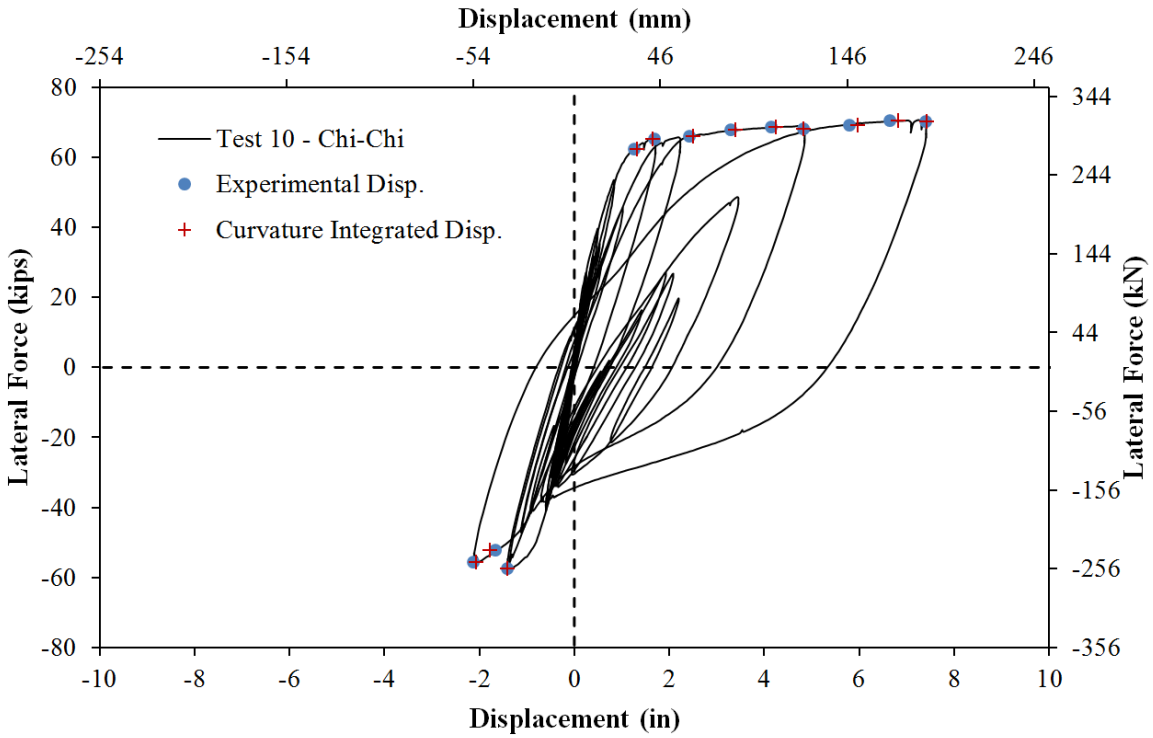

Figure 2-90. Test 10 – Comparison of Measured and Optotrak Integrated Displacements

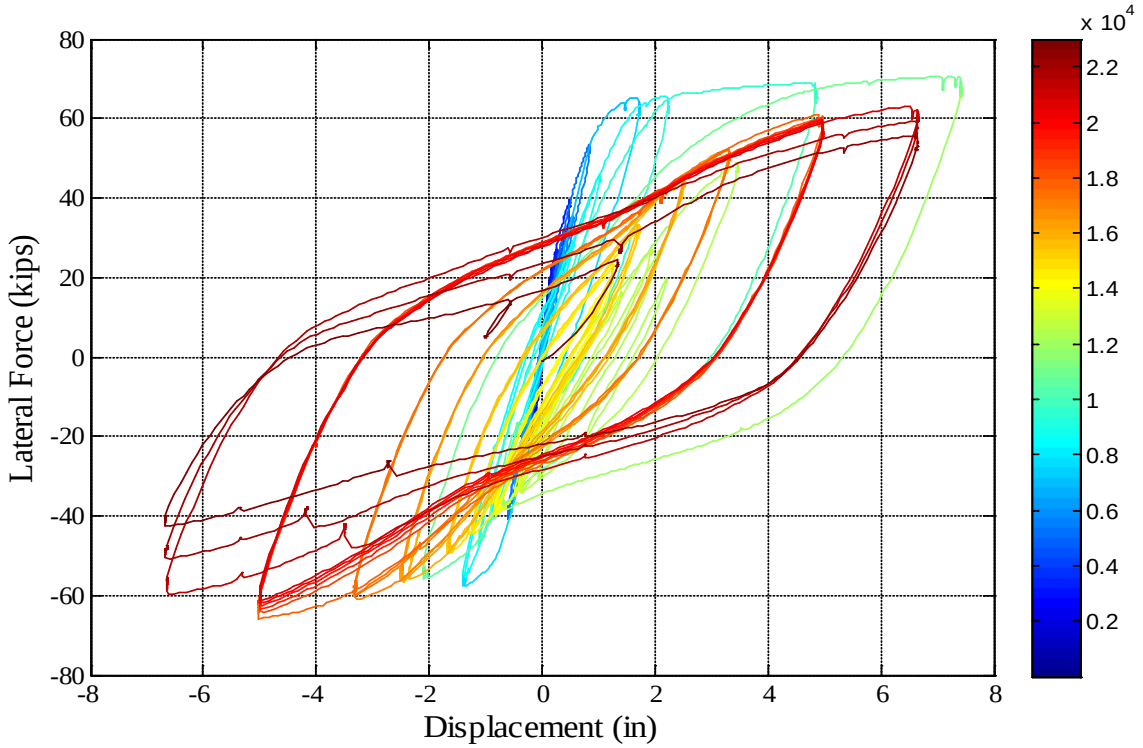

Figure 2-91. Test 10 and 10b – Complete Hysteretic Response with an Elapsed Time Color Bar

2.1.3.4. Test 10b Symmetric Three Cycle Set Aftershock Experimental Observations:

Since buckling did not occur during the Chichi load history, a second symmetric three cycle set load history was conducted on the specimen with degraded stiffness but no losses in strength, similar to Test 8b conducted after the Chilean load history. The extreme fiber South reinforcement bar S3 buckled after reversal from ($\mu_6^{-1} = -5.01$"). Due to the asymmetric nature of the Chichi load history, the South side of the specimen was subjected to low tensile demands but high compressive demands during the peak displacement cycle to ($\mu_{8.9}^{17.31} = 7.40$"). The purpose of the cyclic aftershock study shifted to determine if continued cycling at ductility six would rupture the previously buckled South reinforcement. After reversal from ($\mu_6^{-3} = -4.98$"), bar S2 buckled as shown in Figure 2-92. Six complete cycles of ductility six where completed without rupturing previously buckled reinforcement on the South side of the specimen, so the load history continued to ductility eight as shown in Figure 2-74. As the load history progressed, visible deterioration of the core concrete on the South side of the specimen over the buckled region occurred due to loss of confinement, which is evident in the left photo in Figure 2-93 taken at ($\mu_8^{+1} = 6.64$").

Additionally, South reinforcement bar S4 buckled during ($\mu_8^{+1} = 6.64$"). Previously buckled reinforcing bar S3 ruptured during ($\mu_8^{-1} = -6.63$"). Bar S1 buckled during the ($\mu_8^{+2} = 6.62$") and previously buckled Bar S2 ruptured during ($\mu_8^{-2} = -6.67$"). During the ($\mu_8^{+3} = 6.63$"), the fifth reinforcing bar on the South side of the specimen buckled. Previously buckled reinforcing bar S4 ruptured during ($\mu_8^{-3} = -6.67$"). . The test was concluded with five buckled bars on the South side of the specimen and intact reinforcing bars on the North side of the specimen, see Figure 2-93 and Figure 2-94 for photos of South and North sides of the specimen after testing.

The complete hysteretic response for Tests 10 and 10b is shown in Figure 2-91 with an elapsed time color bar to track the progression of the response through both load histories. Buckling of multiple bars during ductility six produced minimal losses in strength during pull cycles when previously buckled reinforcement was placed into tension while push cycles of ductility six did not suffer from losses in strength. During each pull cycle of ductility eight, a previously buckled bar on the South side of the specimen ruptured leading to losses of strength in both the push and pull directions of loading. When the response from Test 10b is compared to the moment curvature prediction, in Figure 2-75, it is clear that there is a larger amount of stiffness degradation at lower ductility cycles in the push direction of loading due to the original asymmetric Chichi load history. The hysteretic response for Tests 9 and 10b are shown in Figure 2-95, and the response for Tests 8b and 10b are compared in Figure 2-96. The hysteretic response for Tests 8b and 10b are similar up to ductility six except test 10b has larger forces in the pull direction due to lower stiffness degradation during the asymmetric Chichi load history compared to the symmetric Chile load history of Test 8.

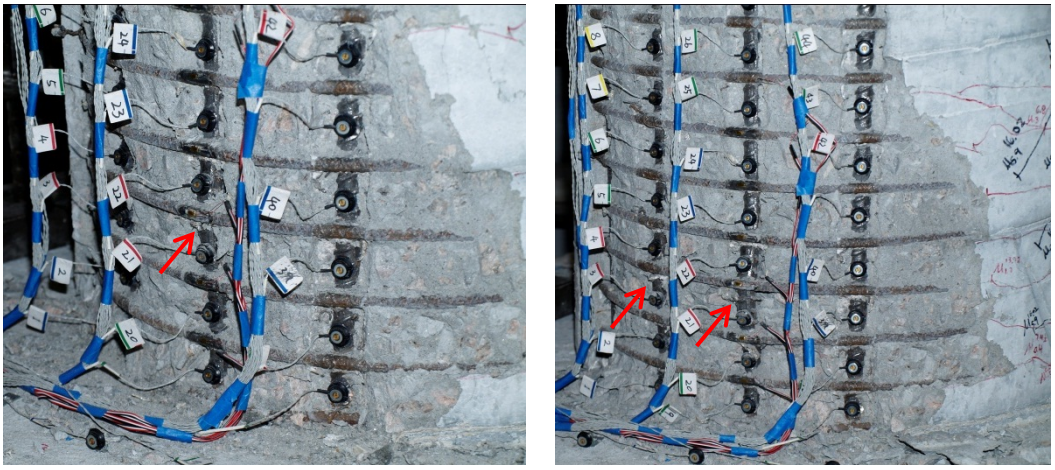

Figure 2-92. Test 10b – (Left) Buckling of Bar S3 after Reversal from ($\mu_6^{-1} = -5.01$") and (Right) Buckling of S2 after Reversal from ($\mu_6^{-3} = -4.98$")

Figure 2-93. Test 10b – (Left) South Side of the Column during ($\mu_8^{+1} = 6.64$") and (Right) South Side of the Column at the End of the Test (Five Buckled and Three Ruptured Bars)

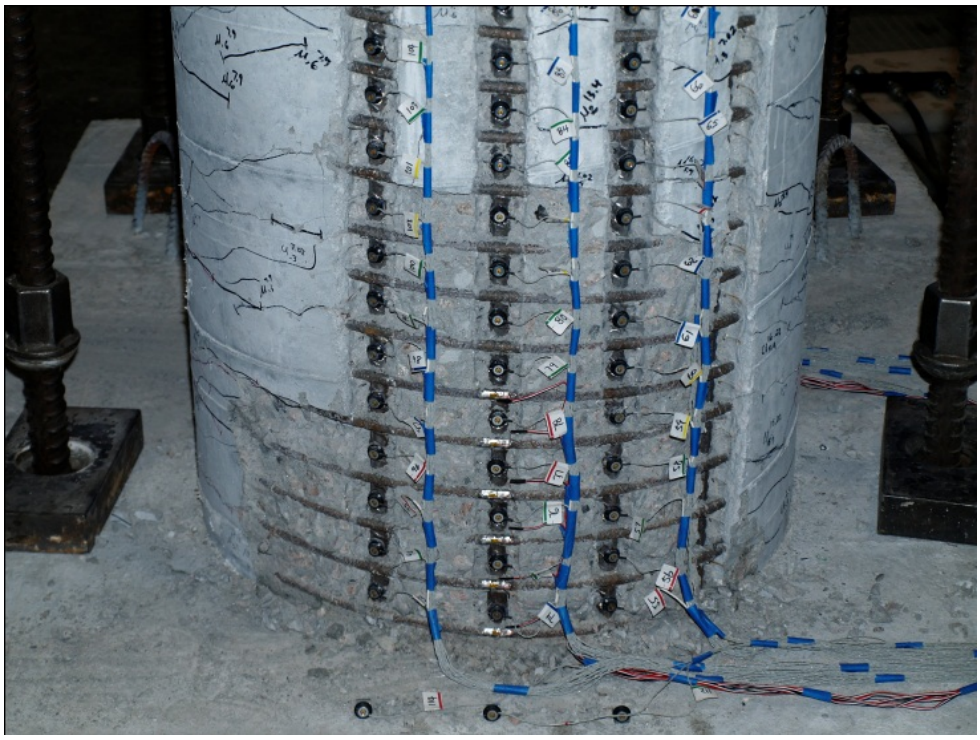

Figure 2-94. Test 10b – North Side of the Column after the Test was concluded with Intact Reinforcement

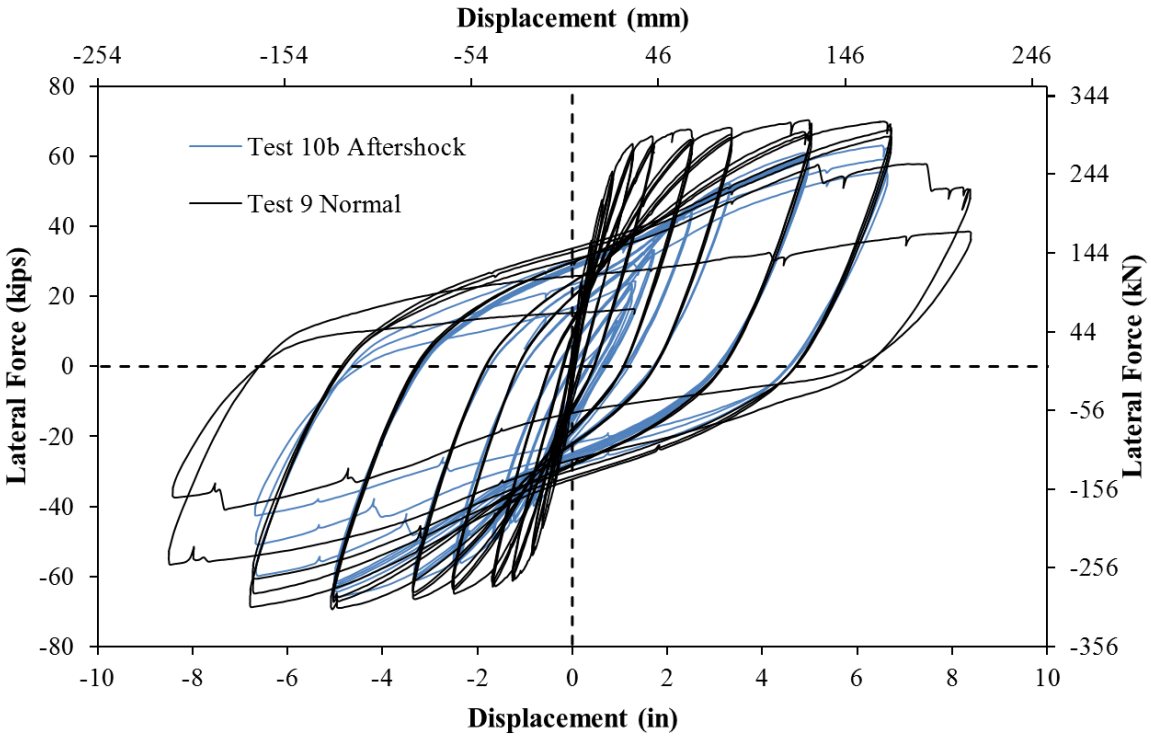

Figure 2-95. Test 10b Cyclic Aftershock and Test 9 Hysteretic Response Comparison

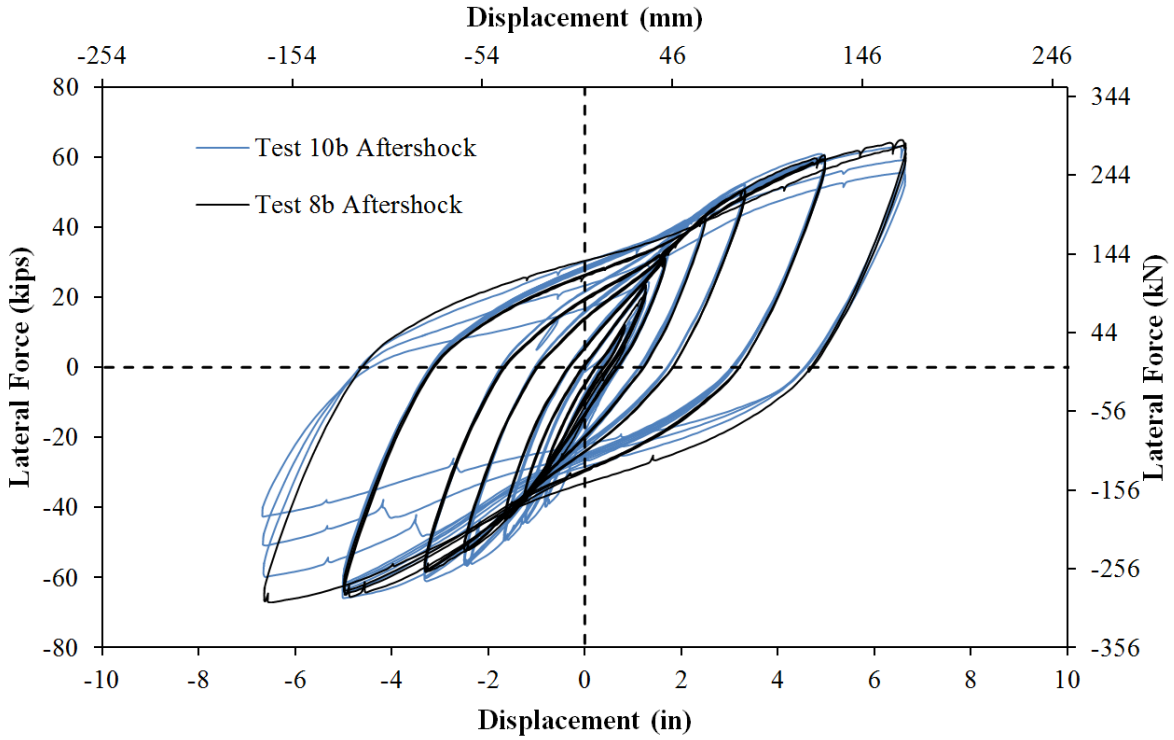

Figure 2-96. Test 10b and 8b Cyclic Aftershock Hysteretic Response Comparison

2.1.3.5. Test 10b Symmetric Three Cycle Set Aftershock Strain Data:

South Reinforcement:

The extreme fiber vertical strain profiles for push and pull cycles of the cyclic aftershock load history are shown in Figure 2-97 and Figure 2-98 respectively. The compressive vertical strain profiles for Bar S3, left half of Figure 2-97, indicate a large amount of measurable deformation prior to visible buckling occurred after reversal from ($\mu_6^{-1} = -5.01$"). Tensile strain measurements for the third gage length above the footing with large compression strains recorded over adjacent gage lengths above and below indicate outward deformation of the reinforcement. Visually, this is supported by the left photo in Figure 2-92 that shows outward deformation over the third gage length when visible buckling was observed during the second push cycle of ductility six. The vertical strain profile shows that measurable deformation over second, third, and fourth gage lengths were recorded over the entire cyclic aftershock test. The measured deformation increased during the fourth ductility level before visible buckling was observed. Once outward deformation of the longitudinal steel occurs, the magnitude of recorded strains is no longer representative of engineering strain. Instead, the vertical strain profiles are shown until visible buckling to highlight the location and propagation of damage.

The complete strain hysteresis for South extreme fiber bar S3 for the gage length centered 5.72" above the footing for Tests 10 and 10b appear in Figure 2-101. This particular gage length captures the outwards deformation of the buckled bar which increases the distance between target markers. The strain hysteresis shows the peak cycle of the Chichi load history with bar S3 in compression, and upon reversal many small ductility cycles failed to place the gage length back into large compression due to the effects of small deformation prior to visible buckling. The recorded strains over the South reinforcement gage length should be in compression after reversal from pull cycles; instead the strain

increases as the column is pushed due to the outward deformation. The opposite phenomenon was observed over adjacent gage lengths where increasing compression strains were observed at locations where the bar begins to straighten back out. The final push cycle in Figure 2-101 represents the push to ($\mu_6^{+2} = 4.97"$) when visible buckling occurred. The recorded data at this stage of the strain hysteresis is affected by measurable deformations prior to buckling.

The strain gage hysteresis for the transverse steel layer overlaying the portion of the extreme fiber South reinforcing bar that later buckled outwards appears in Figure 2-102. After reversal from the peak cycle, the transverse steel maintained a large residual strain over 0.01, even during low ductility cycles. The increased residual strain in the transverse steel affects the column behavior in two distinct ways: (1) Inelastic strains in the transverse steel decrease its effectiveness as a boundary condition restraining buckling of the longitudinal steel explains small measurable deformation prior to visible buckling, and (2) Large residual strains in the transverse steel result in reduced confinement of the core concrete which concentrates further damage at that location. Presumably, if the effectiveness of the transverse steel in confining the core concrete was reduced, repeated cycles could lead to deterioration of the core concrete in the localized region critical to reinforcement buckling. If even small regions of the confined core were to crush, the effect of this crushing is analogous to increasing the demand on the longitudinal steel while cracks are closing since the longitudinal steel would be required to maintain compression zone stability until portions of the core concrete were engaged at potentially greater displacements.

North Reinforcement:

The tensile and compressive vertical strain profiles for extreme fiber bar N3 during push and pull cycles appear in Figure 2-97 and Figure 2-98 respectively. A peak tensile strain of 0.048 was measured 4.33" above the footing on bar N3 during ($\mu_8^{+3} = 6.63"$). This value is lower than the peak tensile strain of 0.052 measured over the same gage length during the original Chichi record at ($\mu_{8.9}^{17.31\,sec} = 7.40"$). Initial strain profiles at low ductility levels are strongly influenced by residual tension strains from previous high ductility cycles during the Chichi record. The compression strains for bar N3 up to ductility six follow the same trend with increasing strain at greater displacements with no sign of measurable deformation.

The complete strain hysteresis for extreme fiber North reinforcing bar N3 appears in Figure 2-99 with an elapsed time color bar to follow the test progression. Since the North reinforcement did not buckled during either load history, stable hysteretic loops were observed for the gage length centered 4.33" above the footing. The transverse steel strain gage hysteresis for the spiral layer which experienced the highest tensile strains overlaying the North un-buckled region appears in Figure 2-100. Large transverse steel strains were not recorded until displacement ductility eight of the cyclic aftershock study.

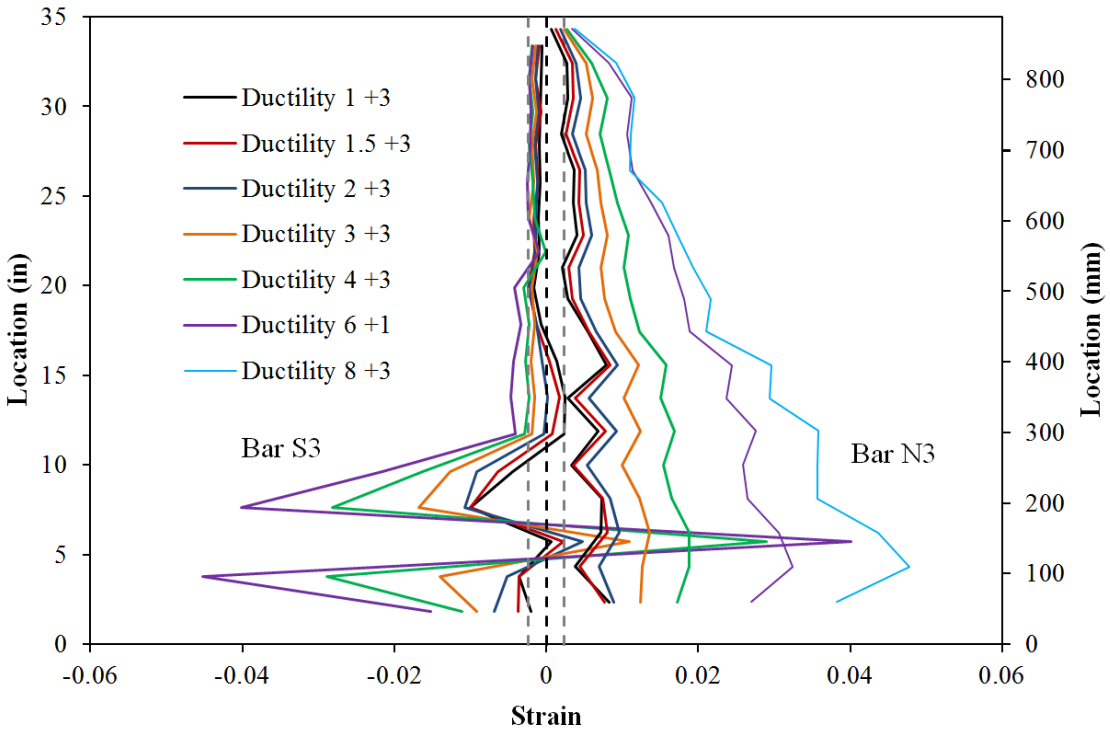

Figure 2-97. Test 10b – Extreme Fiber Vertical Strain Profiles during Push Cycles (Significant Measurable Deformation in Bar S3)

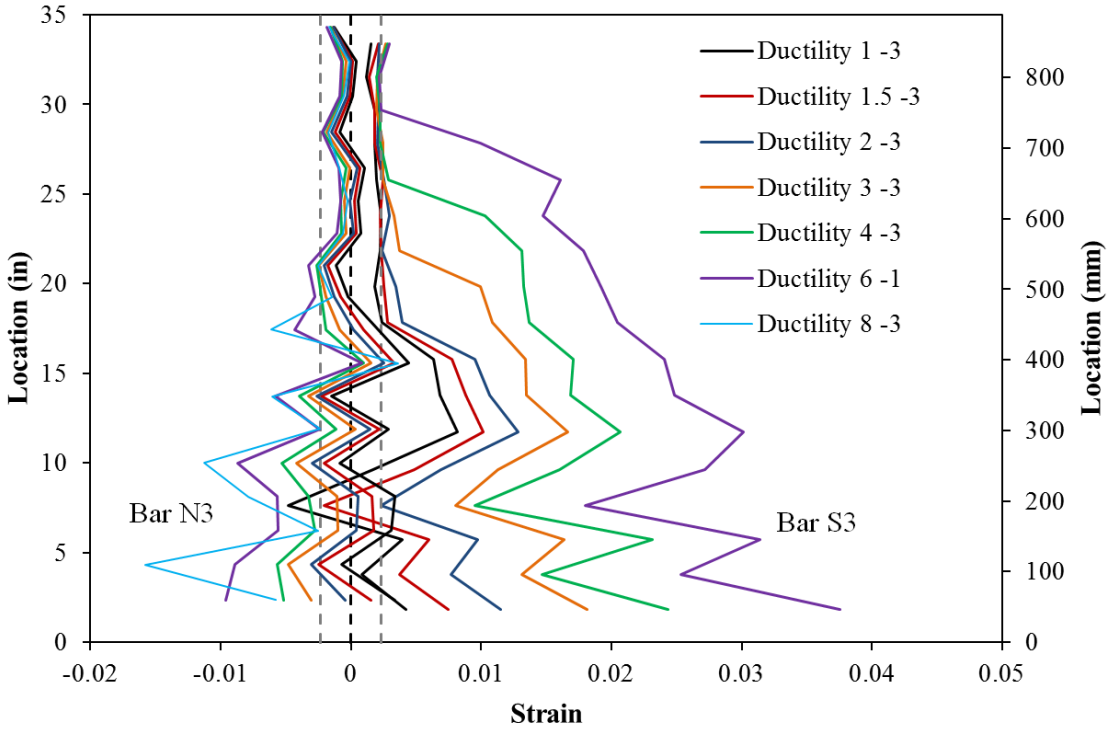

Figure 2-98. Test 10b – Extreme Fiber Vertical Strain Profiles during Pull Cycles

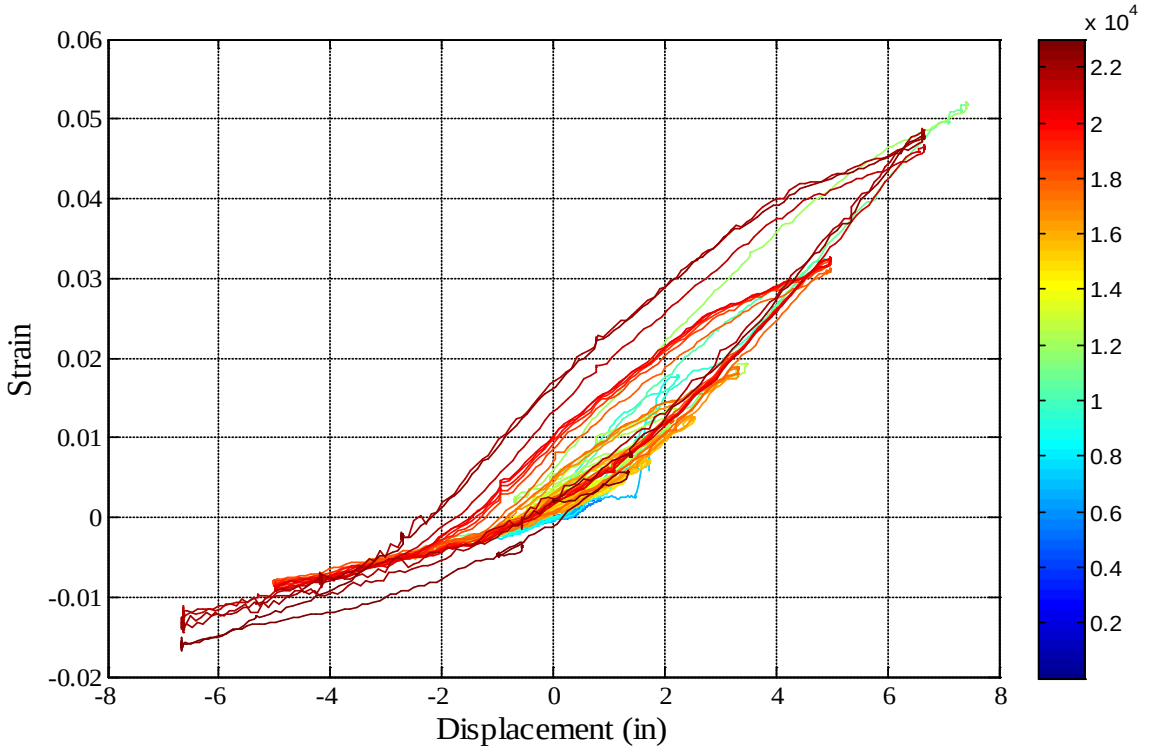

Figure 2-99. Test 10 and 10b – Bar N3 Strain Hysteresis for Gage Length (4.33" Above)

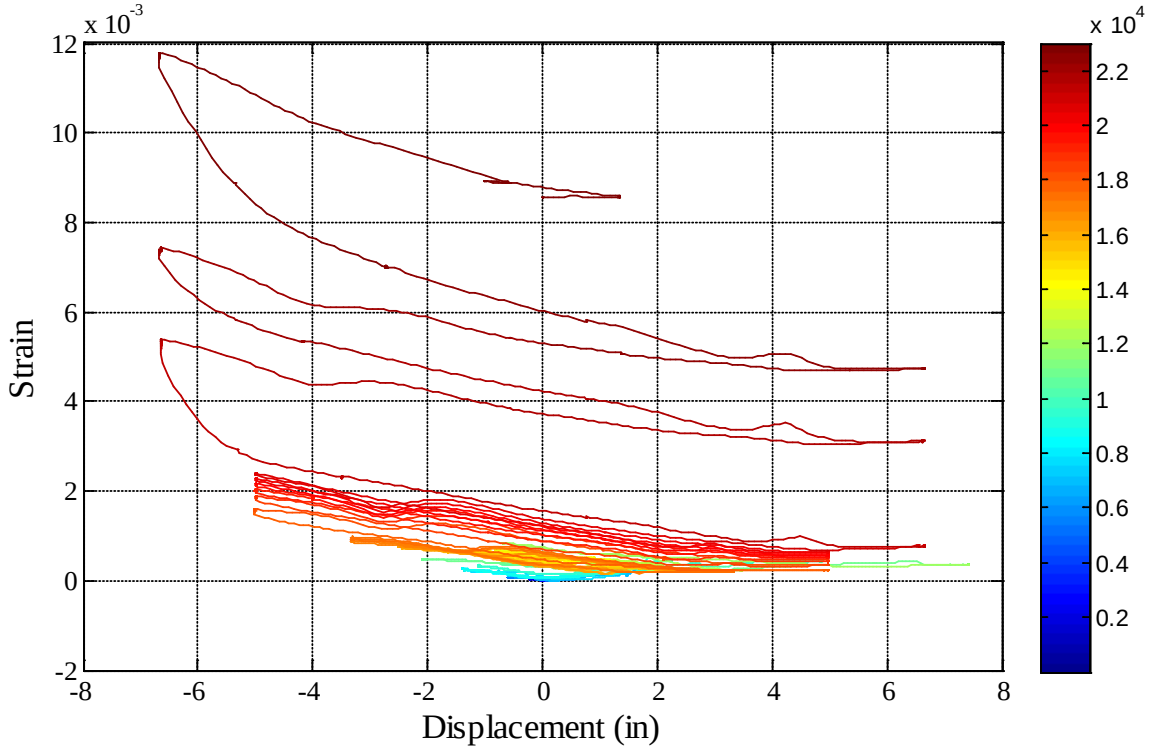

Figure 2-100. Test 10 and 10b – Transverse Steel Strain Gage Hysteresis over North "Unbuckled" Region

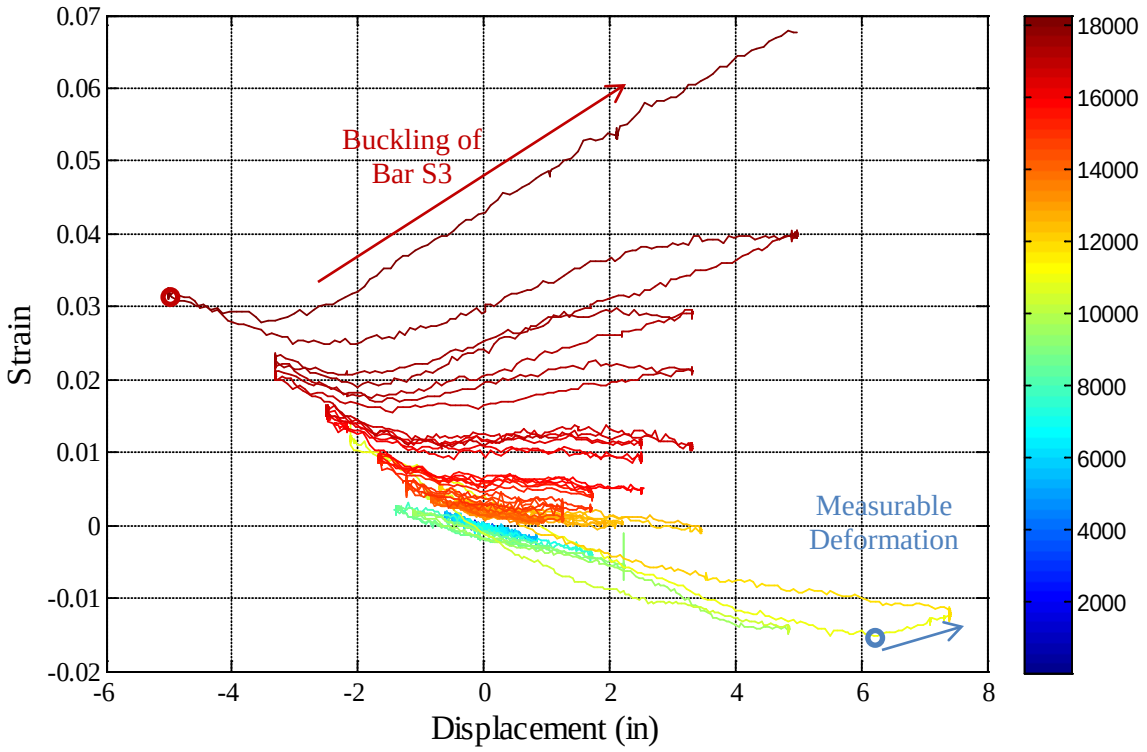

Figure 2-101. Test 10 and 10b – Bar S3 Strain Hysteresis for Gage Length (5.72" Above)

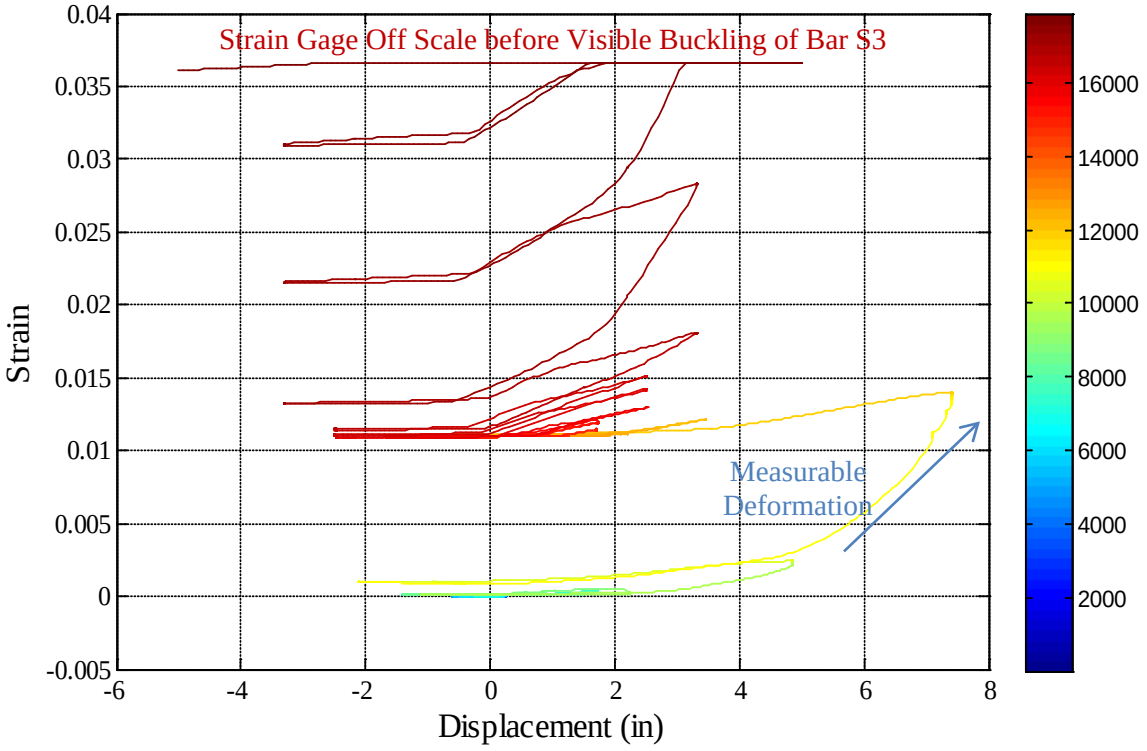

Figure 2-102. Test 10 and 10b – Spiral Strain Gage Hysteresis over South Buckled Region

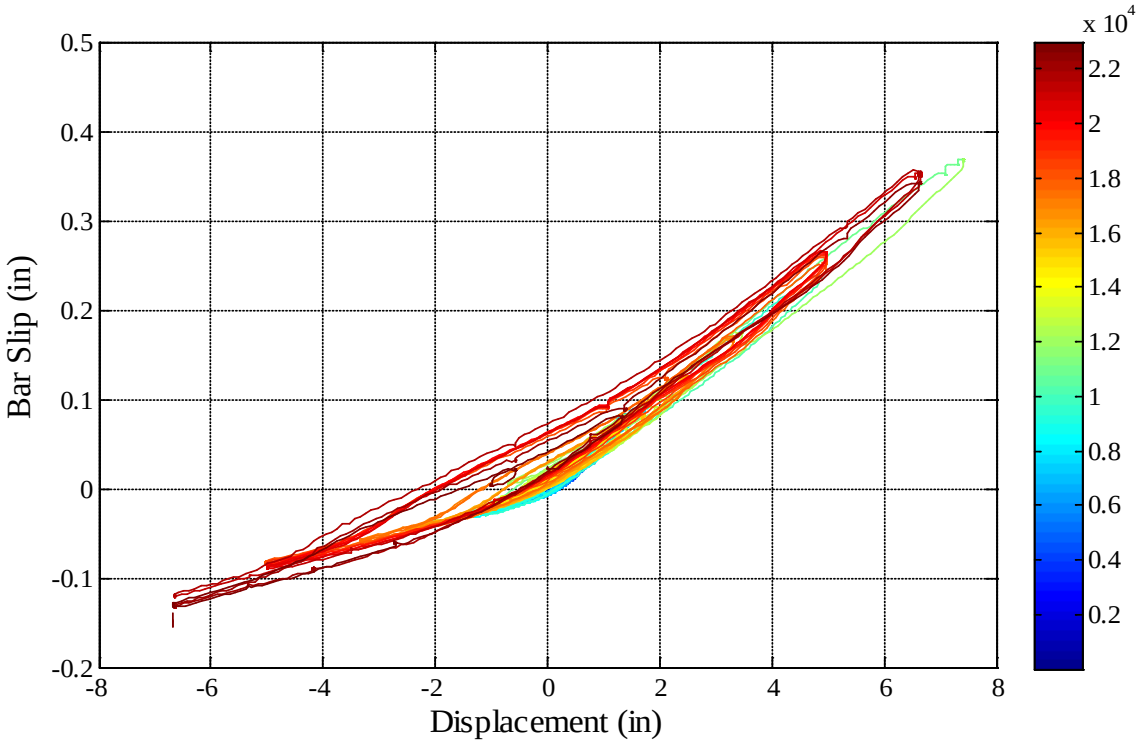

Figure 2-103. Test 10 and 10b – Bar N3 Base Section Slip Hysteresis due to Strain Penetration into the Footing

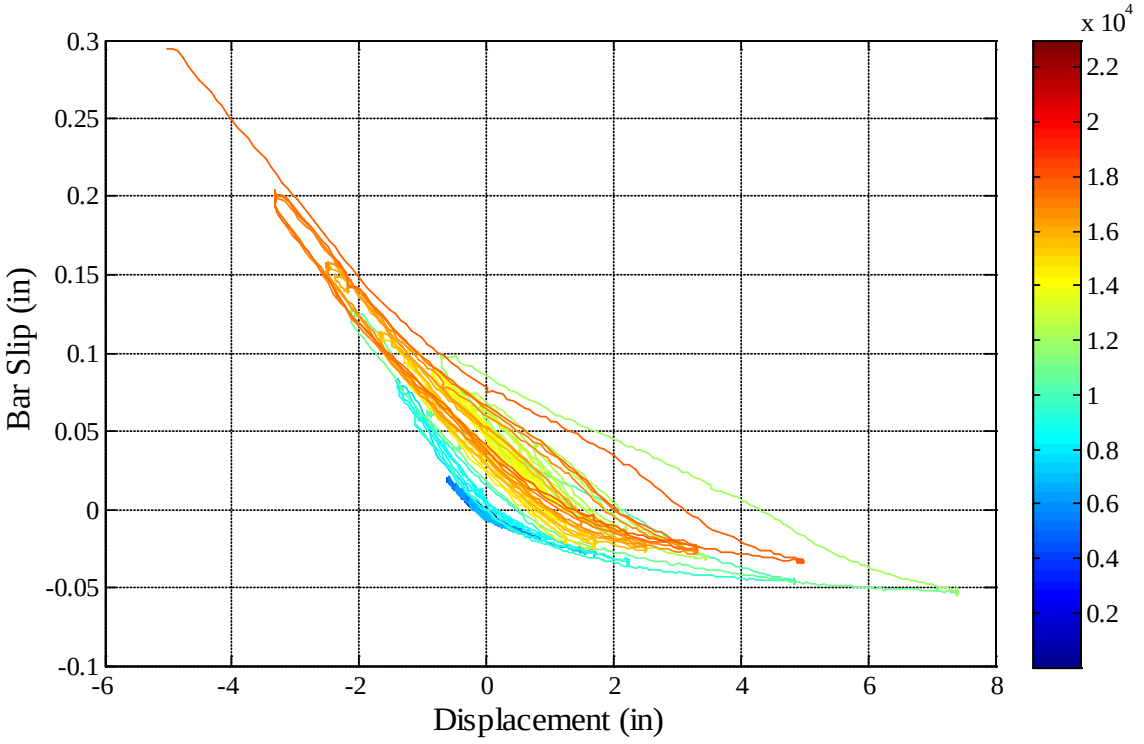

Figure 2-104. Test 10 and 10b – Bar S3 Slip Hysteresis due to Strain Penetration

2.1.4. Test 11 – Kobe Earthquake Load History

Table 2-8. Results Summary for Test 11 – Kobe Earthquake Load History

LOAD HISTORY: Kobe Earthquake Load History

VALUES OF INTEREST:

Concrete Compressive Strength:	$f_c' = 6070psi$
Axial Load:	$P = 170kips$
Analytical First Yield Force:	$F_y' = 46.47kips$
Experimental First Yield Displacement:	$\Delta_y' = 0.62"$
Analytical Nominal Moment Capacity:	$M_n = 495.58kip * ft$
Equivalent Yield Displacement:	$\Delta_y = 0.83"$
Maximum Lateral Force:	$68.0kips$
Maximum Lateral Displacement:	$\mu_{10}^{3.86sec} = 8.28"$
Failure Mode:	Specimen Saved as a Repair Candidate

DAMAGE OBSERVATIONS: (Drift %) [Displacement Ductility, μ_Δ]

First Cracking North:	Unknown Δ during Push to $\mu_{10}^{3.86sec} = 8.28"$
First Cracking South:	Unknown Δ during Pull to $\mu_{-1.5}^{3.44sec} = -1.24"$
Cover Concrete Crushing North:	Unknown Δ during Pull to $\mu_{-6.1}^{4.42sec} = -5.08"$
Cover Concrete Crushing South:	Unknown Δ during Push to $\mu_{10}^{3.86sec} = 8.28"$
Transverse Steel Yield North:	At 1.47" during pull to $\mu_{-2.7}^{7.16sec} = -2.22"$
Transverse Steel Yield South:	At 3.96" during push to $\mu_{10}^{3.86sec} = 8.28"$
Longitudinal Bar Buckling North:	Reversal from $\mu_{9.3}^{6.56sec} = 7.75"$
Longitudinal Bar Buckling South:	Reversal from $\mu_{-6.1}^{4.42sec} = -5.08"$
Longitudinal Bar Fracture North:	Specimen Saved as a Repair Candidate
Longitudinal Bar Fracture South:	Specimen Saved as a Repair Candidate

$*\mu_{10}^{3.86sec} = 8.28"$ represents a push cycle 3.86 seconds into the Kobe earthquake record which produced a peak displacement of 8.28” and a displacement ductility of 10

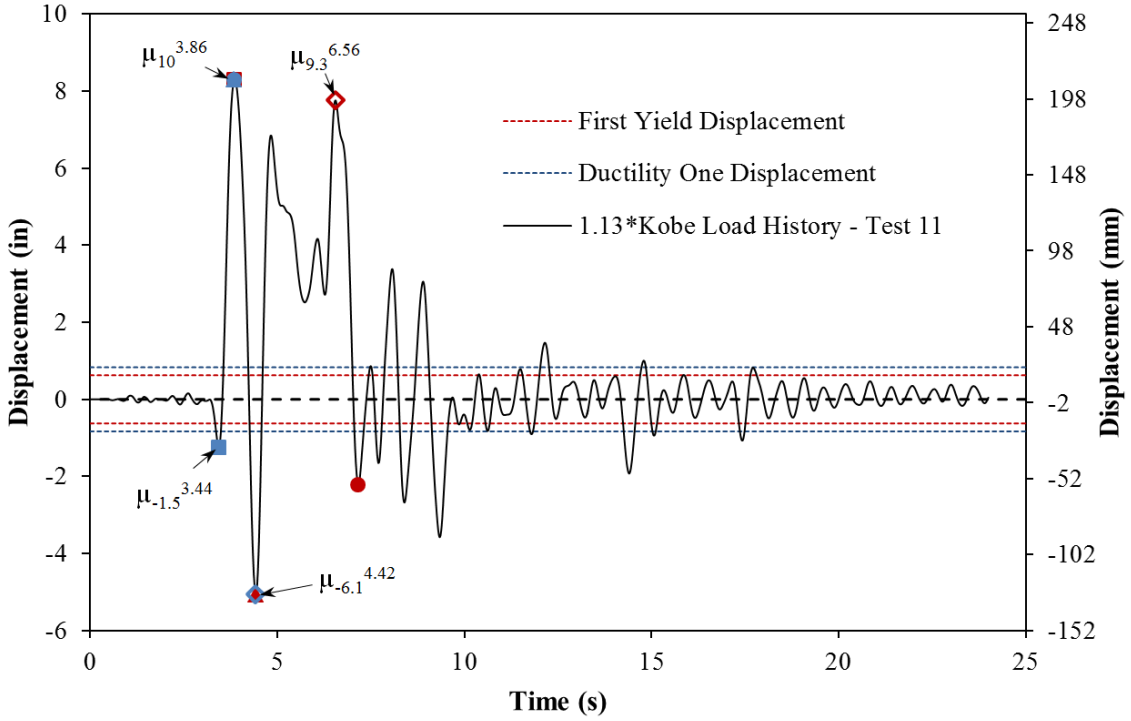

Figure 2-105. Test 11 – Kobe Earthquake Load History

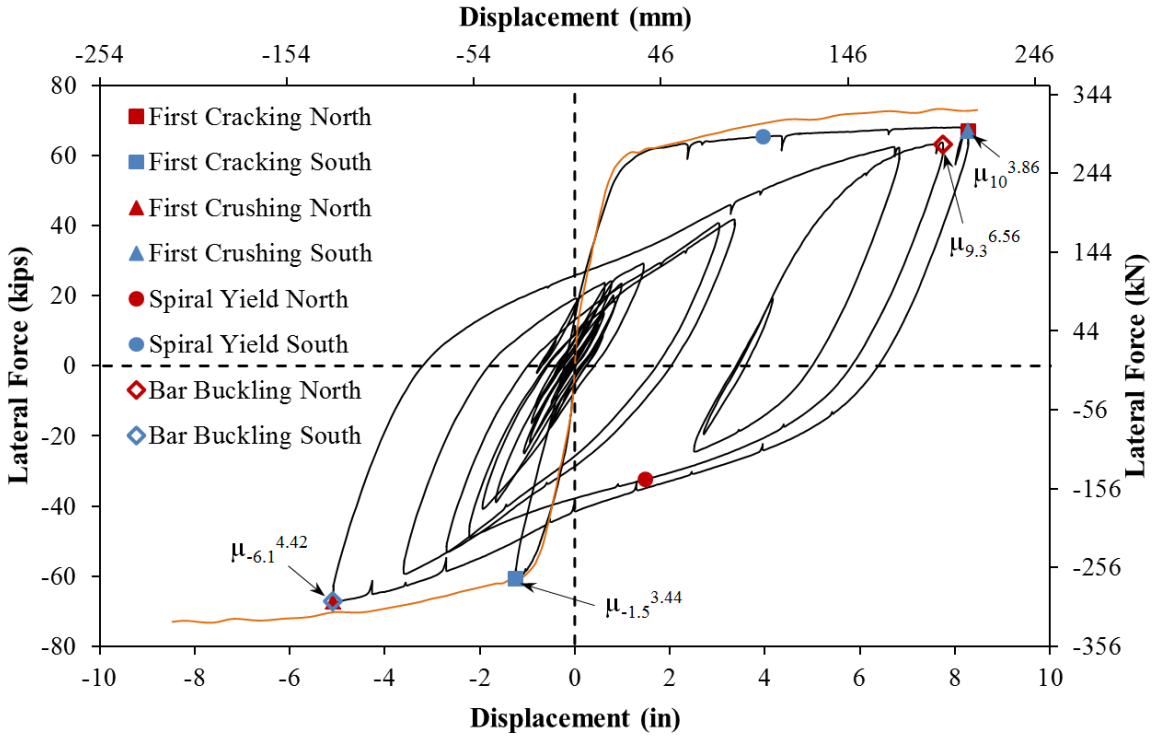

Figure 2-106. Test 10 – Kobe Earthquake Lateral Force vs. Top Column Displacement Response

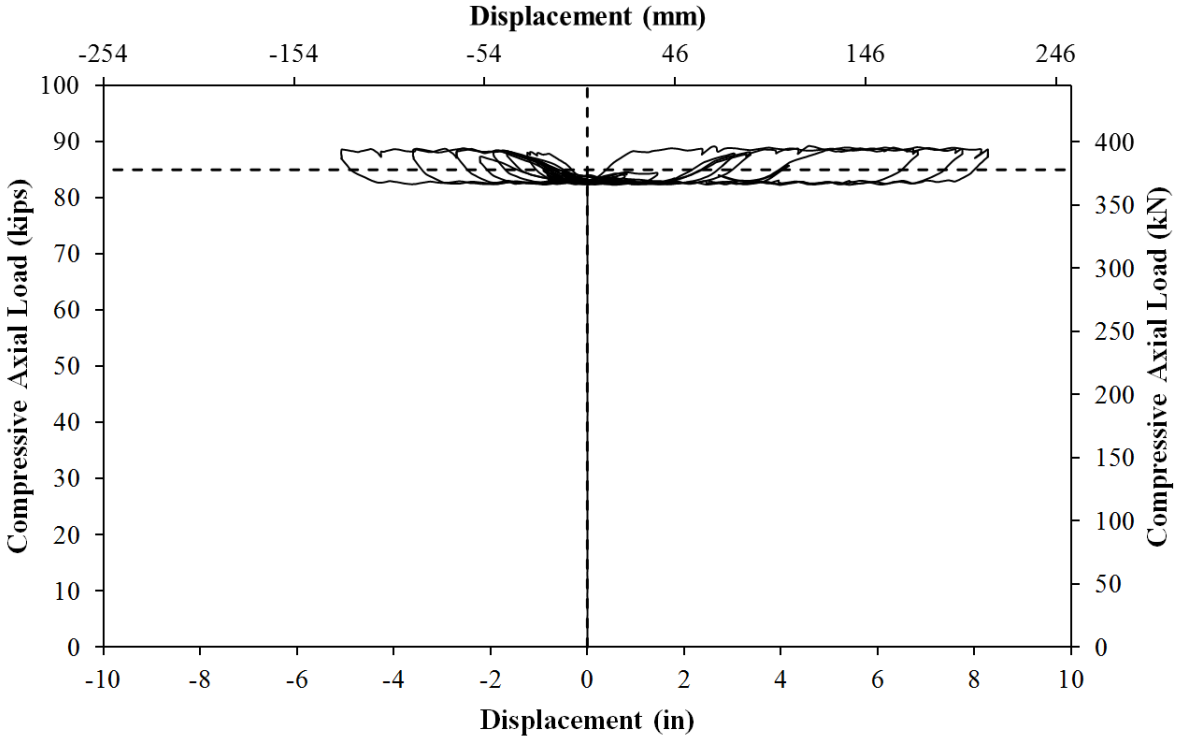

Figure 2-107. Test 11 – Compressive Axial Load from One Jack (Total = 2*Value)

2.1.4.1. Test 11 Kobe Earthquake Load History:

The analytical top column displacement history for the scaled Kobe earthquake, see Figure 2-105, was determined using fiber-based numerical simulation in OpenSees. A 1.13x scaled version of the 1995 Kobe Japan earthquake was selected because it contains a near monotonic cycle to the peak displacement ductility of ten in one direction followed by the largest reversal to the peak cycle in the opposing direction of loading. In previous time history based tests, buckling did not occur during the Chile or Chichi records scaled to displacement ductility 8.7 and 8.9 respectively. The results from the asymmetric Chichi record suggest that high ductility cycles can decrease the effectiveness of transverse steel as a boundary condition restraining the longitudinal steel. A peak displacement level consistent with ductility ten was chosen to increase the level of tension strain in the steel to evaluate the steel tensile strain limit. The Kobe displacement history is unique since the peak cycle occurs early without previous cyclic ramp up, and in a near monotonic fashion. The resulting lateral force vs. top column displacement history for the Kobe earthquake is shown in Figure 2-106.

The North reinforcement was exposed to a tensile strain of 0.059 during the peak cycle, but did not initially buckle after the first large reversal of loading. Instead, the North extreme fiber bar buckled after the second largest push cycle with elastic transverse steel restraint prior to bar buckling. The transverse steel on the South side of the specimen experienced inelastic strains over 0.015 during the largest push cycle of the load history. Since the transverse steel was less effective as a boundary condition restraining buckling, the South reinforcement buckled after reversal from the largest pull cycle with a tensile strain of only 0.033. The Kobe earthquake points out the effects of load history on the longitudinal steel buckling mechanism.

2.1.4.2. Test 11 Kobe Earthquake Experimental Observations:

The first cycle of loading consisted a of small pull cycle to ductility 1.5, where cracks were measured at 0.75mm at approximate 5" spacing on the South side of the specimen. The Chile and Chichi records contained a cyclic ramp up to the peak cycle in contrast to the near monotonic push cycle to the peak displacement in the Kobe load history at ($\mu_{10}^{3.86\,sec} = 8.28"$). The crack distribution on the North side of the specimen can be seen in the left photo of Figure 2-108, while the extent of crushing on the South side of the specimen appears in the middle photo. During the largest pull cycle at ($\mu_{-6.1}^{4.42\,sec} = -5.08"$), the concrete on the North side of the specimen crushed and the reinforcement did not show signs of visible buckling even though large tensile strains occurred during the near monotonic push cycle.

The South side of the specimen was exposed to large compressive strains during the near monotonic push cycle. The dilation of the core concrete caused large strains in the transverse steel which decrease its effectiveness as a boundary condition restraining longitudinal bar buckling during subsequent push cycles. The extreme fiber South reinforcing bar buckled after reversal from the peak cycle in the pull direction at ($\mu_{-6.1}^{4.42\,sec} = -5.08"$), as shown in the left photo of Figure 2-109. Buckling on the South side of the specimen after reversal from such a low level of displacement required both a decrease in the effectiveness of the transverse steel, and large tensile cracks which would increase the compressive demand on the South reinforcement while the cracks are closing. The extreme fiber North reinforcing bar visibly buckled after reversal from the second largest push cycle at ($\mu_{9.3}^{6.56\,sec} = 7.75"$), as shown in the right photo of Figure 2-109. Additional deformation in previously buckled bars S3 and N3 occurred during the remainder of the load history as shown in Figure 2-110. The specimen was saved as a repair candidate with a single buckled extreme fiber bar on each side of the specimen, but without significant loss in strength.

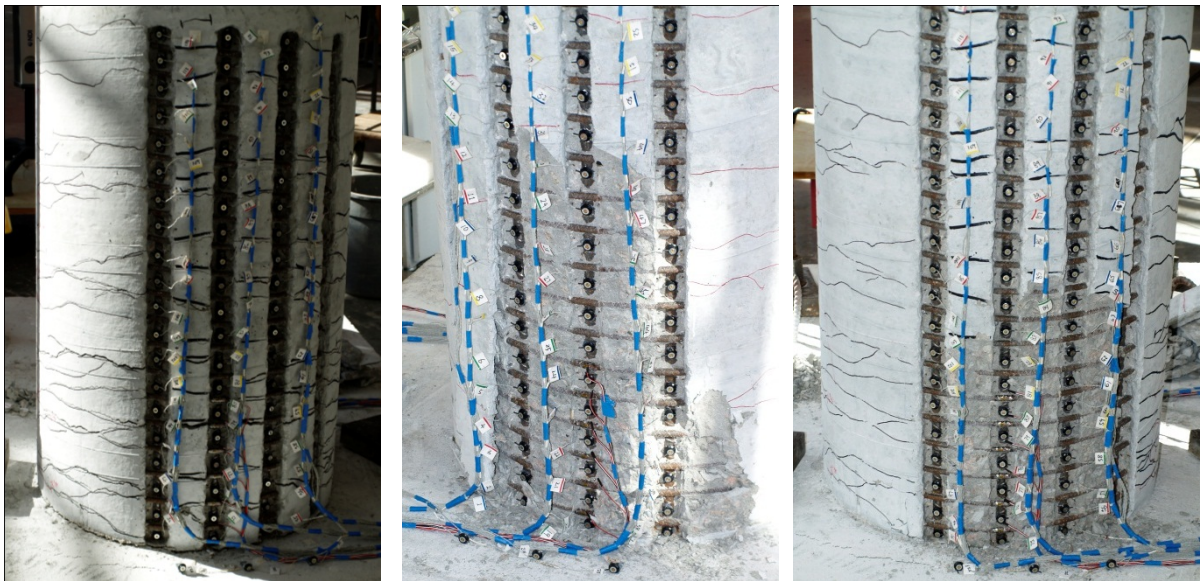

Figure 2-108. Test 11 – (Left and Middle) North and South Sides of Specimen during ($\mu_{10}^{3.86\,sec} = 8.28"$) and (Right) North Side of the Specimen during ($\mu_{-6.1}^{4.42\,sec} = -5.08"$)

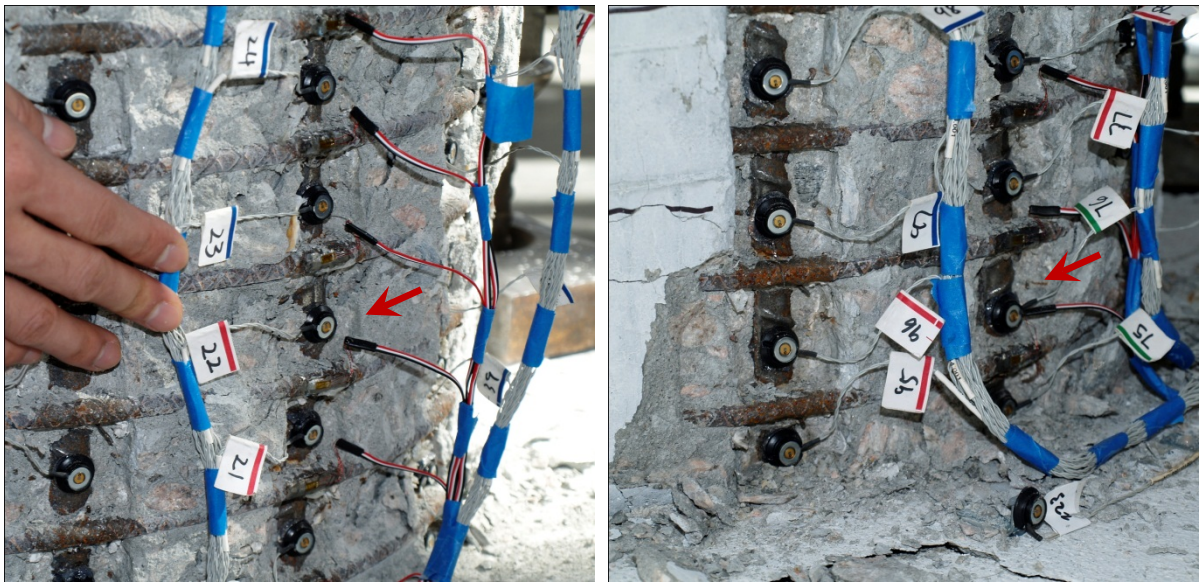

Figure 2-109. Test 11 – (Left) Buckling of Bar S3 after Reversal from ($\mu_{-6.1}^{4.42\,sec} = -5.08$") and (Right) Buckling of Bar N3 after Reversal from ($\mu_{9.3}^{6.56\,sec} = 7.75$")

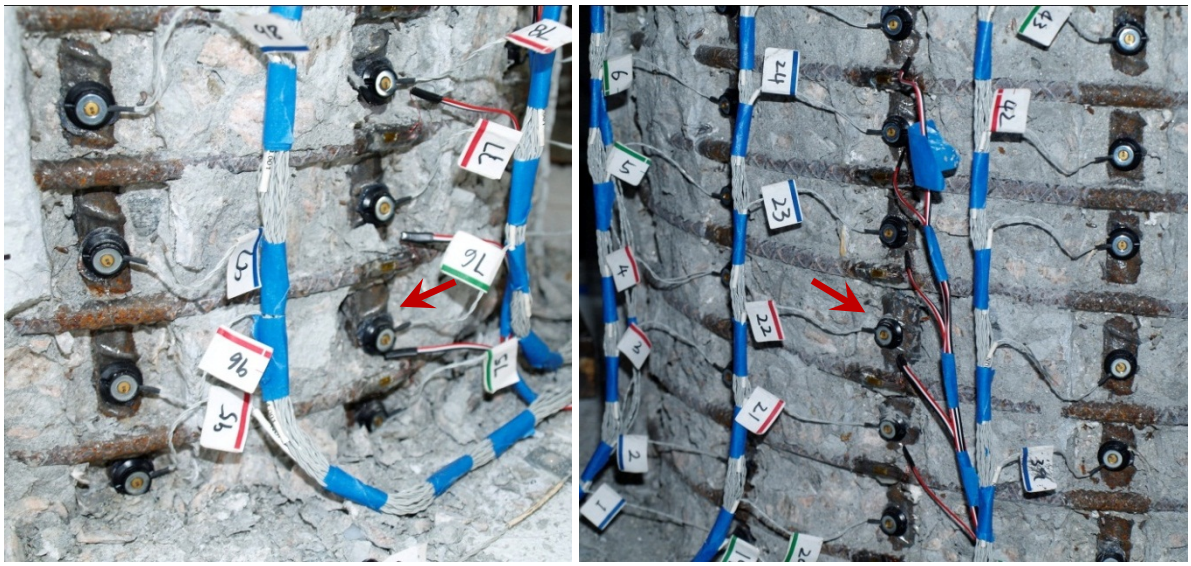

Figure 2-110. Test 11 – (Left) Additional Deformation in North Buckled Region and (Right) Additional Deformation in South Buckled Region

2.1.4.3. Test 11 Kobe Earthquake Load History Strain Data:

North Reinforcement:

The extreme fiber vertical strain profiles for push and pull cycles appear in Figure 2-111 and Figure 2-112. The vertical strain profiles in the push direction are all from the backbone curve of the near monotonic push cycle which occurred 3.86 seconds into the Kobe load history, see Figure 2-105. The lowest gage lengths on each side of the specimen were blocked by debris for most of the push cycle. The pull cycle vertical strain profiles mainly show the reversal from the peak displacement, and are therefore highly influenced by residual strains. The spiral layer placed closed to the footing-column interface remained elastic due to the additional confinement provided by the footing. The spiral strains on the North side of the specimen, see Figure 2-114, remained elastic during the peak pull cycle to ($\mu_{-6.1}^{4.42\,sec} = -5.08$").

Since bar buckling happened so early into the load history, only a few cycles contain usable strain data. The relationship between tensile strain and displacement for Bar N3 during push cycles before bar buckling is shown in Figure 2-115. Moment curvature analysis significantly over predicts the measured tensile strains at higher displacements. The relationship between strain and displacement for each extreme fiber bar during pull cycles appears in Figure 2-116 and Figure 2-117.

The strain hysteresis for the buckled region of the North extreme fiber bar, 3.33" above the footing, appears in Figure 2-121. The peak tensile strain over the North buckled region is slightly lower than the maximum tensile strain sustained by bar N3 since they occur over different gage lengths. The strain values after reversal from ($\mu_{9.3}^{6.56\,sec} = 7.75$") no longer represent engineering strain since visible bar buckling occurred. After this point, the reinforcement is never placed back into compression, indicating an outward deformation of the reinforcement over this location which matches test observations. The transverse steel strain gage hysteresis for the spiral layer overlaying the North buckled region appears in Figure 2-122. The transverse steel restraining the North reinforcement did not yield until reversal from ($\mu_{9.3}^{6.56\,sec} = 7.75$"), which was when visible buckling was observed in the test. Since the transverse steel on the North side of the specimen did not yield during the largest pull cycle, the inelastic spiral layers are due solely to bar buckling.

South Reinforcement:

The measured compressive strains in bar S3 during the peak cycle, see Figure 2-118, are under predicted by moment curvature analysis. This is likely due to the inelastic layers of transverse steel in this region. The measured strains in the lowest six spiral layers on the South side of the specimen during the push cycle to ($\mu_{10}^{3.86\,sec} = 8.28$") are shown in Figure 2-113. A single layer of transverse steel entered the inelastic range at a displacement ductility of five. The compressive demand continued to increase during the push to ($\mu_{10}^{3.86\,sec} = 8.28$") until five layers of transverse steel were inelastic.

The longitudinal steel strain hysteresis over the South buckled region, 7.13" above the footing, appears in Figure 2-119. While the entire strain hysteresis is shown, only the data before buckling occurred, upon reversal from ($\mu_{-6.1}^{4.42\,sec} = -5.08$"), represents engineering strains. This particular gage length was over the outward buckled region of the bar that expands during buckling. This explains the erroneous tensile strains measured during a cycle which should have placed the reinforcement in compression. The transverse steel strain gage hysteresis over the South buckled region appears in Figure 2-120. Transverses steel strains over 0.015 were measured during the peak

push cycle to ($\mu_{10}^{3.86\,sec} = 8.28$"). The measured spiral strains sharply increase after reversal from ($\mu_{-6.1}^{4.42\,sec} = -5.08$") when visible buckling was observed. The strain gage quickly goes off scale and no longer provides meaningful data.

2.1.4.4. Test 11 Kobe Load History Curvature and Strain Penetration Data:

Vertical curvature profiles for push and pull cycles before bar buckling appear in Figure 2-123 and Figure 2-124. The curvature profiles during pull cycles seem to be affected by residual strains from the peak displacement cycle to ($\mu_{10}^{3.86\,sec} = 8.28$"). The plastic portions of the curvature profiles during pull cycles are less linear when compared to profiles in other tests. The variation of curvatures measured in the lowest 18" above the footing remain effectively constant during the pull cycle to ($\mu_{-6.1}^{4.42\,sec} = -5.08$"). The base section rotations attributable to strain penetration during push and pull cycles appear in Figure 2-125 and Figure 2-126 respectively. The extreme fiber bars were blocked by fallen debris for large portions of the test, but adjacent instrumented bars remained visible allowing for rotation measurements. A comparison of the measured top column displacements and the integrated displacements from the curvature data and base rotation profiles appear in Figure 2-127. The Optotrak integrated displacements match the measured string potentiometer displacements well throughout the entire range of response.

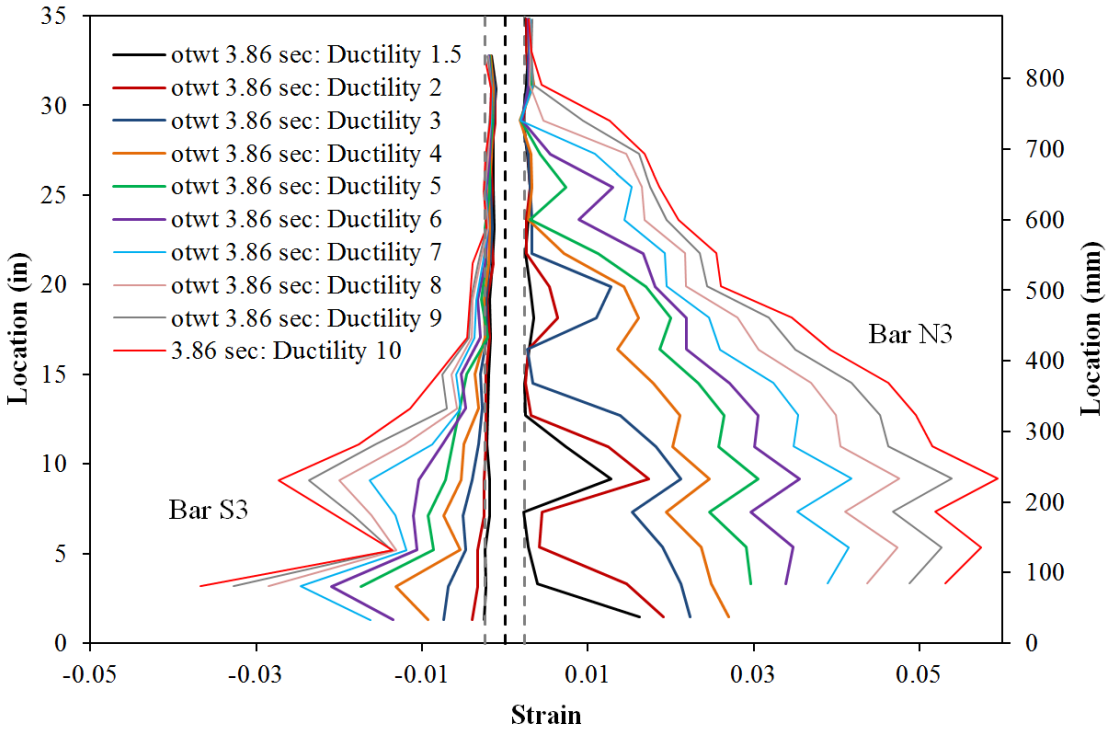

Figure 2-111. Test 11 – Extreme Fiber Vertical Strain Profiles during Push Cycles

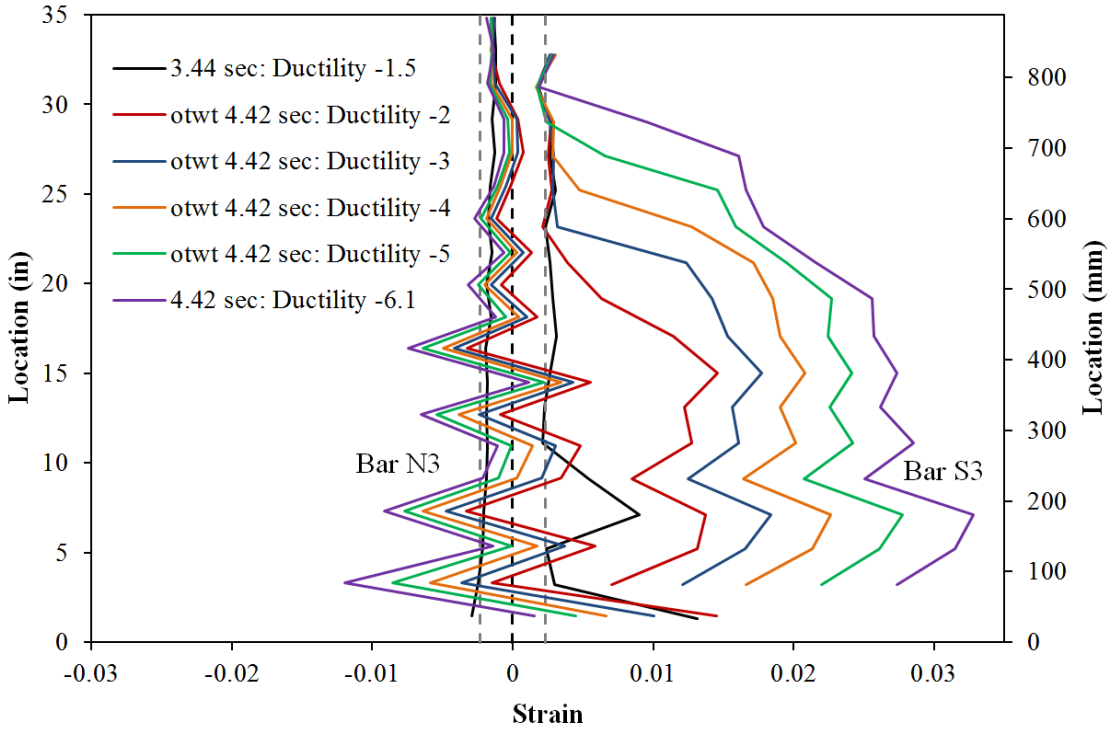

Figure 2-112. Test 11 – Extreme Fiber Vertical Strain Profiles during Pull Cycles

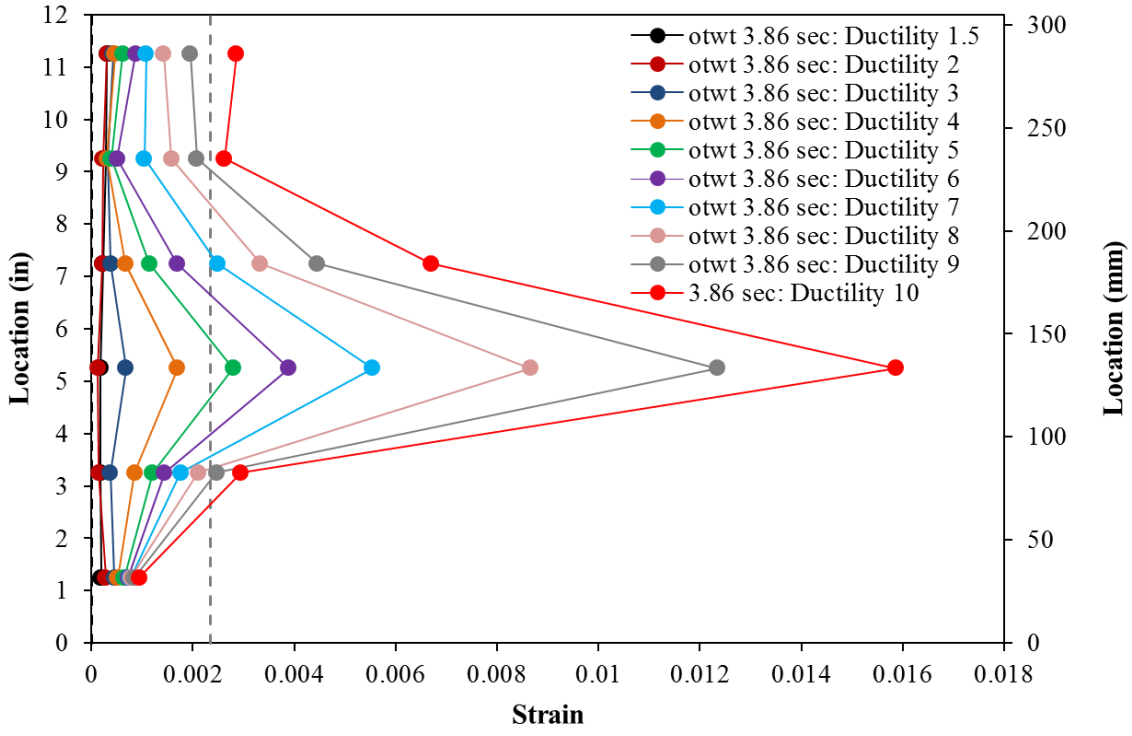

Figure 2-113. Test 11 – Transverse Steel Strains for Lowest Six Spiral Layers on the South Side during Push Cycles

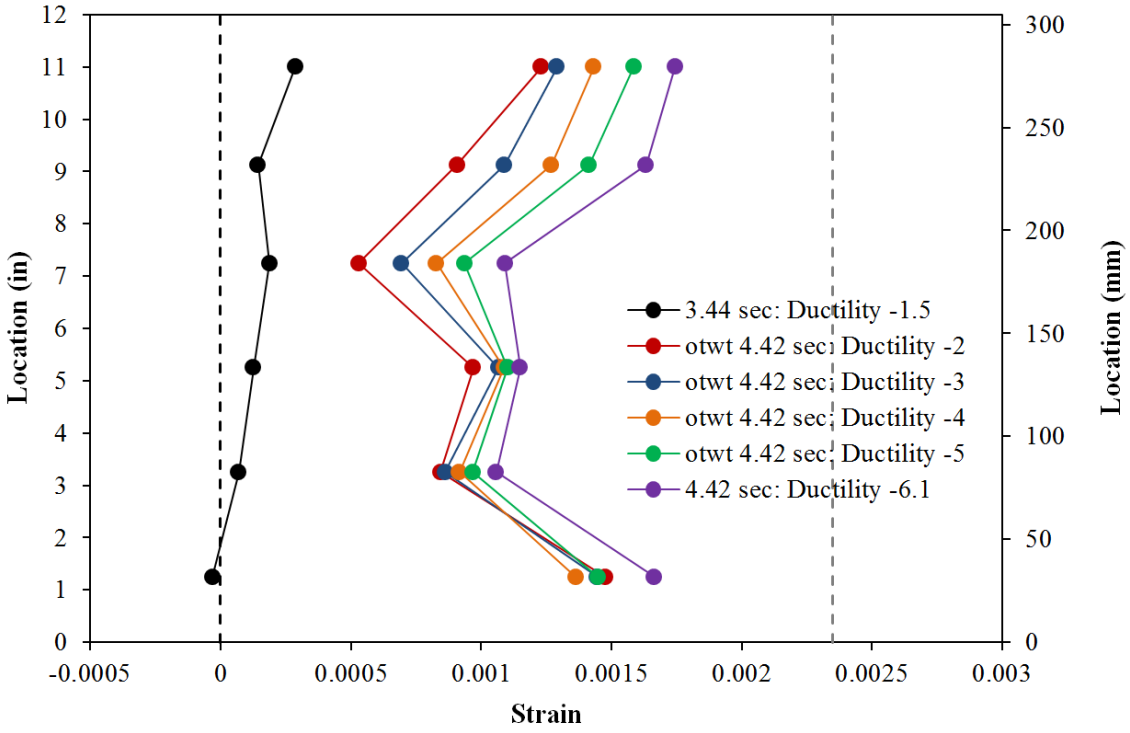

Figure 2-114. Test 11 – Transverse Steel Strains for Lowest Six Spiral Layers on the North

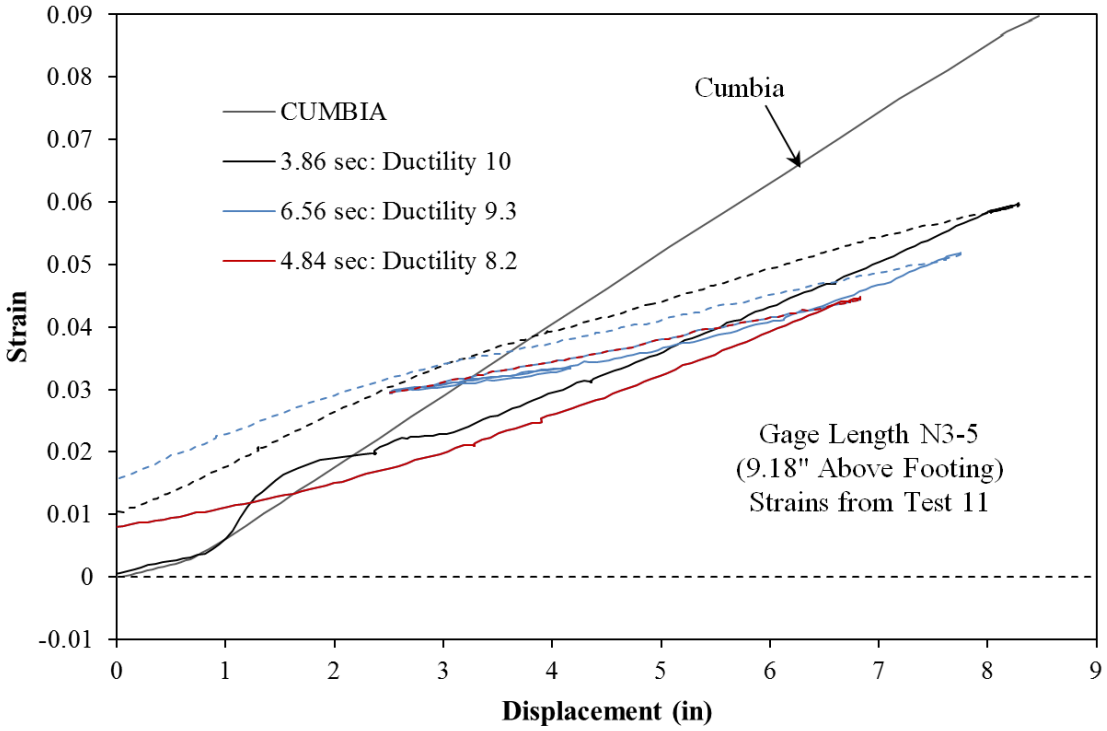

Figure 2-115. Test 11 – Tensile Strain and Displacement for Bar N3 during Push Cycles

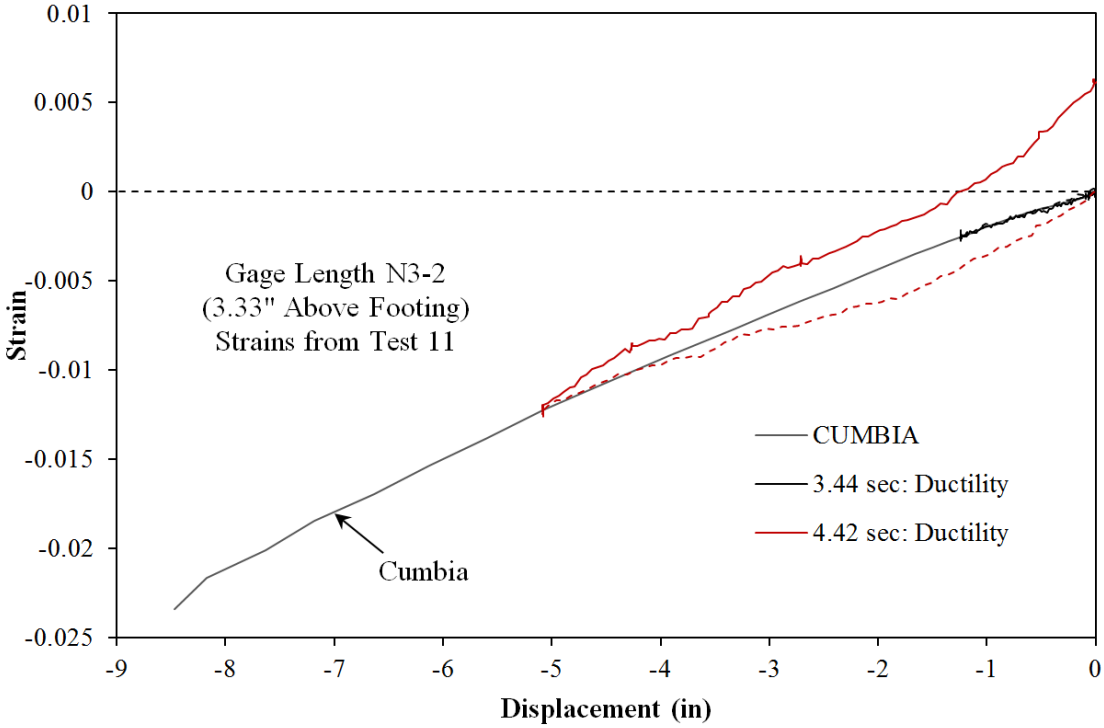

Figure 2-116. Test 11 – Compressive Strain and Displacement for Bar N3 for Pull Cycles

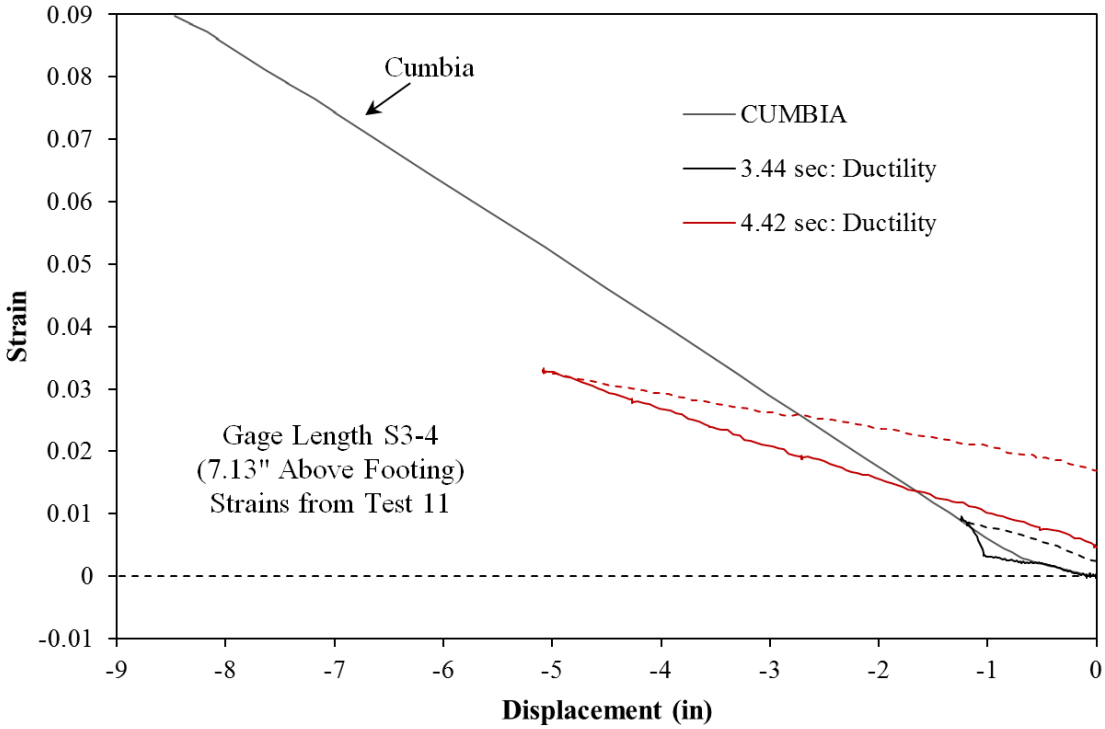

Figure 2-117. Test 11 – Tensile Strain and Displacement for Bar S3 during Pull Cycles

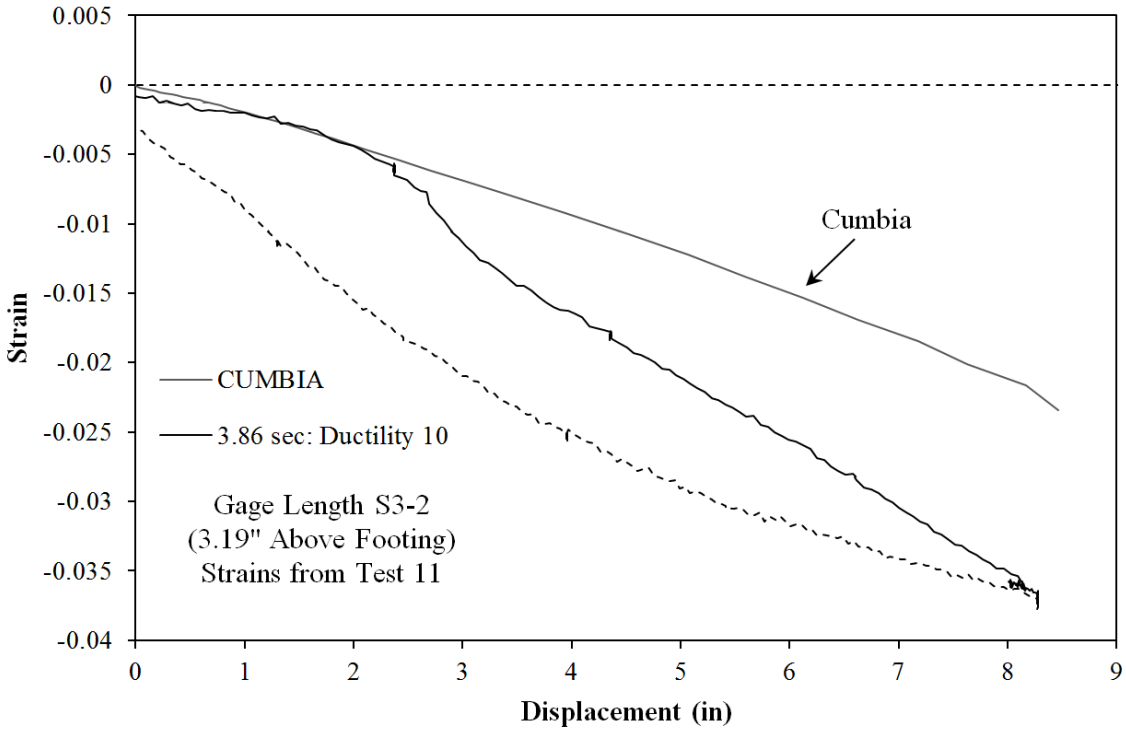

Figure 2-118. Test 11 – Compressive Strain and Displacement for Bar S3 for Push Cycles

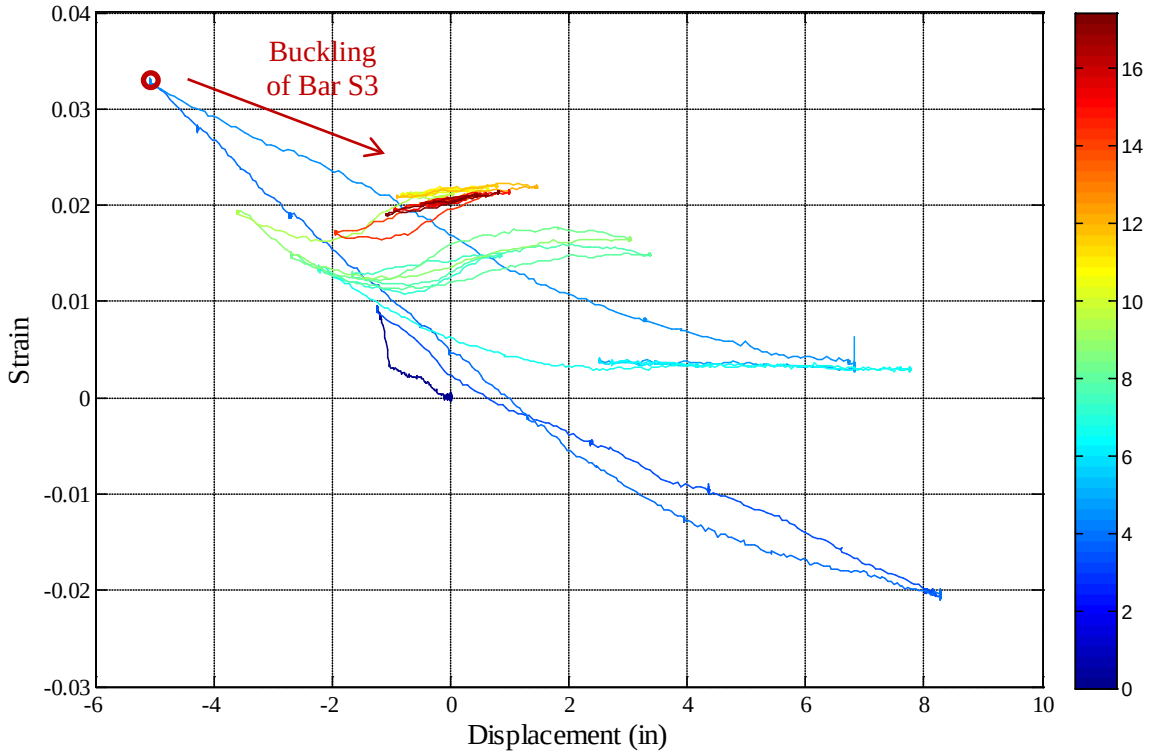

Figure 2-119. Test 11 – Bar S3 Strain Hysteresis over South Buckled Region (7.13" Above Footing)

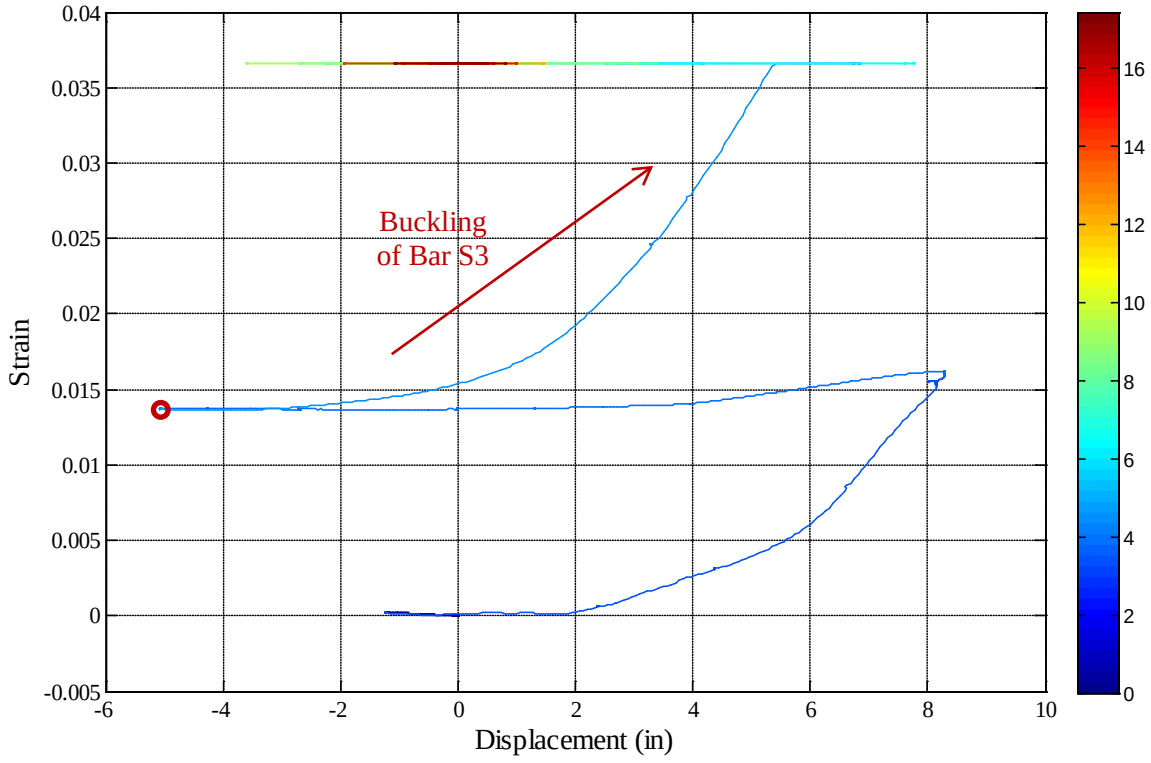

Figure 2-120. Test 11 – Transverse Steel Strain Hysteresis over South Buckled Region

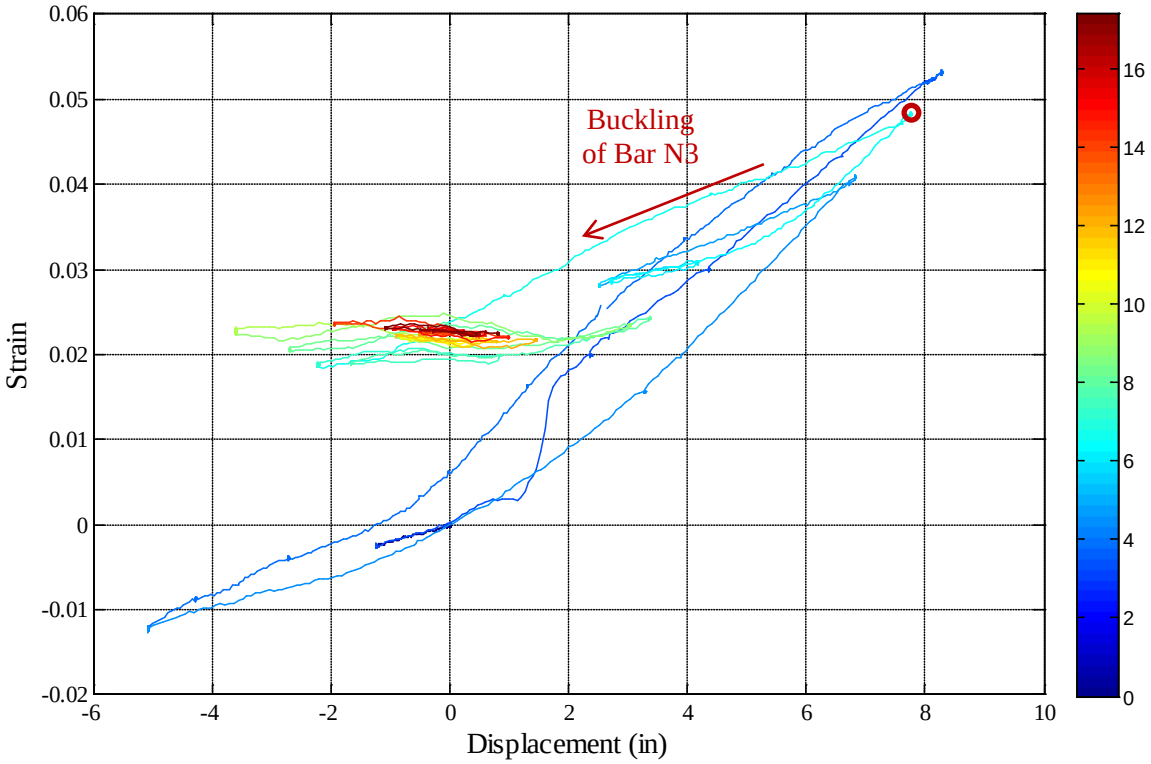

Figure 2-121. Test 11 – Bar N3 Strain Hysteresis over North Buckled Region (3.33" Above Footing)

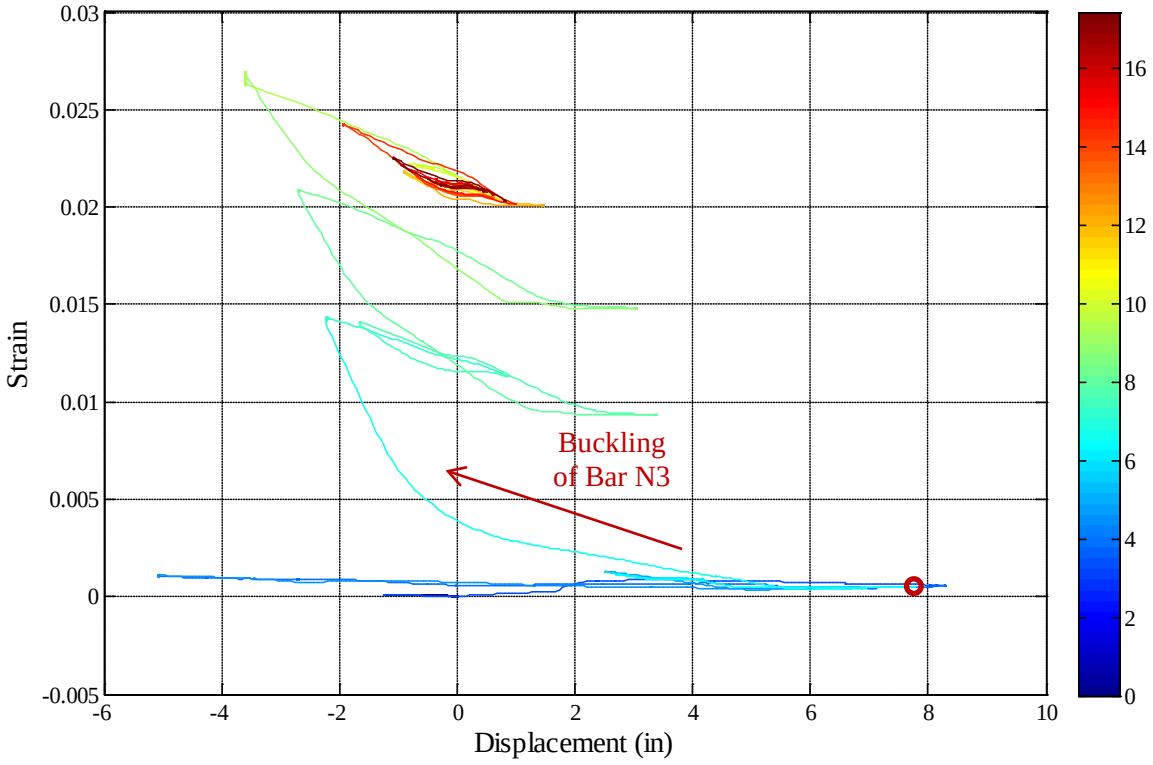

Figure 2-122. Test 11 – Transverse Steel Strain Hysteresis over North Buckled Region

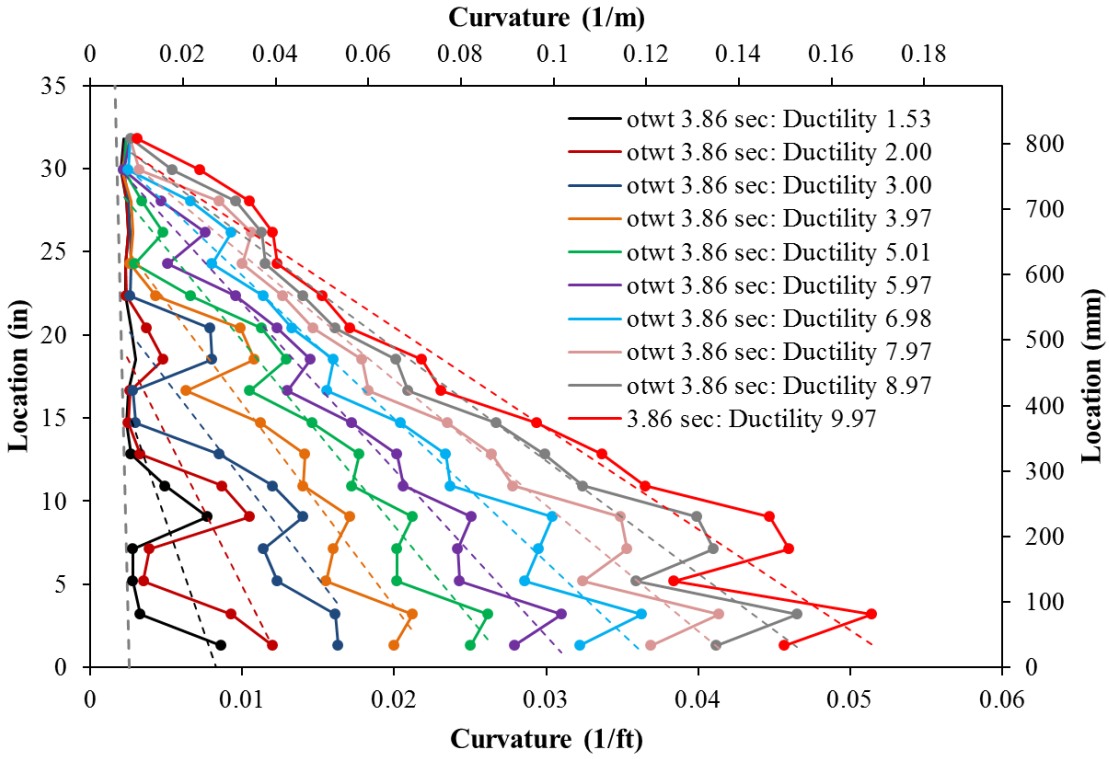

Figure 2-123. Test 11 – Vertical Curvature Profiles for Push Cycles with Linear Plastic Curvature Least Squared Error Lines

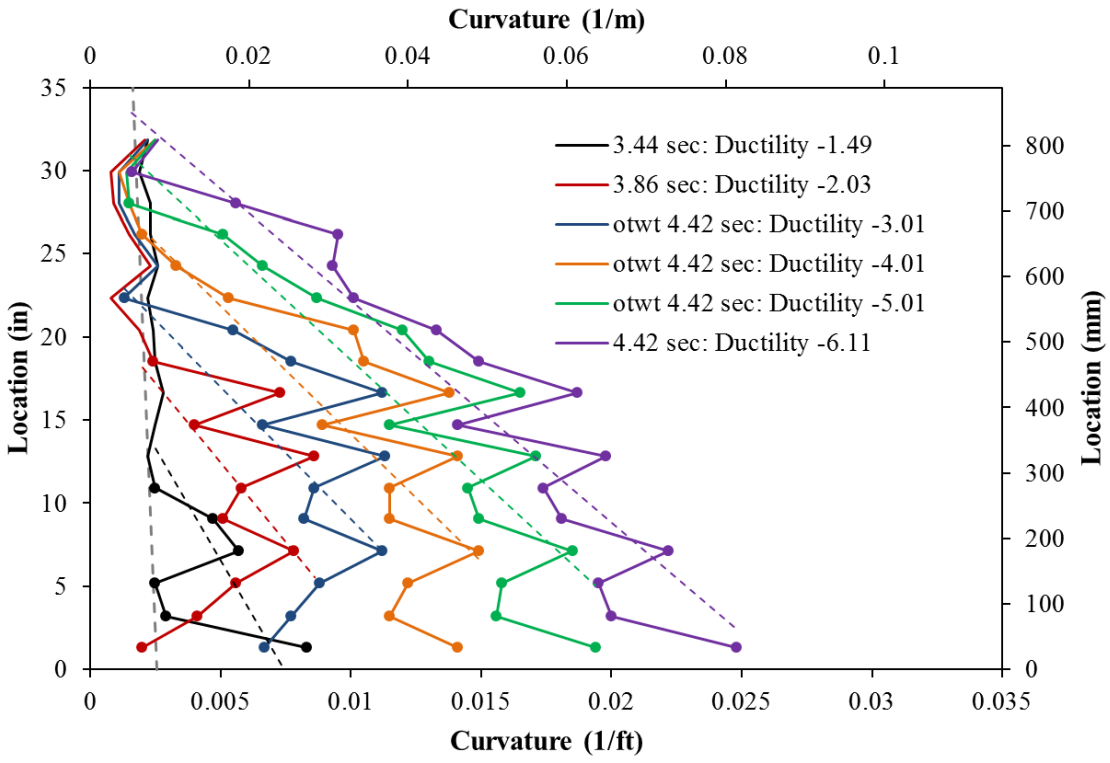

Figure 2-124. Test 11 – Vertical Curvature Profiles for Pull Cycles

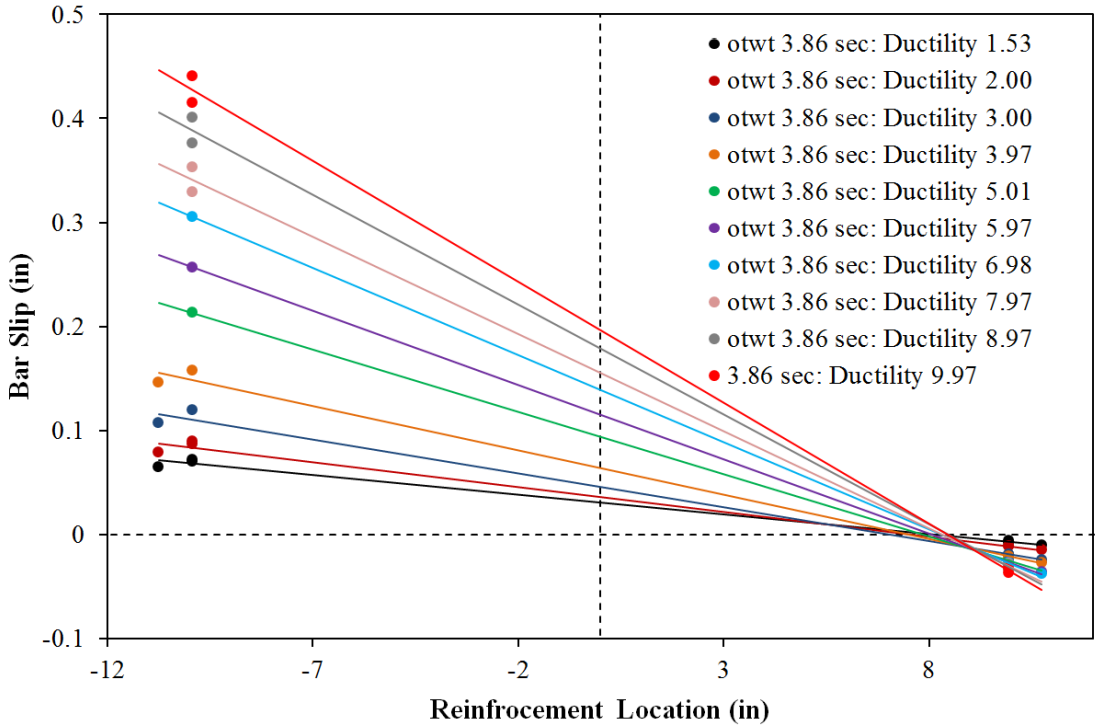

Figure 2-125. Test 11 – Base Rotation Attributable to Strain Penetration during Push Cycles

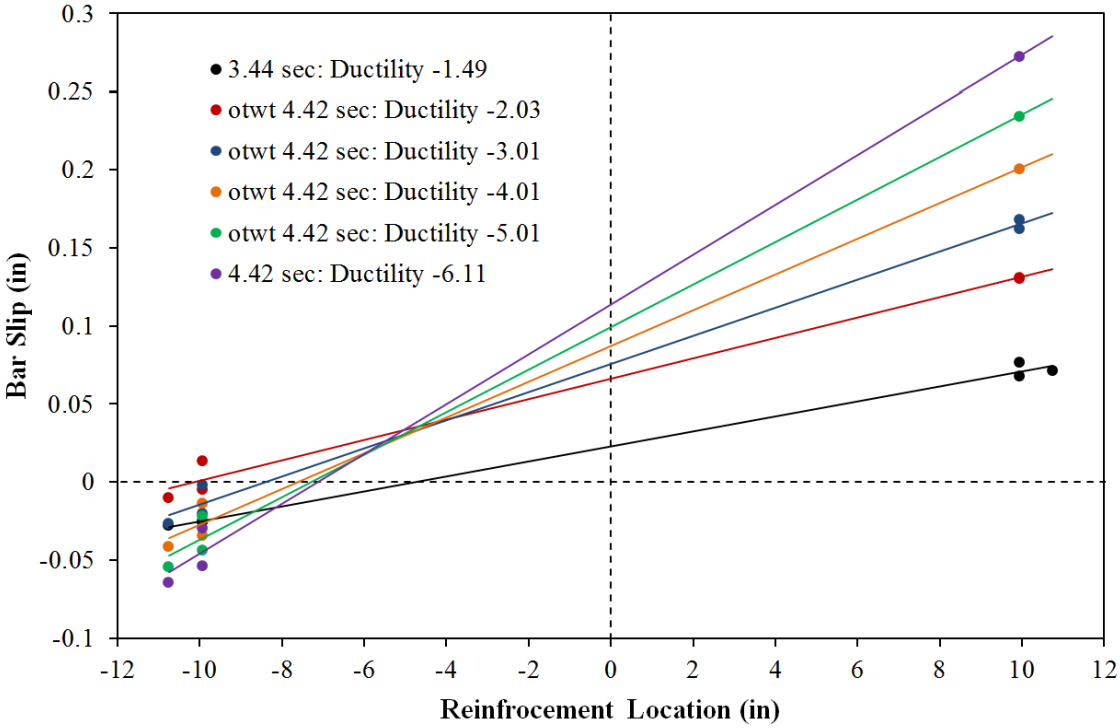

Figure 2-126. Test 11 – Base Rotation Attributable to Strain Penetration during Pull Cycles

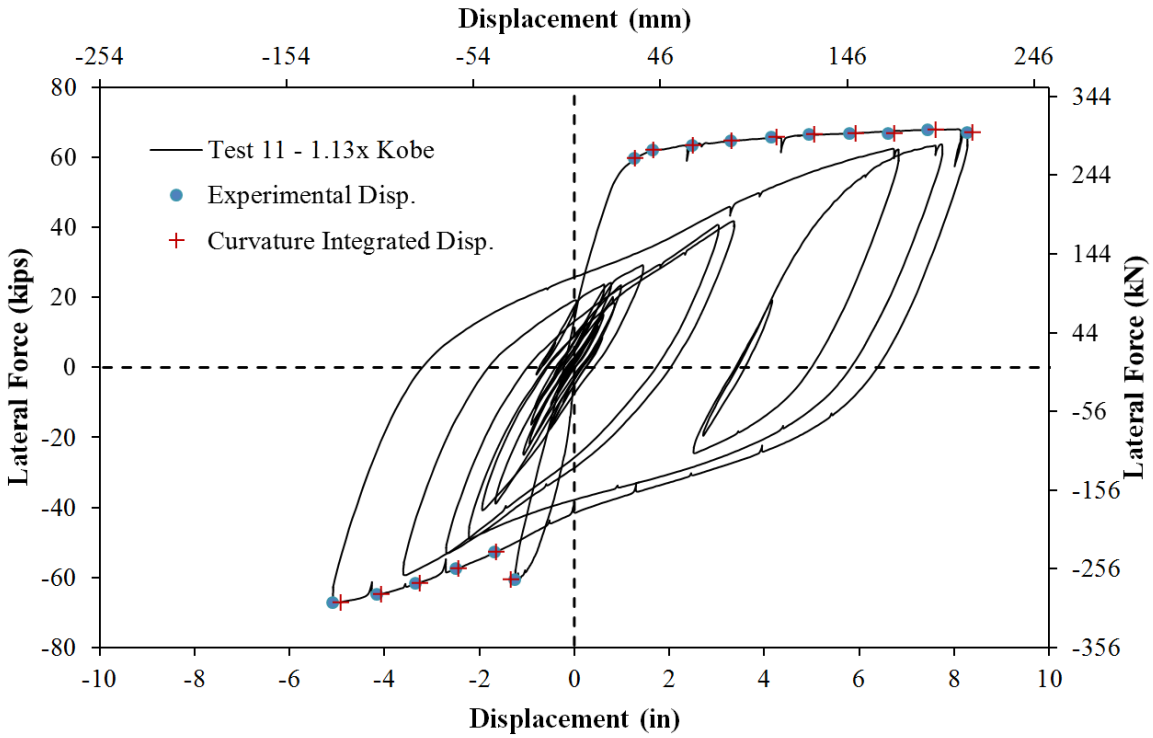

Figure 2-127. Test 11 – Comparison of Measured and Integrated Displacements

2.1.5.Test 12 – Japan 2011 Earthquake Load History

Table 2-9. Results Summary for Test 12 – Japan 2011 Earthquake Load History

LOAD HISTORY: Japan 2011 Earthquake Load History

VALUES OF INTEREST:

Concrete Compressive Strength:	$f_c' = 6100psi$
Axial Load:	$P = 170kips$
Analytical First Yield Force:	$F_y' = 46.5kips$
Experimental First Yield Displacement:	$\Delta_y' = 0.62"$
Analytical Nominal Moment Capacity:	$M_n = 494.5kip * ft$
Equivalent Yield Displacement:	$\Delta_y = 0.83"$
Maximum Lateral Force:	$72.6kips$
Maximum Lateral Displacement:	$\mu_{9.9}^{68.62sec} = 8.22"$
Failure Mode:	Specimen Saved as a Repair Candidate after Buckling of Extreme Fiber Reinforcement

DAMAGE OBSERVATIONS: (Drift %) [Displacement Ductility, μ_Δ]

First Cracking North:	$\mu_{0.5}^{44.26sec} = 0.39"$
First Cracking South:	$\mu_{-0.3}^{43.98sec} = -0.26"$
Cover Concrete Crushing North:	$\mu_{-2.2}^{61.80sec} = -1.85"$
Cover Concrete Crushing South:	$\mu_{2.1}^{48.83sec} = 1.77"$
Transverse Steel Yield North:	At $-5.02"$ during pull to $\mu_{-7.9}^{66.88sec} = -6.53"$
Transverse Steel Yield South:	At $5.70"$ during push to $\mu_{9.9}^{68.62sec} = 8.22"$
Longitudinal Bar Buckling North:	Reversal from $\mu_{9.9}^{68.62sec} = 8.22"$
Longitudinal Bar Buckling South:	Did Not Visibly Buckle
Longitudinal Bar Fracture North:	Specimen Saved as a Repair Candidate
Longitudinal Bar Fracture South:	Specimen Saved as a Repair Candidate

$*\mu_{9.9}^{68.62sec} = 8.22"$ represents a push cycle 68.62 seconds into the Japan 2011 earthquake record which produced a peak displacement of 8.22” and a displacement ductility of 9.9

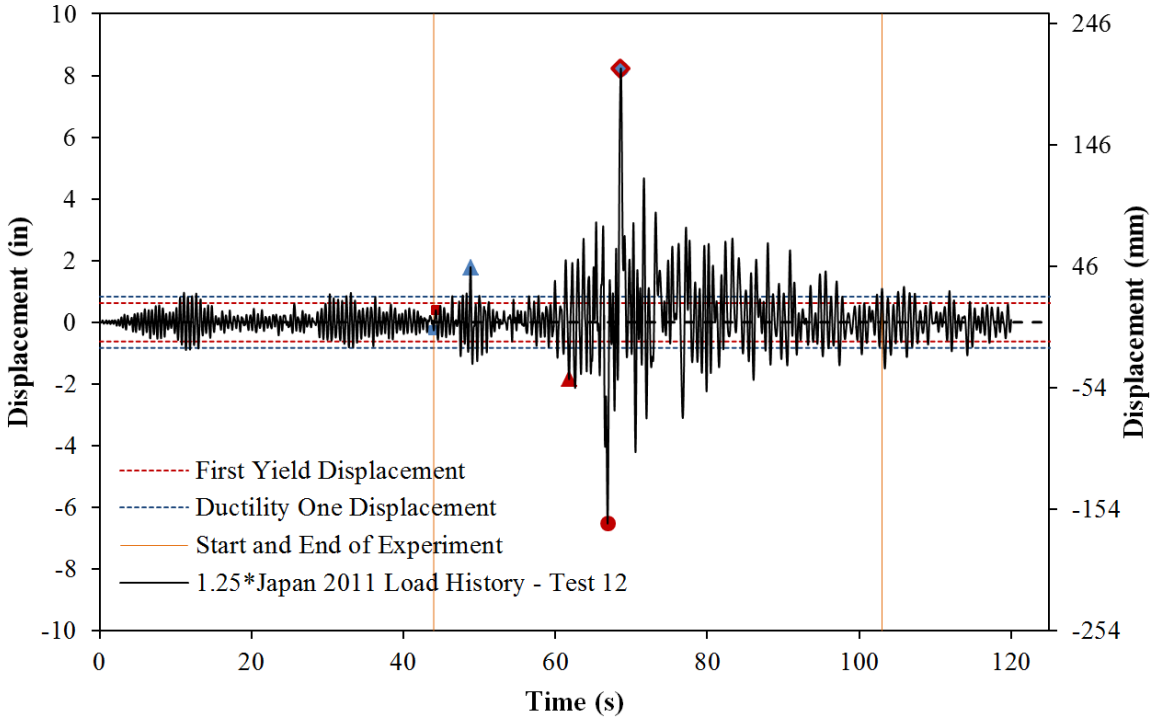

Figure 2-128. Test 12 – Complete Japan 2011 Load History Scaled to Displacement Ductility Ten (1.25*Recorded Accelerations)

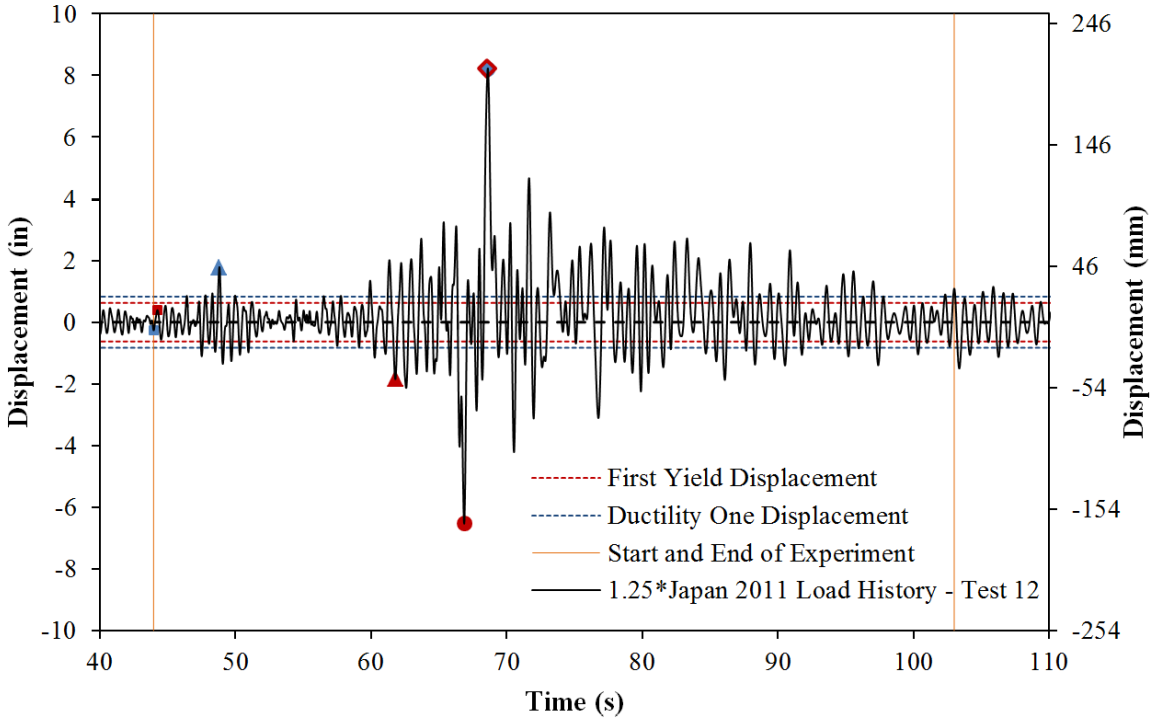

Figure 2-129. Test 12 – Experimental Portion of the Japan 2011 Earthquake Load History

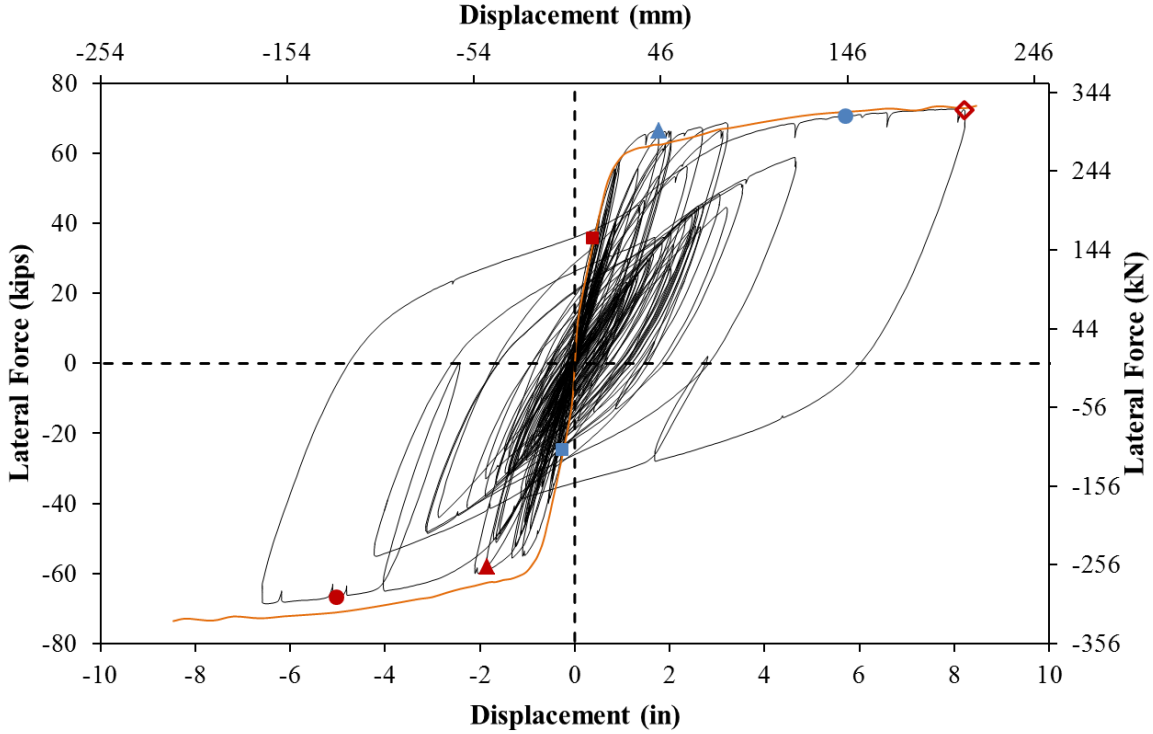

Figure 2-130. Test 12 – Japan 2011 Lateral Force vs. Top Column Displacement Response

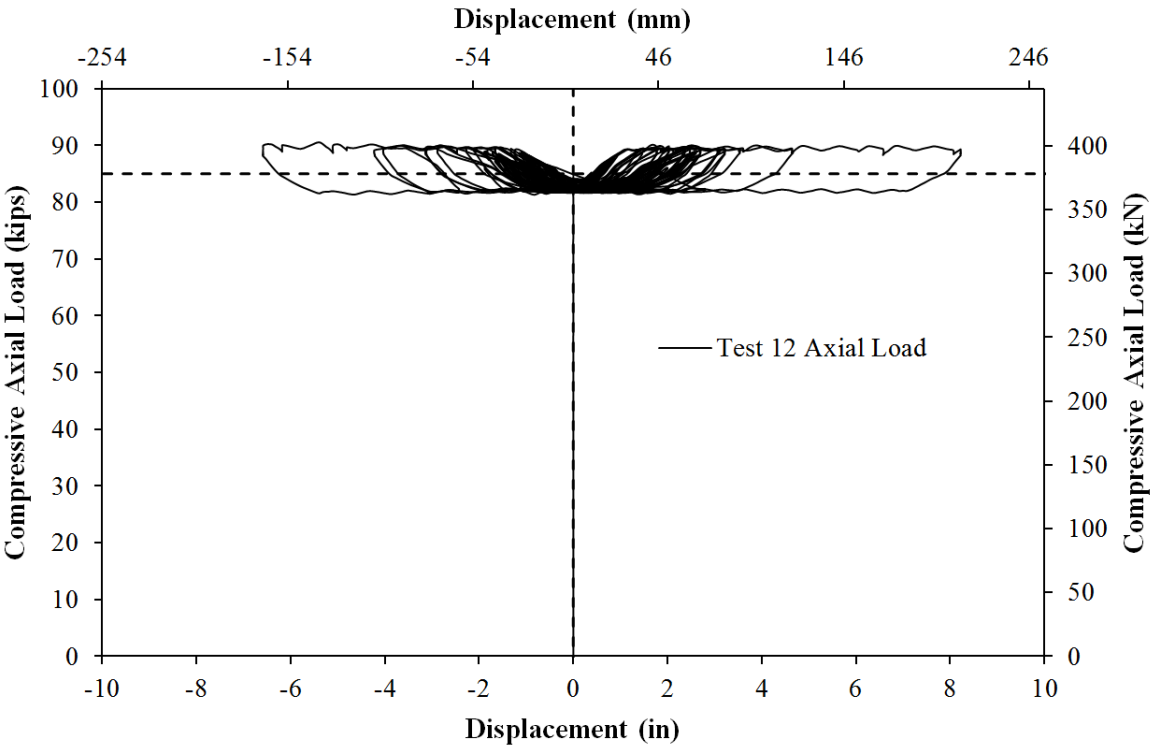

Figure 2-131. Test 12 – Compressive Axial Load from One Jack (Total = 2*Value)

2.1.5.1. Test 12 Japan 2011 Earthquake Load History Experimental Observations:

The analytical top column displacement history for the scaled Japan 2011 earthquake, which appears in Figure 2-128, was determined using fiber-based numerical simulation in OpenSees. A 1.25x scaled version of the 2011 Japan earthquake was selected to reach a displacement ductility of ten during the largest cycle. In previous time history based tests, buckling did not occur during the Chile or Chichi records scaled to displacement ductility 8.7 and 8.9 respectively. The results from the Chichi and Kobe records suggest that high ductility cycles can decrease the effectiveness of transverse steel as a boundary condition restraining the longitudinal steel. A peak displacement ductility level of ten was chosen to increase the level of tension strain in the steel to evaluate the steel tensile strain limit which leads to buckling of longitudinal steel upon reversal of loading. The initial portion of the Japan 2011 earthquake contained reversals around ductility one which have little large impact on the remainder of the test. The portion of the load history recreated in the experiment is shown in Figure 2-129. The resulting lateral force vs. top column displacement response for the Japan 2011 record appears in Figure 2-130.

The first cycle for the experimental test reached ($\mu_{-0.3}^{43.98sec} = -0.26$"), as shown in Figure 2-128. The first cracks on the South side of the specimen measured 0.1mm at a lateral force of -24.63 kips which is over half of the first yield force. The load history prior to this point contained many cycles of loading around a displacement ductility of one, which were not included in the experimental test. The beginning cycles omitted from the experimental displacement history should not have a large impact on the relationship between strain and displacement or damage within the section. Cracks measuring 0.2mm on the North side of the specimen were measured during ($\mu_{0.5}^{44.26sec} = 0.39$"), with a lateral force of 35.69 kips which is around 75% of the first yield force.

Cracks on the South side of the specimen were measured at 0.4mm during ($\mu_{-1.3}^{47.53\,sec} = -1.10$") as shown in the left photo of Figure 2-132. The crack distribution on the North side of the specimen during ($\mu_{2.1}^{48.83\,sec} = 1.77$") appears in the middle and right photos of Figure 2-132. Crack widths on the North side of the specimen measured 2mm and the cover concrete on the South side of the specimen began to crush as shown in the left photo of Figure 2-133. The extent of crushing on the South side of the specimen extended 10" above the footing during ($\mu_{2.4}^{61.36sec} = 2.02$"), while crack widths on the North side of the column measured 2.5mm. Crushing usually begins after a visual flaking which was observed on the North side of the specimen during ($\mu_{-2.2}^{61.80\,sec} = -1.85$"), as shown in the right photo of Figure 2-133. The extent of crushing on the North side of the specimen extended 7" above the footing during ($\mu_{-2.1}^{65.83\,sec} = -1.71$") as shown in the right photo of Figure 2-134.

The largest cycle in the pull direction of loading occurred during ($\mu_{-7.9}^{66.88\,sec} = -6.53$") with additional crushing on the North side of the specimen, see Figure 2-135. The peak cycle in the push direction at ($\mu_{9.9}^{68.62\,sec} = -8.22$") was concluded without visible buckling on the South side of the specimen as shown in Figure 2-136. A peak lateral load of 72.1 kips was recorded during the peak cycle of the Japan 2011 load history. Upon reversal of loading from ($\mu_{9.9}^{68.62\,sec} = 8.22$"), which placed the North side of the specimen under large tensile strains, the extreme fiber North reinforcing bar N3 buckled on the way to ($\mu_{2.0}^{68.95\,sec} = 1.68$") as shown in the left photo of Figure 2-137. Even though the reversal only brought the specimen to a lower ductility in the same direction of loading as the peak cycle, a lateral load of -27.40 kips was recorded due to hysteretic offset from the peak displacement cycle. Therefore, visible buckling was observed while the cracks on the North side of the specimen remained open and the North reinforcement was the sole source of compression zone stability. After a small push cycle to ($\mu_{3.4}^{69.12\,sec} = 2.80$"), a second reinforcing bar N4 on the North side of the specimen buckled on the way to ($\mu_{-1.4}^{69.41\,sec} = -1.14$") as shown in the right photo of

Figure 2-137. The rest of the load history progressed without any additional buckled reinforcement or rupture of buckled reinforcement. The deformation in the previously buckled bars increased and the core concrete over the North buckled region began to deteriorate as the load history progressed, see Figure 2-138. Visible buckling of the South reinforcement was never observed, although very slight deformation over the bottom three transverse steel spacing was noticed. This deformation never visibly increased with additional cycles.

Figure 2-132. Test 12 – (Left) South Crack Distribution during ($\mu_{-1.3}^{47.53\ sec} = -1.10$") and (Middle & Right) North Crack Distribution during ($\mu_{2.1}^{48.83\ sec} = 1.77$")

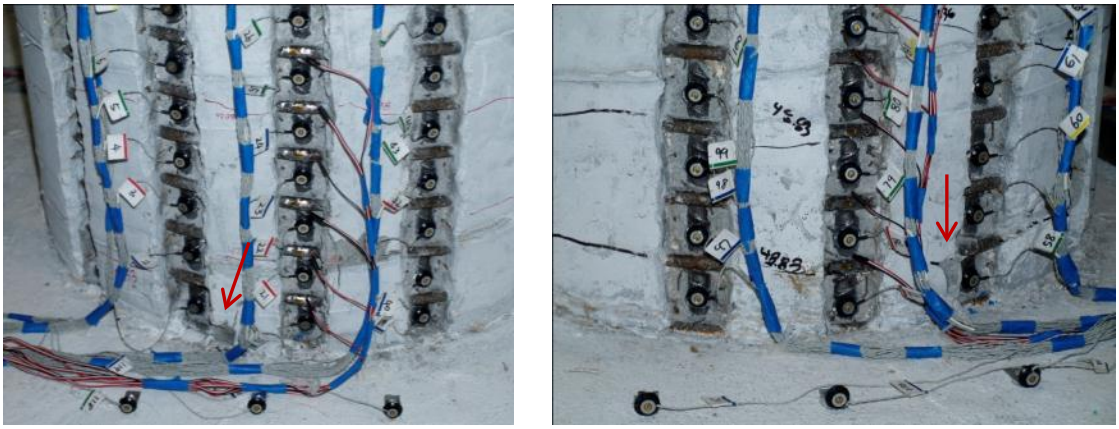

Figure 2-133. Test 12 – First Signs of Crushing (Left) South Side of the Specimen during ($\mu_{2.1}^{48.83\ sec} = 1.77$") and (Right) North Side of the Specimen during ($\mu_{-2.2}^{61.80\ sec} = -1.85$")

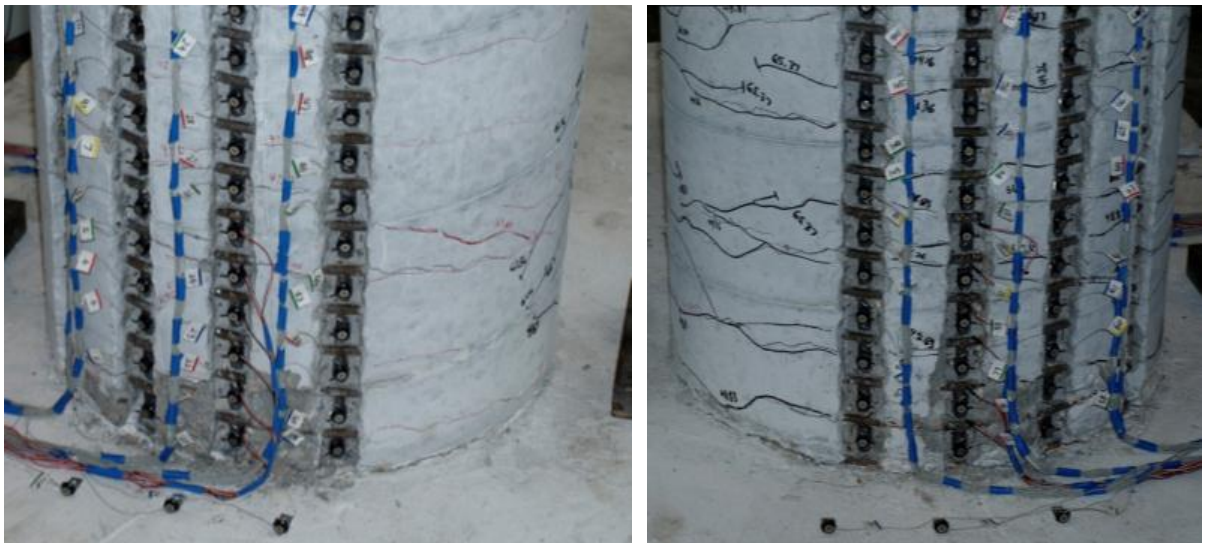

Figure 2-134. Test 12 – (Left) Crushing on the South side of the specimen during ($\mu_{2.4}^{61.36\,sec} = 2.02$") and (Right) Crushing on the North side of the specimen during ($\mu_{-2.1}^{65.83\,sec} = -1.71$")

Figure 2-135. Test 12 – Peak Pull Cycle at ($\mu_{-7.9}^{66.88\,sec} = -6.53$") – (Left) Back Side of the Specimen, (Middle) South Side, and (Right) North Side

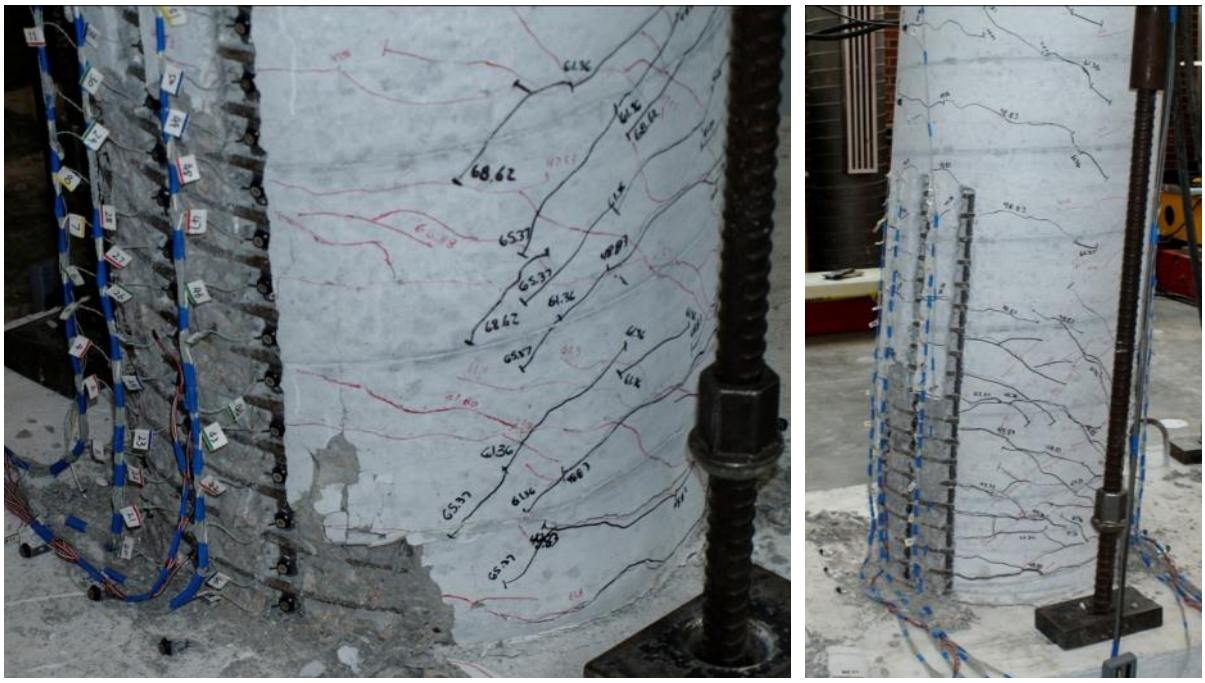

Figure 2-136. Test 12 – Peak Push Cycle in the Japan 2011 Load History at ($\mu_{9.9}^{68.62sec} = 8.22$")

Figure 2-137. Test 12 – (Left) Buckling of Extreme Fiber Bar N3 after Reversal from ($\mu_{9.9}^{68.62\,sec} = 8.22$") and (Right) Buckling of Bar N4 at ($\mu_{-1.4}^{69.4\,sec} = -1.14$")

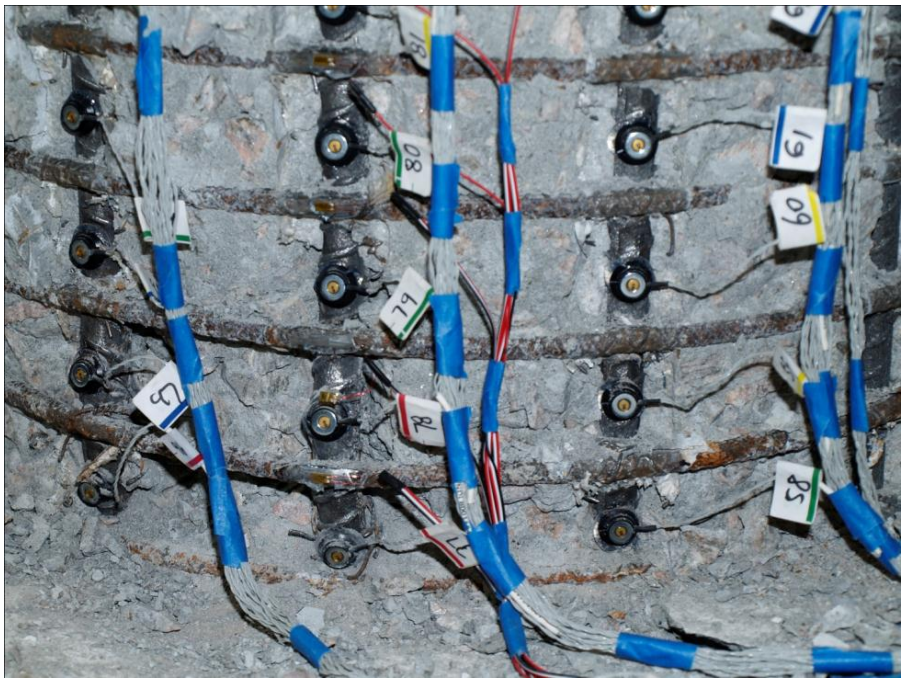

Figure 2-138. Test 12 – Increased Deformation in the Buckled bars toward the End of the Load History

2.1.5.2. Test 12 Japan 2011Earthquake Strain Data:

North Reinforcement:

Specific strain data observation points along the backbone curve of cyclic response were chosen for analysis, see Figure 2-139. The extreme fiber vertical strain profiles for push and pull cycles appear in Figure 2-140 and Figure 2-141 respectively. The corresponding transverse steel strains for the lowest six spiral layers on the South and North sides of the column in compression appear in Figure 2-142 and Figure 2-143.

Bar N3 buckled after reversal from a peak tensile strain of 0.058, measured 3.57" above the footing, during the peak push cycle ($\mu_{9.9}^{68.62\,sec} = 8.22"$). The peak compressive strain of -0.021 measured 3.57" above the footing in bar N3 during ($\mu_{-7.9}^{66.88\,sec} = -6.53"$) preceded the peak tensile cycle which caused buckling upon reversal of loading. The location of the largest tensile and compressive strains coincides with the location of outward buckling later in the test. The relationship between tensile strain and displacement from when the column was vertical to the peak of push cycles for extreme fiber bar N3 appears in Figure 2-144. The relationship between compressive strain and displacement for bar N3 appears in Figure 2-145. During initial pull cycles, the moment curvature prediction matches the recorded compressive strains well, but during the peak pull cycle to ($\mu_{-7.9}^{66.88\,sec} = -6.53"$) the recorded strains begin to exceed the moment curvature prediction at an increasing rate.

The strain hysteresis for the buckled region of bar N3, 3.75" above the footing, appears in Figure 2-149 with an earthquake time color bar to track the progression of the test. The peak tensile and compressive strains for bar N3 were measured over this gage length during the largest push and pull cycles respectively. The transverse steel strain gage hysteresis for the spiral layer overlaying the North buckled region appears in Figure 2-150. The strain in the transverse steel went into the inelastic range during the largest pull cycle to ($\mu_{-7.9}^{66.88\,sec} = -6.53"$). A data marker was placed at the location when the transverse steel strain began to sharply increase during the reversal from

($\mu_{9.9}^{68.62\ sec} = 8.22"$), indicating outward deformation over buckled extreme fiber bar N3. A similar data label is shown on the bar N3 strain hysteresis. Measured strains past this point no longer represent engineering strain, but are included to illustrate the progression of damage. Similarly, the strain gage placed over the transverse steel quickly goes off scale preventing further measurement.

South Reinforcement:

A peak compressive strain of -0.032 was measured 7.88" above the footing for extreme fiber bar S3. The relationship between compressive strain and displacement from when the column was vertical to the peak of push cycles appears in Figure 2-147 for bar S3. The recorded compressive strains match up well with the moment curvature prediction up to the peak cycle at ($\mu_{9.9}^{68.62\ sec} = 8.22"$). The relationship between tensile strain and displacement is shown in Figure 2-146.

The strain hysteresis for extreme fiber bar S3 appears in Figure 2-151 with an earthquake time color bar to track the progression of the test. The transverse steel strain hysteresis for the spiral layer restraining the potential outward deformed region of bar S3 is shown in Figure 2-152. The transverse steel strain sharply increased during the peak push cycle at ($\mu_{9.9}^{68.62\ sec} = 8.22"$). Since visible buckling was not observed for the South reinforcement, this sharp increase is attributed to large compressive demand in the region. The strain hysteresis in Figure 2-151 would suggest that measurable deformation occurred after the peak pull cycle. This particular gage length was never placed back into compression due to outward deformation during push cycles. The potential deformation cannot be visually verified by test results since bar buckling on the South side of the specimen was not observed. In previous tests, the measurable deformation was verified by buckling in the same region later in the test.

2.1.5.3. Test 12 Japan 2011 Earthquake Curvature and Strain Penetration Data:

Vertical curvature profiles for push and pull cycles along the backbone curve of cyclic response appear in Figure 2-153 and Figure 2-154. The least squared error lines show that higher ductility cycles have a linear distribution of plastic curvature similar to previous tests. The base rotations attributable to strain penetration of longitudinal reinforcement into the footing are shown in Figure 2-155 and Figure 2-156 respectively. The measured displacement of the base section was obtained from the LED placed closest to the footing-column interface. The slip hysteresis for extreme fiber bars N3 and S3 appear in Figure 2-157 and Figure 2-158 respectively. The top column displacement from the Optotrak may be determined by integrating the measured curvature distribution, extrapolating the base rotation to the center of loading, and assuming a linear distribution of curvature above the instrumented region which aligns the equivalent yield curvature at the base section. A comparison of the Optotrak integrated and measured top column displacements, in Figure 2-159, shows that the two methods agree throughout the entire range of displacements.

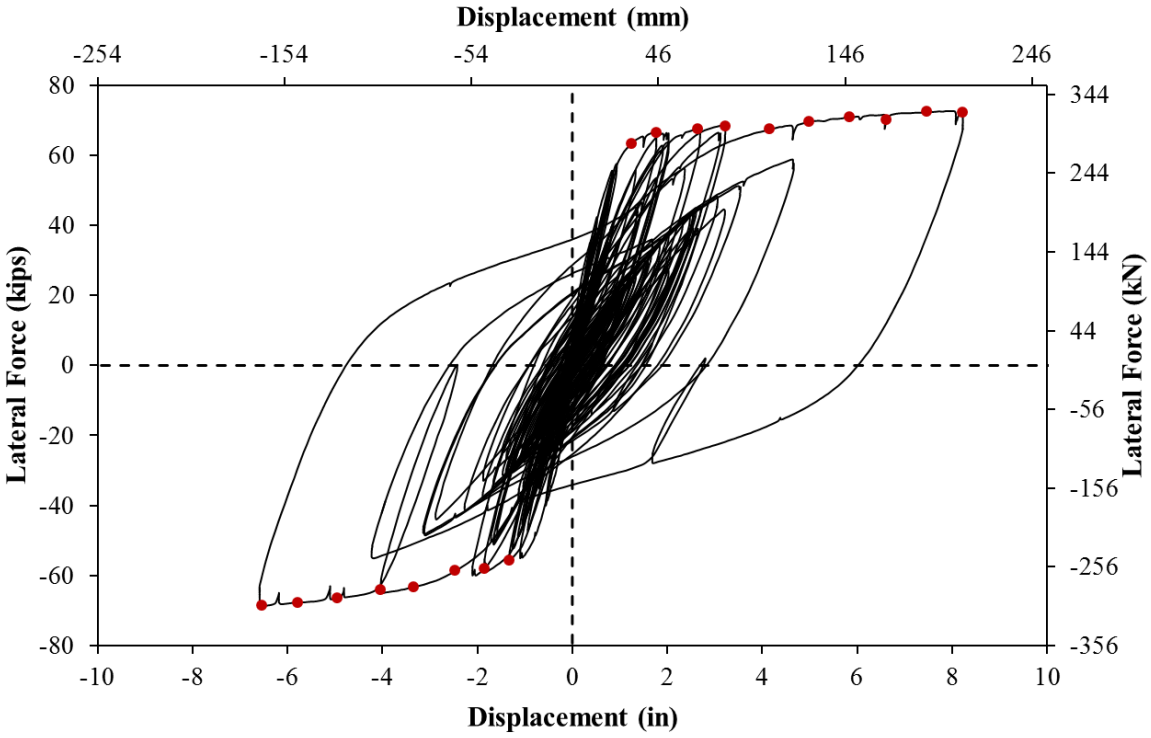

Figure 2-139. Test 12 – Strain Data Observation Points along the Backbone Curve

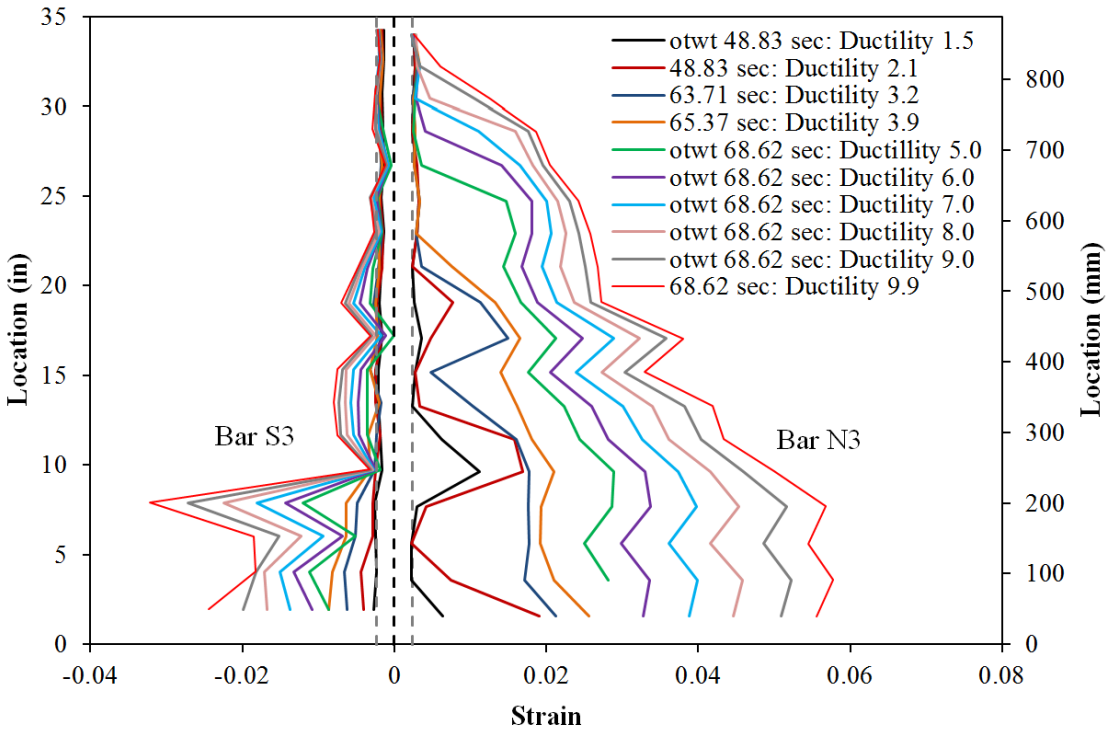

Figure 2-140. Test 12 – Extreme Fiber Vertical Strain Profiles during Push Cycles

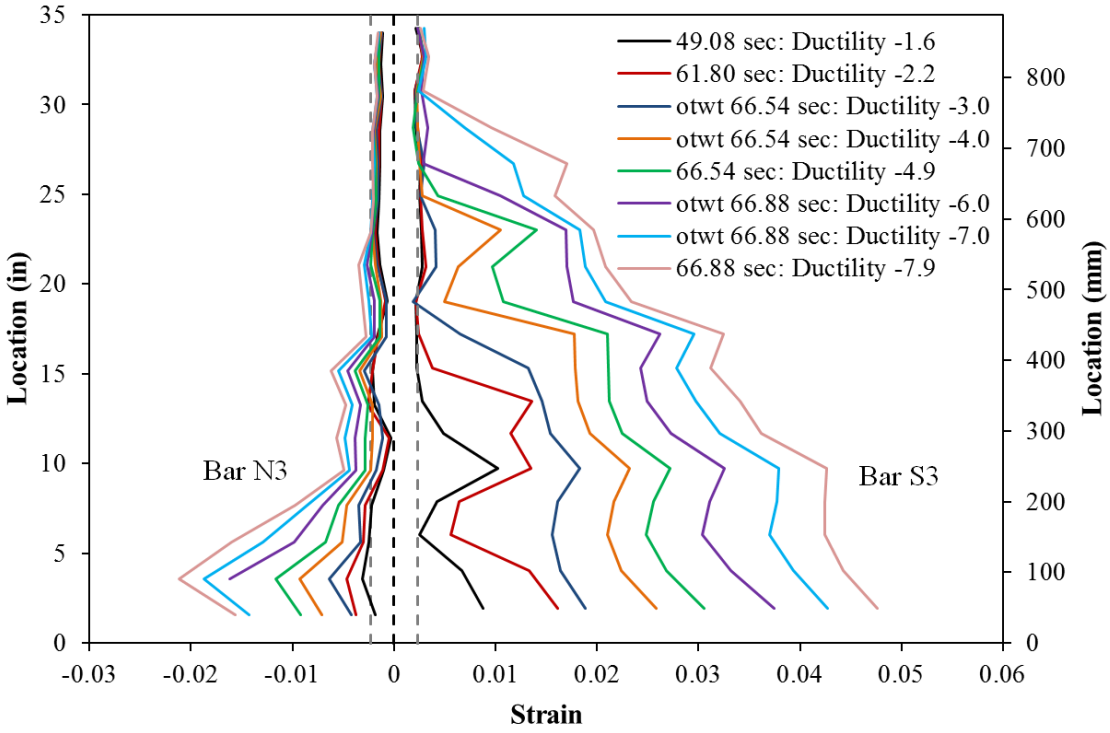

Figure 2-141. Test 12 – Extreme Fiber Vertical Strain Profiles during Pull Cycles

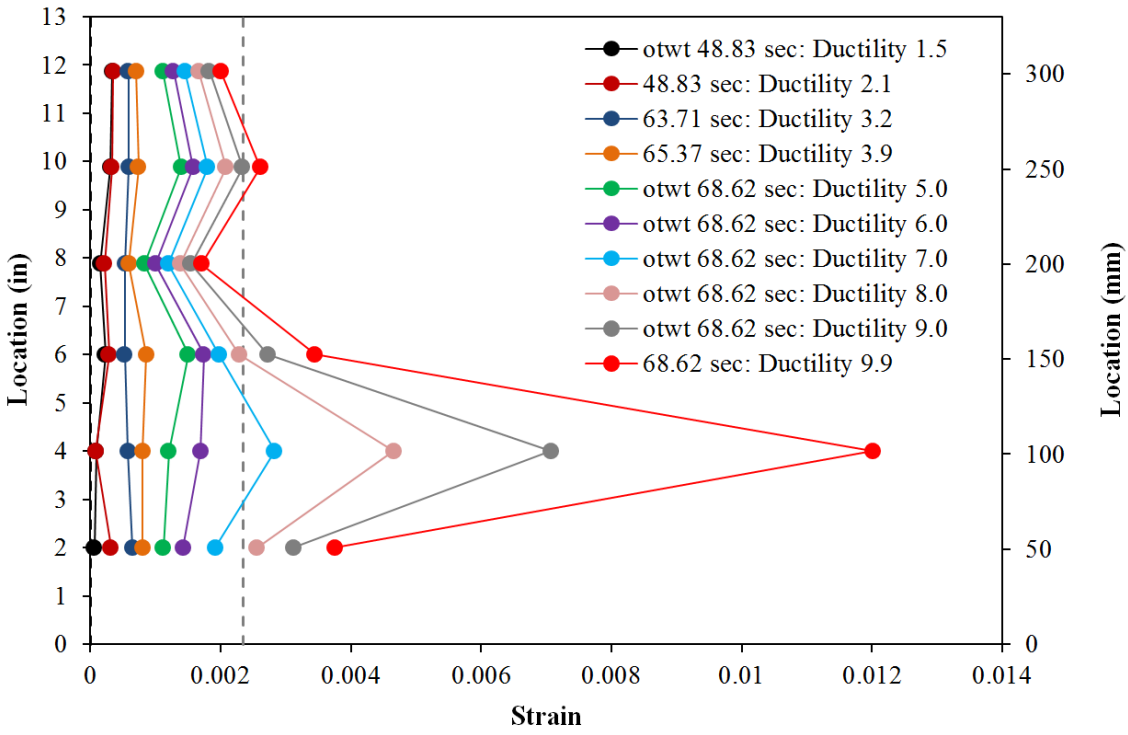

Figure 2-142. Test 12 – Transverse Steel Strains for Six Lowest Spiral Layers on the South Side during Push Cycles

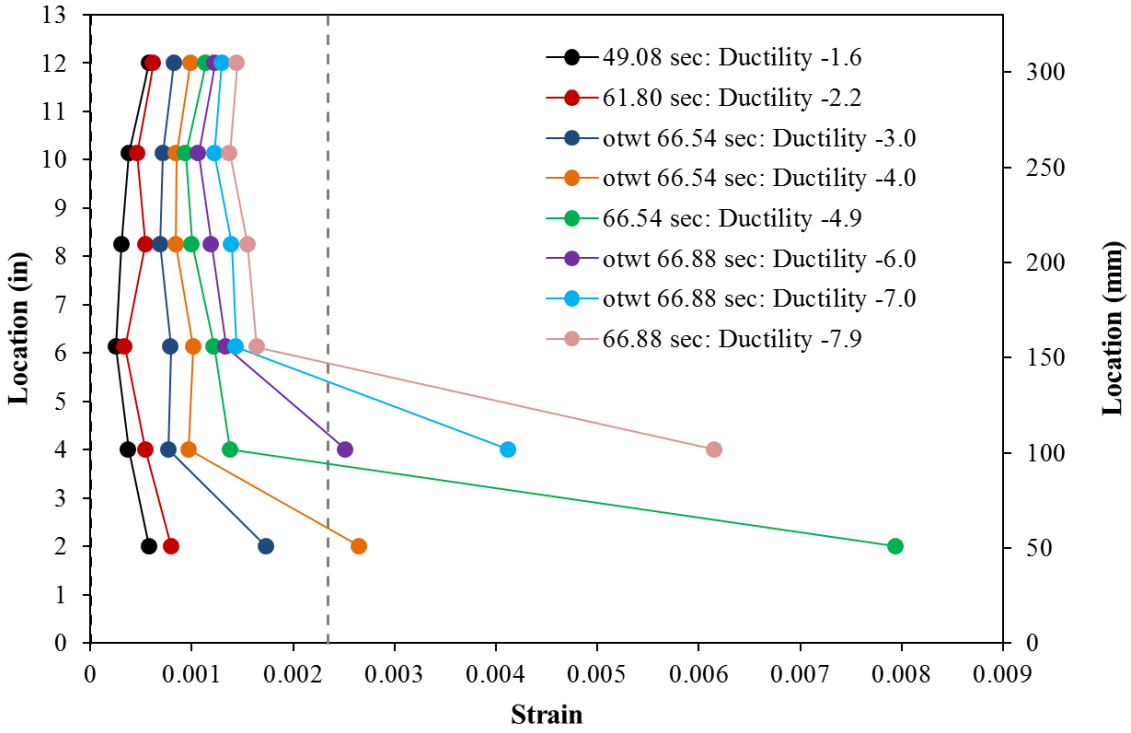

Figure 2-143. Test 12 – Transverse Steel Strains on the North Side during Pull Cycles

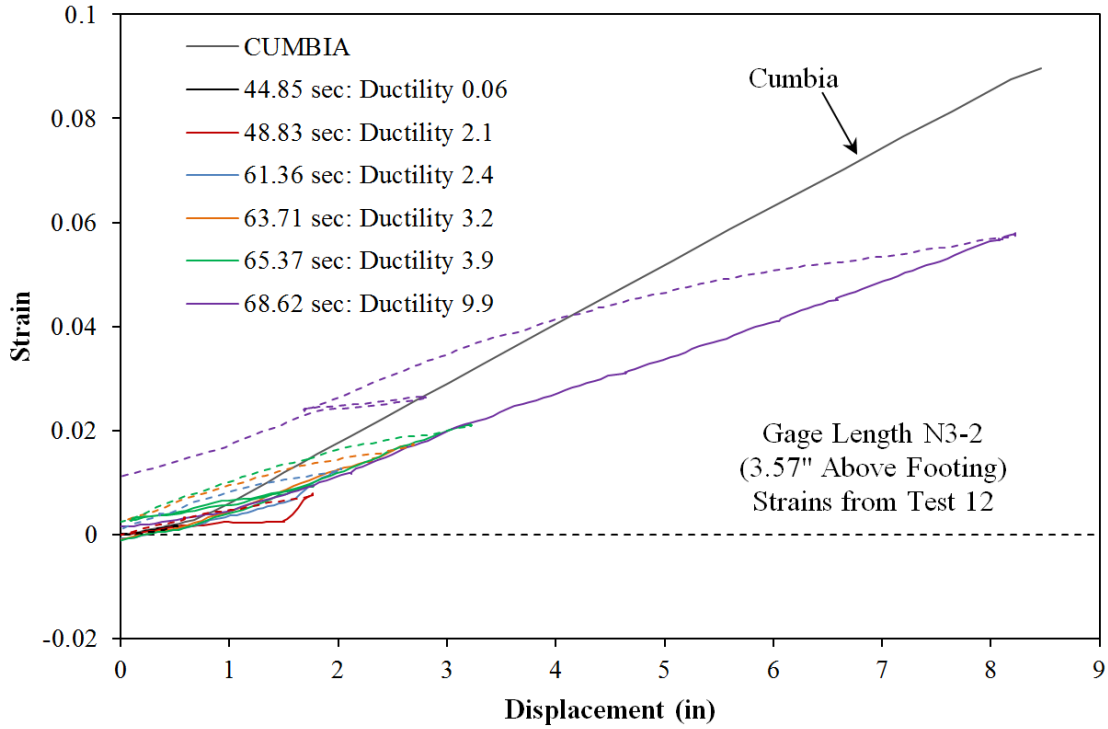

Figure 2-144. Test 12 – Relationship between Tensile Strain and Displacement for Bar N3 during Push Cycles

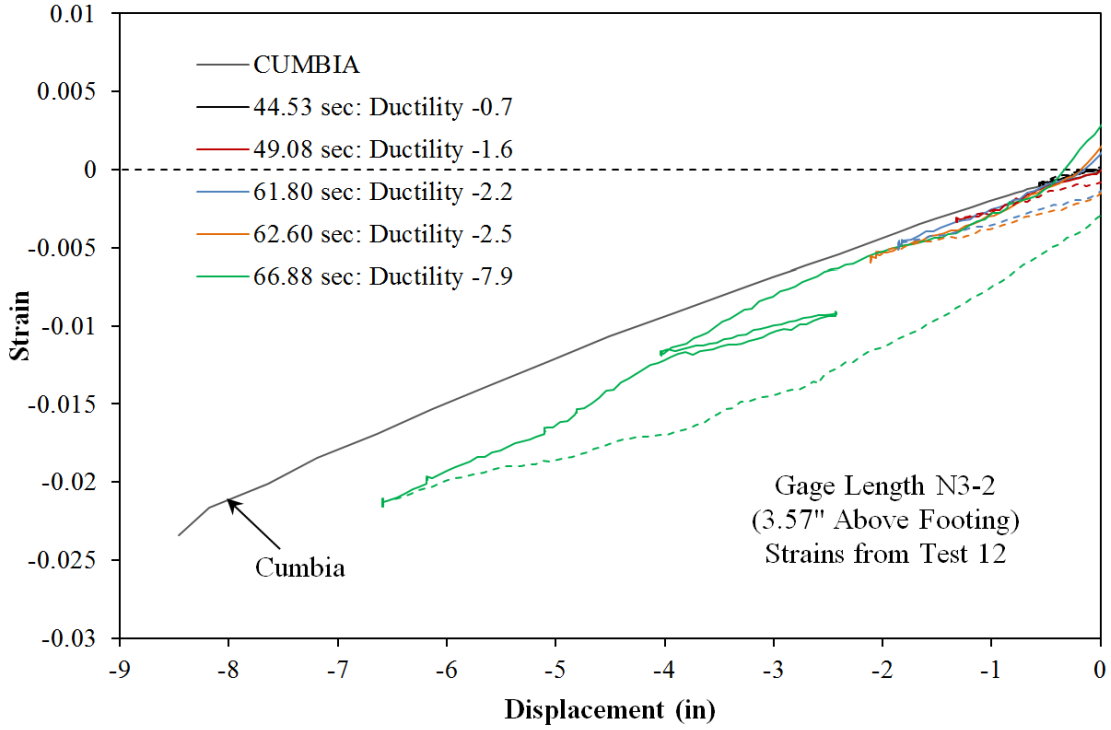

Figure 2-145. Test 12 – Compressive Strain and Displacement for Bar N3 during Pull Cycles

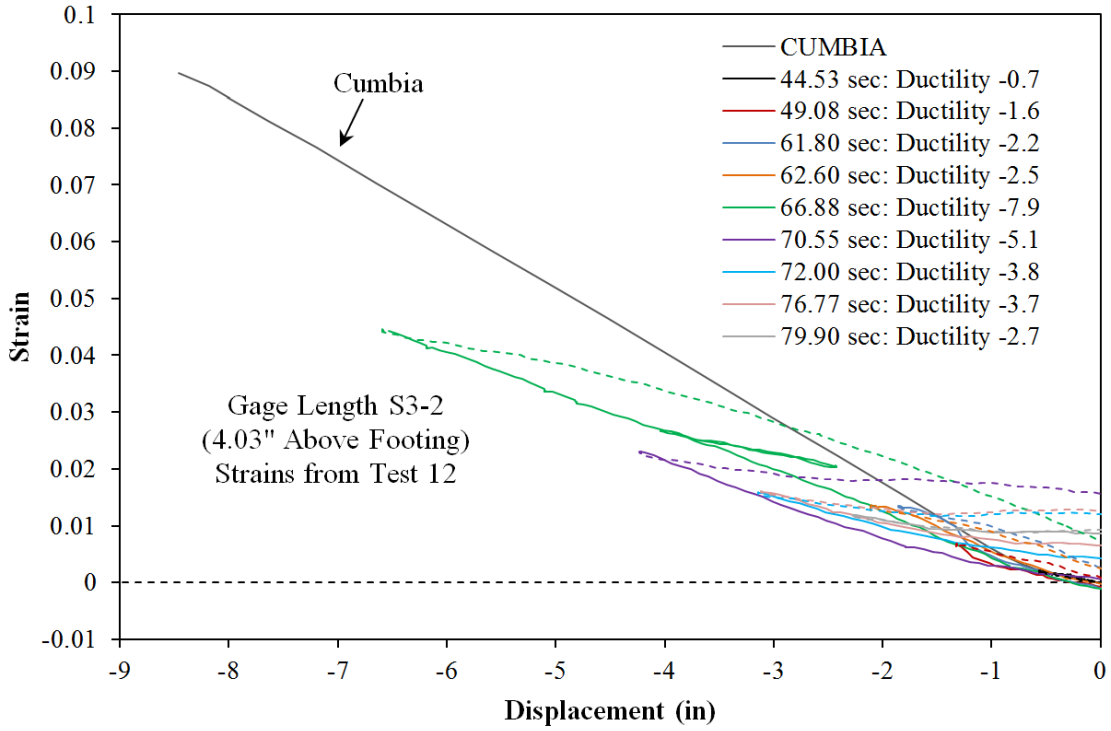

Figure 2-146. Test 12 – Relationship between Tensile Strain and Displacement for Bar S3 during Pull Cycles

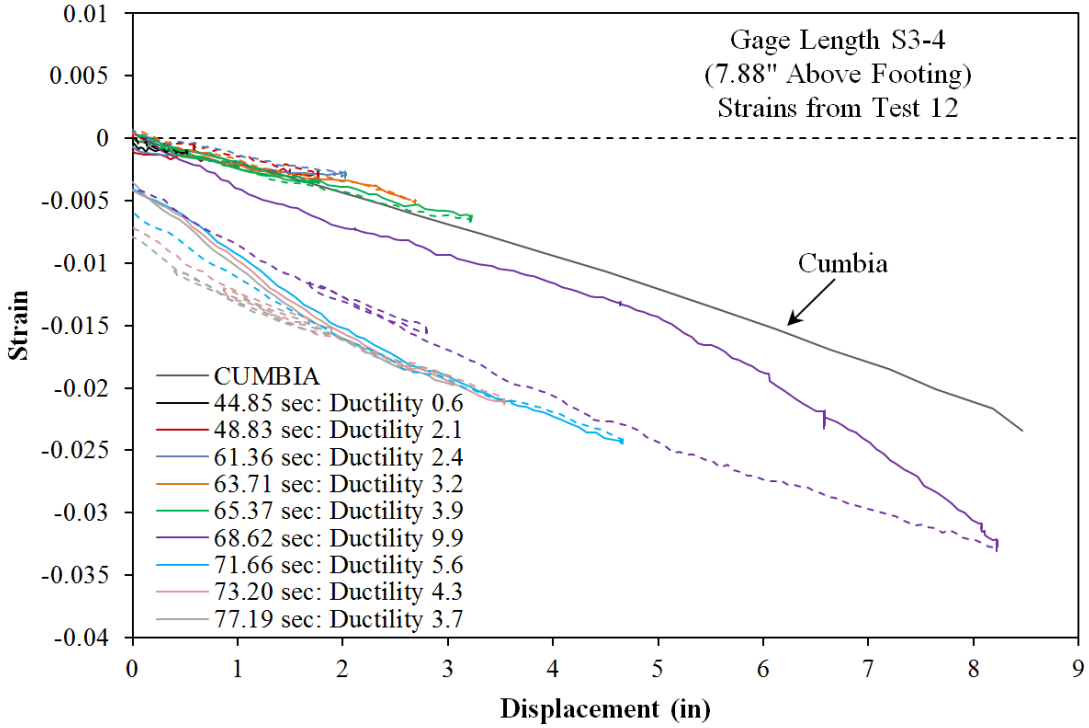

Figure 2-147. Test 12 – Compressive Strain and Displacement for Bar S3 during Pull Cycles

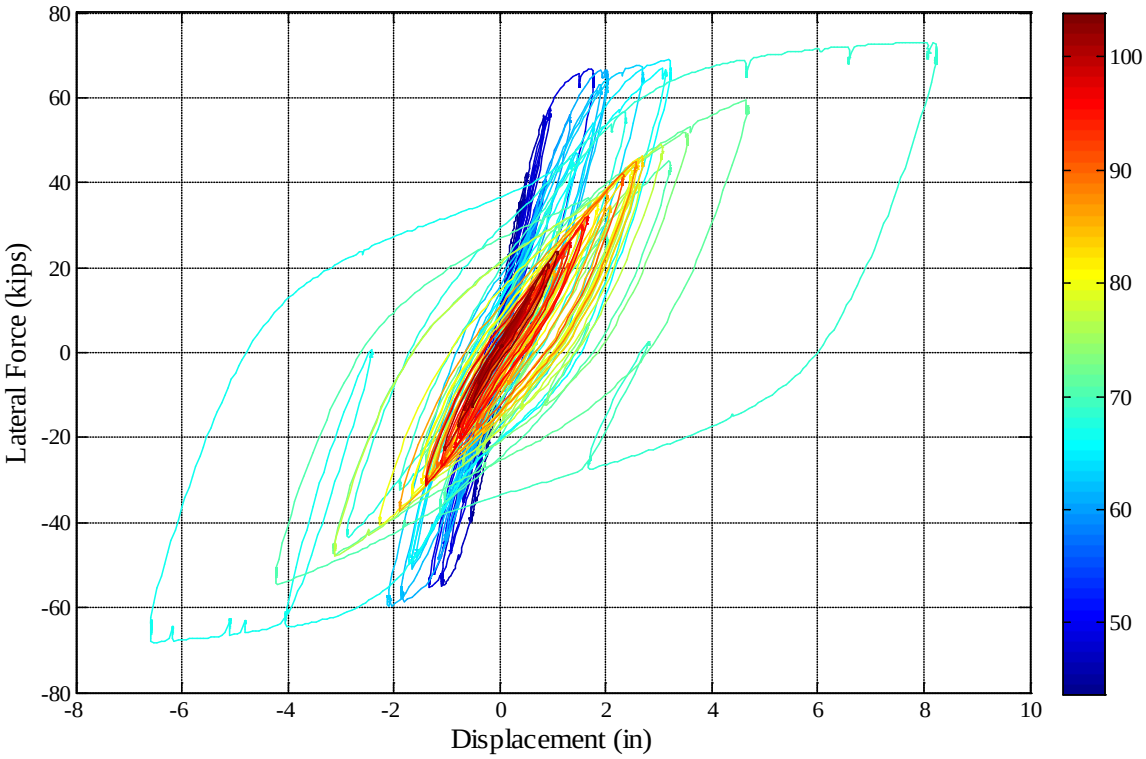

Figure 2-148. Test 12 – Hysteretic Response with an Earthquake Time Color Bar for the Japan 2011 Record

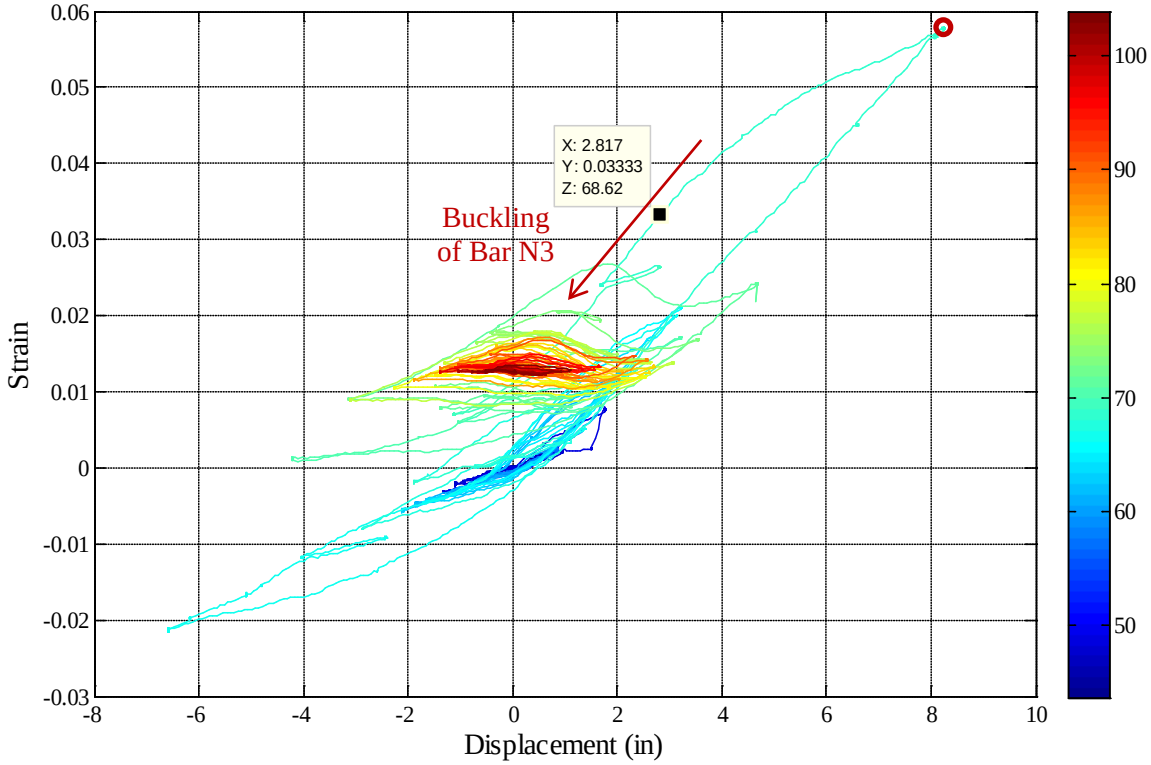

Figure 2-149. Test 12 – North Extreme Fiber Bar N3 Strain Hysteresis (1.56" Above)

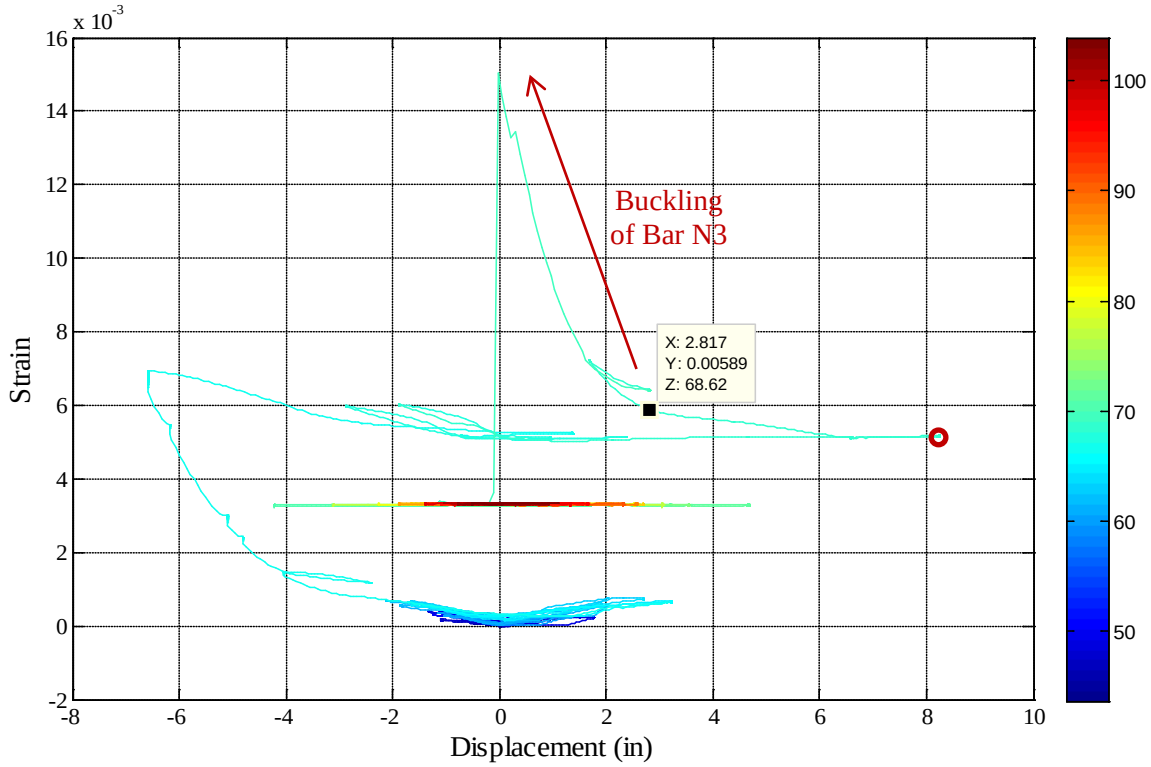

Figure 2-150. Test 12 – Transverse Steel Strain Hysteresis over North Buckled Region

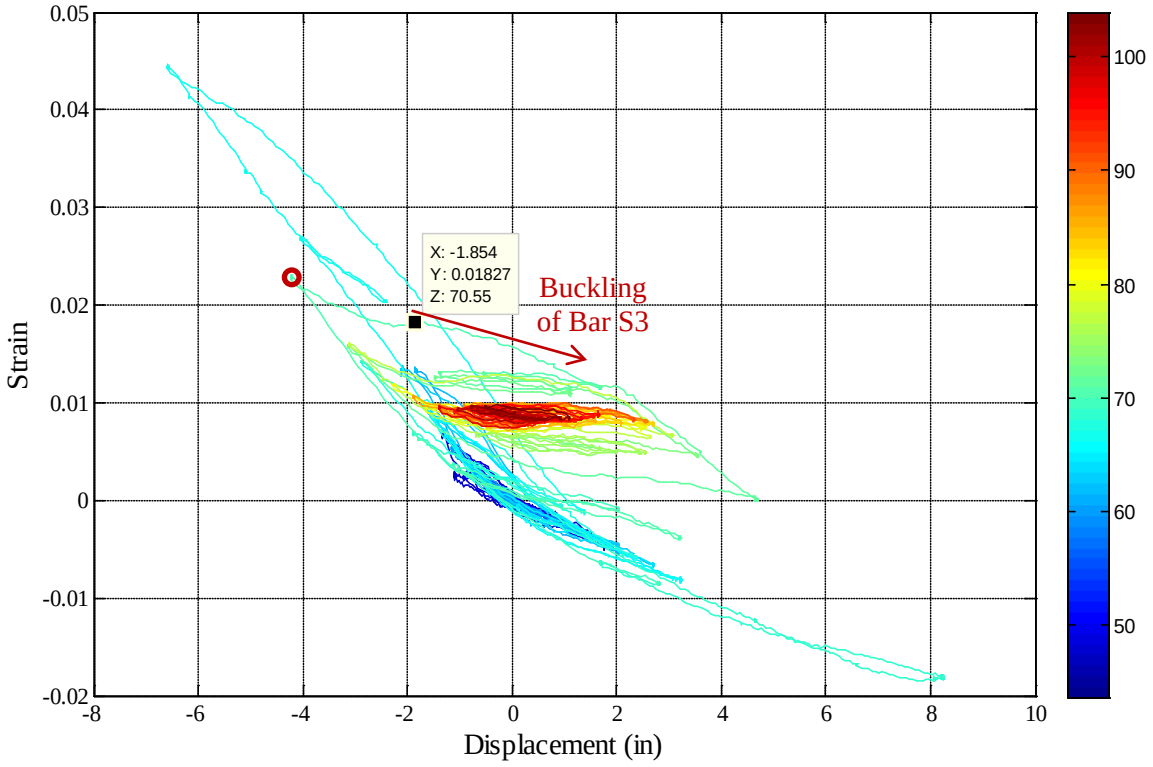

Figure 2-151. Test 12 – South Extreme Fiber Bar S3 Strain Hysteresis (4.03" Above)

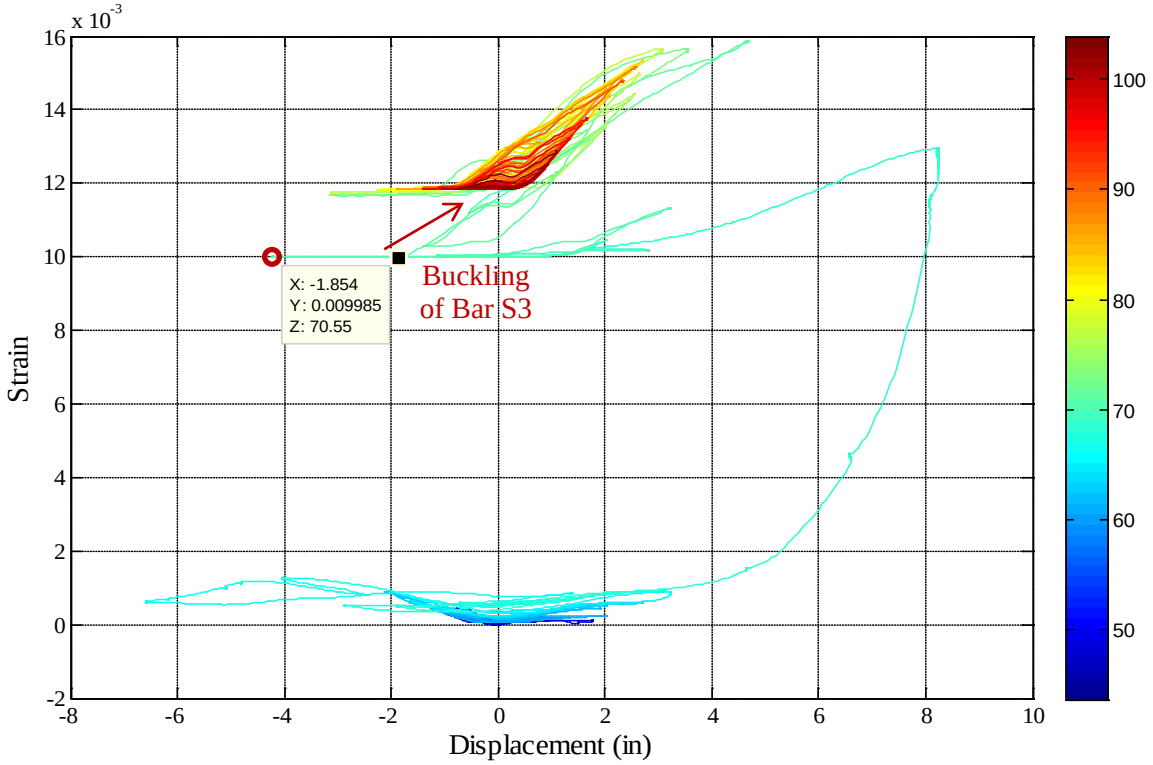

Figure 2-152. Test 12 – Transverse Steel Strain Gage Hysteresis over South "Measurable Deformation Region"

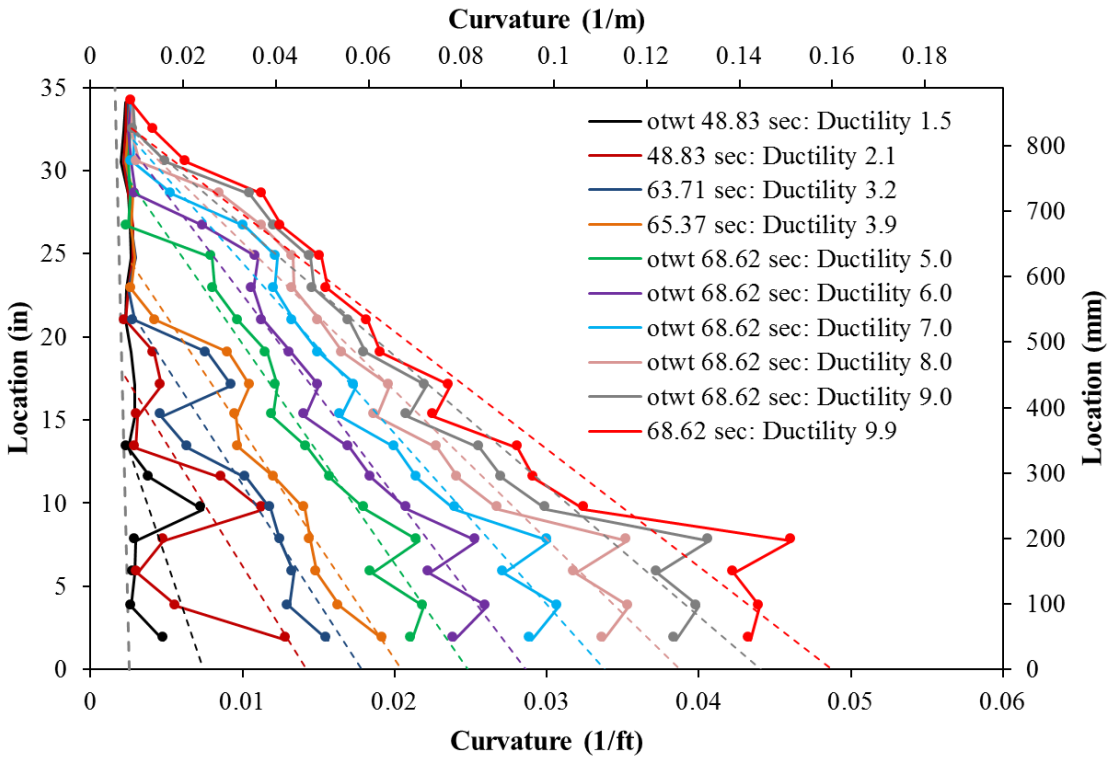

Figure 2-153. Test 12 – Vertical Curvature Profiles during Push Cycles

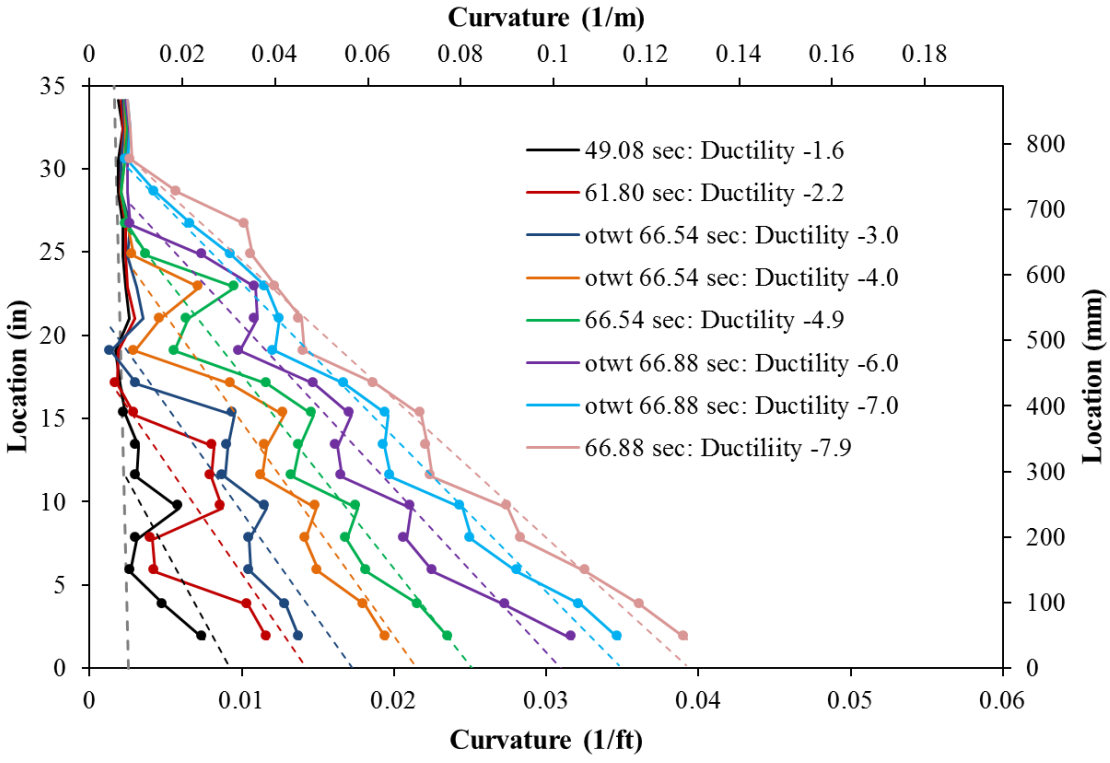

Figure 2-154. Test 12 – Vertical Curvature Profiles during Pull Cycles

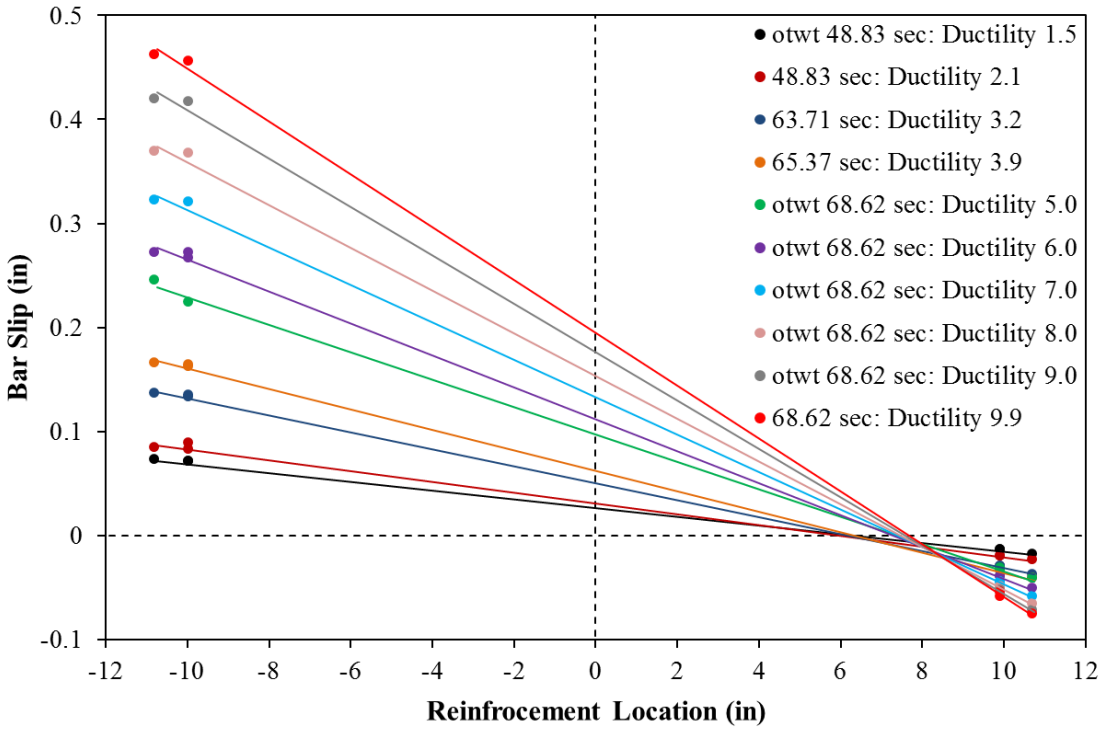

Figure 2-155. Test 12 – Base Rotation due to Strain Penetration during Push Cycles

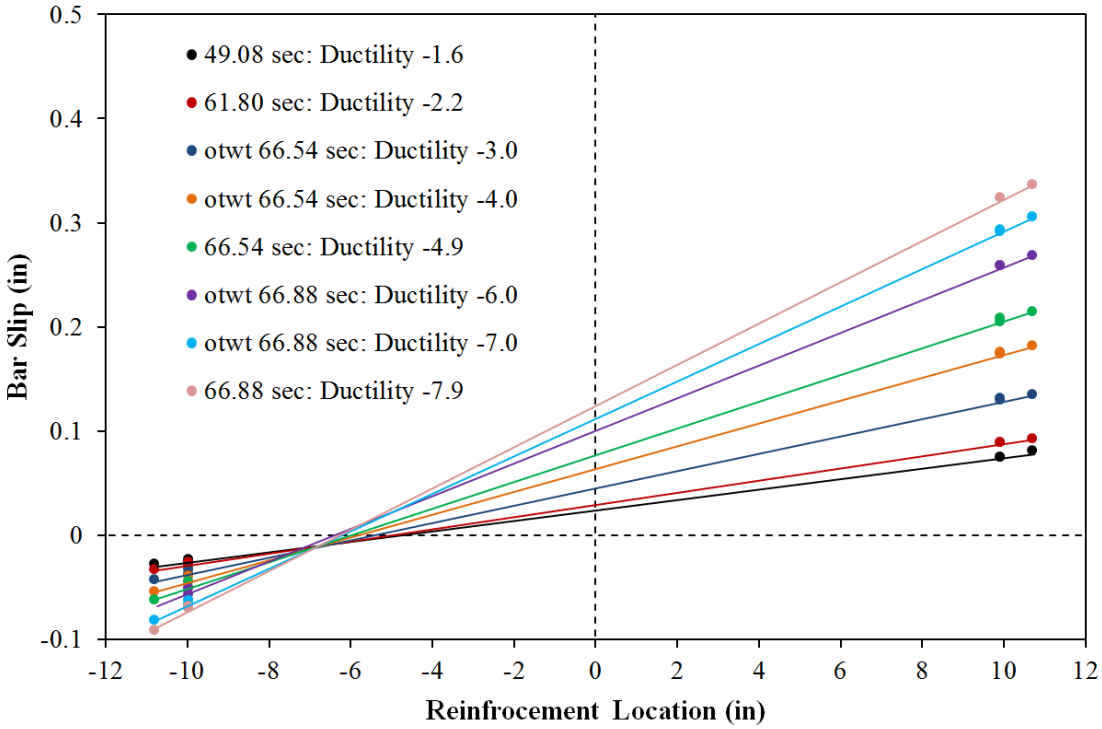

Figure 2-156. Test 12 – Base Rotation due to Strain Penetration during Pull Cycles

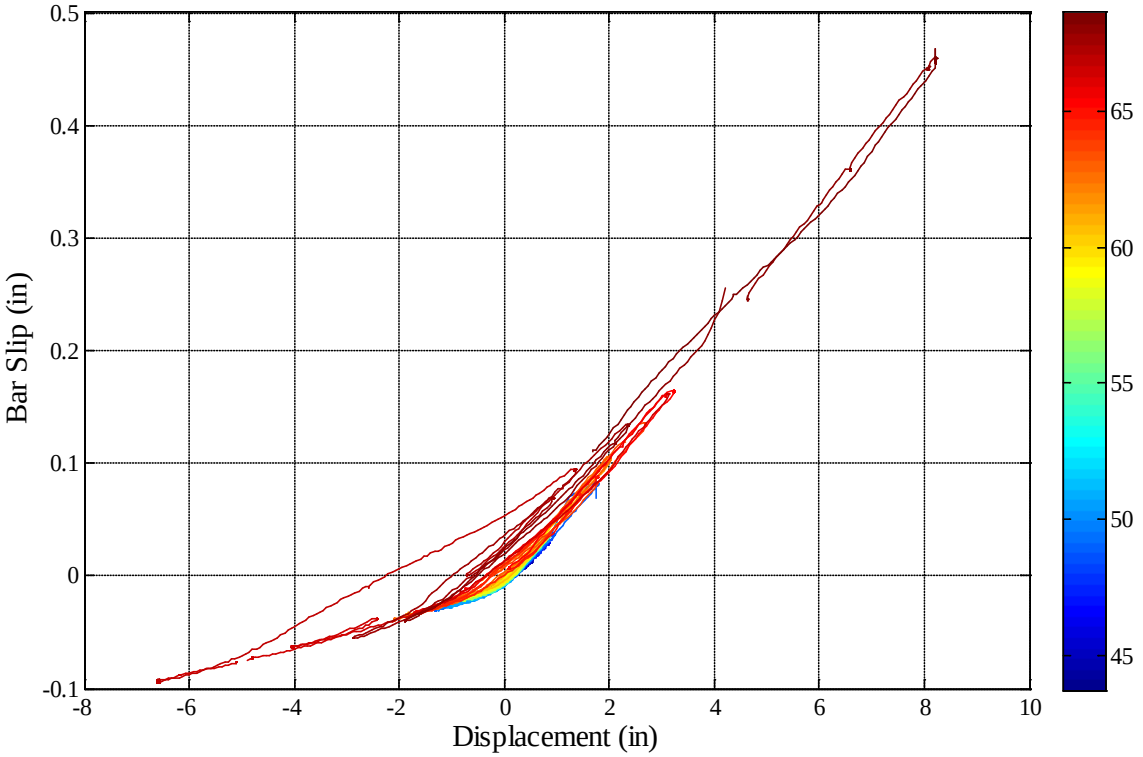

Figure 2-157. Test 12 – Bar N3 Base Section Slip Hysteresis due to Strain Penetration into the Footing (Shown Until Bar Buckling)

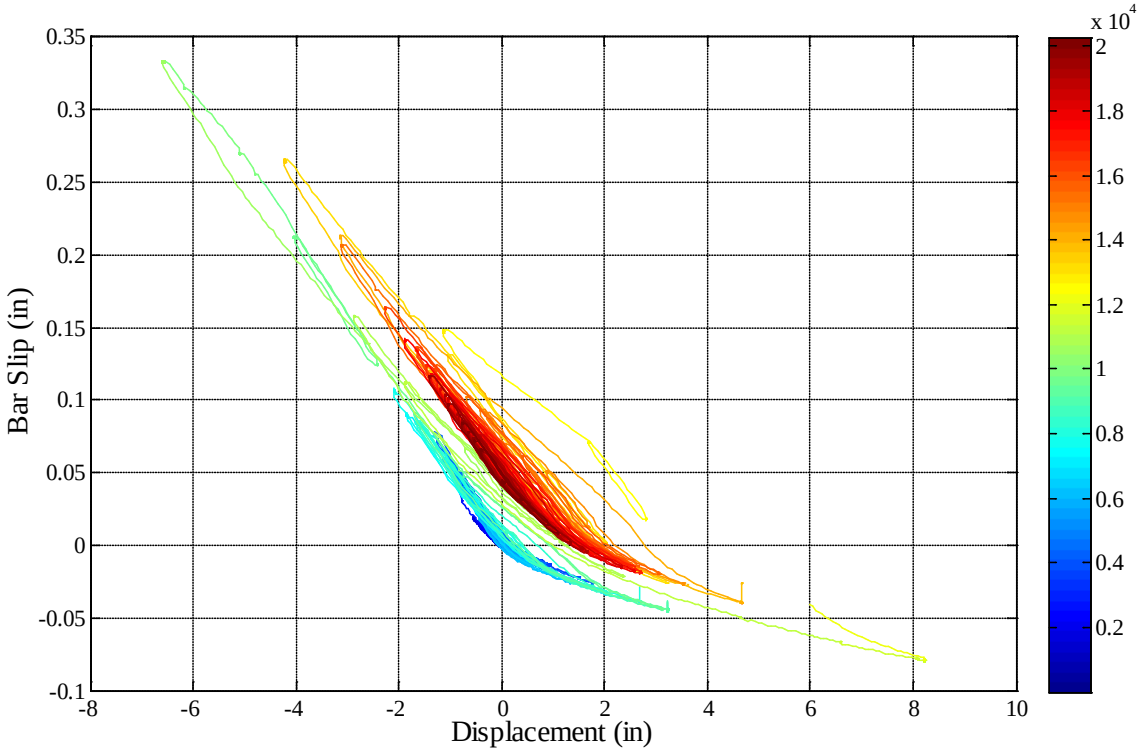

Figure 2-158. Test 12 – Bar S3 Base Section Slip Hysteresis due to Strain Penetration

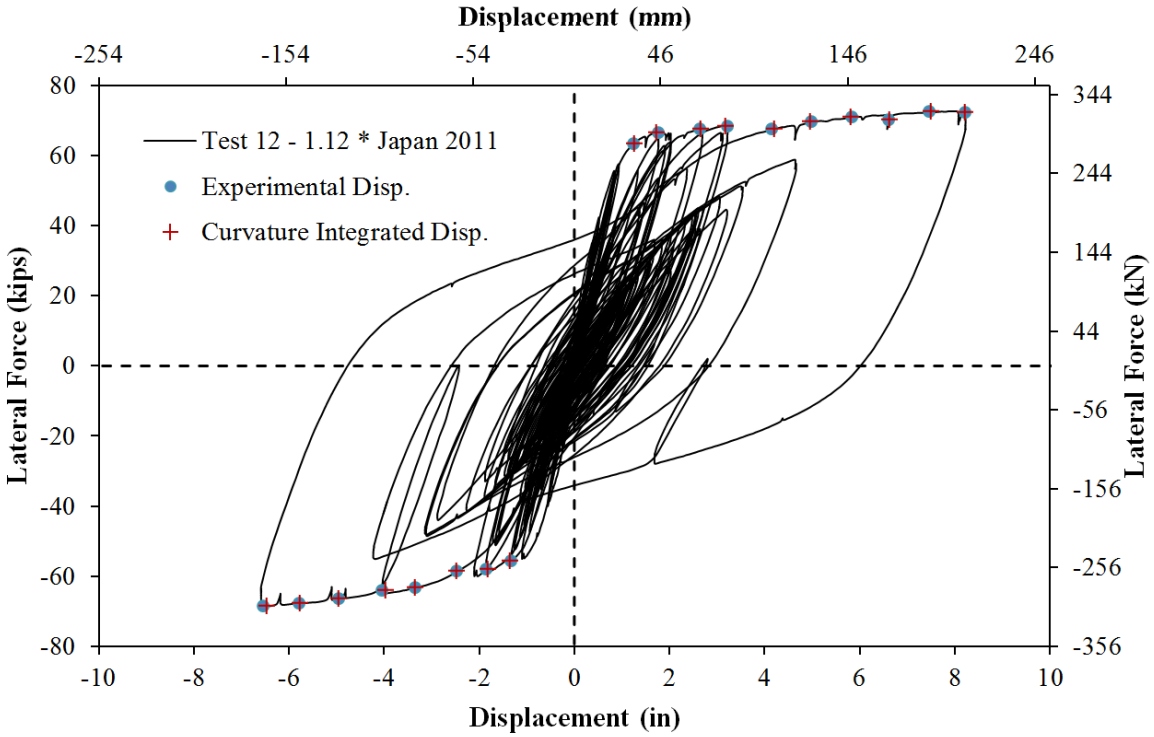

Figure 2-159. Test 12 – Comparison of Measured and Optotrak Integrated Top Column Displacements

2.2. Transverse Steel Variable Tests 13-18 Experimental Results

The effect of transverse steel detailing on restraint of longitudinal bars was the main variable for Tests 13-18. The same column geometry and longitudinal reinforcement were utilized with variable spiral detailing as shown in Figure 1-7. Load history was maintained as a variable for Tests 16-18 which had the same transverse steel detailing. The following transverse volumetric steel ratios were investigated: $(4A_{sp}/(D's)) = 0.5\%$ ($6d_{bl}$ spacing), 0.7%, 1% (previous test series), and two separate detailing arrangements for 1.3%. The research team believes that both volumetric ratio and spacing of the transverse steel are important when describing buckling restraint. Two columns were tested with 1.3% transverse steel, one with a #3 spiral at 1.5" spacing and another with a #4 spiral at 2.75" spacing. To evaluate the effect of a smaller bar at the same spacing a specimen was tested with a #3 spiral at 2.75" spacing.

An engineer has the most control over varying the size and spacing of transverse steel to improve buckling resistance. Previously tested specimens 8-12 utilized a #3 spiral at 2" pitch $(4A_{sp}/(D's)) =$ 1%.. During the Kobe and Japan 2011 load histories, a peak displacement ductility of ten was necessary to provide sufficient tensile strain to buckle reinforcement upon reversal. At ductility ten, the compression zone had sufficient demand to produce inelastic transverse steel which decreased its effectiveness in restraining the longitudinal reinforcement for the remainder of the load history. Even though this side of the specimen was subjected to much lower levels of tensile strain, the reinforcement still buckled due to the inelastic transverse steel. This implies that a compressive strain limit related to excessive yielding of the transverse steel may also be related to reinforcement bar buckling.

Table 2-10. Column Property Summary for Transverse Steel Variable Tests 13-18

Test	Load History	D (in)	L/D	Long. Steel (ρ_l)	Spiral Detailing (ρ_s)	f'c (psi)	P/f'c*Ag
13	Three Cycle Set	24	4	16 #6 bars (1.6%)	#4 at 2.75" (1.3%)	6097	6.2%
14	Three Cycle Set	24	4	16 #6 bars (1.6%)	#3 at 4" (0.5%)	6641	5.7%
15	Three Cycle Set	24	4	16 #6 bars (1.6%)	#3 at 2.75" (0.7%)	7232	5.2%
16	Three Cycle Set	24	4	16 #6 bars (1.6%)	#3 at 1.5" (1.3%)	6711	5.6%
17	Llolleo 1985	24	4	16 #6 bars (1.6%)	#3 at 1.5" (1.3%)	7590	5.0%
17b	Cyclic Aftershock	24	4	16 #6 bars (1.6%)	#3 at 1.5" (1.3%)	7590	5.0%
18	Darfield 2010	24	4	16 #6 bars (1.6%)	#3 at 1.5" (1.3%)	7807	4.8%
18b	Cyclic Aftershock	24	4	16 #6 bars (1.6%)	#3 at 1.5" (1.3%)	7807	4.8%

Table 2-11. Material Property Summary for Longitudinal and Transverse Reinforcement

Longitudinal Reinforcement	ε_y	f_y (ksi)	ε_h	f_h (ksi)	ε_u	f_u (ksi)
Tests 8-12	0.00235	68.1	0.0131	68.2	0.1189	92.8
Tests 13-18	0.00235	68.1	0.0146	68.2	0.1331	94.8

Transverse Steel	Yield Stress, f_y (ksi)
Tests 8-12 (#3 Spiral)	74.1
Tests 13-18 (#3 Spiral)	64.6
Tests 13-18 (#4 Spiral)	69.9

2.2.1. Test 13 – Symmetric Three Cycle Set Load History (#4 Spiral at 2.75" Spacing)

Table 2-12. Results Summary for Test 13 – Symmetric Three Cycle Set Load History

LOAD HISTORY: Symmetric Three Cycle Set Load History

VALUES OF INTEREST:

Transverse Steel Detailing:	#4 Spiral at 2.75" Spacing (1.3%)
Concrete Compressive Strength:	$f_c' = 6097psi$
Axial Load:	$P = 170kips$
Analytical First Yield Force:	$F_y' = 46.5kips$
Experimental First Yield Displacement:	$\Delta_y' = 0.60"$
Analytical Nominal Moment Capacity:	$M_n = 498.7kip * ft$
Equivalent Yield Displacement:	$\Delta_y = 0.81"$
Maximum Lateral Force:	$70.9kips$
Failure Mode:	Fracture of Previously Buckled Reinforcement

DAMAGE OBSERVATIONS: (Drift %) [Displacement Ductility, μ_Δ]

First Cracking North:	$1/2Fy' = 0.17"$
First Cracking South:	$-1/2Fy' = -0.16"$
Cover Concrete Crushing North:	$\mu_2^{-1} = -1.61"$
Cover Concrete Crushing South:	$\mu_2^{+1} = 1.60"$
Transverse Steel Yield North:	At $-4.78"$ during pull to $\mu_6^{-3} = -4.85"$
Transverse Steel Yield South:	At $4.17"$ during push to $\mu_8^{+2} = 6.46"$
Longitudinal Bar Buckling North:	Reversal from $\mu_8^{+1} = 6.46"$
Longitudinal Bar Buckling South:	Reversal from $\mu_8^{-1} = 6.48"$
Longitudinal Bar Fracture North:	At $-0.79"$ during push to $\mu_{10}^{+1} = 8.06"$
Longitudinal Bar Fracture South:	At $-2.51"$ during pull to $\mu_{10}^{-2} = -8.12"$

*$\mu_{10}^{-2} = -8.12"$ represents the second pull cycle of displacement ductility ten which reached a peak displacement of -8.12 inches

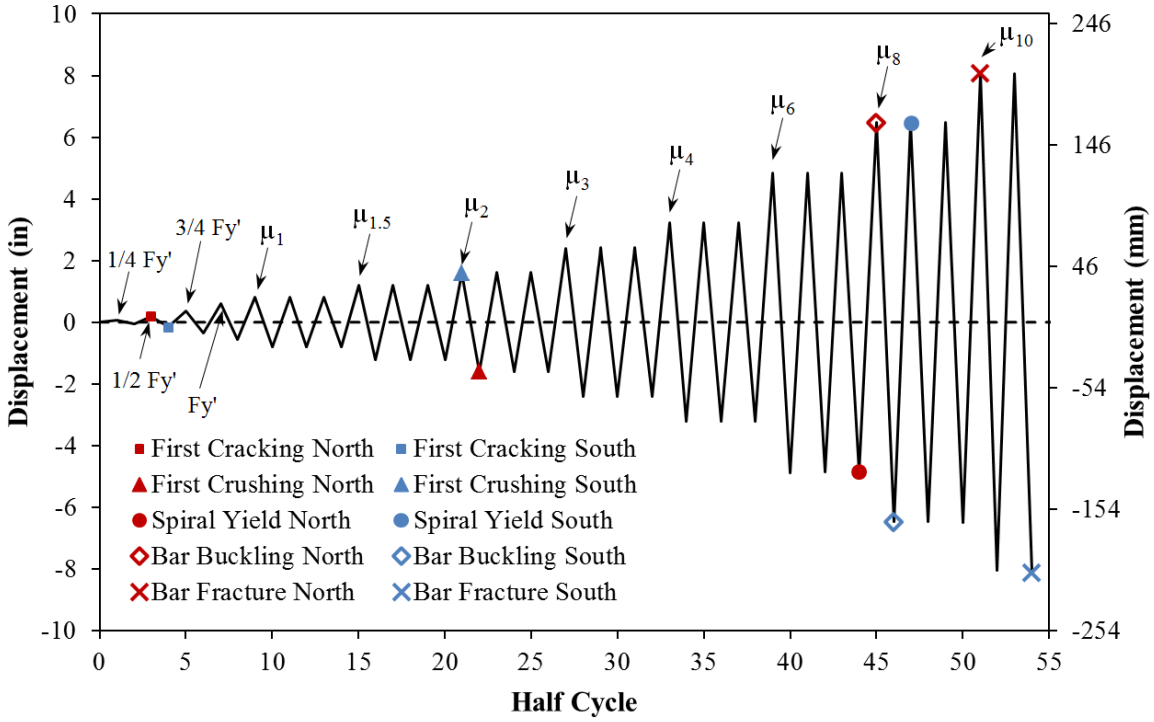

Figure 2-160. Test 13 – Symmetric Three Cycle Set Load History

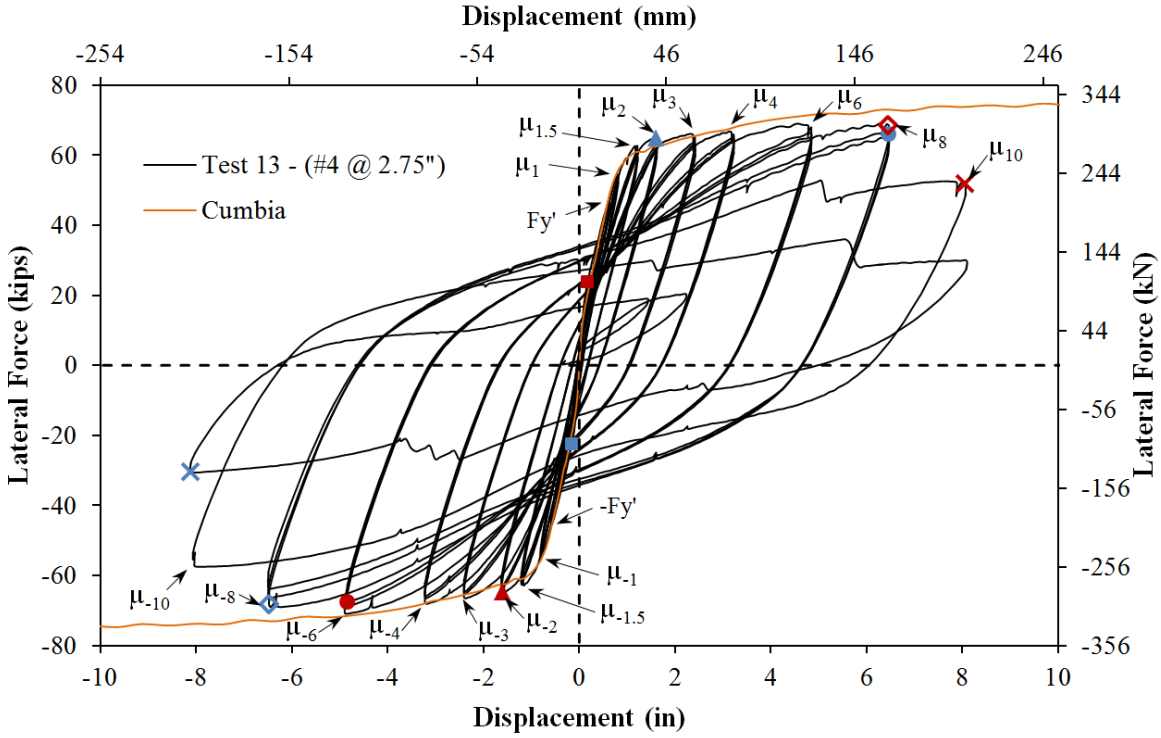

Figure 2-161. Test 13 – Lateral Force vs. Top Column Displacement Response

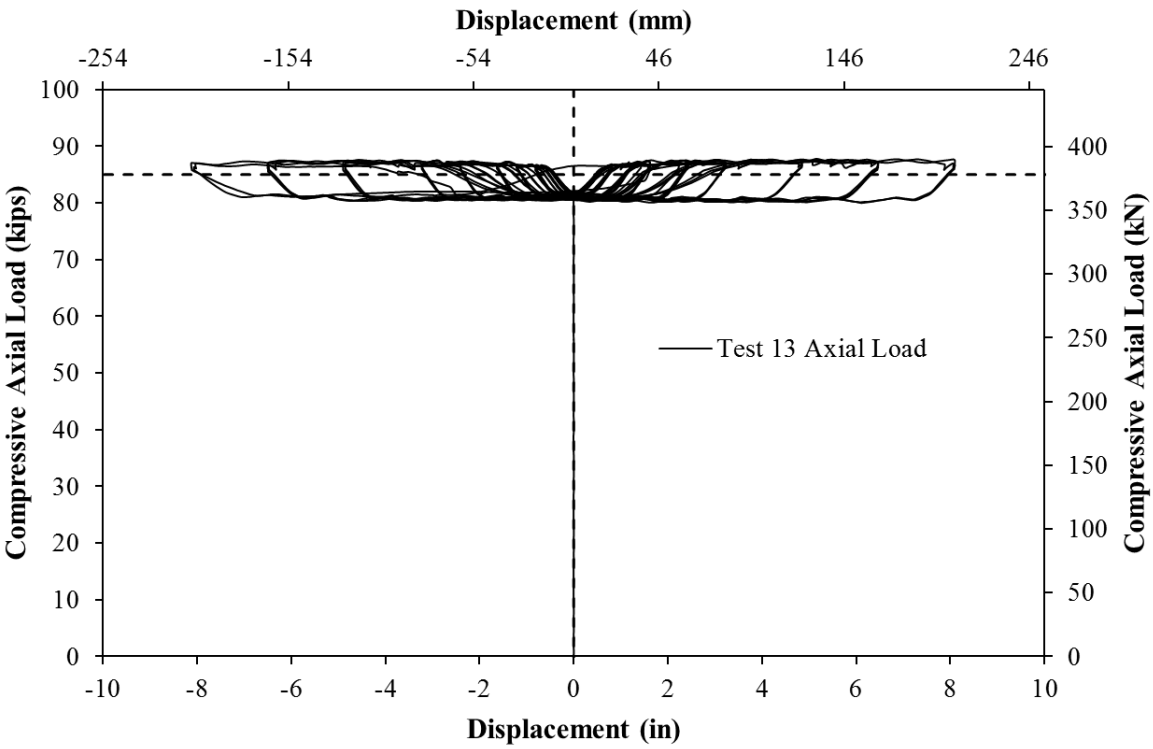

Figure 2-162. Test 13 – Compressive Axial Load from One Jack (Total = 2*Value)

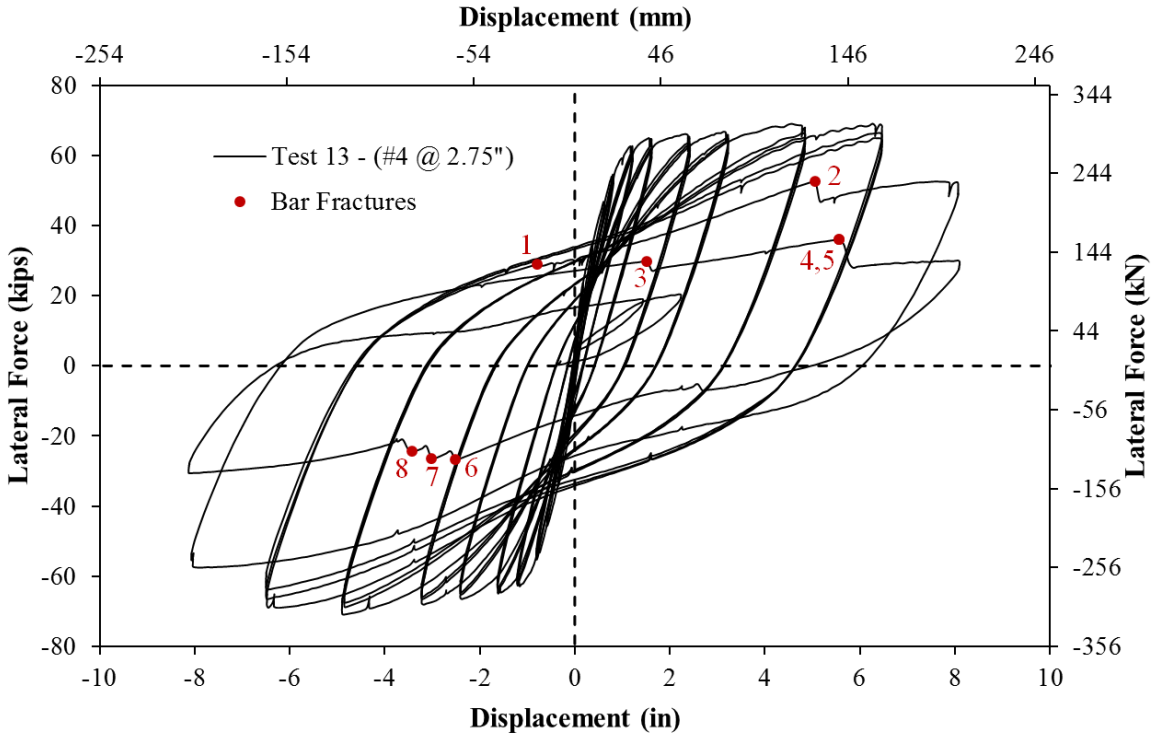

Figure 2-163. Test 13 – Bar Fracture History of Previously Buckled Reinforcement

2.2.1.1. Test 13 – Symmetric Three Cycle Set (#4 @ 2.75") Experimental Observations:

The first yield force for the tested material and geometric properties was determined using moment curvature analysis (Test 13: Cumbia Fy' = 46.5 kips with f'c = 6097 psi) compared to (Test 9: Cumbia Fy' = 46.9 kips with f'c = 6814 psi). The predicted first yield force for both test series, 7-12 and 13-18, are remarkably similar due to the near identical longitudinal reinforcement properties for both batches of steel. The first yield displacement for the thirteenth test was obtained as an average for the first yield push and pull cycles ($\Delta'_y = 0.60$") compared to ($\Delta'_y = 0.63$") for the ninth test. Vertical strain profiles for both push and pull cycles up to the first yield force appear in Figure 2-164 with a dashed line representing the yield strain of the longitudinal reinforcement. The equivalent yield displacement, used to determine the displacement ductility levels ($\mu_{\Delta 1} = 1 * \Delta_y$), is then calculated as $\Delta_y = \Delta'_y(M_n/M'_y) = 0.81$" for Test 13 compared to $\Delta_y = 0.84$" for Test 9. The full symmetric three cycle set load history appears in Figure 2-160 and the resulting lateral force vs. top column displacement hysteresis is shown in Figure 2-161.

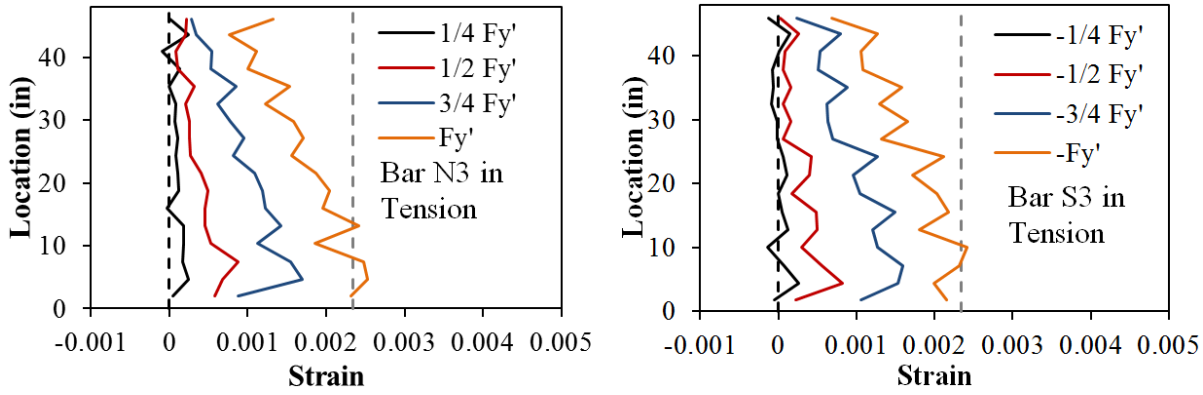

Figure 2-164. Test 13 – Vertical Strain Profiles for Extreme Fiber Reinforcement (Dashed Yield Line)

The first cracks on the North side of the specimen where measured at 0.1mm at approximate 8" spacing during the push cycle to ½Fy'. Cracks of the same width and approximate spacing where measured on the South side of the specimen during the -½Fy' pull cycle. The cracks on the North side of the specimen increased to 0.2mm at 4" spacing during the push cycle to ¾Fy'. Larger 0.3mm crack widths at a greater spacing of 8" were measured on the South side of the specimen during -¾Fy'. Up until the first yield force was reached, the cracks were all horizontal without any inclination on the sides of the specimen with greater shear stress. The change in orientation of flexural shear cracks with increased ductility demands appears in Figure 2-170. Cracks on the North side of the specimen increased to 0.3mm width at approximate 4" spacing during the first yield push cycle. During the first yield pull cycle cracks increased to 0.4mm width at 5" spacing.

During ($\mu_1^{+3} = 0.81$"), crack widths measured 0.4mm at 4" spacing on the North side of the specimen. On the opposite side of the specimen crack widths were measured at 0.5mm at 5" spacing during ($\mu_1^{-3} = -0.80$"). Visible flaking which occurs just before cover concrete crushing was apparent on both sides of the specimens after the first push and pull cycles of ductility 1.5. This flaking did not lead to crushing during subsequent cycles at displacement ductility 1.5. Cracks on the North side of the specimen measured 1.1mm, while the South side measured 1.25mm during the third push and pull cycles of ductility 1.5 respectively. Concrete cover crushing 2" above the footing occurred on the South side of the specimen during ($\mu_2^{+1} = 1.60$"). Similarly, crushing over 2" on the North side of the specimen was observed during the ($\mu_2^{-1} = -1.61$"). Cracks on the North and South

sides of the specimens measured 1.5mm and 2mm during the third push and pull cycles of ductility two respectively. After three complete cycles at ductility three, the extent of crushing increased to 10" on the North and 7" on the South side of the specimen. The load history continued through ductility six with additional inclined flexural shear cracks and increased extent of crushing, but without buckling of the longitudinal steel.

After reversal from ($\mu_8^{+1} = 6.46"$), extreme fiber bar N3 and adjacent bar N2 buckled as shown in the left photo of Figure 2-167. During the second push cycle of ductility eight, South reinforcing bar S4 visibly buckled, see the left photo of Figure 2-168. The South extreme fiber bar S3 did not show signs of visible buckling while adjacent bar S4 deformed out of plane at the location where more prominent buckling later occurred. During the second and third pull cycles of ductility eight the deformation in the North buckled bars increased and an additional bar N4 buckled as shown in the right photo of Figure 2-167. The buckled deformation of both the North and South reinforcement occurred between layers of transverse steel (#4 at 2.75" spacing). Buckling over two to three layers of transverse steel was observed in previous tests with a #3 spiral at 2" spacing.

During ($\mu_{10}^{+1} = 8.07"$), two of the previously buckled North reinforcing bars ruptured and South reinforcing bars S2 and S3 buckled, see Figure 2-169. Rupture of the North reinforcing bar N3 occurred before the bar straightened out in tension. While this has never been observed in previous tests, it is likely a consequence of the more severe buckled profile between layers of transverse reinforcement. Losses in strength from reinforcement ruptures are shown in Figure 2-163 on the hysteretic response. Three additional North reinforcing bars ruptured during the ($\mu_{10}^{+2} = 8.06"$). Three previously buckled reinforcing bars on the South side of the specimen ruptured during ($\mu_{10}^{-2} = -8.12"$). The test was concluded with a total of eight ruptured reinforcing bars and a considerable loss of strength in each direction of loading.

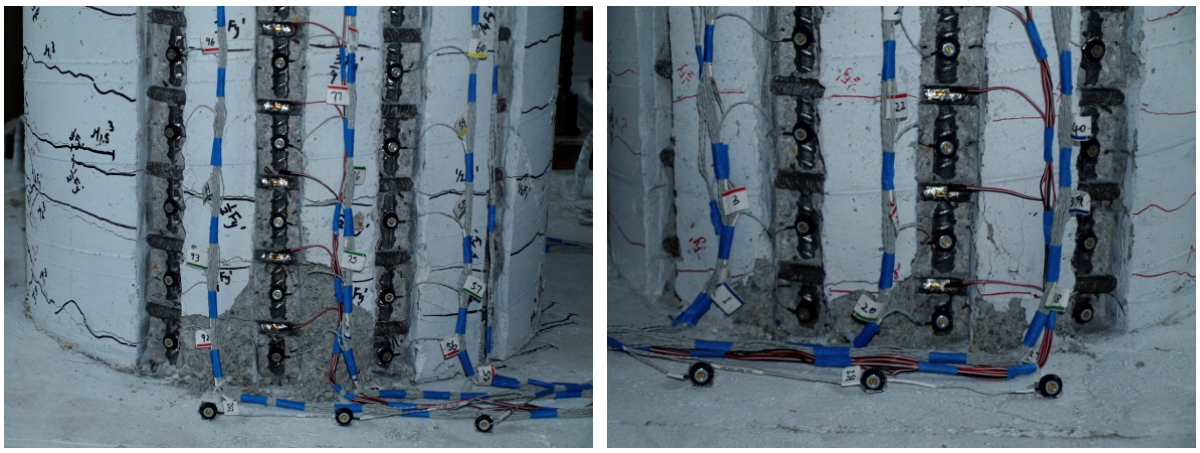

Figure 2-165. Test 13 – Concrete Cover Crushing at the End of Ductility Two (Left - North) and (Right - South)

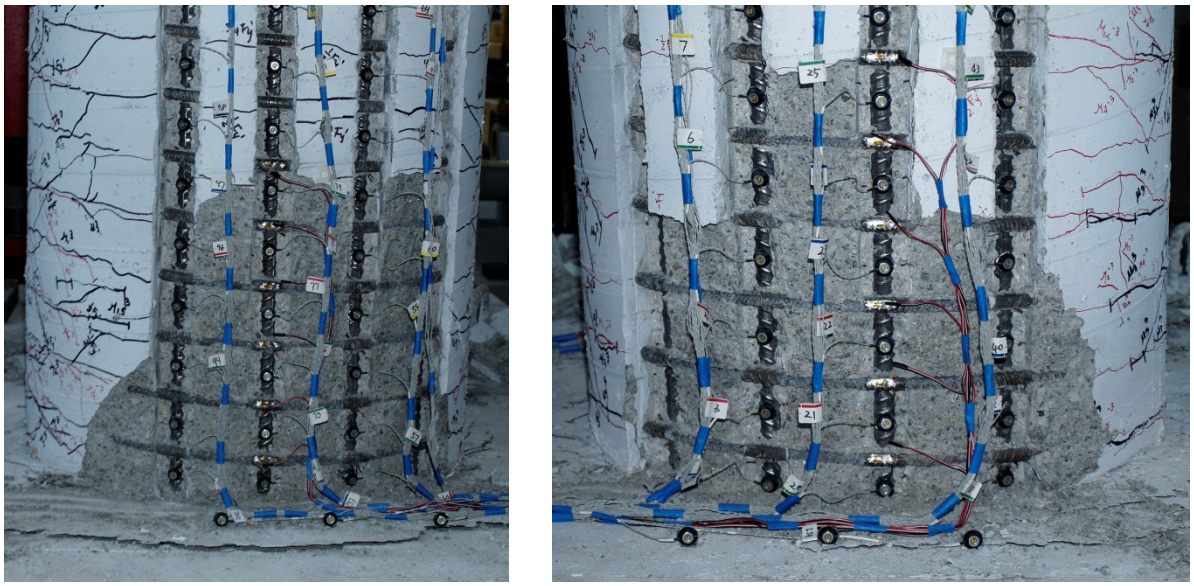

Figure 2-166. Test 13 – Extent of Crushing at the End of Ductility Six (Left - North) and (Right - South)

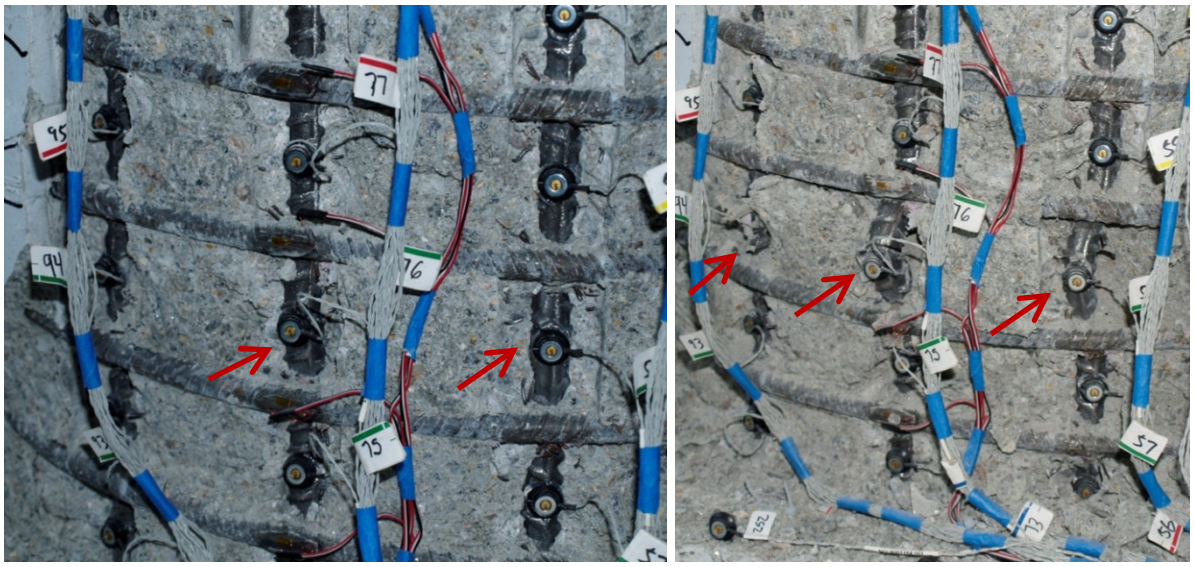

Figure 2-167. Test 13 – (Left) Buckling of South Reinforcing Bars N2 and N3 during ($\mu_8^{-1} = -6.48$") and (Right) Increased deformation in North Buckled Bars ($\mu_8^{-3} = -6.50$")

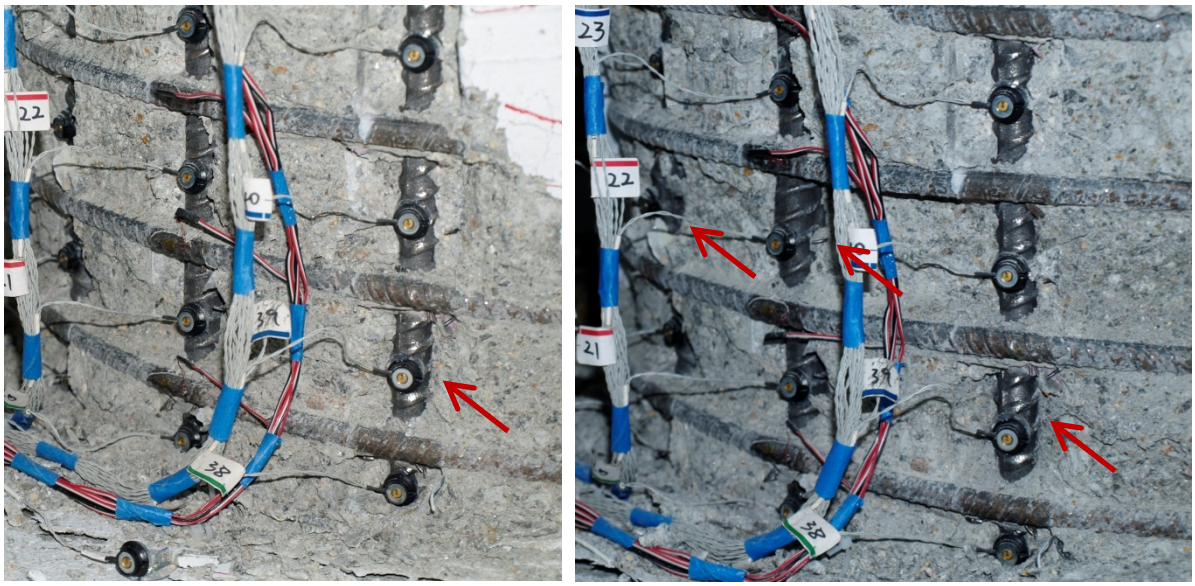

Figure 2-168. Test 13 – Buckling of South Reinforcing Bar S4 during ($\mu_8^{+2} = 6.46$") and (Right) Buckling of Bar S2 and S3 during ($\mu_{10}^{+1} = 8.07$")

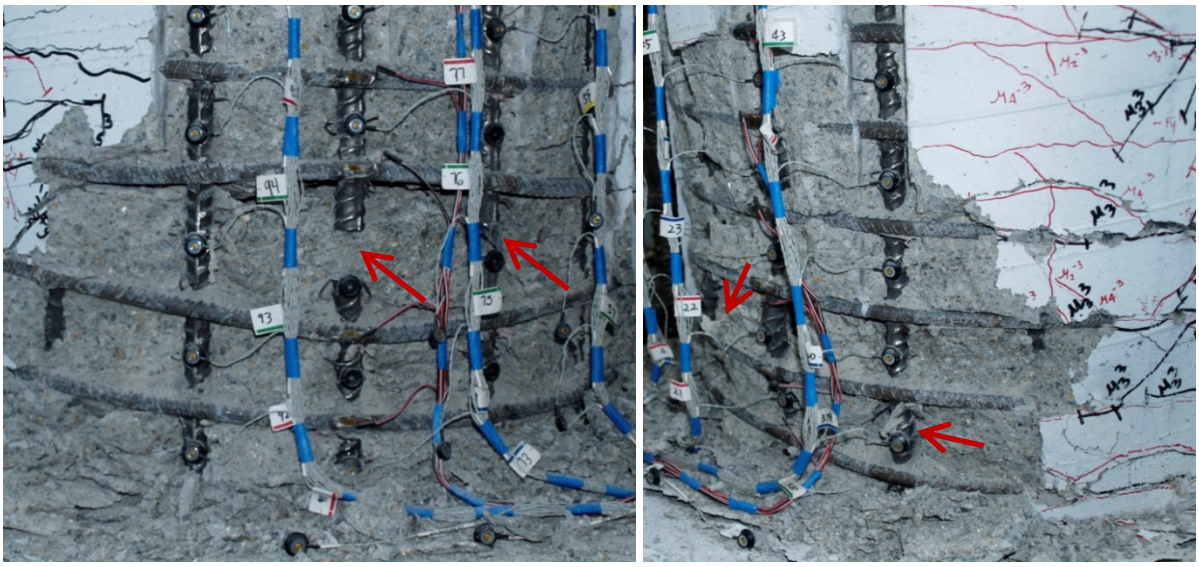

Figure 2-169. Test 13 – (Left) Rupture of North Reinforcement Bars N2 and N3 during ($\mu_{10}^{+1} = 8.07$") and (Right) Additional Deformation in South Bars during ($\mu_{10}^{+2} = 8.06$")

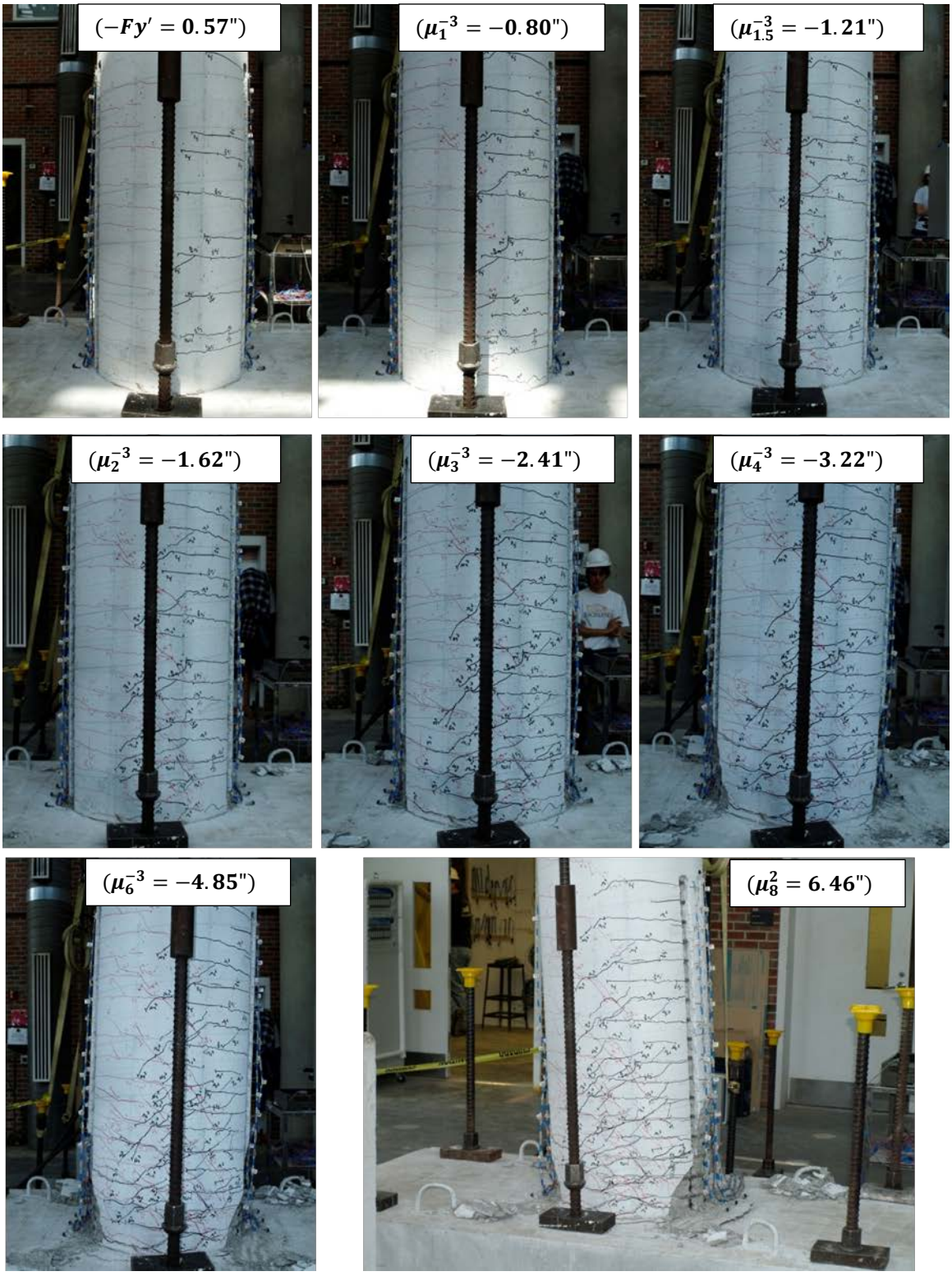

Figure 2-170. Test 13 – Crack Progression on the Back Side of the Specimen

2.2.1.2. Test 13 – Symmetric Three Cycle Set (#4 @ 2.75") Strain Data:

North Reinforcement:

Extreme fiber vertical strain profiles during push and pull cycles appear in Figure 2-171 and Figure 2-172 respectively. These figures show both extreme fiber bars on the same graph to illustrate the effects of tension shift on strain profiles. As the hinge rotates about inclined flexural shear cracks, compressive strains are concentrated at the base and tensile strains are fanned out to a greater height following the crack distribution. Just above the footing cracks remain horizontal, but above this base section the flexural shear cracks are inclined as shown in Figure 2-170. Due to the effects of tension shift, the tensile strains at the beginning of an inclined flexural shear crack do not coincide with the perceived moment demand at that location based on its height above the footing and the applied lateral load.

A peak tensile strain of 0.047, at a height of 2.03" above the footing, was measured in North extreme fiber bar N3 during ($\mu_8^{+1} = 6.46"$). It is notable that a higher peak tensile strain of 0.050 was measured 2.2" above the footing in the adjacent North reinforcement bar N4. Bar N2 and N3 visually buckled after reversal from ($\mu_8^{+1} = 6.46"$), leaving bar N4 intact. During the next pull cycle bar N4 visually buckled. The largest compressive strain in bar N3 of -0.017, located 2.03" above the footing, was measured during ($\mu_6^{+3} = 4.85"$). The relationship between tensile strain and displacement for bar N3 appears in Figure 2-175 for the largest tensile gage length 2.03" above the footing. Each curve in the graph represents the tensile strains measured from when the column was vertical to the peak of the given cycle of the load history. The gray line represents the moment curvature prediction for the relationship between strain and displacement from the Cumbia program developed at NCSU. During higher displacement ductility cycles, the measured tensile strains are significantly lower than the moment curvature prediction. The relationship between compressive strain and displacement for bar N3 appears in Figure 2-176. Buckling of bar N3 during the first pull cycle of ductility eight above the largest compressive gage length did not have a large impact on the relationship between compressive strain and displacement for this gage length, see the left photo of Figure 2-167.

The strain hysteresis for the buckled region of extreme fiber North reinforcing bar N3 appears in Figure 2-179. The transverse steel strain hysteresis for a layer of transverse steel close to the buckled region is shown in Figure 2-180. The peak displacement cycle at ($\mu_8^{+1} = 6.46"$) prior to visible buckling after reversal of load appears as a small red circle in both figures. A data label at the same displacement appears in both figures which represents the time when the buckled bar began to rapidly increase the tensile strain in the transverse steel restraint. The compressive demand during ($\mu_6^{+3} = 4.85"$) was not enough to cause the transverse steel to enter the nonlinear range.

South Reinforcement:

The peak compressive strain in bar S3 of -0.0174 was measured 1.82" above the footing during ($\mu_8^{+1} = 6.46"$). A peak tensile strain of 0.047, centered 7.18" above the footing, was measured in bar S3 at ($\mu_8^{-1} = 6.48"$). The lowest tensile gage length for bar S3 was blocked by debris during ductility eight, so larger tensile strains may have occurred over this region. To illustrate this point, the vertical strain profile for adjacent bar S4 appears in Figure 2-181. The largest tensile strain in bar S4 of 0.051 was measured 1.82" above the footing during ($\mu_8^{-1} = 6.48"$). Bar S4 was the first South reinforcement to visibly buckle after reversal from ($\mu_8^{-1} = 6.48"$). The strain hysteresis for the buckled region of bar S4 can be seen in Figure 2-182. The relationship between strain and displacement for push and pull cycles for extreme fiber bar S3 appears in Figure 2-178 and Figure 2-177 respectfully.

2.2.1.3. Test 13 – Symmetric Three Cycle Set (#4 @ 2.75") Curvature and Strain Penetration Data:

The cross section curvature for each horizontal section above the footing is determined by connecting the strain measurements from all six instrumented bars with a least squared error line. The curvature is then extracted from the slope of the least squared error line as shown in Figure 2-185. Vertical curvature profiles are plotted for push and pull cycles as shown in Figure 2-186 and Figure 2-187 respectively. These figures show that plastic curvatures have a linear distribution at higher displacement ductility levels. The extent of plastic curvatures above the footing can be calculated by determining where the linear plastic curvature distribution intersects the triangular yield curvature shown as a grey dashed line. The dashed lines for each curvature distribution represent a least squared error linear fit to the plastic portion of the measured curvatures. The data points used to create the least squared error lines appear as circle data markers.

LEDs placed closest to the footing-column interface on the six reinforcing bars can track the base section rotation due to strain penetration of longitudinal reinforcement into the footing. The measured base rotations for push and pull cycles appear in Figure 2-190 and Figure 2-191 respectively. Compared to previous tests, the bar slip profiles are shifted down slightly. Inspection of the measured slip hysteresis for extreme fiber bars N3 and S3 in Figure 2-188 and Figure 2-189 shows that each bar shifted downwards after the tests began. A possible explanation for why this occurred is not available, since this was not observed in any of the other experiments. A comparison of the measured top column displacement and the Optotrak integrated displacements appear in Figure 2-192. The Optotrak displacement was obtained by integrating the measured curvature profile, extrapolating the base rotation to the center of loading, and assuming an elastic curvature distribution above the instrumented region.

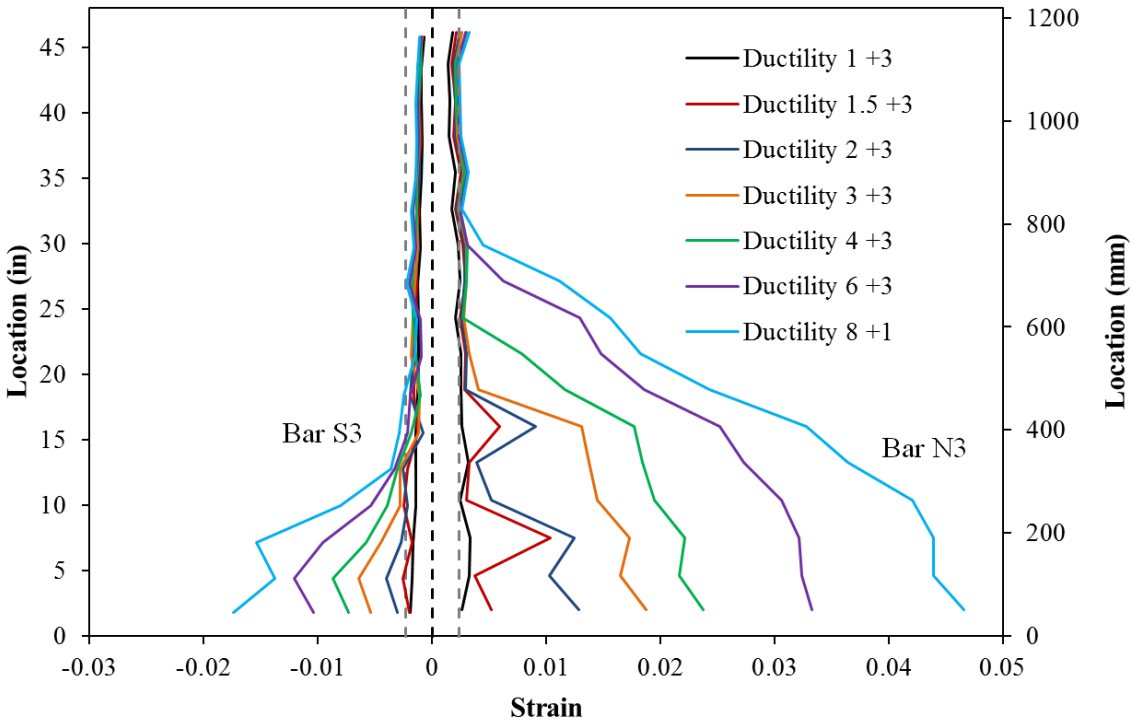

Figure 2-171. Test 13 – Extreme Fiber Vertical Strain Profiles during Push Cycles

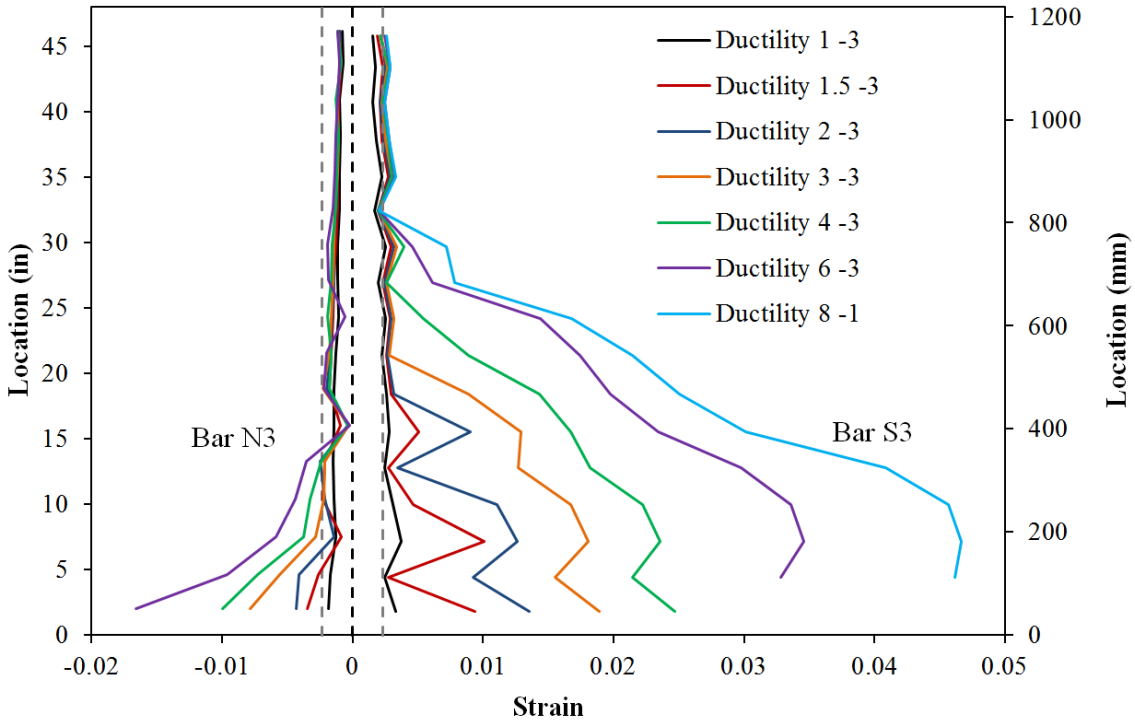

Figure 2-172. Test 13 – Extreme Fiber Vertical Strain Profiles during Pull Cycles

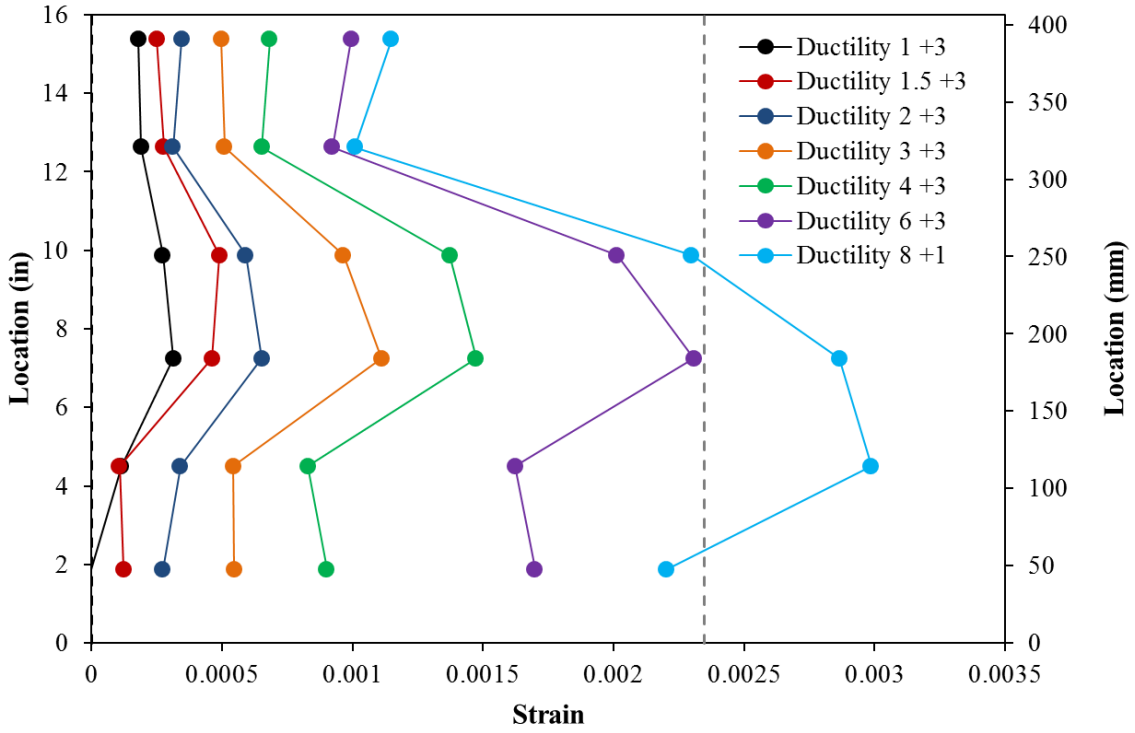

Figure 2-173. Test 13 – Transverse Steel Strains for the Lowest Six Spiral Layers on the South Side of the Specimen during Push Cycles

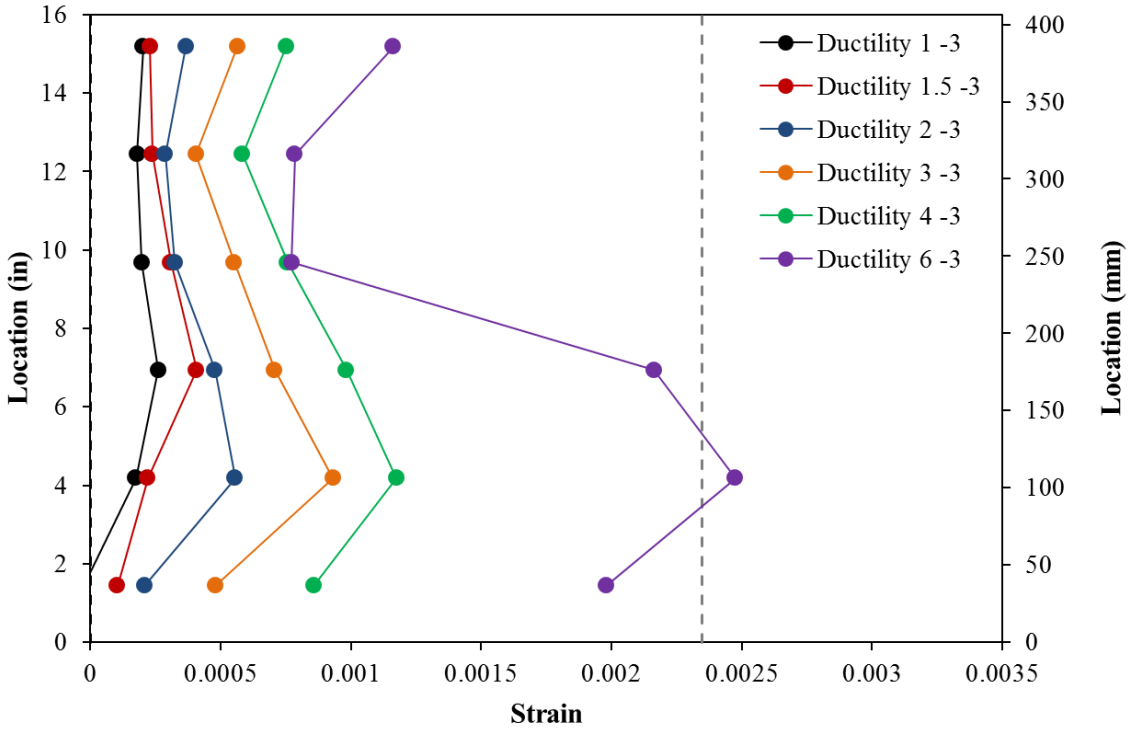

Figure 2-174. Test 13 – Spiral Strains on the North Side during Pull Cycles

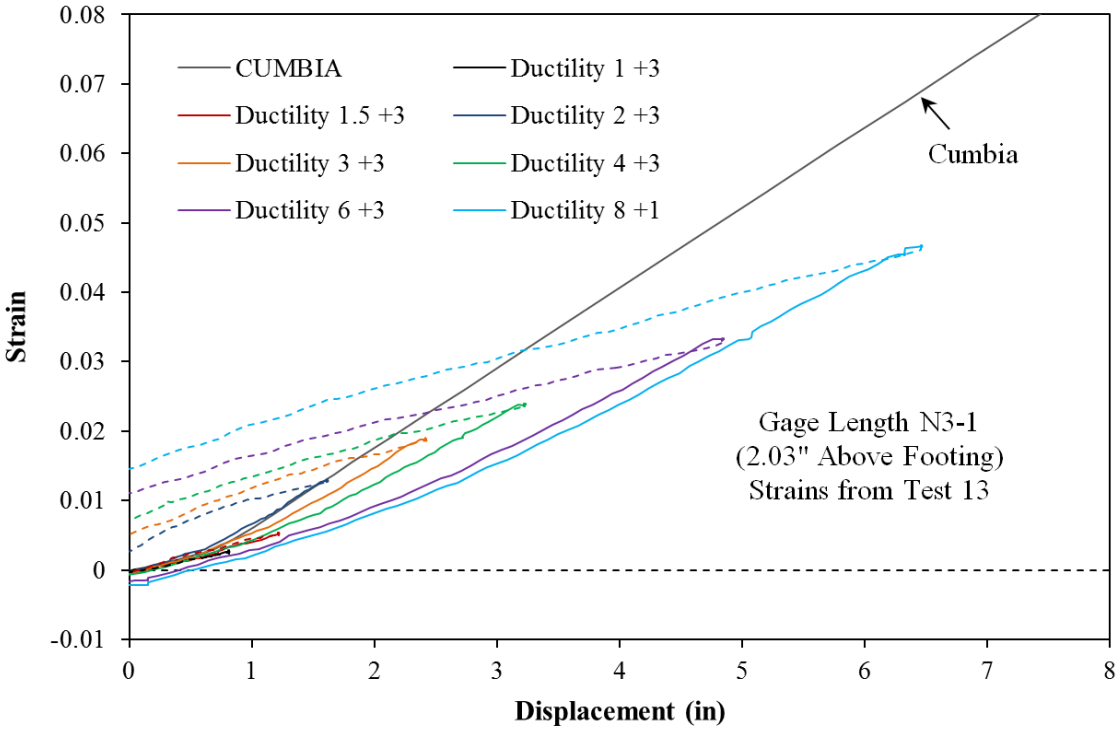

Figure 2-175. Test 13 – Tensile Strain and Displacement for Bar N3 during Push Cycles

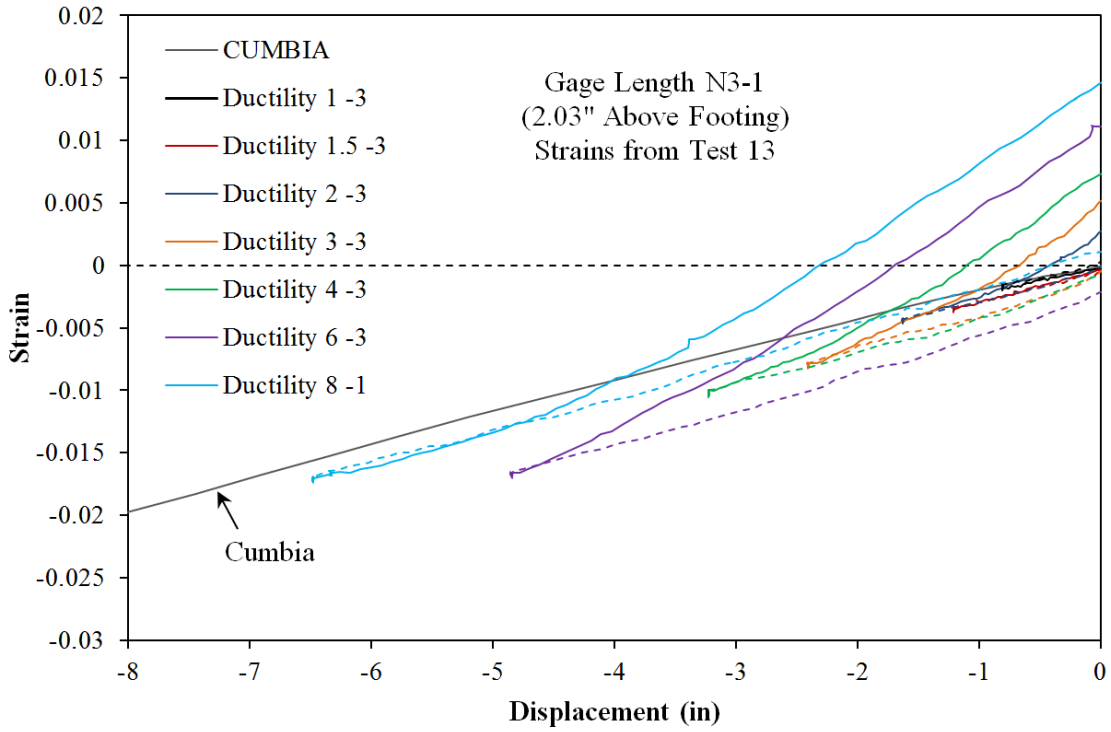

Figure 2-176. Test 13 – Compressive Strain and Displacement for Bar N3 during Pull Cycles

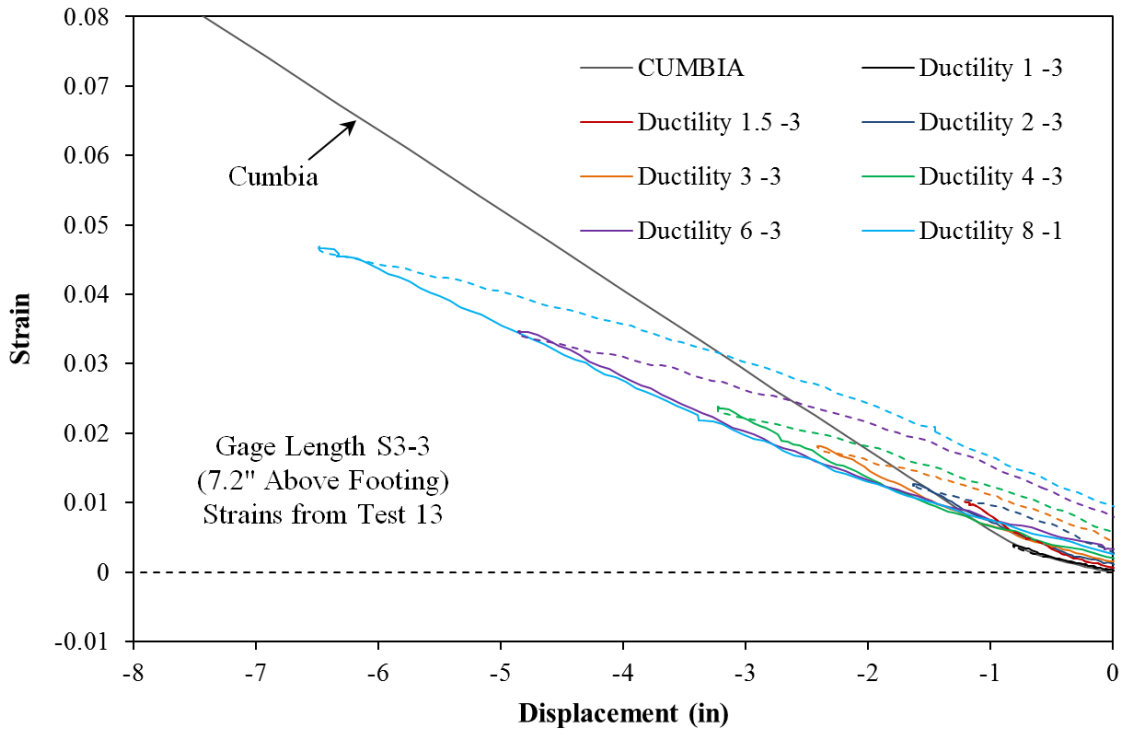

Figure 2-177. Test 13 – Tensile Strain and Displacement for Bar S3 during Pull Cycles

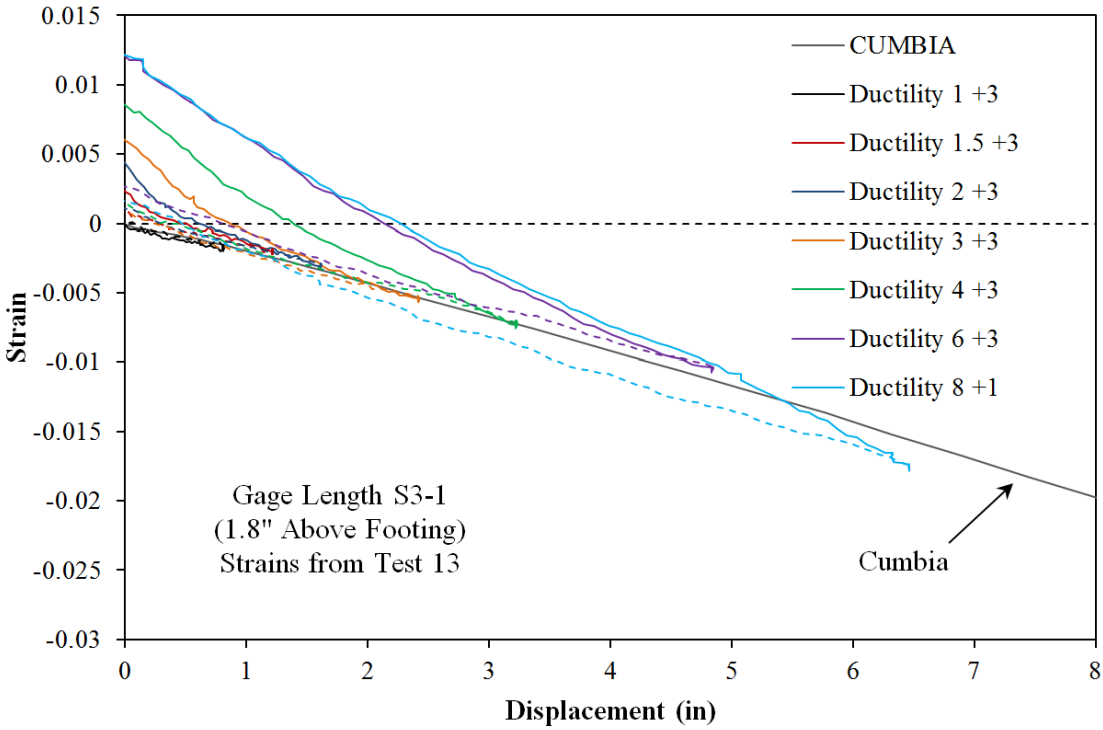

Figure 2-178. Test 13 – Compressive Strain and Displacement for Bar S3 during Push Cycles

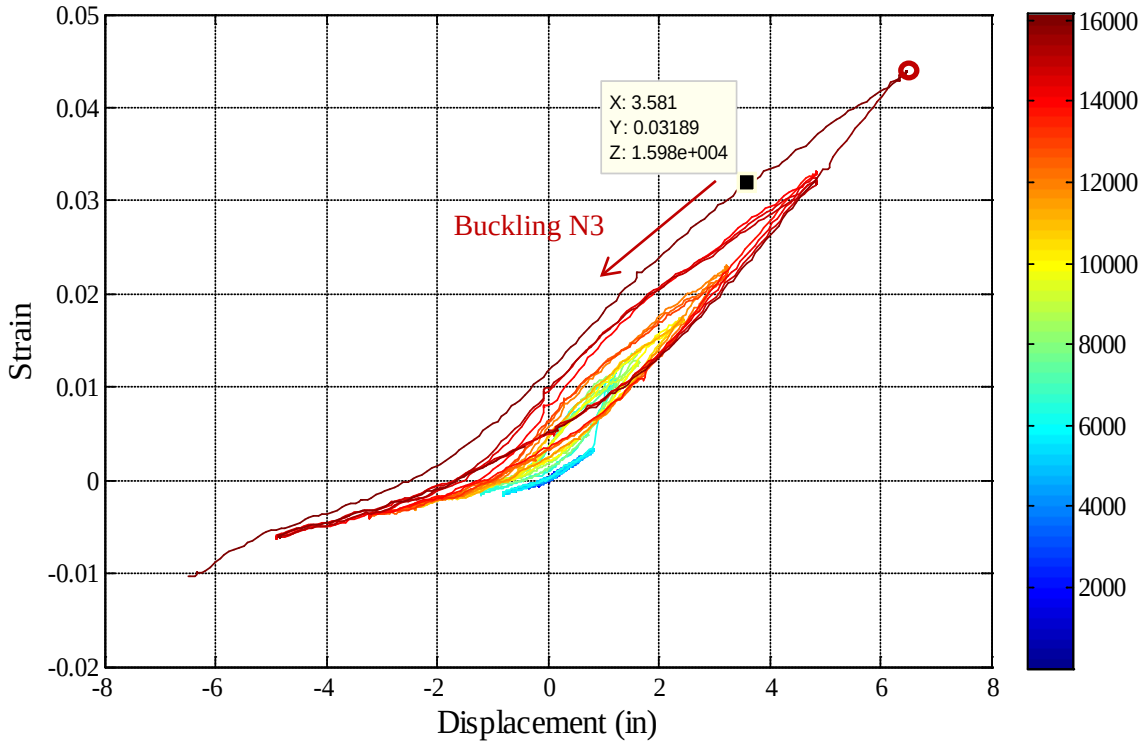

Figure 2-179. Test 13 – Bar N3 Strain Hysteresis (Buckled Region 7.48" Above the Footing)

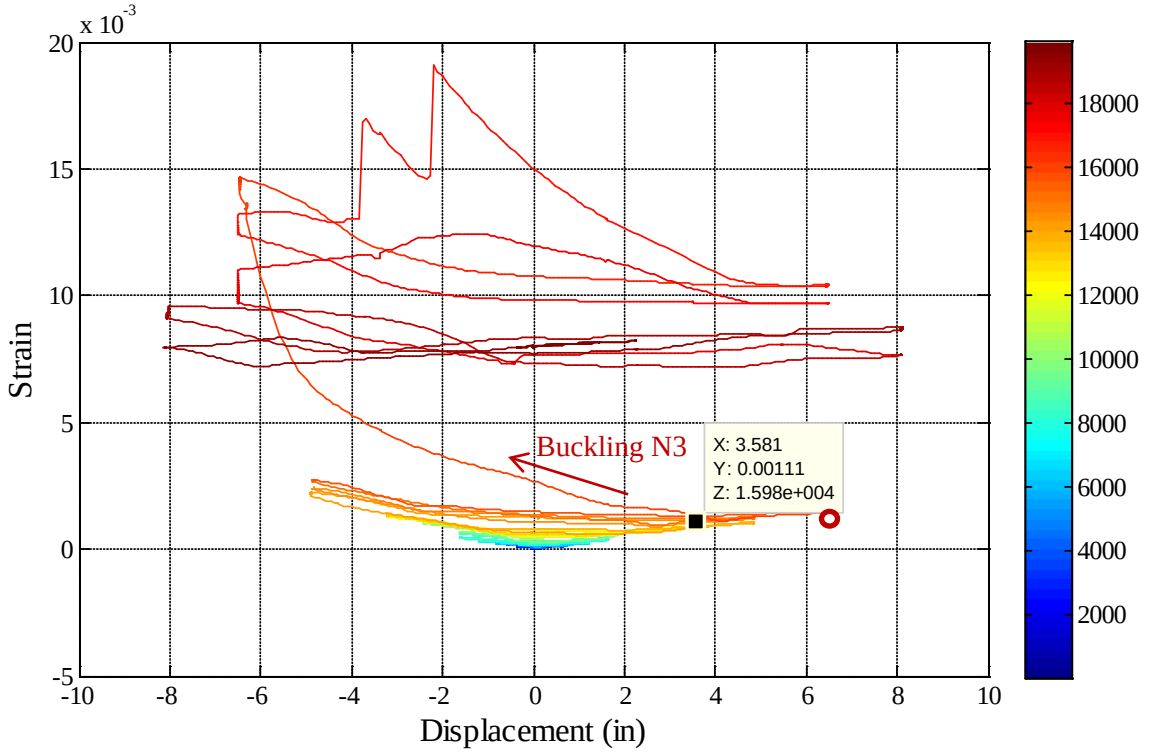

Figure 2-180. Test 13 – Transverse Steel Strain Hysteresis for the Spiral Layer Overlaying the Buckled Region of Bar N3

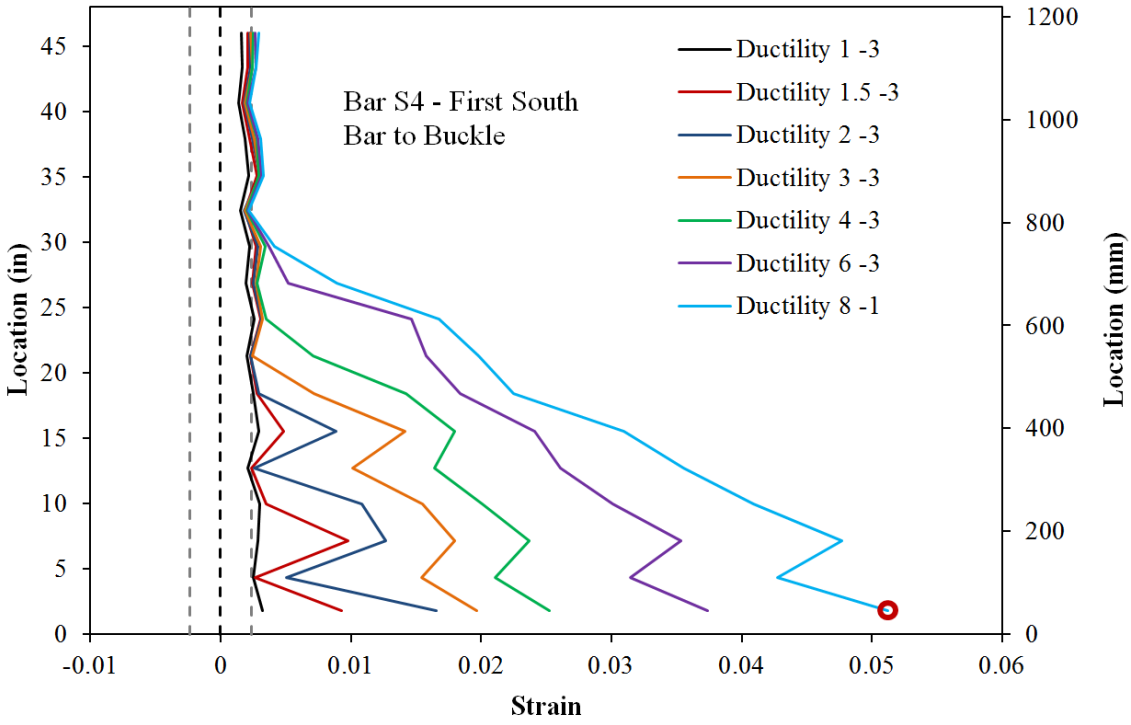

Figure 2-181. Test 13 – Tensile Vertical Strain Profile for Bar S4 (First South Bar to Buckle)

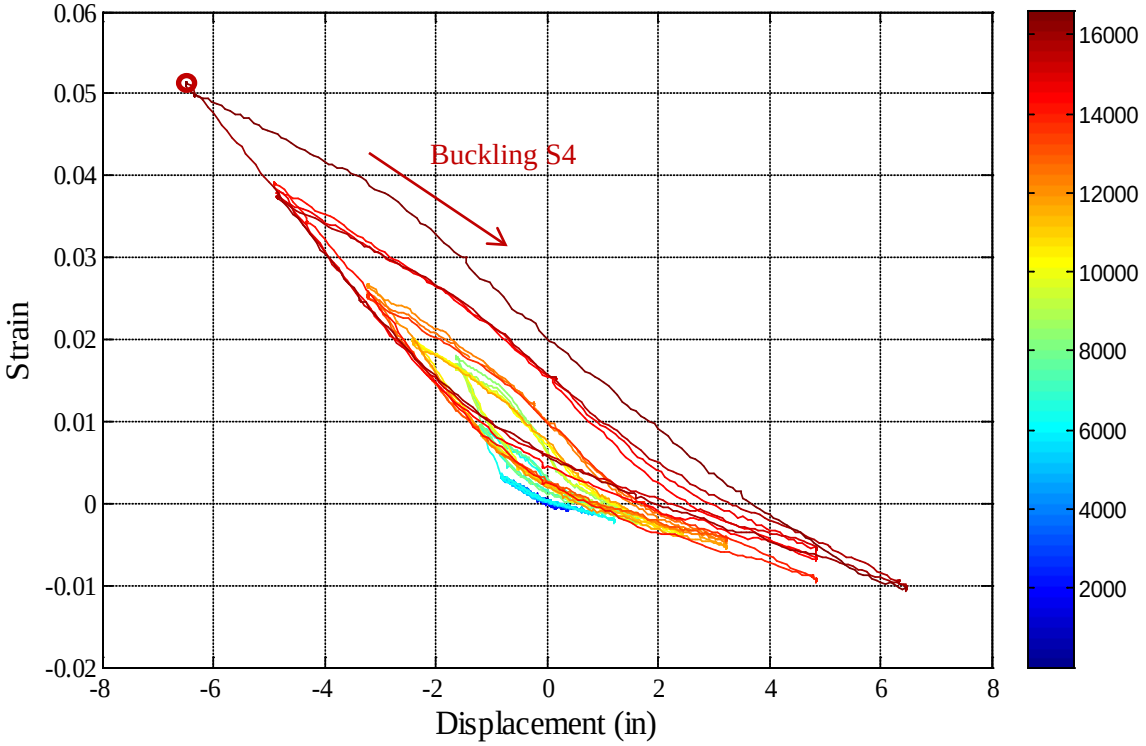

Figure 2-182. Test 13 – Bar S4 Strain Hysteresis (Buckled Region 1.82" Above the Footing)

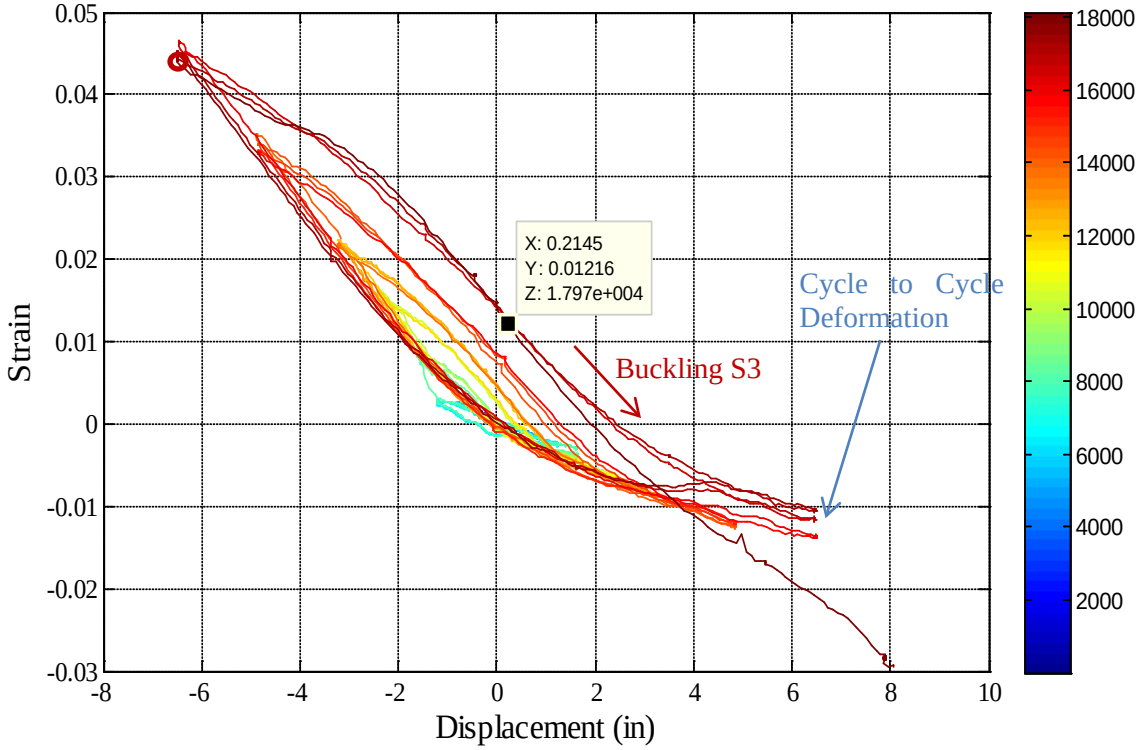

Figure 2-183. Test 13 – Bar S3 Strain Hysteresis (Buckled Region 4.41" Above the Footing)

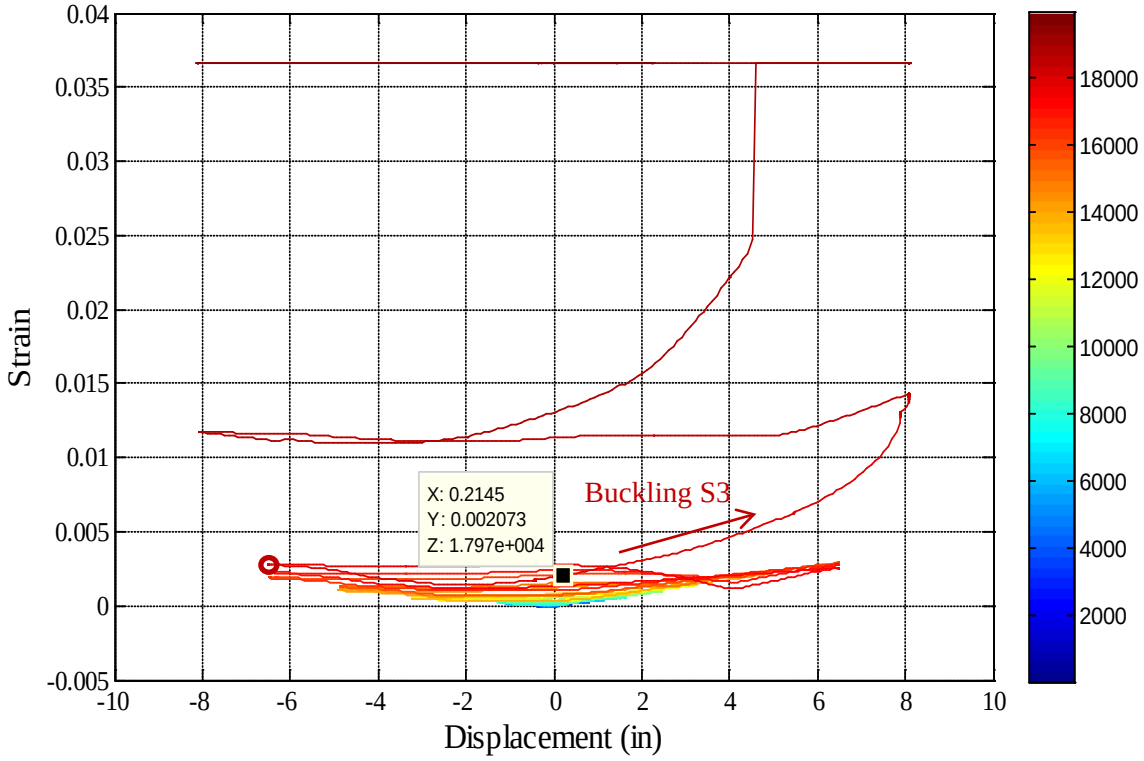

Figure 2-184. Test 13 – Transverse Steel Strain Hysteresis over the South Buckled Region

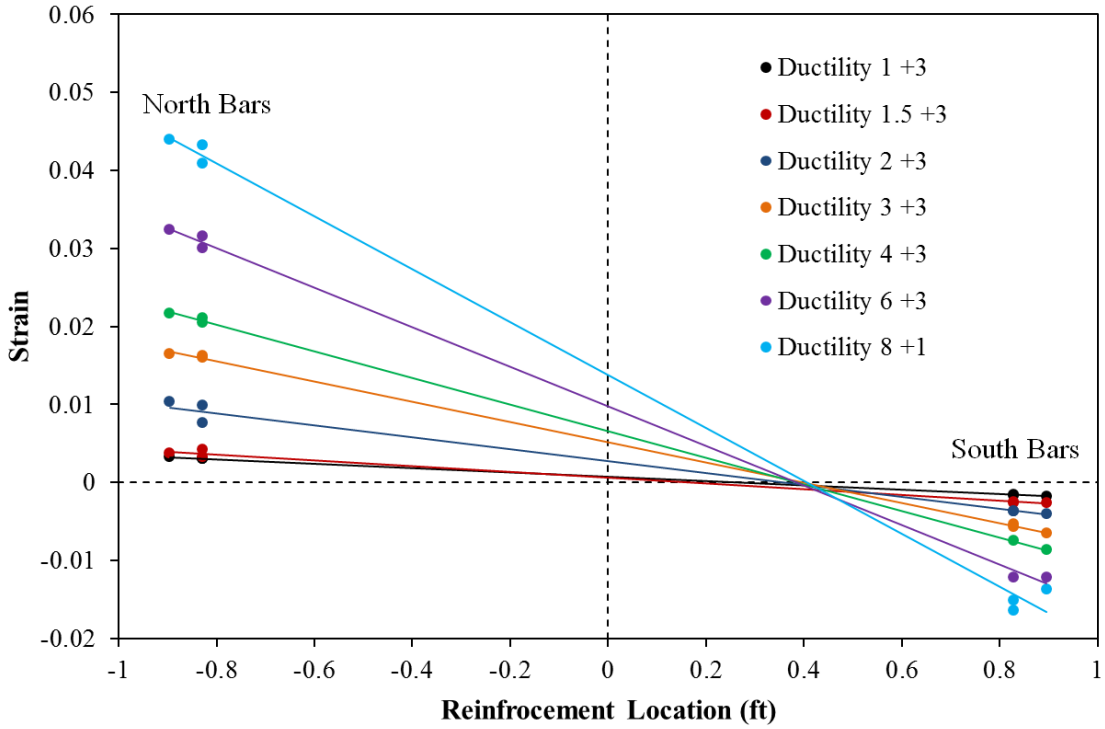

Figure 2-185. Test 13 – Method of Determining Cross Section Curvature from Six Instrumented Bars (Slope of Least Squared Error Line)

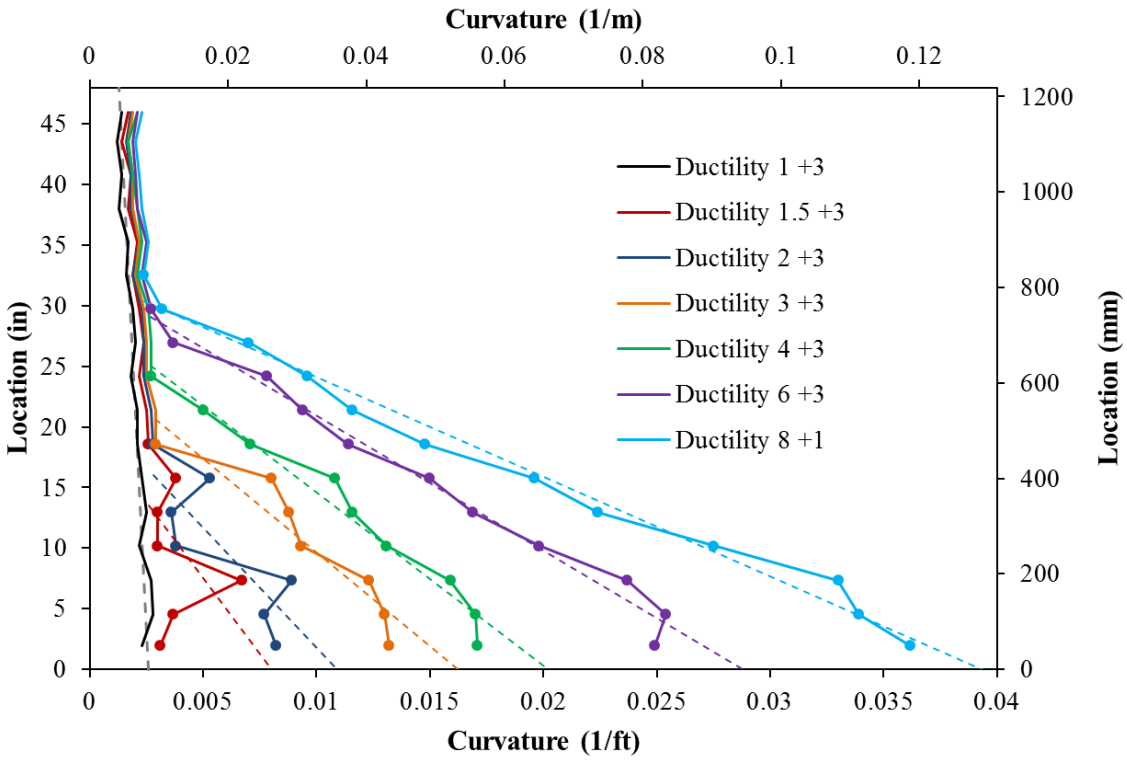

Figure 2-186. Test 13 – Vertical Curvature Profiles during Push Cycles

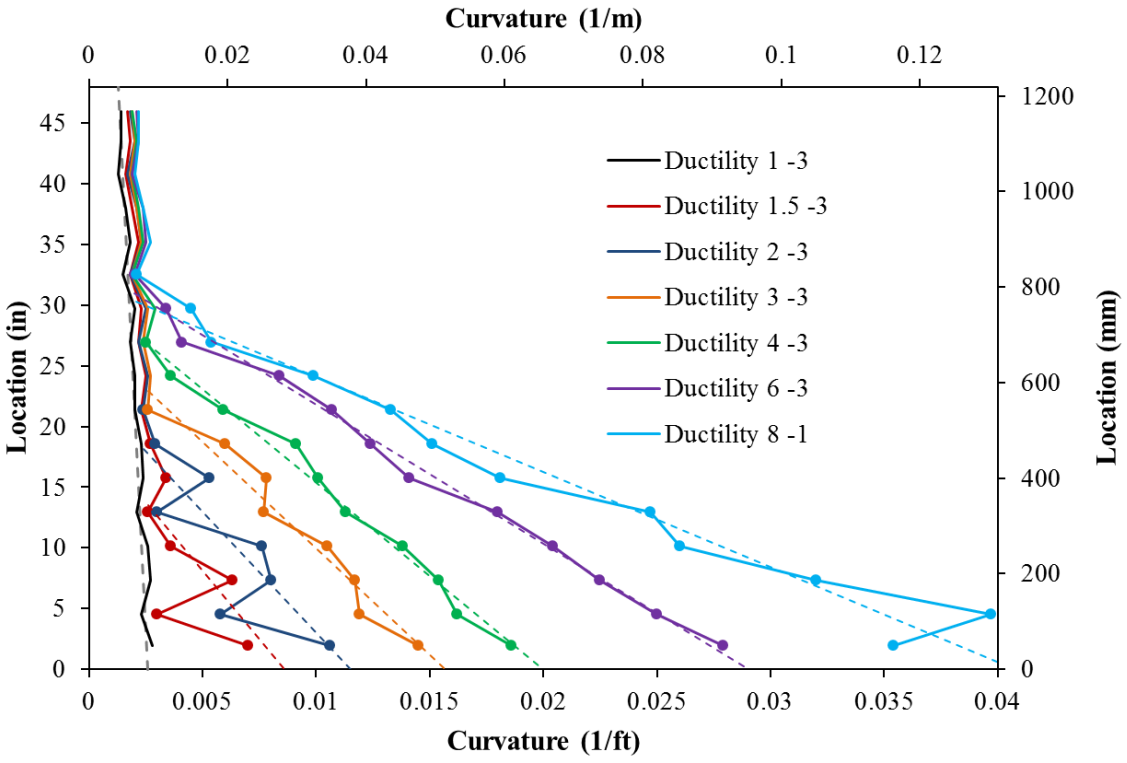

Figure 2-187. Test 13 – Vertical Curvature Profiles during Pull Cycles with Linear Least Squared Error Lines

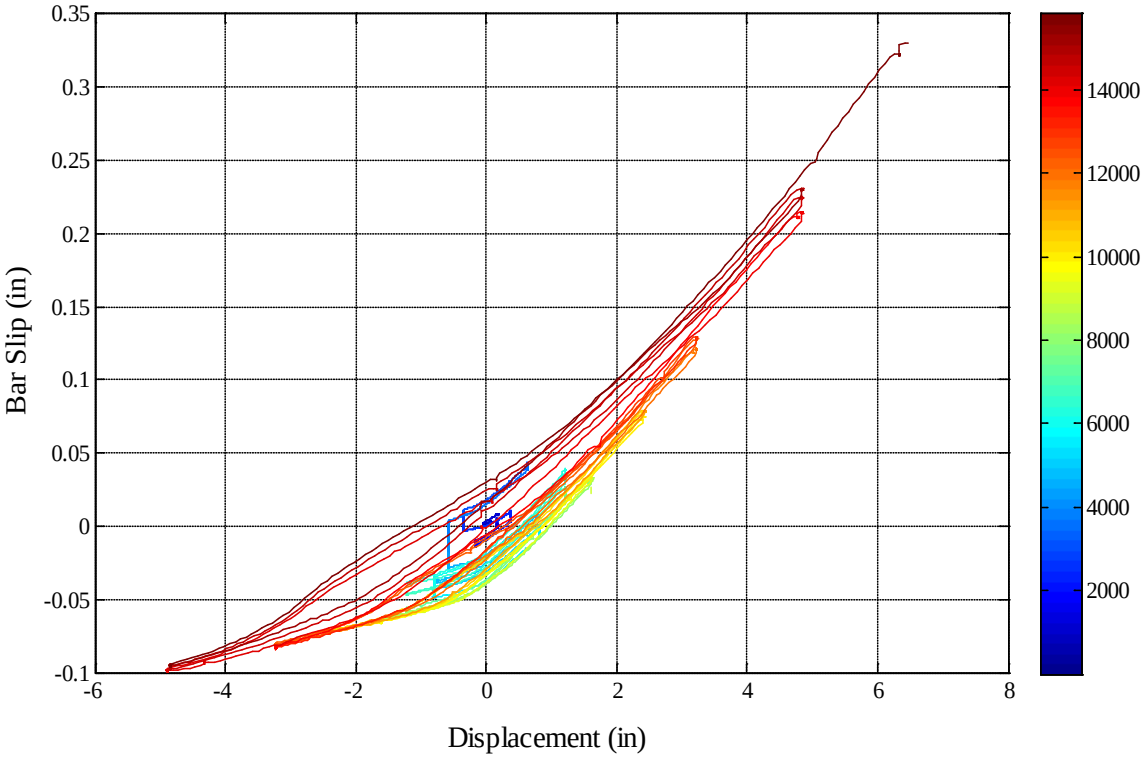

Figure 2-188. Test 13 – Bar N3 Base Section Slip Hysteresis due to Strain Penetration

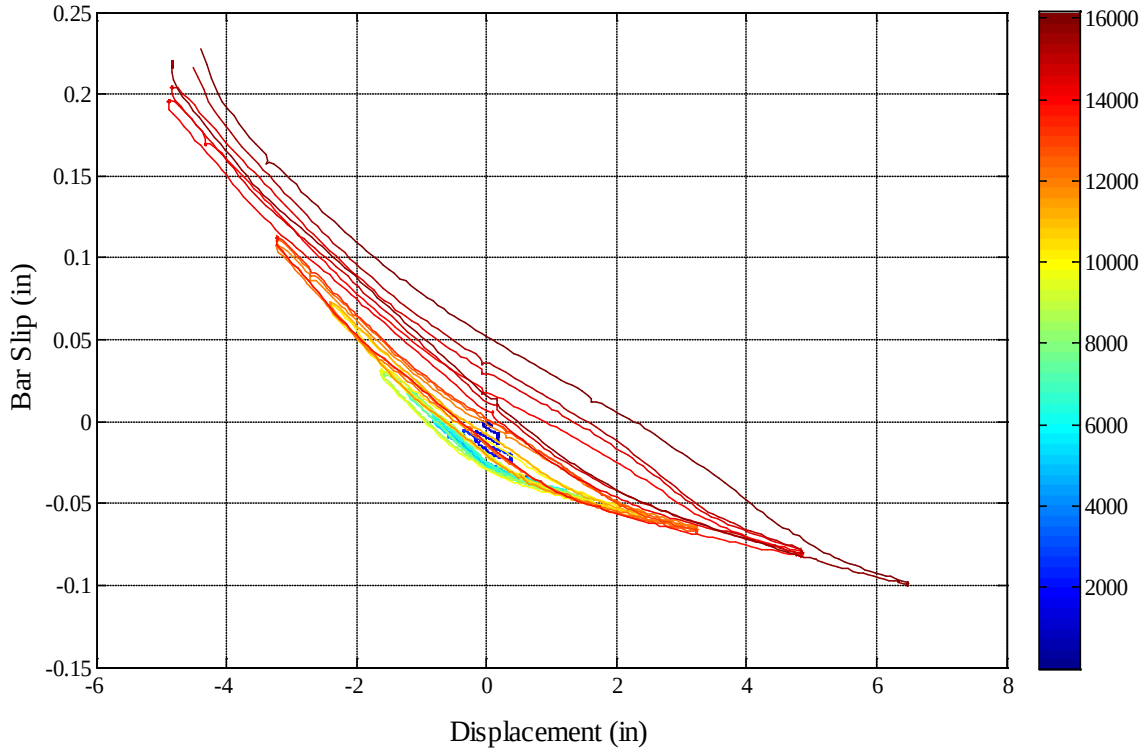

Figure 2-189. Test 13 – Bar S3 Base Section Slip Hysteresis due to Strain Penetration

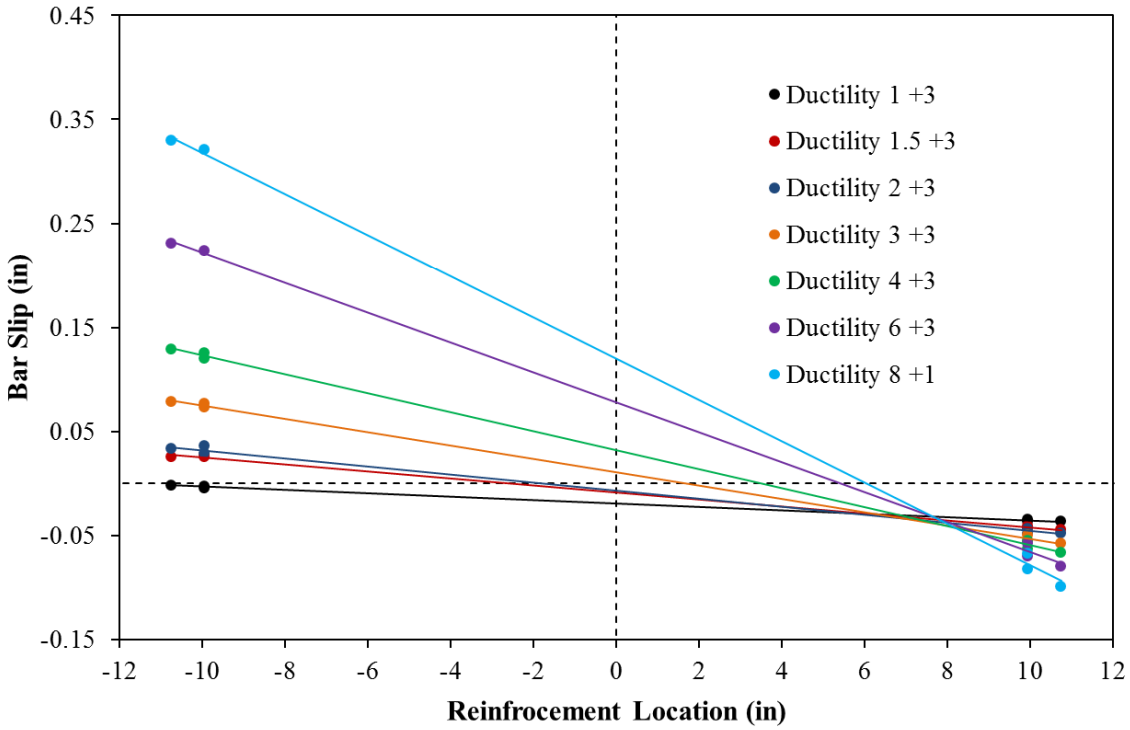

Figure 2-190. Test 13 – Base Rotations during Push Cycles due to Strain Penetration of Reinforcement into the Footing

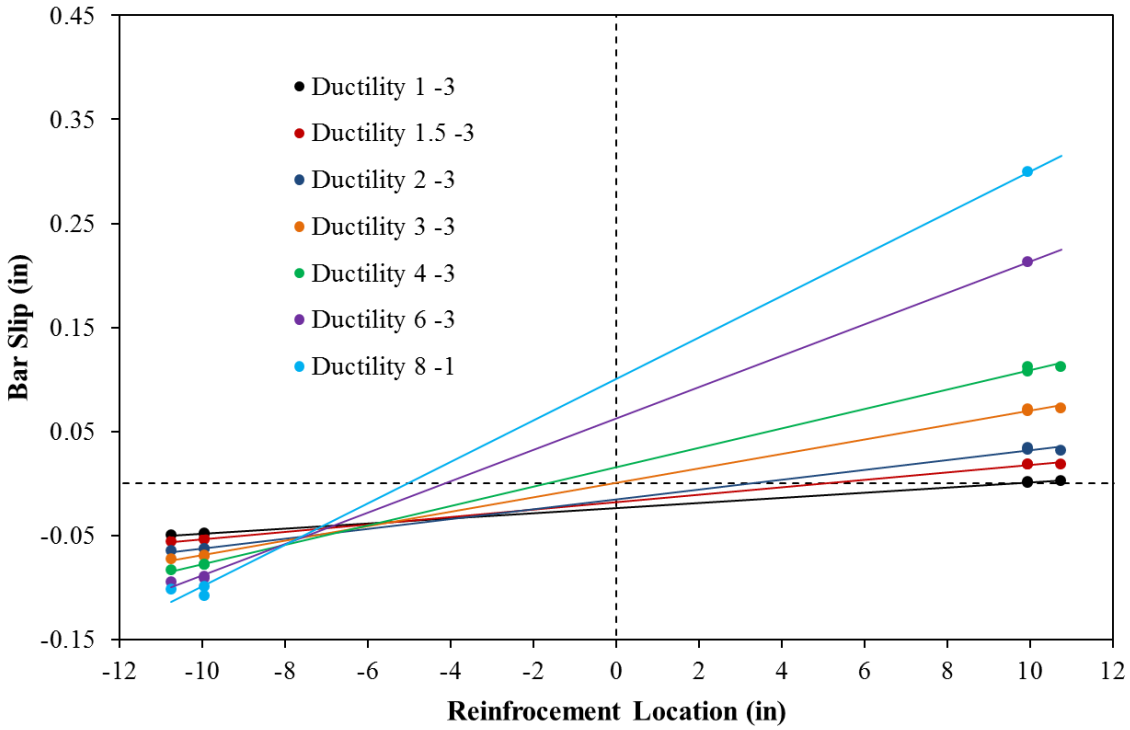

Figure 2-191. Test 13 – Base Rotations during Pull Cycles due to Strain Penetration

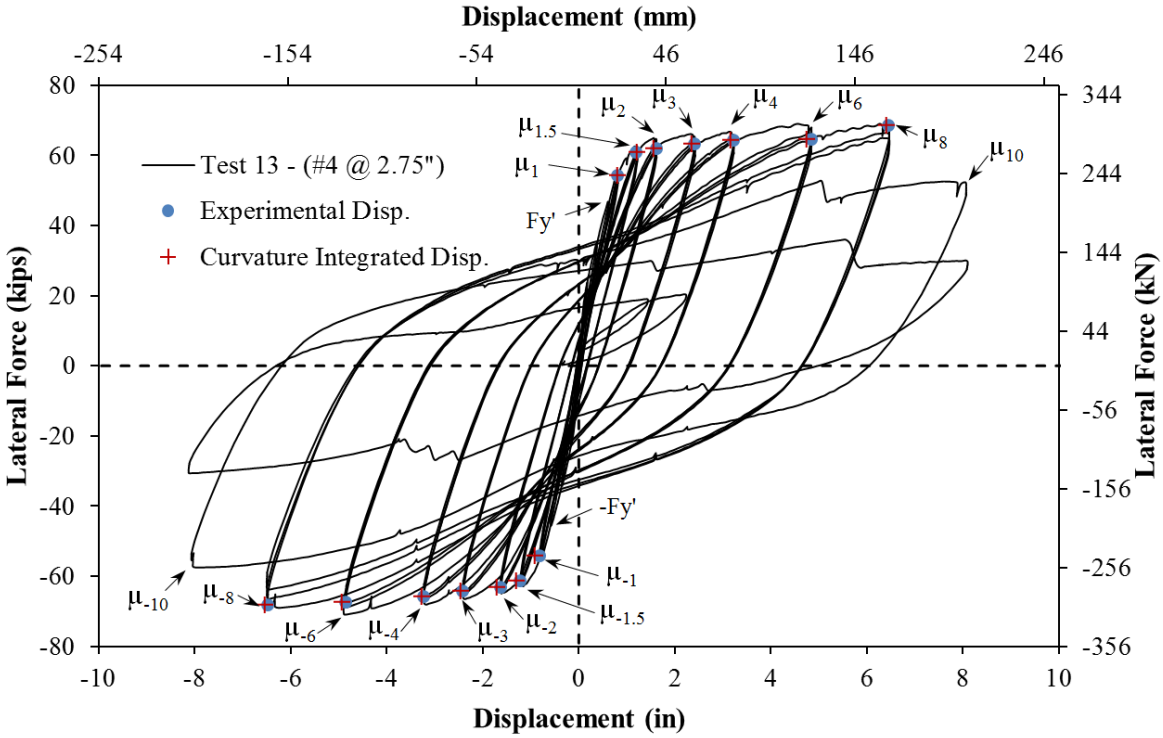

Figure 2-192. Test 13 – Comparison of Measured and Optotrak Integrated Displacements

2.2.2. Test 14 – Symmetric Three Cycle Set Load History (#3 Spiral at 4" Spacing)

Table 2-13. Results Summary for Test 14 – Symmetric Three Cycle Set Load History

LOAD HISTORY: Symmetric Three Cycle Set Load History

VALUES OF INTEREST:

Transverse Steel Detailing:	#3 Spiral at 4" Spacing (0.5%)
Concrete Compressive Strength:	$f_c' = 6641psi$
Axial Load:	$P = 170kips$
Analytical First Yield Force:	$F_y' = 47.0kips$
Experimental First Yield Displacement:	$\Delta_y' = 0.60"$ (*From Test 13, See Discussion)
Analytical Nominal Moment Capacity:	$M_n = 499.7kip * ft$
Equivalent Yield Displacement:	$\Delta_y = 0.80"$
Maximum Lateral Force:	$69.1kips$
Failure Mode:	Fracture of Previously Buckled Reinforcement

DAMAGE OBSERVATIONS: (Drift %) [Displacement Ductility, μ_Δ]

First Cracking North:	**Intended Cycle to $1/2Fy' = 0.42"$
First Cracking South:	**Intended Cycle to $-1/2Fy' = -0.45"$
Cover Concrete Crushing North:	$\mu_{1.5}^{-3} = -1.19"$
Cover Concrete Crushing South:	$\mu_{1.5}^{+3} = 1.20"$
Transverse Steel Yield North:	At $-0.25"$ during pull to $\mu_6^{-1} = -4.80"$
Transverse Steel Yield South:	At 3.84" during push to $\mu_6^{+1} = 4.80"$
Longitudinal Bar Buckling North:	Reversal from $\mu_6^{+1} = 4.80"$
Longitudinal Bar Buckling South:	Reversal from $\mu_6^{-1} = -4.80"$
Longitudinal Bar Fracture North:	At $-3.46"$ during push to $\mu_8^{+2} = 6.40"$
Longitudinal Bar Fracture South:	At $-2.81"$ during pull to $\mu_8^{-1} = -6.39"$

*$\mu_8^{-1} = -6.39"$ represents the first pull cycle of displacement ductility eight which reached a peak displacement of -6.39 inches

** Initial cycles of the load history affected by load cell problems, refer to Figure 2-193.

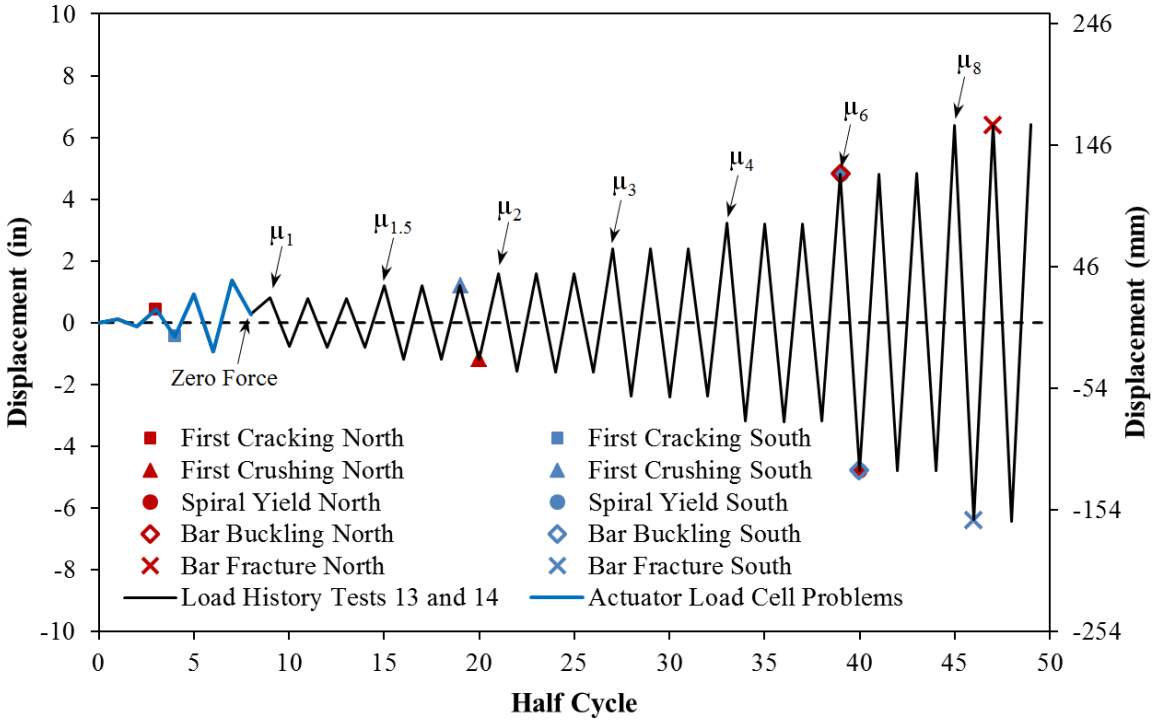

Figure 2-193. Test 14 – Symmetric Three Cycle Set Load History (Same as Test 13 Except for Initial Cycles without a Properly Functioning Actuator Load Cell)

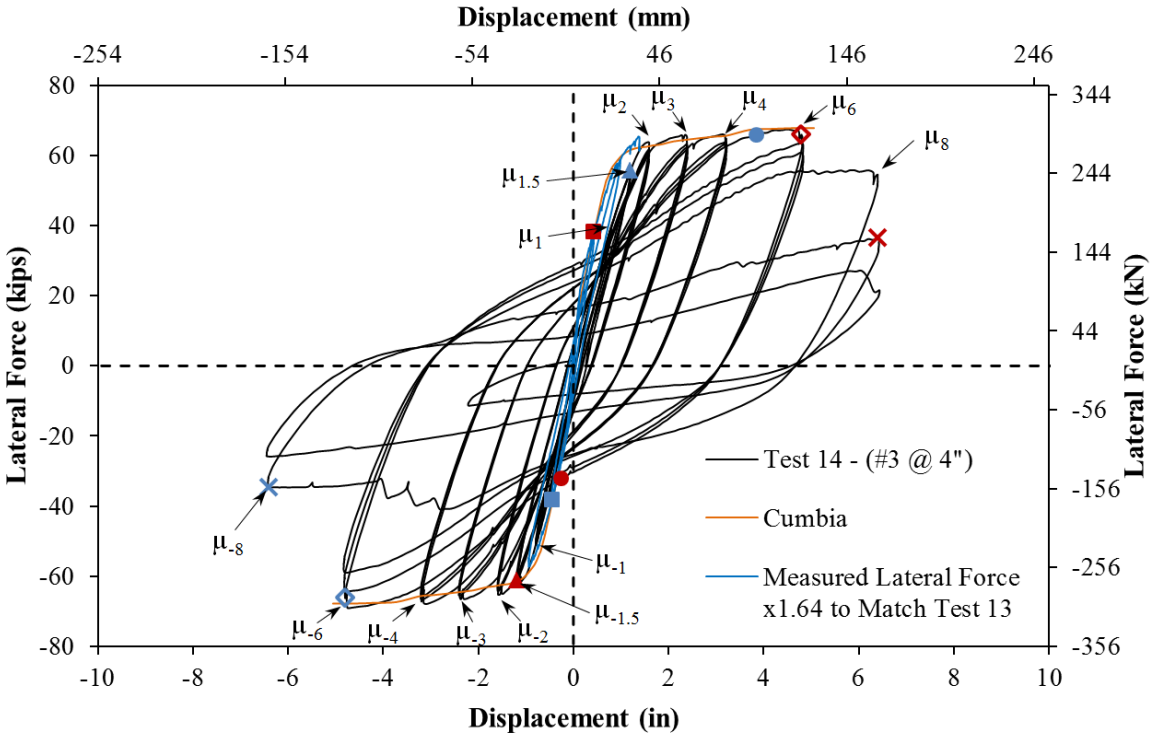

Figure 2-194. Test 14 – Lateral Force vs. Top Column Displacement Response

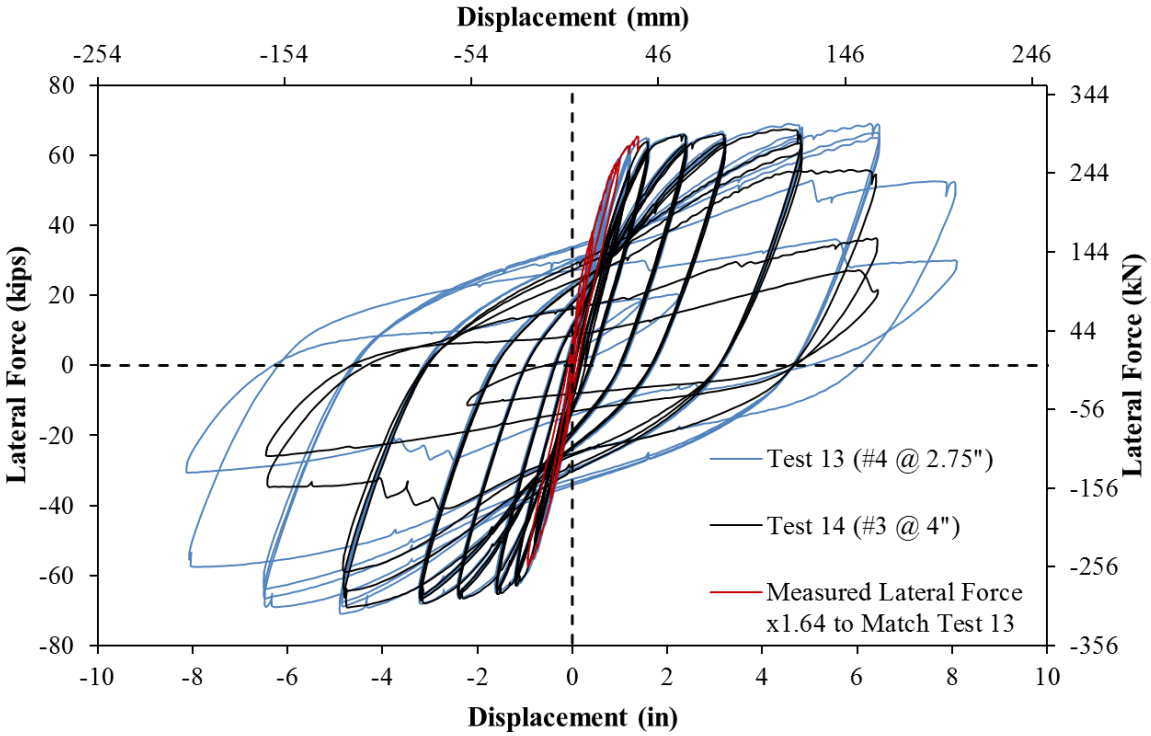

Figure 2-195. Test 14 – Method to Determining Appropriate Scale Factor for Initial Cycles Affected by Load Cell Problems with Test 13 Response

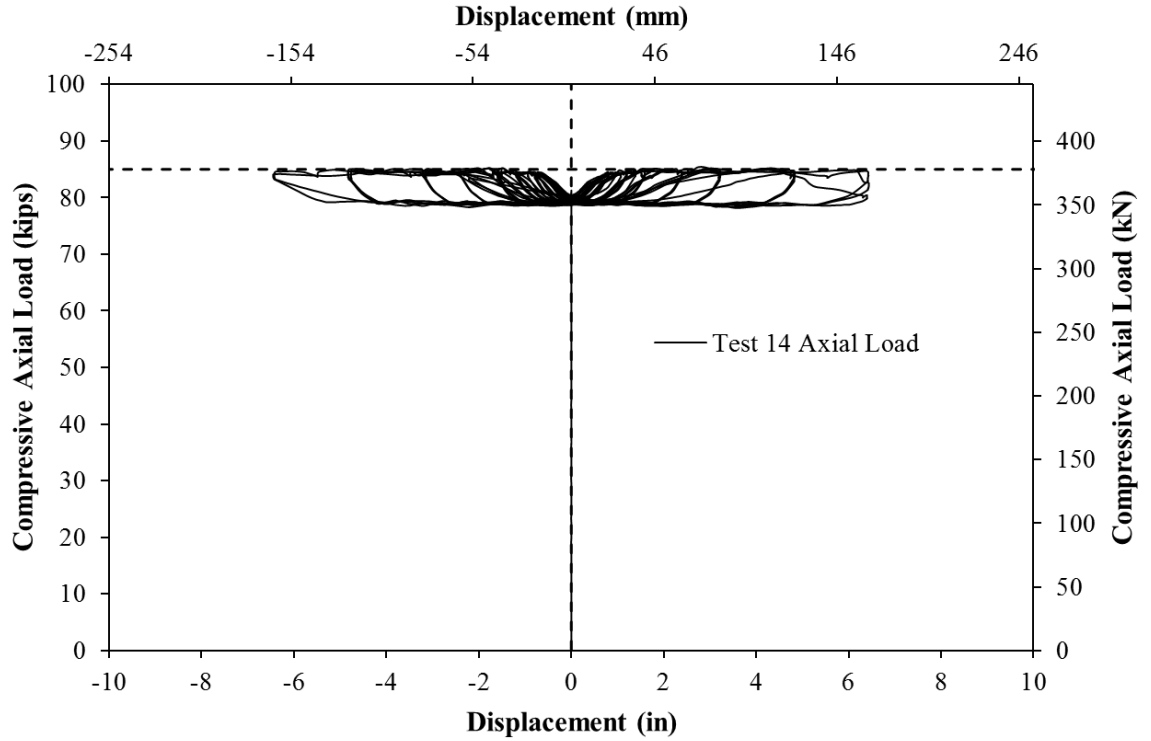

Figure 2-196. Test 14 – Compressive Axial Load from One Jack (Total = 2*Value)

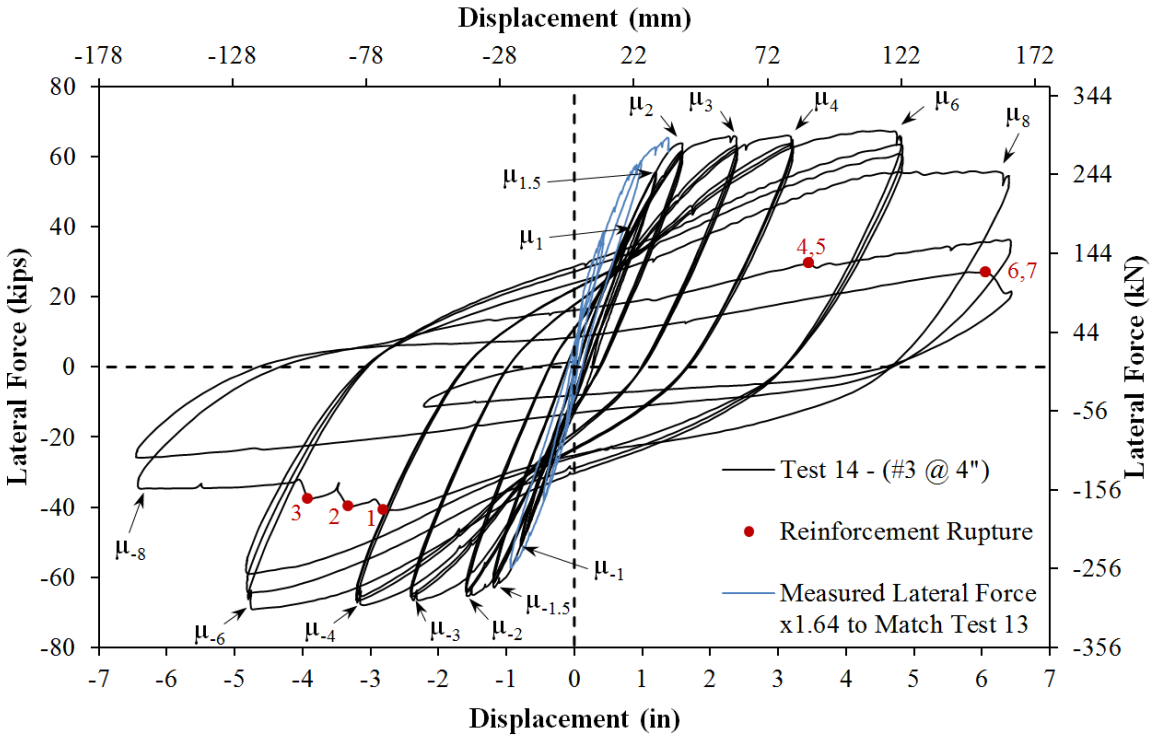

Figure 2-197. Test 14 – Rupture History of Previously Buckled Reinforcement

Figure 2-198. Test 14 – (Left) Test Setup and Specimen at ($\mu_8^{+2} = 6.40$") and (Right) Two Target Markers within Each 4" Transverse Steel Spacing

2.2.2.1. Test 14 – Symmetric Three Cycle Set (#3 @ 4") Experimental Observations:

The first yield force for the tested material and geometric properties was determined using moment curvature analysis (Test 14: Cumbia Fy' = 46.97 kips with f'c = 6641 psi) compared to (Test 13: Cumbia Fy' = 46.48 kips with f'c = 6097 psi). During the early cycles of the Test 14 load history, it became apparent that the actuator load cell was not functioning properly. This was noticed because the forces were considerably lower than expected at low levels of displacement. Initially, this problem was not attributed to the actuator load cell and several small cycles were conducted to try and pin down the specific cause of the problem. During these cycles, the specimen was pushed past the first and equivalent yield displacements in both directions of loading, see Figure 2-193. In the push direction of loading the specimen went past displacement ductility 1.5 and in the pull direction the displacement was just past ductility one. It was determined that the only thing that could have caused this issue is an incorrect actuator load cell reading, and upon inspection a damaged cable connection was found. The cable was replaced and the actuator load cell began recording the correct lateral force for the remainder of the test.

At this point of the test, there was no way to go back and redo the elastic cycles to the first yield displacement due to the slight stiffness degradation from inelastic cycles in each direction of loading. For this reason, the first yield displacement from Test 13 was used for Test 14. The first yield displacement for the thirteenth test was obtained as an average for the first yield push and pull cycles ($\Delta'_y = 0.60"$). Extreme fiber vertical strain profiles, for Test 14, at the first yield displacement appear in Figure 2-199 and Figure 2-200 for push and pull cycles respectively. The first yield displacement from Test 13 is also appropriate for Test 14 based on the vertical strain profiles which have strains just past yield at the locations of large cracks.

The equivalent yield displacement, used to determine the displacement ductility levels ($\mu_{\Delta n} = \mathrm{n} * \Delta_y$), is then calculated as $\Delta_y = \Delta'_y(M_n/M'_y) = 0.80"$ for Test 14 compared to $\Delta_y = 0.81"$ for Test 13. The full symmetric three cycle set load history appears in Figure 2-193 and the resulting lateral force vs. top column displacement hysteresis is shown in Figure 2-194. Past tests in the load history research program suggest that cycles at lower displacement ductility levels, such as those prior to fixing lateral load issue, should not have an impact on later cycles at larger displacements. The concrete cover on the South side of the specimen remained intact during the largest overload cycle. It did cause stiffness degradation which decreased the force during lower displacement ductility levels in the three cycle set load history.

Since the actuator load is calibrated based on a linear curve relating voltage to lateral force which passes through the origin, a constant scale factor can be used to transform the incorrect data to a better approximation of the actual lateral force. The backbone curves of reinforced concrete bridge columns with similar material properties should remain similar, so this was used to calibrate the scale factor to relate the incorrect lateral force of Test 14 to the backbone curve of Test 13. As shown in Figure 2-195, a constant scale factor of 1.64 gave the best approximation of the actual lateral force during early cycles affected by the damaged load cell cable.

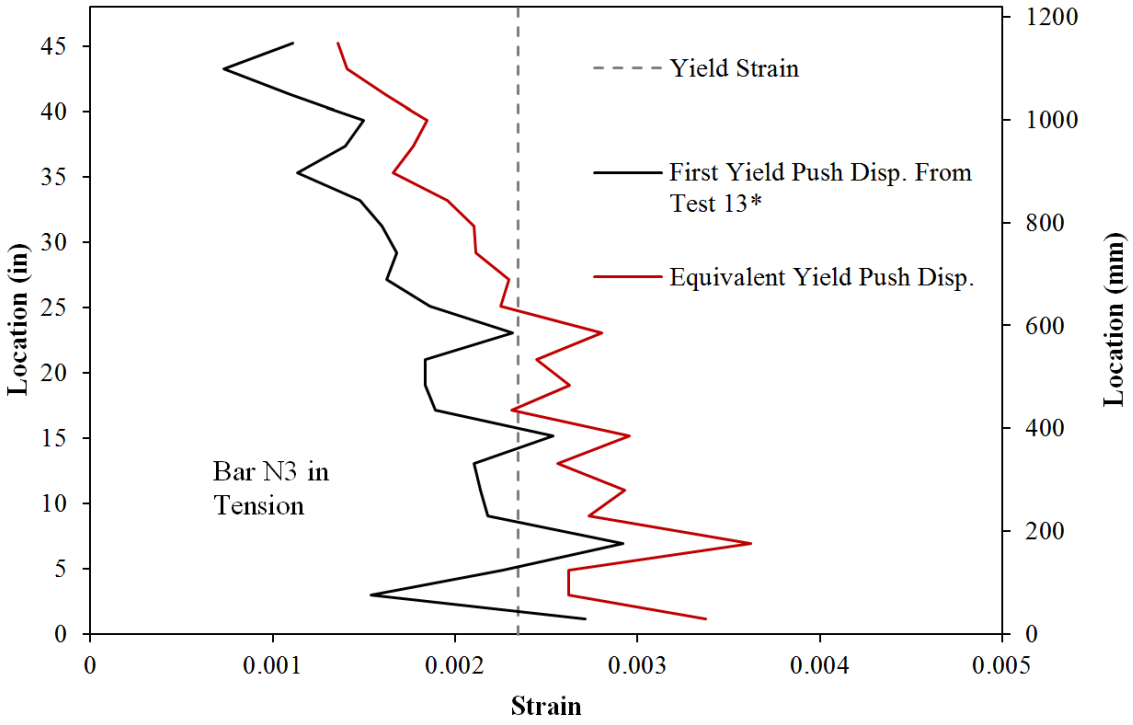

Figure 2-199. Test 14 – Vertical Strain Profiles for North Extreme Fiber Bar N3 during the First Excursions to Δ_y' (Test 13) and Δ_y

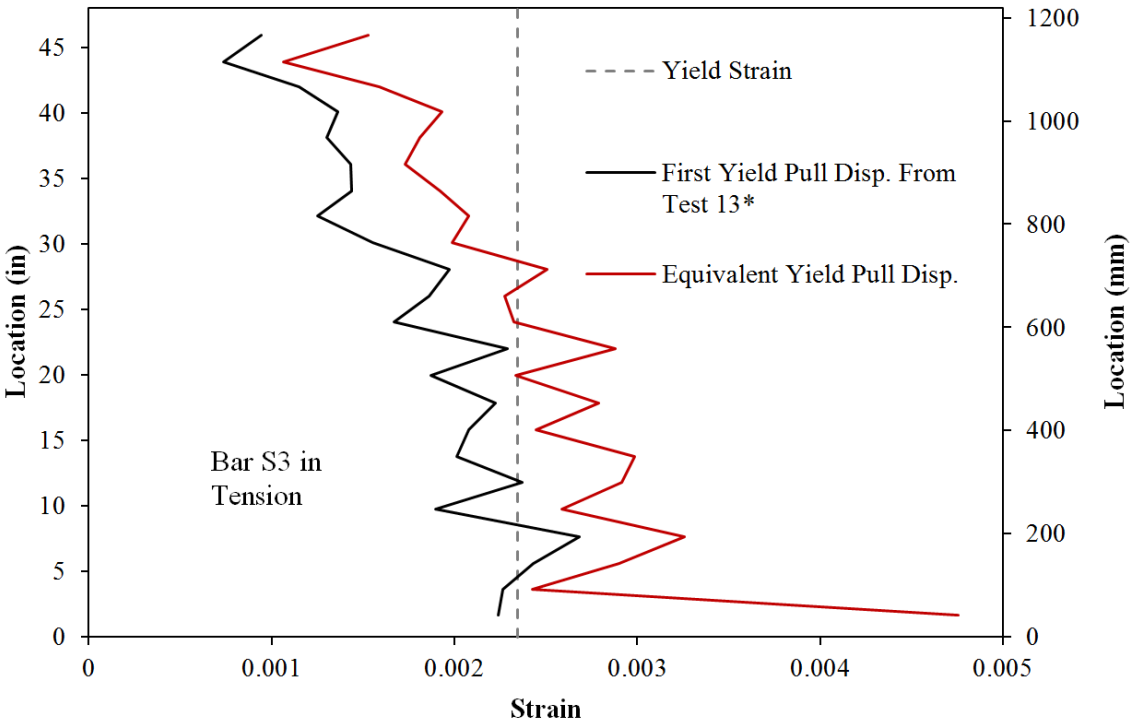

Figure 2-200. Test 14 – Bar S3 Strain Profiles during $-\Delta_y'$ (Test 13) and $-\Delta_y$

Even though the initial cycles were did not reach the proper level of force expected in a symmetric three cycle set load history, information on the crack location, width, and orientation were still taken at the peak of each cycle. The first half cycle was intended to reach ¼ Fy', but since the actuator load cell cable was damaged, the actual displacement at this intended lateral force was greater. This initial cycle and the subsequent reversal to -¼ Fy' were not large enough to cause cracking in the specimen. The third half cycle intended to reach ½ Fy' pushed the specimen to 0.42" and 0.3mm cracks at 8" spacing were observed. As expected, the cracks occurred at the level of the transverse steel. The same crack width and spacing was observed during the pull cycle to -½ Fy'. The cycle intended for ¾ Fy' reached a displacement of 0.91". Note that this is larger than the equivalent yield displacement of 0.80". The largest crack width measured 0.6mm at 4" spacing which followed the locations of transverse steel. During the intended pull cycle to -¾ Fy' at -0.94", 0.75mm crack widths were measured at 4" spacing.

The next cycle was intended to reach Fy', but the specimen was paused and the actuator load cell connection problem was determined. The peak displacement reached prior to pausing and reversing the load to zero force was 1.38". Note that this is equal to a displacement ductility of 1.73, therefore latter cycles in the load history to ductility 1 and 1.5 in the push direction have a loss of stiffness due to this overload. In the pull direction of loading only the ductility one cycles are affected by stiffness degradation from the displacement ductility -1.13 cycle.

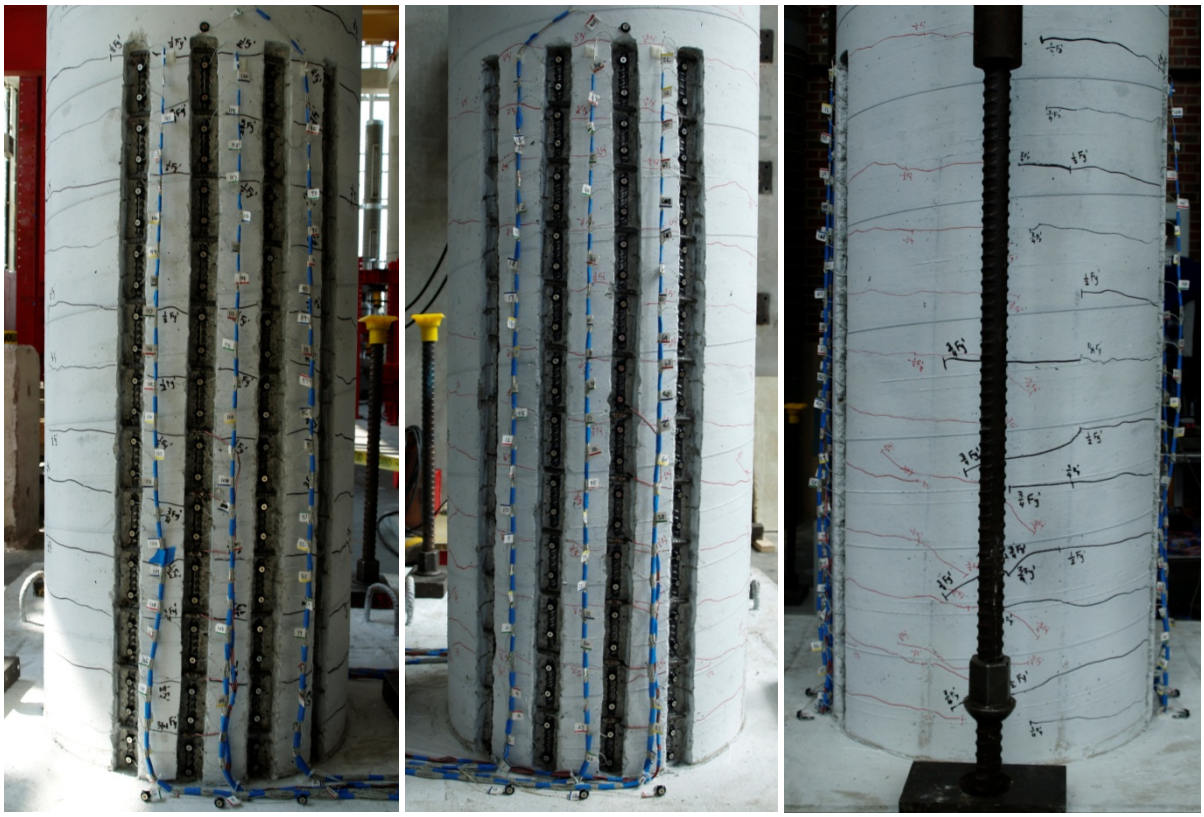

Figure 2-201. Test 14 – Crack Distribution after All Cycles with Actuator Load Cell Errors (No Notable Limit States Reached)

During ($\mu_1^{+3} = 0.79"$), 0.75mm crack widths at 4" spacing were measured. This is very similar to the crack widths and spacing observed during the intended ¾ Fy' cycle earlier in the load history to ductility 1.13. The same crack width and spacing were measured during ($\mu_1^{-3} = -0.79"$). At ($\mu_{1.5}^{+1} = 1.19"$) visible flaking of the cover concrete was observed on the South side of the specimen which usually occurs just before crushing. Crushing over the bottom two inches of the cover concrete on the south side occurred during ($\mu_{1.5}^{+3} = 1.20"$), as shown in the left photo of Figure 2-202. During this same cycle cracks on the North side of the specimen were measured at 1.25mm at 4" spacing. The extent of crushing on the North side of the specimen reached 7" above the footing during ($\mu_{1.5}^{-3} = 1.19"$), see the right photo of Figure 2-202. Here, the cracks on the South side of the specimen increased to 1.5mm width at 4" spacing. Cracks on the North side of the specimen measured 1.5mm at 4" spacing at ($\mu_2^{+3} = 1.58"$) while the extent of crushing on the South side of the specimen extended 7" above the footing. The extent of crushing on the North side of the specimen did not increase during ductility two, but it spread to other uncrushed locations near the base of the column. The extent of crushing on the South side of the specimen increased to 10" above the footing and widened during ($\mu_3^{+3} = 2.40"$). The crushing on North side of the specimen widened, but did not increase in height during ductility three.

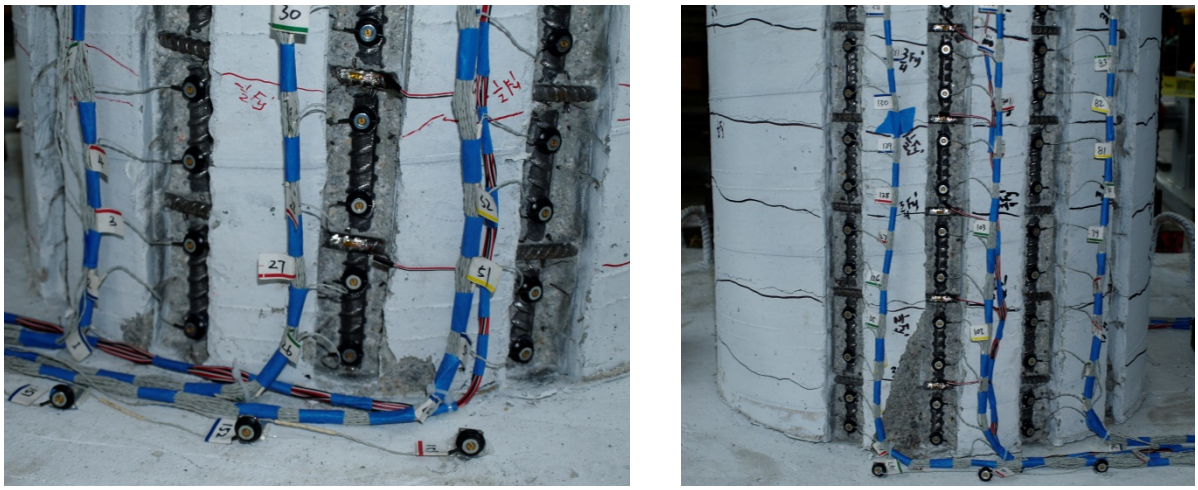

Figure 2-202. Test 14 – (Left) South Cover Crushing during ($\mu_{1.5}^{+3} = 1.20"$) and (Right) Cover Crushing on the North Side of the Specimen at ($\mu_{1.5}^{-3} = 1.19"$)

The extent of crushing on the North and South sides of the specimen during the third cycle of ductility four is shown in Figure 2-203. Extreme fiber North reinforcing bar N3 buckled after reversal from ($\mu_6^{+1} = 4.80"$), see the left photo of Figure 2-203. All three instrumented bars on the South side of the specimen (S2, S3, and S4) buckled after reversal from ($\mu_6^{-1} = -4.80"$), as shown in the right photo of Figure 2-204. During the reversal from ($\mu_6^{+2} = 4.82"$), additional North reinforcement bars N2 and N4 buckled, see Figure 2-205. North reinforcing bars N1 and N5 buckled during ($\mu_6^{-3} = -4.80"$). At the end of ductility six there was 9% strength loss in the push direction of loading and 12% strength loss in the pull direction due to buckled reinforcing bars and loss of confinement prior to rupture. On the way to ($\mu_8^{+1} = 6.40"$), South reinforcing bar S1 buckled. While the longitudinal steel on the North side of the specimen was in tension, the separation of the deformed spiral in Figure 2-206 highlights the effect of loss of confinement due to buckled bars. During ($\mu_8^{-1} = -6.39"$), previously buckled South reinforcing bars S2, S3, and S4 ruptured causing a 48% loss in strength, see Figure 2-207. On the way to ($\mu_8^{+2} = 6.40"$), previously buckled North reinforcing bars N2 and N3 ruptured causing a 45% loss in strength as shown in the left photo of

Figure 2-208. North reinforcement bars N4 and N5 ruptured on the way to ($\mu_8^{+2} = 6.40$") causing a 67% loss in strength. The test was concluded at this time and photos which show the specimen after instrumentation and debris were removed appear in Figure 2-208. A photo progression of the crack propagation on the back side of the specimen is shown in Figure 2-209.

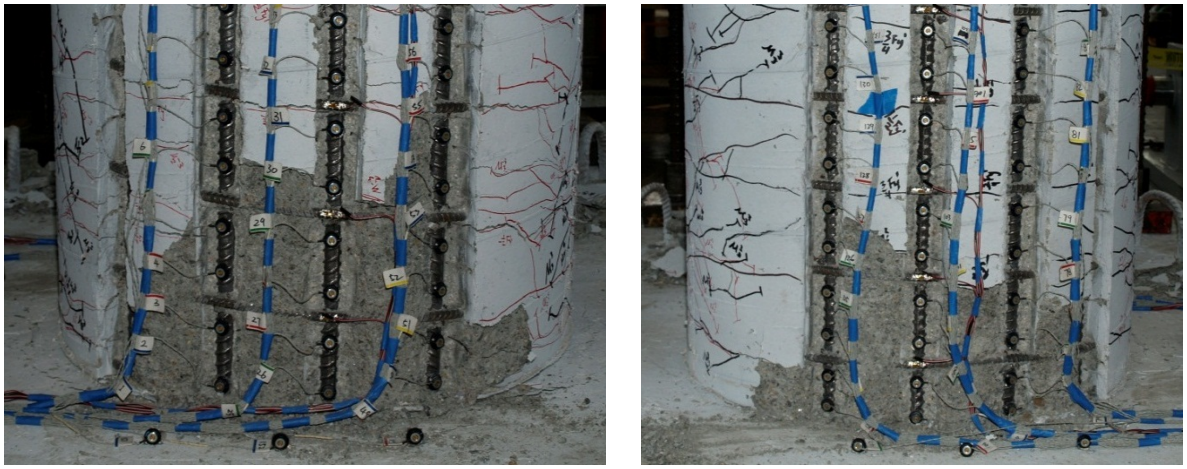

Figure 2-203. Test 14 – (Left) Extent of Crushing on the South Side of the Specimen during ($\mu_4^{+3} = 3.19$") and (Right) Extent of Crushing on the North Side during ($\mu_4^{-3} = 3.20$")

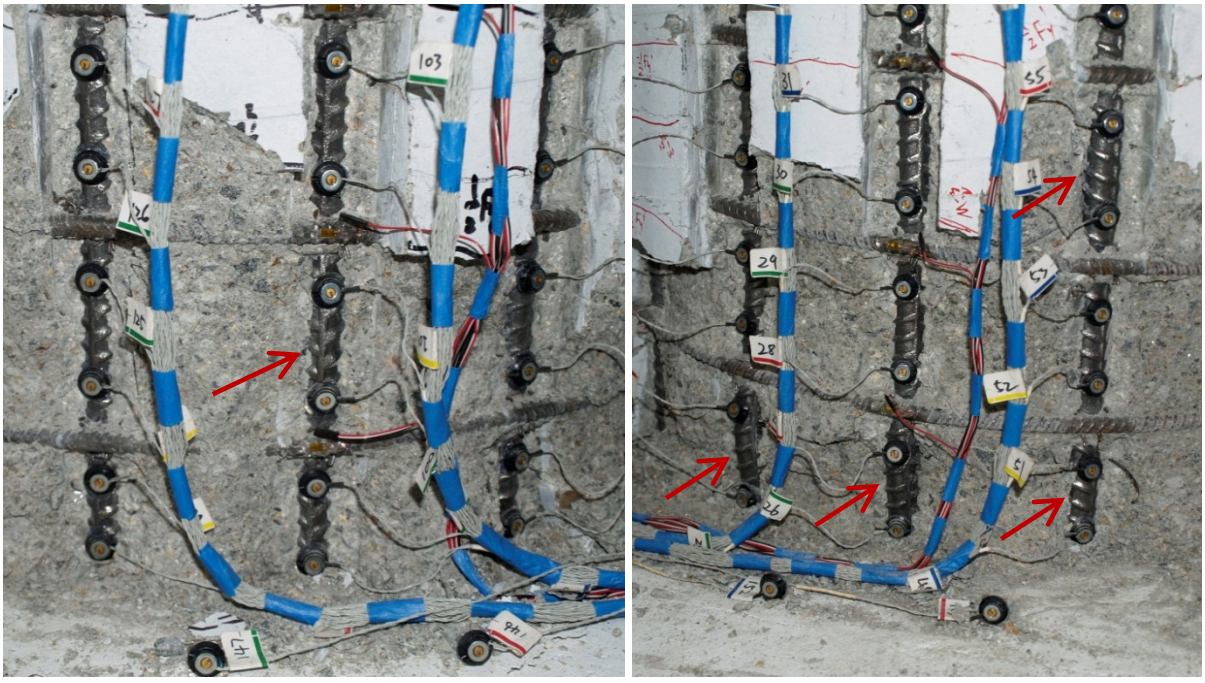

Figure 2-204. Test 14 – (Left) Buckling of Bar N3 during ($\mu_6^{-1} = -4.80$") and (Right) Buckling of South Reinforcing Bars S2, S3, and S4 during ($\mu_6^{+2} = 4.82$")

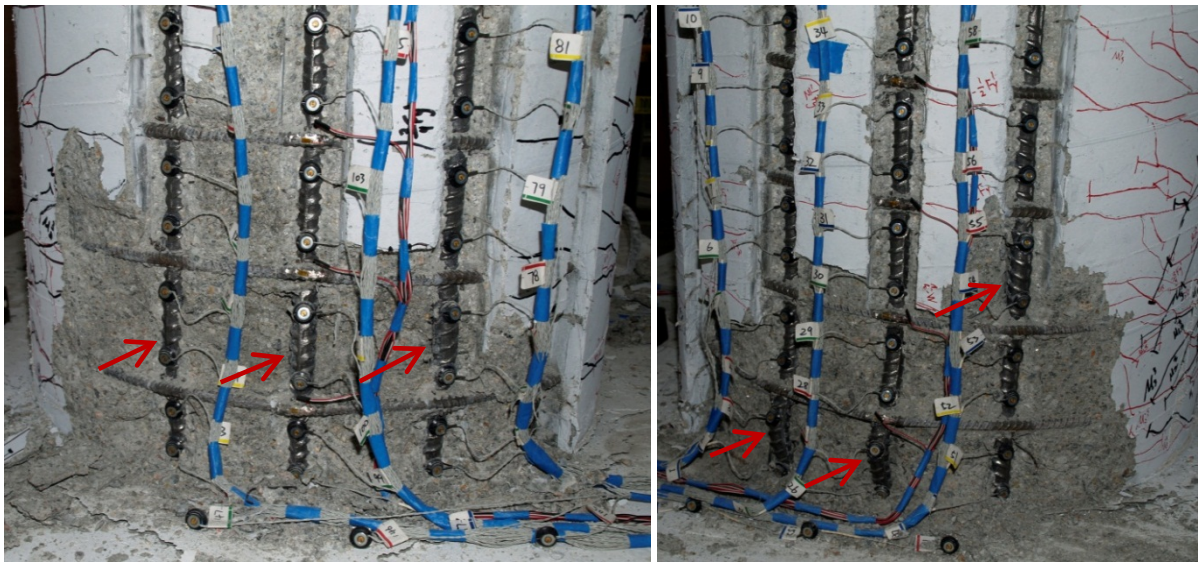

Figure 2-205. Test 14 – (Left) Buckling of Additional North Reinforcing Bars N2 and N4 during ($\mu_6^{-2} = -4.80$") and (Right) Additional Deformation in Buckled Bars S2, S3, and S4 during ($\mu_6^{+3} = 4.83$")

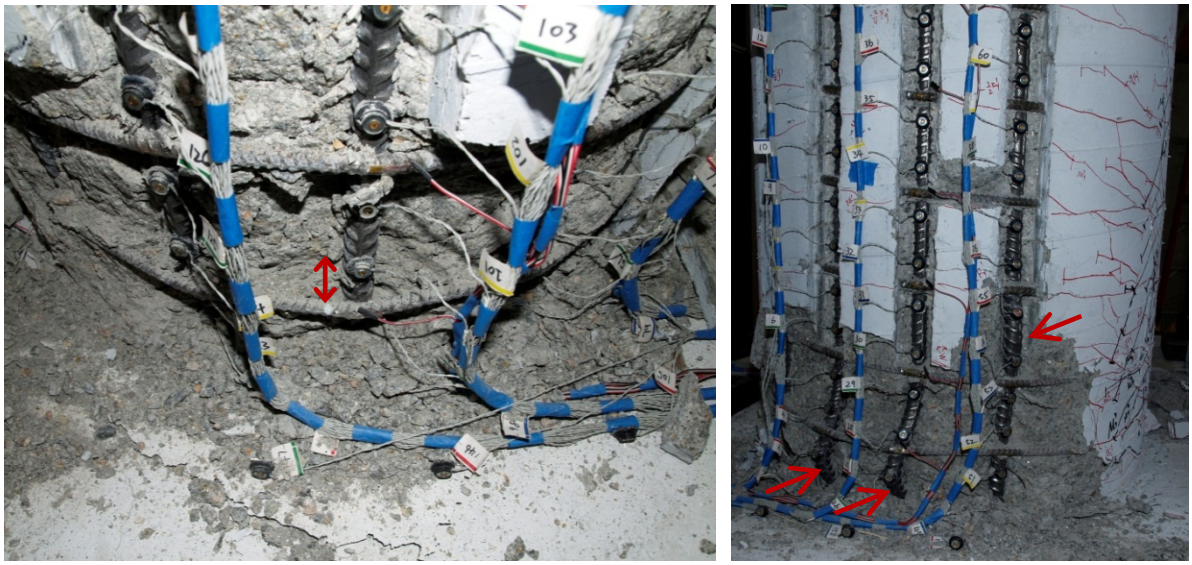

Figure 2-206. Test 14 – (Left) Separation of Deformed Spiral Layer from Buckled Bar N3 Placed Back into Tension ($\mu_8^{+1} = 6.40$") and (Right) Additional Deformation in Buckled South Reinforcing Bars S1, S2, S3, and S4 during ($\mu_8^{+1} = 6.40$")

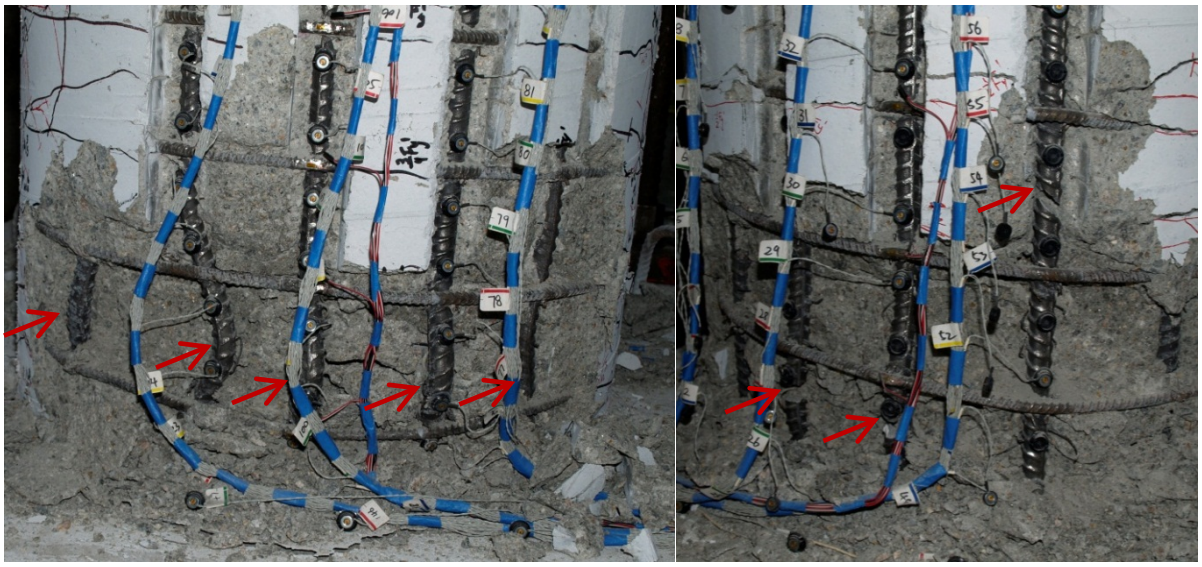

Figure 2-207. Test 14 – (Left) Additional Deformation in North Buckled Bars during ($\mu_8^{-1} = -6.39$") and (Right) Rupture of South Buckled Bars S2, S3, and S4 during ($\mu_8^{-1} = -6.39$")

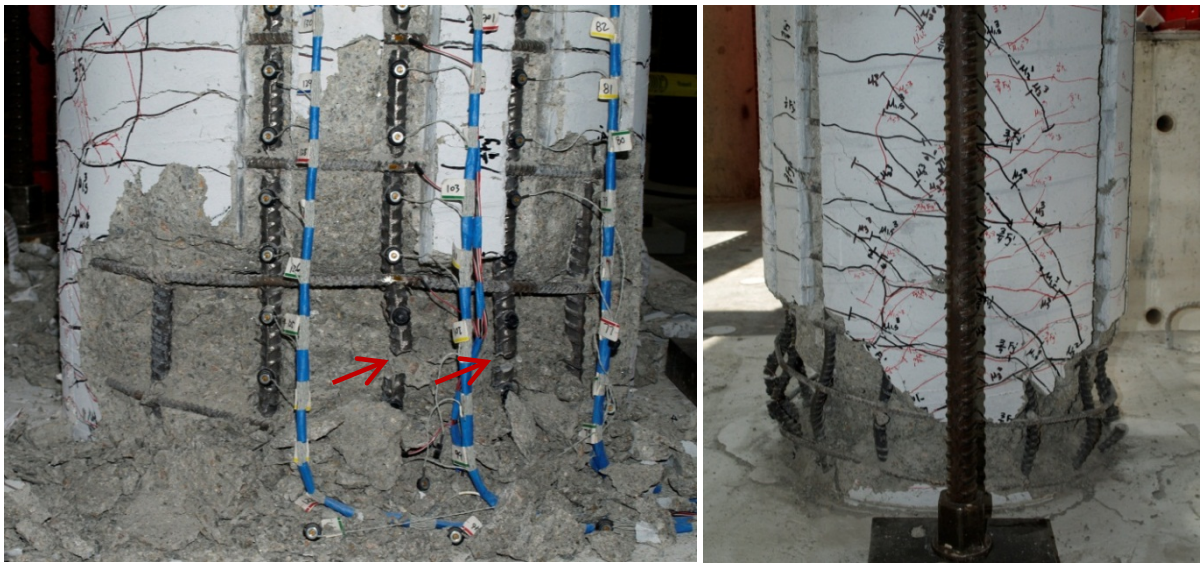

Figure 2-208. Test 14 – (Left) Rupture of North Buckled Bars N2 and N3 during ($\mu_8^{+2} = 6.40$") and (Right) Front of the Specimen after the Conclusion of the Test

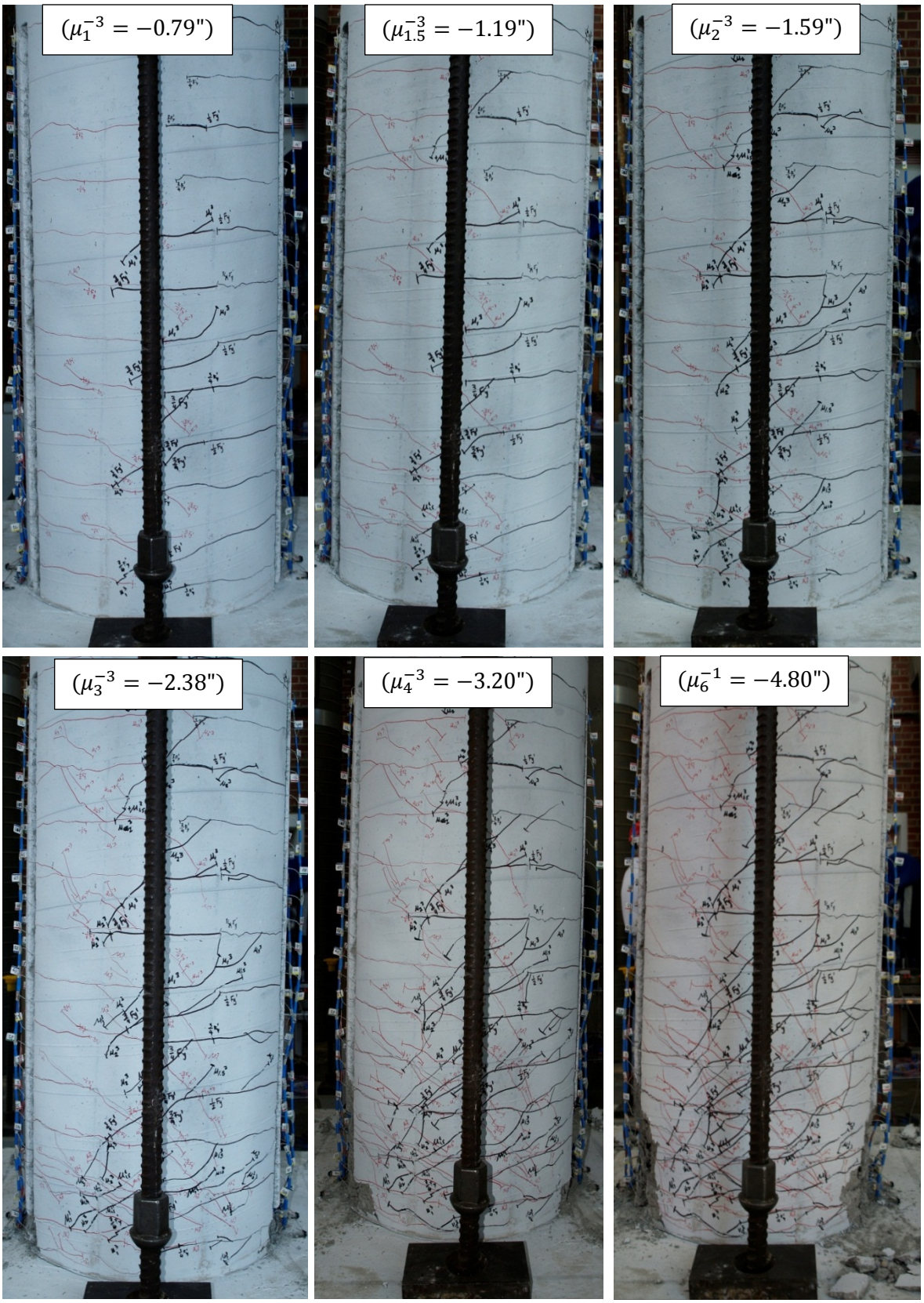

Figure 2-209. Test 14 – Crack Propagation and Orientation on the Back Side of the Specimen

2.2.2.2. Test 14 – Symmetric Three Cycle Set (#3 @ 4") Strain Data:

North Reinforcement:

Vertical strain profiles for each extreme fiber bar during push and pull cycles appear in Figure 2-210 and Figure 2-211 respectively. Measured strains at the first occurrence of ductility 1 and 1.5 are also shown due to the initial overload cycles while the actuator load cell problems were being resolved. A peak tensile strain of 0.0348, at a height of 6.95" above the footing, was measured for extreme fiber bar N3 during ($\mu_6^{+1} = 4.80"$) before the bar buckled after reversal of load. The relationship between tensile strain and displacement for this gage length appears in Figure 2-214. Similar to previous tests, the moment curvature prediction for the relationship between strain and displacement begins to over predict the tensile strains at higher displacements at an increasing rate. The largest compressive strain of -0.011, located 4.92" above the footing, was measured during ($\mu_4^{-3} = -3.20"$). The relationship between compressive strain and displacement for bar N3 during pull cycles appears in Figure 2-217 for the gage length 4.92" above the footing. Here the measured compressive strains are slightly larger than the moment curvature prediction, but the overall trend is captured through displacement ductility three.

The strain hysteresis for the largest tensile gage length on extreme fiber bar N3 is shown in Figure 2-218 with an color bar to track the progression of the test. The strain hysteresis is plotted through ($\mu_6^{-1} = -4.80"$) when the bar buckled. Prior to bar buckling, the spiral layers on the North side of the specimen remained elastic, as shown in Figure 2-213. After reversal from ($\mu_6^{+1} = 4.80"$), the relationship between strain and displacement begins to break away from the trend around 1" which agrees with the visual buckling observation. This gage length is centered over a layer of transverse steel with the largest tensile crack. Since the outward buckling of bar N3 occurred between layers of transverse steel, this particular gage length just above the outward buckled region shortens as the deformation increases. To illustrate this point, the strain hysteresis over the outward buckled region of bar N3, located 4.92" above the footing, appears in Figure 2-219. The transverse steel strain gage hysteresis for a spiral layer restraining buckled bar N3 is shown in Figure 2-220. In all three graphs, buckling looks like it occurred between 0-1" of displacement after reversal from ($\mu_6^{+1} = 4.80"$). Here the gage length over the outward buckled region begins to rapidly elongate and the transverse steel restraint tensile strain sharply increases. Before buckling, the transverse steel was elastic on the North side of the specimen, see Figure 2-213.

South Reinforcement:

A peak tensile strain of 0.035 in extreme fiber bar S3 was measured 3.61" above the footing during ($\mu_6^{-1} = -4.80"$). Debris was blocking the lowest gage length of bar S3 during this cycle, so it is unclear whether higher strains occurred. The relationship between tensile strain and displacement for bar S3 is shown in Figure 2-216 for the gage length located 3.61" above the footing. A peak compression strain of -0.0152 was measured 7.62" above the footing during ($\mu_6^{+1} = 4.80"$). This particular gage length did not have the largest compressive strains during earlier cycles. The relationship between compressive strain and displacement for the gage length 3.61" above the footing appears in Figure 2-215. The measured strains match the moment curvature prediction through the entire range of displacements. For the gage length 7.62" above the footing, the compression strain sharply increased during the first push cycle of ductility six where the largest compressive strains in bar S3 were measured.

Transverse steel strains in the lowest six spiral layers on the South side of the specimen are shown in Figure 2-212. During ($\mu_6^{+1} = 4.80"$), the compressive demand on the South side of the specimen

lead to inelastic transverse steel. The strain hysteresis for the gage length overlaying the outward buckled region of bar S3, 3.61" above the footing, appears in Figure 2-221. After reversal from a peak tensile strain of 0.035 at ($\mu_6^{-1} = -4.80$"), the relationship between strain and displacement begins to break from the trend around 1" which agrees with visible buckling observations during the test. The transverse steel strain gage hysteresis for a spiral layer over the South buckled region is shown in Figure 2-222.

2.2.2.3. Test 14 – Symmetric Three Cycle Set (#3 @ 4") Curvature and Strain Penetration:

Vertical curvature profiles for push and pull cycles appear in Figure 2-223 and Figure 2-224 respectively. Plastic curvatures at higher ductility levels have a linear distribution as shown by the linear least squared error lines. The base section reinforcement slip measured at the footing-column interface can be monitored using the Optotrak system. The slip hysteresis for North and South extreme fiber bars appears in Figure 2-225 and Figure 2-226. The base section rotation due to strain penetration during push and pull cycles is shown in Figure 2-227 and Figure 2-228 respectively. The top column displacement can be calculated by integrating the measured curvature profiles, extrapolating the base section rotation to the center of loading, and assuming an elastic curvature distribution above the instrumented region. A comparison of measured and integrated top column displacements appears in Figure 2-229.

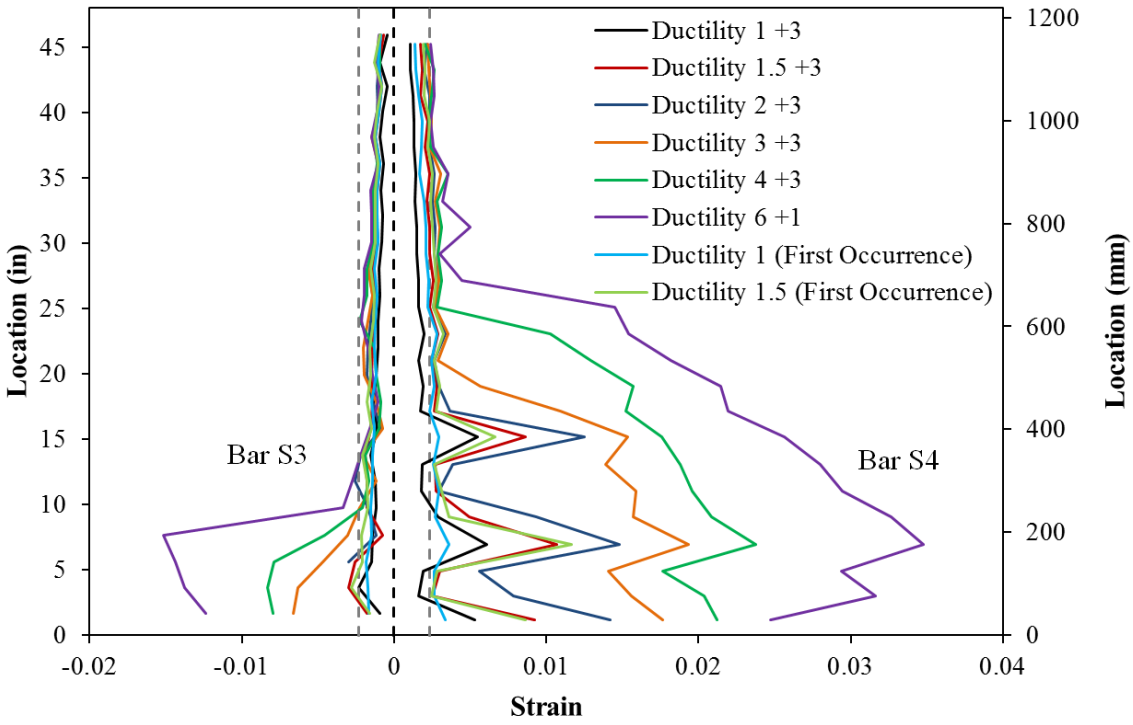

Figure 2-210. Test 14 – Extreme Fiber Vertical Strain Profiles for Push Cycles

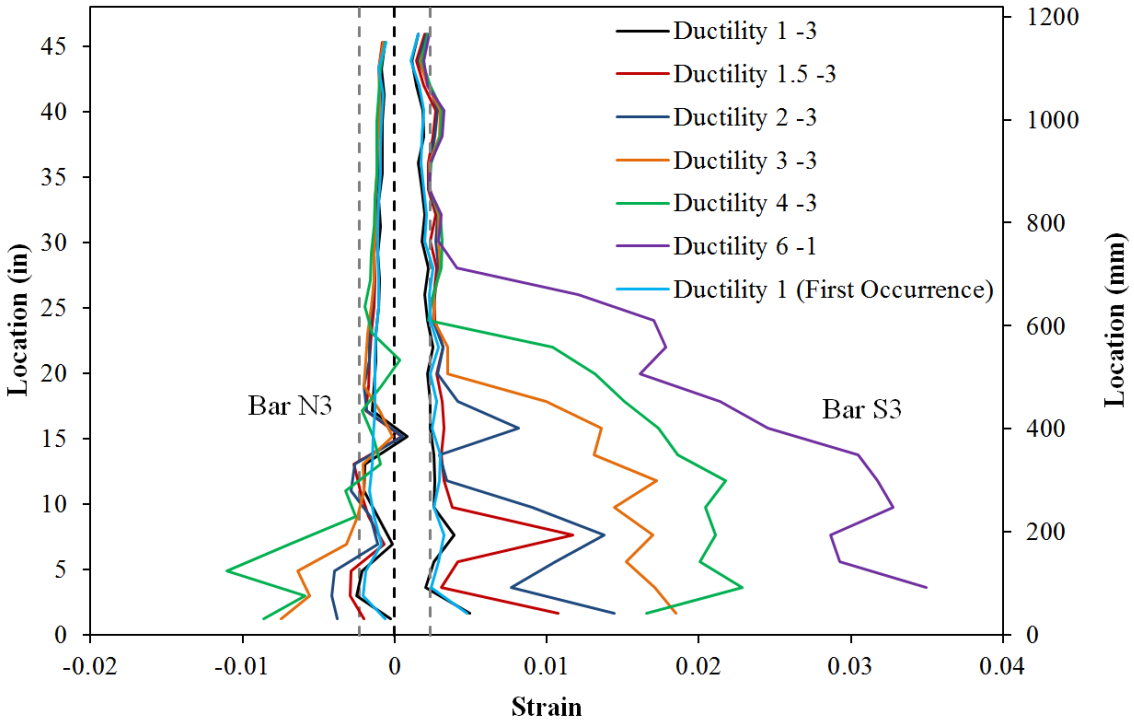

Figure 2-211. Test 14 – Extreme Fiber Vertical Strain Profiles during Pull Cycles

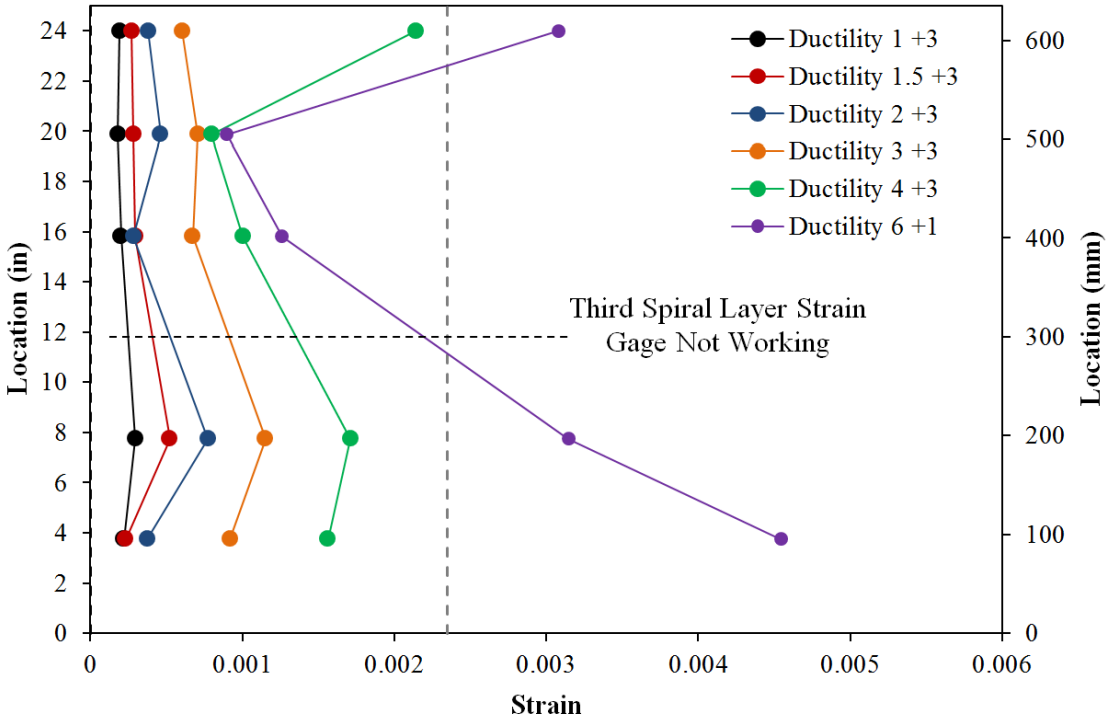

Figure 2-212. Test 14 – Transverse Steel Strains in the Lowest Six Spiral Layers on the South Side of the Specimen during Push Cycles

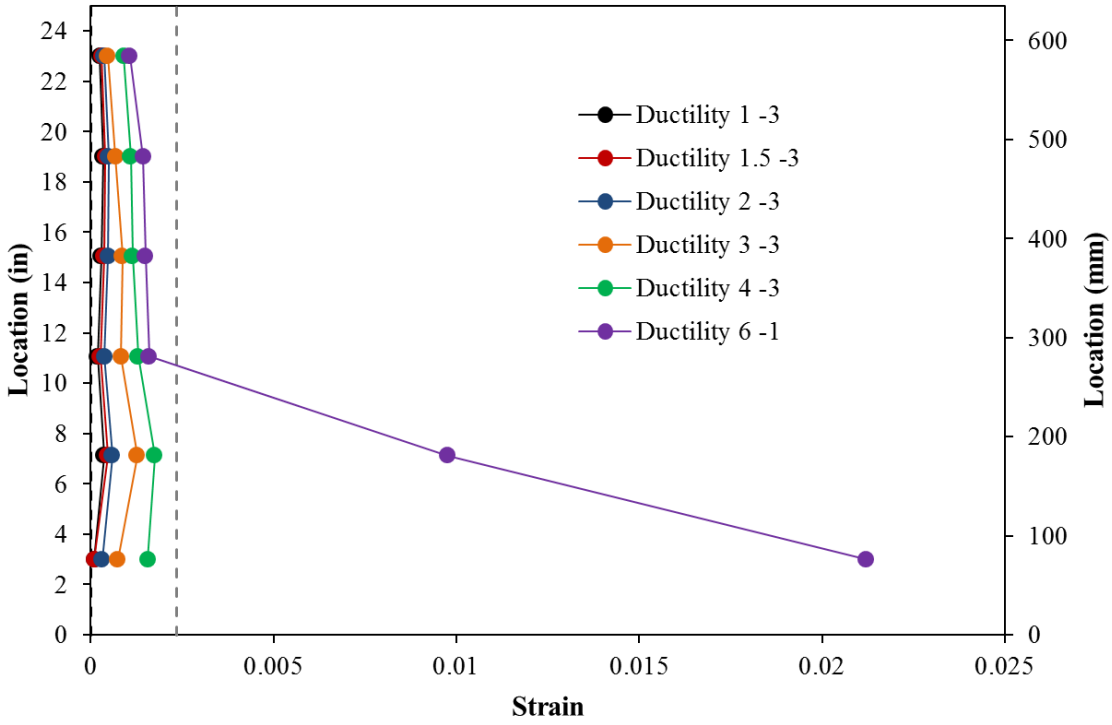

Figure 2-213. Test 14 – Spiral Strains on the on the North Side during Pull Cycles

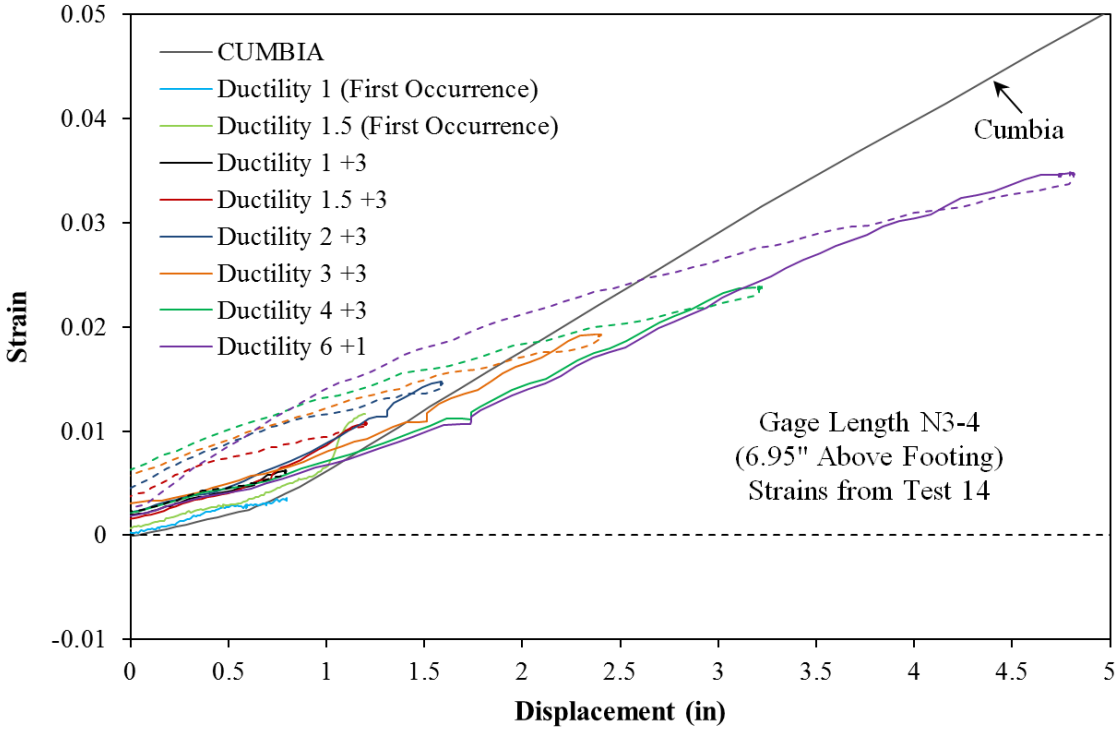

Figure 2-214. Test 14 – Strain and Displacement Relationship for Extreme Fiber Bar N3 during Push Cycles (6.95" Above Footing)

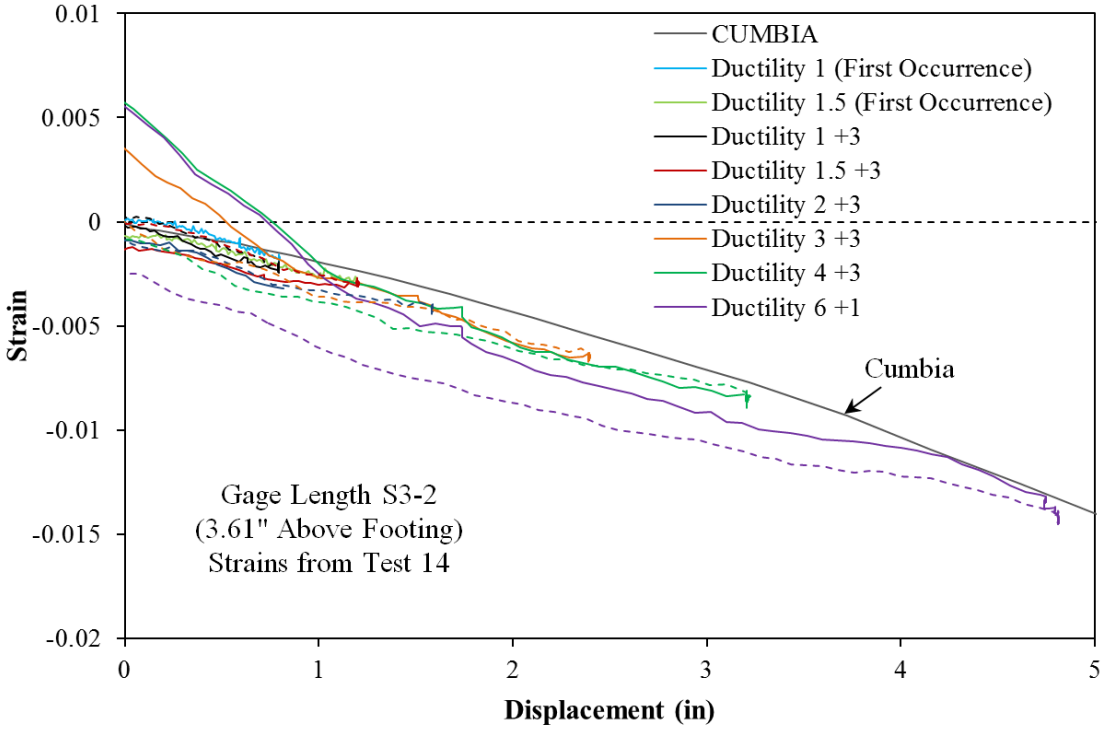

Figure 2-215. Test 14 – Compressive Strain and Displacement for Bar S3 (3.61" Above)

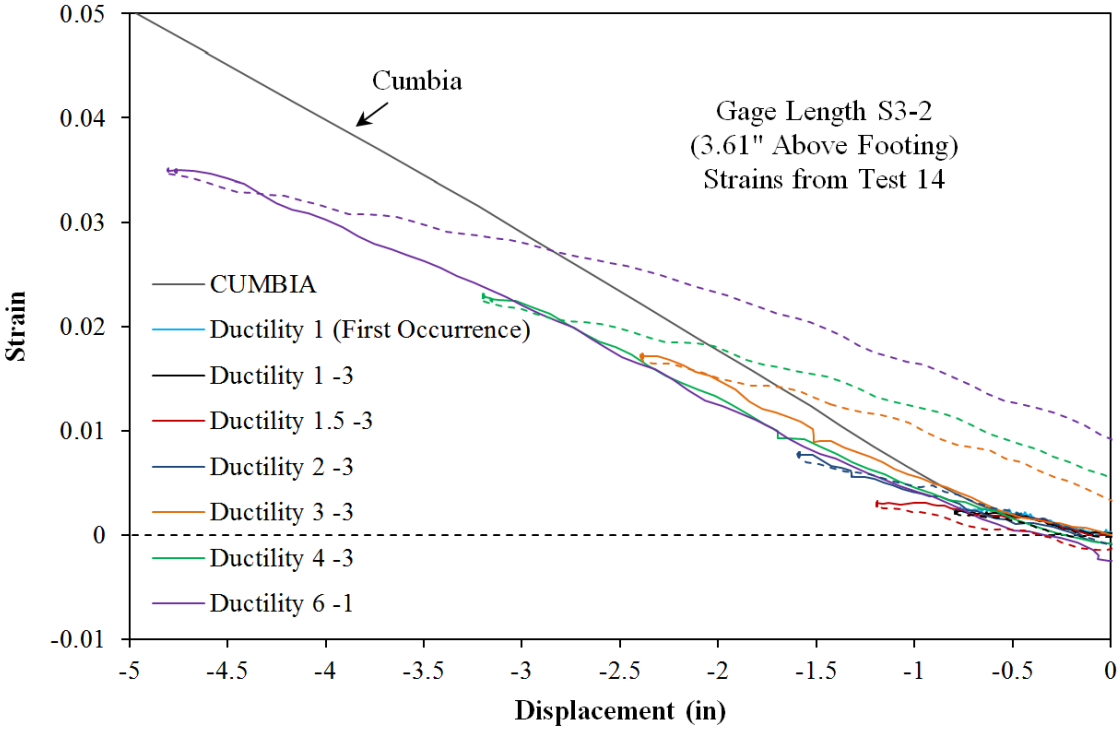

Figure 2-216. Test 14 – Tensile Strain and Displacement for Bar S3 (3.61” Above)

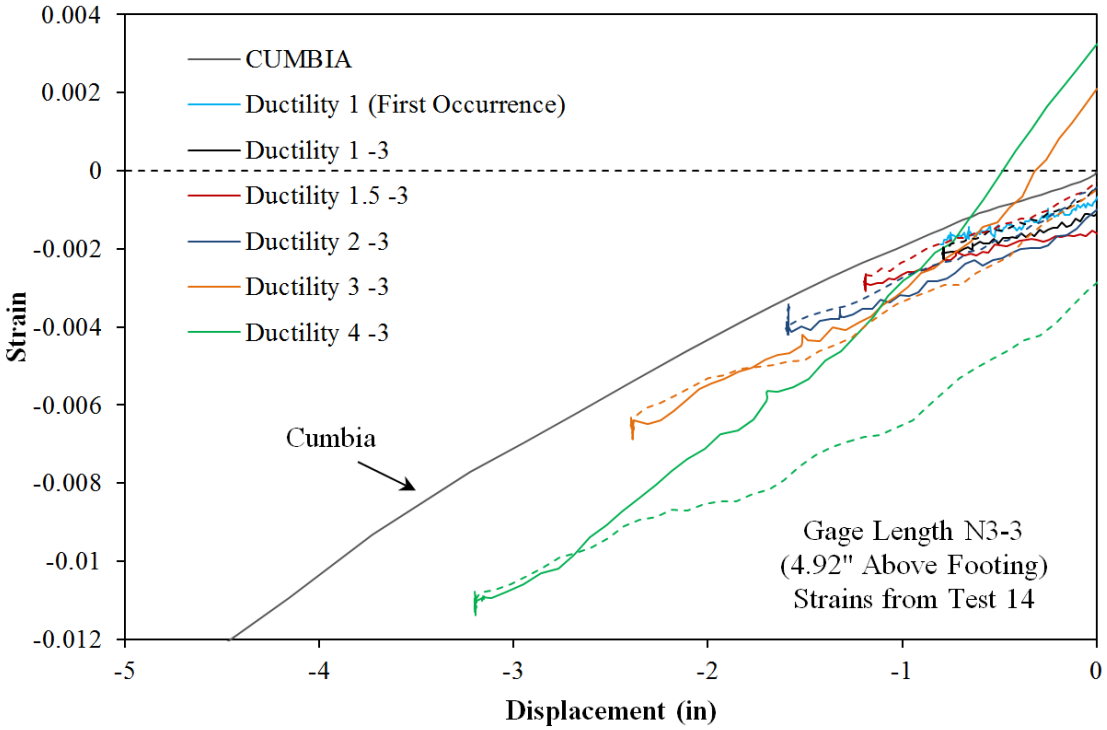

Figure 2-217. Test 14 – Strain and Displacement Relationship for Extreme Fiber Bar N3 during Pull Cycles (4.92" Above Footing)

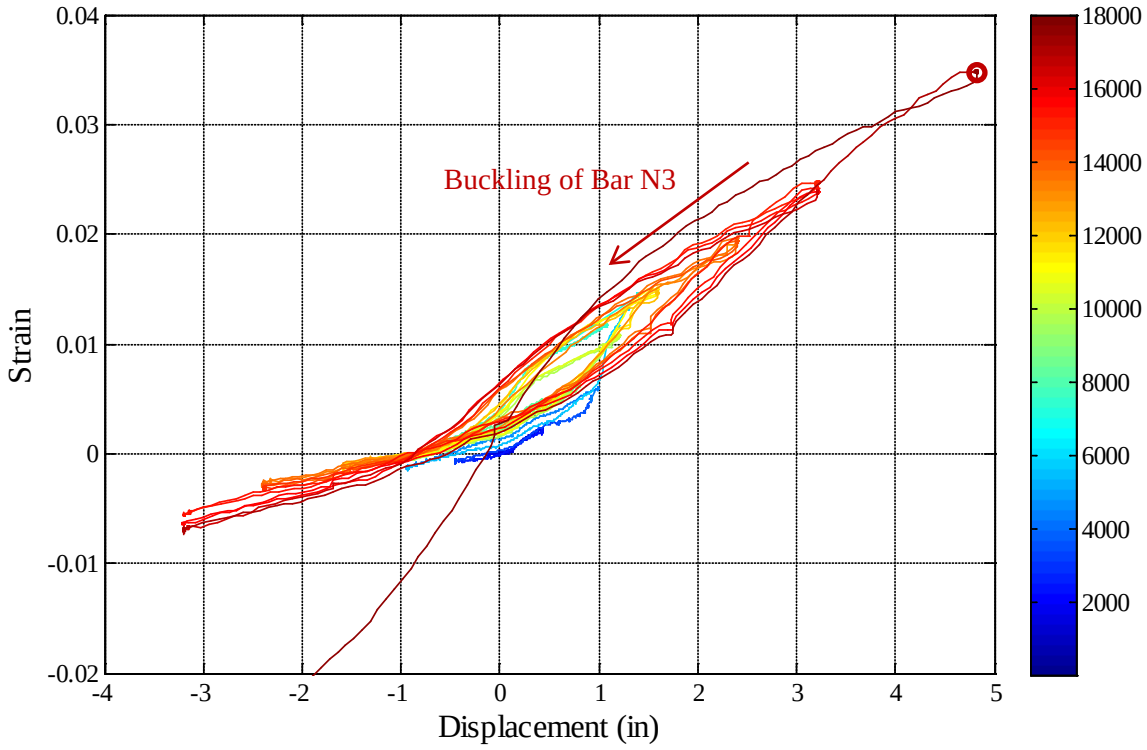

Figure 2-218. Test 14 – Bar N3 Strain Hysteresis (6.95” Above Footing)

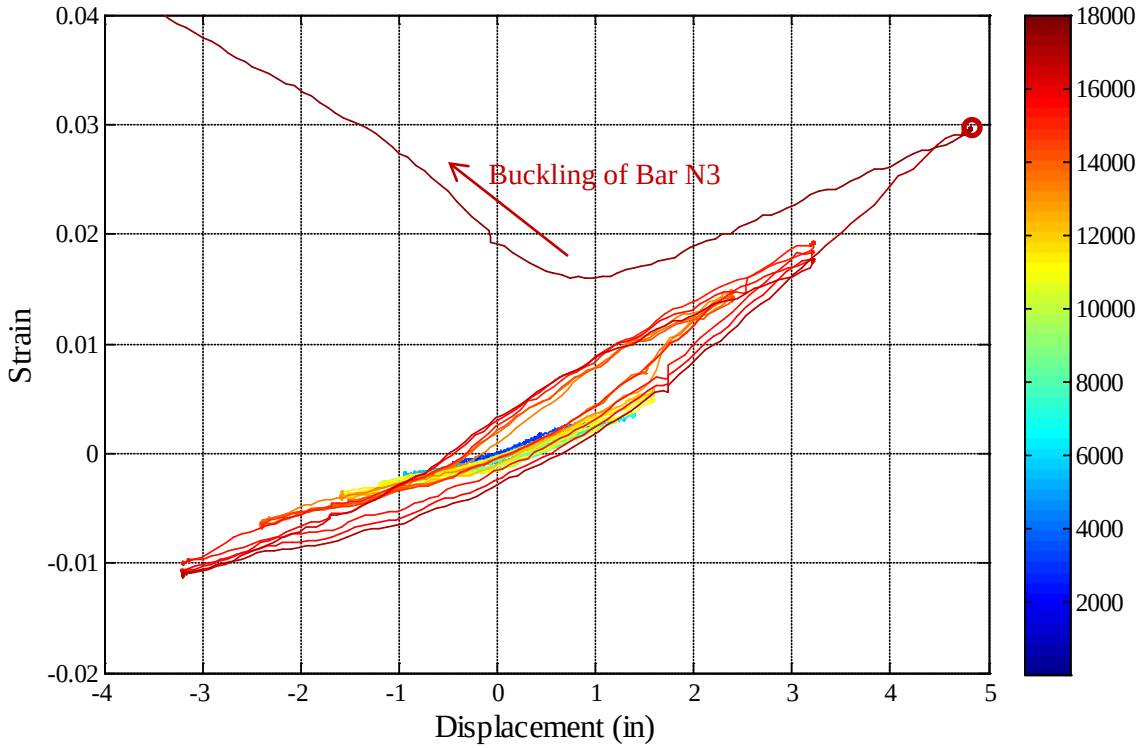

Figure 2-219. Test 14 – Bar N3 Strain Hysteresis (4.92" Above Footing)

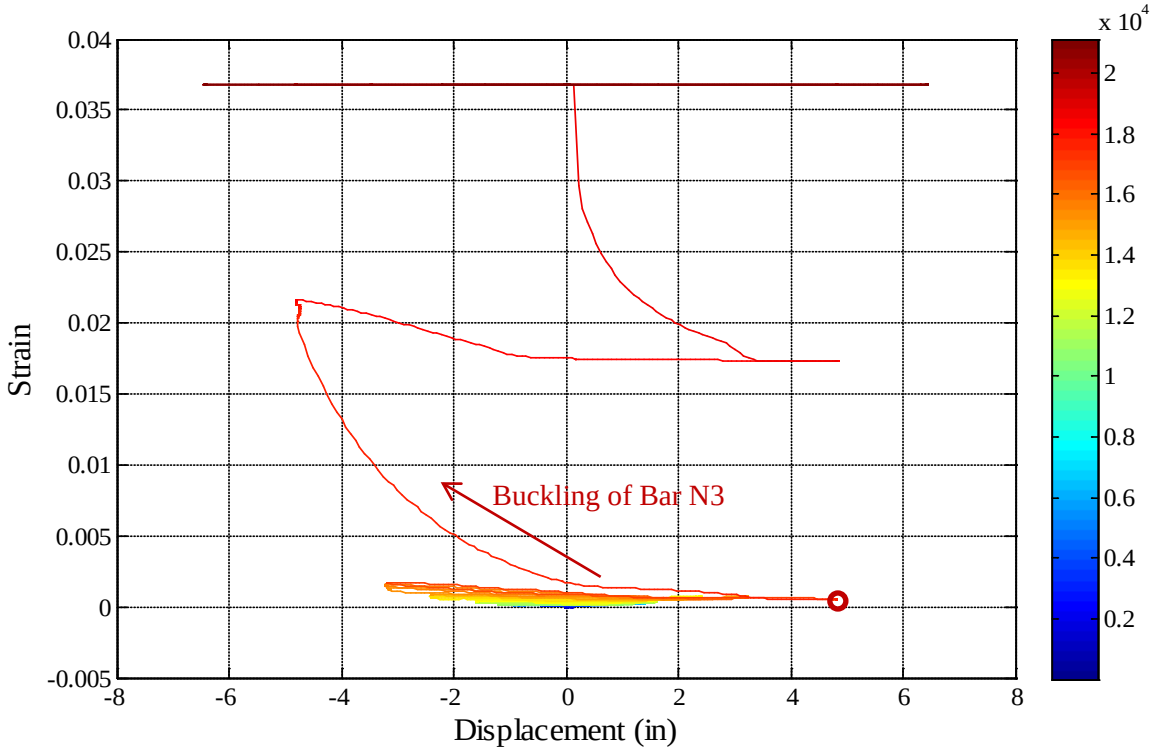

Figure 2-220. Test 14 – Transverse Steel Strain Gage Hysteresis over North Buckled Region

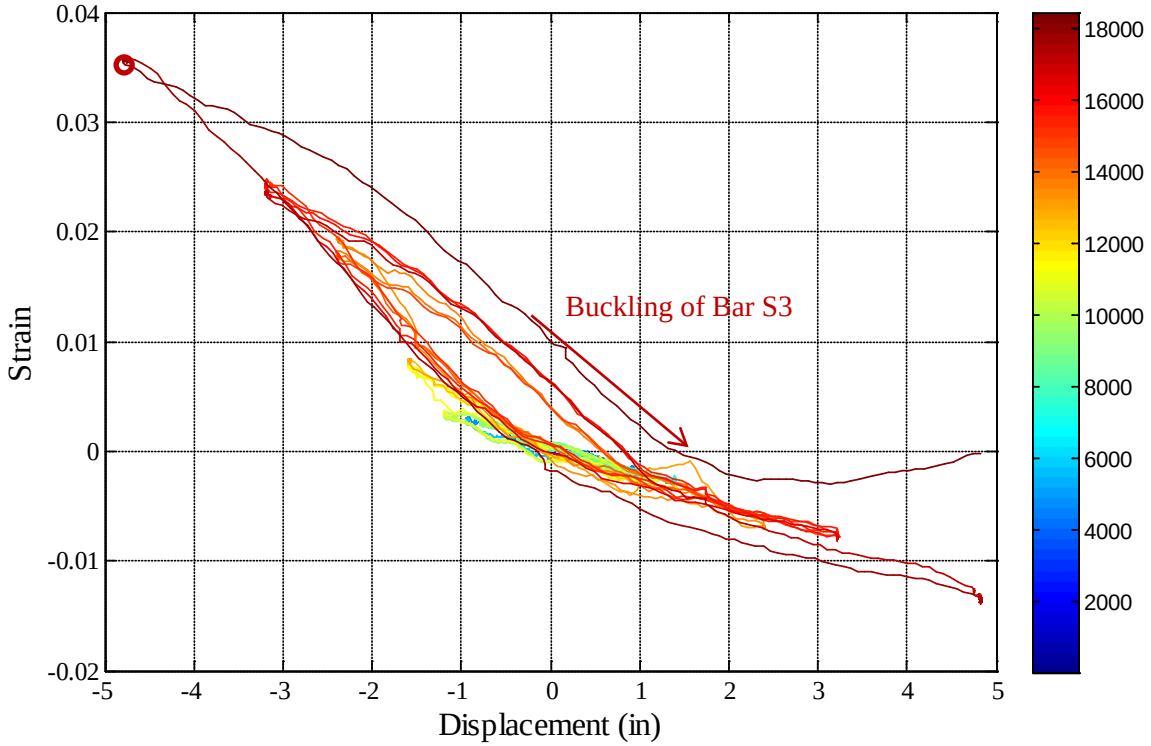

Figure 2-221. Test 14 – Bar S3 Strain Hysteresis (3.61" Above Footing)

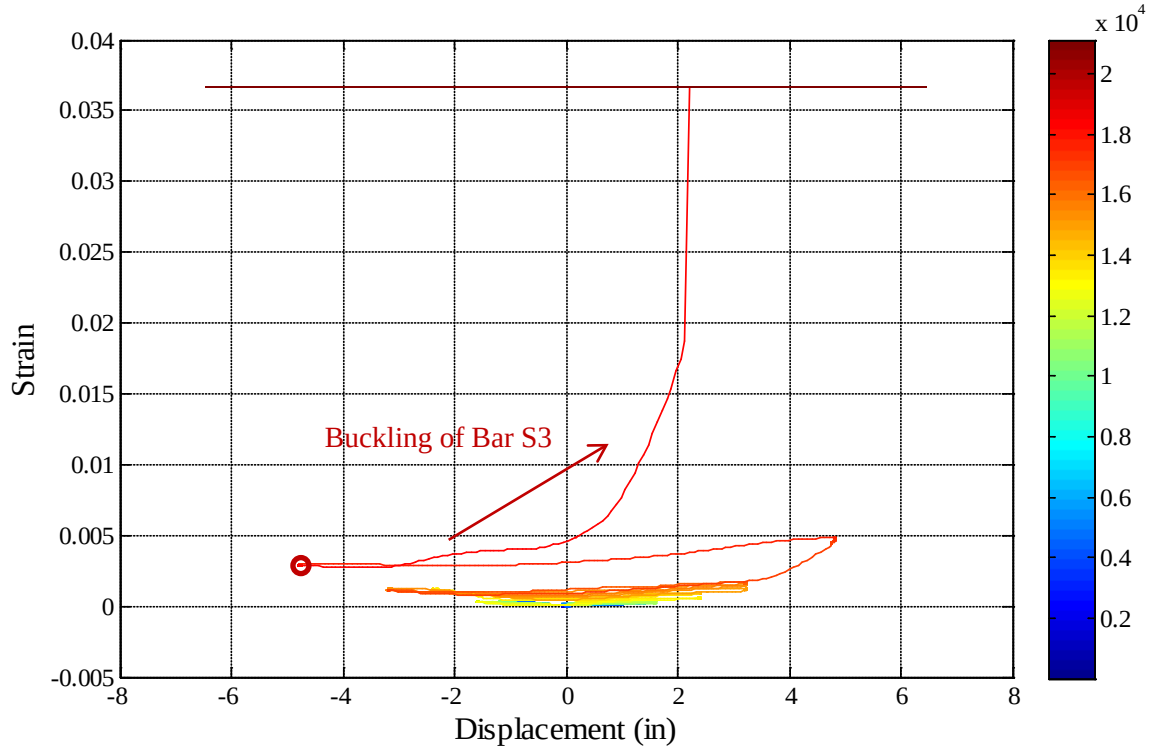

Figure 2-222. Test 14 – Transverse Steel Strain Gage Hysteresis Over South Buckled Region

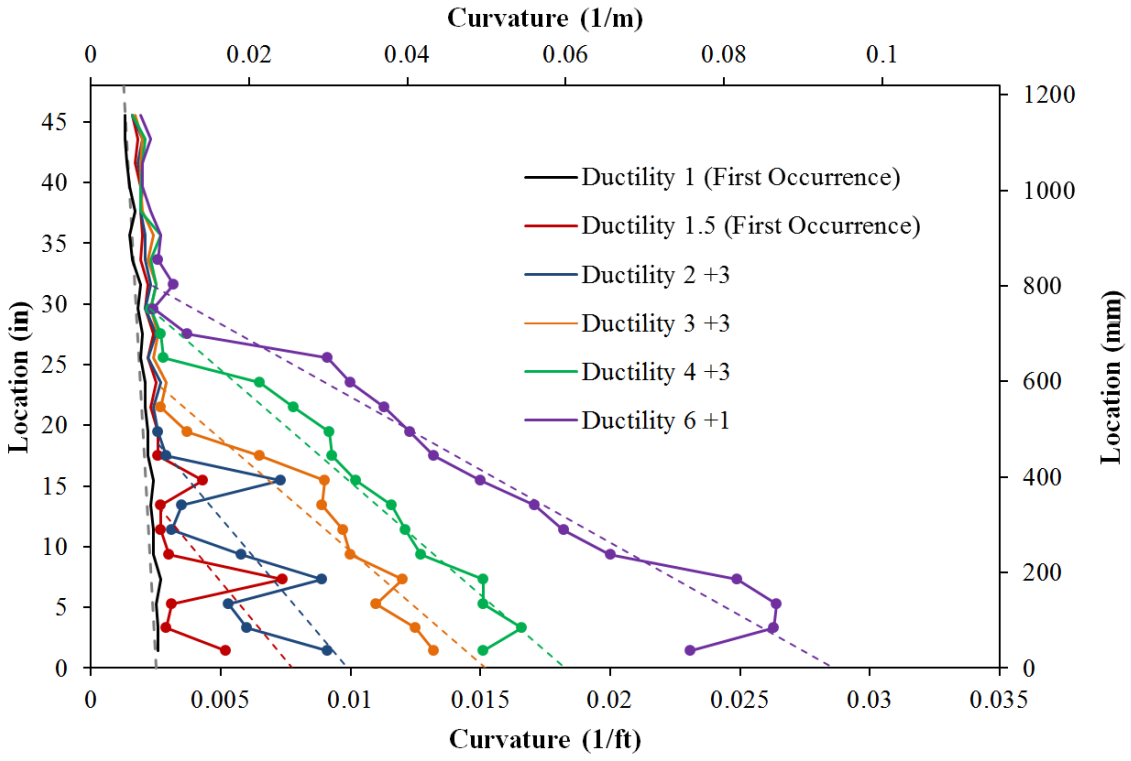

Figure 2-223. Test 14 – Vertical Curvature Profiles during Push Cycles

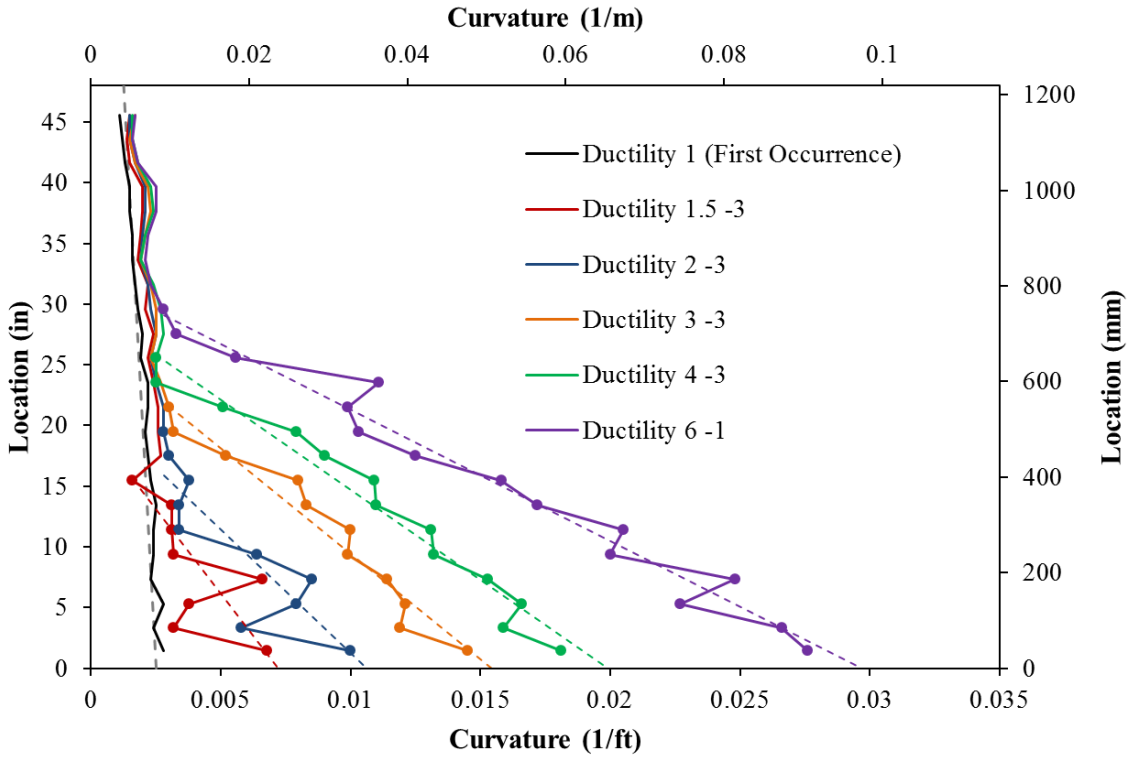

Figure 2-224. Test 14 – Vertical Curvature Profiles during Pull Cycles

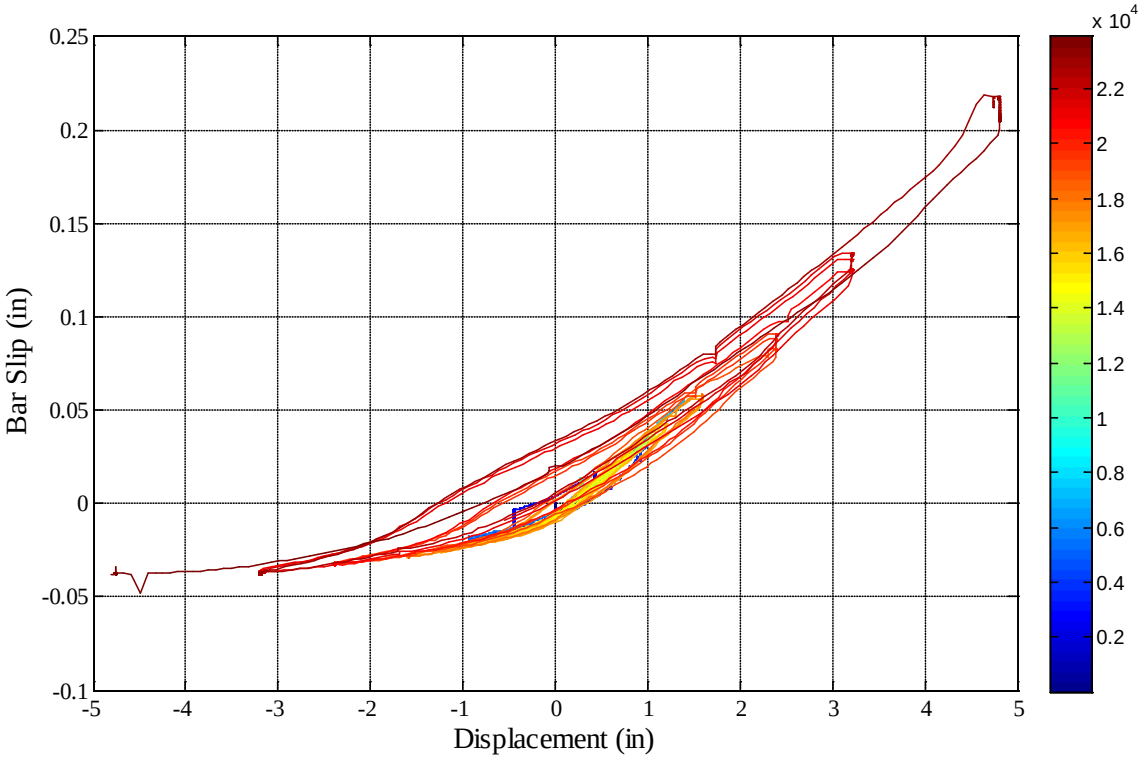

Figure 2-225. Test 14 – Bar N3 Base Section Slip Hysteresis due to Strain Penetration into the Footing

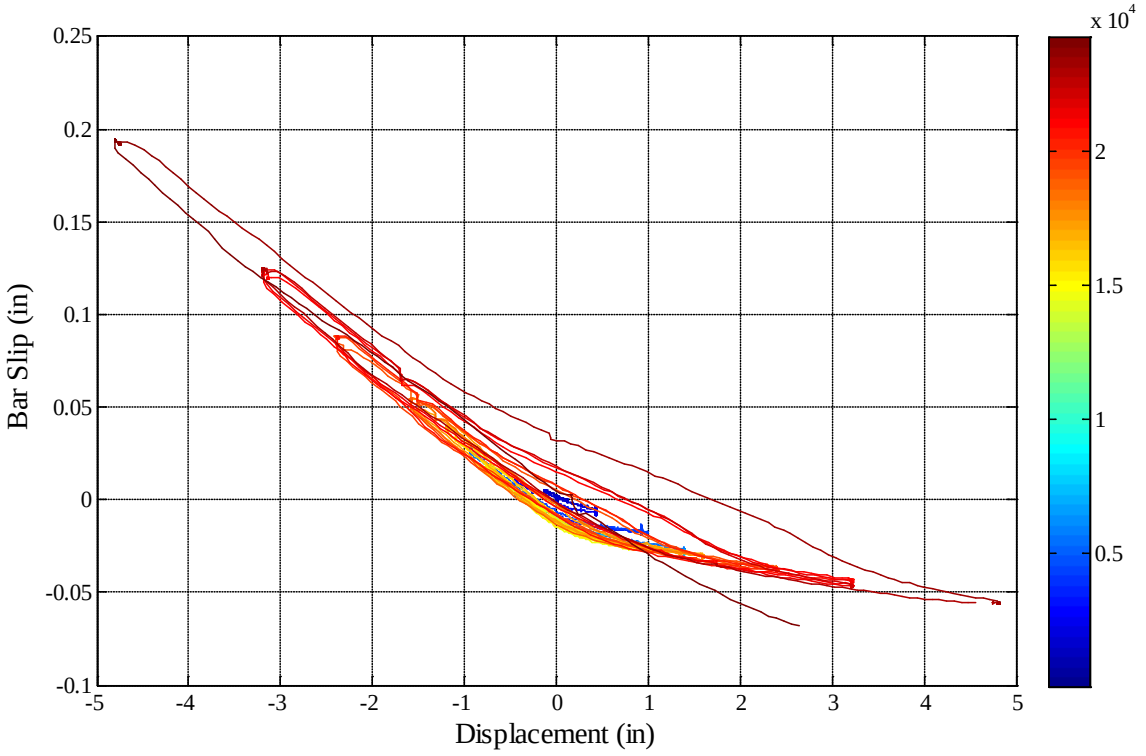

Figure 2-226. Test 14 – Bar S4 Slip Hysteresis due to Strain Penetration into the Footing

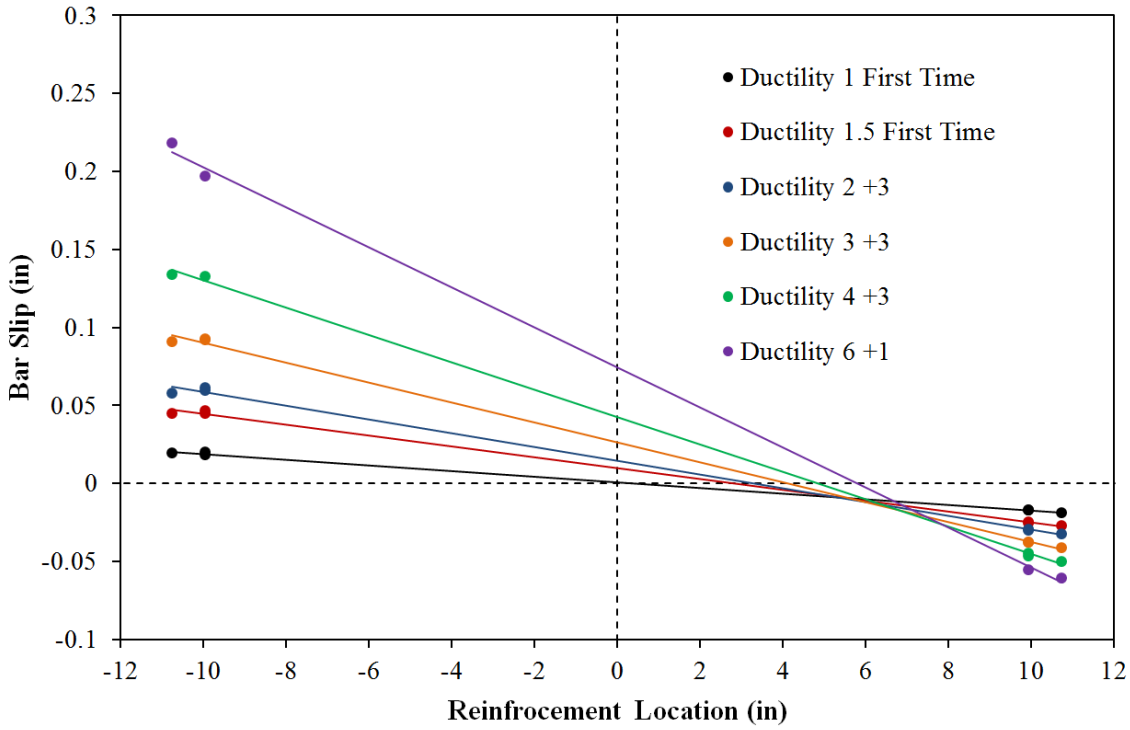

Figure 2-227. Test 14 – Base Section Rotation due to Strain Penetration during Push Cycles

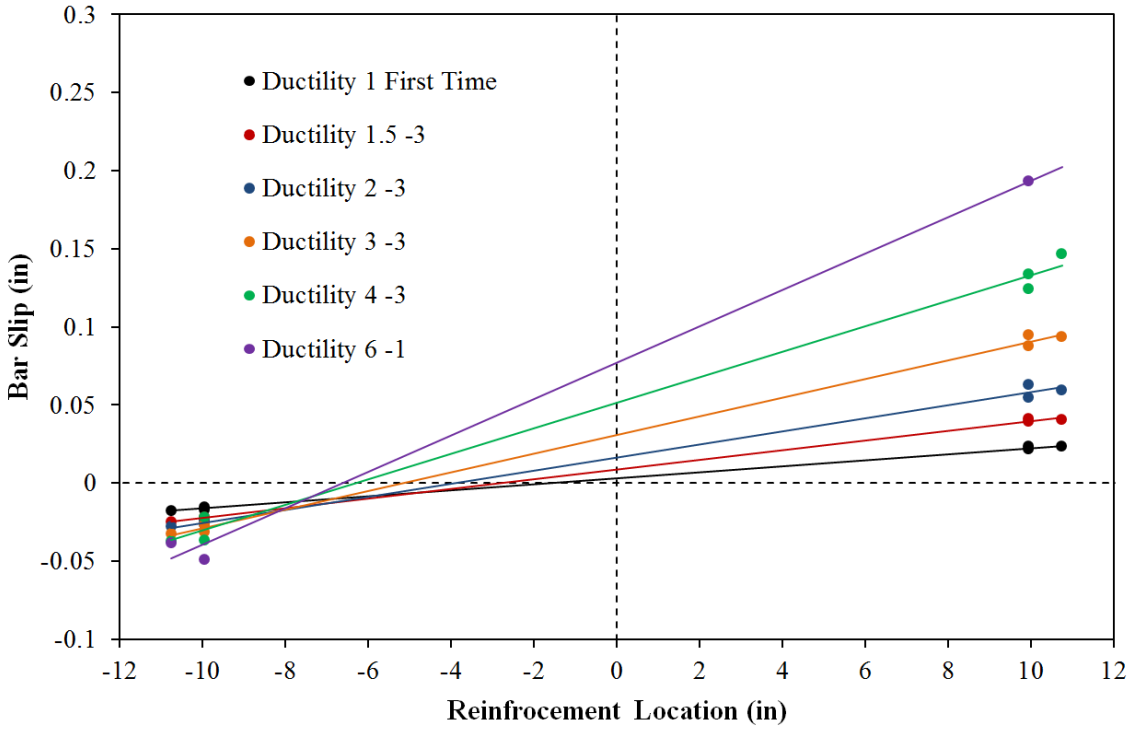

Figure 2-228. Test 14 – Base Section Rotation due to Strain Penetration during Pull Cycles

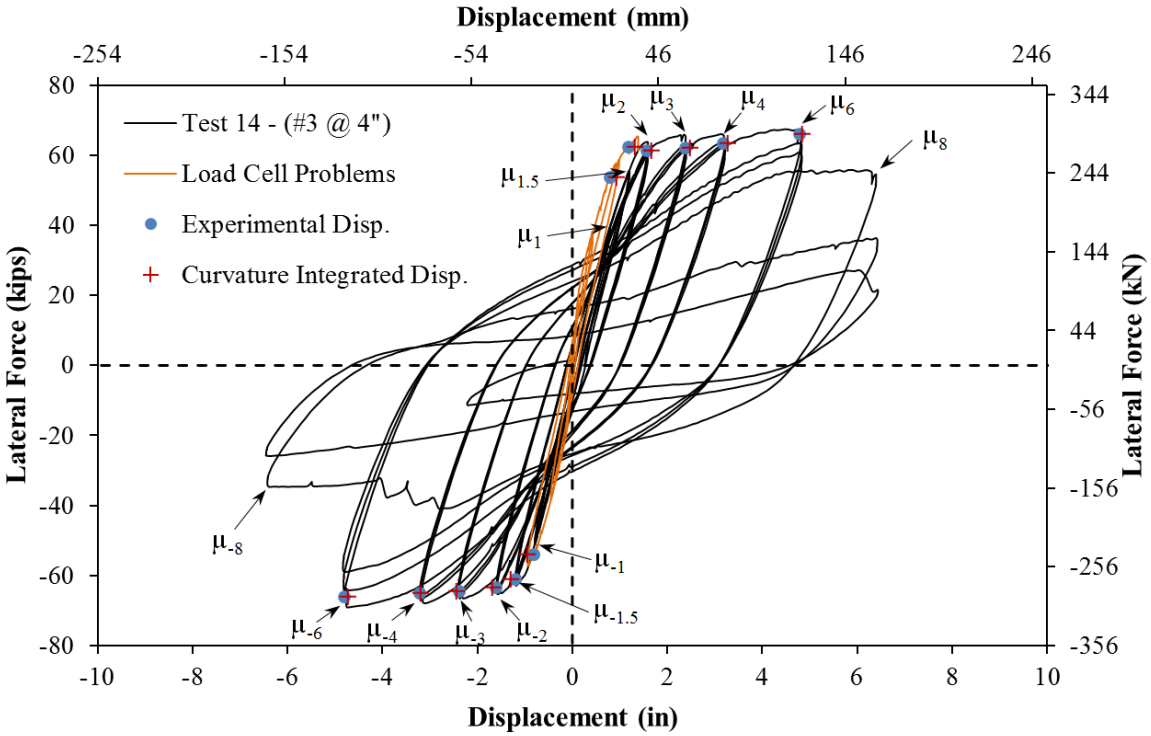

Figure 2-229. Test 14 – Comparison of Measured and Optotrak Integrated Top Column Displacements

2.2.3.Test 15 – Symmetric Three Cycle Set Load History (#3 Spiral at 2.75" Spacing)

Table 2-14. Results Summary for Test 15 – Symmetric Three Cycle Set Load History

LOAD HISTORY: Symmetric Three Cycle Set Load History

VALUES OF INTEREST:

Transverse Steel Detailing:	#3 Spiral at 2.75" Spacing (0.7%)
Concrete Compressive Strength:	$f_c' = 7232psi$
Axial Load:	$P = 170kips$
Analytical First Yield Force:	$F_y' = 47.1kips$
Experimental First Yield Displacement:	$\Delta_y' = 0.62"$
Analytical Nominal Moment Capacity:	$M_n = 506.9kip * ft$
Equivalent Yield Displacement:	$\Delta_y = 0.84"$
Maximum Lateral Force:	$68.6kips$
Failure Mode:	Fracture of Previously Buckled Reinforcement

DAMAGE OBSERVATIONS: (Drift %) [Displacement Ductility, μ_Δ]

First Cracking North:	$1/2Fy' = 0.16"$
First Cracking South:	$-1/2Fy' = -0.20"$
Cover Concrete Crushing North:	$\mu_{1.5}^{-3} = -1.25"$
Cover Concrete Crushing South:	$\mu_2^{+1} = 1.68"$
Transverse Steel Yield North:	At $-1.89"$ during pull to $\mu_6^{-1} = -5.00"$
Transverse Steel Yield South:	At $2.08"$ during push to $\mu_4^{+2} = 3.33"$
Longitudinal Bar Buckling North:	Reversal from $\mu_6^{+2} = 5.00"$
Longitudinal Bar Buckling South:	Reversal from $\mu_6^{-1} = -5.00"$
Longitudinal Bar Fracture North:	At $3.91"$ during push to $\mu_8^{+2} = 6.67"$
Longitudinal Bar Fracture South:	At $-2.54"$ during pull to $\mu_8^{-1} = -6.69"$

*$\mu_8^{-1} = -6.69"$ represents the first pull cycle of displacement ductility eight which reached a peak displacement of -6.69 inches

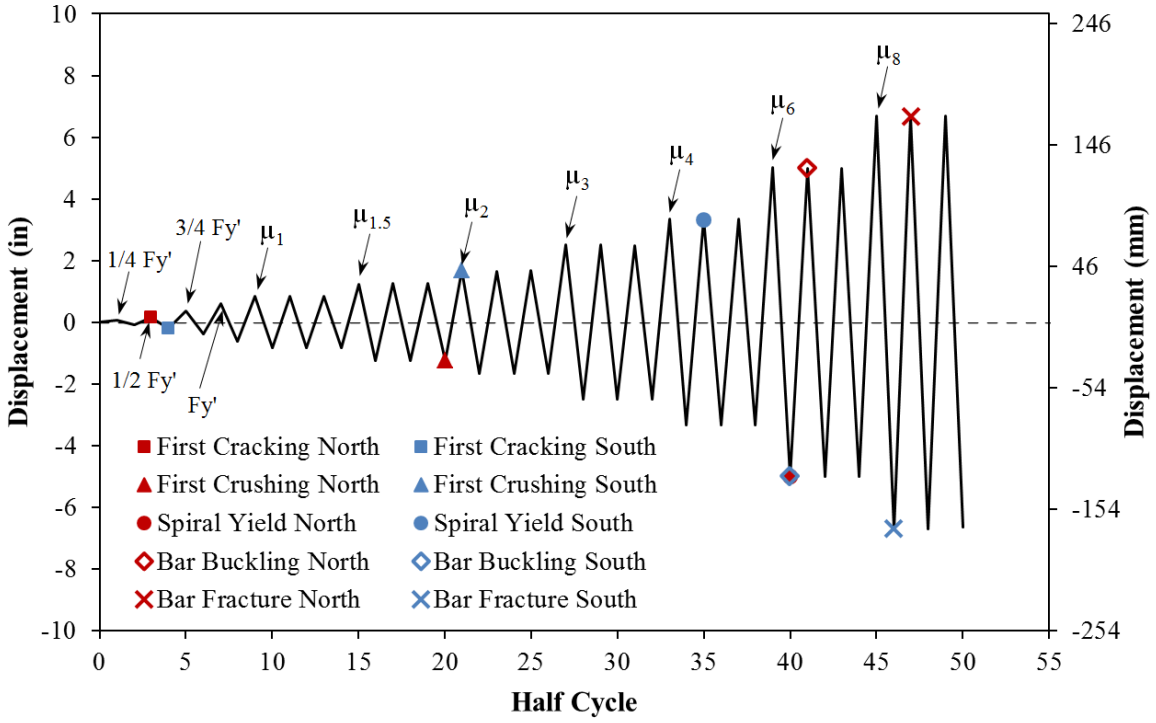

Figure 2-230. Test 15 – Symmetric Three Cycle Set Load History

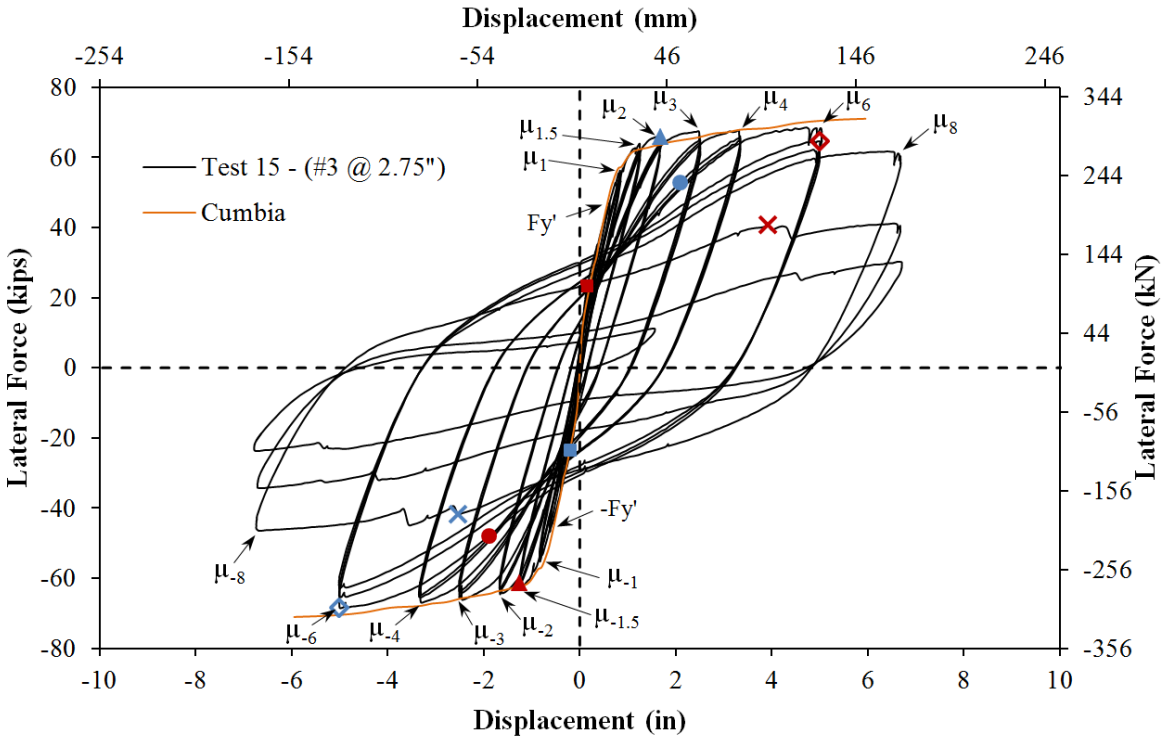

Figure 2-231. Test 15 – Lateral Force vs. Top Column Displacement Response

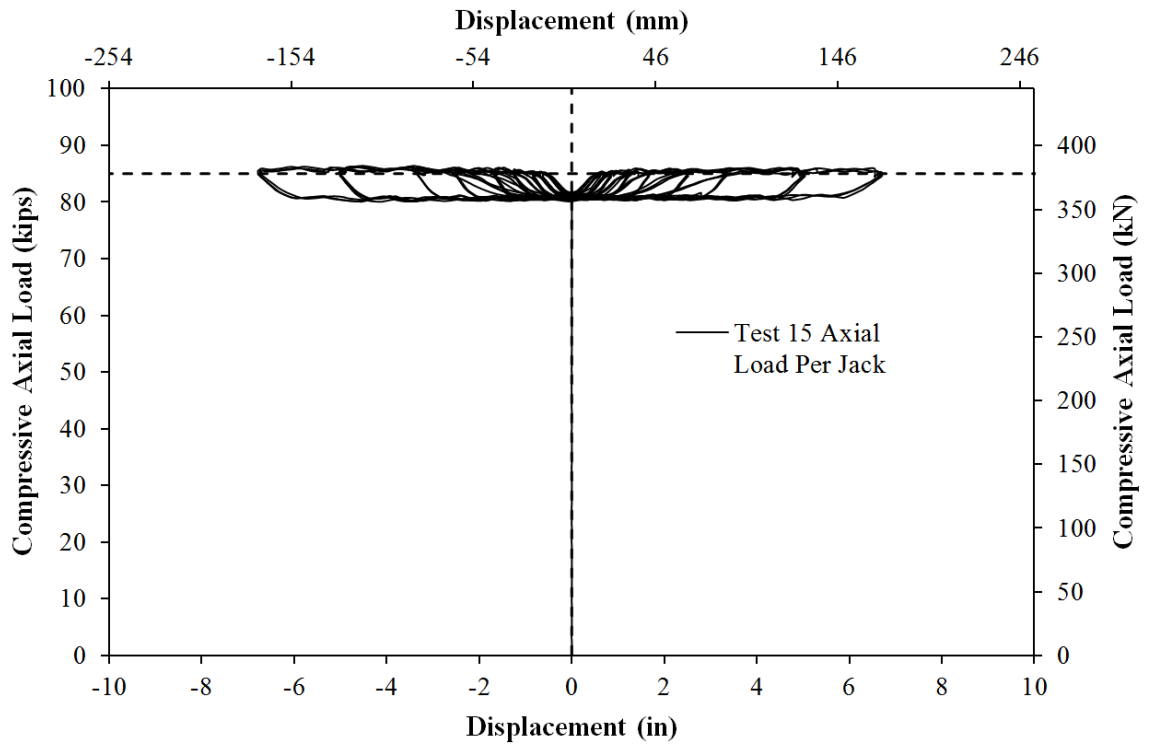

Figure 2-232. Test 15 – Compressive Axial Load from One Jack (Total = 2*Value)

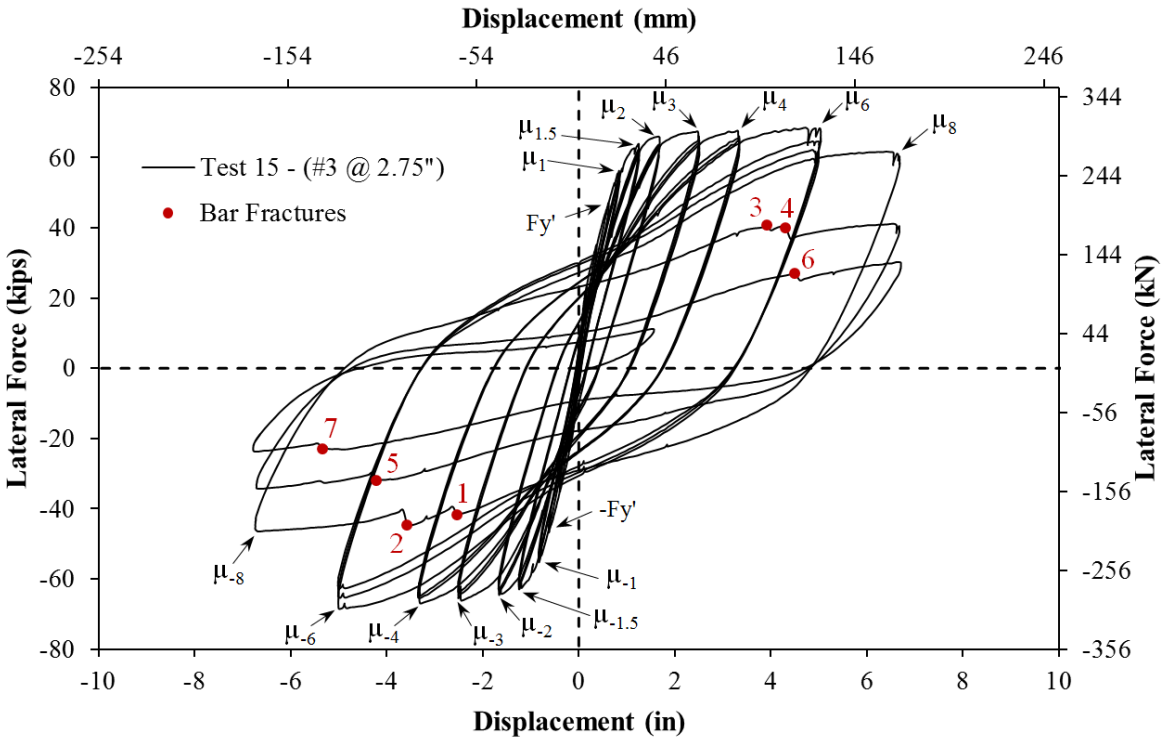

Figure 2-233. Test 15 - Rupture History of Previously Buckled Reinforcement

2.2.3.1. Test 15 – Symmetric Three Cycle Set (#3 @ 2.75") Experimental Observations:

The first yield force for the tested material and geometric properties was determined using moment curvature analysis (Test 15: Cumbia Fy' = 47.11 kips with f'c = 7232 psi). The first yield displacement was obtained as an average for the first yield push and pull cycles ($\Delta'_y = 0.62$"). Vertical strain profiles for both extreme fiber bars during push and pull cycles up to the first yield force appear in Figure 2-234 with a dashed line representing the yield strain of the longitudinal reinforcement. The equivalent yield displacement, used to determine the displacement ductility levels ($\mu_{\Delta n} = \mathrm{n} * \Delta_y$), is then calculated as $\Delta_y = \Delta'_y(M_n/M'_y) = 0.84$" for Test 15. The full symmetric three cycle set load history appears in Figure 2-230 and the resulting lateral force vs. top column displacement hysteresis is shown in Figure 2-231. The monotonic moment curvature prediction agrees well with the backbone curve of the cyclic response.

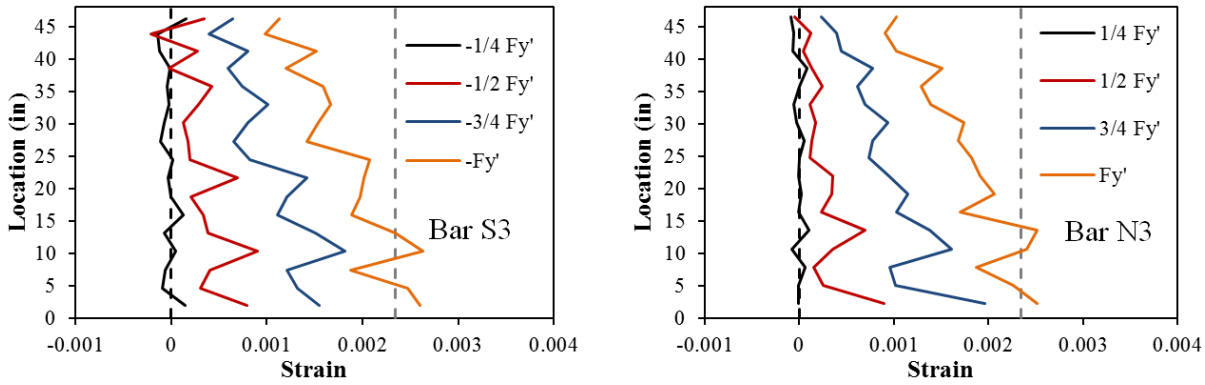

Figure 2-234. Test 15 – Vertical Strain Profiles for Extreme Fiber Reinforcement before Yield (Grey Dashed Yield Strain Line)

The test began with cycles in ¼ Fy' (first yield force) increments in each direction of loading until the first yield force was reached. The first cracks on the North side of the specimen measured 0.1mm at approximate 10" spacing at $(1/2Fy' = 23.27kips)$. Cracks on the South Side of the specimen measured 0.1mm at approximate 10" spacing during $(-1/2Fy' = -23.47kips)$. The largest crack widths on the North side of the specimen reached 0.2mm at approximate 5" spacing at $(3/4Fy' = 35.23kips)$. Cracks measured at 0.3mm with 5" spacing were observed on the South side of the specimen during $(-3/4Fy' = -35.16kips)$. During the first yield push cycle $(Fy' = 47.13kips,$ 0.62"), the largest crack widths measured 0.35mm at approximate 5" spacing. During the subsequent pull cycle $(-Fy' = -46.81kips, -0.63")$, crack widths reached 0.4mm on the South side of the specimen. The crack distribution at first yield is shown in Figure 2-235. The progression of the crack distribution on the back side of the specimen is shown in Figure 2-245. Cracks on the North side of the specimen measured 0.5mm at approximate 4" spacing during $(\mu_1^3 = 0.85")$. After reversal, cracks on the South side reached 0.55mm at 5" spacing during $(\mu_1^{-3} = -0.84")$. Visible flaking of the cover concrete in compression, which is a precursor to crushing, was observed on the South side of the specimen during $(\mu_{1.5}^{+1} = 1.24")$. A similar observation on the North side of the specimen occurred during $(\mu_{1.5}^{-1} = -1.24")$.

Cracks on the North side of the specimen measured 1mm during $(\mu_{1.5}^{+3} = 1.25")$. Crushing of the cover concrete on the North side of the specimen was observed during $(\mu_{1.5}^{-3} = -1.25")$, see the left photo of Figure 2-236. Here, the largest crack width on the South side of the specimen reached 1.25mm. Crushing on the South side of the specimen did not occur until $(\mu_2^{+1} = 1.68")$, as shown in the right photo of Figure 2-236. The largest crack width on the North side of the specimen measured

1.25mm during ($\mu_2^{+3} = 1.66$"). The extent of crushing on the South side of the specimen increased to 13" above the footing during ($\mu_3^{+3} = 2.49$"), as shown in the right photo of Figure 2-237. On the North side of the specimen, the extent of crushing reached 10 ¾" above the footing during ($\mu_3^{-3} = -2.51$"). The extent of crushing on the South side of the specimen reached 24 ½" above the footing during ($\mu_6^{+1} = 5.01$"). Crushing on the North side of the specimen reached 16 ¼" above the footing at ($\mu_6^{-1} = -5.00$"), as shown in the left photo of Figure 2-238. The first push and pull cycles of ductility six were concluded without visible buckling on either side of the specimen.

South reinforcing bars S2 and S3 visibly buckled on the way to ($\mu_6^{+2} = 5.00$"), as shown in Figure 2-239. Buckling of the two South bars caused a 5.5% loss of strength from the peak load of 68.37 kips measured during ($\mu_6^{+1} = 5.01$"). North reinforcing bars N2 and N3 visibly buckled on the way to ($\mu_6^{-2} = -5.01$"), as shown in Figure 2-240. Buckling of the two North bars caused a 5% loss of strength from the peak load of -68.51 kips, which occurred during ($\mu_6^{-1} = -5.00$"). An additional South reinforcing bar S4 buckled during ($\mu_6^{+3} = 4.99$) and the outward deformation in bars S2 and S3 increased, which lead to a 9.3% loss in strength. North reinforcing bar N4 buckled during ($\mu_6^{-3} = -5.00$") causing a 8.1% loss in strength relative to the peak load in the pull direction. During the first push cycle of ductility eight, an 11.75% loss of strength was observed without additional buckling or rupture of reinforcement. The effect of buckling on confinement loss is highlighted by observed permanent deformation in spiral layers over the North reinforcement when the bar was placed back into tension, see Figure 2-241.

Previously buckled bars S2 and S3 ruptured in tension during ($\mu_8^{-1} = -6.69$"), see Figure 2-242. Rupture of the two South bars lead to a 32.2% total loss in strength, as shown in Figure 2-233 on the force vs. displacement response. During ($\mu_8^{+2} = 6.67$"), South bars S1 and S5 buckled and previously buckled North reinforcing bars N2 and N3 ruptured in tension, as shown in Figure 2-243. This caused a 40.72% total loss of strength in the push direction of loading. During ($\mu_8^{-2} = -6.71$"), North bars N1 and N5 buckled and an additional bar S4 ruptured in tension leading to a 50.1% loss in strength. North bar N4 ruptured during ($\mu_8^{+3} = 6.70$") causing a 55.9% loss in strength. During the final cycle of the load history ($\mu_8^{-3} = -6.66$"), South bar S1 ruptured leading to a total loss in strength of 65.4%. Photos of the specimen after the test was concluded appear in Figure 2-244.

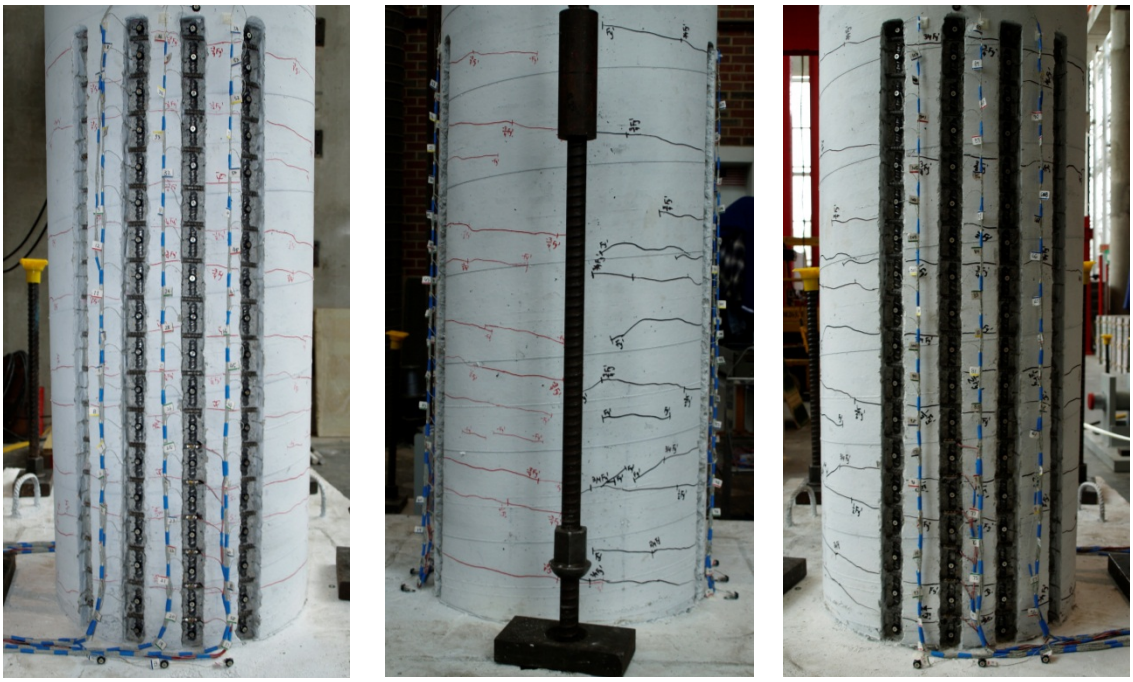

Figure 2-235. Test 15 – Crack Distribution during First Yield Push ($F_y^{'} = 0.62$") and Pull ($-F_y^{'} = -0.63$") Cycles

Figure 2-236. Test 15 – (Left) Crushing on the North Side of the Specimen during ($\mu_{1.5}^{-3} = -1.25$") and (Right) Crushing on the South Side during ($\mu_2^{+1} = 1.68$")

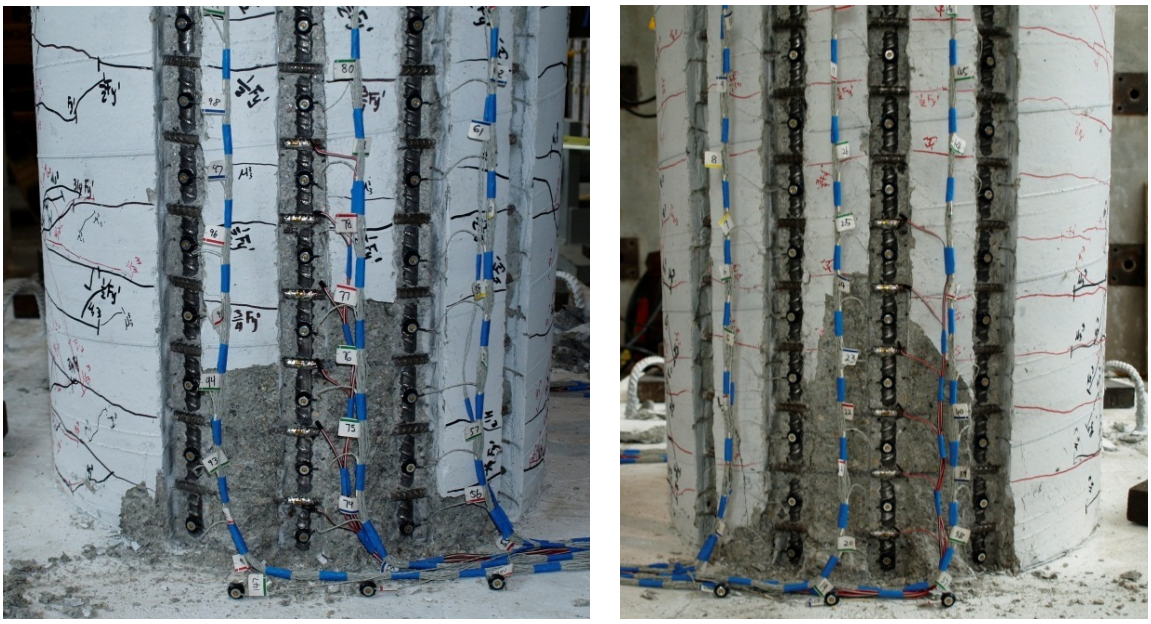

Figure 2-237. Test 15 – (Left) Crushing on the North Side of the Specimen during ($\mu_3^{-3} = -2.51$") and (Left) Crushing on the South Side during ($\mu_3^{+3} = 2.49$")

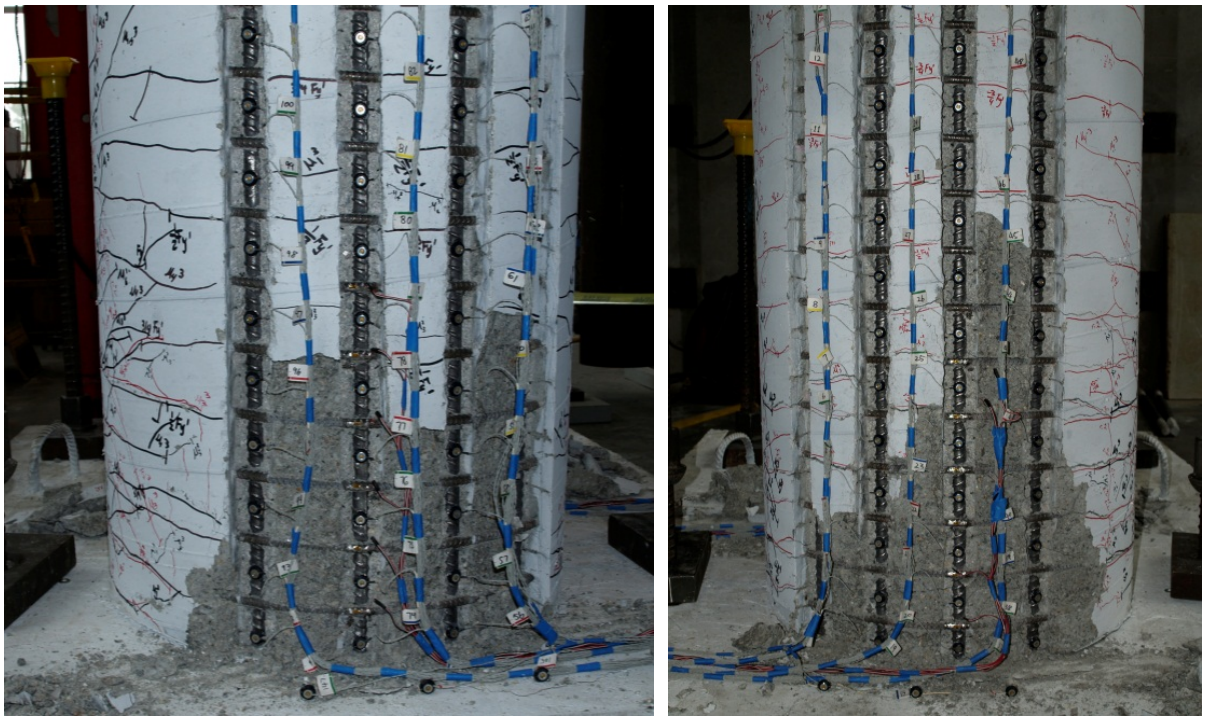

Figure 2-238. Test 15 – (Left) Extent of Crushing on the North Side of the Specimen during ($\mu_6^{-1} = -5.00$") and (Right) Crushing on the South Side during ($\mu_6^{+1} = 5.01$") *(Both Prior to Buckling)*

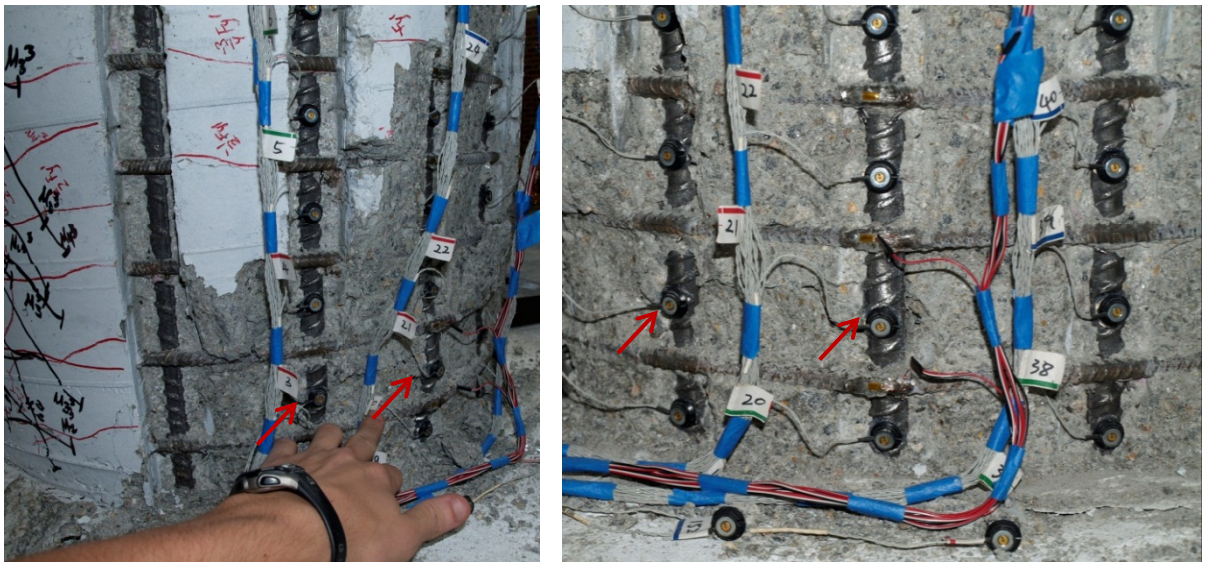

Figure 2-239. Test 15 – Buckling of South Reinforcing Bars S2 and S3 during ($\mu_6^{+2} = 5.00$")

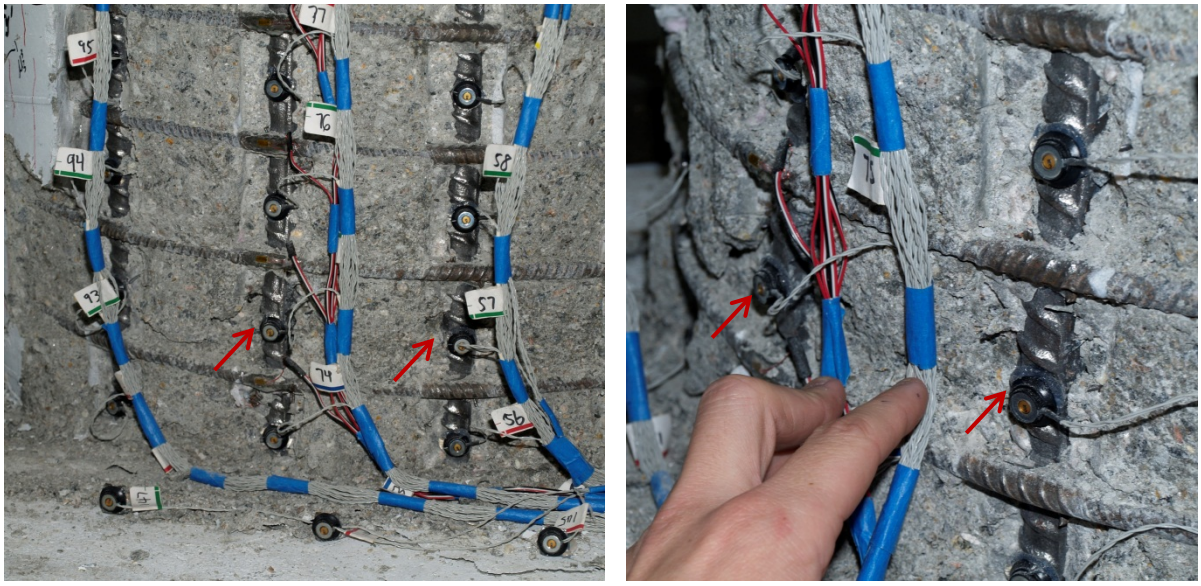

Figure 2-240. Test 15 – Buckling of Bars N2 and N3 during ($\mu_6^{-2} = -5.01$")

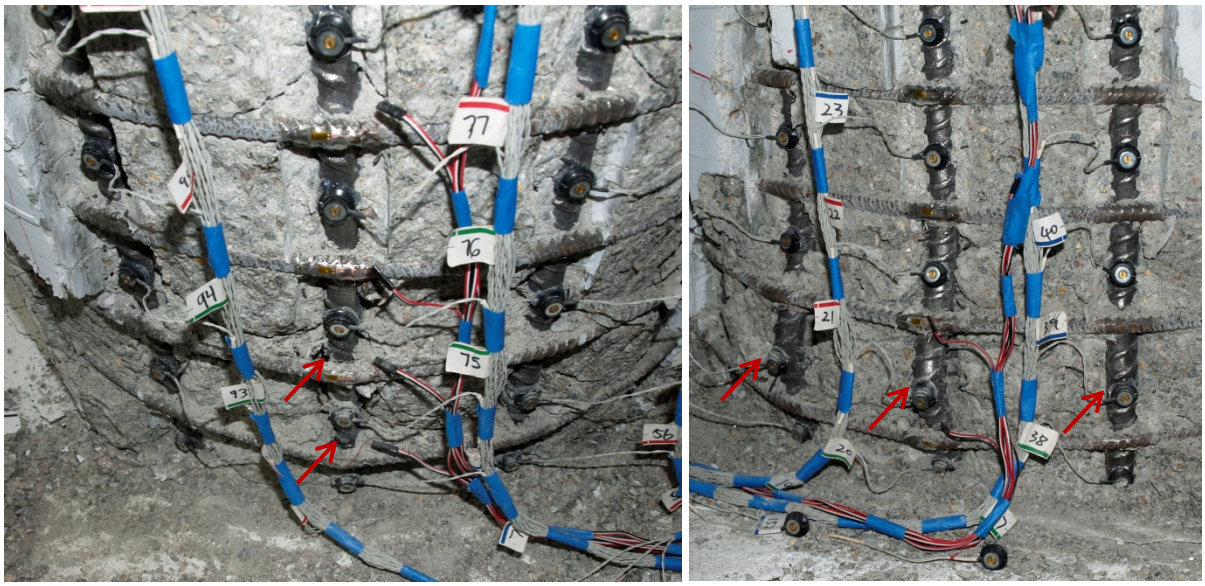

Figure 2-241. Test 15 – (Left) Permanent Deformation in Spiral Layers Overlaying North Buckled Bars during ($\mu_8^{+1} = 6.68$") and (Right) Additional Deformation of Buckled Bars S2, S3, and S4 during ($\mu_8^{+1} = 6.68$")

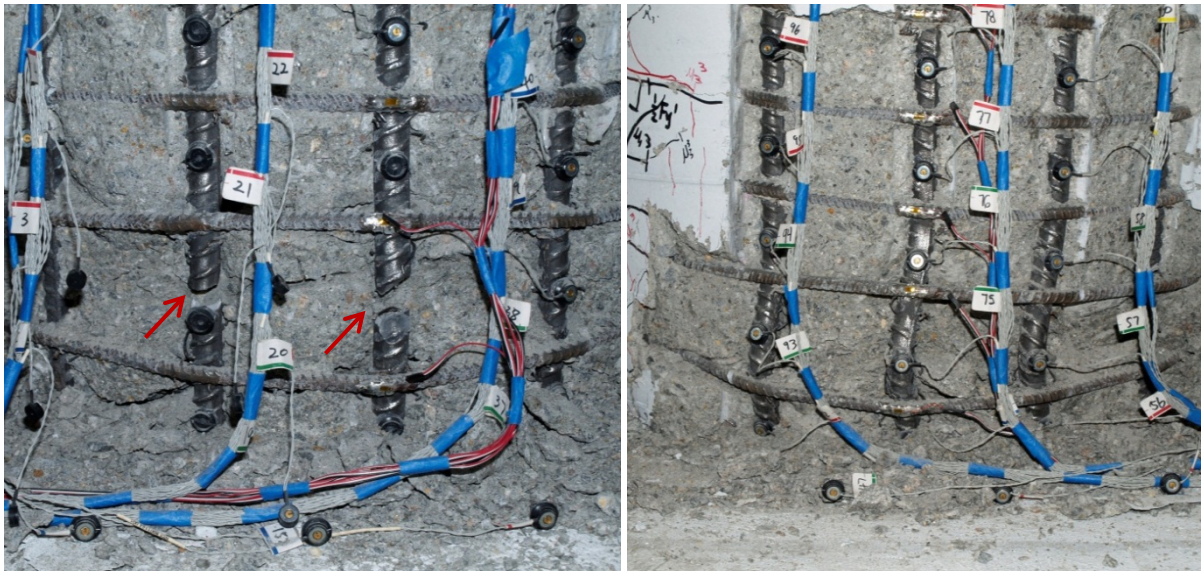

Figure 2-242. Test 15 – (Left) Rupture of Previously Buckled South Bars S2 and S3 during ($\mu_8^{-1} = -6.69$") and (Right) Additional Deformation in North Buckled Bars N2, N3, and N4 during ($\mu_8^{-1} = -6.69$")

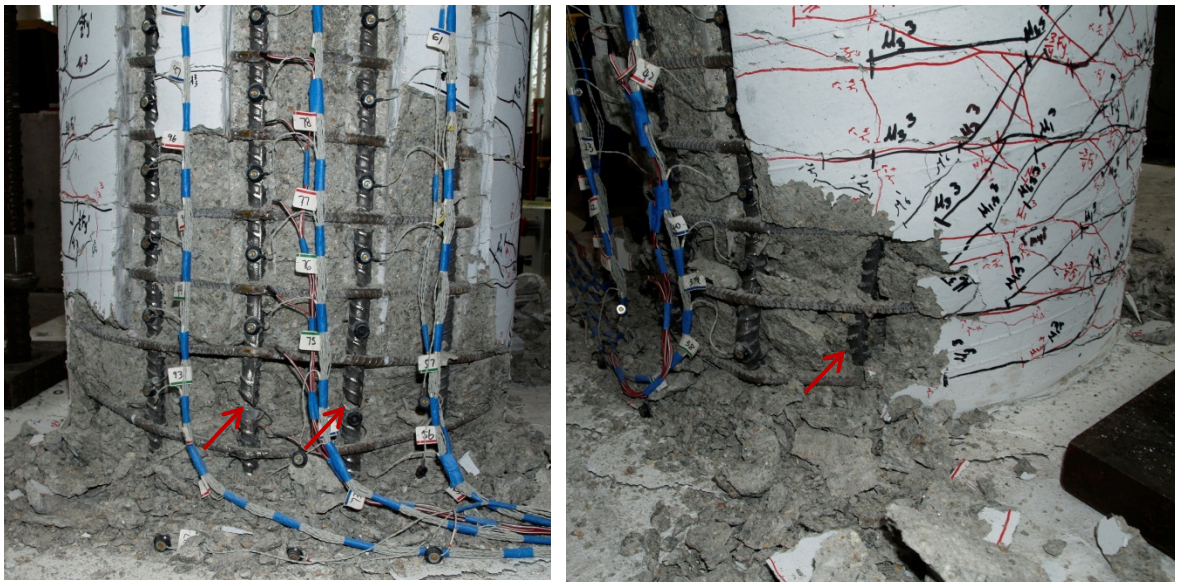

Figure 2-243. Test 15 – (Left) Rupture of Previously Buckled Bars N2 and N3 during ($\mu_8^{+2} = 6.67$") and (Right) Buckling of Bar S1 and S5 during ($\mu_8^{+2} = 6.67$")

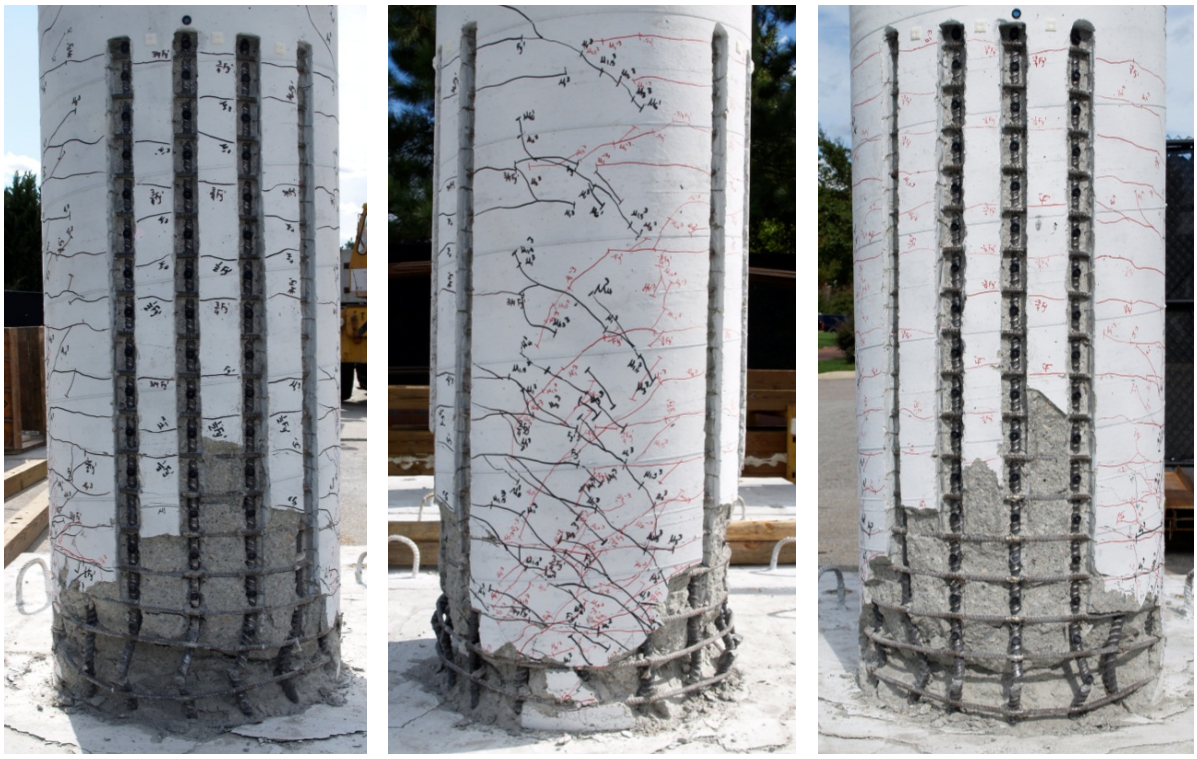

Figure 2-244. Test 15 – After the Test: (Left) North Side of the Specimen, (Middle) Front, and (Right) South

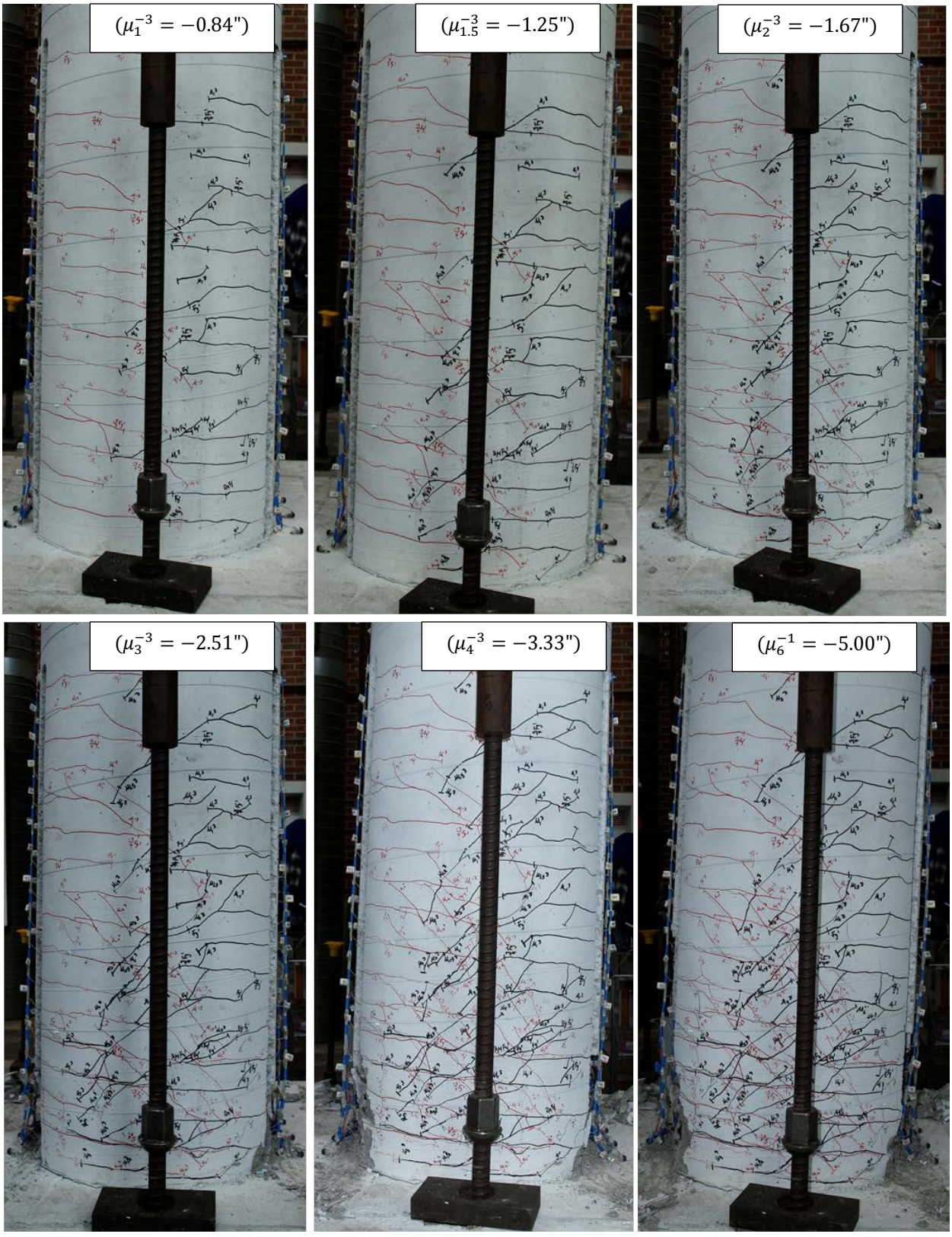

Figure 2-245. Test 15 – Crack Progression on the Back Side of the Specimen

2.2.3.2. Test 15 – Symmetric Three Cycle Set (#3 @ 2.75") Strain Data:

North Reinforcement:

Extreme fiber vertical strain profiles for push and pull cycles appear in Figure 2-246 and Figure 2-247 respectively. As the hinge rotates about inclined flexural shear cracks, compressive strains are clumped at the base and tensile strains are fanned out to a greater height following the crack distribution. Near the footing cracks remain effectively horizontal, but above the base section flexural shear cracks are inclined as shown in Figure 2-245. The effects of tension shift increase as the cracks become more inclined at higher ductility levels. A peak tensile strain of 0.0372 was measured 2.31" above the footing for bar N3 during ($\mu_6^{+1} = 5.01$"). Bar N3 did not buckle until reversal from ($\mu_6^{+2} = 5.00$"), when the peak tensile strain was 0.0365. The relationship between tensile strain and displacement for this gage length appears in Figure 2-250. The solid line contains data during the push cycle loading up to the peak displacement and the dashed line represents the subsequent reversal of load. Similar to previous tests, the moment curvature prediction for the relationship between strain and displacement begins to over predict the tensile strains at higher displacements at an increasing rate. The largest compressive strain of -0.0199, located 7.89" above the footing, was measured during ($\mu_6^{-1} = -5.00$"). The peak compressive strain of -0.0199 in bar N3 is 54.3% larger than the original Mander ultimate concrete compressive strain of -0.0129. The relationship between compressive strain and displacement for bar N3, gage length centered 2.31" above the footing, during pull cycles appears in Figure 2-253. Here the measured compressive strains are slightly larger than the moment curvature prediction, but the overall trend is captured. At the section 7.89" above the footing, the relationship between strain and displacement does not match as well at higher ductility levels.

The strain hysteresis for the largest tensile gage length, 2.31" above the footing, on extreme fiber bar N3 is shown in Figure 2-254 with an elapsed time color bar to track the progression of the test. The strain hysteresis is plotted through ($\mu_6^{-2} = -5.01$") when the bar visibly buckled. After reversal from ($\mu_6^{+2} = 5.00$"), the relationship between strain and displacement begins to break away from the trend at around zero displacement. This gage length is centered over a layer of transverse steel where the largest crack was located. Since the outward buckled deformation of bar N3 occurred between layers of transverse steel, this particular gage length just below the outward buckled region shortens with increased deformation. To illustrate this point, the strain hysteresis over the outward buckled region of bar N3, located 5.11" above the footing, appears in Figure 2-255. The transverse steel strain gage hysteresis for a spiral layer restraining buckled bar N3 is shown in Figure 2-256. In all three graphs, buckling looks like it occurred between 0-2" of displacement after reversal from ($\mu_6^{+2} = 5.00$"). Here the gage length over the outward buckled region begins to rapidly elongate and the transverse steel restraint tensile strain sharply increases. The transverse steel restraint on the North side of the specimen went into the inelastic range during ($\mu_6^{-1} = -5.00$"), as shown in Figure 2-249. Even though the transverse steel was inelastic during this cycle, visibly buckling was not observed. The strain hysteresis for bar N3, located 5.11" above the footing, in Figure 2-255 shows that some measurable deformation occurred during ($\mu_6^{-1} = -5.00$"). The curve which represents the reversal from μ_6^{+1} to μ_6^{-1} breaks away from the trend set by previous cycles.

South Reinforcement:

A peak tensile strain of 0.0347 was measured 4.64" above the footing on bar S3 during ($\mu_6^{-1} = -5.00$"). When the loading of the specimen was paused at μ_6^{-1}, debris was removed and the peak tensile strain over the base gage length measured 0.0378. The relationship between tensile strain and displacement for bar S3 is shown in Figure 2-252 for the gage length located 4.64" above the footing.

A peak compression strain of -0.0233 was measured 7.47” above the footing on bar S3 during ($\mu_6^{+1} = 5.01"$). The peak value is 80.6% larger than the original Mander (1988) ultimate concrete compressive strain of -0.0129. The relationship between compressive strain and displacement for the gage length 2.03” above the footing on bar S3 during push cycles appears in Figure 2-251. This gage length represents the base section where a peak compression strain of -0.0115 was measured during ($\mu_6^{+1} = 5.01"$). The measured strains match the moment curvature prediction well throughout the entire range of displacements.

The strain hysteresis for the gage length overlaying the outward buckled region of bar S3, 4.64” above the footing, appears in Figure 2-257. After reversal from a peak tensile strain of 0.0378 at ($\mu_6^{-1} = -5.00"$), the relationship between strain and displacement begins to break from the trend around -3” which agrees with visible buckling observations. The transverse steel strain gage hysteresis for a spiral layer restraining the top portion of the outward buckled region is shown in Figure 2-258. The strain hysteresis for the spiral layer restraining the lower portion of the outward buckled region appears in Figure 2-259. The second spiral layer above the footing was inelastic by the time the specimen reached ($\mu_6^{+1} = 5.01"$), see Figure 2-248. The South reinforcing bars S2 and S3 buckled during the push cycle to ($\mu_6^{+2} = 5.00"$). The measured strain in the upper spiral layer continued to rapidly increase while the lower spiral layer entered the inelastic range for the first time. The data suggests that buckling of bar S3 began at around -3”.

2.2.3.3. Test 15 – Symmetric Three Cycle Set (#3 @ 2.75”) Curvature and Strain Penetration Data:

Vertical curvature profiles are plotted for push and pull cycles as shown in Figure 2-260 and Figure 2-261 respectively. These figures show that plastic curvatures have a linear distribution at higher displacement ductility levels. As the displacements increase, the base curvatures become larger and the extent of plastic curvatures reach higher above the footing. The effects of strain penetration of longitudinal reinforcement into the footing can be measured with the LEDs placed closest to the footing-column interface. The slip hysteresis for the North and South extreme fiber bars appear in Figure 2-262 and Figure 2-263. The base rotation attributable to strain penetration is obtained by looking at the measured slip of all six instrumented bars, as shown in Figure 2-264 and Figure 2-265 for push and pull respectively. The base rotation is equal to the slop of the least squared error line connecting the measured values. The top column displacement can be determined using the Optotrak system by integrating the measured curvatures, extrapolating the base rotation to the center of loading, and assuming an elastic distribution of curvature above the instrumented region. A comparison of the measured top column displacements and the Optotrak integrated displacements appears in Figure 2-266. The two methods agree well throughout the entire test.

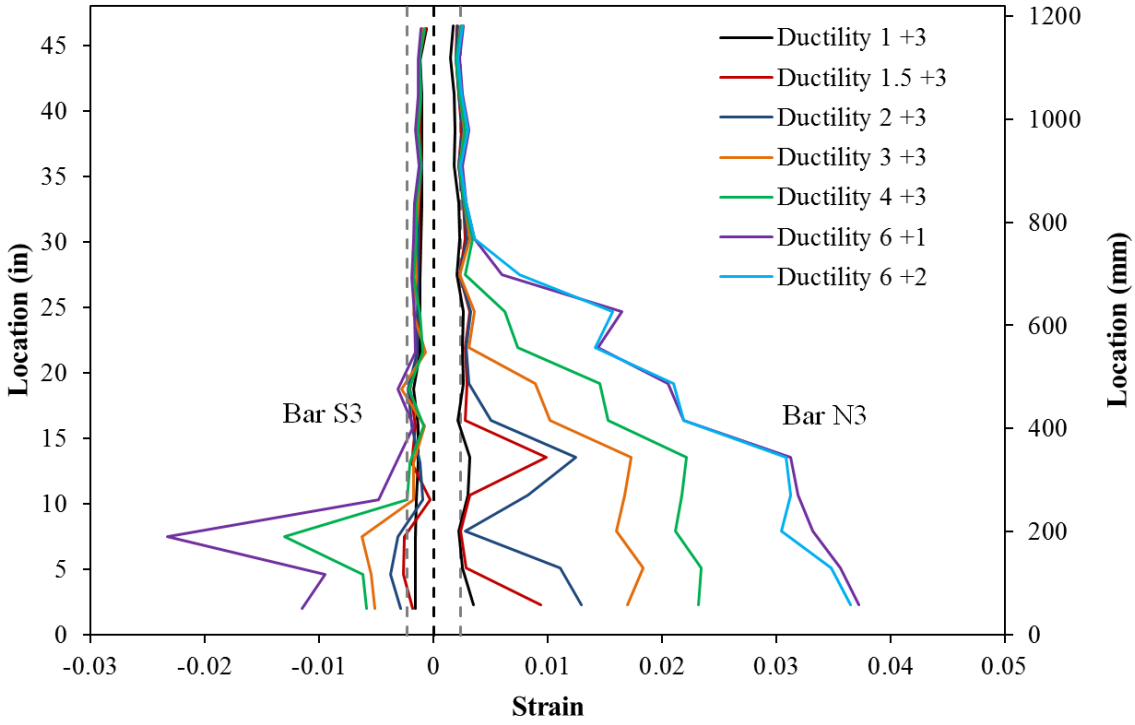

Figure 2-246. Test 15 – Extreme Fiber Vertical Strain Profiles during Push Cycles

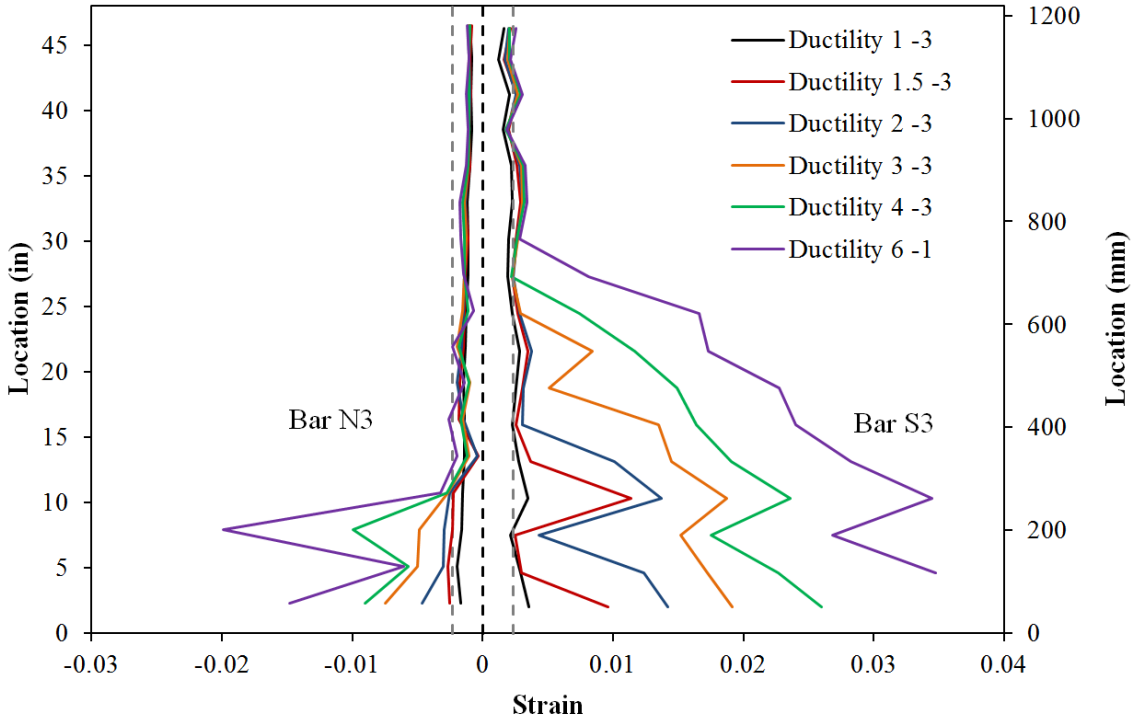

Figure 2-247. Test 15 – Extreme Fiber Vertical Strain Profiles during Pull Cycles

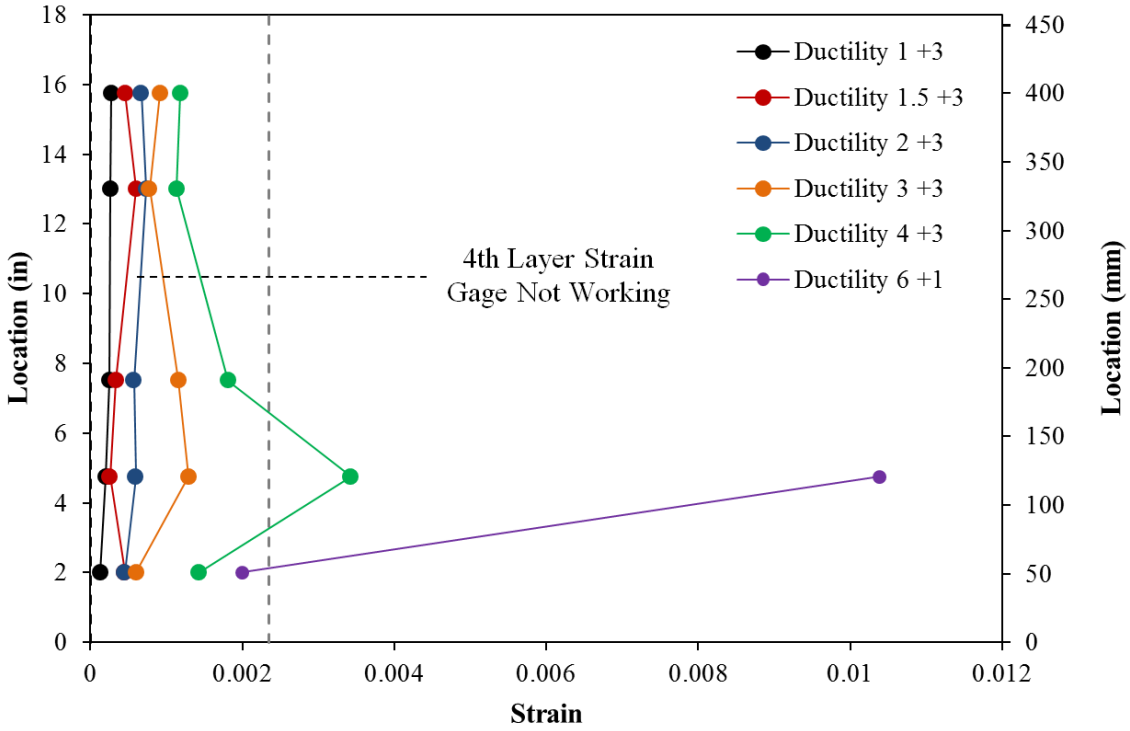

Figure 2-248. Test 15 – Transverse Steel Strains on the South Side of the Specimen during Push Cycles

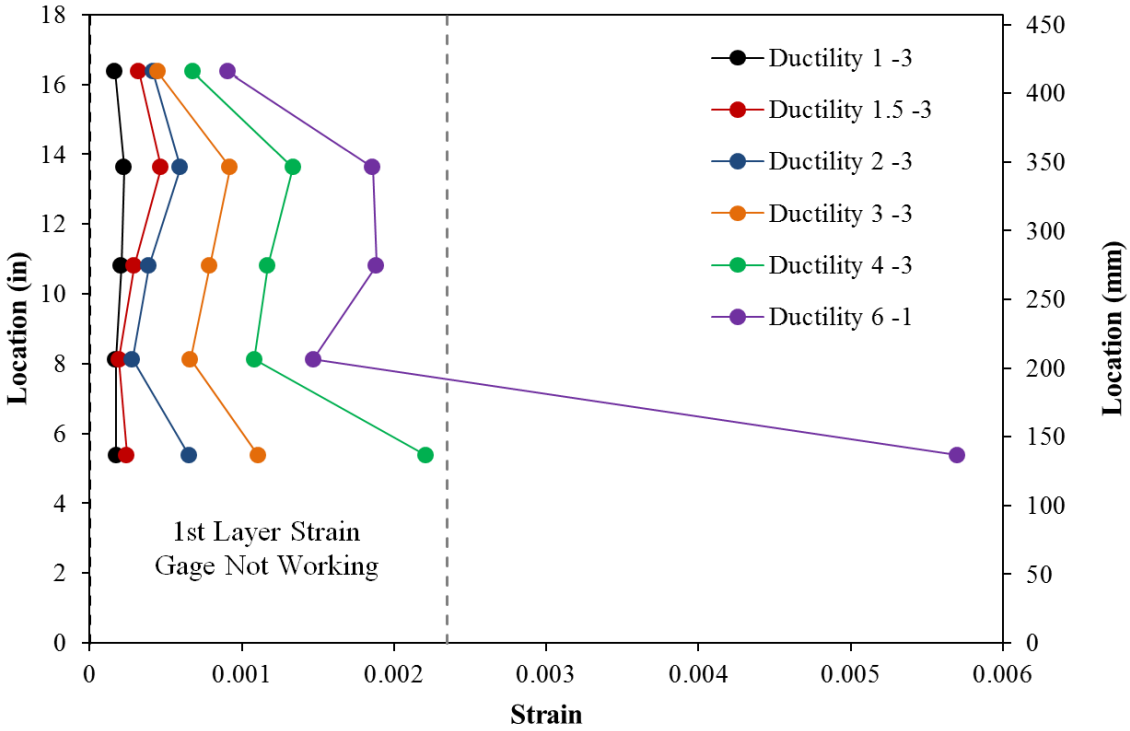

Figure 2-249. Test 15 – North Spiral Strains during Pull Cycles

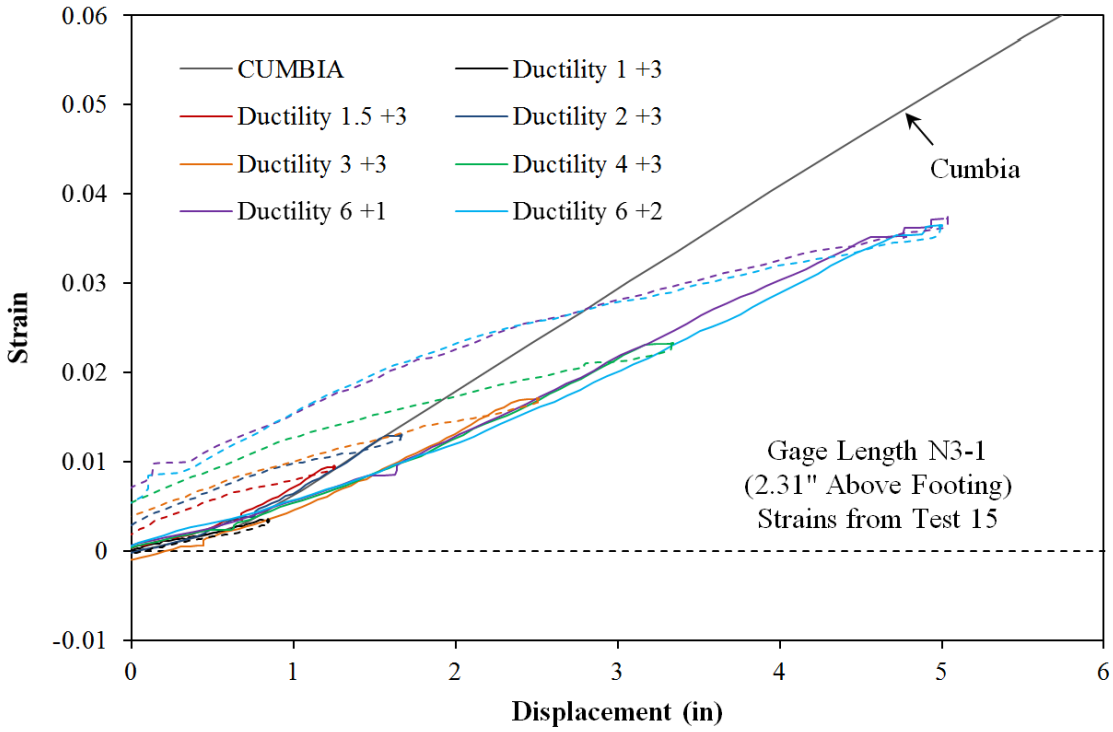

Figure 2-250. Test 15 – Tensile Strain and Displacement for Bar N3 during Push Cycles

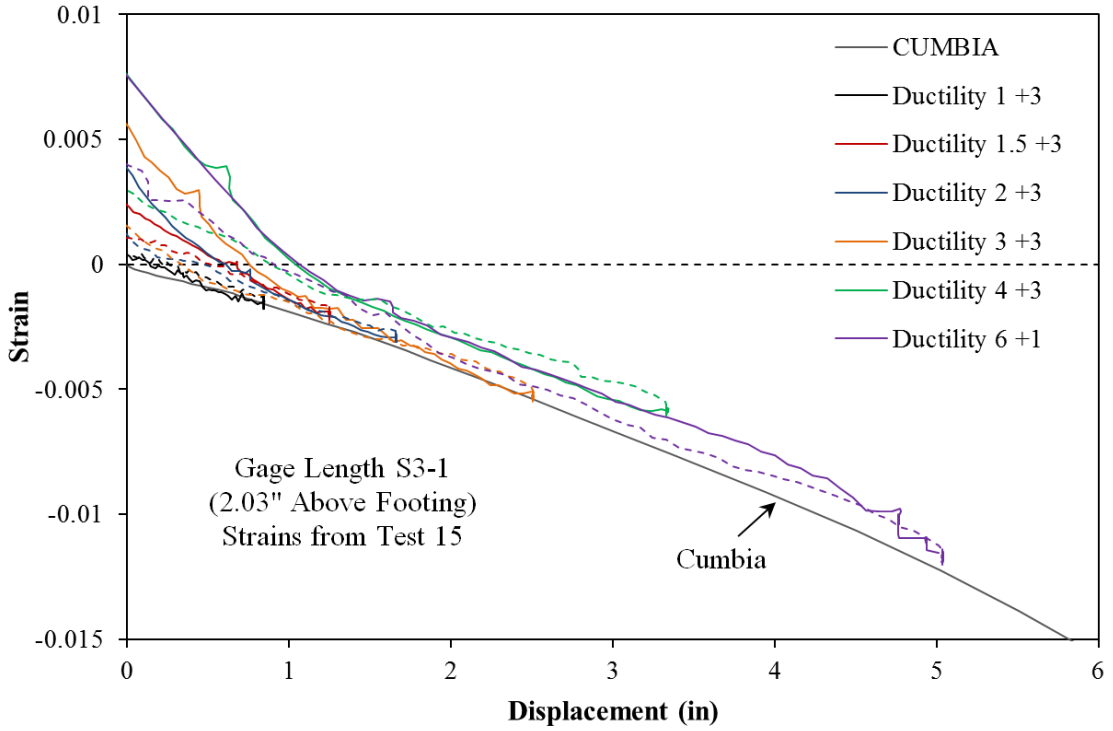

Figure 2-251. Test 15 – Compressive Strain and Displacement for Bar S3 during Push Cycles

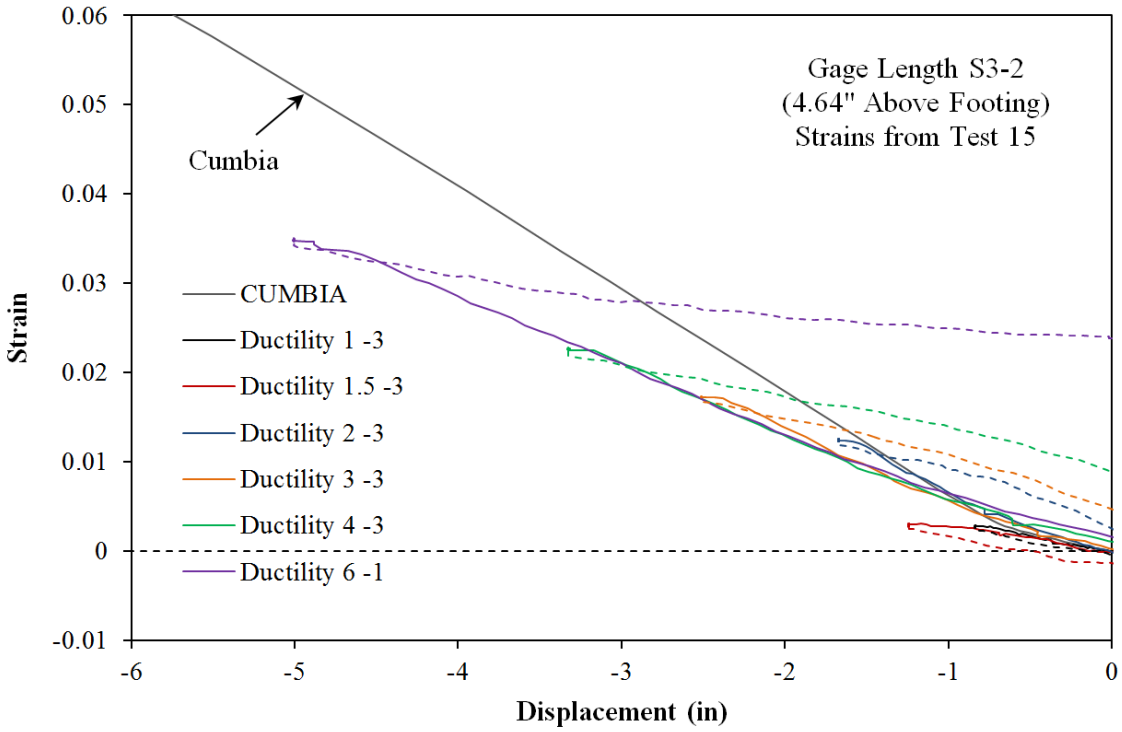

Figure 2-252. Test 15 – Tensile Strain and Displacement for Bar S3 during Pull Cycles

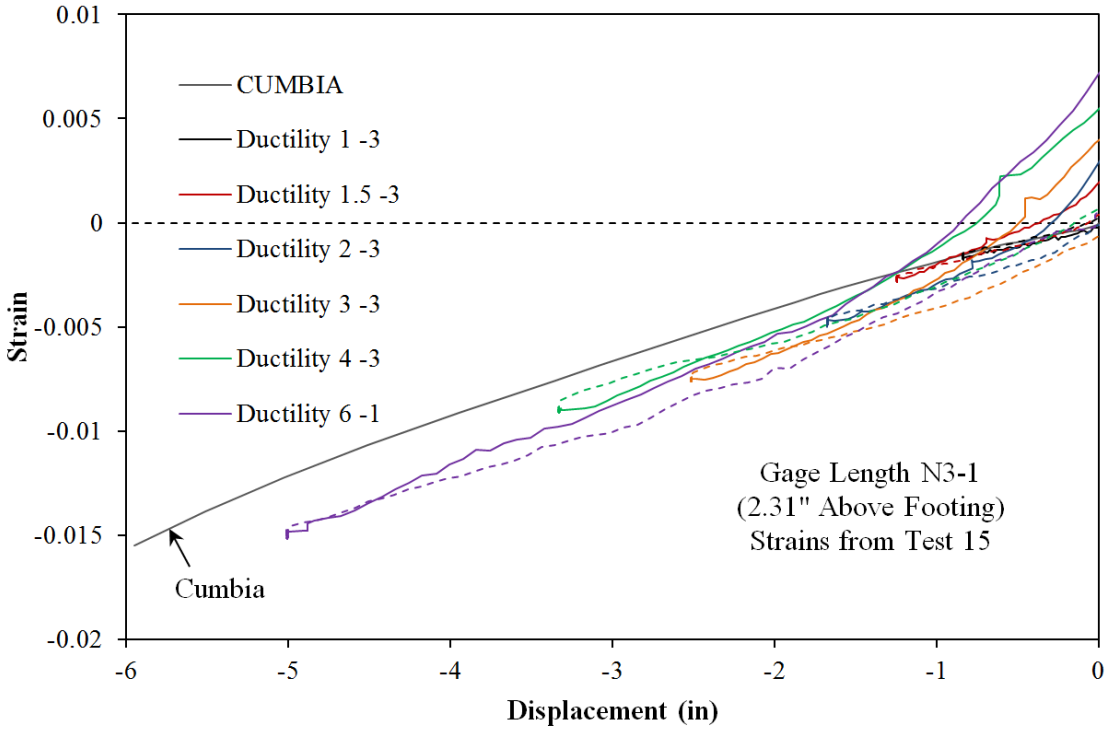

Figure 2-253. Test 15 – Tensile Strain and Displacement for Bar N3 during Pull Cycles

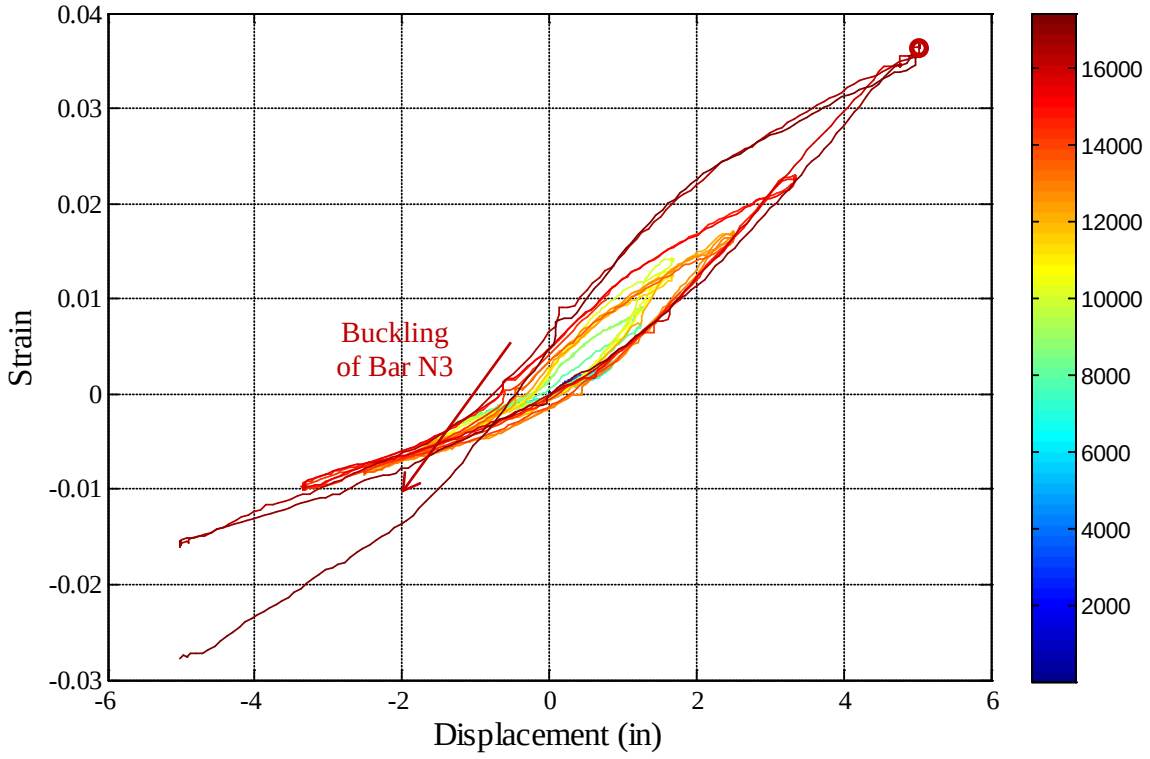

Figure 2-254. Test 15 – Strain Hysteresis over the Buckled Region of Bar N3 (2.31" Above the Footing)

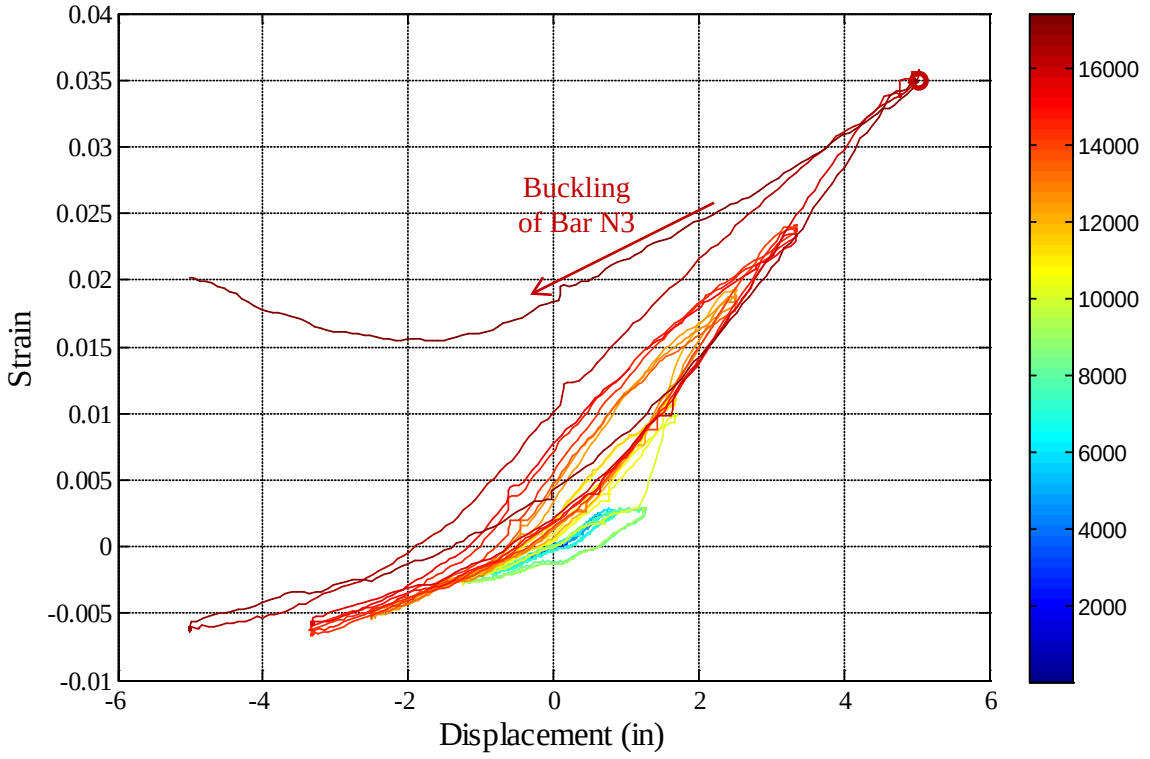

Figure 2-255. Test 15 – Bar N3 Strain Hysteresis (5.11" Above the Footing)

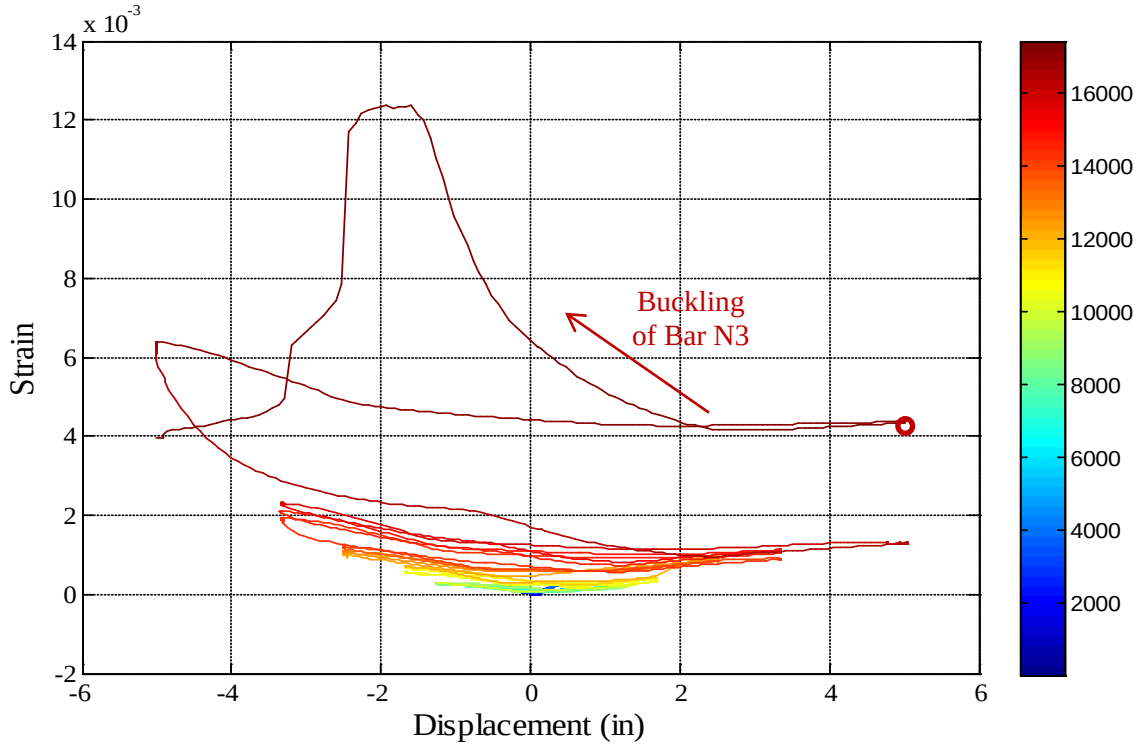

Figure 2-256. Test 15 – Transverse Steel Strain Hysteresis over the Buckled Region of Bar N3

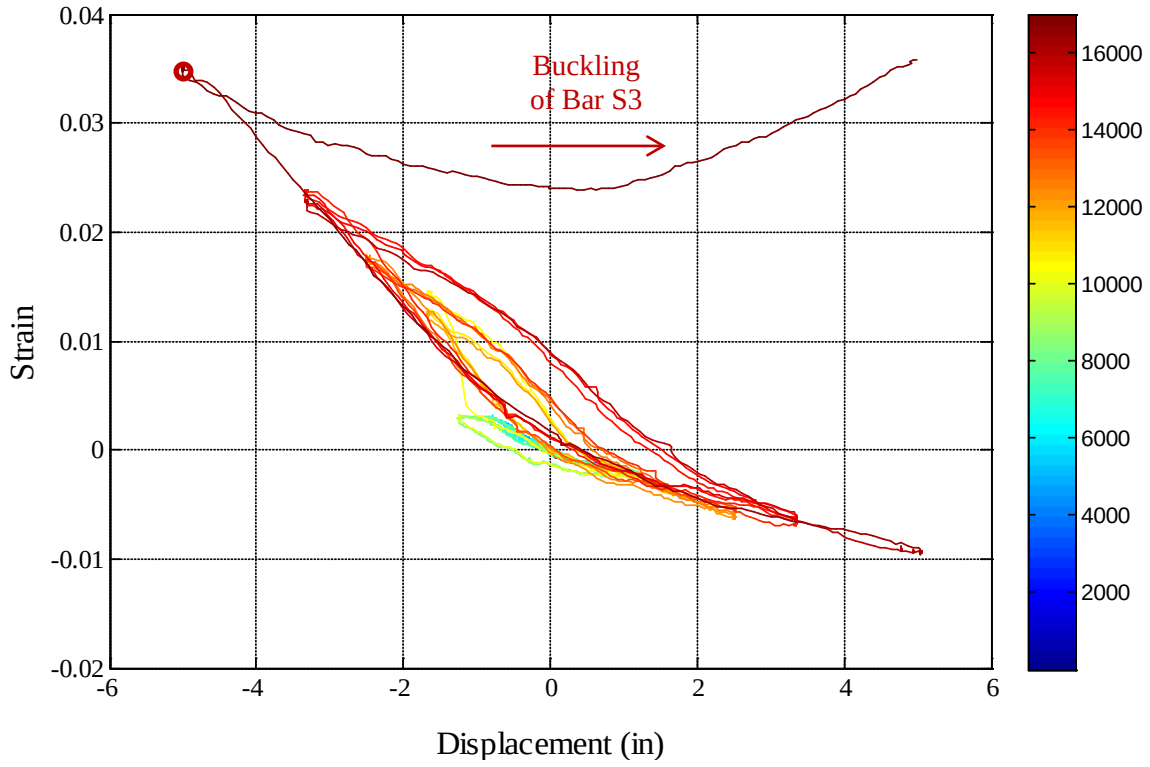

Figure 2-257. Test 15 – Strain Hysteresis over the Buckled Region of Bar S3 (4.64" Above the Footing)

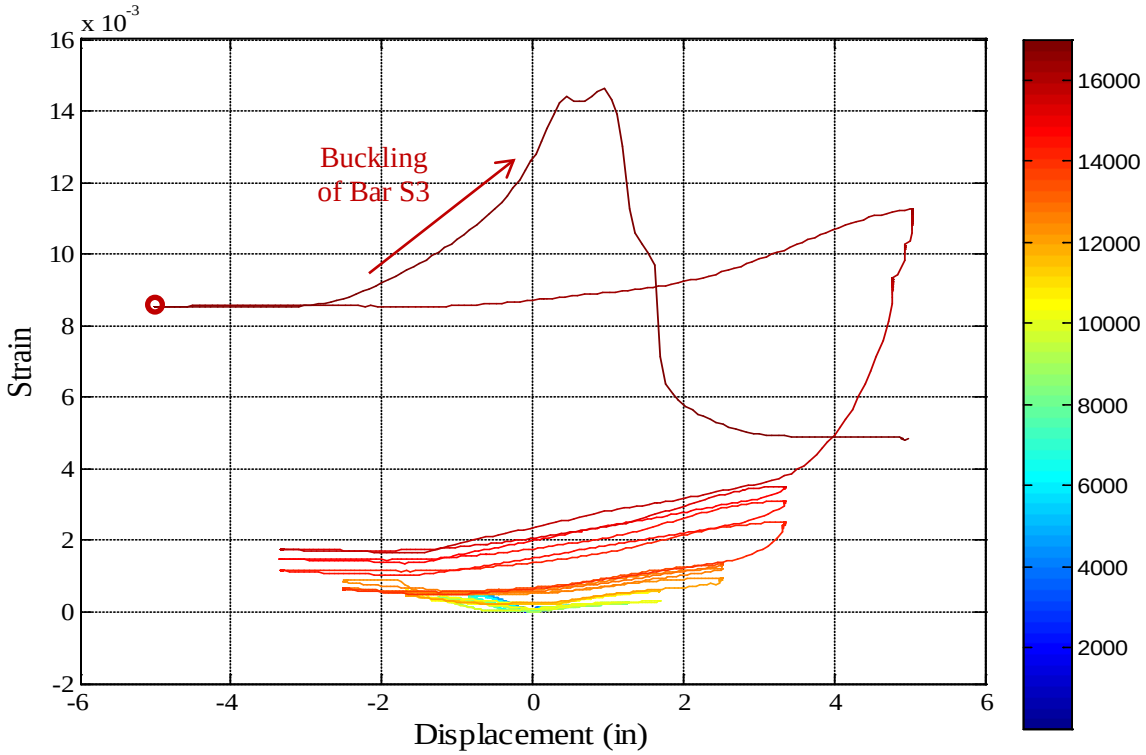

Figure 2-258. Test 15 – Transverse Steel Strain Gage Hysteresis over the Buckled Region of Bar S3 (2nd Layer above the Footing)

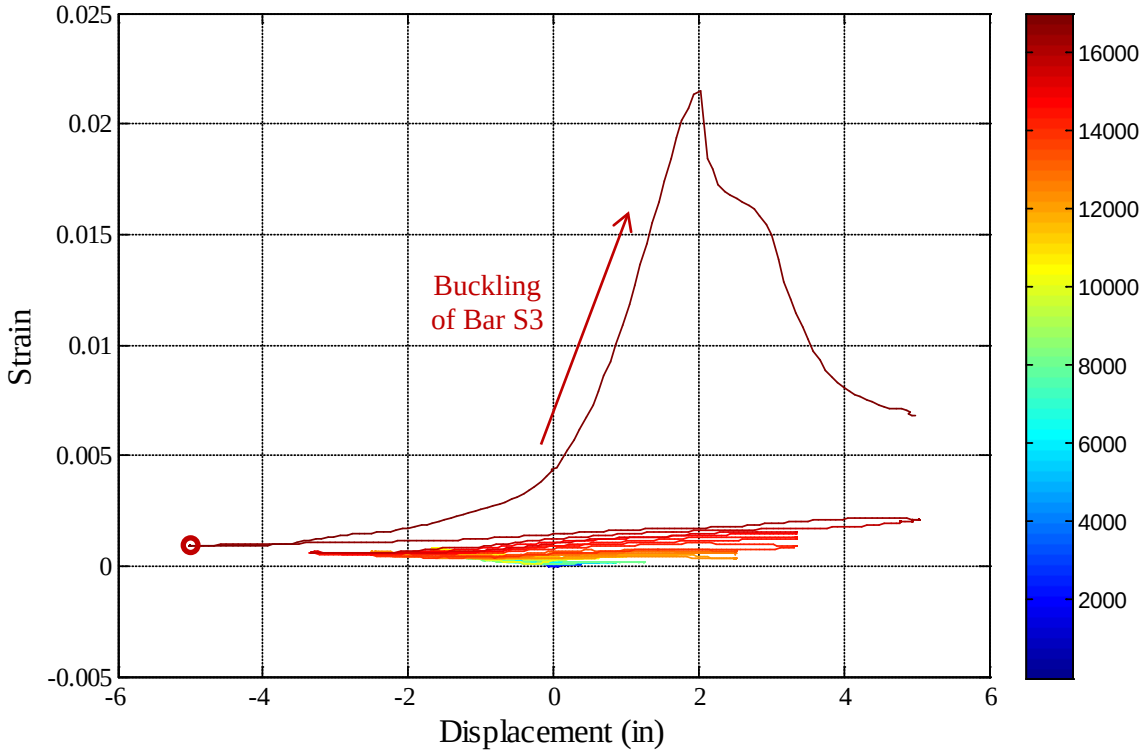

Figure 2-259. Test 15 – South Side Transverse Steel Hysteresis (1st Layer Above)

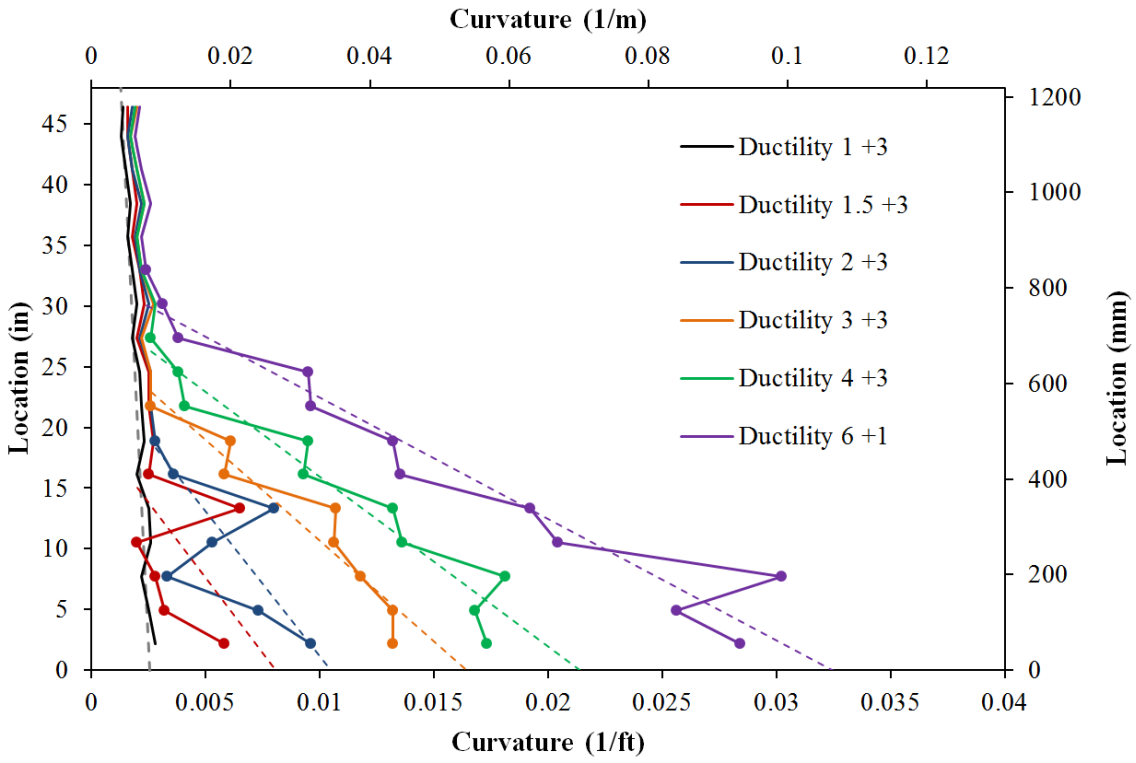

Figure 2-260. Test 15 – Vertical Curvature Profiles during Push Cycles

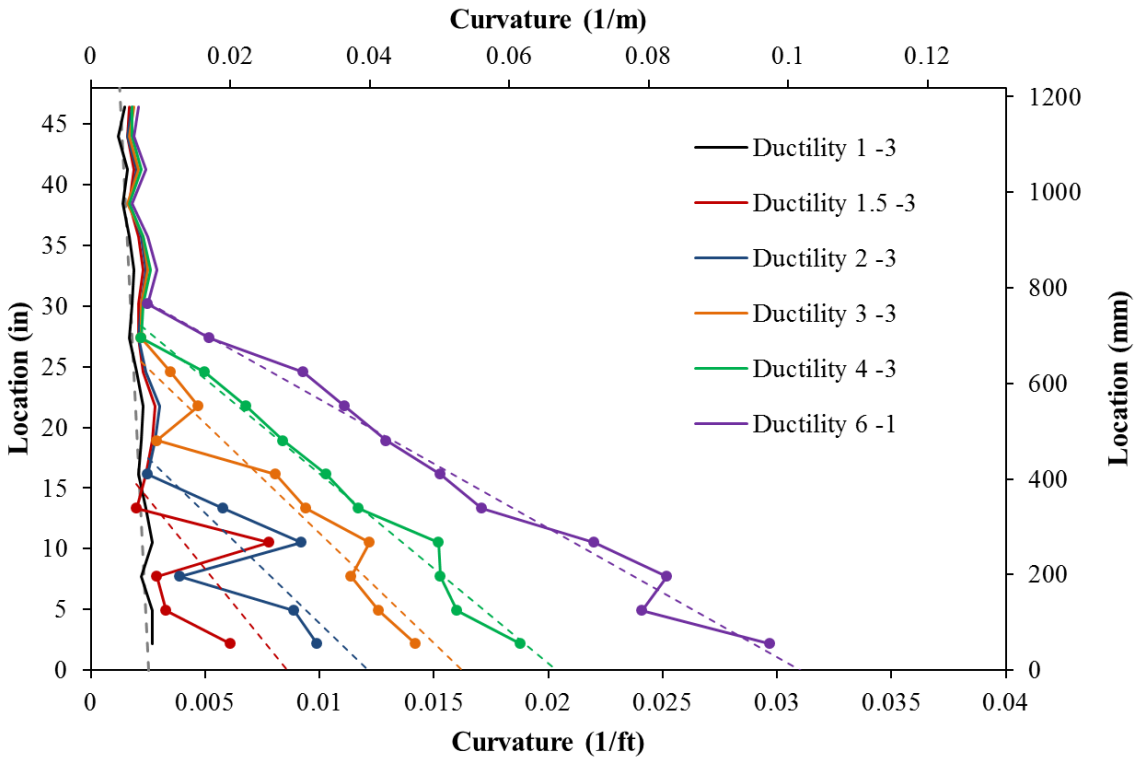

Figure 2-261. Test 15 – Vertical Curvature Profiles during Pull Cycles

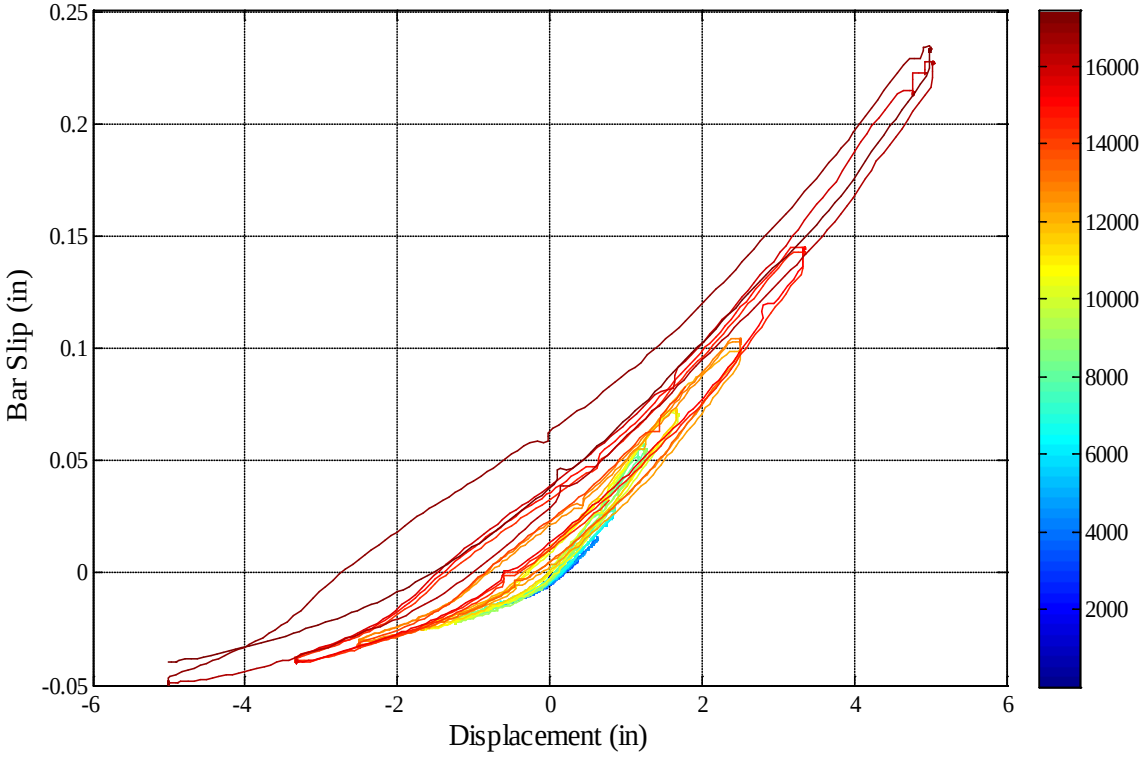

Figure 2-262. Test 15 – Bar N3 Base Section Slip Hysteresis due to Strain Penetration

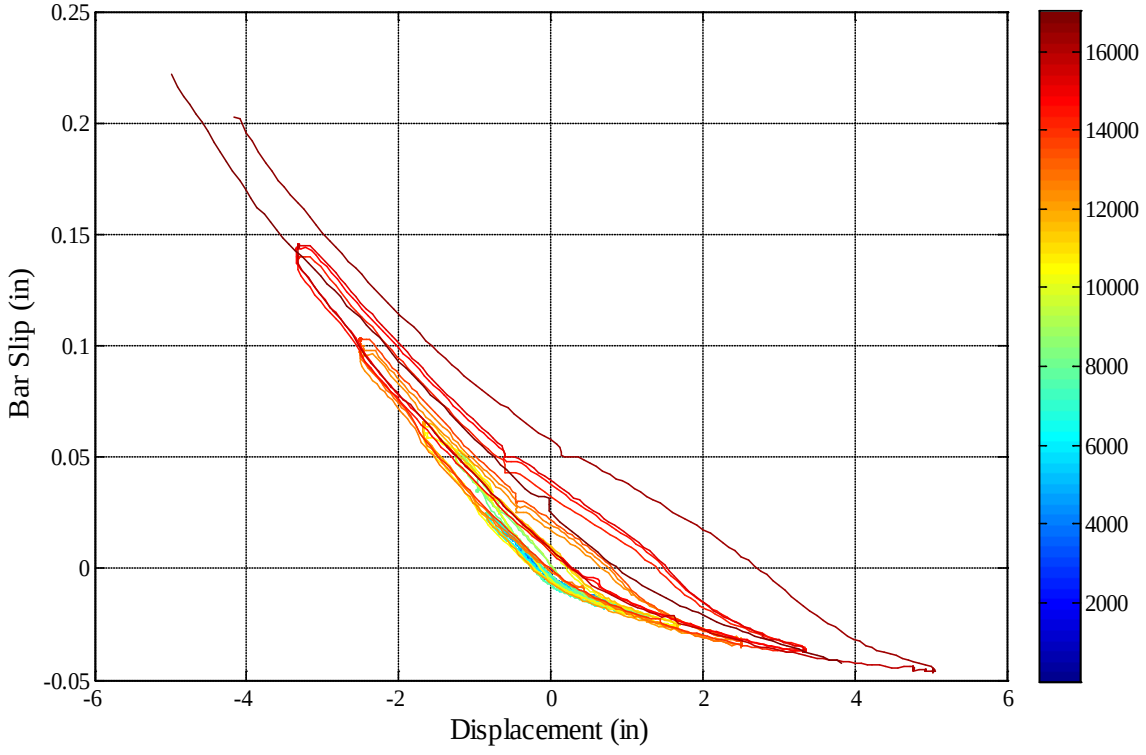

Figure 2-263. Test 15 – Bar S3 Slip Hysteresis due to Strain Penetration

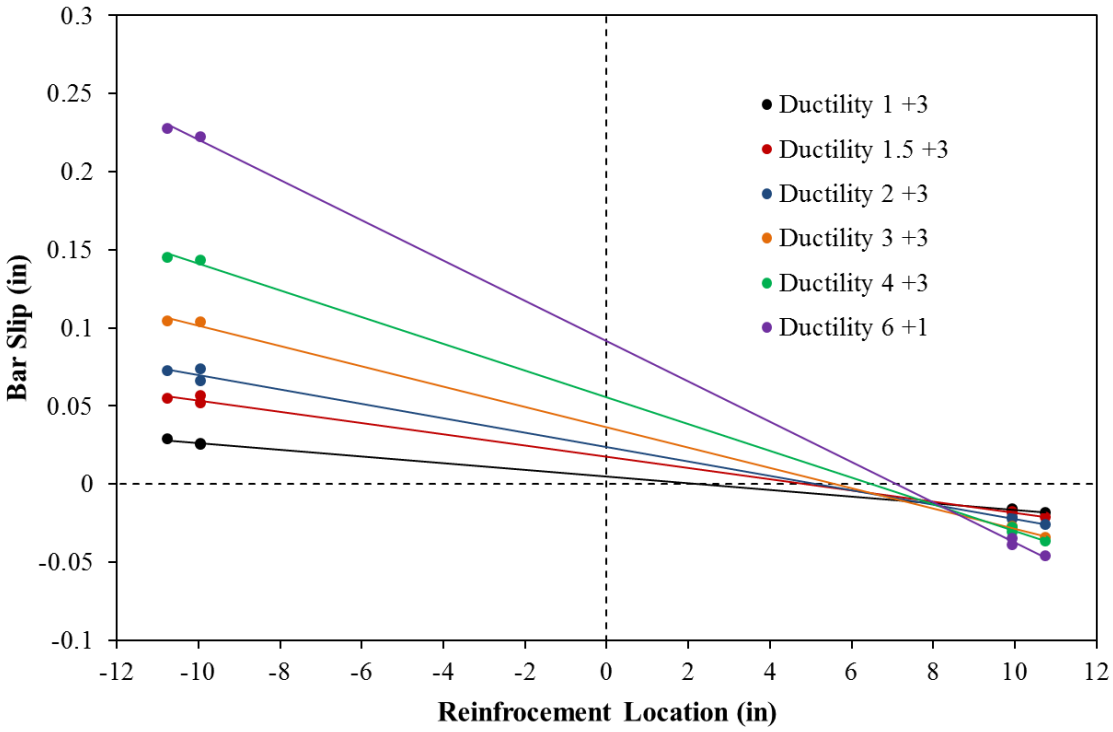

Figure 2-264. Test 15 - Base Rotation due to Strain Penetration during Push Cycles

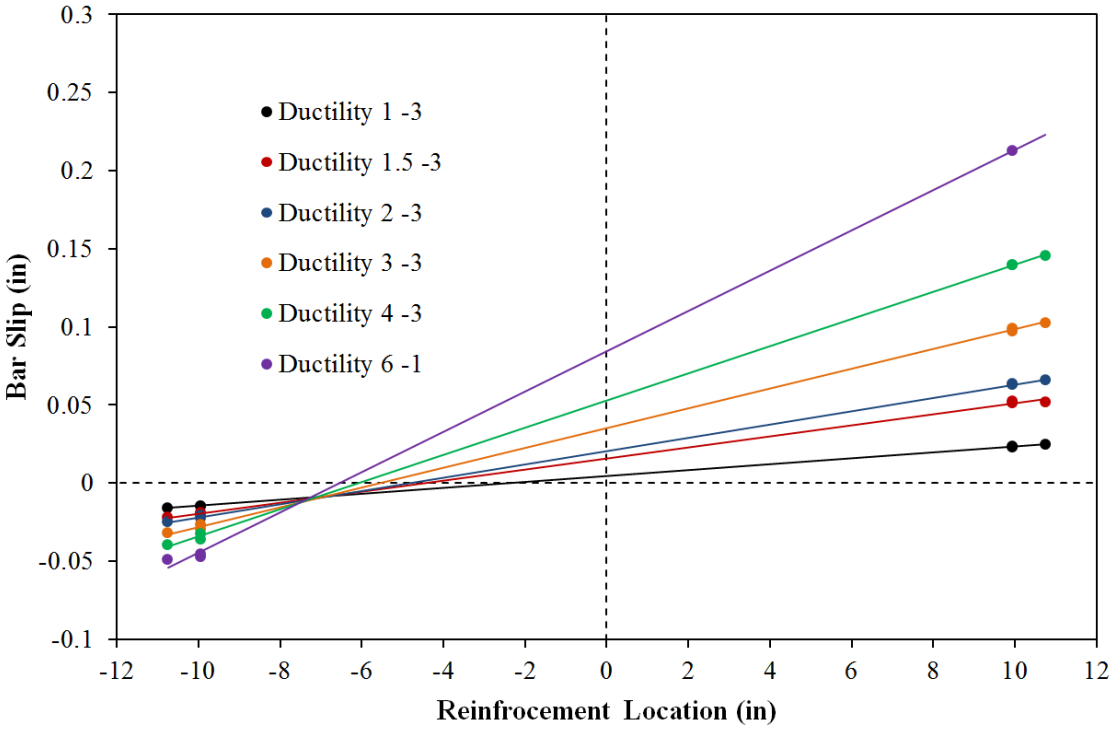

Figure 2-265. Test 15 – Base Rotation due to Strain Penetration during Pull Cycles

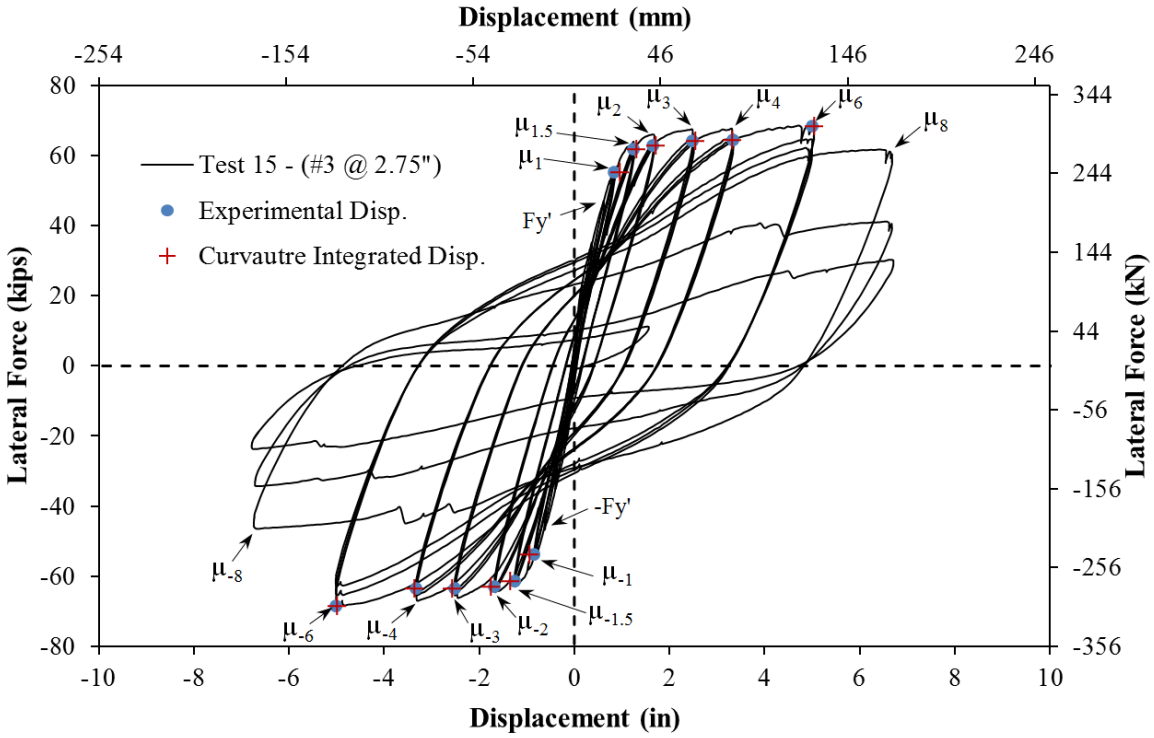

Figure 2-266. Test 15 – Comparison of Measured and Optotrak Integrated Top Column Displacements

2.2.4.Test 16 – Symmetric Three Cycle Set Load History (#3 Spiral at 1.5" Spacing)

Table 2-15. Results Summary for Test 16 – Symmetric Three Cycle Set Load History

LOAD HISTORY: Symmetric Three Cycle Set Load History

VALUES OF INTEREST:

Transverse Steel Detailing:	#3 Spiral at 1.5" Spacing (1.3%)
Concrete Compressive Strength:	$f_c' = 6711psi$
Axial Load:	$P = 170kips$
Analytical First Yield Force:	$F_y' = 46.8kips$
Experimental First Yield Displacement:	$\Delta_y' = 0.62"$
Analytical Nominal Moment Capacity:	$M_n = 503.2kip * ft$
Equivalent Yield Displacement:	$\Delta_y = 0.83"$
Maximum Lateral Force:	$70.7kips$
Failure Mode:	Fracture of Previously Buckled Reinforcement

DAMAGE OBSERVATIONS: (Drift %) [Displacement Ductility, μ_Δ]

First Cracking North:	$1/2Fy' = 0.17"$
First Cracking South:	$-1/2Fy' = -0.19"$
Cover Concrete Crushing North:	$\mu_2^{-3} = -1.65"$
Cover Concrete Crushing South:	$\mu_2^{+1} = 1.66"$
Transverse Steel Yield North:	At $-4.98"$ during pull to $\mu_6^{-1} = -4.98"$
Transverse Steel Yield South:	At 3.80" during push to $\mu_6^{+1} = 4.99"$
Longitudinal Bar Buckling North:	Reversal from $\mu_6^{+2} = 5.00"$
Longitudinal Bar Buckling South:	Reversal from $\mu_6^{-1} = -4.98"$
Longitudinal Bar Fracture North:	At 3.68" during push to $\mu_{10}^{+2} = 8.32"$
Longitudinal Bar Fracture South:	At $-2.64"$ during pull to $\mu_{10}^{-1} = -8.34"$

*$\mu_{10}^{-1} = -8.34"$ represents the first pull cycle of displacement ductility ten which reached a peak displacement of -8.34 inches

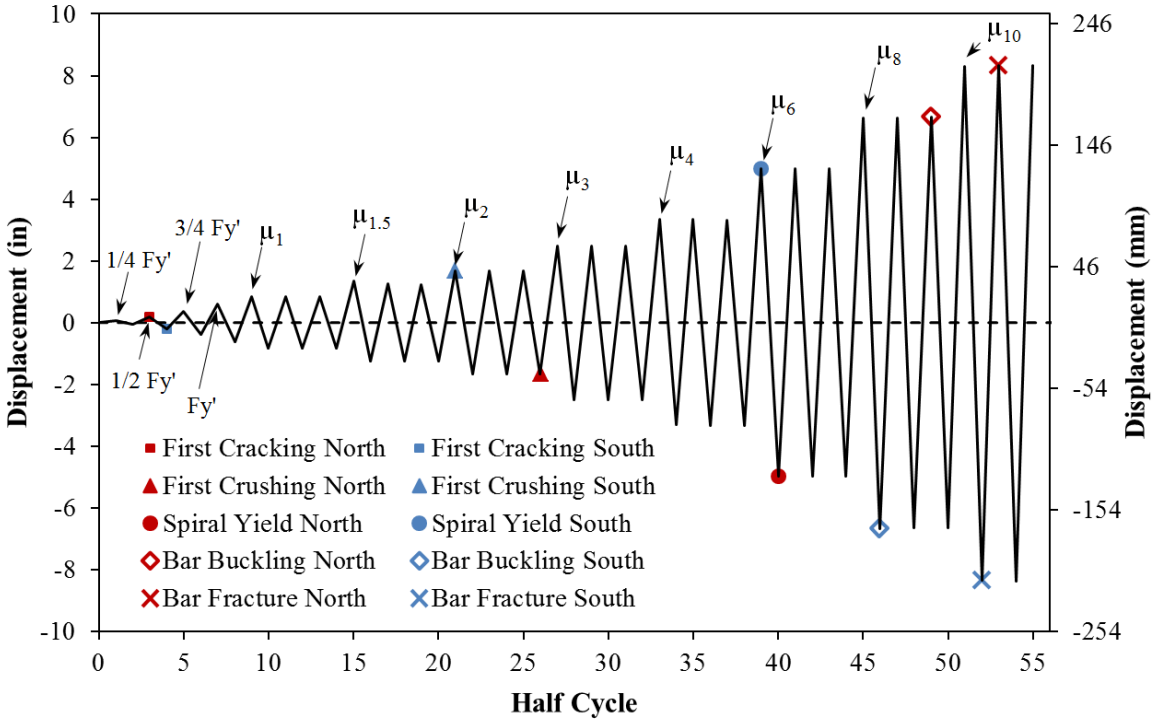

Figure 2-267. Test 16 – Symmetric Three Cycle Set Load History

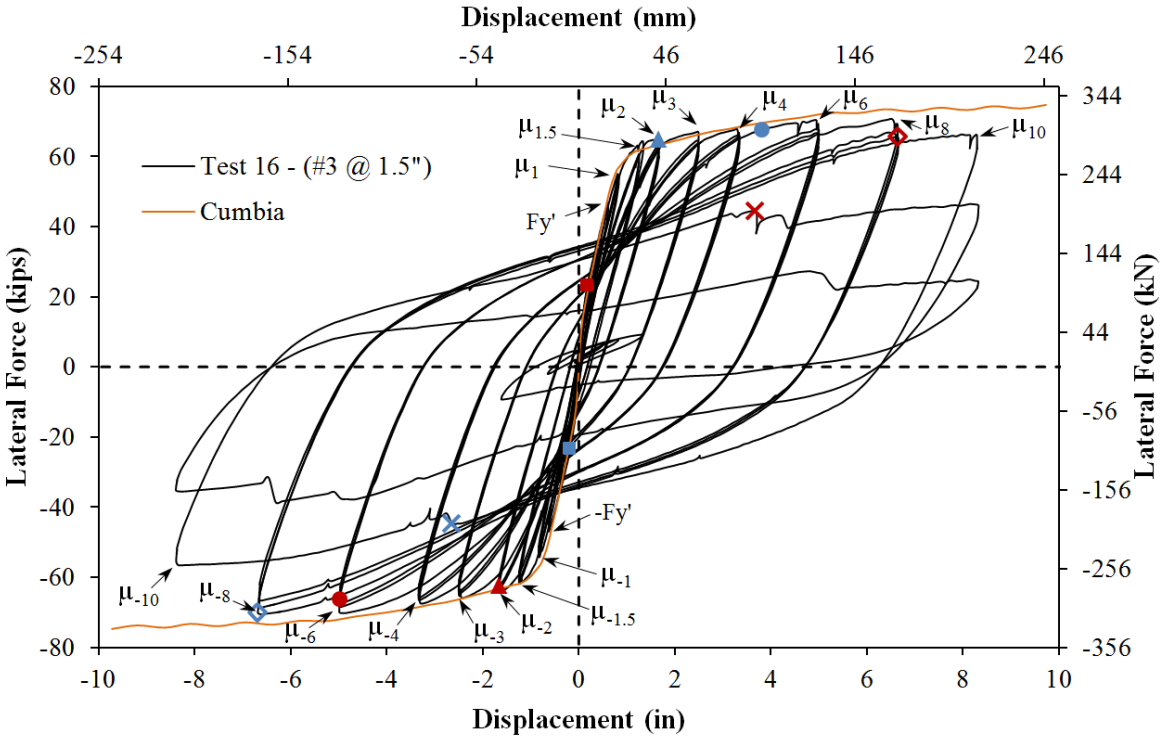

Figure 2-268. Test 16 – Symmetric Three Cycle Set Load History

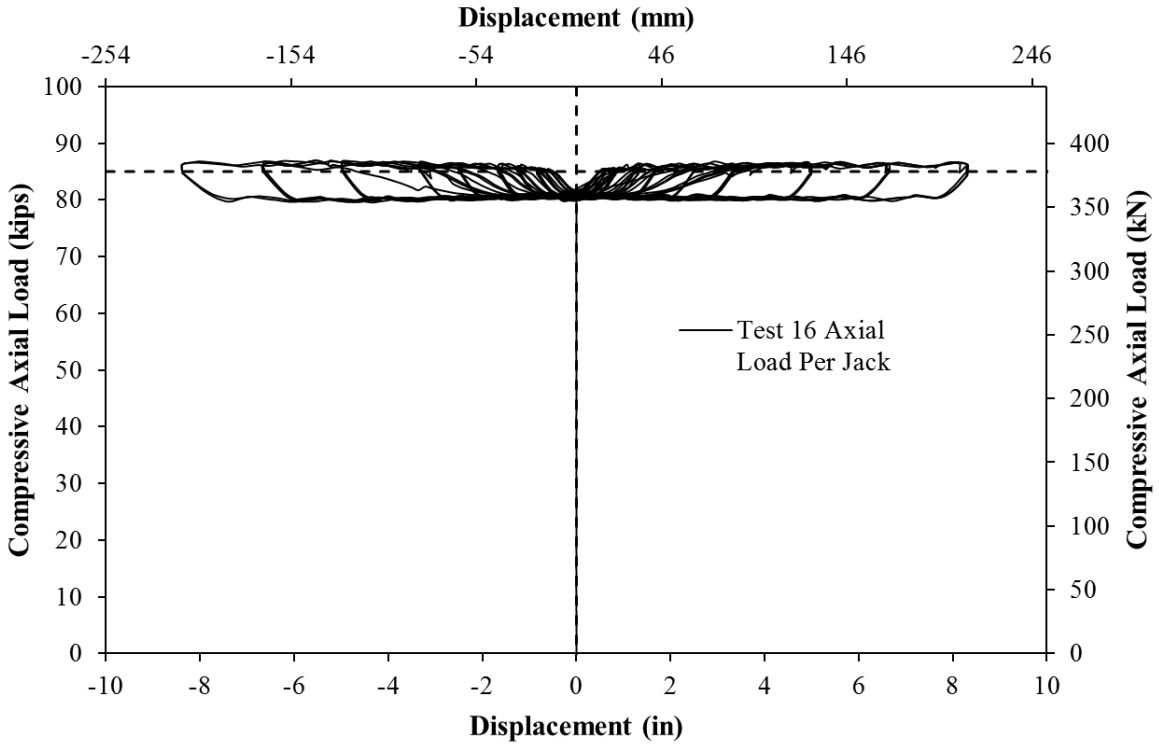

Figure 2-269. Test 16 – Compressive Axial Load from One Jack (Total = 2*Value)

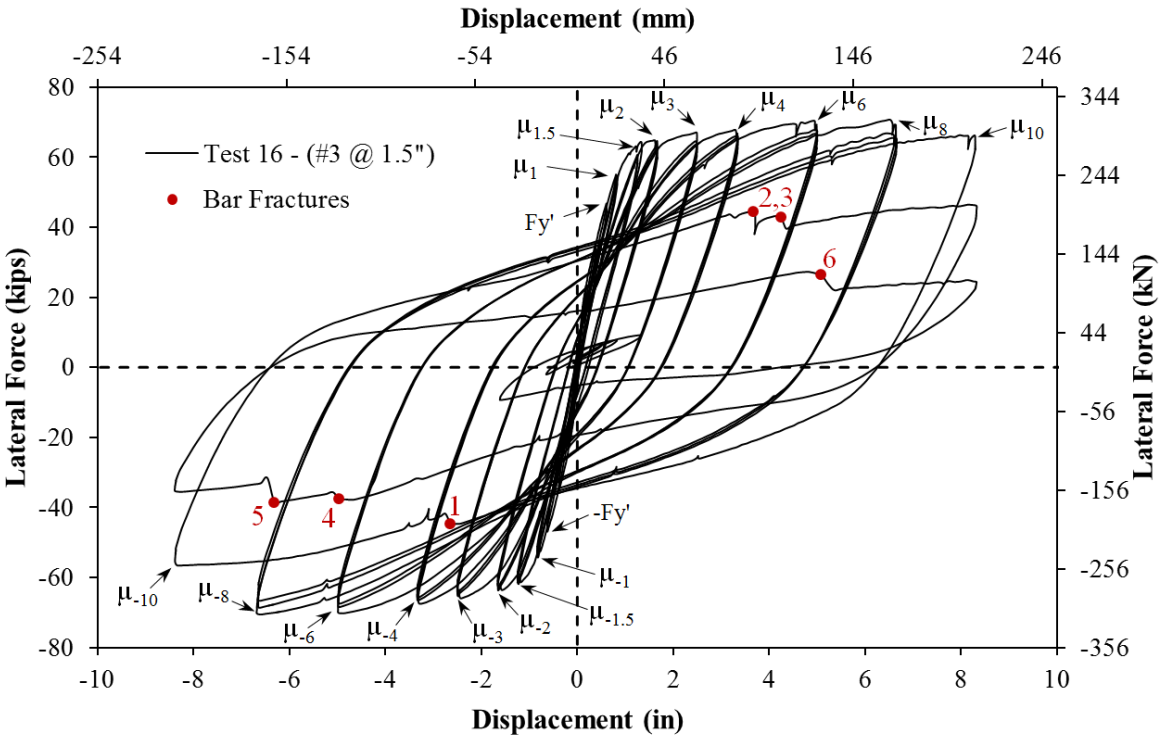

Figure 2-270. Test 16 – Bar Fracture History of Previously Buckled Reinforcement

2.2.4.1. Test 16 – Symmetric Three Cycle Set (#3 @ 1.5") Experimental Observations:

The test began with cycles in ¼ Fy' (first yield force) increments in each direction of loading until the first yield force was reached. The first cracks on the North side of the specimen measured 0.1mm at approximate 9" spacing at $(1/2Fy' = 23.30\ kips)$. Cracks on the South Side of the specimen measured 0.1mm at approximate 7" spacing during $(-1/2Fy' = -23.40\ kips)$. The largest crack widths on the North side of the specimen reached 0.2mm at approximate 6" spacing at $(3/4Fy' = 35.06\ kips)$. Cracks measuring 0.3mm with 6" spacing were observed on the South side of the specimen during $(-3/4Fy' = -34.46\ kips)$. During the first yield push cycle $(Fy' = 46.85\ kips,$ 0.61"), the largest crack widths measured 0.3mm at approximate 6" spacing. During the subsequent pull cycle $(-Fy' = -46.92\ kips, -0.63")$, crack widths reached 0.4mm at approximate 5" spacing on the South side of the specimen. The crack distribution at first yield is shown in Figure 2-271. The progression of the crack distribution on the back side of the specimen is shown in Figure 2-279. Cracks on the North side of the specimen measured 0.6mm at approximate 4" spacing during $(\mu_1^{+3} = 0.83")$. After reversal, cracks on the South side reached 0.6mm at 6" spacing at $(\mu_1^{-3} = -0.84")$.

Visible flaking of the cover concrete in compression, which is a precursor to crushing, was observed on the South side of the specimen during $(\mu_{1.5}^{+1} = 1.34")$. While the displacement for this cycle was intended to reach 1.25", a slight overload to 1.34" occurred. The largest crack width on the North side of the specimen measured 0.9mm, located 10" above the footing, during $(\mu_{1.5}^{+3} = 1.24")$. Crushing on the South side of the specimen 2" above the footing was observed during $(\mu_2^{+1} = 1.66")$, see the left photo of Figure 2-272. Visible cover concrete flaking on the North side of the specimen did not occur until $(\mu_2^{-1} = -1.66")$. During $(\mu_2^{-3} = -1.65")$, the largest crack width on the South side of the specimen measured 1.5mm and cover concrete crushing on the North side of the specimen reached 5" above the footing as shown in the right photo of Figure 2-272. The extent of crushing on the South side of the specimen reached 15" above the footing during $(\mu_3^{+3} = 2.50")$, as shown in the left photo of Figure 2-273. Crushing on the North side of the specimen extended 11" above the footing during $(\mu_3^{-3} = -2.50")$, see the right photo of Figure 2-273. During $(\mu_4^{+3} = 3.33")$ and $(\mu_4^{-3} = -3.33")$ the extent of crushing on the South and North side of the specimen reached 15" and 13" above the footing respectively.

Crushing on the North and South sides of the specimen both reached 25" above the footing during $(\mu_6^{+3} = 5.00")$ and $(\mu_6^{-3} = -4.99")$, as shown in Figure 2-274. After reversal from $(\mu_8^{-1} = -6.68")$, South extreme fiber bar S3 buckled as shown in the left and middle photos of Figure 2-275. After reversal from $(\mu_8^{+3} = 6.65")$, North extreme fiber bar N3 and adjacent bar N2 buckled, see the right photo of Figure 2-275. Even though rupture of the North reinforcement did not occur during $(\mu_{10}^{+2} = 8.32")$, a 5.7% loss in strength was observed due only to buckled bars on each side of the specimen during $(\mu_{10}^{+1} = 8.29")$. An additional South reinforcing bar S2 buckled during $(\mu_{10}^{+1} = 8.29")$, as shown in the left photo of Figure 2-276. During $(\mu_{10}^{-1} = 8.34")$, previously buckled South reinforcing bar S3 ruptured causing a 19.5% loss in strength, see the right photo of Figure 2-276. North reinforcing bars N1 and N4 also buckled during $(\mu_{10}^{-1} = 8.34")$, see the left photo of Figure 2-277. Previously buckled North bars N2 and N3 ruptured during $(\mu_{10}^{+2} = 8.32")$, leading to a 33.4% total loss in strength, see the right photo of Figure 2-277. Additional South reinforcing bars S1 and S4 buckled during $(\mu_{10}^{+2} = 8.32")$, as shown in Figure 2-278. Previously buckled South bars S2 and S4 ruptured during $(\mu_{10}^{-2} = -8.39")$, causing a 49.7% total loss in strength. During $(\mu_{10}^{+3} = 8.32")$, North bars N1 and N5 ruptured leading to a total 64.7% loss in strength. At this time the test was concluded. A graph plotting the rupture locations and corresponding losses in strength on the hysteretic response appears in Figure 2-270.

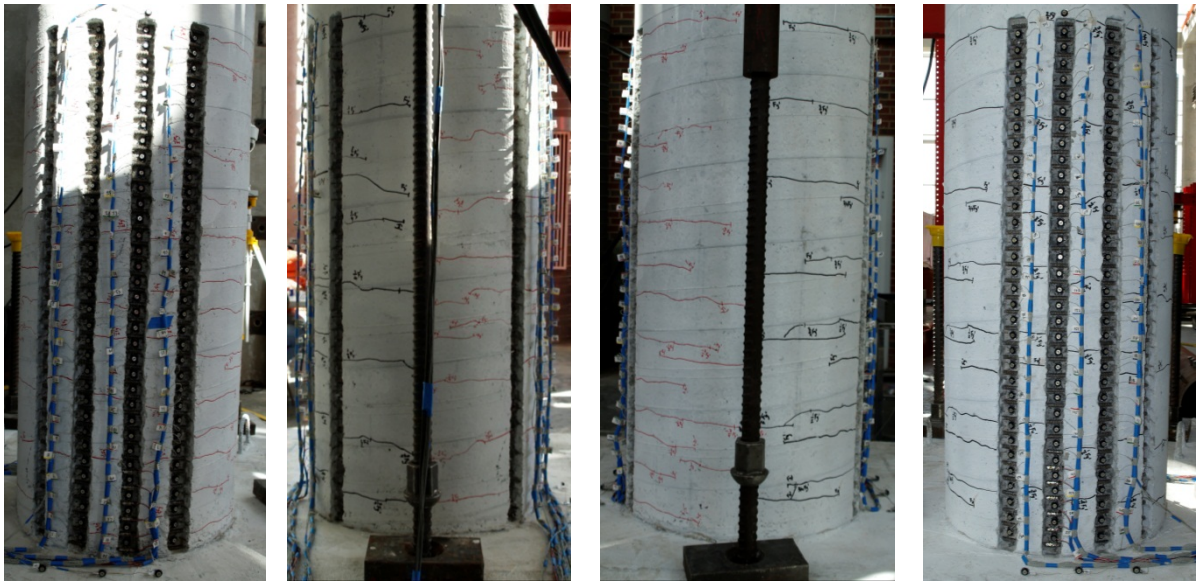

Figure 2-271. Test 16 – Crack Distribution at First Yield (Left) South, (Middle-Left) Front, (Middle-Right) Back, (Right) North

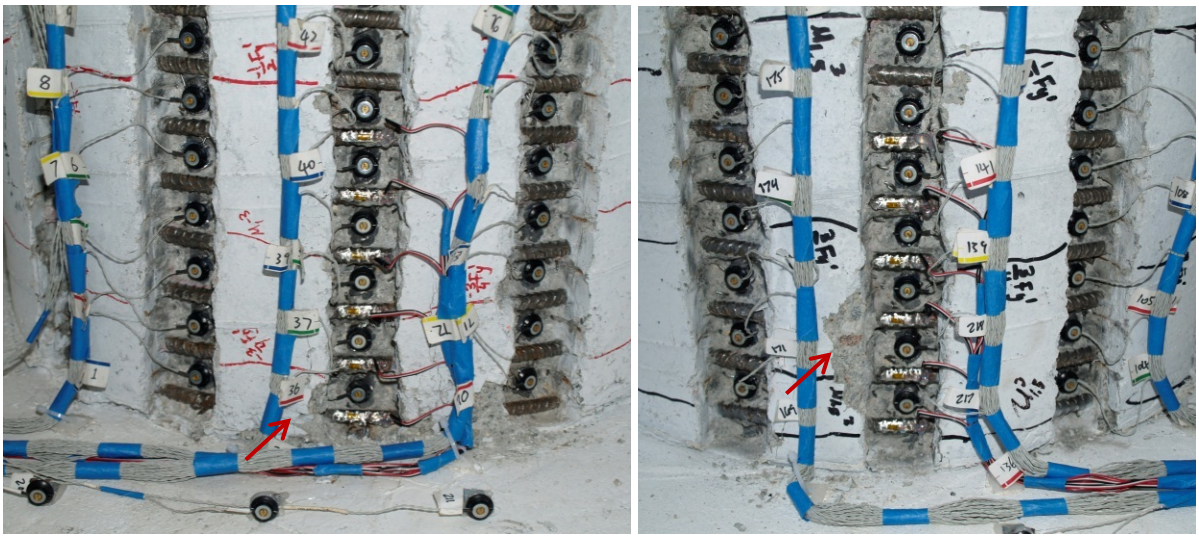

Figure 2-272. Test 16 – (Left) South Crushing during ($\mu_2^{+1} = 1.66$") and (Right) North Crushing during ($\mu_2^{-3} = -1.65$")

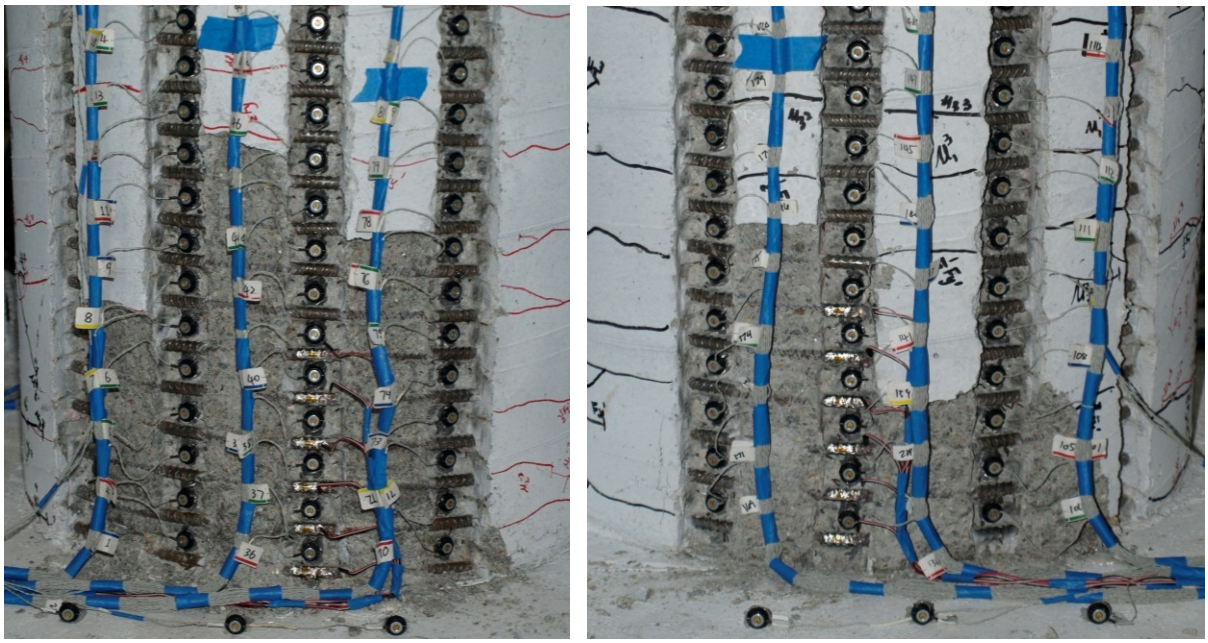

Figure 2-273. Test 16 – (Left) South Crushing during ($\mu_3^{+3} = 2.50$") and (Right) North Crushing during ($\mu_3^{-3} = -2.50$")

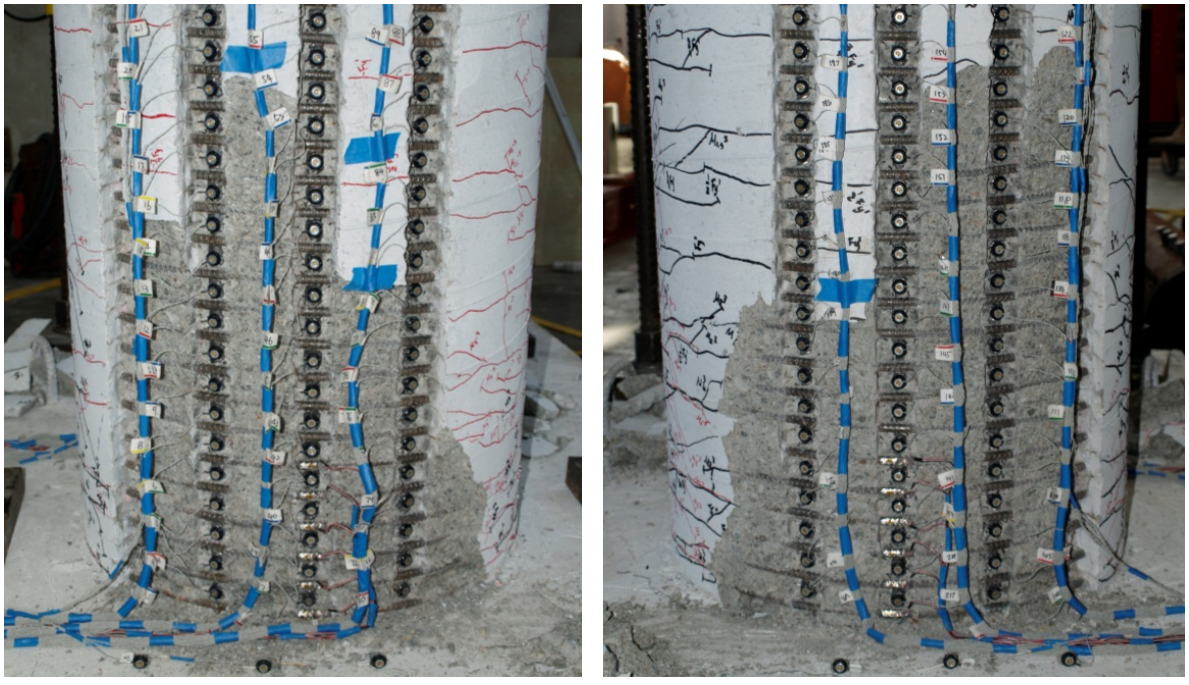

Figure 2-274. Test 16 – (Left) South Crushing during ($\mu_6^{+3} = 5.00$") and (Right) North Crushing during ($\mu_6^{-3} = -4.99$")

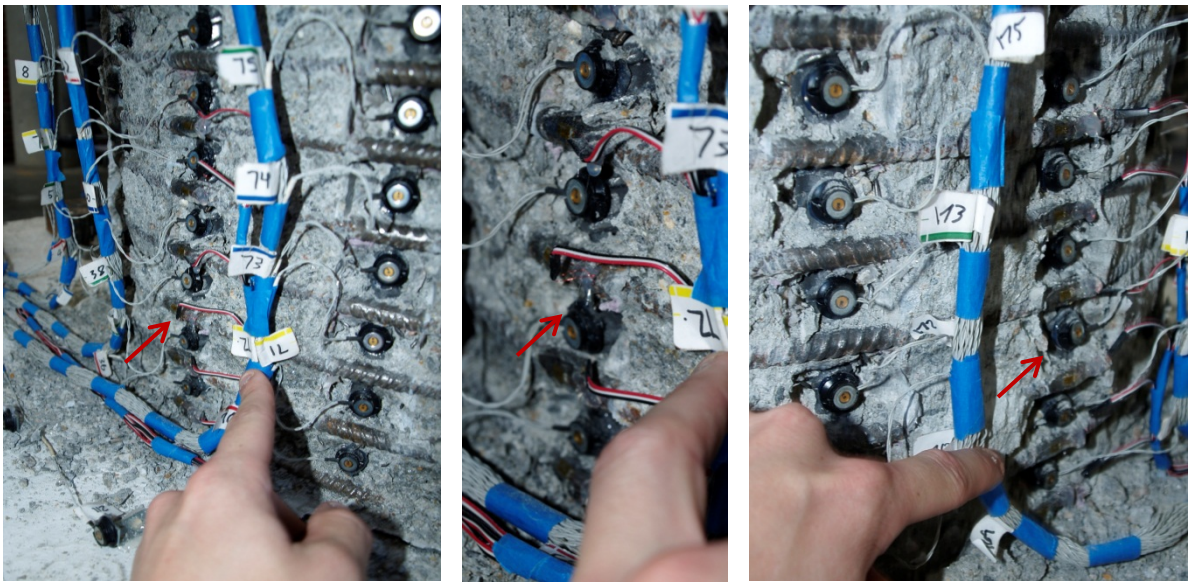

Figure 2-275. Test 16 – (Left and Middle) Buckling of Bar S3 during ($\mu_8^{+2} = 6.64$") and (Right) Buckling of Bar N2 and N3 during ($\mu_8^{-3} = 6.66$")

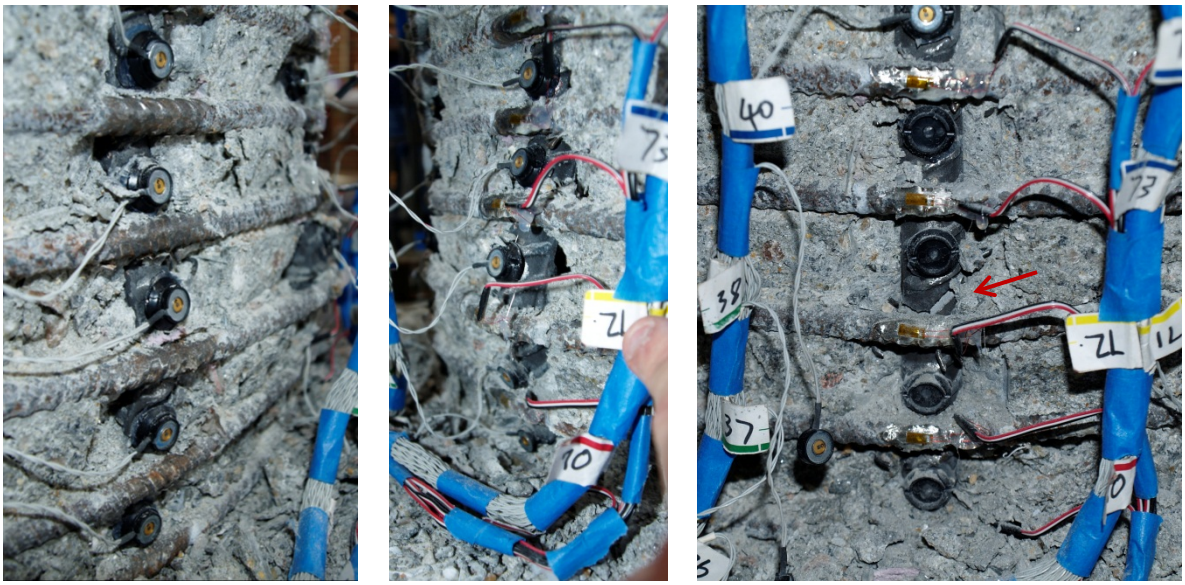

Figure 2-276. Test 16 – (Left) Buckling of Bar S2 during ($\mu_{10}^{+1} = 8.29$"), (Middle) Increased Deformation in Bar S3 during ($\mu_{10}^{+1} = 8.29$"), and (Right) Rupture of Bar S3 during ($\mu_{10}^{-1} = -8.34$")

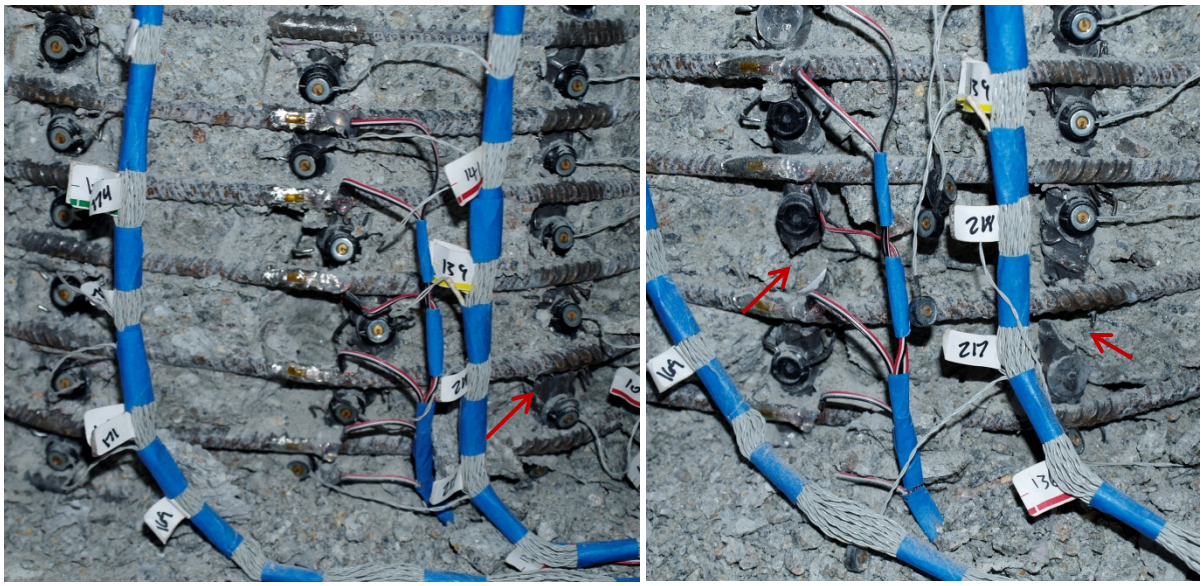

Figure 2-277. Test 16 – (Left) Buckling of N1 and N4 during ($\mu_{10}^{-1} = -8.34$") and (Right) Rupture of N2 and N3 during ($\mu_{10}^{+2} = 8.32$")

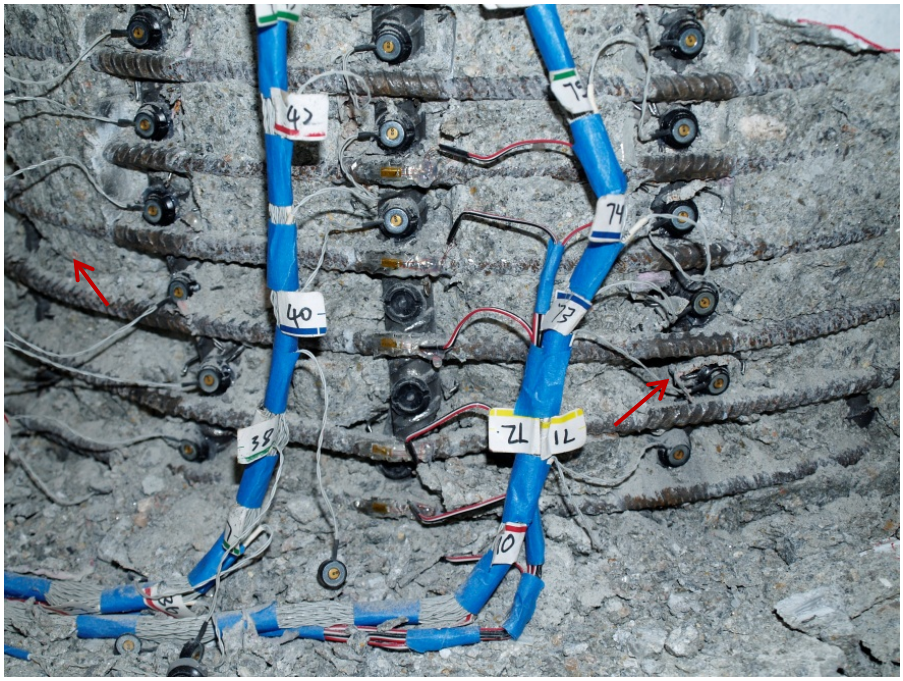

Figure 2-278. Test 16 – Buckling of S1 and S4 during ($\mu_{10}^{+2} = 8.32$")

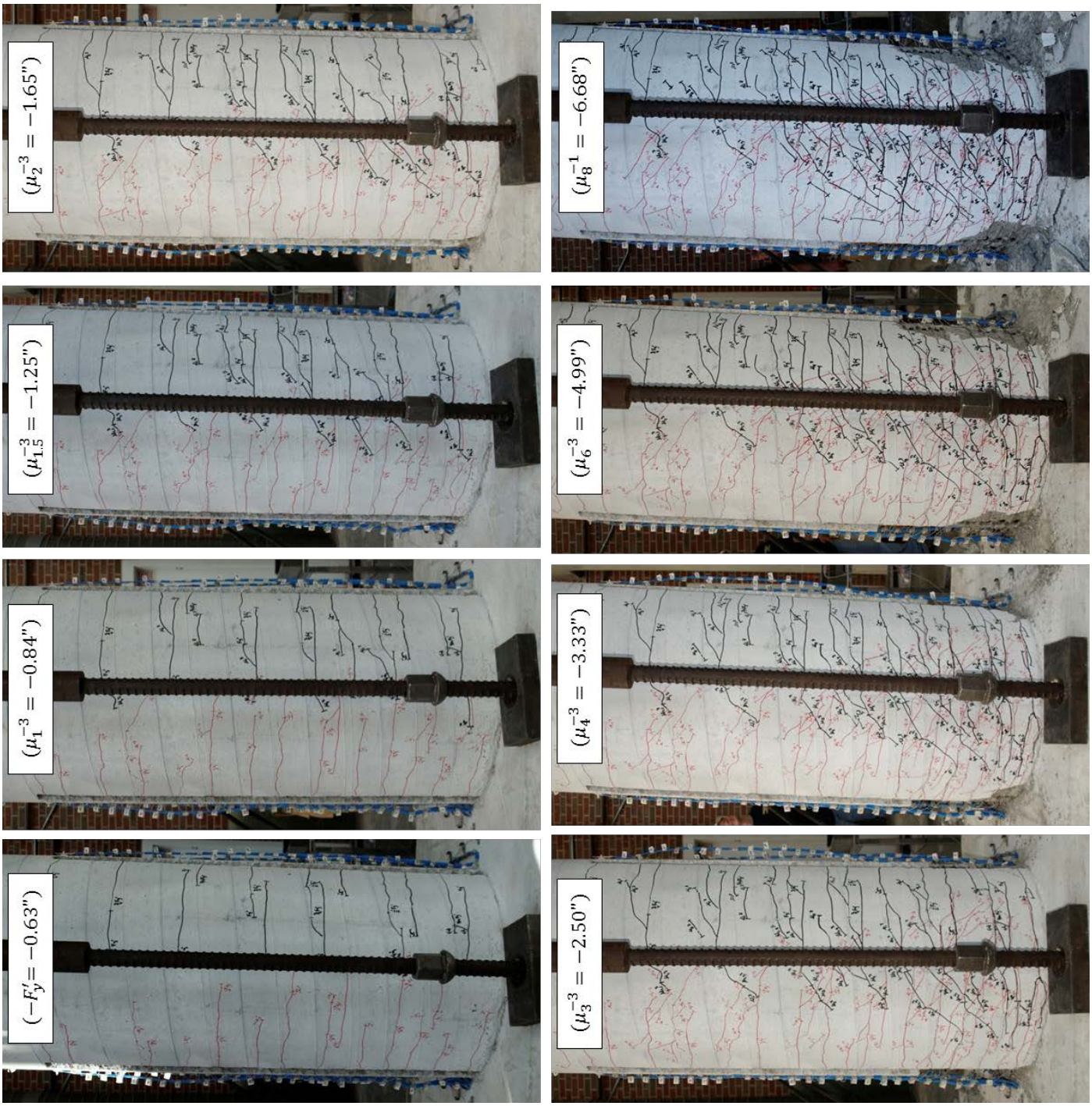

Figure 2-279. Test 16 – Crack Progression on the Back Side of the Specimen (North to the Right and South to the Left)

2.2.4.2. Test 16 – Symmetric Three Cycle Set (#3 @ 1.5") Strain Data:

North Reinforcement:

Extreme fiber vertical strain profiles for push and pull cycles appear in Figure 2-280 and Figure 2-281 respectively. These figures show both extreme fiber bars on the same graph to illustrate the effects of tension shift on strain profiles. Compressive strains are concentrated near the base of the column while tensile strains are fanned out to a greater height above the footing following the inclined crack distribution shown in Figure 2-279. The compressive vertical strain profile for North extreme fiber bar N3 during pull cycles appears in the left half of Figure 2-281. While the overall shape of the compressive strain profile matches past observations, a single gage length located 14.8" above the footing shows tensile strains during compressive cycles. The calculations for this gage length have been checked, and an explanation for why this may occur is not available. At this same height on adjacent bars N2 and N4, compressive strains were measured as expected.

A peak tensile strain of 0.056, located 3.40" above the footing, was measured for North extreme fiber bar N3 during ($\mu_8^{+3} = 6.65"$). Bar N3 buckled after reversal from this peak tensile strain. The relationship between tensile strain and displacement for this gage length appears in Figure 2-284. The solid line contains data during the push cycle loading up to the peak and the dashed line represents the subsequent reversal of load. Similar to previous tests, the moment curvature prediction for the relationship between strain and displacement begins to over predict the tensile strains at higher displacements at an increasing rate. The largest compressive strain of -0.0187, located 7.70" above the footing, was measured during ($\mu_8^{-1} = -6.68"$). The relationship between compressive strain and displacement for bar N3, gage length centered 7.7" above the footing, during pull cycles appears in Figure 2-287. Here the measured compressive strains deviate above or below the prediction depending on the displacement range, but the overall trend is captured.

The strains in the lowest six transverse steel layers restraining North extreme fiber bar N3 are plotted in Figure 2-283. The individual data points are from strain gages attached to each spiral layer at a specific height above the footing. The data points are connected with lines only to show trends for the particular displacement level. The vertical grey dashed line represents the yield strain of the transverse reinforcement. A single transverse steel layer, located 3.5" above the footing, entered the inelastic range during ($\mu_6^{-3} = -4.99"$). Compressive demands during ($\mu_8^{-1} = -6.68"$), led to three layers of transverse steel going into the inelastic range. Prior to buckling, the strain in the three inelastic spiral layers increased during ($\mu_8^{-2} = -6.64"$), even though the displacement level remained the same. When bar N3 latter buckled during ($\mu_8^{-3} = -6.66"$) the tensile strain for these spiral layers rapidly increased as they accommodated the outward deformation of the bar.

The strain hysteresis over the outward buckled region of bar N3, gage length located 3.40" above the footing, appears in Figure 2-288. It is clear that there was some measurable outward deformation during ($\mu_8^{-2} = -6.64"$), as shown by the blue arrow in Figure 2-288. Visible Buckling occurred after reversal from ($\mu_8^{+3} = 6.65"$), here the outward deformation begins to rapidly increase as indicated by the red arrow. The transverse steel strain gage hysteresis for the layer over the outward buckled region of bar N3 appears in Figure 2-289. The measurable deformation during ($\mu_8^{-2} = -6.64"$), shown by the blue arrow, increases the inelastic tensile strain in the spiral layer. Visible bar buckling after reversal from ($\mu_8^{+3} = 6.65"$) leads to a rapid increase in the spiral strain causing the gage to go beyond its measurable range.

South Reinforcement:

A peak tensile strain of 0.052 on bar S3 was measured 7.76" above the footing during ($\mu_8^{-1} = -6.68"$). The relationship between tensile strain and displacement for bar S3 is shown in Figure 2-286 for the gage length located 7.76" above the footing. The same comments on the accuracy of the moment curvature prediction for the North reinforcement bar N3 also apply to bar S3. A peak compression strain of -0.0303 was measured 4.89" above the footing during ($\mu_8^{+1} = 6.64"$). The relationship between compressive strain and displacement for the gage length 4.89" above the footing on bar S3 during push cycles appears in Figure 2-285. The measured strains match the moment curvature prediction well through ductility two, but at higher ductility levels the measured compressive strains are significantly larger than the prediction. The peak compressive strain of -0.0303 measured in bar S3 is 57% larger than the original Mander (1988) ultimate concrete compressive strain of -0.0193.

The strains in the lowest six transverse steel layers restraining South extreme fiber bar S3 are plotted in Figure 2-282. Compressive demands during ($\mu_6^{+3} = 6.64"$), led to two layers of transverse steel exceeding the yield strain. Prior to buckling, the strain in the two inelastic spiral layers increased and a third layer entered the inelastic range during ($\mu_8^{+1} = 6.64"$). The strain hysteresis for the outward buckled region of extreme fiber bar S3, gage length located 3.37" above the footing, appears in Figure 2-290. The strain gage hysteresis for the spiral layer overlaying the outward buckled region of bar S3 appears in Figure 2-291. Visible buckling of bar S3 occurred after reversal from ($\mu_8^{-1} = -6.68"$). During this reversal outward deformation over bar S3 occurred as shown by the increased tensile strains in Figure 2-290. As the bar deformed outwards, the spiral restraint tensile strain began to rapidly increase until the strain gage exceeded its maximum value by going off scale.

2.2.4.3. Test 16 – Symmetric Three Cycle Set (#3 @ 1.5") Curvature and Strain Penetration Data:

The cross section curvature for each horizontal section above the footing is determined by connecting the strain measurements from all six instrumented bars with a least squared error line. The curvature is then extracted from the slope of the least squared error line, see Figure 2-292. Vertical curvature profiles are plotted for push and pull cycles as shown in Figure 2-293 and Figure 2-294 respectively. These figures show that plastic curvatures have a linear distribution at higher displacement ductility levels. The extent of plastic curvatures above the footing can be calculated by determining where the linear plastic curvature distribution intersects the triangular yield curvature distribution, shown as a grey dashed line. The dashed lines for each curvature distribution represent a least squared error linear fit to the plastic portion of the measured curvatures. The data points used to create the least squared error lines appear as circle data markers.

The target marker on each bar placed closest the footing-column interface can be used to create slip hysteresis and horizontal slip profiles attributable to strain penetration. The slip hysteresis for extreme fiber bars N3 and S3 appear in Figure 2-295 and Figure 2-296 respectively. The peak tensile slip of each bar exceeds 0.4in during displacement ductility eight. If the tensile and compressive slip of all of the instrumented bars is plotted along the cross section depth, the base rotation attributable to strain penetration may be calculated. The slip profiles for push and pull cycles appear in Figure 2-297 and Figure 2-298 respectively. The rotation of the base section can be extracted from the slope of the least squared error line connecting all six measured bar slips.

Combining the curvatures over the instrumented region (4ft above the footing), bar slip profiles, and an elastic curvature assumption above the instrumented region, the top column displacement can be calculated. This top column displacement calculated from the Optotrak system is compared to the top

column displacement measured with a string potentiometer at the center of loading in Figure 2-299. The calculated displacements match well over the entire range of response indicating that shear displacements are negligible in comparison to flexural displacements. A bar chart which plots the components of top column displacement for each displacement ductility level appears in Figure 2-300. Strain penetration accounts for between 25-35% of the top column displacement throughout the entire range of response.

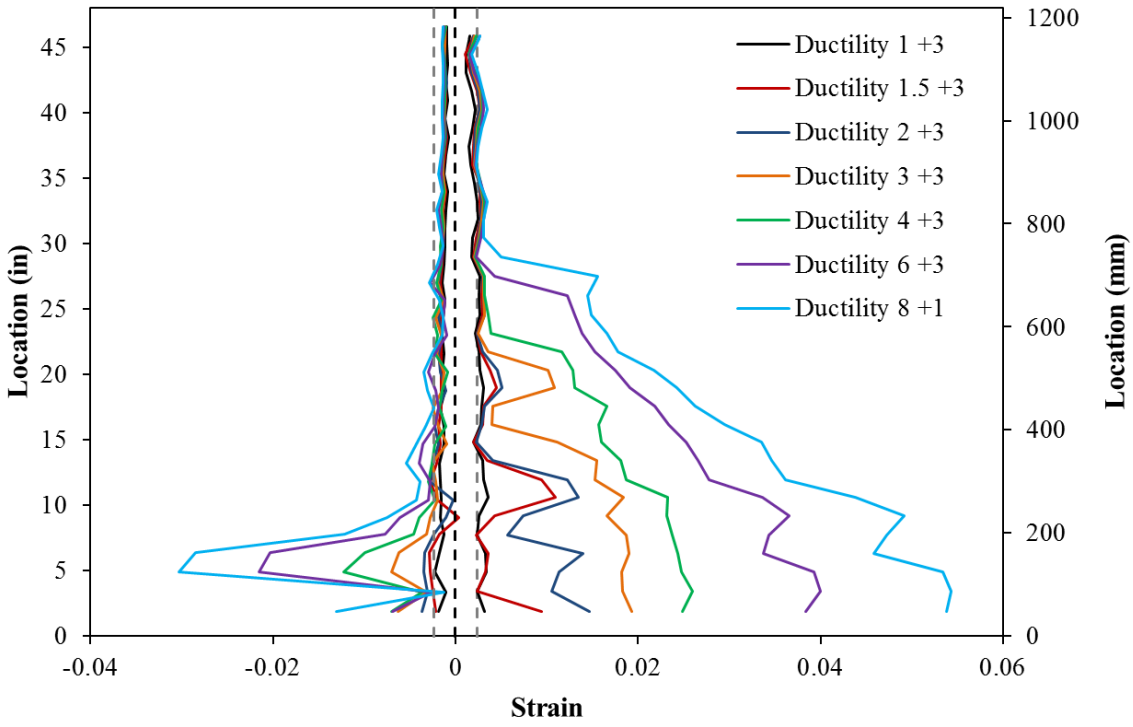

Figure 2-280. Test 16 – Extreme Fiber Vertical Strain Profiles during Push Cycles

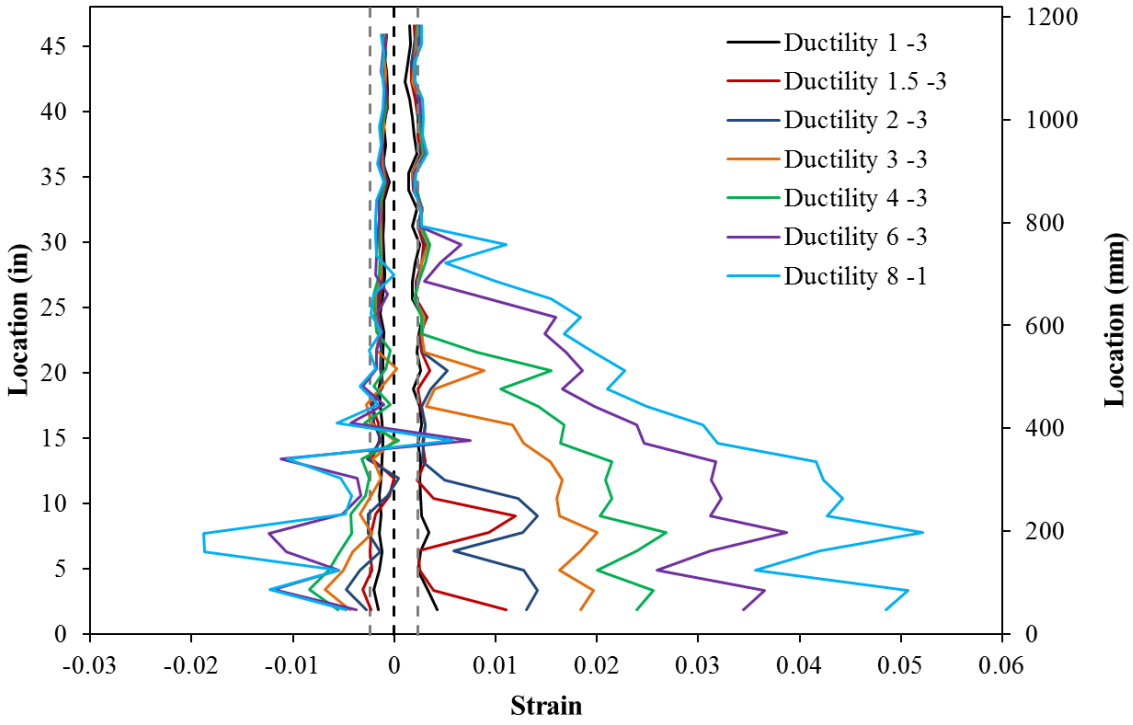

Figure 2-281. Test 16 – Extreme Fiber Vertical Strain Profiles during Pull Cycles

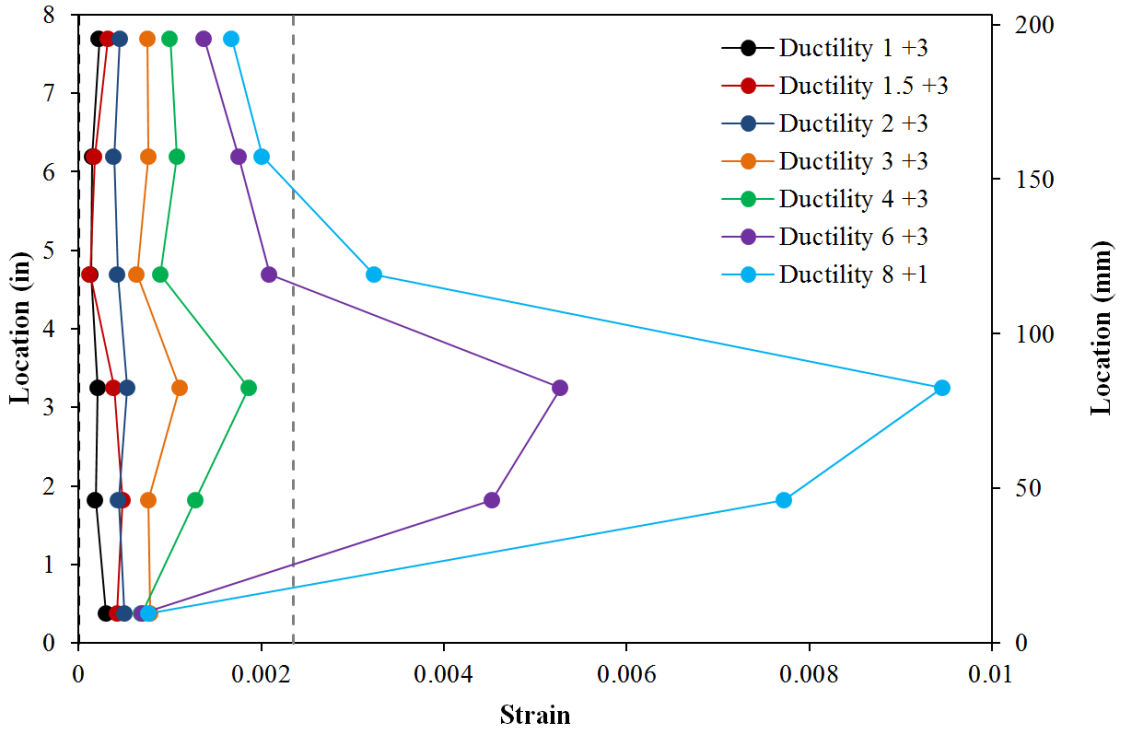

Figure 2-282. Test 16 – Transverse Steel Strains for Lowest Six Spiral Layers on the South Side Placed into Compression during Push Cycles

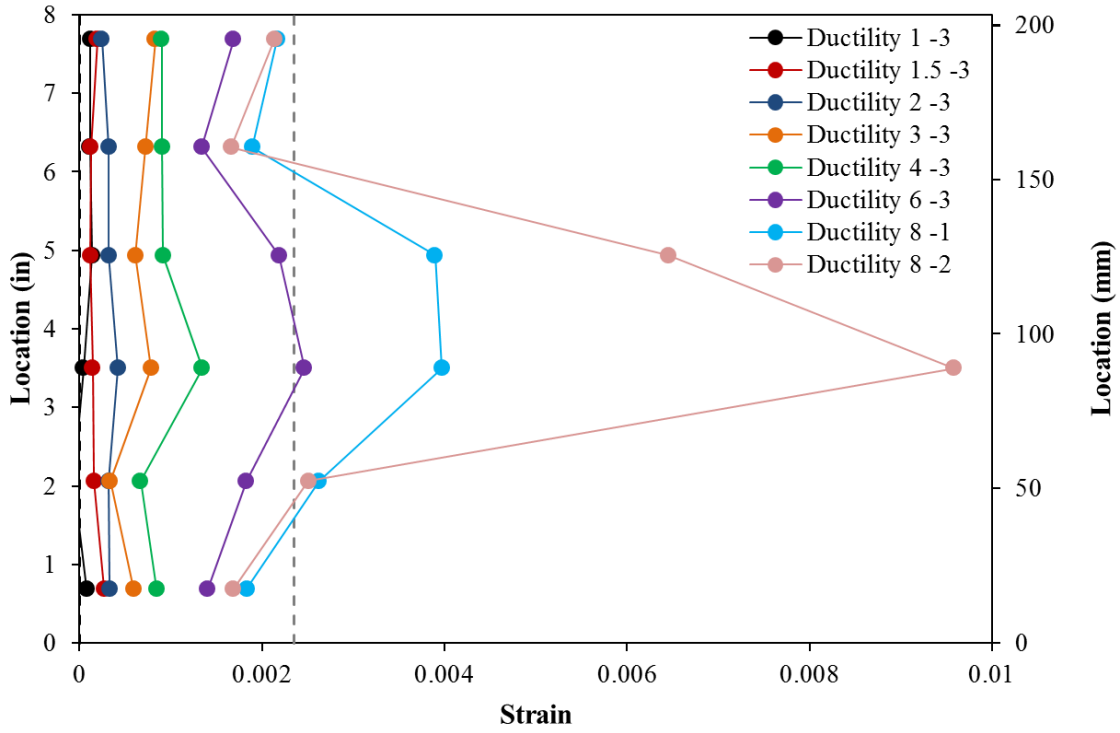

Figure 2-283. Test 16 – Lowest Six Spiral Layers on the North Side during Pull Cycles

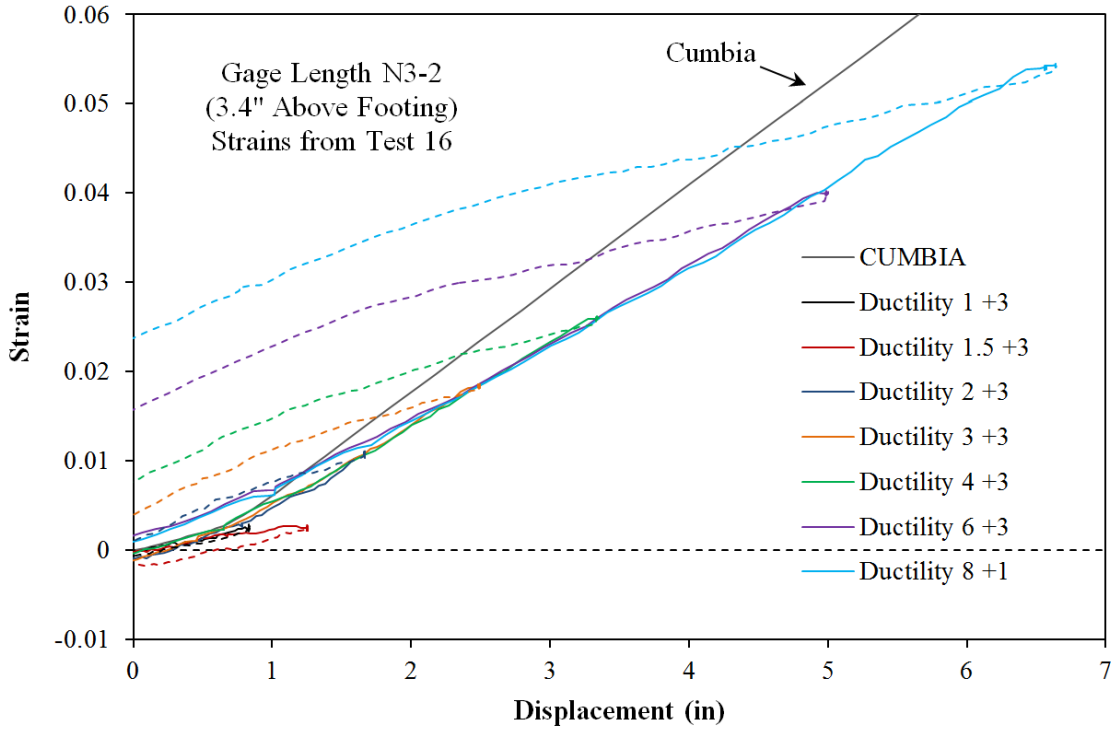

Figure 2-284. Test 16 – Tensile Strain and Displacement for Bar N3 during Push Cycles (3.4" Above Footing)

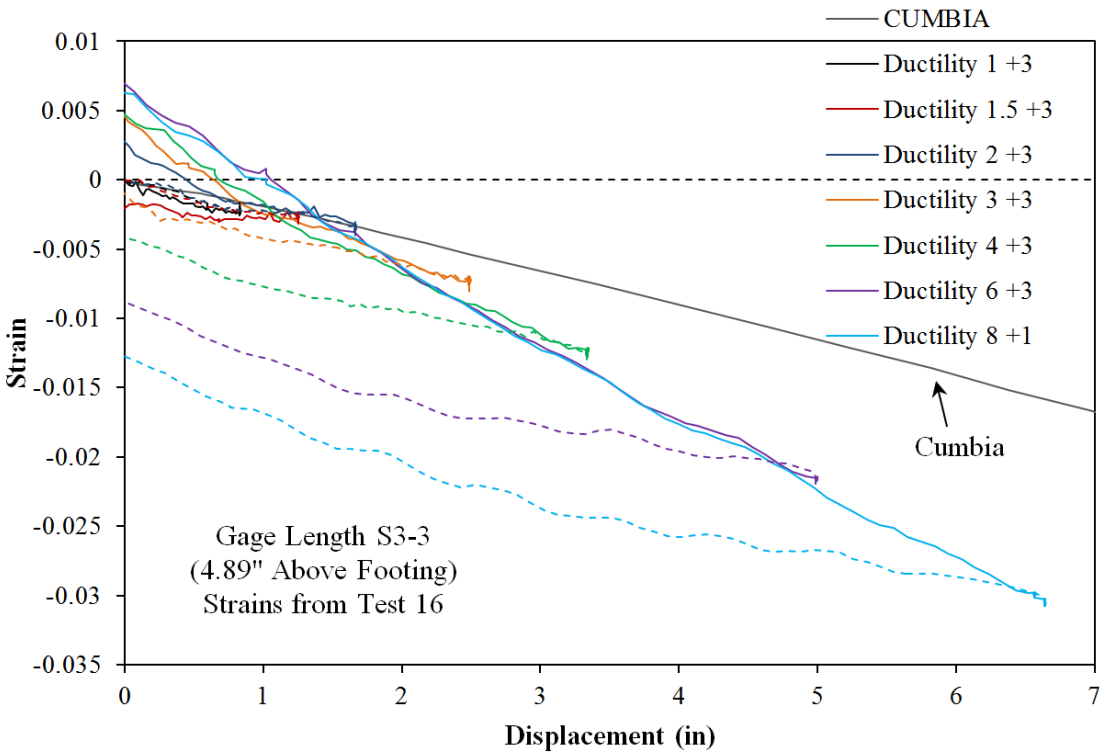

Figure 2-285. Test 16 – Compressive Strain and Displacement for Bar S3 (4.89” Above)

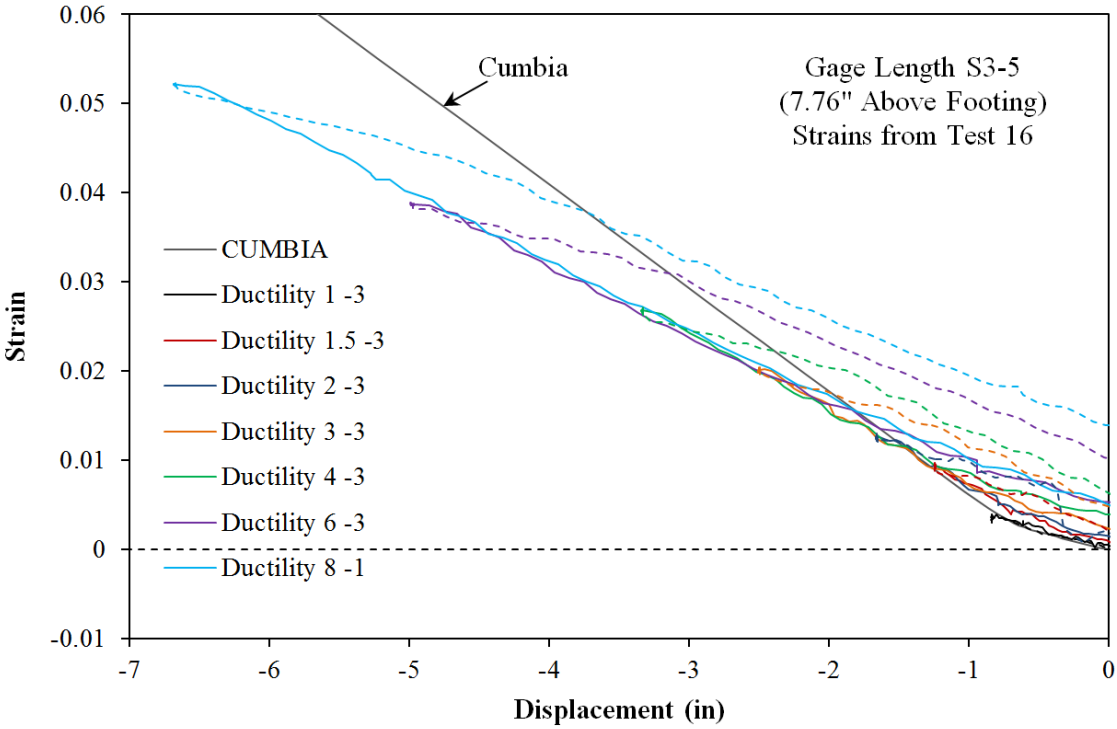

Figure 2-286. Test 16 – Tensile Strain and Displacement for Bar S3 (7.76” Above)

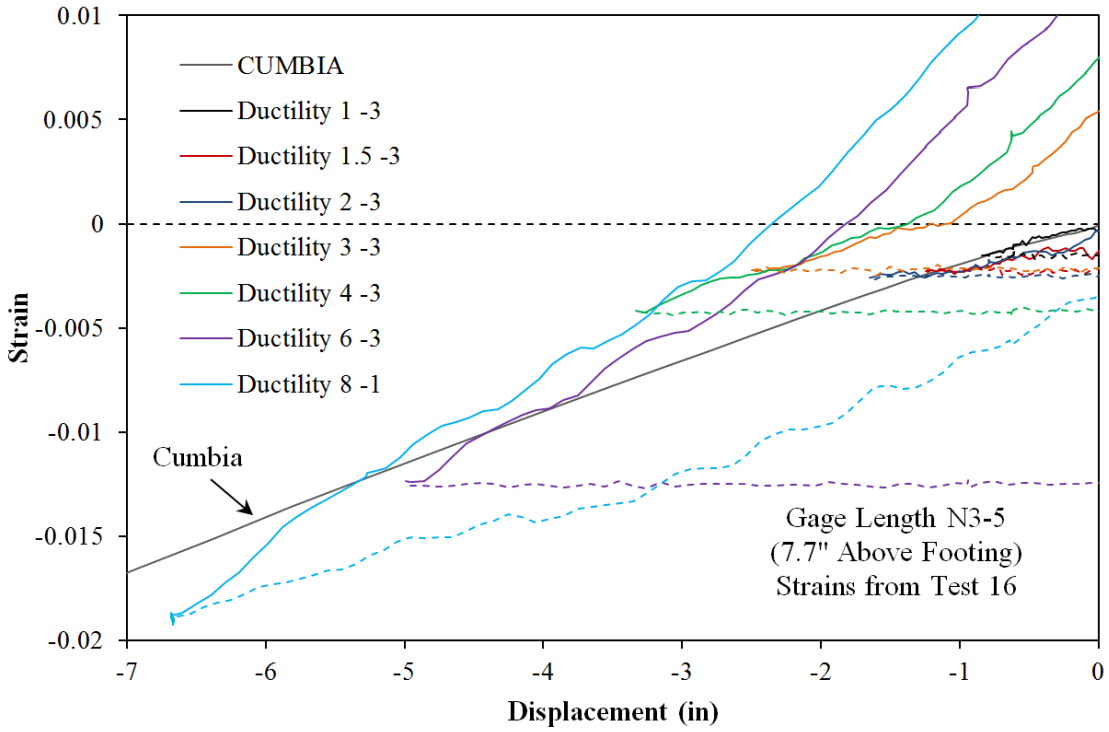

Figure 2-287. Test 16 – Compressive Strain and Displacement for Bar N3 (7.7” Above)

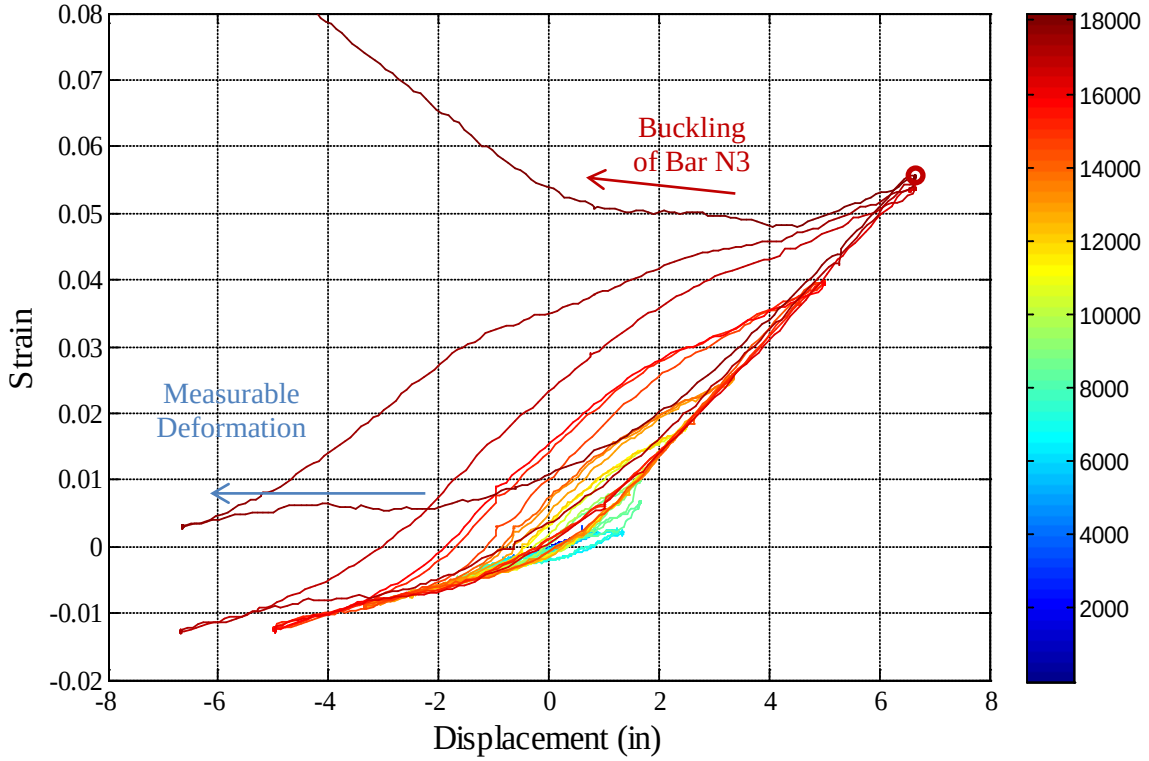

Figure 2-288. Test 16 – Strain Hysteresis over the Buckled Region of Bar N3 (3.4” Above the Footing)

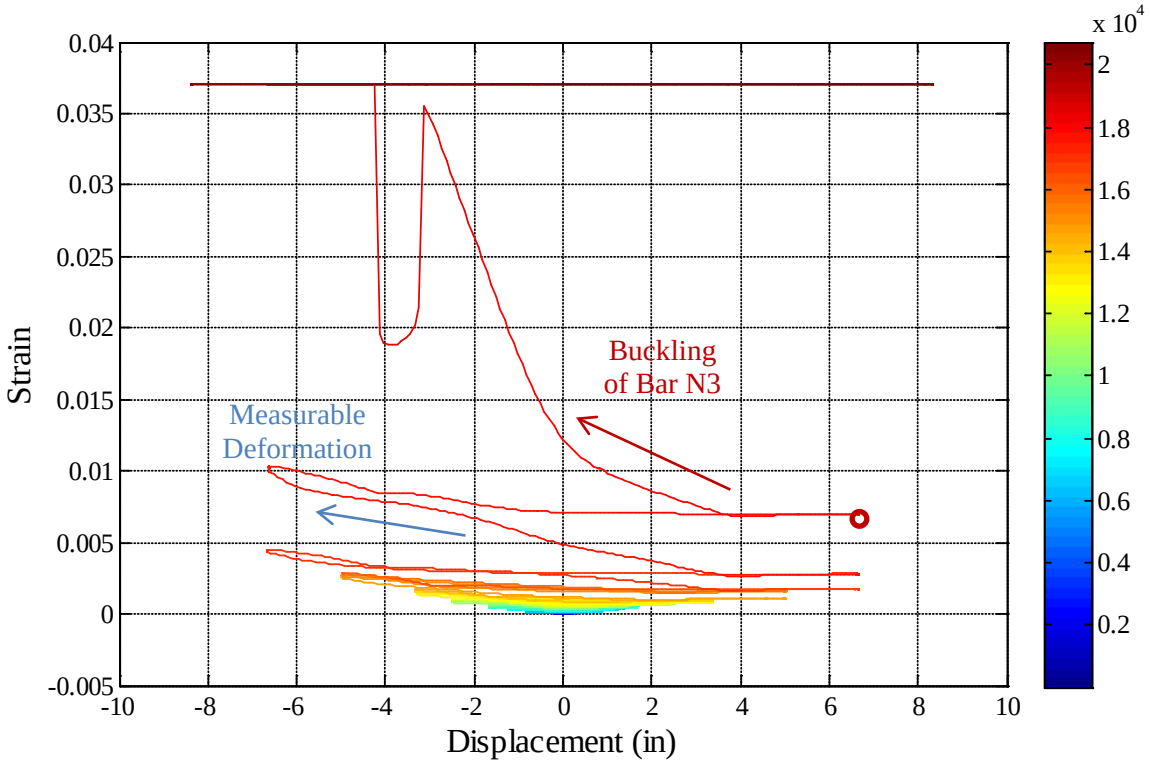

Figure 2-289. Test 16 – Transverse Steel Strain Gage Hysteresis over the Buckled Region of Bar N3

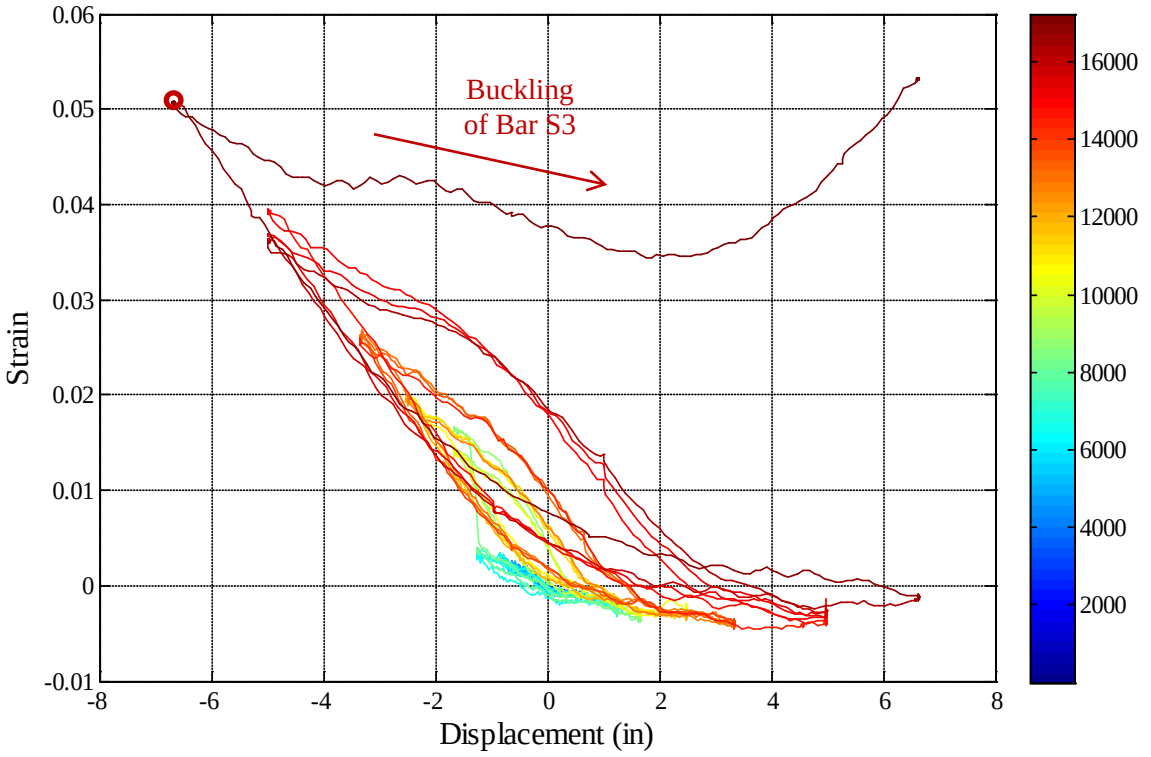

Figure 2-290. Test 16 – Strain Hysteresis over the Buckled Region of Bar S3 (3.37” Above)

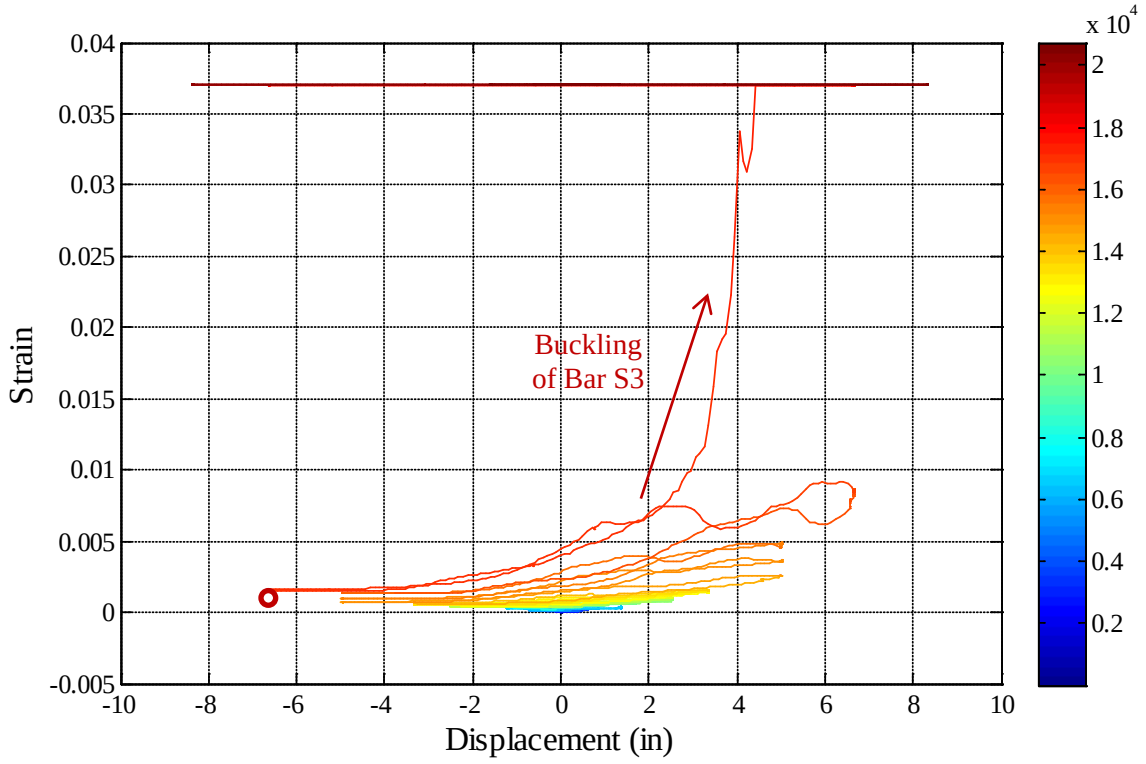

Figure 2-291. Test 16 – Spiral Strain Gage Hysteresis over the Buckled Region of Bar S3

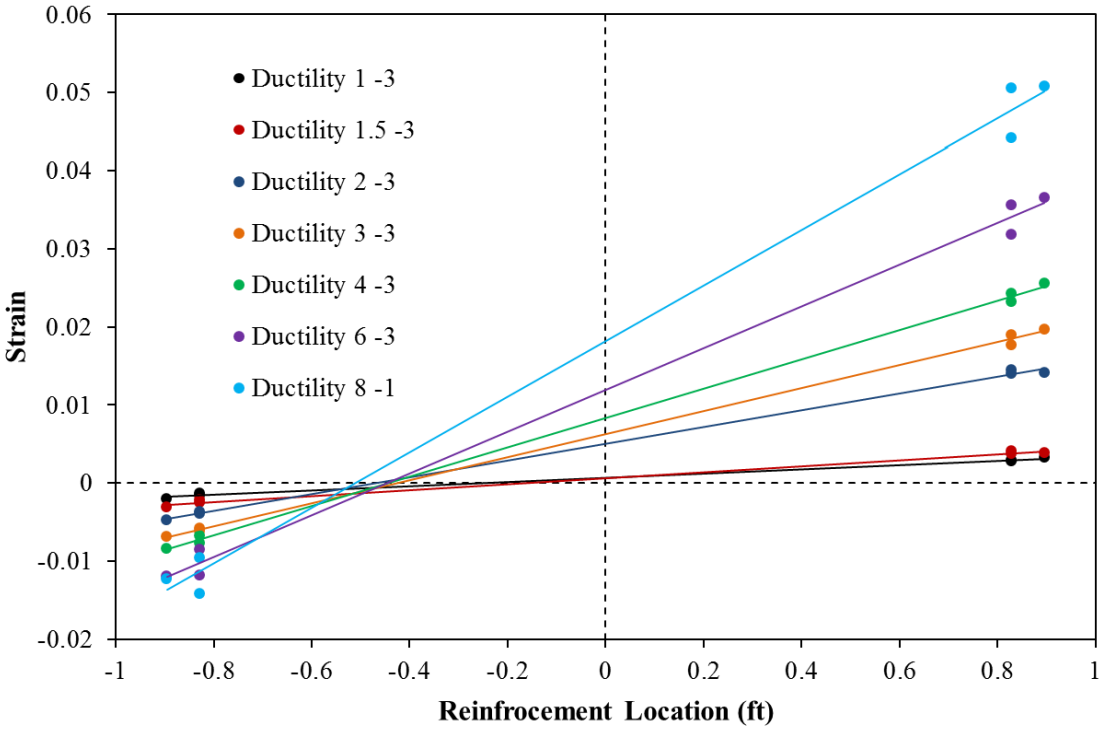

Figure 2-292. Test 16 – Method of Determine Cross Section Curvature through Slope of Least Squared Error Line

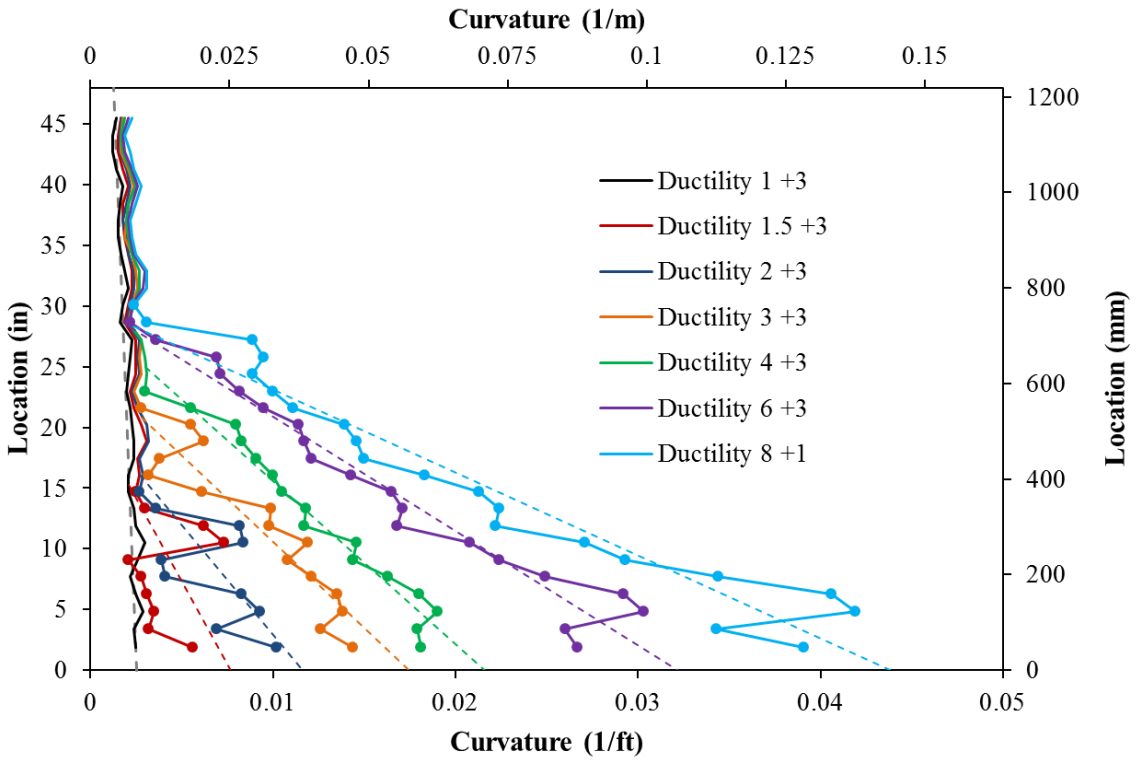

Figure 2-293. Test 16 – Vertical Curvature Profiles during Push Cycles with Linearized Plastic Curvature Least Squared Error Lines

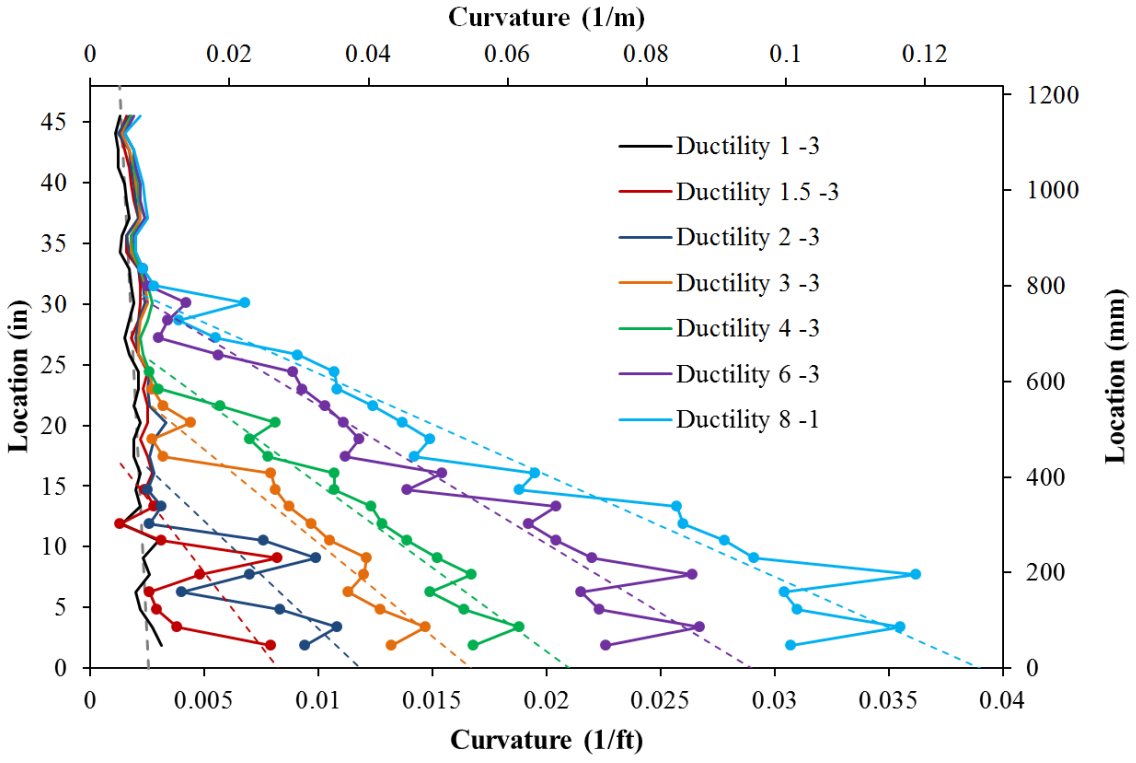

Figure 2-294. Test 16 – Vertical Curvature Profiles during Pull Cycles

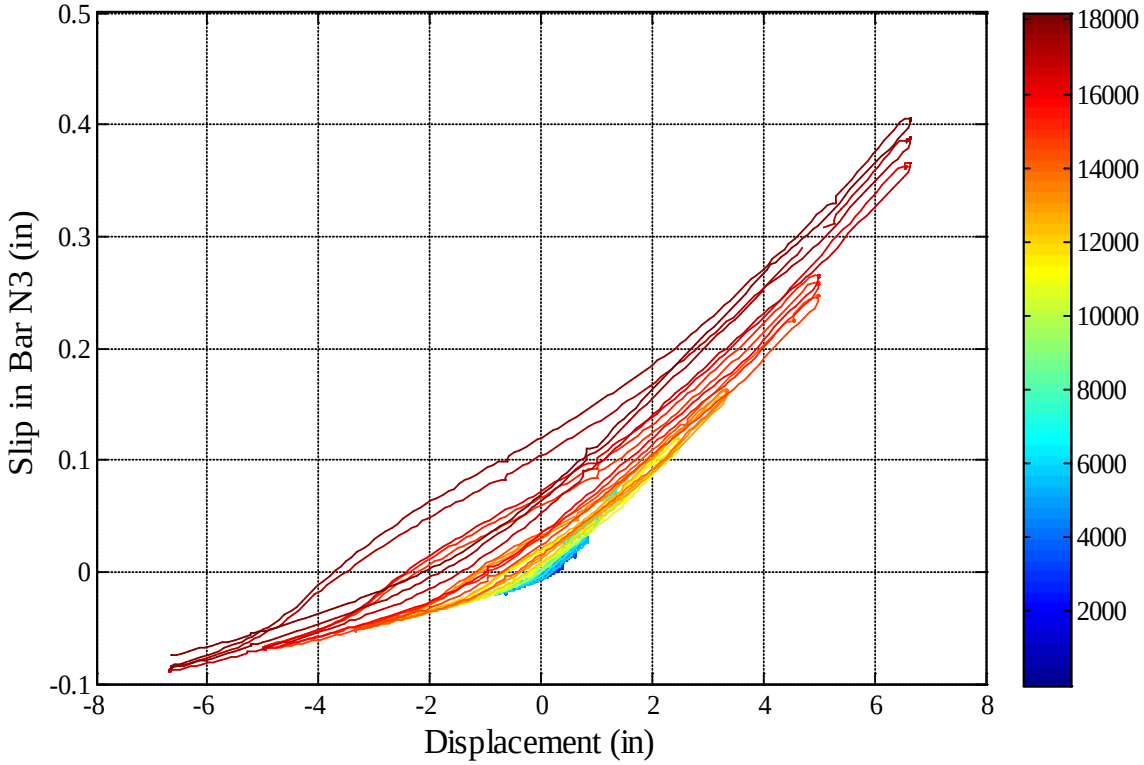

Figure 2-295. Test 16 – Extreme Fiber Bar N3 Slip Hysteresis due to Strain Penetration

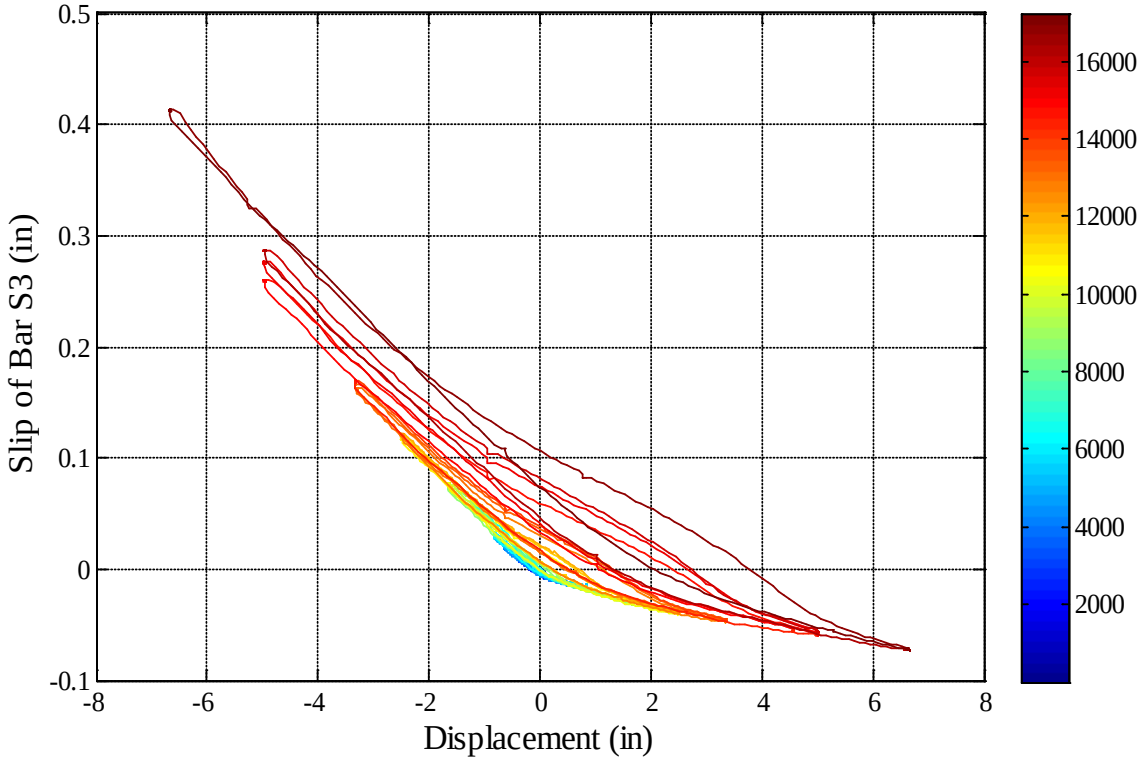

Figure 2-296. Test 16 – Extreme Fiber Bar S3 Slip Hysteresis due to Strain Penetration

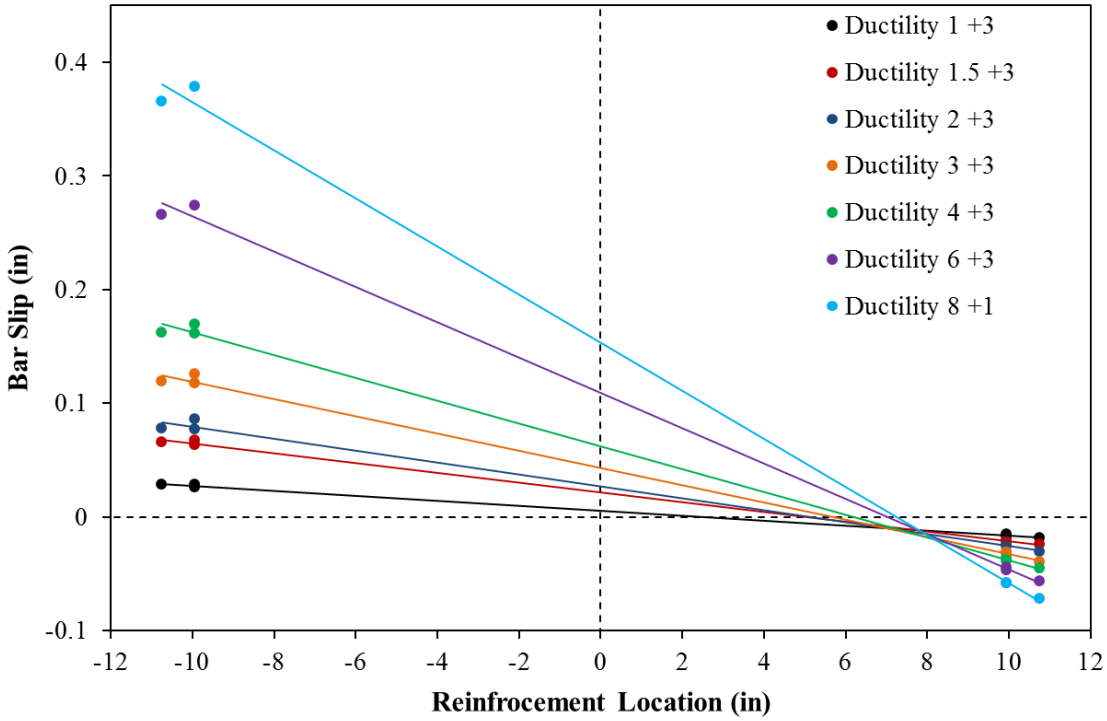

Figure 2-297. Test 16 – Slip Profile of All Six Instrumented Bars to Obtain the Base Section Rotation during Push Cycles

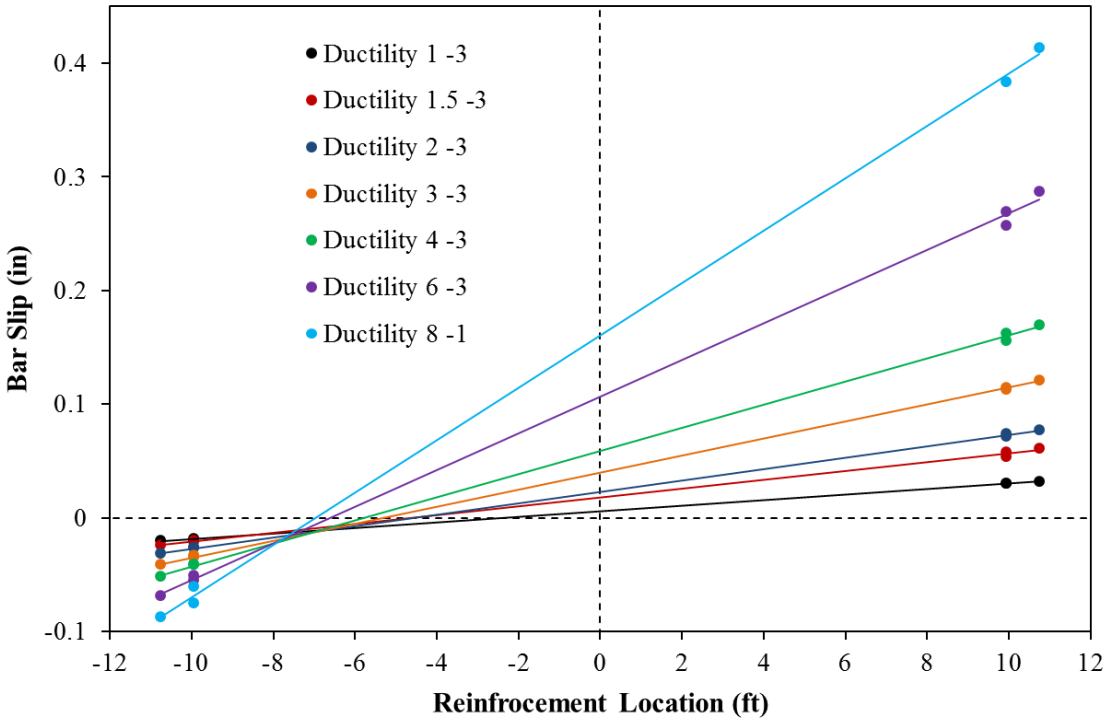

Figure 2-298. Test 16 – Base Section Rotation due to Strain Penetration during Pull Cycles

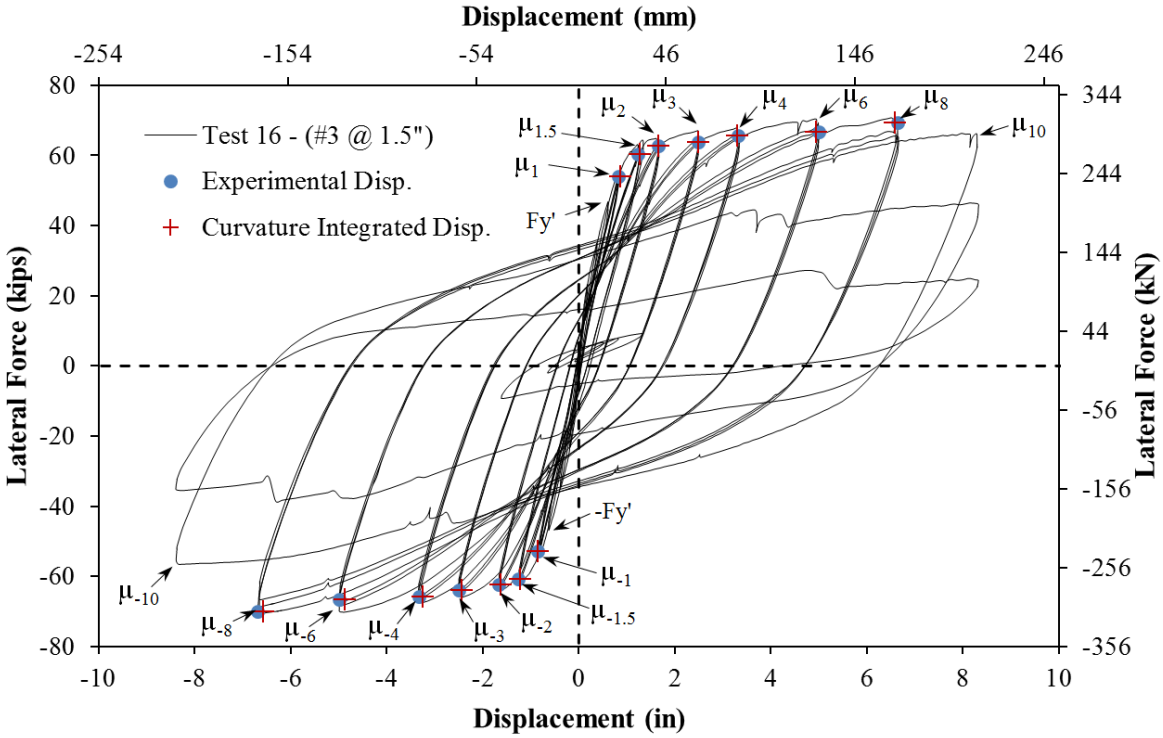

Figure 2-299. Test 16 – Comparison of Experimentally Measured and Optotrak Curvature Integrated Displacements

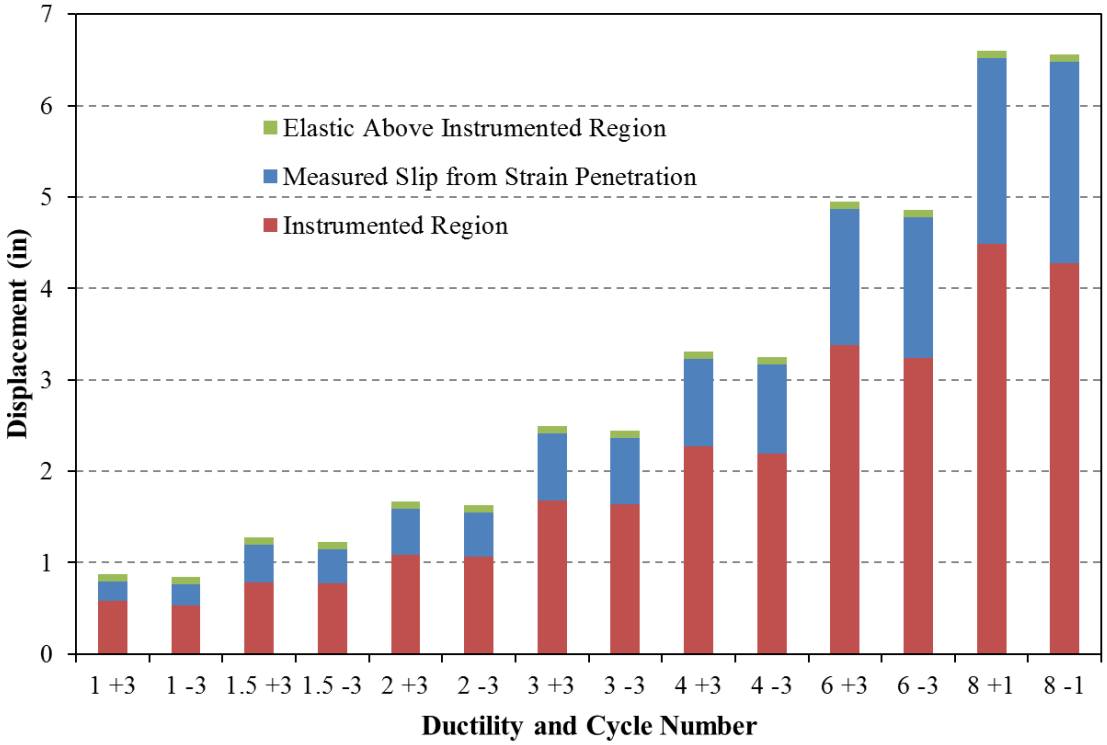

Figure 2-300. Test 16 – Optotrak Integrated Deformation Components

2.2.5. Test 17 – Chile 1985 Earthquake and Cyclic Aftershock Load History

Table 2-16. Results Summary for Test 17 – Chile 1985 Earthquake Load History

LOAD HISTORY: Chile 1985 Earthquake Load History

VALUES OF INTEREST:

Concrete Compressive Strength:	$f_c' = 7590psi$
Axial Load:	$P = 170kips$
Analytical First Yield Force:	$F_y' = 47.5kips$
Experimental First Yield Displacement:	$\Delta_y' = 0.62"$ *From Test 16
Analytical Nominal Moment Capacity:	$M_n = 509.2kip * ft$
Equivalent Yield Displacement:	$\Delta_y = 0.83"$
Maximum Lateral Force:	$72.0kips$
Maximum Lateral Displacement:	$\mu_{9.0}^{32.76\,sec} = 7.49"$
Failure Mode:	No significant damage from earthquake.

DAMAGE OBSERVATIONS: (Drift %) [Displacement Ductility, μ_Δ]

First Cracking North:	During cycle to $\mu_{1.0}^{10.50\,sec} = 0.84"$
First Cracking South:	During cycle to $\mu_{-0.6}^{10.29\,sec} = -0.49"$
Cover Concrete Crushing North:	$\mu_{-1.9}^{16.27\,sec} = -1.60"$
Cover Concrete Crushing South:	$\mu_{2.0}^{15.32\,sec} = 1.67"$
Transverse Steel Yield North:	At $-4.02"$ otwt $\mu_{-5.4}^{18.52\,sec} = -4.49"$
Transverse Steel Yield South:	At 4.5" otwt $\mu_{9.0}^{32.76\,sec} = 7.49"$

*$\mu_{9.0}^{32.76\,sec} = 7.49"$ represents a push cycle 32.76 seconds into the earthquake load history which reached a peak displacement of 7.49” and a displacement ductility of 9.0

Table 2-17. Results Summary for Test 17b – Cyclic Aftershock Load History

LOAD HISTORY: Symmetric Three Cycle Set Aftershock after Chile 1985

DAMAGE OBSERVATIONS: (Drift %) [Displacement Ductility, μ_Δ]

Longitudinal Bar Buckling North:	Reversal from $\mu_6^{+2} = 4.99"$
Longitudinal Bar Buckling South:	Reversal from $\mu_6^{-2} = -5.00"$
Failure Mode:	Specimen Saved as a Repair Candidate after Each Extreme Fiber Longitudinal Bar Buckled

*$\mu_6^{+2} = 4.99"$ represents the second push cycle of displacement ductility six which reached a peak displacement of 4.99”

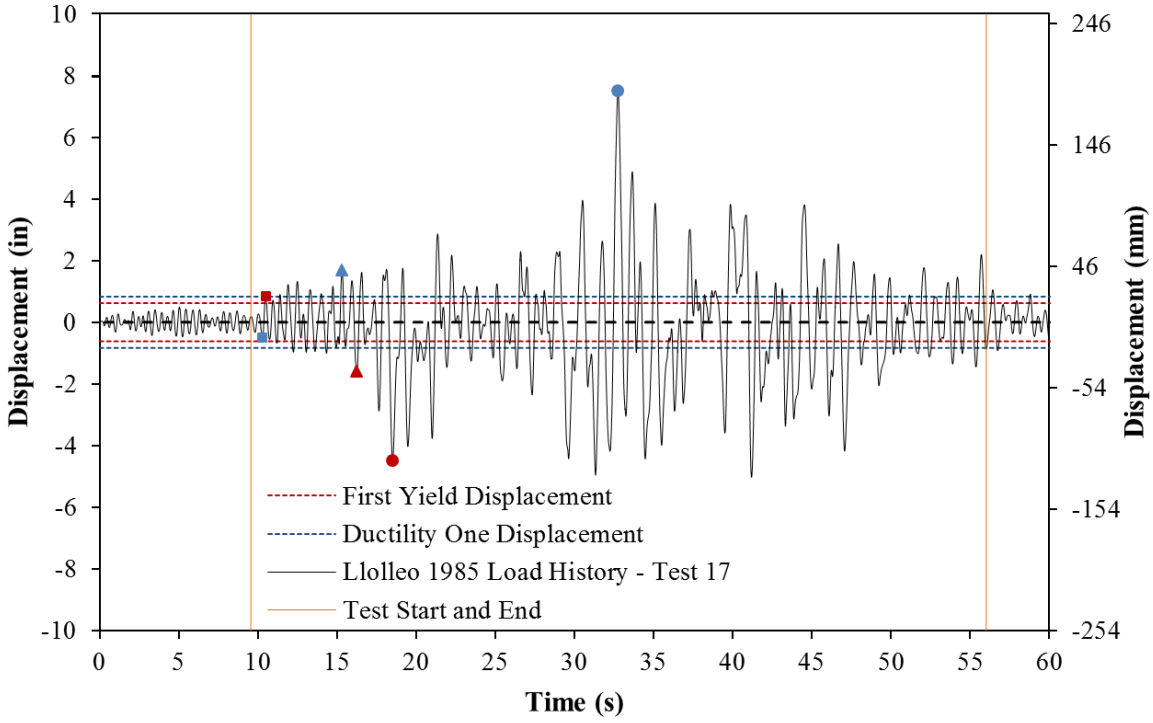

Figure 2-301. Test 17 – Llolleo Chile 1985 Earthquake Load History

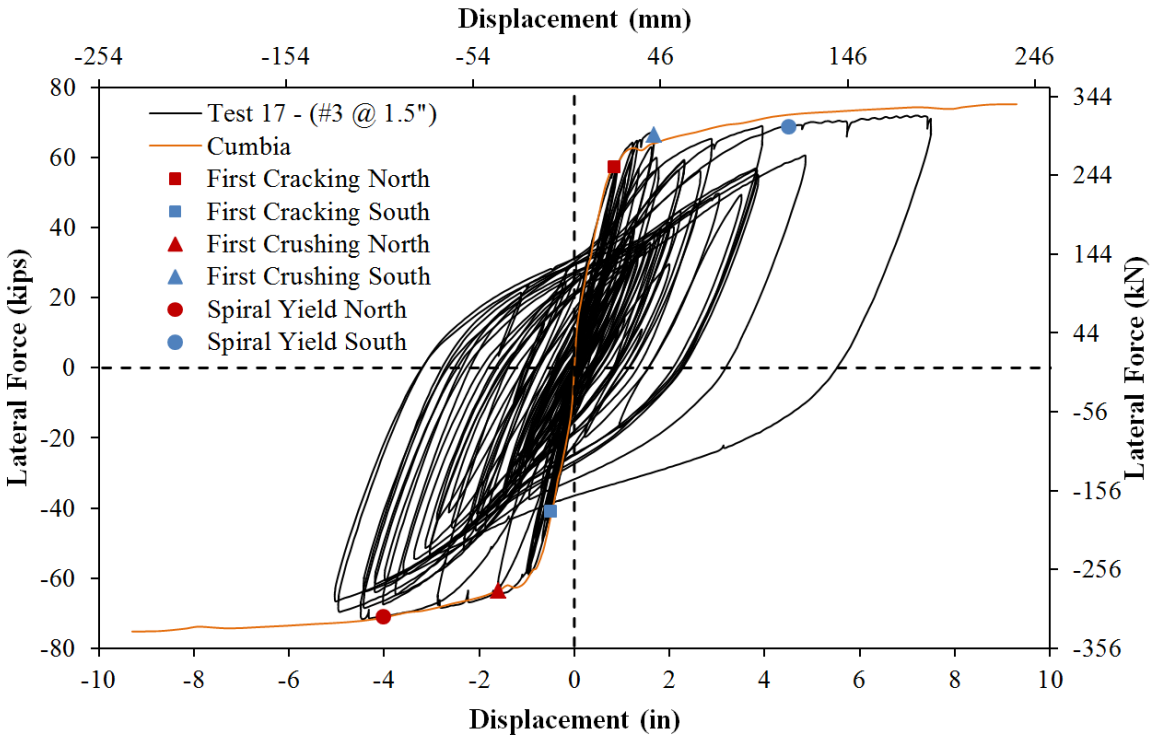

Figure 2-302. Test 17 – Lateral Force vs. Top Column Displacement Hysteretic Response

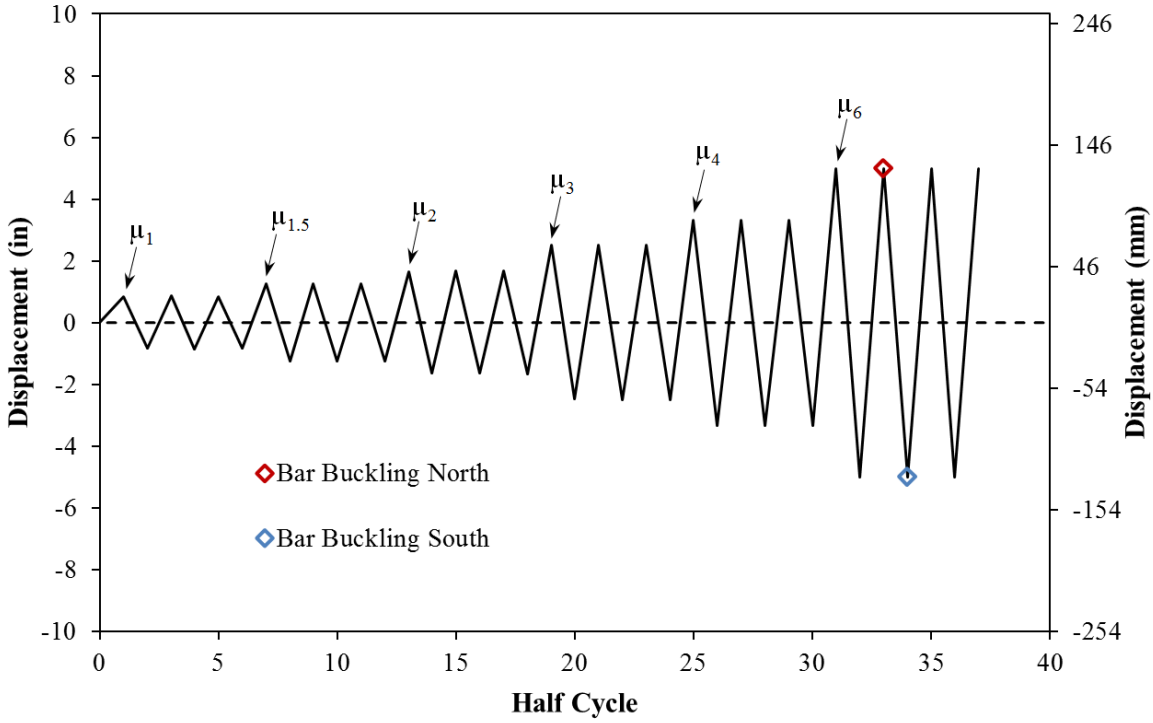

Figure 2-303. Test 17b – Symmetric Three Cycle Set Aftershock Load History

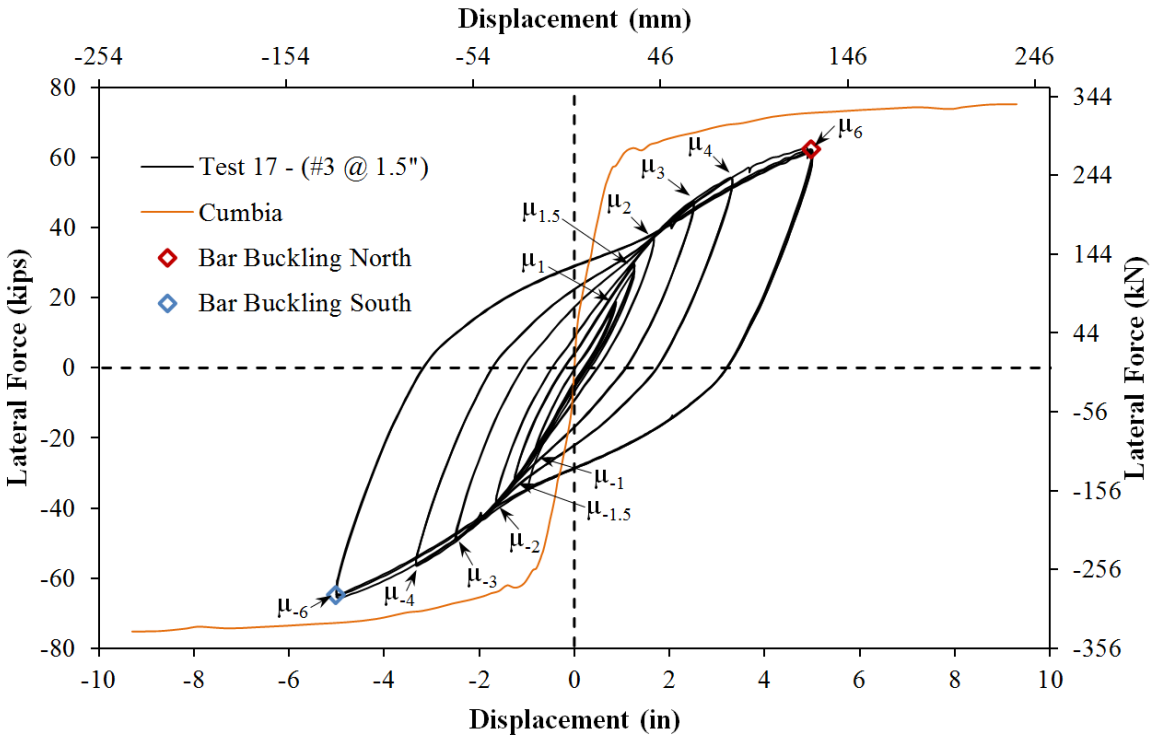

Figure 2-304. Test 17b – Lateral Force vs. Top Column Displacement Hysteretic Response

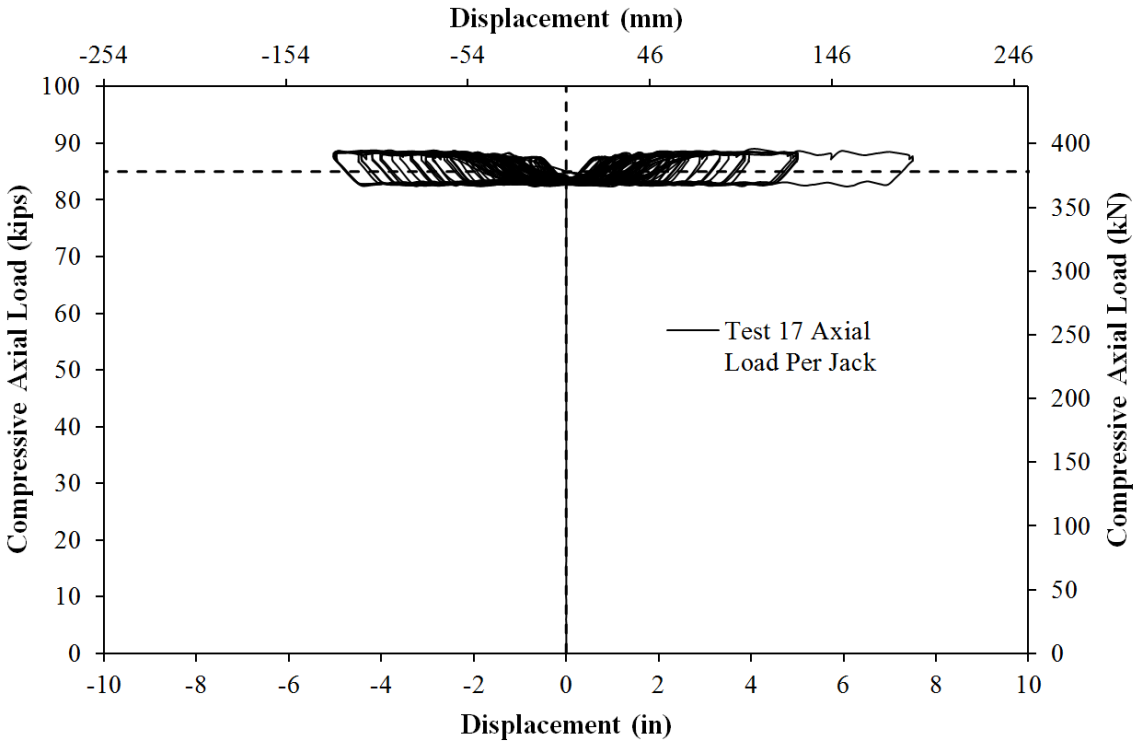

Figure 2-305. Test 17 – Compressive Axial Load from One Jack (Total = 2*Value)

2.2.5.1. Test 17 – Llolleo Chile 1985 Earthquake Load History (#3 @ 1.5"):

A scaled version of the Llolleo 1985 Chile earthquake load history, with a peak displacement ductility of nine, was chosen for Test 17. The top column displacement history, in Figure 2-301, was obtained using numerical analysis in OpenSees with a force-based fiber element to model the column and a zero-length strain penetration element to model the effects of strain penetration. The acceleration input of the Llolleo 1985 Chile earthquake was multiplied by 2.16 to produce a peak displacement ductility of nine. The resulting experimental lateral force vs. top column displacement response for the Llolleo 1985 Chile earthquake load history appears in Figure 2-302. The first yield displacement for Test 16, which contained the same spiral detailing as Test 17, was obtained as an average of the experimental first yield push and pull cycles ($\Delta'_y = 0.62"$). To determine if this first yield displacement is applicable to Test 17, the tensile strain profile at ($\Delta'_y = 0.62"$) for each extreme fiber bar appears in Figure 2-306. At the first yield displacement, the tensile strains in both extreme fiber reinforcing bars reached yield. The equivalent yield displacement, used to determine the displacement ductility levels ($\mu_{\Delta n} = \mathrm{n} * \Delta_y$), was then calculated as $\Delta_y = \Delta'_y(M_n/M'_y) = 0.84"$ for Test 16. The displacement ductility levels for Test 16, see Figure 2-306, are also applicable for Test 17.

Previous Tests 8-12 focused on the effects of load history on reinforcement buckling. For the detailing of Tests 8-12 (#3 @ 2", 1% volumetric ratio), it was found that reinforcement bar buckling occurred during displacement ductility eight of a three cycle set laboratory load history. Subsequent earthquake load history based tests scaled to displacement ductility (Test 8 - Chile 2010, 8.7) and (Test 10 - Chi-Chi 1999, 8.9) did not produce buckling of longitudinal steel. Instead, earthquake load histories scaled to ductility ten (Test 11 - Kobe 1995, 10) and (Test 12 – Japan 2011, 9.9) buckled reinforcing bars. The balanced repeated cycles of increasing ductility of the symmetric three cycle set

load history appear to be more damaging than the load histories produced by historical earthquake records. To buckle reinforcing bars, the earthquake load histories were required to reach larger peak displacement ductility.

For the previous Test 16 (also #3 @ 1.5", 1.3% volumetric ratio), a column with the same transverse steel detailing produced bar buckling during ductility eight of a symmetric three cycle set load history. The Llolleo 1985 Chile load history for Test 17 was scaled to displacement ductility nine to further evaluate the effect of load history on accumulated strains in the longitudinal and transverse steel. Based on previous test observations, an earthquake load history scaled to ductility nine is not expected to produce bar buckling. The Llolleo 1985 Chile top column displacement history contains a large number of inelastic reversals of generally high amplitude both before and after the peak displacement. The push direction of loading is dominated by a single large push cycle to ductility nine with many smaller reversals which range between ductility four and six. In the opposing direction of loading, there are a large number of reversals within the range of ductility four to six which appear both before and after the peak displacement.

After conclusion of the Llolleo 1985 Chile load history, the specimen had crushed cover concrete and degraded stiffness, but the longitudinal steel had not visibly buckled. The state of the specimen resembled Tests 8 and 10 where the reinforcement did not visibly buckle during the earthquake load history. Specimens 8, 10, and now 17 were subjected to a symmetric three cycle set aftershock to study the effect of degraded stiffness and strain accumulation on post-earthquake performance during a controlled load history. The displacement history and hysteretic response for the symmetric three cycle set aftershocks study for Test 17 appear in Figure 2-303 and Figure 2-304 respectively. Visible bar buckling was observed on both sides of the specimen during ductility six of the cyclic aftershock study of Test 17b.

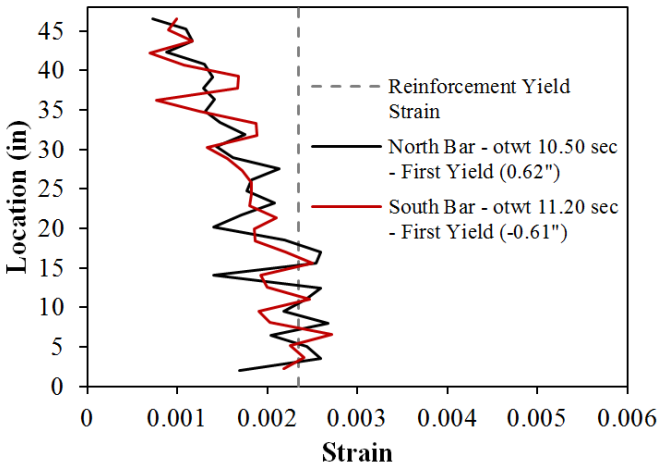

Analytical Fy'	46.80	kips
Experimental Δy'	0.62	in
Analytical My'	374.44	kip-ft
Analytical Mn	503.19	kip-ft
μ1	0.83	in
μ1.5	1.25	in
μ2	1.66	in
μ3	2.50	in
μ4	3.33	in
μ6	4.99	in
μ8	6.65	in
μ10	8.32	in
μ12	9.98	in

Figure 2-306. Test 17 – (Left) Tensile Strain Profiles at the First Yield Displacement of Test 16 and (Right) Displacement Ductility Levels from Test 16 (Also Apply for Test 17)

2.2.5.2. Test 17 – Llolleo Chile 1985 Earthquake (#3 @ 1.5") Experimental Observations:

The Llolleo 1985 Chile earthquake load history begins with a series of cycles below the first yield displacement, followed by cycles below ductility two as shown in Figure 2-301. Since the initial elastic cycles are not expected to affect the relationship between strain and displacement during later inelastic cycles, they were excluded from the experimental load history to save time. Crack widths on the North side of the specimen reached 0.45mm at approximate 6" spacing during ($\mu_{1.0}^{10.50\,sec}$ =

0.84"), as shown in the left photo of Figure 2-307. The format for the cycle naming system is as follows: ($\mu_{1.0}^{10.50\,sec} = 0.84$") represents the peak of the push cycle 10.50 seconds into the Llolleo earthquake load history which reached a displacement of 0.84" and a displacement ductility of 1.0. During ($\mu_{1.5}^{11.91\,sec} = 1.22$"), the largest crack width on the North side of the specimen increased to 1mm. Crack widths on the South side of the specimen reached 0.5mm in width and approximate 6" spacing at ($\mu_{-1.2}^{12.25\,sec} = -0.96$"), see the right two photos of Figure 2-307.

Visible flaking of cover concrete, which precedes crushing, was observed on the South side of the specimen during ($\mu_{1.6}^{12.50\,sec} = 1.32$"), as shown in the left photo of Figure 2-308. Cover concrete crushing over the lowest 5" of the South side of the column occurred during ($\mu_{2.0}^{15.32\,sec} = 1.67$"), see the right photo of Figure 2-308. Also during this cycle, crack widths on the North side of the specimen reached 1.5mm at approximate 6" spacing. Cover concrete crushing on the North side of the specimen over 3.5" occurred during ($\mu_{-1.9}^{16.27\,sec} = -1.60$"), see the left photo of Figure 2-309. The extent of crushing on the North side increased to 18.5" above the footing during ($\mu_{-3.5}^{17.66\,sec} = -2.87$"), as shown in the right photo of Figure 2-309. The extent of crushing on the North side of the specimen reached 24" above the footing during ($\mu_{-5.4}^{18.52\,sec} = -4.49$"), see the left photo of Figure 2-310. The extent of crushing on the South side of the specimen reached 21.5" above the footing during ($\mu_{3.5}^{21.36\,sec} = 2.89$"). The crack distribution on the South and back sides of the specimen appear in the middle and right photos of Figure 2-310.

During ($\mu_{4.7}^{30.52\,sec} = 3.95$") and ($\mu_{-6.0}^{31.34\,sec} = -4.96$") crushing on the South and North sides of the specimen did not increase in height, but rather widened to previously uncrushed areas around the column base as shown in Figure 2-311. At the peak cycle of the load history ($\mu_{9.0}^{32.76\,sec} = 7.49$"), the extent of crushing on the South side of the specimen reached 25" above the footing. Photos of each side of the specimen during the peak cycle of the Llolleo earthquake load history appear in Figure 2-312. The remainder of the earthquake load history contained a large number of cycles below ductility six. Visible bar buckling was not observed during the remainder of the load history.

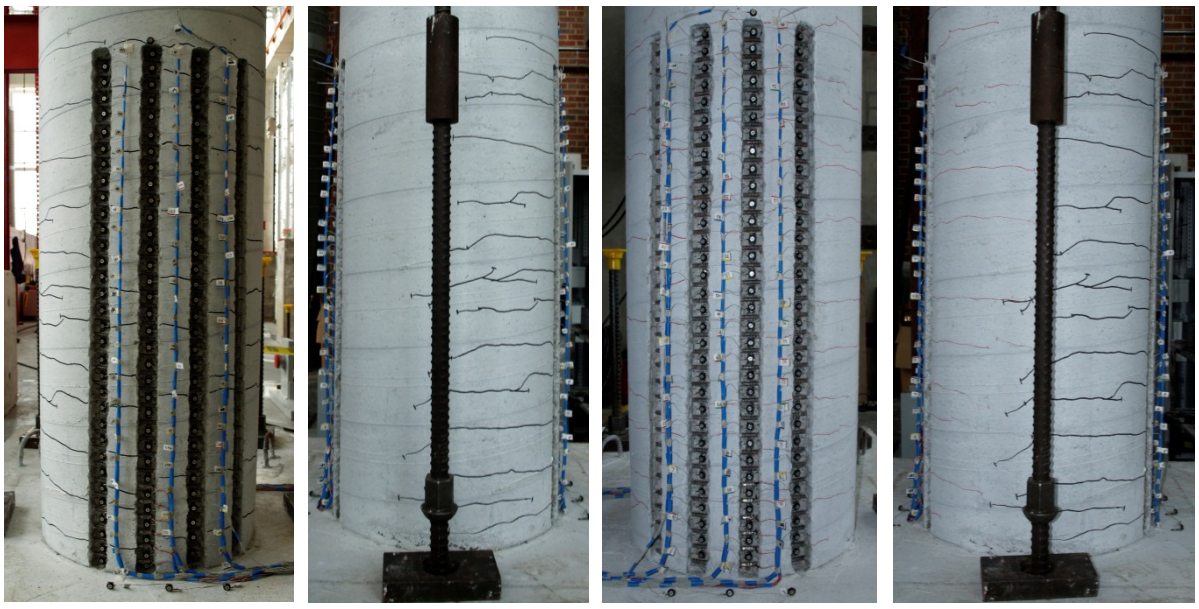

Figure 2-307. Test 17 – (Left) North Crack Distribution during ($\mu_{1.0}^{10.50\,sec} = 0.84$"), (Mid-Left) Back Side during ($\mu_{1.5}^{11.91\,sec} = 1.22$"), (Mid-Right) South Side during ($\mu_{-1.2}^{12.25\,sec} = -0.96$"), and (Right) Back Side during ($\mu_{-1.2}^{12.25\,sec} = -0.96$")

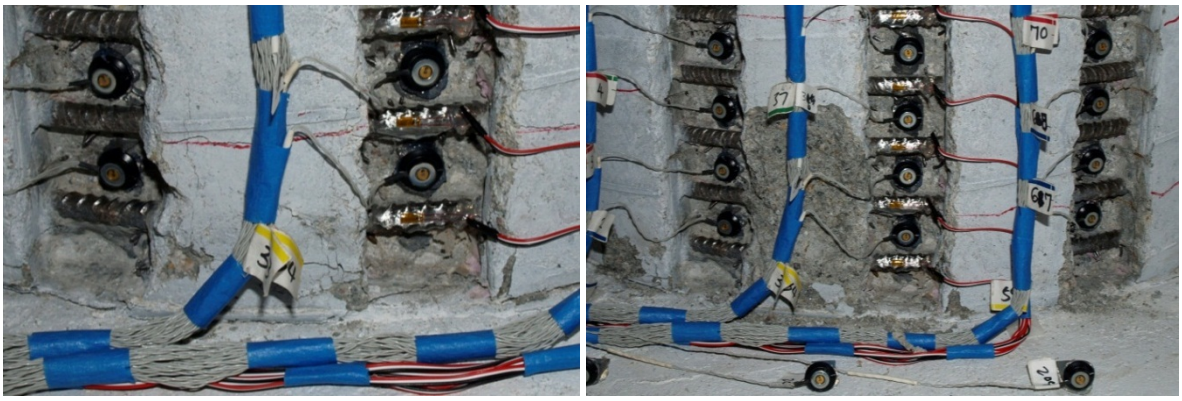

Figure 2-308. Test 17 – (Left) Cover Concrete Flaking Preceding Crushing on the South Side during ($\mu_{1.6}^{12.50\,sec} = 1.32$"), (Right) Crushing on the South Side during ($\mu_{2.0}^{15.32\,sec} = 1.67$")

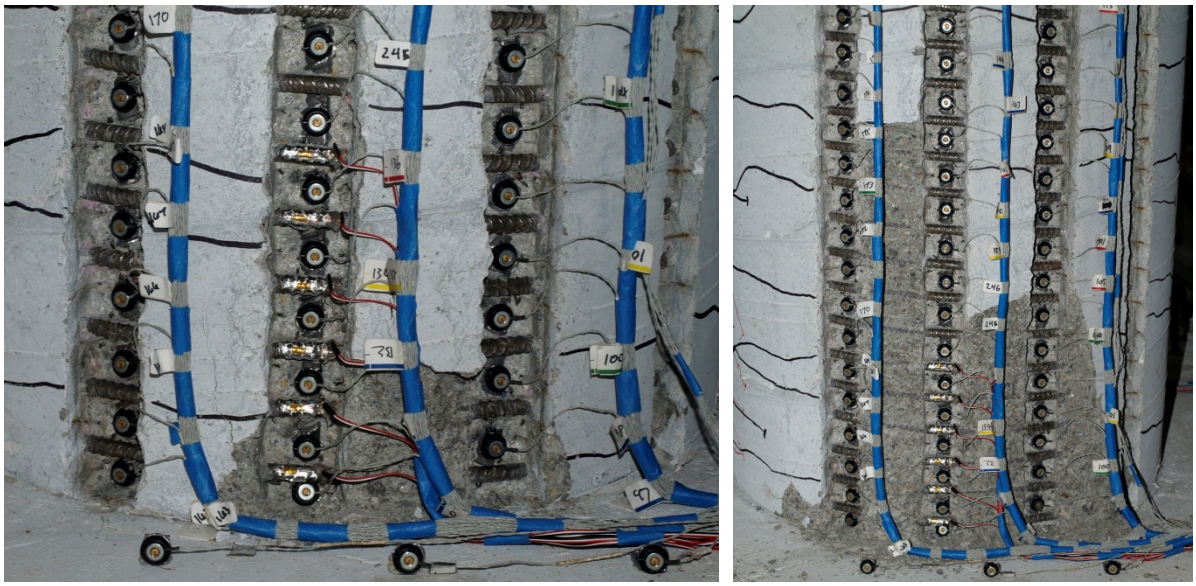

Figure 2-309. Test 17 – (Left) North Cover Concrete Crushing during ($\mu_{-1.9}^{16.27\,sec} = -1.60$") and (Right) Extent of Crushing on the North Side during ($\mu_{-3.5}^{17.66\,sec} = -2.87$")

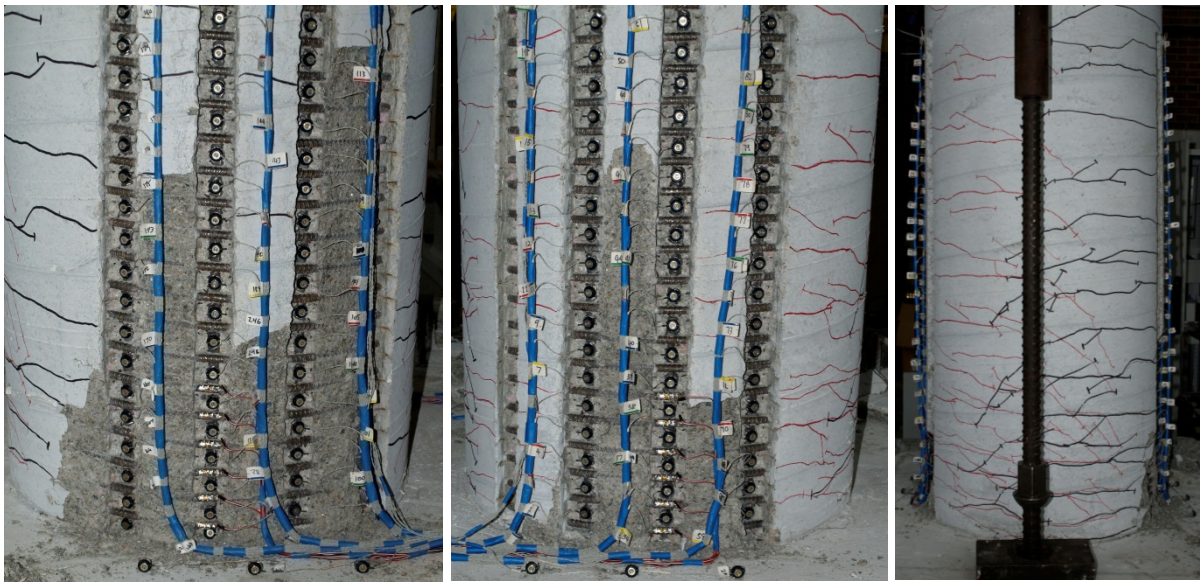

Figure 2-310. Test 17 – (Left) Extent of Crushing on the North Side during ($\mu_{-5.4}^{18.52\ sec} = -4.49$"), (Middle) Extent of Crushing on the South Side during ($\mu_{3.5}^{21.36\ sec} = 2.89$"), and (Right) Crack Distribution on the Back Side during ($\mu_{3.5}^{21.36\ sec} = 2.89$")

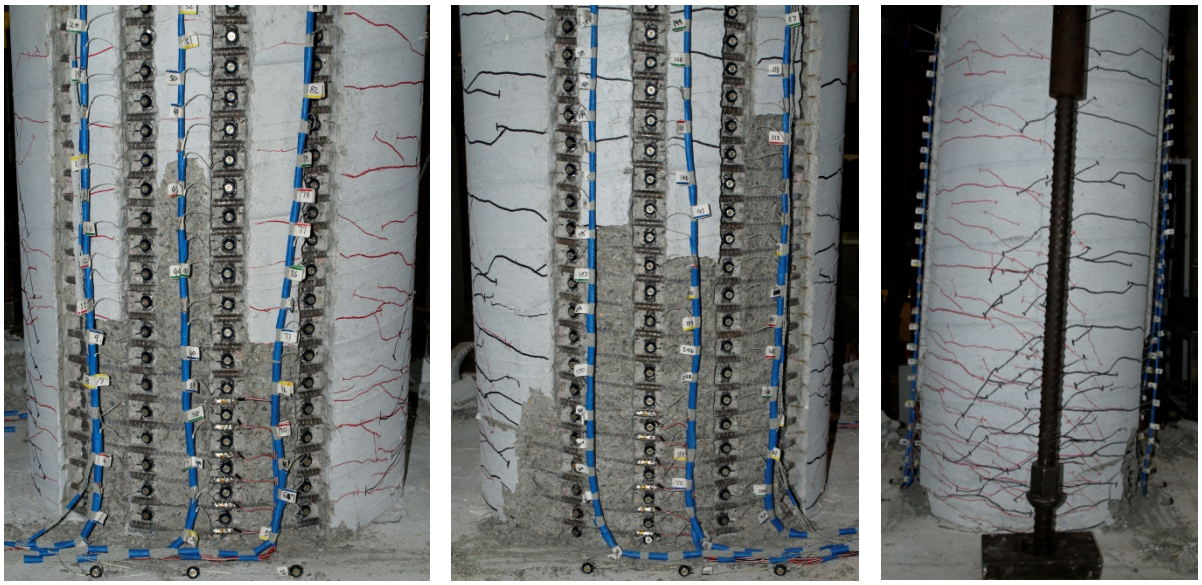

Figure 2-311. Test 17 – (Left) Extent of Crushing on the South during ($\mu_{4.7}^{30.52\ sec} = 3.95$"), (Middle) Crushing on the North Side during ($\mu_{-6.0}^{31.34\ sec} = -4.96$"), and (Right) Crack Distribution on the Back Side during ($\mu_{-6.0}^{31.34\ sec} = -4.96$")

Figure 2-312. Test 17 – (Left, Middle, and Right) South, Back, and North Side of the Specimen during ($\mu_{9.0}^{32.76\,sec} = 7.49"$) Respectively

2.2.5.3. Test 17b – Cyclic Aftershock Load History (#3 @ 1.5") Experimental Observations:

Since bar buckling did not occur during the earthquake record, a symmetric three cycle set load history was conducted to determine the effect of degraded stiffness and strain accumulation on column behavior. The displacement ductility levels for the cyclic aftershock matched those from the symmetric three cycle set load history of Test 16. No notable damage was observed during cycles from displacement ductility one to four. The extreme fiber reinforcement remained visibly straight without noticeable outward deformation. Visible buckling of the North extreme fiber bar N3 occurred during ($\mu_6^{-2} = -5.00"$), as shown in Figure 2-313. Visible outward deformation was observed 3.5" above the footing on bar N3 as well as slight rotation of LEDs above and below where the bar begins to straighten back out.

During the subsequent push cycle to ($\mu_6^{+3} = 5.00"$), the South extreme fiber bar S3 visibly buckled as shown in Figure 2-314. Outward deformation was observed 8" above the footing over the highest transverse steel layer instrumented with a strain gage. During the next pull cycle to ($\mu_6^{-3} = -5.00"$), the deformation in buckled bar N3 increased as shown in the left photo of Figure 2-315. Permanent deformation in spiral layers overlaying bar N3 was observed during ($\mu_6^{+4} = 5.00"$), see the middle photo of Figure 2-315. During this cycle, the outward deformation in buckled bar S3 increased as shown in the right photo of Figure 2-315. A fourth cycle at ductility six was conducted to verify that the outward deformation in bar S3 would increase over the same location giving a stronger indication of observable bar buckling during the previous cycle. After this cycle, the test was concluded with buckling of each extreme fiber bar, but without any strength loss or rupture of reinforcement. The specimen was saved as a repair candidate for a separate research project.

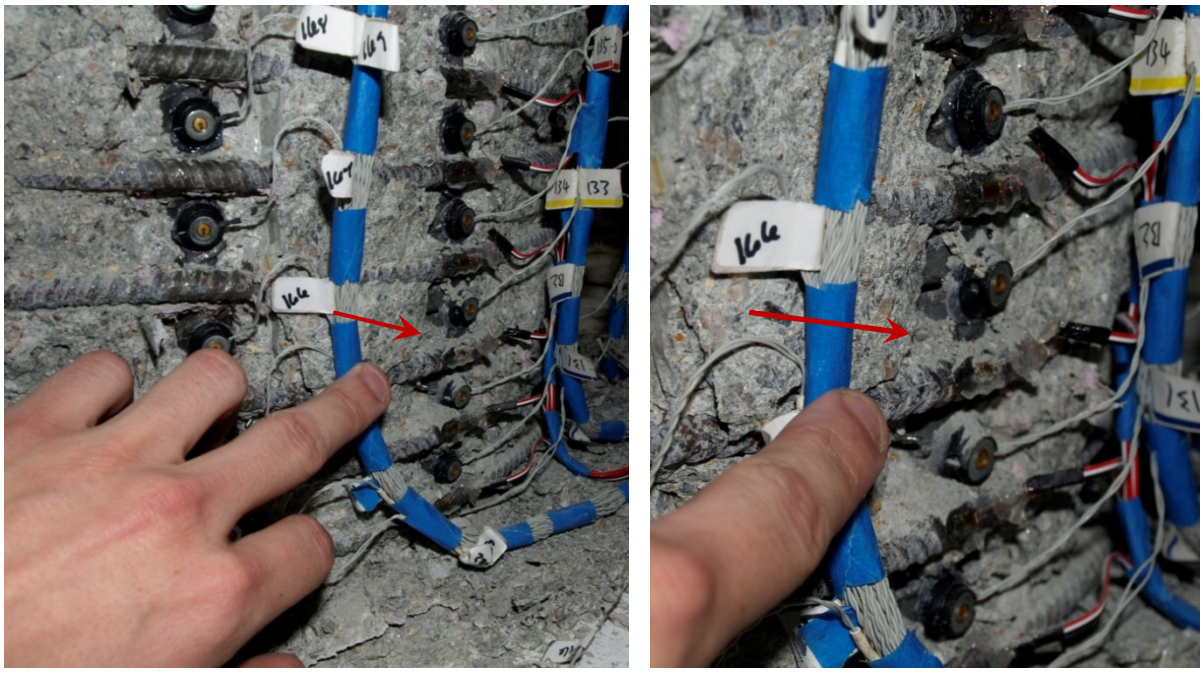

Figure 2-313. Test 17 – (Left and Right) Buckling of North Reinforcing Bar N3 during ($\mu_6^{-2} = -5.00$") of the Cyclic Aftershock Load History

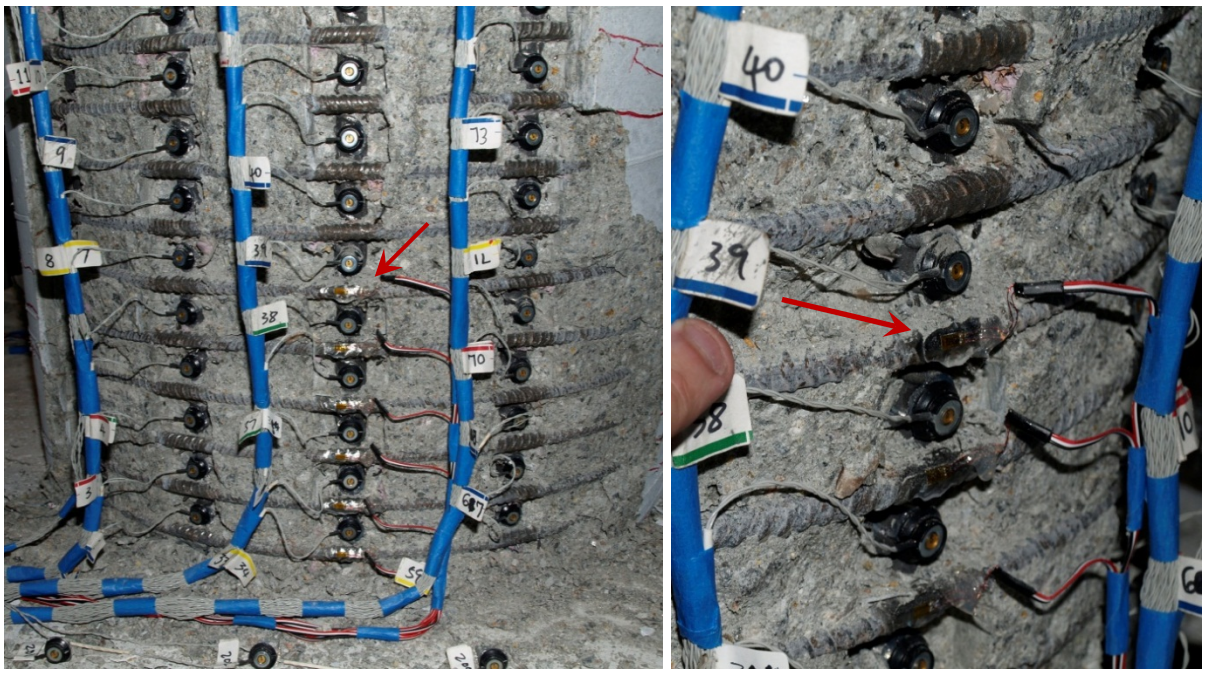

Figure 2-314. Test 17 – (Left and Right) Buckling of South Reinforcing Bar S3 during ($\mu_6^{+3} = 5.00$") of the Cyclic Aftershock

Figure 2-315. Test 17 – (Left) Additional Deformation in Buckled Bar N3 during ($\mu_6^{-3} = -5.00$"), (Middle) Permanent Deformation in Spiral Layers over Buckled Region of Bar N3 during ($\mu_6^{+4} = 5.00$"), and (Right) Additional Deformation in Buckled Bar S3 during ($\mu_6^{+4} = 5.00$")

2.2.5.4. Test 17 – Llolleo Chile 1985 Earthquake (#3 @ 1.5") Strain Data:

North Reinforcement:

Since the peaks of cycles during the earthquake load history do not align with the ductility levels of a traditional three cycle set load history, intermediate cycles along the backbone curve were selected for strain data analysis, see Figure 2-316. Extreme fiber vertical strain profiles for push and pull cycles appear in Figure 2-317 and Figure 2-318 respectively. A peak tensile strain of 0.055, located 3.56" above footing, was measured for Bar N3 during ($\mu_{9.0}^{32.76\,sec} = 7.49$"). The relationship between tensile strain and displacement for this gage length appears in Figure 2-321. Each line represents a single push cycle which began with the column at zero displacement and ended at the peak during a continuous push cycle. The solid line contains data during the push cycle loading up to the peak displacement and the dashed line represents the subsequent reversal of load. The peak tensile strain of 0.055 was not sufficient to produce visible bar buckling after reversal of load. Similar to previous tests, the moment curvature prediction for the relationship between strain and displacement begins to over predict the tensile strains at higher displacements at an increasing rate. The largest compressive strain of -0.023 for bar N3, located 2.05" above the footing, was measured during ($\mu_{-6.0}^{41.20\,\mathrm{sec}} = -5.02$"). The relationship between compressive strain and displacement for this gage length appears in Figure 2-325. The recorded strains match the trend predicted by moment curvature analysis through ($\mu_{-3.5}^{17.66\,sec} = -2.87$"), but during later cycles the measured strains are larger than expected.

The transverse steel strains measured over the lowest six spiral layers overlaying the North reinforcement were plotted in Figure 2-320. Even though the peak compressive strains were measured 2.05" and 6.45" above the footing, the layer of transverse steel located 3.6" above the footing went furthest into the inelastic range during the Llolleo load history. The outward buckled region of bar N3 latter formed at this location during the ductility six of the cyclic aftershock, as shown in Figure 2-313. The peak tensile strains for bar N3 were located 3.56" above the footing. As previously mentioned, the residual growth strains measured for this gage were large, as shown in Figure 2-321. One possible explanation for the observations noted above is that measureable outward

deformation occurred over the gage length 3.56” above the footing on bar N3 prior to visible bar buckling. It is not immediately obvious that this occurred because a large amount of growth strain could, perhaps, outweigh future compressive strains during subsequent cycles. Some amount of measureable outward deformation would increase the residual growth strain, increase the demand on the layer of transverse steel overlaying the bar, and agree with the location of visible bar buckling observations during the cyclic aftershock study.

South Reinforcement:

A peak tensile strain of 0.0387 on bar S3 was measured 2.26” above the footing during ($\mu_{-6.0}^{41.20\ \mathrm{sec}} = -5.02"$). The relationship between tensile strain and displacement for this gage length is shown in Figure 2-324. The same comments on the accuracy of the moment curvature prediction for bar N3 also apply to bar S3. A peak compression strain of -0.0392 on bar S3 was measured 9.53” above the footing during ($\mu_{9.0}^{32.76\ sec} = 7.49"$). The measured peak compression strain is 2.2 times the calculated Mander (1988) ultimate concrete compressive strain of -0.0179. The relationship between compressive strain and displacement for the gage length 5.12” above the footing on bar S3 during push cycles appears in Figure 2-322. The measured compressive strains begin to deviate away from the prediction after a displacement ductility of 3.5. The gage length centered 9.53” above the footing with the largest compressive strain during ($\mu_{9.0}^{32.76\ sec} = 7.49"$) appears in Figure 2-323. The relationship between compressive strain and displacement matches well until 5” of displacement during the push cycle to ($\mu_{9.0}^{32.76\ sec} = 7.49"$), when the measured compression strains begin to sharply increase. Closer inspection of the transverse steel strains for spiral layers restraining the South bar during push cycles, in Figure 2-319, provides an explanation for measured increase in compressive strains. The transverse steel layer 8” above the footing first goes inelastic during ductility six, at approximately 5”, during the push cycle to ($\mu_{9.0}^{32.76\ sec} = 7.49"$). It appears that the transverse steel layer entering the inelastic range influenced the relationship between compressive strain and displacement for the gage length 9.53” above the footing.

2.2.5.5. Test 17 – Llolleo Chile 1985 (#3 @ 1.5”) Curvature and Strain Penetration Data:

Vertical curvature profiles are plotted for push and pull cycles in Figure 2-326 and Figure 2-327 respectively. These figures show that plastic curvatures have a linear distribution at higher displacement ductility levels. The dashed lines for each curvature distribution represent a least squared error linear fit to the plastic portion of the measured curvatures. The data points used to create the least squared error lines appear as circle data markers. The target marker on each bar placed closest the footing-column interface can be used to create slip hysteresis and horizontal slip profiles attributable to strain penetration. The slip hysteresis for extreme fiber bars N3 and S3 appear in Figure 2-328 and Figure 2-329 respectively. The peak tensile slip of North extreme fiber bar N3 exceeds 0.45” during displacement ductility nine. If the tensile and compressive slip of all of the instrumented bars is plotted along the cross section depth, the base rotation attributable to strain penetration may be calculated. The slip profiles for push and pull cycles appear in Figure 2-330 and Figure 2-331 respectively. The rotation of the base section can be extracted from the slope of the least squared error line connecting all six measured bar slips. The total displacement could be calculated as the addition of the column flexure, strain penetration, and shear displacement components. The measured string potentiometer displacements from Test 17 were compared to the displacements obtained from curvature diagram integration and slip profile extrapolation to the center of loading in Figure 2-332. The measured and integrated top column displacements match well throughout the entire range of displacements indicating that shear displacements, which were not directly accounted for, must be small and thus negligible.

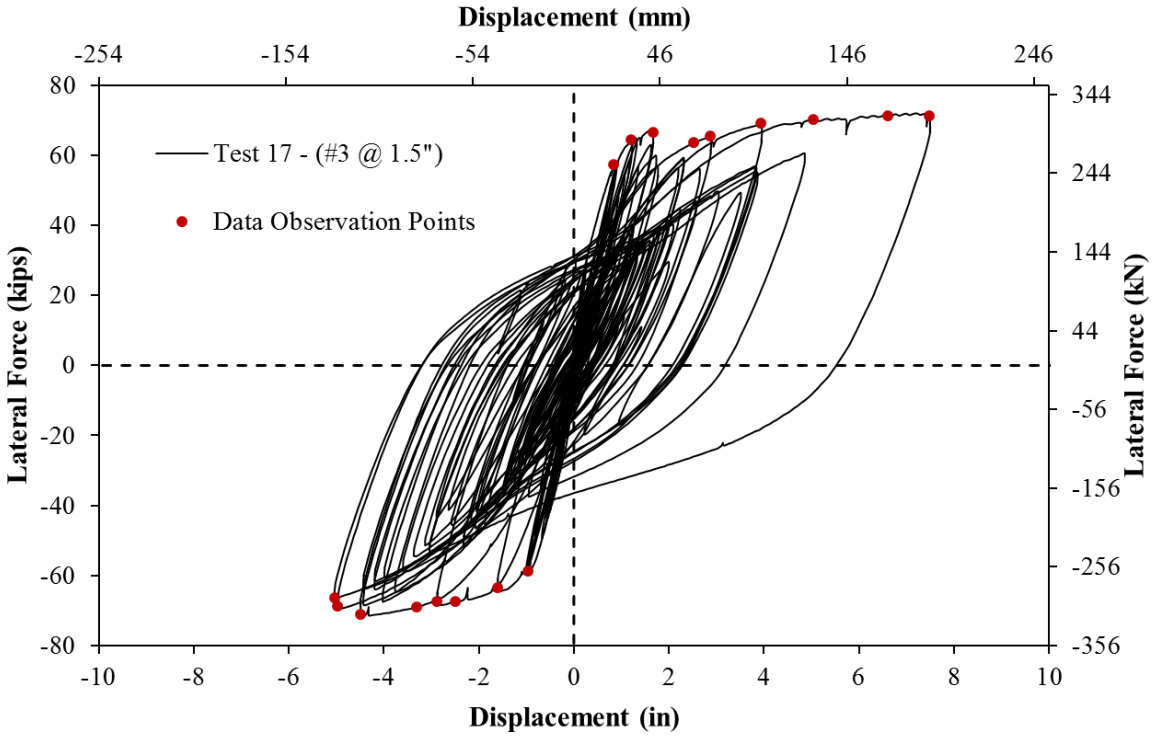

Figure 2-316. Test 17 – Llolleo Earthquake Force vs. Displacement Response with Strain Data Observation Points along the Backbone Curve of Cyclic Response

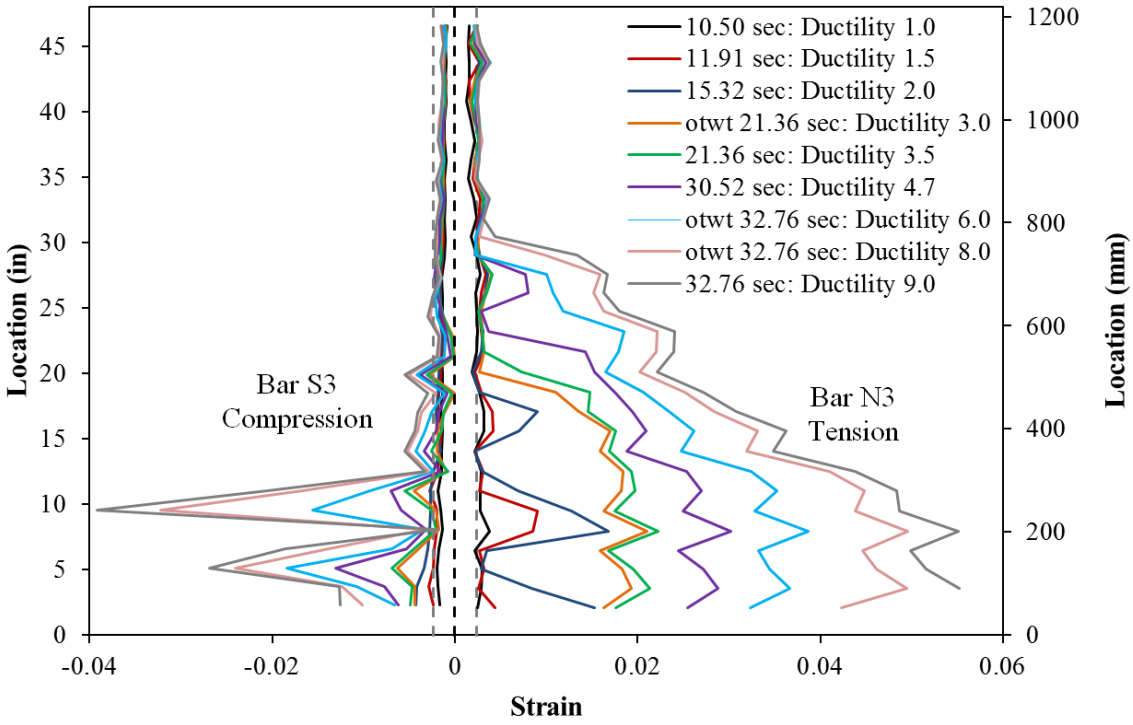

Figure 2-317. Test 17 – Extreme Fiber Vertical Strain Profiles during Push Cycles

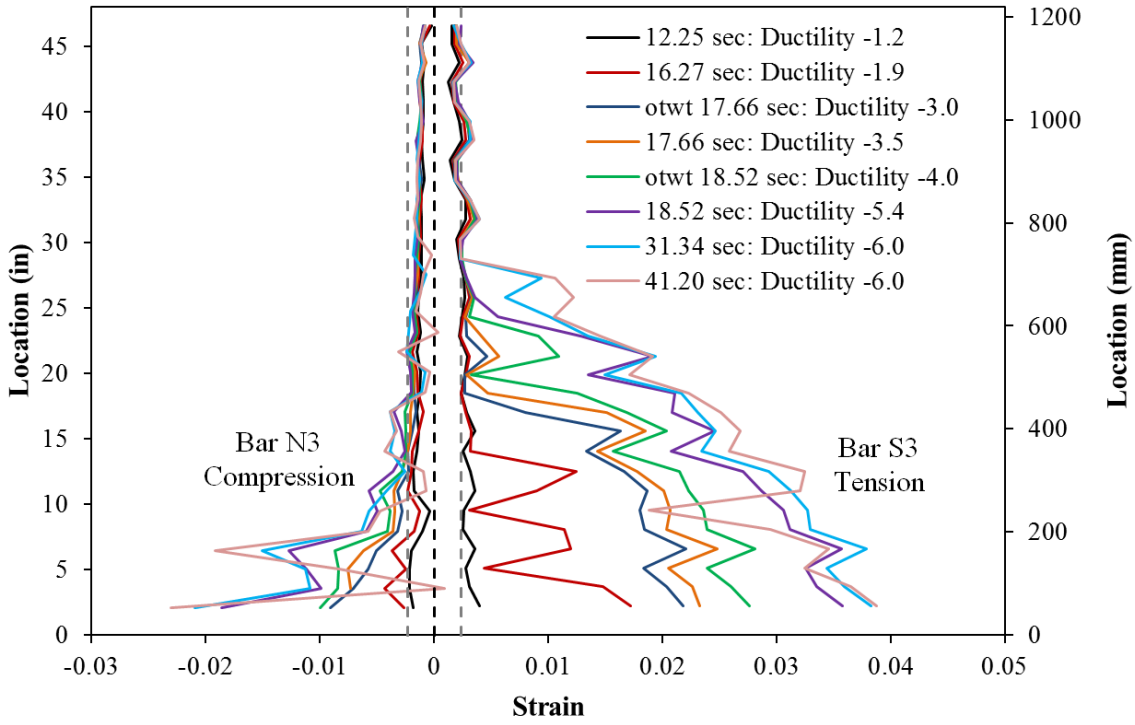

Figure 2-318. Test 17 – Extreme Fiber Vertical Strain Profiles during Pull Cycles

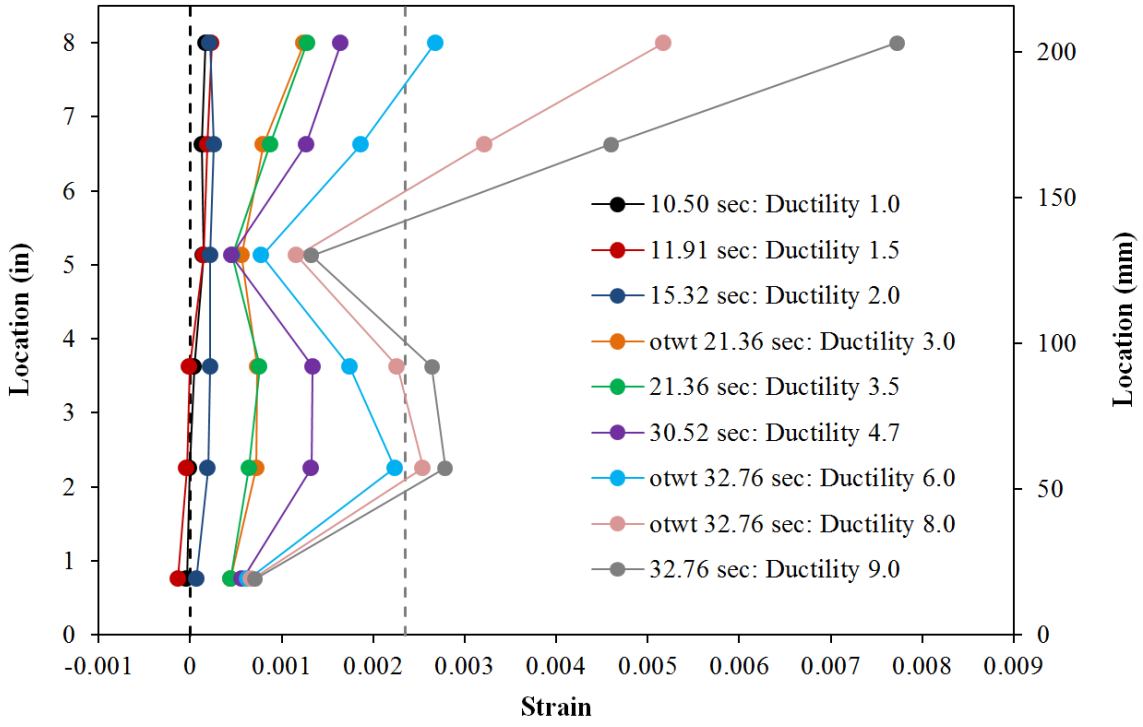

Figure 2-319. Test 17 – Strain in the Lowest Six South Spiral Layers during Push Cycles (Vertical Gray Dashed Line Represents Yield Strain)

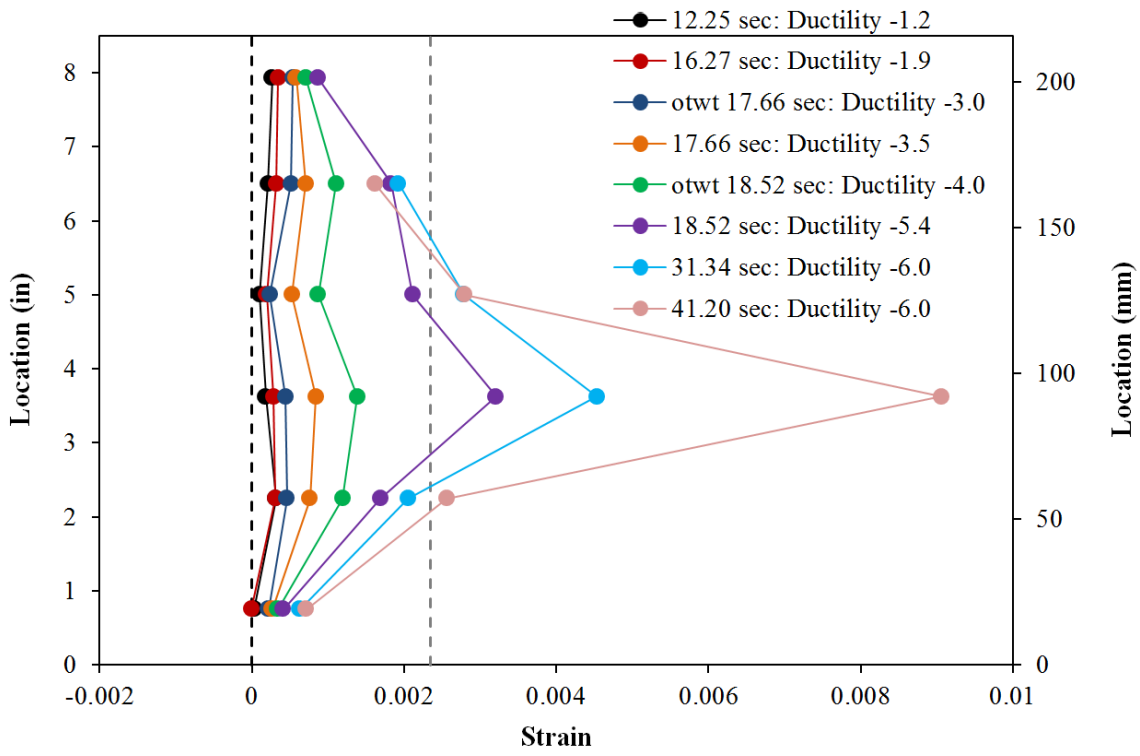

Figure 2-320. Test 17 – Strain in the Lowest Six North Spiral Layers during Pull Cycles

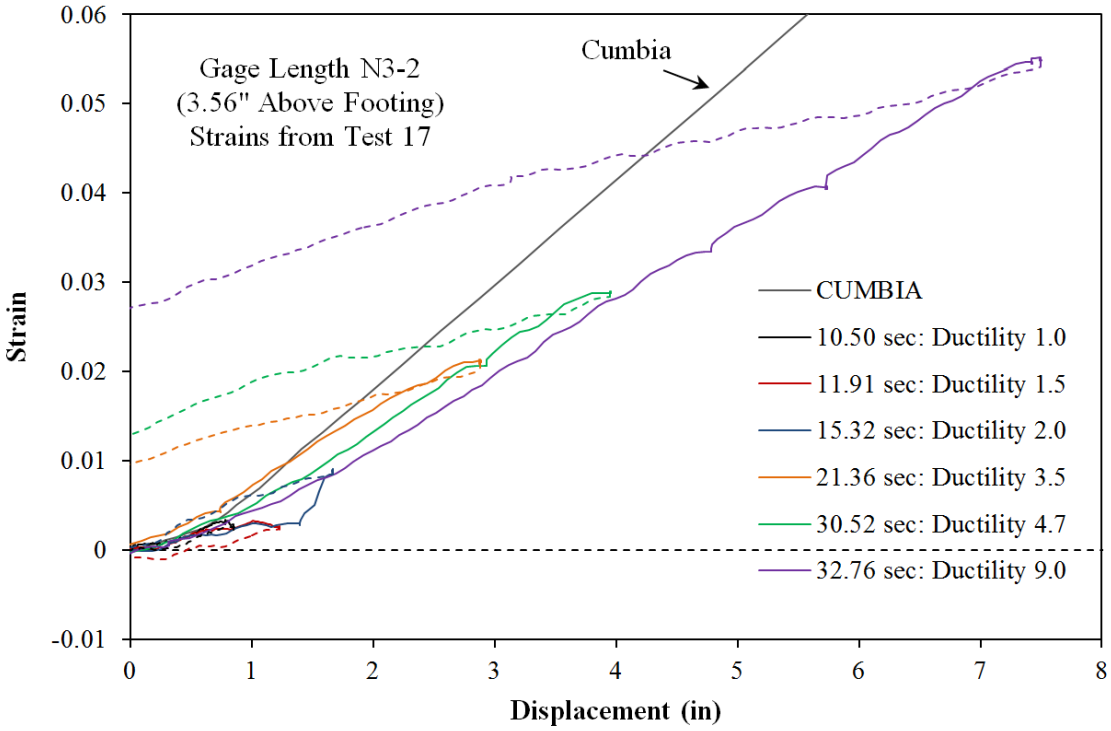

Figure 2-321. Test 17 – Tensile Strain and Disp. during Push Cycles (Bar N3, 3.56” Above)

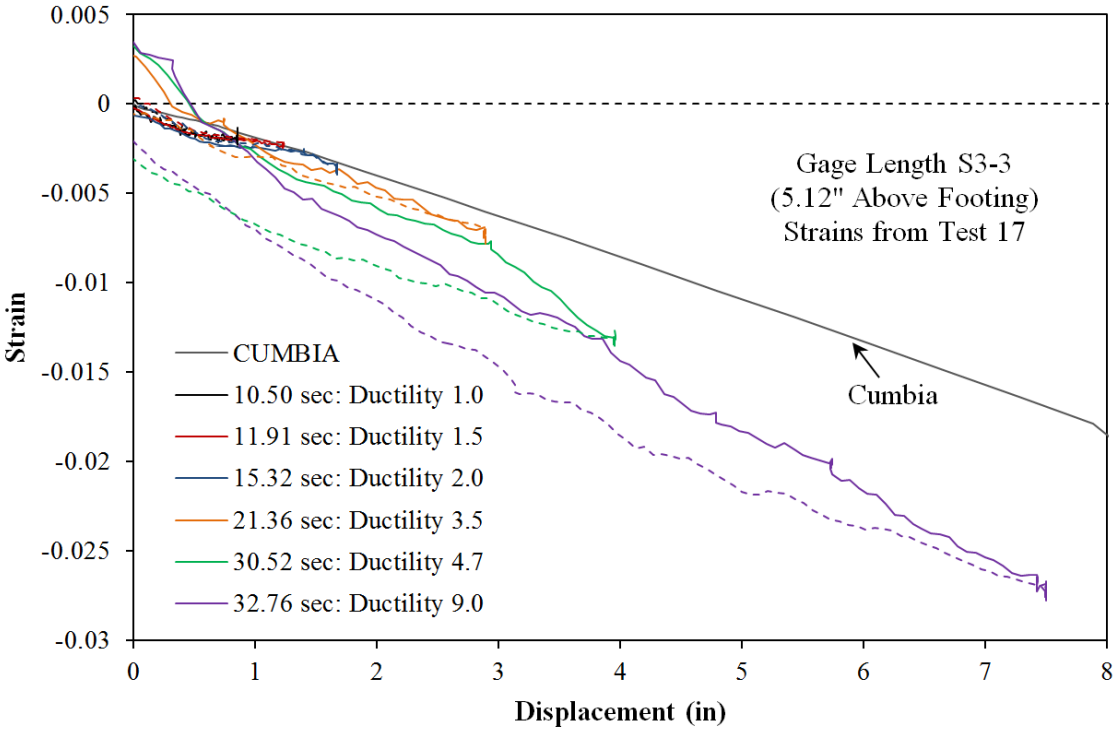

Figure 2-322. Test 17 – Compressive Strain and Disp. for Push Cycles (Bar S3, 5.12” Above)

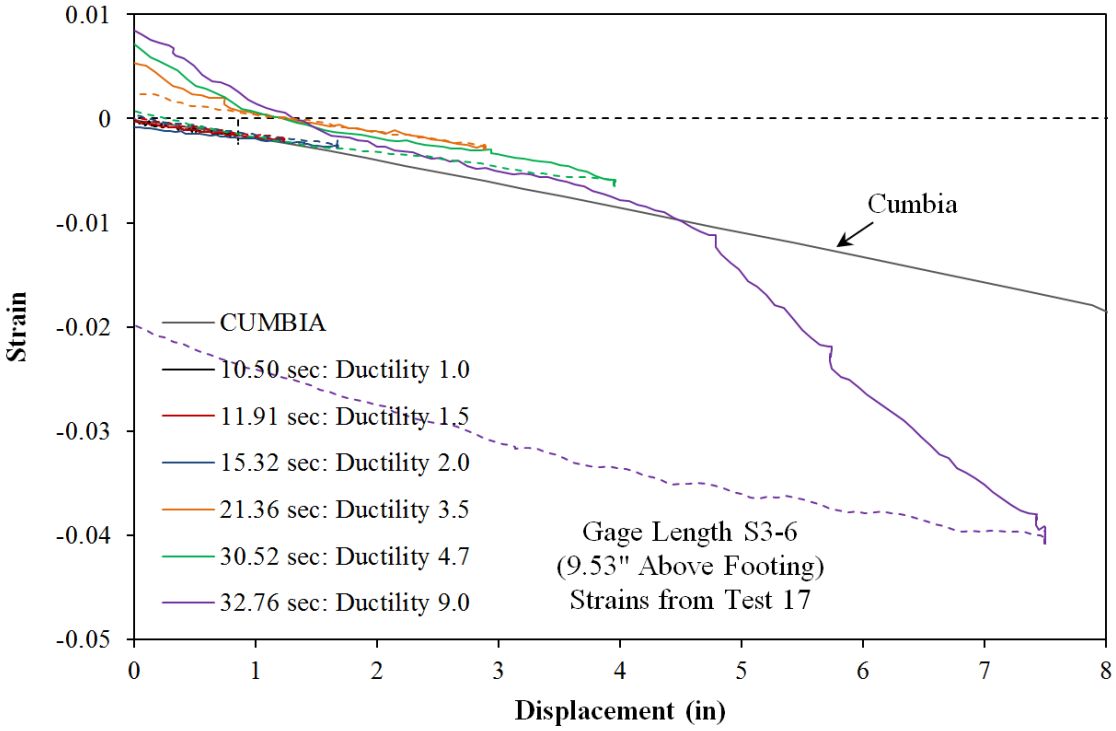

Figure 2-323. Test 17 – Compressive Strain and Disp. for Push Cycles (Bar S3, 9.53” Above)

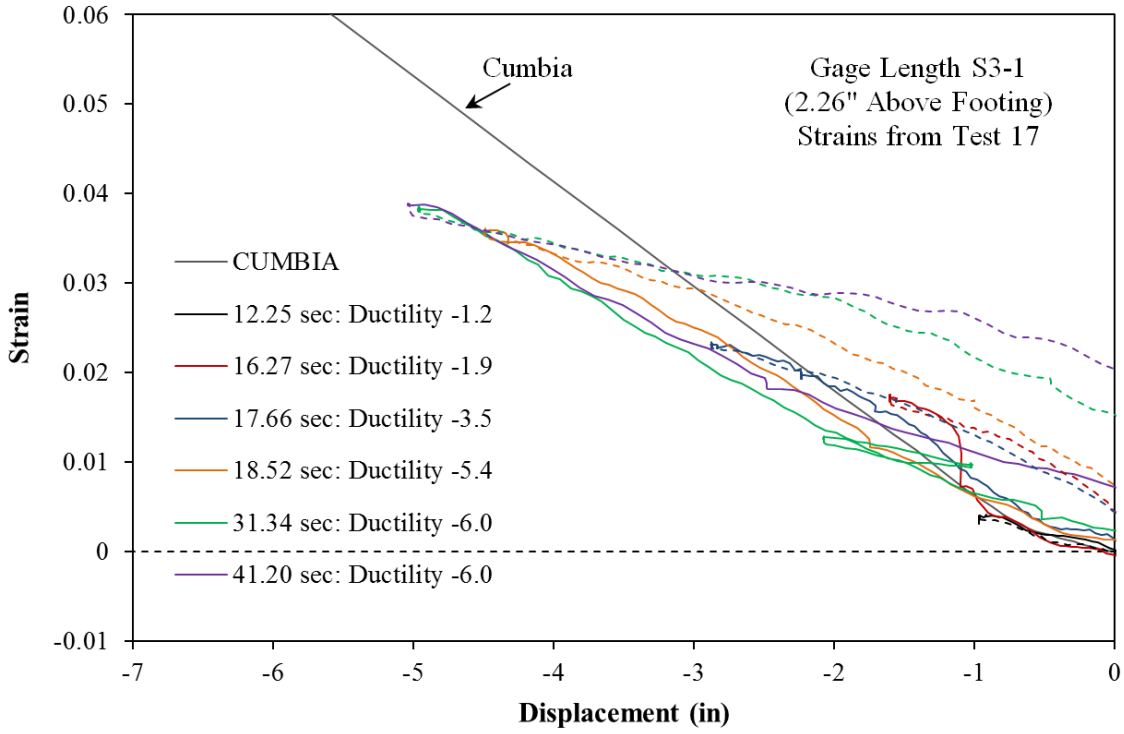

Figure 2-324. Test 17 – Tensile Strain and Disp. for Pull Cycles (Bar S3, 2.26" Above)

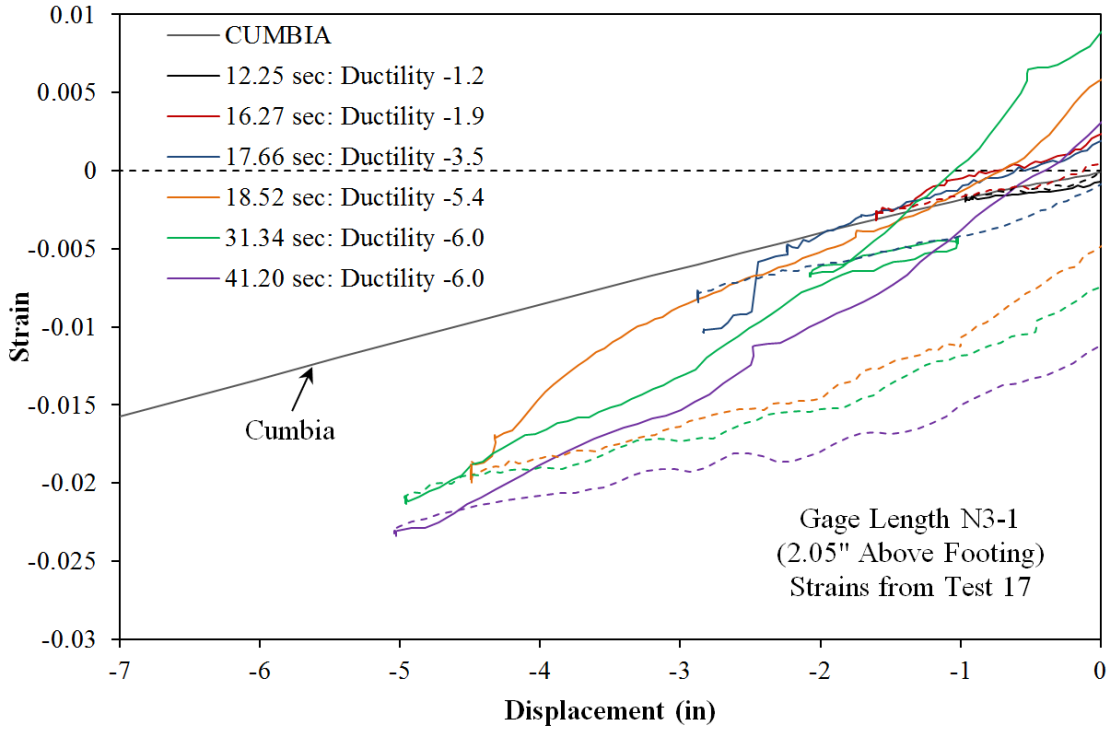

Figure 2-325. Test 17 – Compressive Strain and Disp. for Pull Cycles (Bar N3, 2.05" Above)

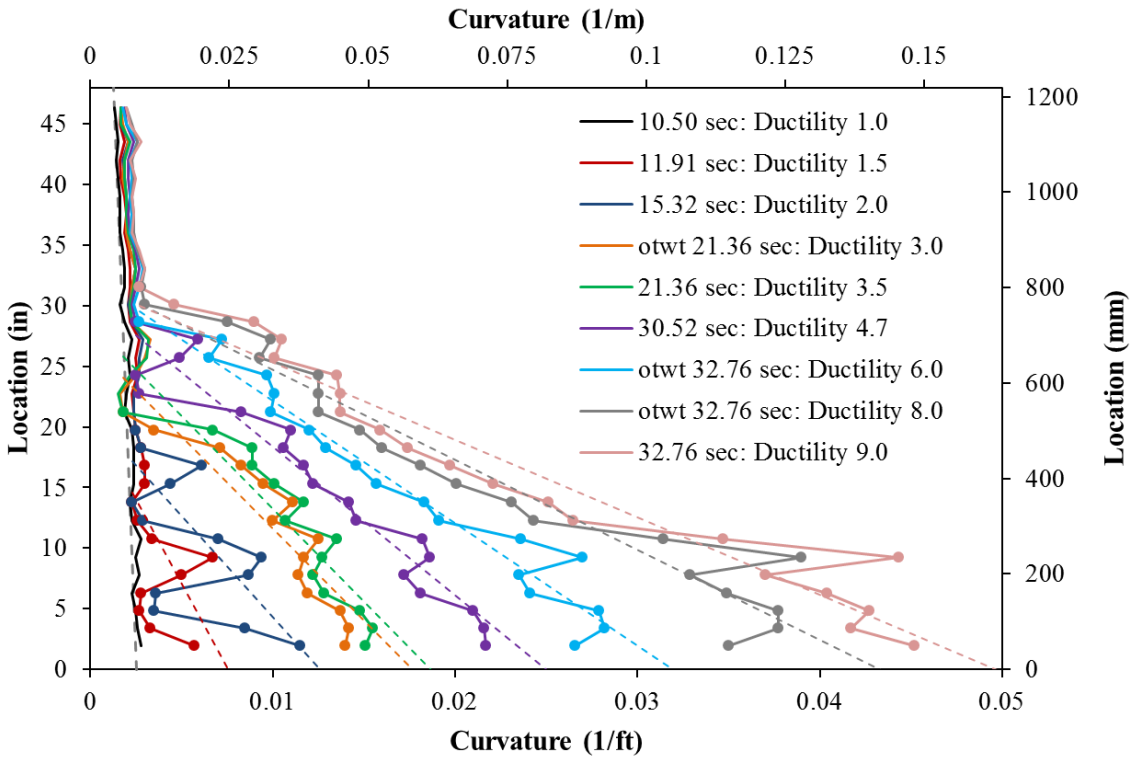

Figure 2-326. Test 17 – Vertical Curvature Profiles during Push Cycles with Linear Plastic Curvature Least Squared Error Lines

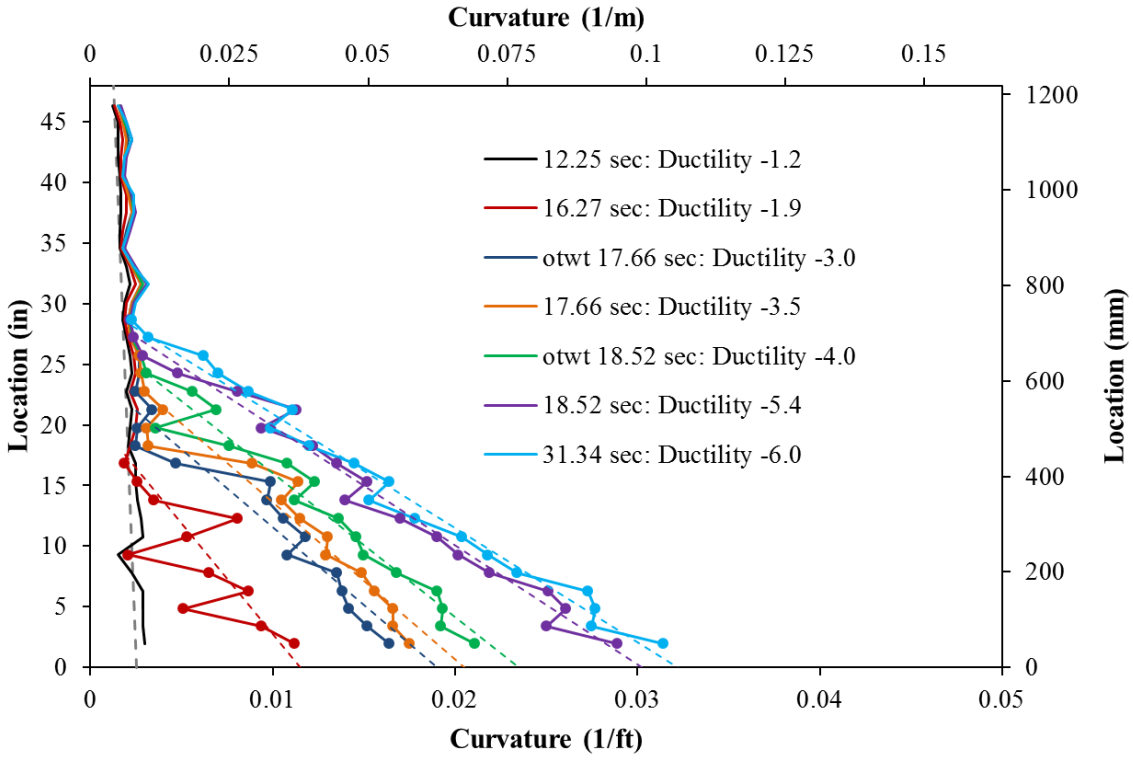

Figure 2-327. Test 17 – Vertical Curvature Profiles during Pull Cycles

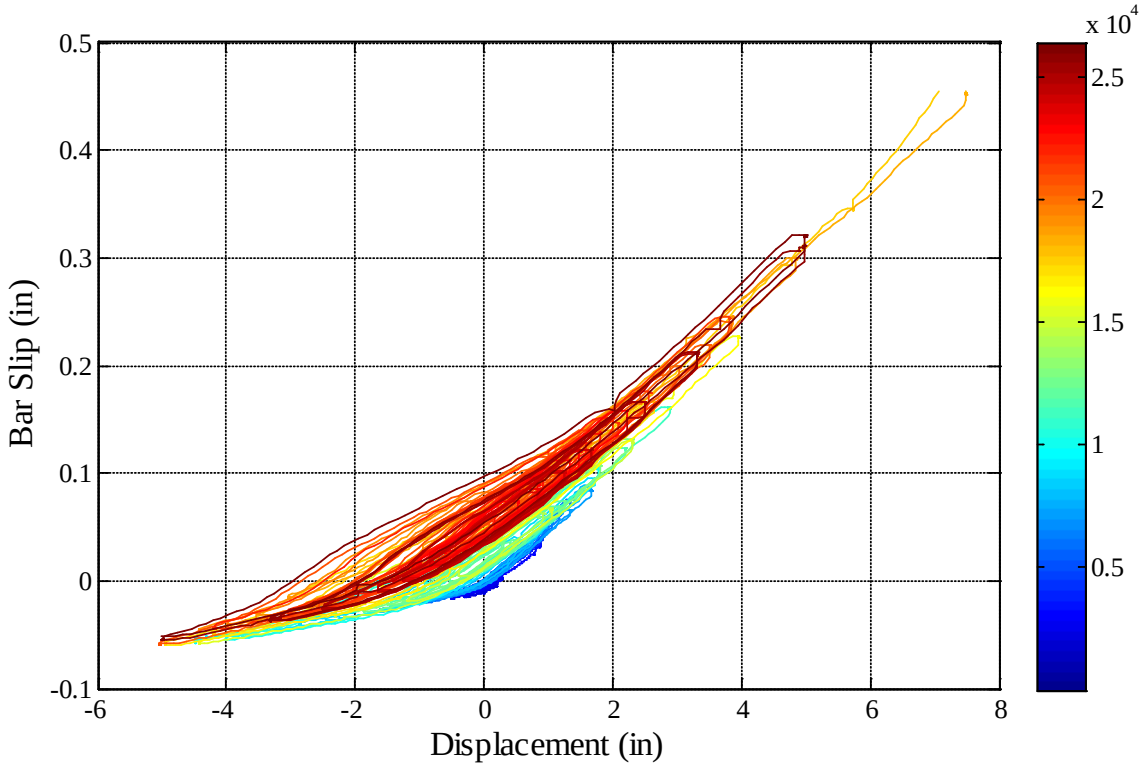

Figure 2-328. Test 17 – Bar N3 Slip Hysteresis at the Footling-Column Interface

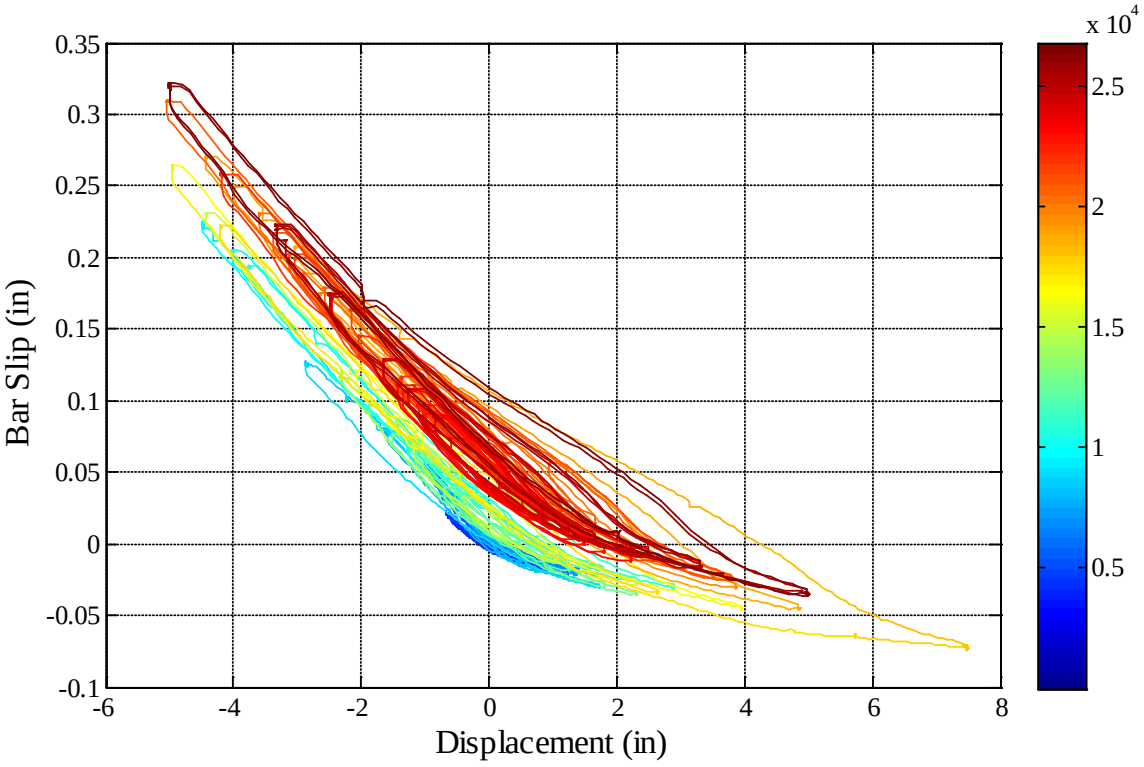

Figure 2-329. Test 17 – Bar S3 Slip Hysteresis at the Footing-Column Interface

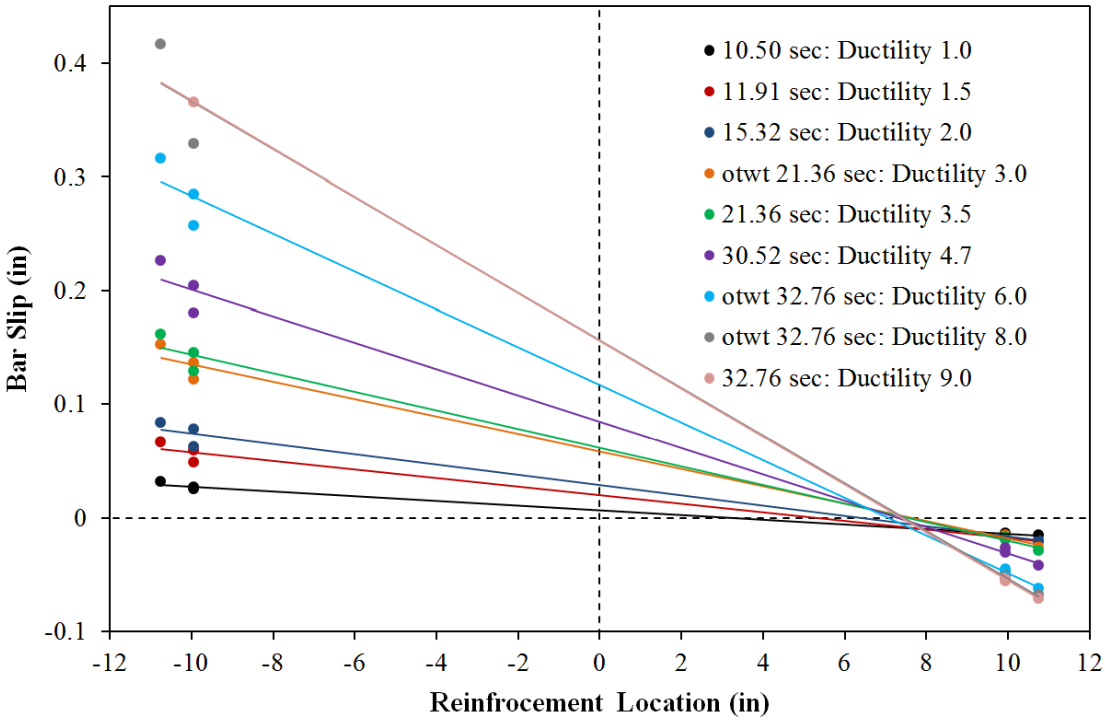

Figure 2-330. Test 17 – Slip Profiles for All Six Instrumented Bars to Obtain Base-Section Rotation during Push Cycles

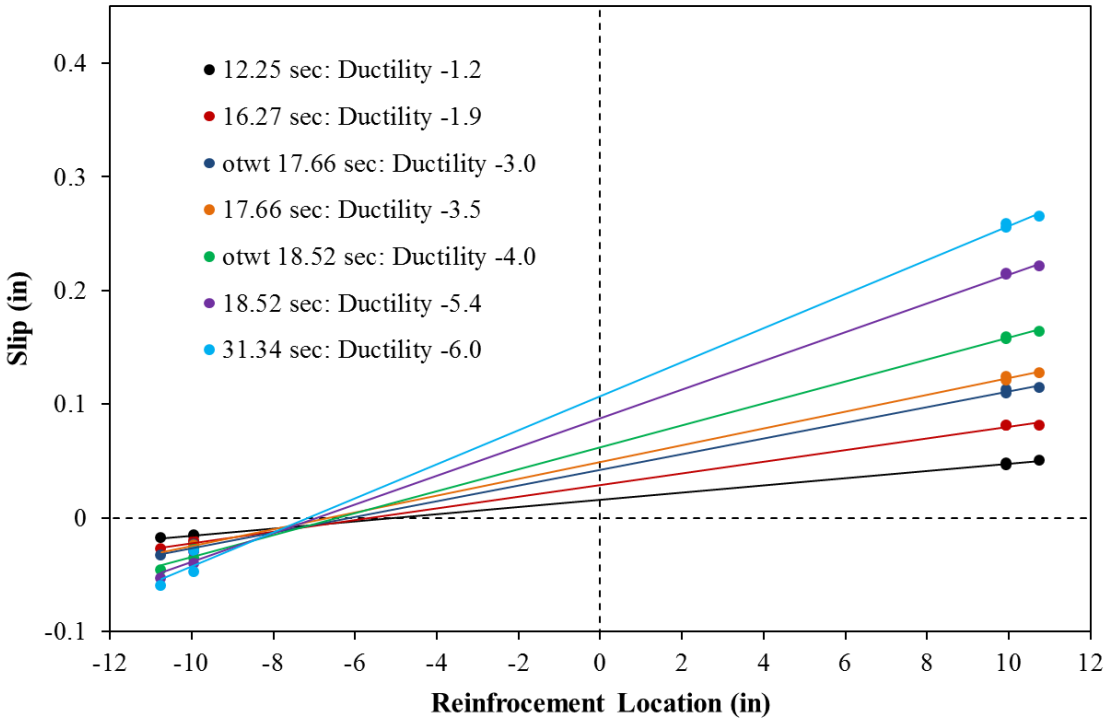

Figure 2-331. Test 17 – Slip Profiles for All Six Instrumented Bars due to Strain Penetration

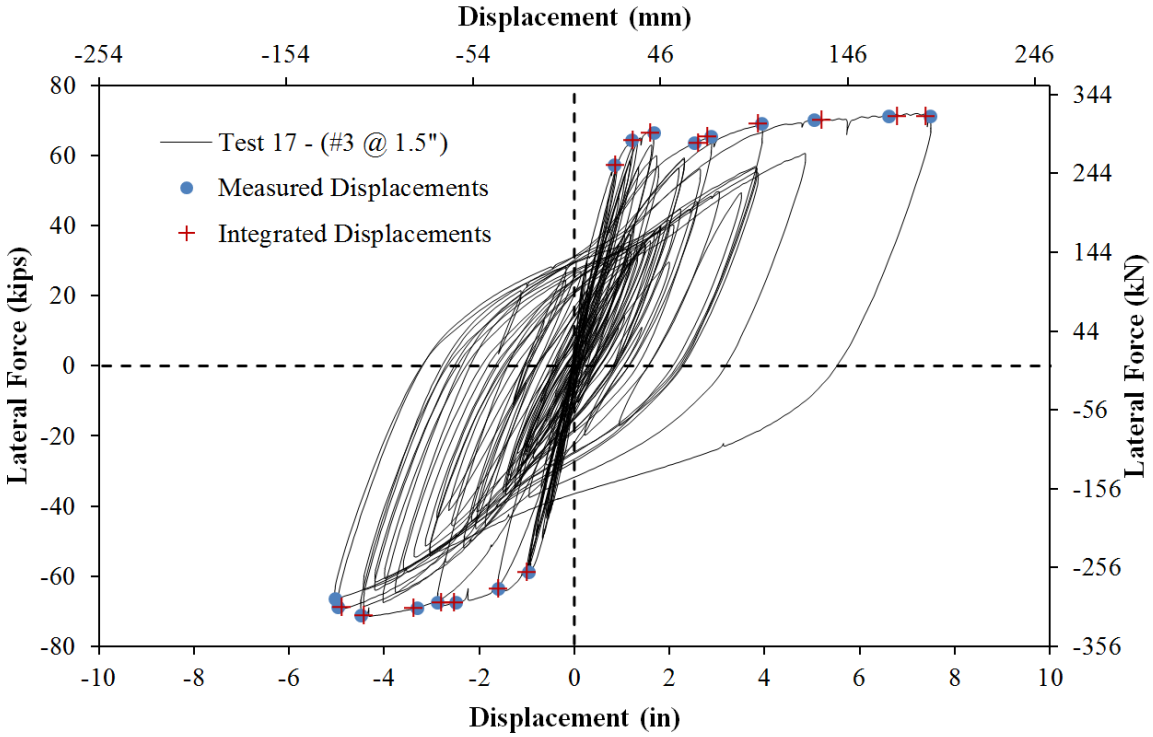

Figure 2-332. Test 17 – Comparison of Measured and Optotrak Integrated Displacements

2.2.5.6. Test 17b – Cyclic Aftershock Load History (#3 @ 1.5") Strain Data:

North Reinforcement:

Extreme fiber vertical strain profiles for the cyclic aftershock load history appear in Figure 2-333 and Figure 2-334 for push and pull cycles respectively. The shape of the tensile strain profiles during the cyclic aftershock resemble each other since the specimen rotates about crack profiles induced during higher ductility cycles of the Llolleo load history. The compressive vertical strain profiles are highly influenced by the measureable outward deformation 3.56" above the footing. The height of potential outward deformation coincides with the location where the bar later visually buckled. The gage lengths above and below 3.56" show greater compressive strains at the location where the bar begins to straighten back out. The recorded strains over these gage lengths are not accurate representations of engineering strains due to the deformation. The graphs are plotted in order to show the location and severity of the deformation.

The complete strain hysteresis for the outward buckled region of bar N3 appears in Figure 2-335 for the gage length 3.56" above the footing. A peak tensile strain of 0.055, located 3.56" above footing, was measured for North extreme fiber bar N3 during ($\mu_{9.0}^{32.76\,sec} = 7.49"$). The peak tensile strain is marked by a small blue circle along with a blue arrow after reversal which represents the beginning of the measurable outward deformation. The transverse steel strain gage hysteresis for the spiral layer over the outward buckled region of bar N3 appears in Figure 2-336. After reversal from the peak displacement, while the cracks on the north side still remained open, the transverse steel strain starts to increase indicating additional demand caused by restraint of bar N3. The peak displacement prior to reinforcement buckling during the cyclic after shock study of ($\mu_6^{-2} = -5.00"$) is marked by a small red circle on the longitudinal and transverse steel strain hysteresis. Following the red line in

both hysteresis, the measured strains in the longitudinal steel deviate further from the previous cycle and the transverse steel restraint strain rapidly increases.

South Reinforcement:

The compressive strain profiles for bar S3 indicate measurable outward deformation 8.06” above the footing. At this height the outward deformation increased the measured tensile strain during cycles where the South reinforcing bar should be placed into compression. The compressive strains above and below the outward deformations reached higher compressive strains where the bar straightens back out. The longitudinal steel strain hysteresis for bar S3, over the outward buckled region 8.06" above the footing, appears in Figure 2-337. A strain hysteresis for the gage length above the outward buckled region 9.5” above the footing is shown in Figure 2-338. The transverse steel strain hysteresis, 8” above the footing, for the layer of transverse steel overlaying the outward buckled region of bar S3 appears in Figure 2-339. A blue data point marker on all three hysteresis marks the point at which the measured compression strain 9.5” above the footing started to rapidly increase during the push to ($\mu_{9.0}^{32.76\,sec} = 7.49"$). As the gage length at 9.5” increased in compressive strain, the measured strains for the gage length below at 8.06” decreased. Coinciding with these two observations the transverse steel layer 8” above the footing entered the inelastic range. The strain hysteresis for the gage length 9.5” above the footing, in Figure 2-338, operates about a permanent downward shift decreasing the strain at a given displacement for the remainder of the test. Deviation after the blue data point for the gage length 8.06” above the footing, in Figure 2-337, indicates some measurable outward deformation. Tensile strains were observed during latter cycles of the load history which should have placed the gage length into compression, which further indicate measurable outward deformation. For the portion of the load history between ($\mu_{9.0}^{32.76\,sec} = 7.49"$) of the Llolleo earthquake and ($\mu_{6}^{+1} = 4.99"$) of the cyclic aftershock, the strain in the transverse steel layer 8” above the footing in Figure 2-339 did not sharply increase indicating that the measurable deformation remained small prior to visible bar buckling. Over multiple cycles at ductility six the transverse steel strain gradually increased during each cycle before rapidly increasing during ($\mu_{6}^{+3} = 5.00"$) when the bar visibly buckled.

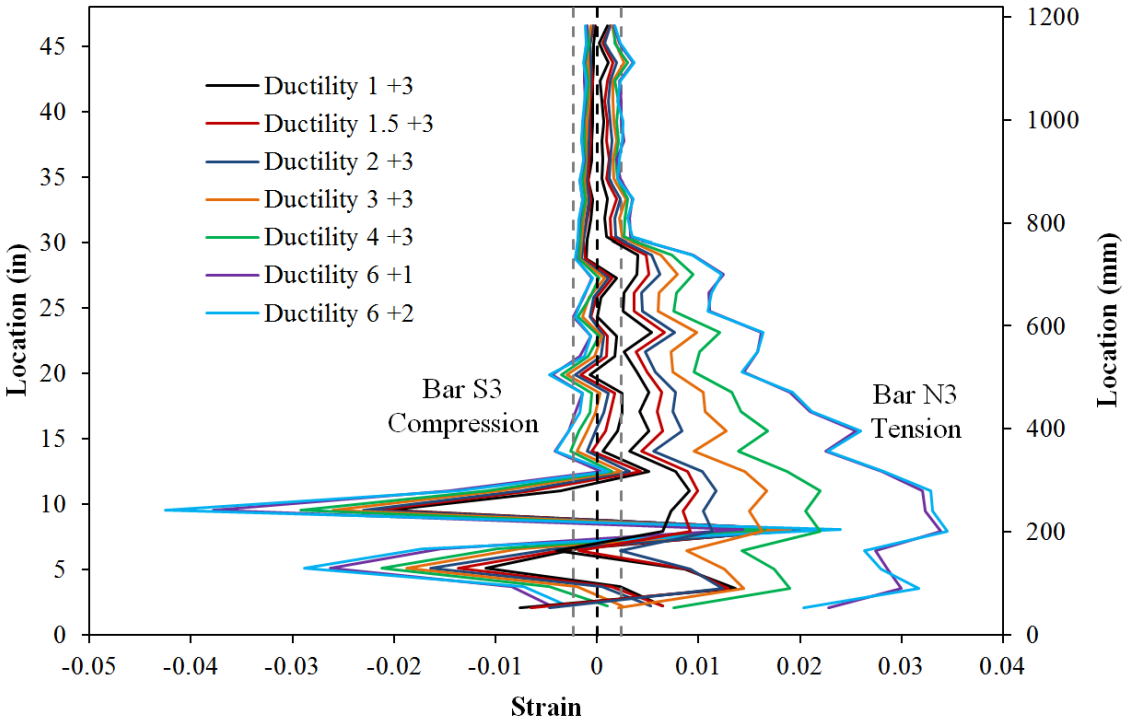

Figure 2-333. Test 17b – Extreme Fiber Vertical Strain Profiles during Push Cycles

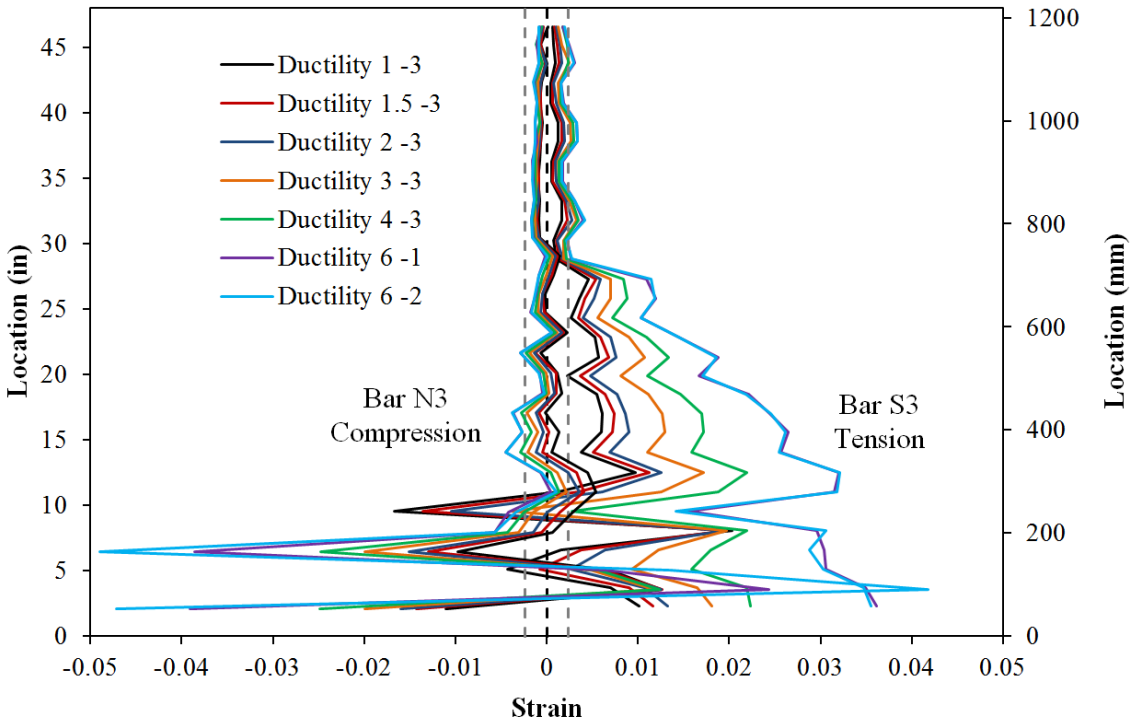

Figure 2-334. Test 17b – Extreme Fiber Vertical Strain Profiles during Pull Cycles

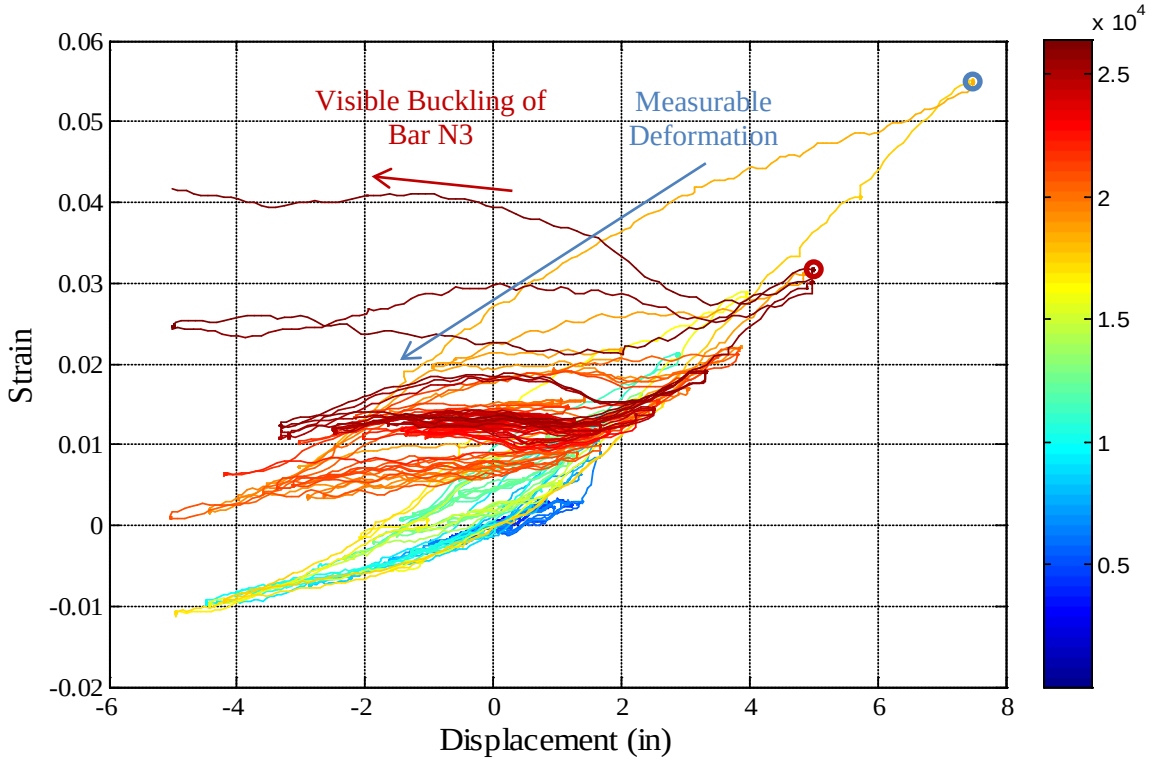

Figure 2-335. Test 17 and 17b – Bar N3 Strain Hysteresis Located 3.56" Above Footing

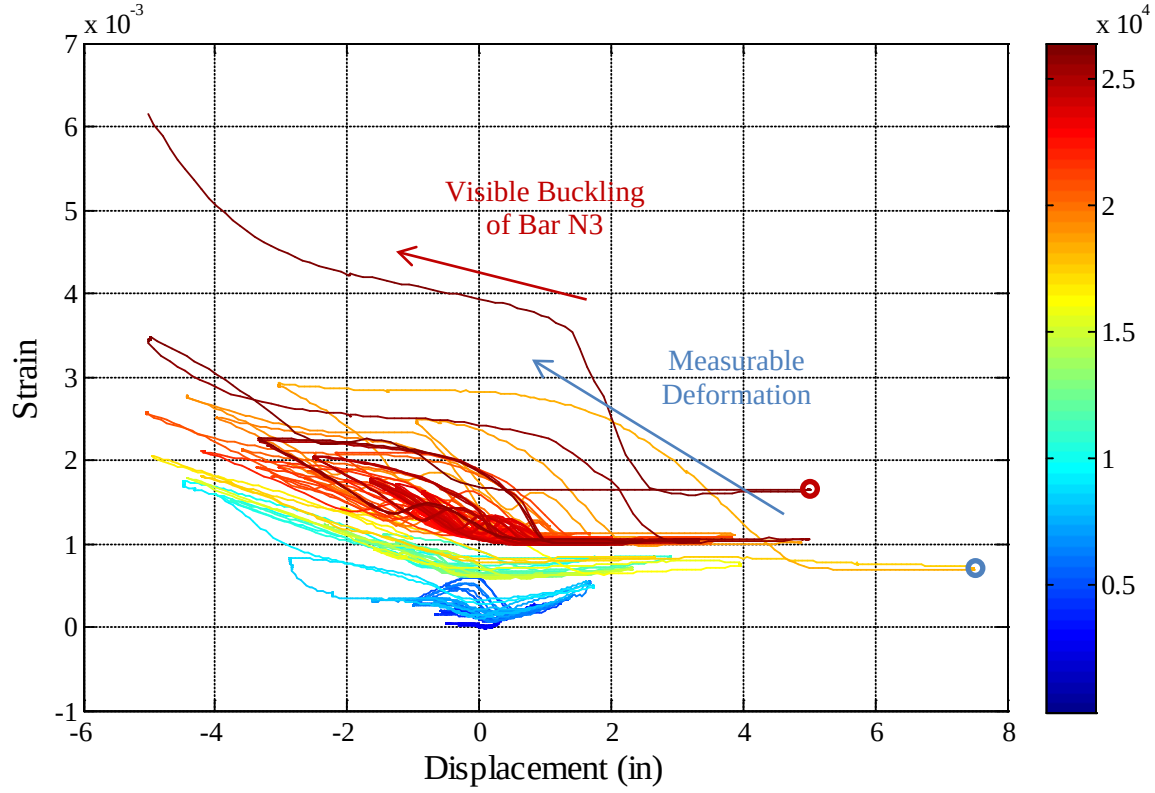

Figure 2-336. Test 17 and 17b – Transverse Steel Strain Hysteresis for the Spiral Layer Overlaying Buckled Bar N3 (2.25" Above the Footing)

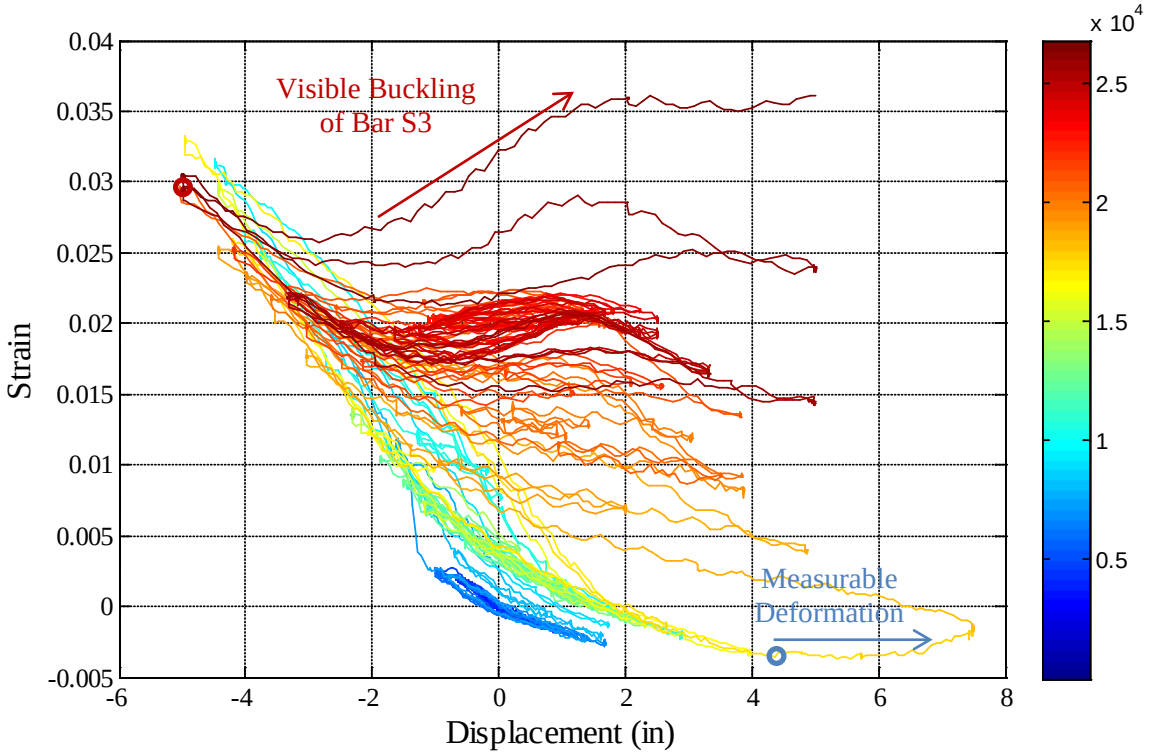

Figure 2-337. Test 17 and 17b – Bar S3 Strain Hysteresis Located 8.06" Above Footing

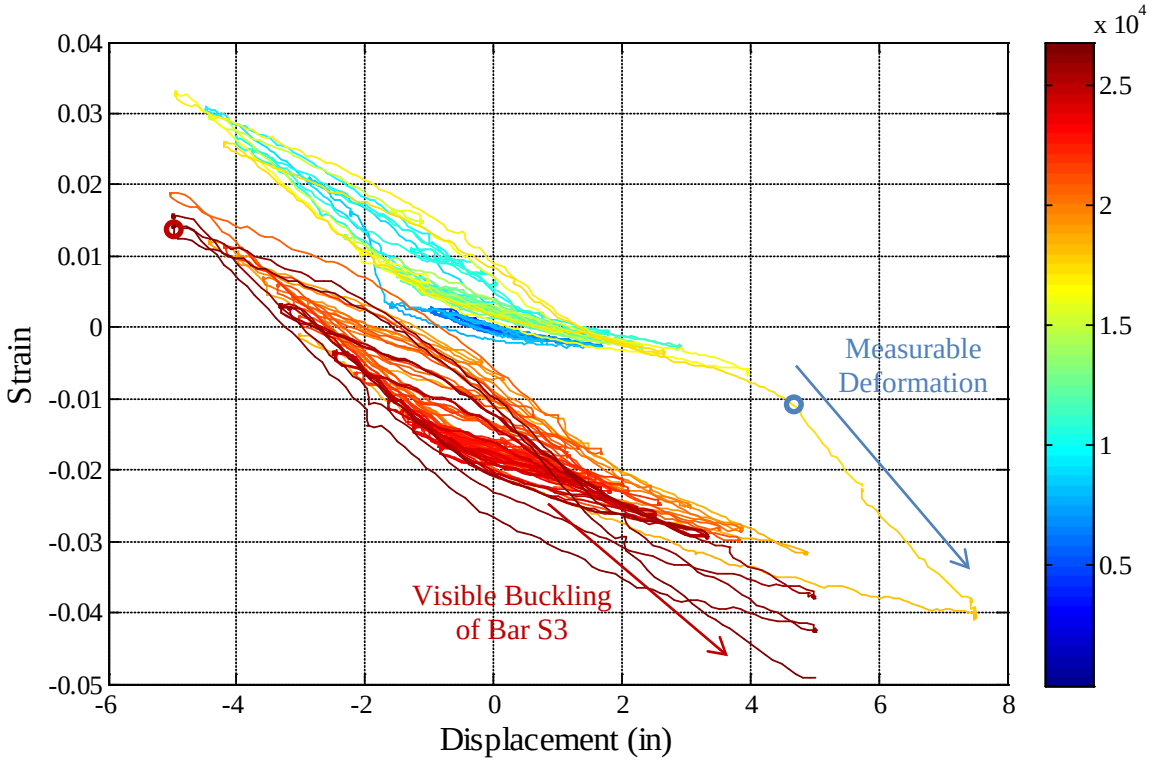

Figure 2-338. Test 17 and 17b – Bar S3 Strain Hysteresis Located 9.53" Above Footing

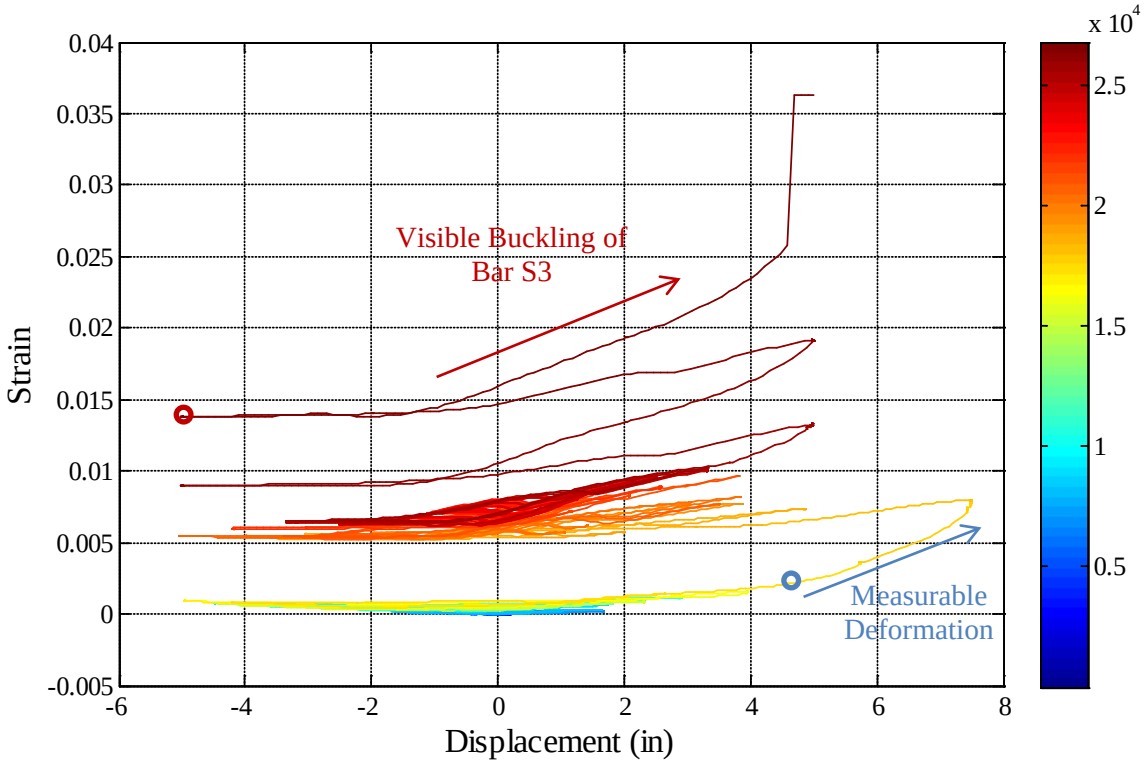

Figure 2-339. Test 17 and 17b – Transverse Steel Strain Hysteresis for the Spiral Layer Overlaying Buckled Bar S3 (8" Above the Footing)

2.2.6. Test 18 – Darfield NZ 2010 Earthquake Load History

Table 2-18. Results Summary for Test 18 – Darfield NZ 2010 Earthquake Load History

LOAD HISTORY: Darfield NZ 2010 Earthquake Load History

VALUES OF INTEREST:

Concrete Compressive Strength:	$f_c' = 7807psi$
Axial Load:	$P = 170kips$
Analytical First Yield Force:	$F_y' = 47.6kips$
Experimental First Yield Displacement:	$\Delta_y' = 0.62"$ *From Test 16
Analytical Nominal Moment Capacity:	$M_n = 510.4kip * ft$
Equivalent Yield Displacement:	$\Delta_y = 0.83"$
Maximum Lateral Force:	$-72.7kips$
Maximum Lateral Displacement:	$\mu_{9.0}^{24.40\ sec} = 7.46"$
Failure Mode:	Single Buckled Bar During Earthquake No Significant Strength Loss Observed

DAMAGE OBSERVATIONS: (Drift %) [Displacement Ductility, μ_Δ]

First Cracking North:	$\mu_{0.2}^{18.12\ sec} = 0.17"$
First Cracking South:	$\mu_{-0.3}^{18.12\ sec} = -0.23"$
Cover Concrete Crushing North:	During the pull to $\mu_{-2.7}^{23.72\ sec} = -2.21"$
Cover Concrete Crushing South:	During the push to $\mu_{9.0}^{24.40\ sec} = 7.46"$
Transverse Steel Yield North:	At $-5.49"$ otwt $\mu_{-7.3}^{25.00\ sec} = -6.05"$
Transverse Steel Yield South:	At $3.70"$ otwt $\mu_{9.0}^{24.40\ sec} = 7.46"$
Bar Buckling South	After Reversal from $\mu_{-7.3}^{25.00\ sec} = -6.05"$

*$\mu_{9.0}^{24.40\ sec} = 7.46"$ represents a push cycle 24.40 seconds into the earthquake load history which reached a peak displacement of 7.46” and a displacement ductility of 9.0

Table 2-19. Results Summary for Test 18b – Cyclic Aftershock Load History

LOAD HISTORY: Symmetric Three Cycle Set Aftershock after Darfield NZ

DAMAGE OBSERVATIONS: (Drift %) [Displacement Ductility, μ_Δ]

Longitudinal Bar Fracture South:	Reversal from $\mu_6^{-2} = -4.99"$
Failure Mode:	Fracture of Previously buckled Reinforcement

*$\mu_6^{-2} = -4.99"$ represents the second pull cycle of displacement ductility six which reached a peak displacement of -4.99”

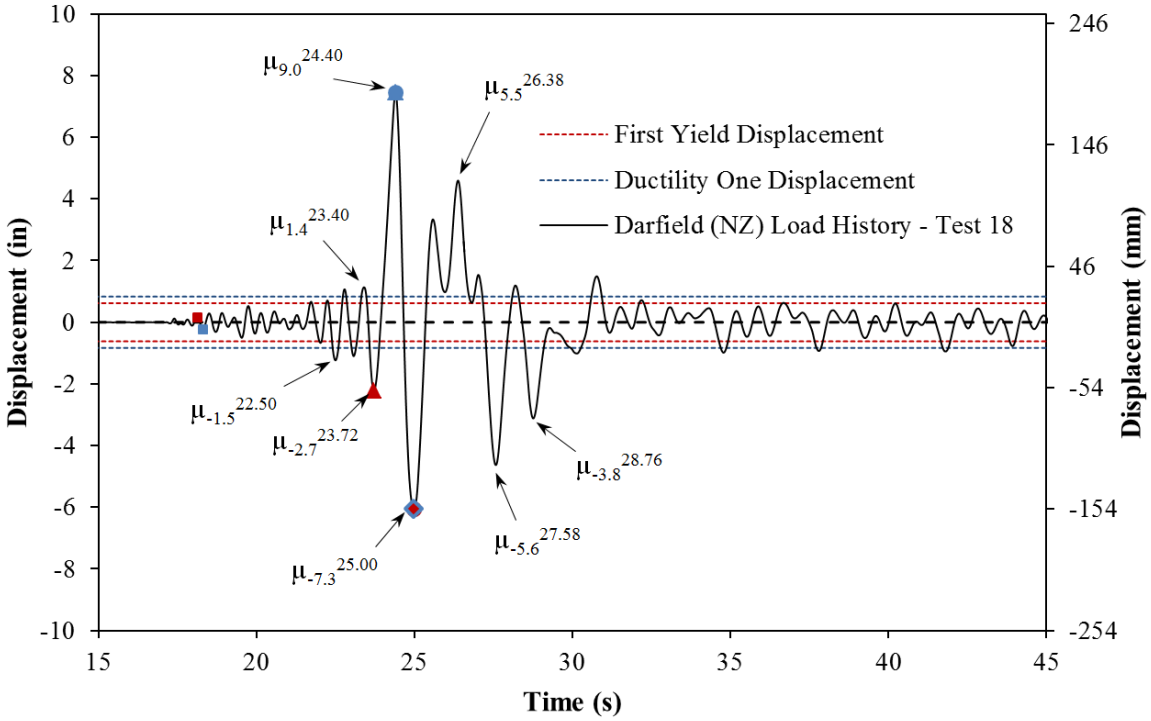

Figure 2-340. Test 18 – Darfield NZ 2010 Earthquake Load History

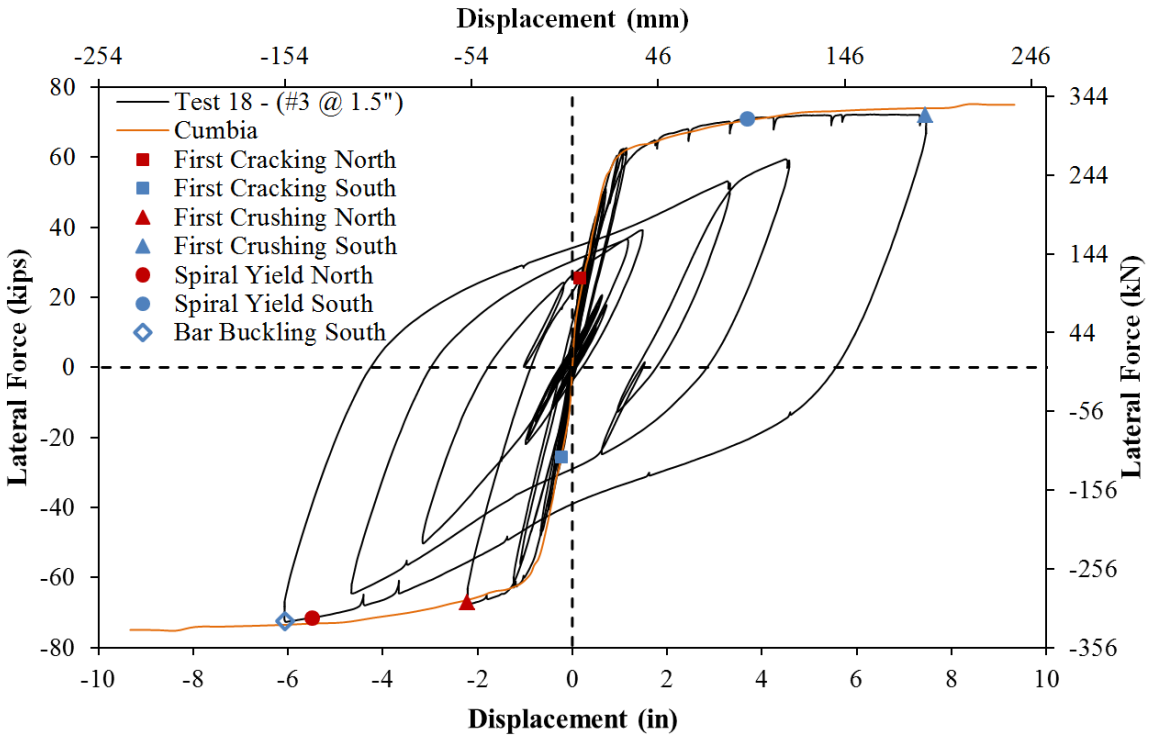

Figure 2-341. Test 18 – Darfield NZ Lateral Force vs. Top Column Displacement Response

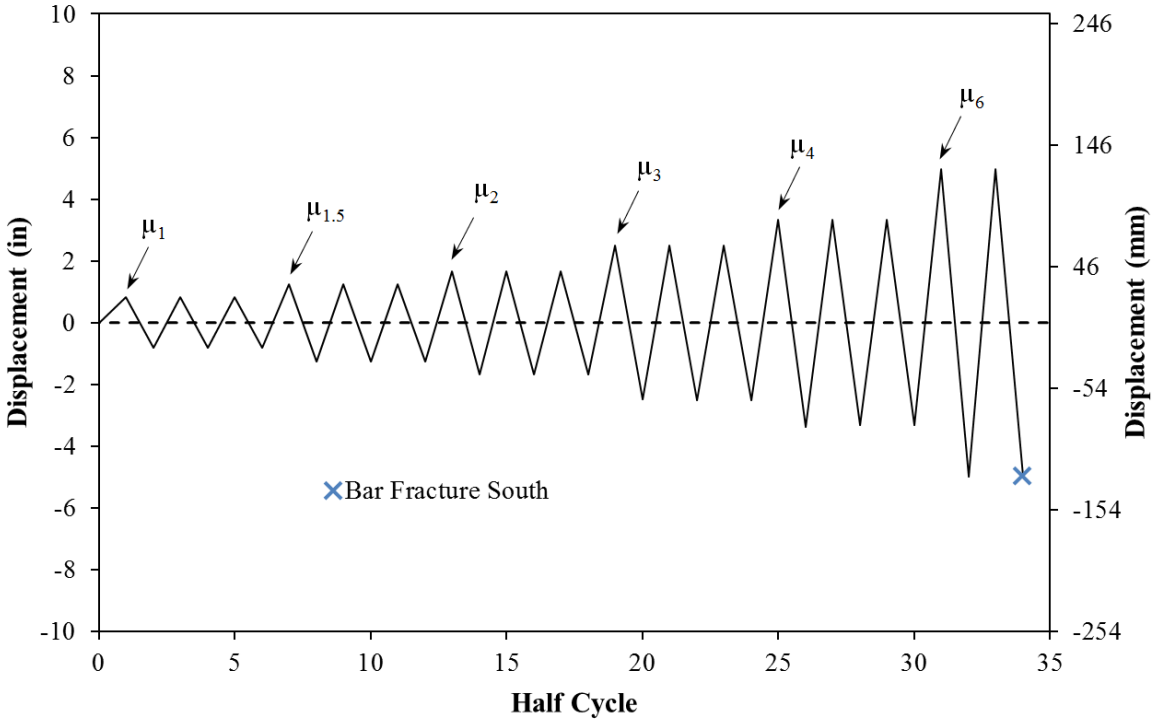

Figure 2-342. Test 18 – Symmetric Three Cycle Set Aftershock Load History

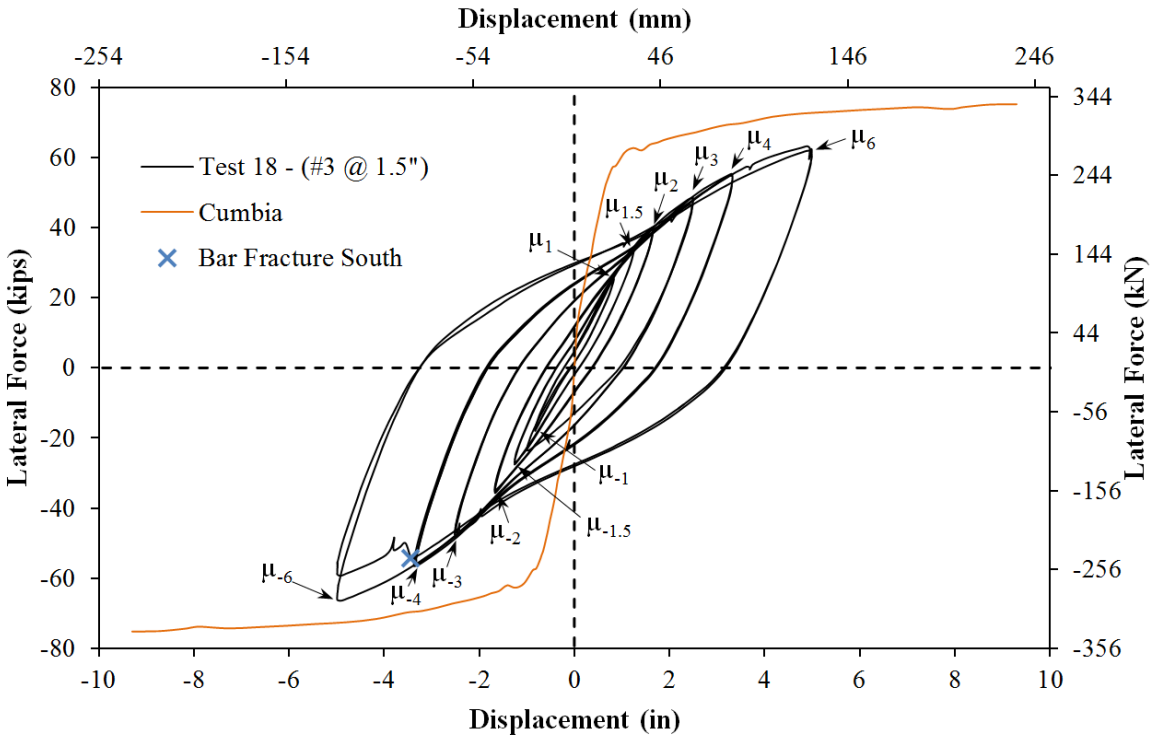

Figure 2-343. Test 18 – Cyclic Aftershock Lateral Force vs. Top Column Displacement Response

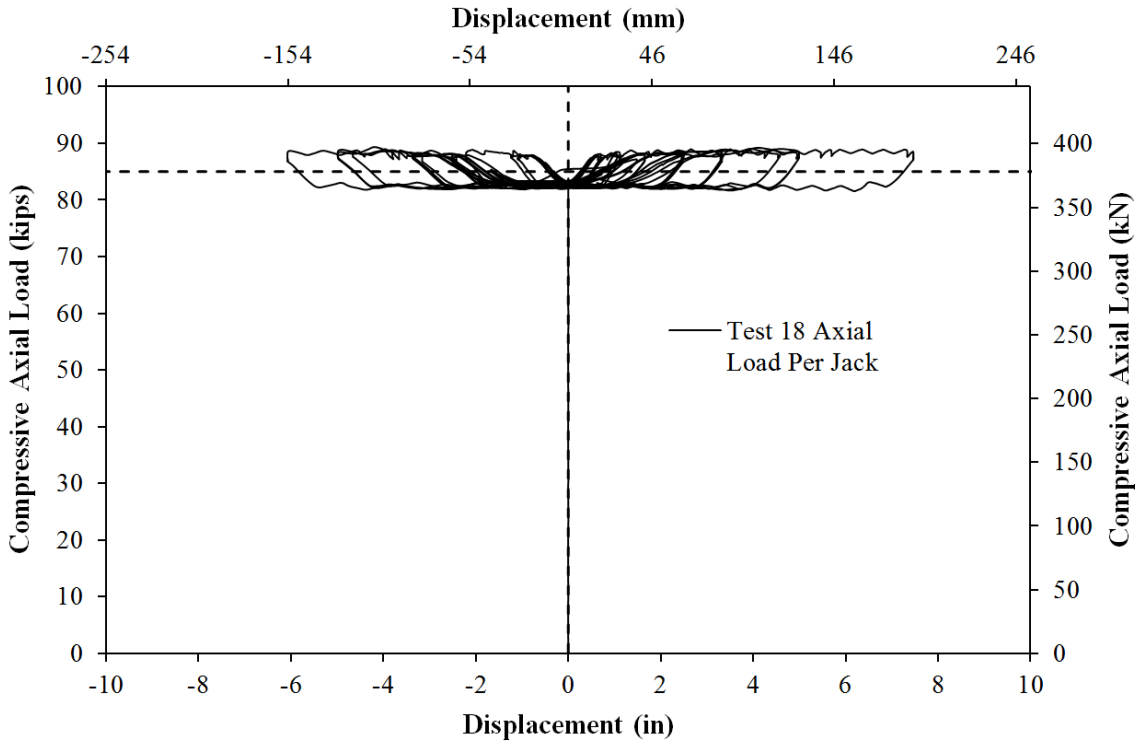

Figure 2-344. Test 18 – Compressive Axial Load from One Jack (Total = 2*Value)

2.2.6.1. Test 18 – Darfield NZ 2010 Earthquake Load History (#3 @ 1.5"):

A scaled version of the Darfield 2010 New Zealand earthquake load history, with a peak displacement ductility of nine, was chosen for Test 18. The top column displacement history, in Figure 2-340, was obtained using numerical analysis in OpenSees with a force-based fiber element to model the column and a zero-length strain penetration element. The acceleration input of the Darfield 2010 earthquake record was multiplied by 0.97 to produce a peak displacement ductility of nine. The analytical top column displacement history was recreated in the lab with a quasi-static loading procedure. The resulting experimental lateral force vs. top column displacement response for the Darfield 2010 load history appears in Figure 2-341. The first yield displacement for Test 16, which had same detailing as Tests 17 and 18, was obtained as an average for the experimental first yield push and pull cycles ($\Delta_y' = 0.62"$). To determine if this first yield displacement is applicable to Test 18, the tensile strain profile at ($\Delta_y' = 0.62"$) for each extreme fiber bar appears in Figure 2-345. At the first yield displacement, the tensile strains in both extreme fiber reinforcing bars reached yield. The equivalent yield displacement, used to determine the displacement ductility levels ($\mu_{\Delta n} = \mathrm{n} * \Delta_y$), was then calculated as $\Delta_y = \Delta_y'(M_n/M_y') = 0.83"$. The displacement ductility levels for Test 16, see Figure 2-345, are also applicable for Tests 17 and 18.

Three columns detailed with a #3 spiral at 1.5" spacing ($4A_{sp}/(D's) = 1.3\%$) were chosen for Tests 16-18. Reinforcement buckling occurred during ductility eight of a symmetric three cycle set load history in Test 16. A scaled version of the 1985 Llolleo Chile earthquake record did not produce bar buckling even though the peak response reached displacement ductility nine. The Llolleo 1985 Chile top column displacement history contains a large number of inelastic reversals of high amplitude both before and after the peak displacement. The top column displacement history for Test 18, which utilized a scaled version of the Darfield 2010 New Zealand record, appears in Figure 2-340. In

comparison, the Darfield load history contains only a few high ductility cycles. The peak cycle in the opposing direction of the maximum response reaches displacement ductility 7.3. While the peak displacement ductility nine cycle is not expected to produce buckling after reversal of loading, it offers the opportunity to study the influence of multiple layers of inelastic transverse steel restraint overlaying the reinforcement placed into tension during the ductility 7.3 reversal.

After conclusion of the Darfield 2010 New Zealand load history, the specimen had crushed cover concrete, degraded stiffness, and a single buckled reinforcing bar on the South side of the specimen. The specimen was subjected to a symmetric three cycle set laboratory load history to evaluate the effect of additional cycles on the buckled region on the South side of the column and to determine what level of displacement is required to induce buckling of the North reinforcement. During ductility six, two additional South reinforcing bars buckled. The tensile demand sustained during repeated cycles at displacement ductility six was sufficient to rupture the extreme fiber South reinforcing bar which buckled during the Darfield load history. The test was concluded with three buckled bars and a single ruptured bar on the South side and unbuckled reinforcement on the North. The specimen is a repair candidate for a separate experimental project.

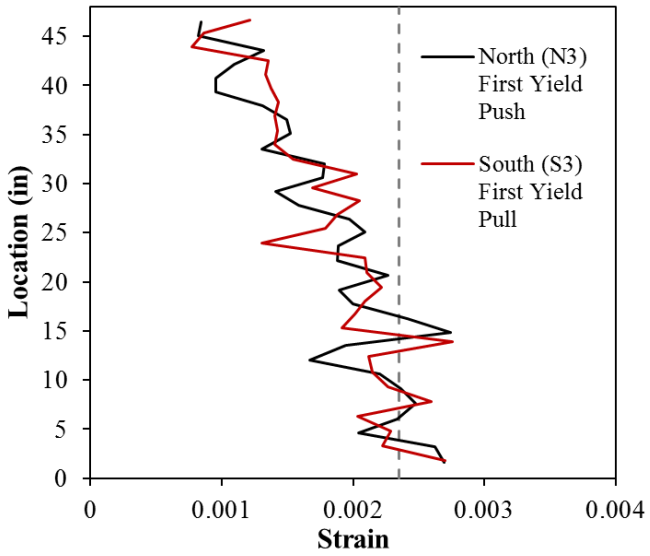

Analytical Fy'	46.80	kips
Experimental Δy'	0.62	in
Analytical My'	374.44	kip-ft
Analytical Mn	503.19	kip-ft
μ1	0.83	in
μ1.5	1.25	in
μ2	1.66	in
μ3	2.50	in
μ4	3.33	in
μ6	4.99	in
μ8	6.65	in
μ10	8.32	in
μ12	9.98	in

Figure 2-345. Test 18 – (Left) Tensile Vertical Strain Profiles Used to Verify Test 16 First yield Displacement and (Right) Displacement Ductility Levels from Test 16 Which Also Apply for Test 18 due to Identical Detailing, Geometry, and Material Properties

2.2.6.2. Test 18 – Darfield NZ 2010 Earthquake (#3 @ 1.5") Experimental Observations:

The beginning of the Darfield 2010 New Zealand load history contains a large number of elastic reversals. The first cracks on the North side of the specimen measured 0.1mm at approximate 9" spacing during ($\mu_{0.2}^{18.12\,sec} = 0.17"$), as shown in the left photo of Figure 2-346. Crack widths reached 0.1mm at approximate 9" spacing on the South side of the specimen during ($\mu_{-0.3}^{18.30\,sec} = -0.23"$), see the middle photo of Figure 2-346. During the pull cycle to ($\mu_{-0.6}^{19.54\,sec} = -0.50"$), in the right photo of Figure 2-346, crack widths on the South side reached 0.3mm at approximate 5" spacing. Cracks on the North side reached 0.4mm at 5" spacing during the pull cycle to ($\mu_{0.6}^{19.74\,sec} = 0.51"$), see the left photo of Figure 2-347. The first cycles exceeding yield for the Darfield load

history occurred during ($\mu_{0.8}^{21.72\,sec} = 0.66$"), when cracks on the North side of the specimen increased to 0.45mm at approximate 5" spacing. Crack widths reached 0.5mm at 5" spacing on the South side of the specimen during ($\mu_{-0.8}^{22.02\,sec} = -0.66$"), see the right two photos of Figure 2-347.

The first cycle exceeding the equivalent yield displacement in the push direction occurred during ($\mu_{-1.5}^{22.50\,sec} = -1.24$"), where crack widths reached 0.8mm at approximate 3-4" spacing. The crack distribution on the front side of the specimen at ($\mu_{1.3}^{22.78\,sec} = 1.04$") appears in the left photo of Figure 2-348. During the pull cycle to ($\mu_{-2.7}^{23.72\,sec} = -2.21$"), crushing on the North side of the specimen extended 16" above the footing. Crack widths on the South side of the specimen reached 2.5mm at 3-4" spacing as shown in Figure 2-348. The displacement when crushing first occurred was not recorded. The following reversal of loading pushed the specimen to the peak displacement of ($\mu_{9.0}^{24.40\,sec} = 7.46$"). The extent of crushing on the South side of the specimen reached 21" above the footing, see the middle photo of Figure 2-349. Additional photos of the specimen at the peak displacement appear in Figure 2-350. Crushing on the North side of the specimen reached 22" above the footing during the pull cycle to ($\mu_{-7.3}^{25.00\,sec} = -6.05$").

North reinforcement exposed to tension during ($\mu_{9.0}^{24.40\,sec} = 7.46$") did not visibly buckle during the large reversal to ($\mu_{-7.3}^{25.00\,sec} = -6.05$"). Large compressive demand during ($\mu_{9.0}^{24.40\,sec} = 7.46$") caused several layers of transverse steel on the South side of the specimen to enter the inelastic range. Inelastic transverse steel layers combined with large tensile strains during ($\mu_{-7.3}^{25.00\,sec} = -6.05$") produced visible reinforcement buckling of the extreme fiber South reinforcing bar during the following reversal of load. Visible buckling of Bar S3 is shown in the right two photos of Figure 2-351 at ($\mu_{4.0}^{25.58\,sec} = 3.32$"). Outward bar buckling occurred over the second and third transverse steel spacings above the footing. The remainder of the Darfield load history contained lower ductility cycles which did not produce any notable damage beyond increasing the buckled deformation in Bar S3.

2.2.6.3. Test 18b – Cyclic Aftershock Load History (#3 @ 1.5") Experimental Observations:

After conclusion of the Darfield 2010 New Zealand load history, the specimen had crushed cover concrete, degraded stiffness, and a single buckled reinforcing bar on the South side of the specimen. Previous earthquake load histories scaled to approximately ductility nine failed to produce visible buckling. The specimen was subjected to a symmetric three cycle set load history, see Figure 2-342, to evaluate the effect of additional cycles on the buckled region on the South side of the column, and to determine what level of displacement is required to induce buckling of the North reinforcement. No notable damage occurred through ductility four of the cyclic aftershock study.

During the first push cycle of displacement ductility six, ($\mu_6^{+1} = 4.99$"), additional South reinforcing bars S2 and S4 buckled as shown in the left photo of Figure 2-352. The outward deformation of previously buckled bar S3 was more severe than at any other point of the load history. On the way to ($\mu_6^{-2} = -4.99$"), previously buckled South reinforcing bar S3 ruptured in tension. The ruptured bar and deformations in several spiral layers are shown in Figure 2-352. The test was concluded with three buckled bars and a single ruptured bar on the South side and unbuckled reinforcement on the North. Cross section equilibrium was distorted beyond the use of additional buckling data for North reinforcement if test were to continue. The specimen was saved as a repair candidate for a separate project.

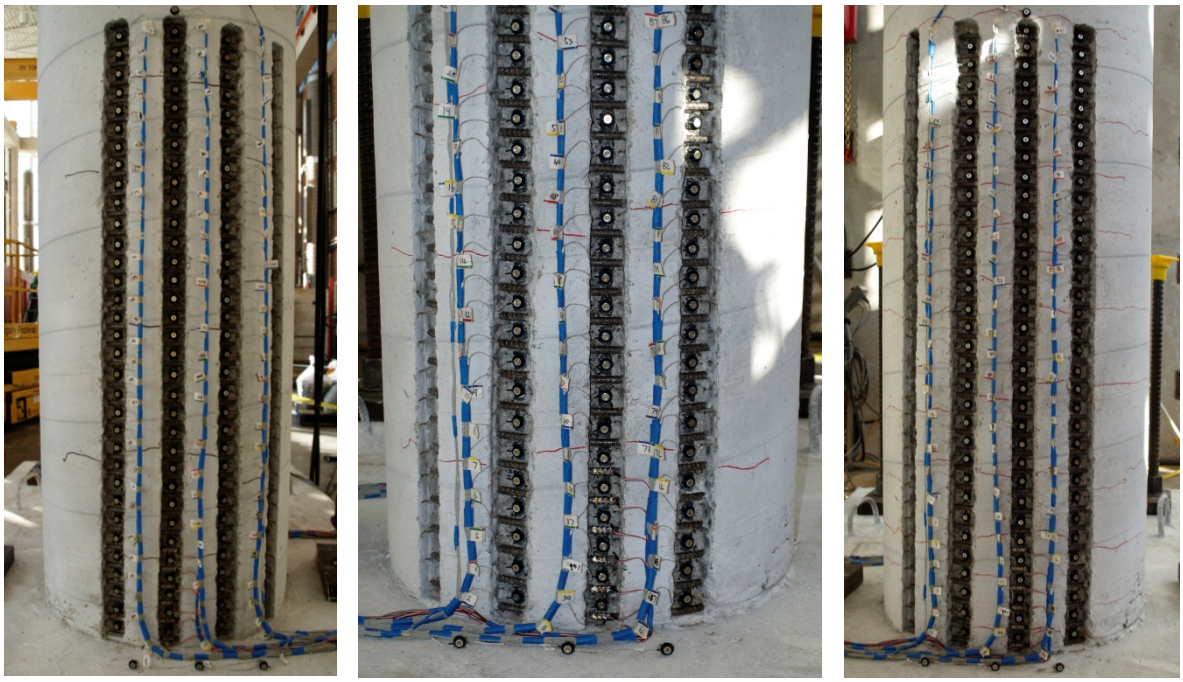

Figure 2-346. Test 18 – (Left) First Cracking on the North Side during ($\mu_{0.2}^{18.12\,sec} = 0.17$"), (Middle) First Cracking on the South Side during ($\mu_{-0.3}^{18.30\,sec} = -0.23$"), and (Right) South Crack Distribution during ($\mu_{-0.6}^{19.54\,sec} = -0.50$")

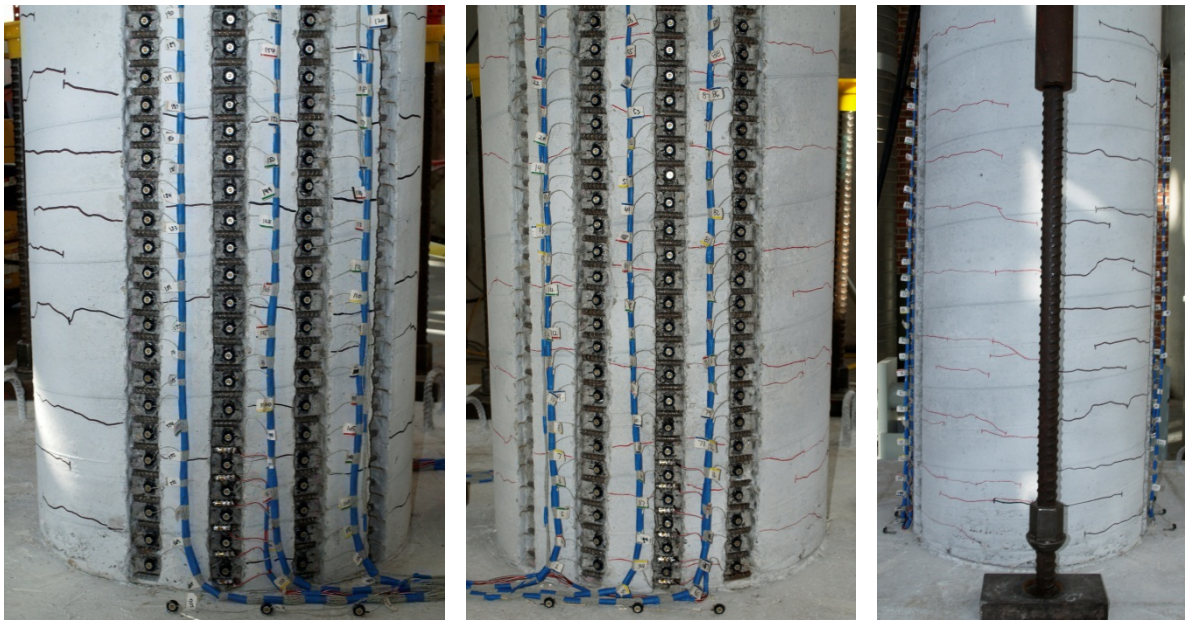

Figure 2-347. Test 18 – (Left) Cracks on the North Side during ($\mu_{0.6}^{19.74\,sec} = 0.51$"), (Middle and Right) Crack Distribution on the South and Back Sides during ($\mu_{-0.8}^{22.02\,sec} = -0.66$")

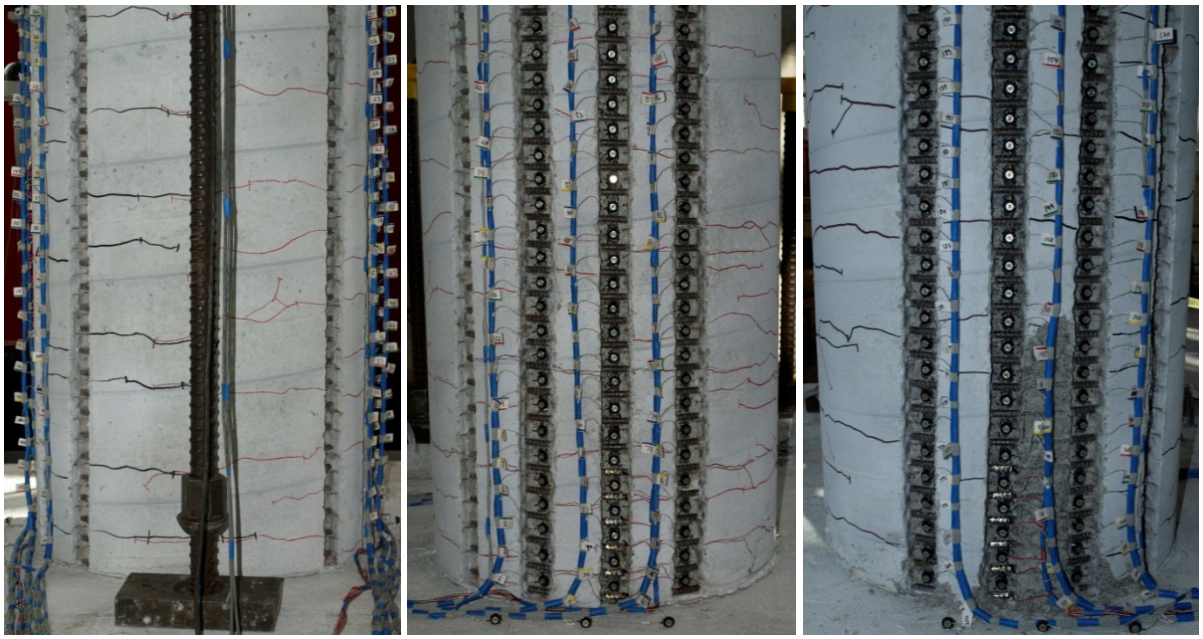

Figure 2-348. Test 18 – (Left) Crack Distribution on the Front Side during ($\mu_{1.3}^{22.78\,sec} = 1.04$"), (Middle) Cracking on the South Side during ($\mu_{-2.7}^{23.72\,sec} = -2.21$"), and (Right) Extent of Cover Concrete Crushing on the North Side at ($\mu_{-2.7}^{23.72\,sec} = -2.21$")

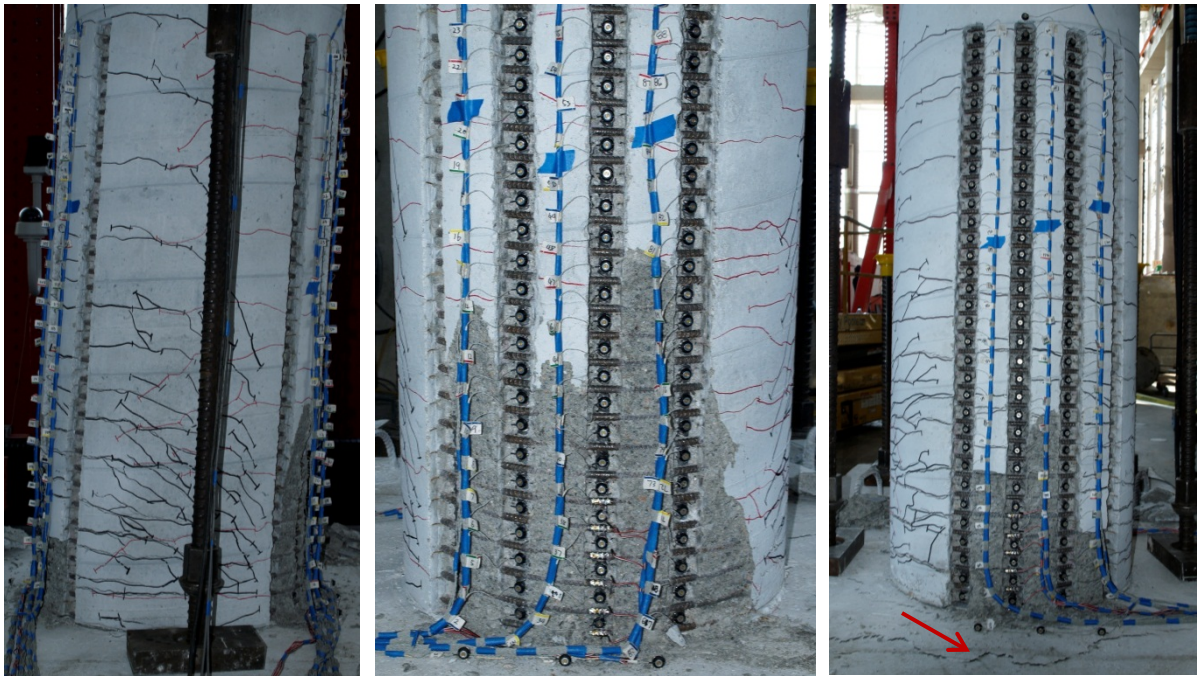

Figure 2-349. Test 18 – (Left) Crack Distribution on the Front Side during the Peak Cycle to ($\mu_{9.0}^{24.40\,sec} = 7.46$"), (Middle) Crushing on the South Side, and (Right) Crack on the Top of the Footing on the North Side of the Column

Figure 2-350. Test 18 – Crack Distribution at Peak Displacement ($\mu_{9.0}^{24.40\,sec} = 7.46$")

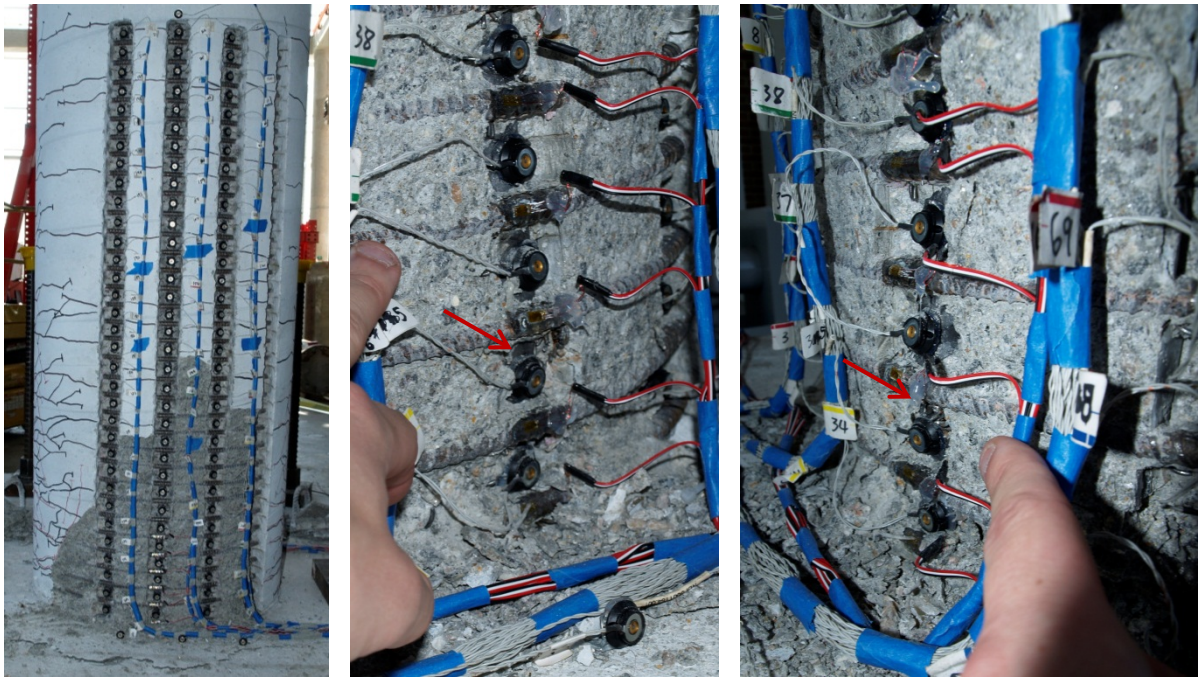

Figure 2-351. Test 18 – (Left) Extent of Crushing on the North Side during ($\mu_{-7.3}^{25.00\,sec} = -6.05$"), (Middle and Right) Visible Buckling of Bar S3 at ($\mu_{4.0}^{25.58\,sec} = 3.32$")

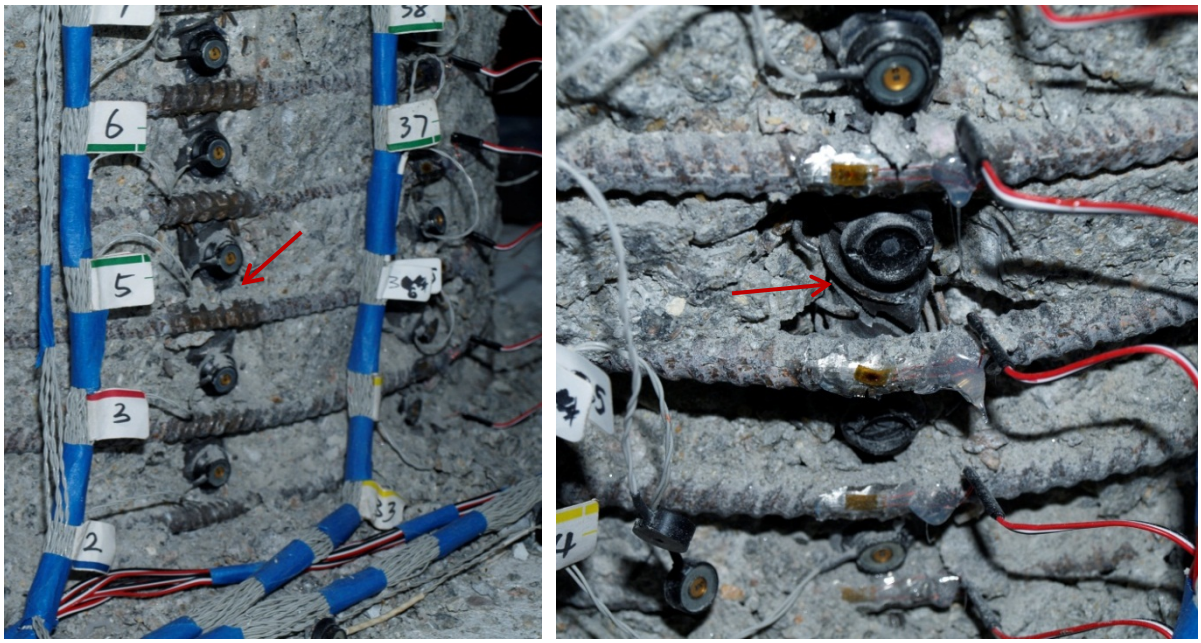

Figure 2-352. Test 18 – (Left) Buckling of Bars S2 and S4 during ($\mu_6^{+1} = 4.99$") and (Right) Rupture of Previously Buckled Bar S3 during ($\mu_6^{-2} = -4.99$")

2.2.6.4. Test 18 – Darfield NZ 2010 Earthquake Load History (#3 @ 1.5") Strain Data:

North Reinforcement:

Since the peaks of cycles during the earthquake load history do not align with the ductility levels of a traditional three cycle set load history, intermediate cycles along the backbone curve were selected for strain data analysis, see Figure 2-353. Extreme fiber vertical strain profiles for push and pull cycles appear in Figure 2-354 and Figure 2-355 respectively. A peak tensile strain of 0.062, located 3.19" above footing, was measured for extreme fiber bar N3 during ($\mu_{9.0}^{24.40\ sec} = 7.46$"). The relationship between tensile strain and displacement for this gage length appears in Figure 2-358. The solid line contains data during the push cycle loading up to the peak displacement and the dashed line represents the subsequent reversal of load. The peak tensile strain of 0.062 was not sufficient to produce visible bar buckling after reversal of load. Similar to previous tests, the moment curvature prediction for the relationship between strain and displacement begins to over predict the tensile strains at higher displacements at an increasing rate.

The largest compressive strain of -0.021 for bar N3, located 1.63" above the footing, was measured during ($\mu_{-7.3}^{25.00\ sec} = -6.05$"). The relationship between compressive strain and displacement for the gage length 4.63" above the footing appears in Figure 2-361. The recorded compressive strains match the moment curvature prediction well. The transverse steel strains measured for the lowest six spiral layers overlaying the North reinforcement are plotted in Figure 2-357. The figure depicts tensile strains in the spiral layers on the North side of the specimen placed into compression during pull cycles. During the peak pull cycle to ($\mu_{-7.3}^{25.00\ sec} = -6.05$"), two spiral layers entered the inelastic range. The strain data for the North reinforcement does not give any indication of measurable deformation during the Darfield load history.

Vertical strain profiles for extreme fiber Bar N3 during push and pull cycles of the cyclic aftershock load history appear in Figure 2-366 and Figure 2-367 respectively. The strain profiles for bar N3 follow a similar shape because the crack distribution was previously set in place during peak cycles of the Darfield load history. The transverse steel strains measured over the lowest six spiral layers overlaying the North reinforcement are plotted against their location above the footing in Figure 2-378. The transverse steel did not re-enter the inelastic range until displacement ductility three of the cyclic aftershock study. During the first and second pull cycles of ductility six, transverse steel strains reached 0.0038 and 0.0039 respectively. The complete strain hysteresis for bar N3, for the gage length 3.19" above the footing, appears in Figure 2-369. A similar strain hysteresis for the gage length 4.63" above the footing is shown in Figure 2-370. The gage length 3.19" above the footing is directly crossed by the largest crack on the North side of the specimen as shown in Figure 2-372. This helps to explain the larger residual strain after the peak cycle evident in the gage length 3.19" above the footing.

South Reinforcement:

A peak tensile strain of 0.0466 on bar S3 was measured 3.31" above the footing during ($\mu_{-7.3}^{25.00\,sec} = -6.05"$). The relationship between tensile strain and displacement for this gage length is shown in Figure 2-360. The same comments on the accuracy of the moment curvature prediction for the North reinforcement also apply to bar S3. The blue dashed line, after reversal from ($\mu_{-7.3}^{25.00\,sec} = -6.05"$), no longer represents engineering strain due to the observed outward buckling over the gage length depicted in Figure 2-351. A peak compression strain of -0.0481 was measured 1.78" above the footing during ($\mu_{9.0}^{24.40\,sec} = 7.46"$). The relationship between compressive strain and displacement for this gage length appears in Figure 2-359. At large displacements, the measured compressive strains are significantly larger than the moment curvature prediction. The measured compression strain of -0.0481 is 2.7 times larger than the Mander ultimate concrete compressive strain of -0.0176. The effect of the large compressive demand on the South side of the specimen can be seen in the transverse steel layers overlaying the extreme fiber bar in Figure 2-356. Two layers of transverse steel enter the inelastic range at displacement ductility six during the constant push cycle to ($\mu_{9.0}^{24.40\,sec} = 7.46"$). By displacement ductility eight, four transverse steel layers went into the inelastic range. The strain gage on the spiral layer 3.56" above the footing went off scale during ($\mu_{9.0}^{24.40\,sec} = 7.46"$).

The strain hysteresis for extreme fiber Bar S3 appears in Figure 2-362 for the gage length 3.31" above the footing which outwardly deformed as the bar buckled. The strain hysteresis for the gage length located 4.83" above the footing appears in Figure 2-363. This gage length coincides with the region where the bar begins to straighten back out. Both graphs are shown to illustrate the effect of inelastic spiral layers on localized compressive demand. The transverse steel strain hysteresis for the spiral layers located 2.06" and 3.56" above the footing appear in Figure 2-364 and Figure 2-365 respectively. The push cycle to ($\mu_{9.0}^{24.40\,sec} = 7.46"$) caused the strain in the transverse steel layer 3.56" above the footing to rapidly increase past 0.016 where the gages go off scale. As this occurred, the instrumentation indicated measurable deformation in bar S3 leading to higher compressive strains in the gage length 4.83" above the footing and lower compressive strains 3.31" above the footing. The location of the measurable deformation agrees with visible bar buckling observations later in the test.

2.2.6.5. Test 18 – Darfield NZ 2010 Earthquake (#3 @ 1.5") Curvature and Strain Penetration Data:

Vertical curvature profiles are plotted for push and pull cycles in Figure 2-373 and Figure 2-374 respectively. These figures show that plastic curvatures have a linear distribution at higher

displacement ductility levels. As the displacements increase, the base curvatures become larger and the extent of plastic curvatures reach higher above the footing. The target marker on each reinforcing bar placed closest the footing-column interface can be used to create slip hysteresis and horizontal slip profiles attributable to strain penetration. The slip hysteresis for North extreme fiber bar N3 appears in Figure 2-377. The peak tensile slip bar N3 exceeds 0.34" at ($\mu_{9.0}^{24.40\,sec} = 7.46$"). If the tensile and compressive slip of all of the instrumented bars is plotted along the cross section depth, the base rotation attributable to strain penetration may be calculated. The slip profiles for push and pull cycles appear in Figure 2-375 and Figure 2-376 respectively. The measured string potentiometer displacements from Test 18 were compared to the displacement obtained from curvature diagram integration and slip profile extrapolation to the center of loading in Figure 2-378. The measured and integrated top column displacements match well with the exception of high ductility data points near ($\mu_{-7.3}^{25.00\,sec} = -6.05$").

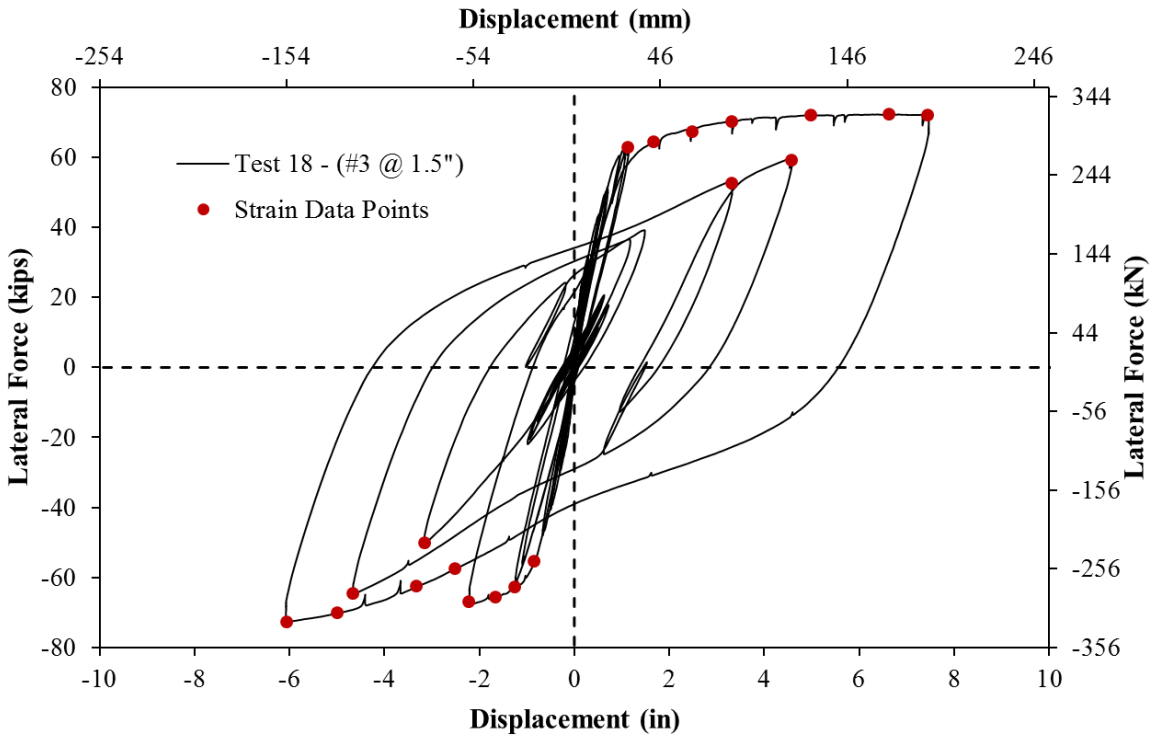

Figure 2-353. Test 18 – Strain Data Observation Points along the Backbone Curve

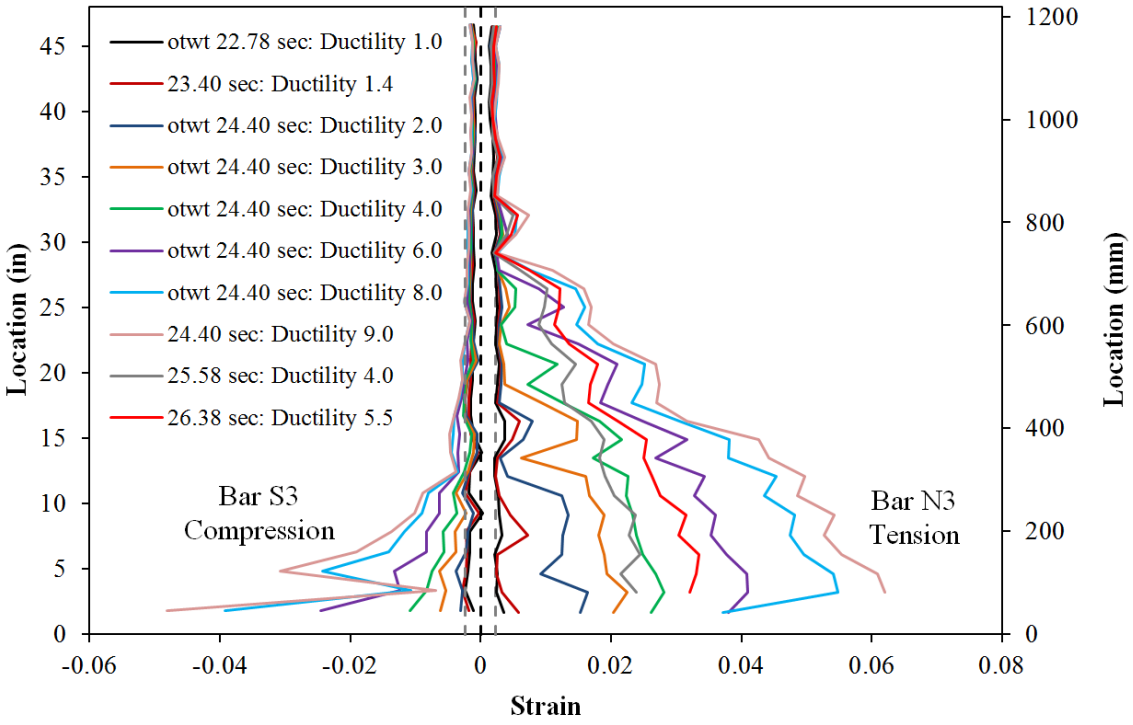

Figure 2-354. Test 18 – Extreme Fiber Vertical Strain Profiles during Push Cycles

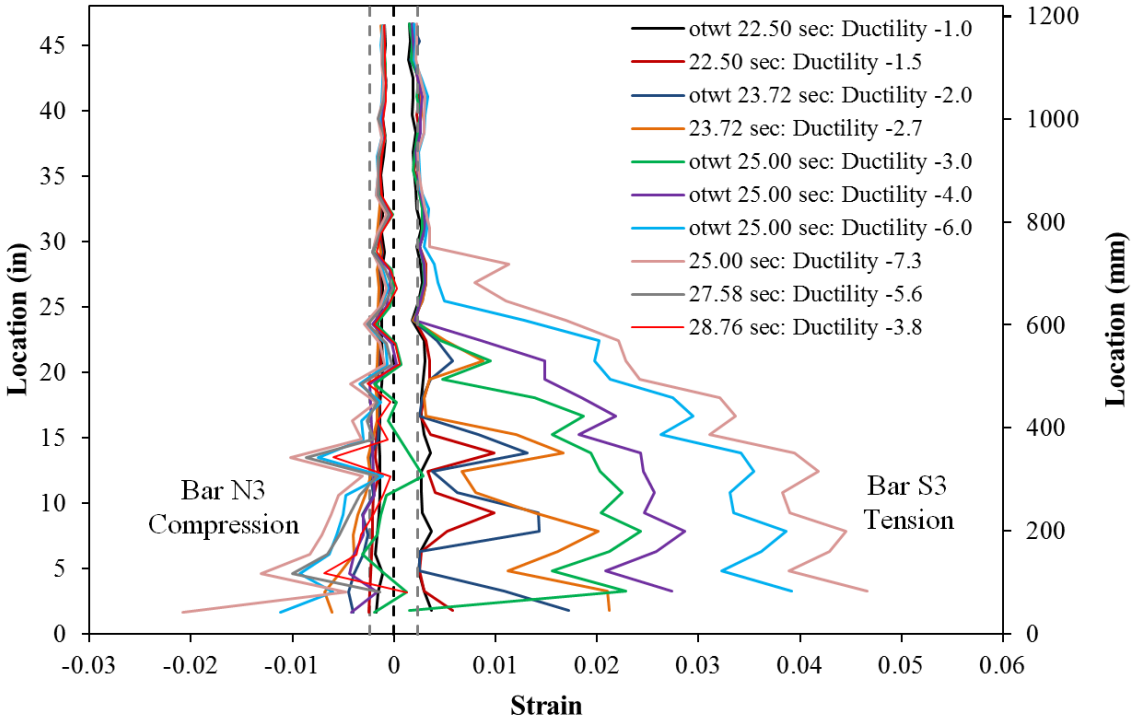

Figure 2-355. Test 18 – Extreme Fiber Vertical Strain Profiles during Pull Cycles

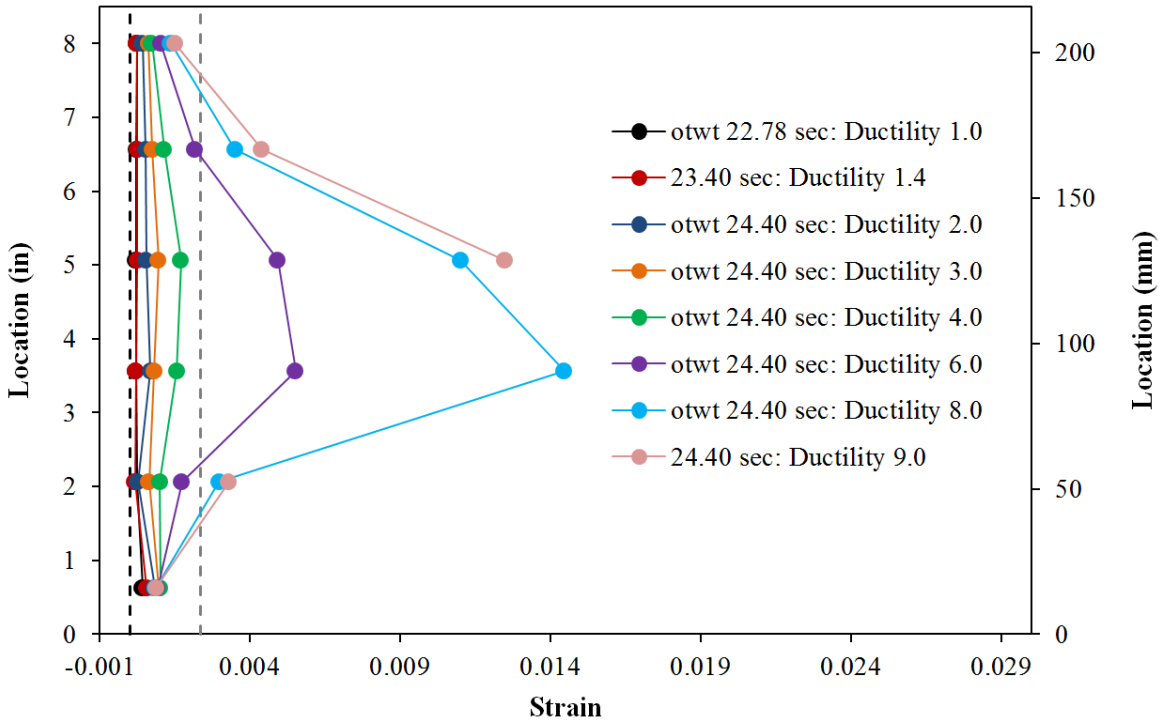

Figure 2-356. Test 18 – Transverse Steel Strains on the South Side during Push Cycles

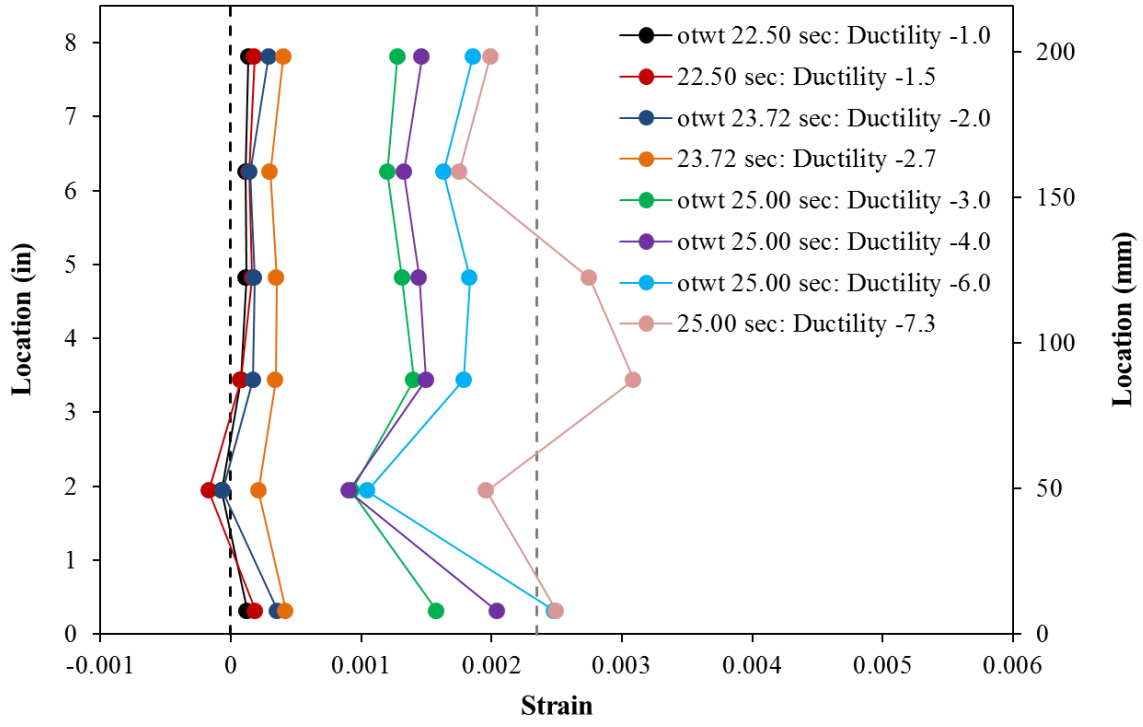

Figure 2-357. Test 18 – Transverse Steel Strains on the North Side during Pull Cycles

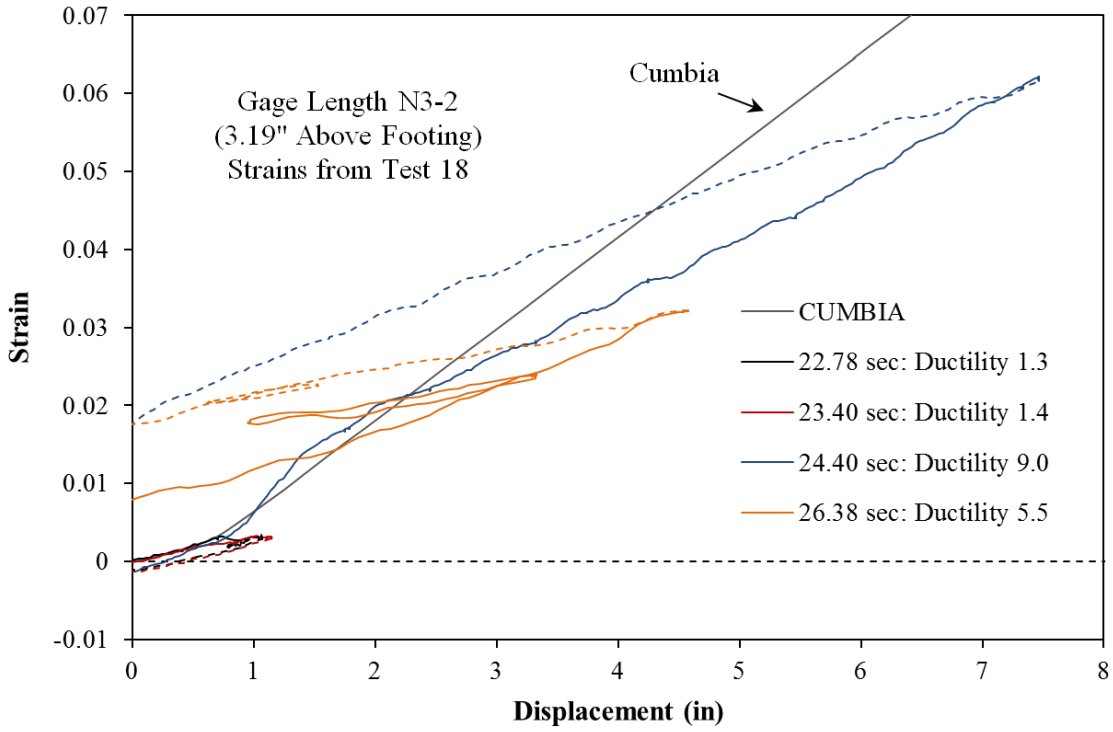

Figure 2-358. Test 18 – Tensile Strain and Displacement for Bar N3 (3.19” Above Footing)

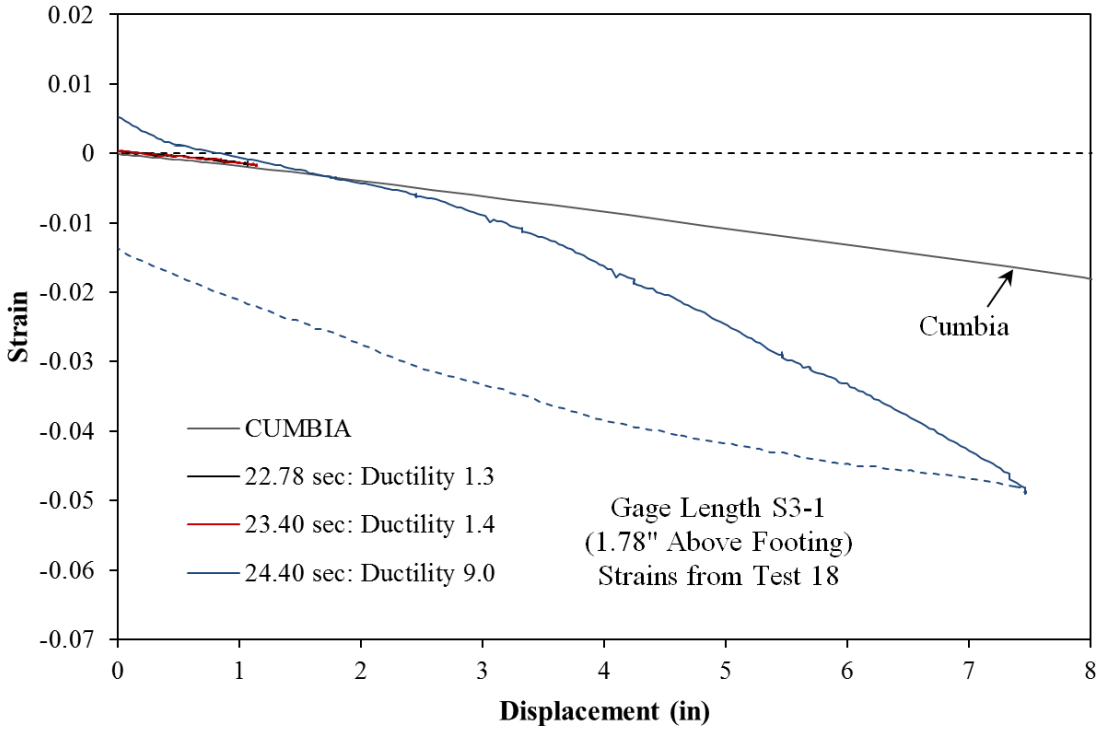

Figure 2-359. Test 18 – Compressive Strain and Displacement for Bar S3 (1.78” Above Footing)

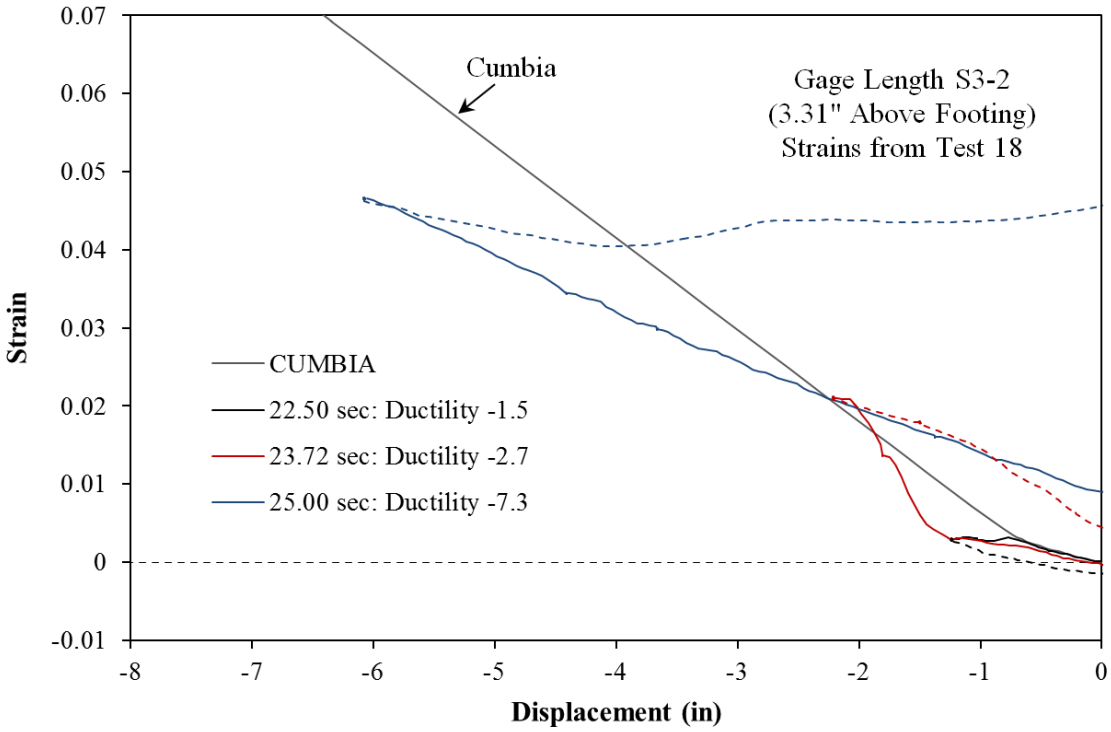

Figure 2-360. Test 18 – Tensile Strain and Displacement for Bar S3 (3.31” Above Footing)

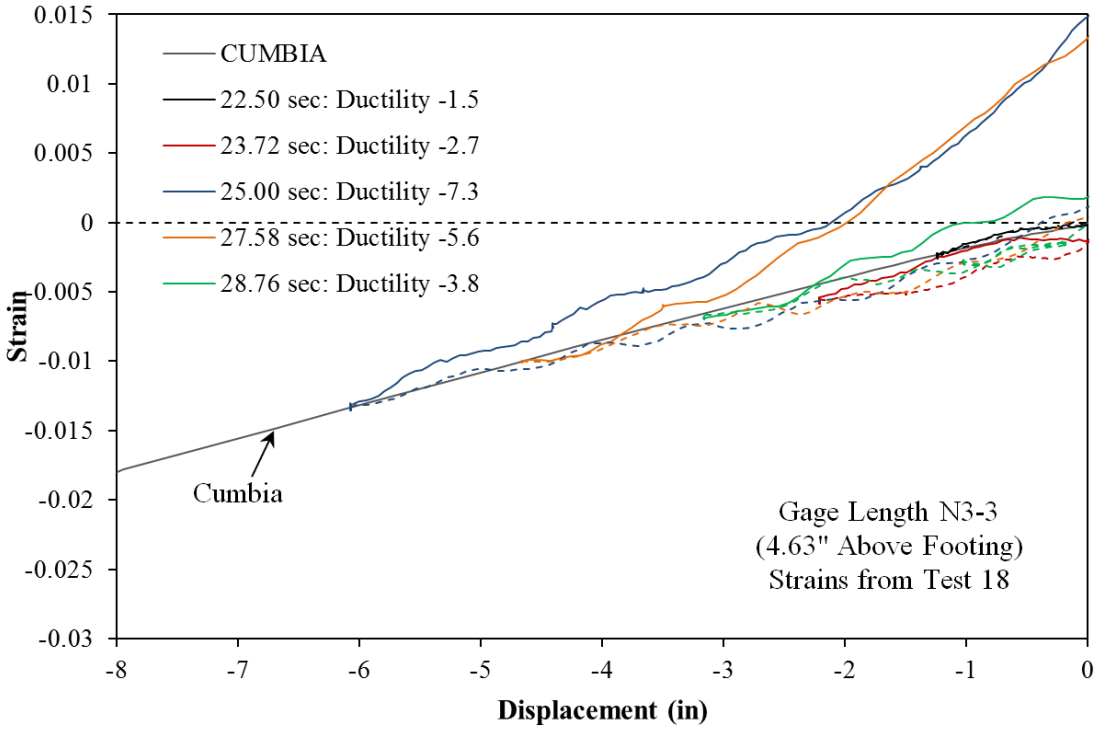

Figure 2-361. Test 18 – Compressive Strain and Displacement for Bar N3 (4.63” Above Footing)

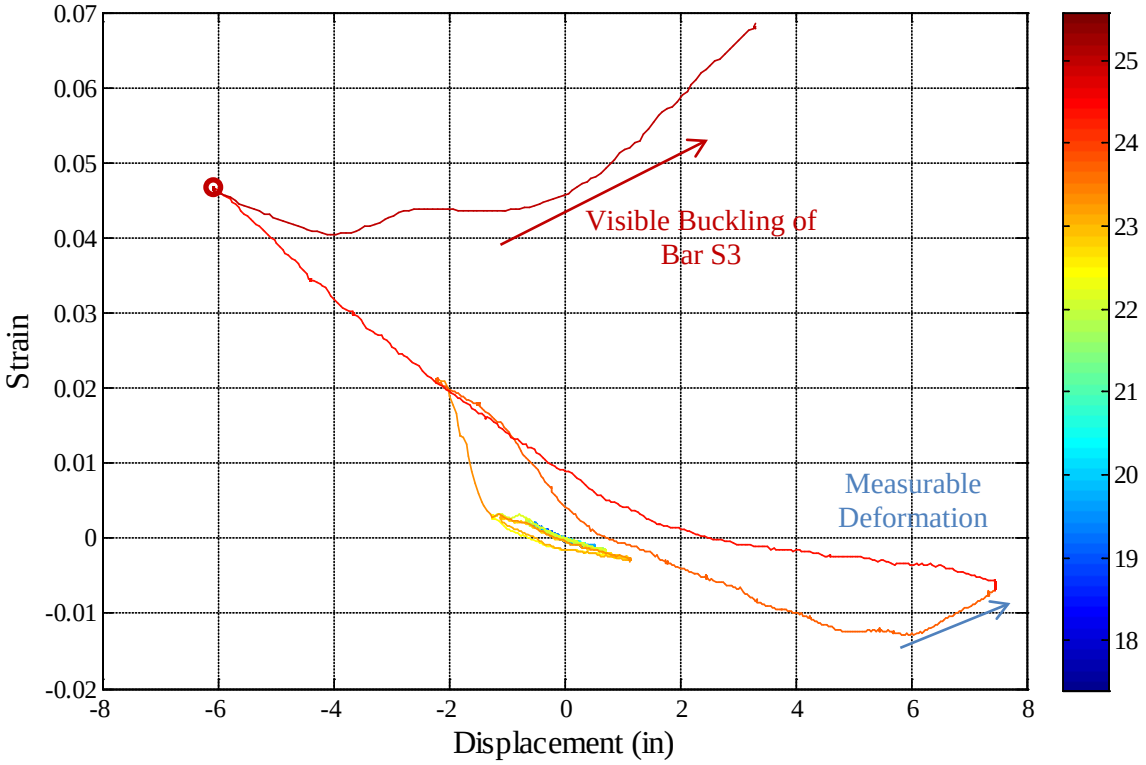

Figure 2-362. Test 18 – Bar S3 Strain Hysteresis for the Gage Length 3.31” Above Footing

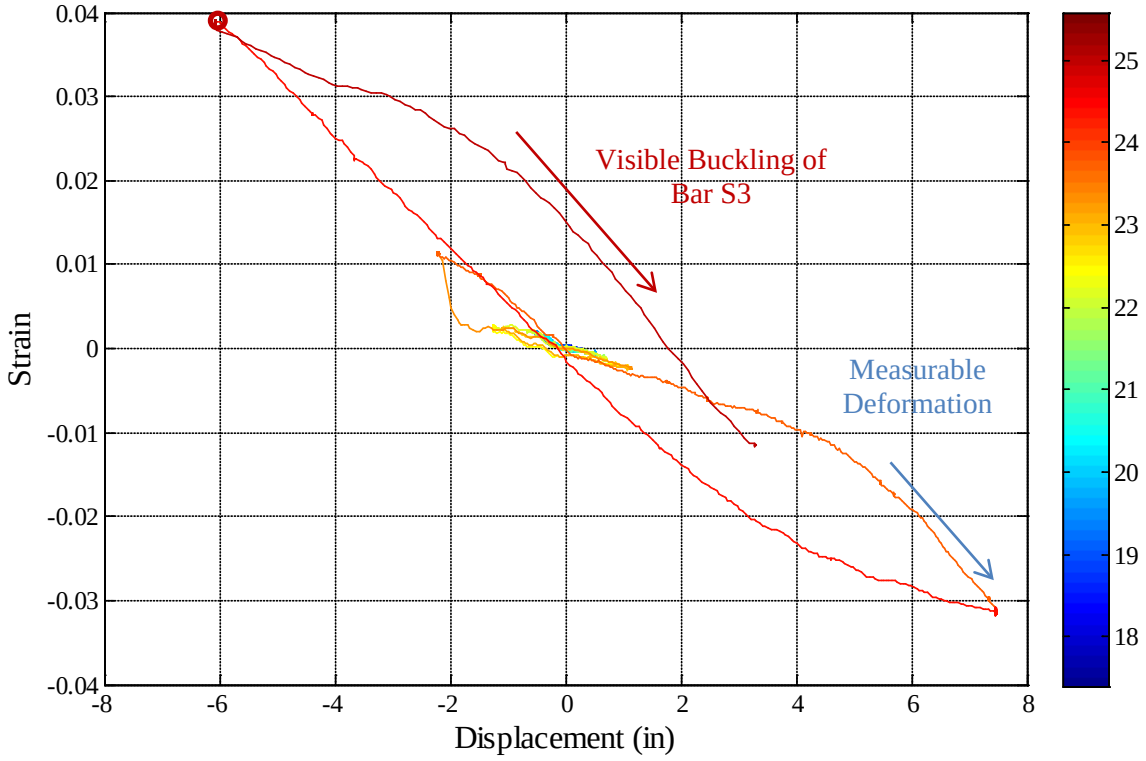

Figure 2-363. Test 18 – Bar S3 Strain Hysteresis for the Gage Length 4.83” Above Footing

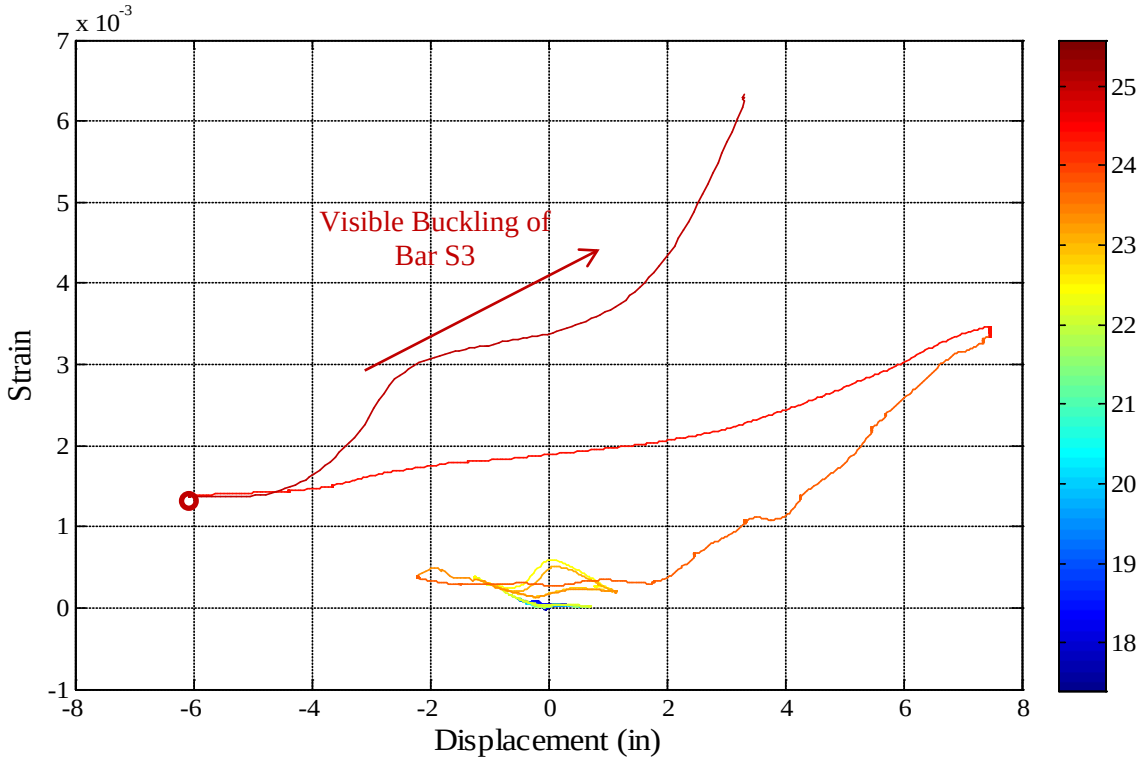

Figure 2-364. Test 18 – Transverse Steel Strain Hysteresis for Spiral Layer 2.06" Above the Footing Restraining Bar S3

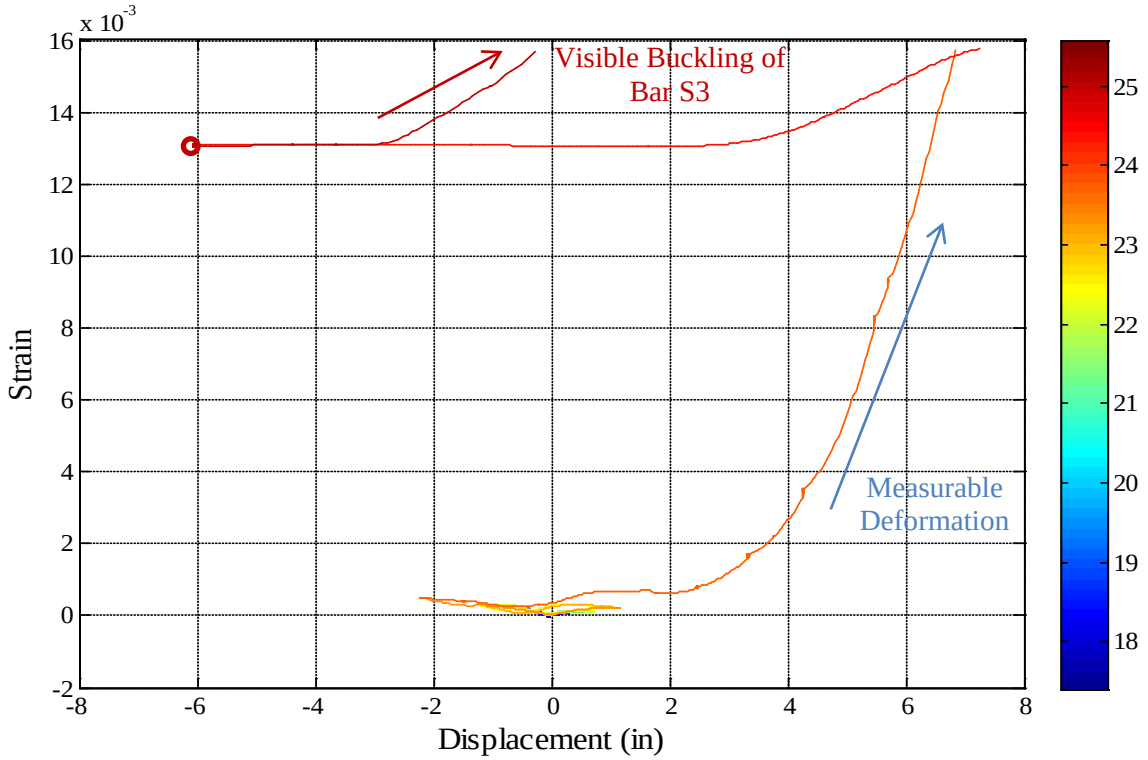

Figure 2-365. Test 18 – Spiral Strain Hysteresis 3.56" Above the footing overlaying Bar S3

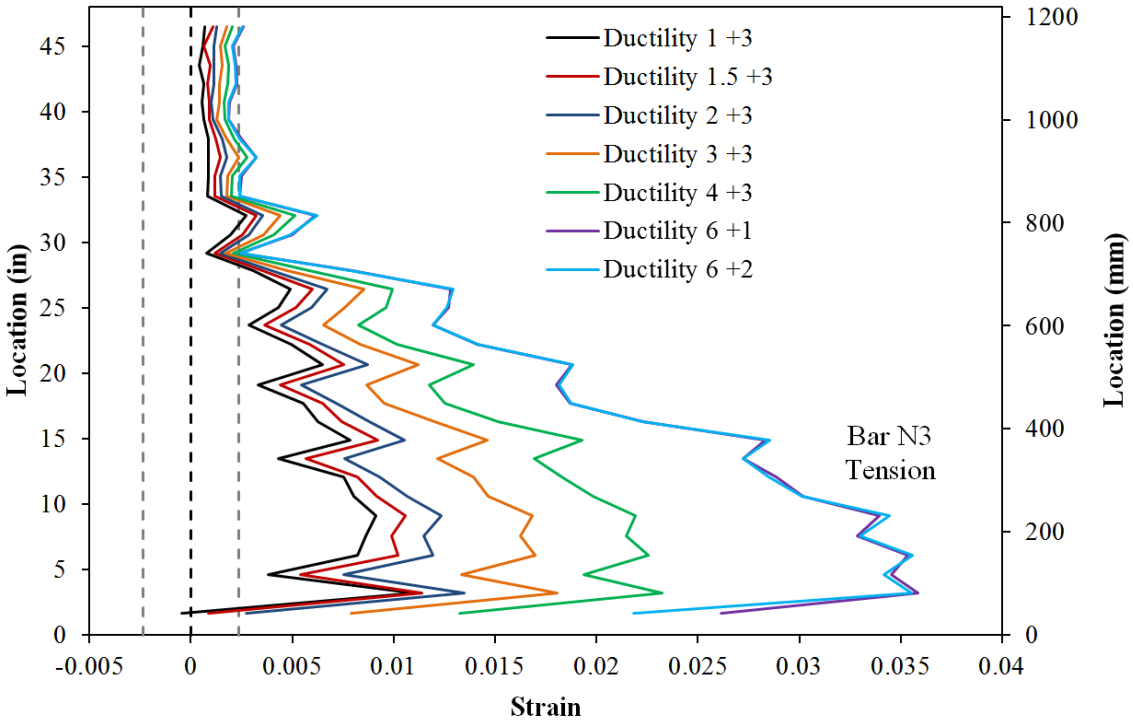

Figure 2-366. Test 18b – Vertical Strain Profiles for Bar N3 during Push Cycles

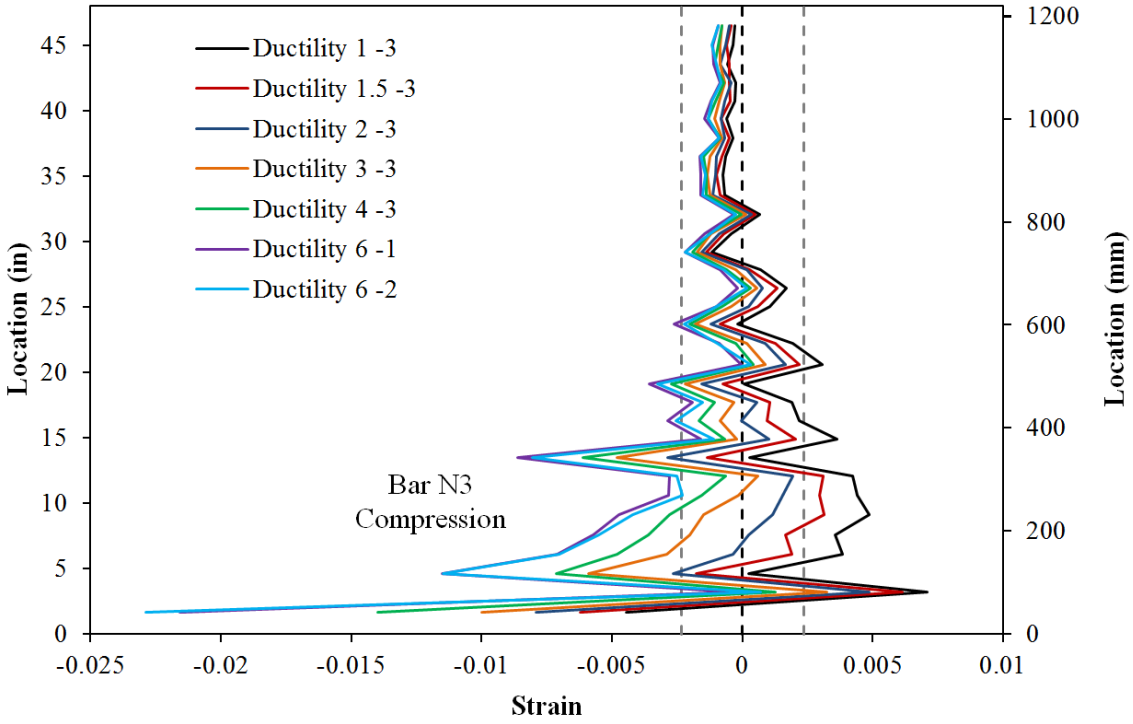

Figure 2-367. Test 18b – Vertical Strain Profiles for Bar N3 during Pull Cycles

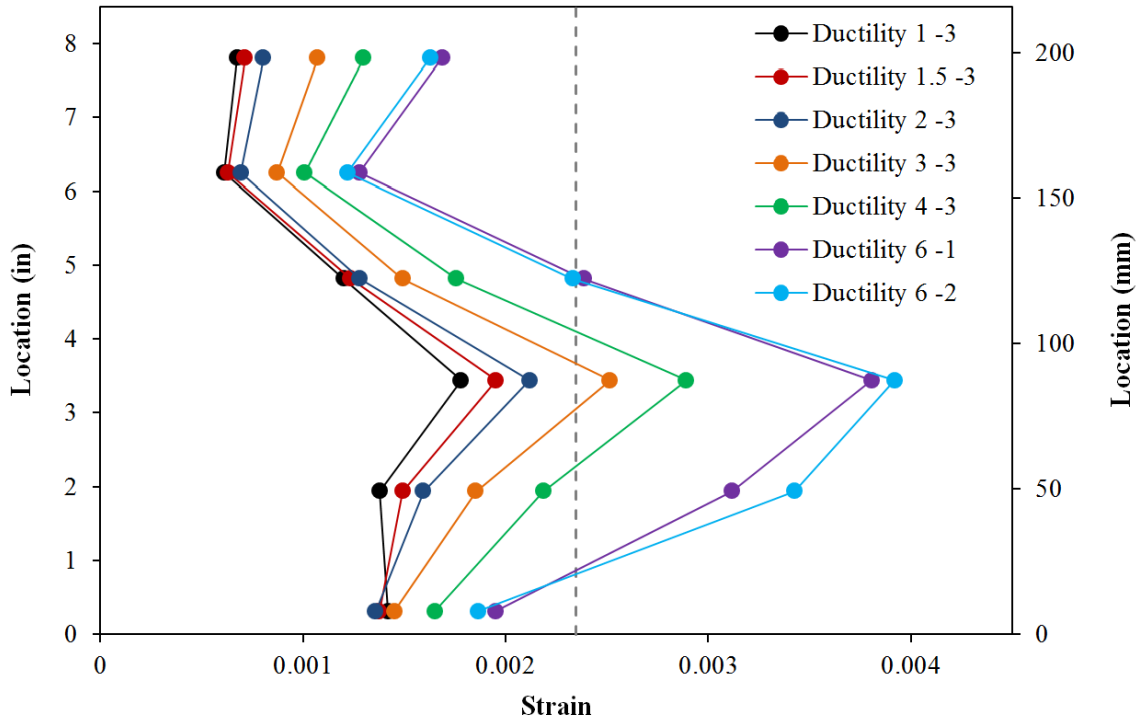

Figure 2-368. Test 18b – Transverse Steel Strains for Spiral Layers overlaying Bar N3 during Pull Cycles

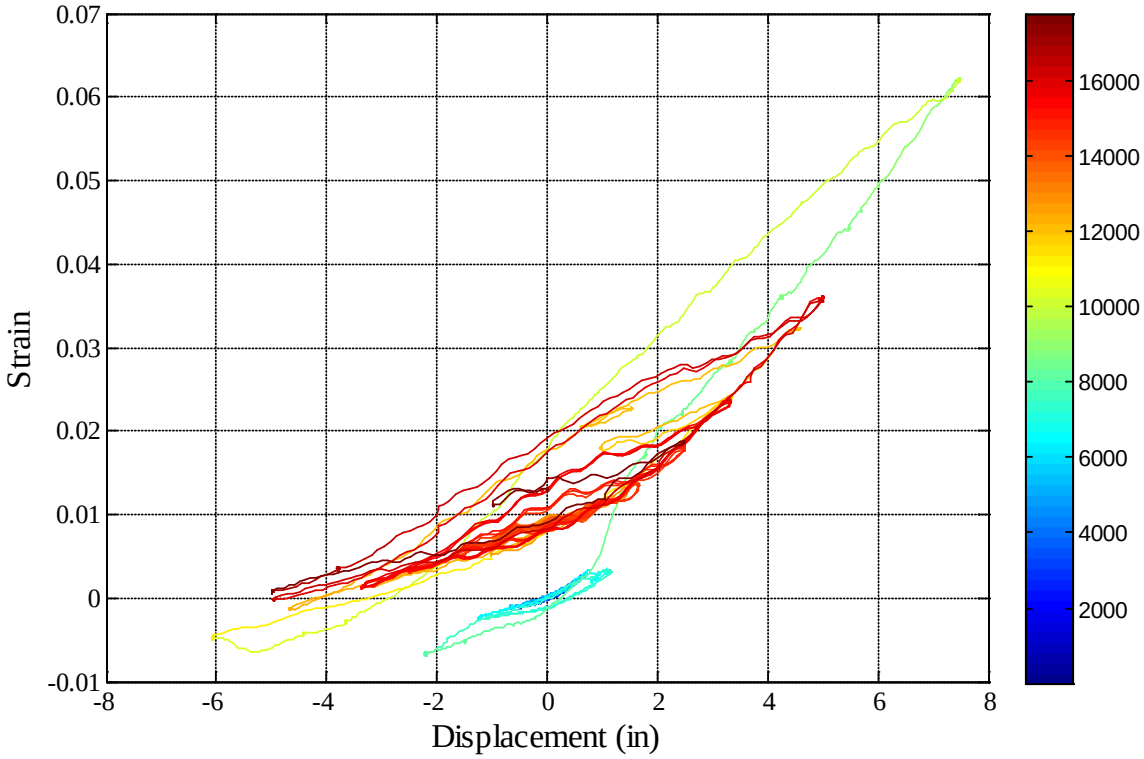

Figure 2-369. Test 18 and 18b – Bar N3 Strain Hysteresis 3.19” Above the Footing

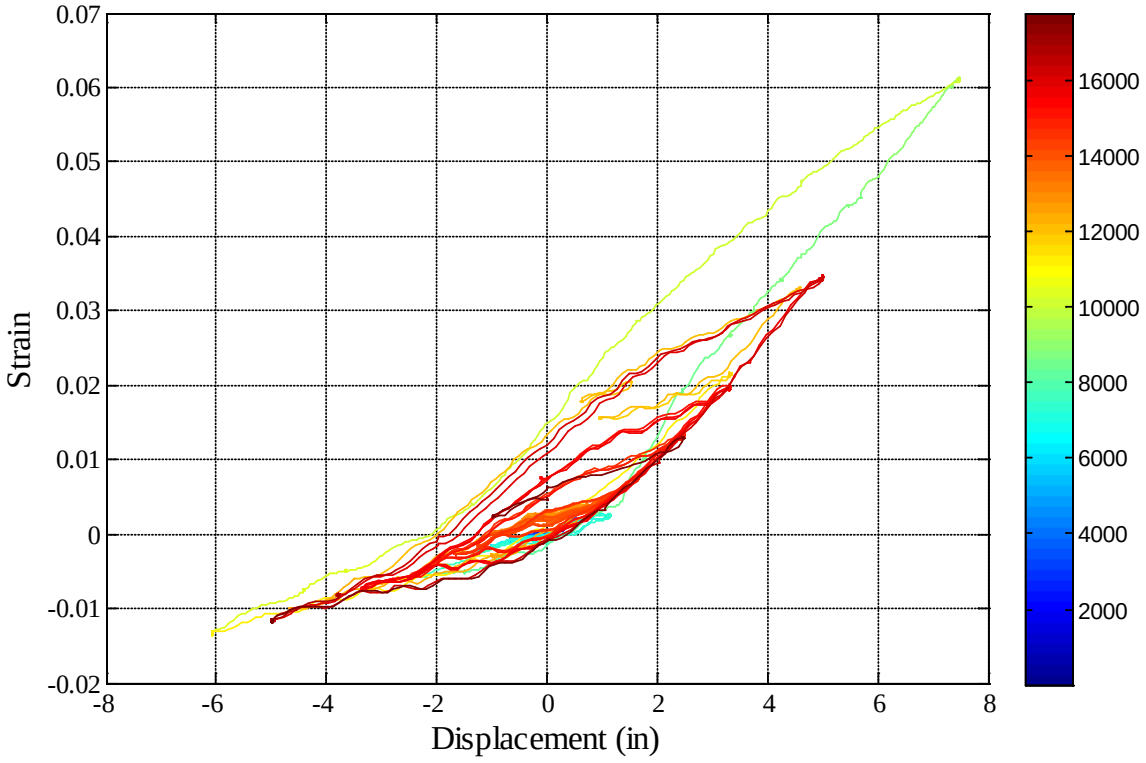

Figure 2-370. Test 18 and 18b – Bar N3 Strain Hysteresis 4.63” Above the Footing

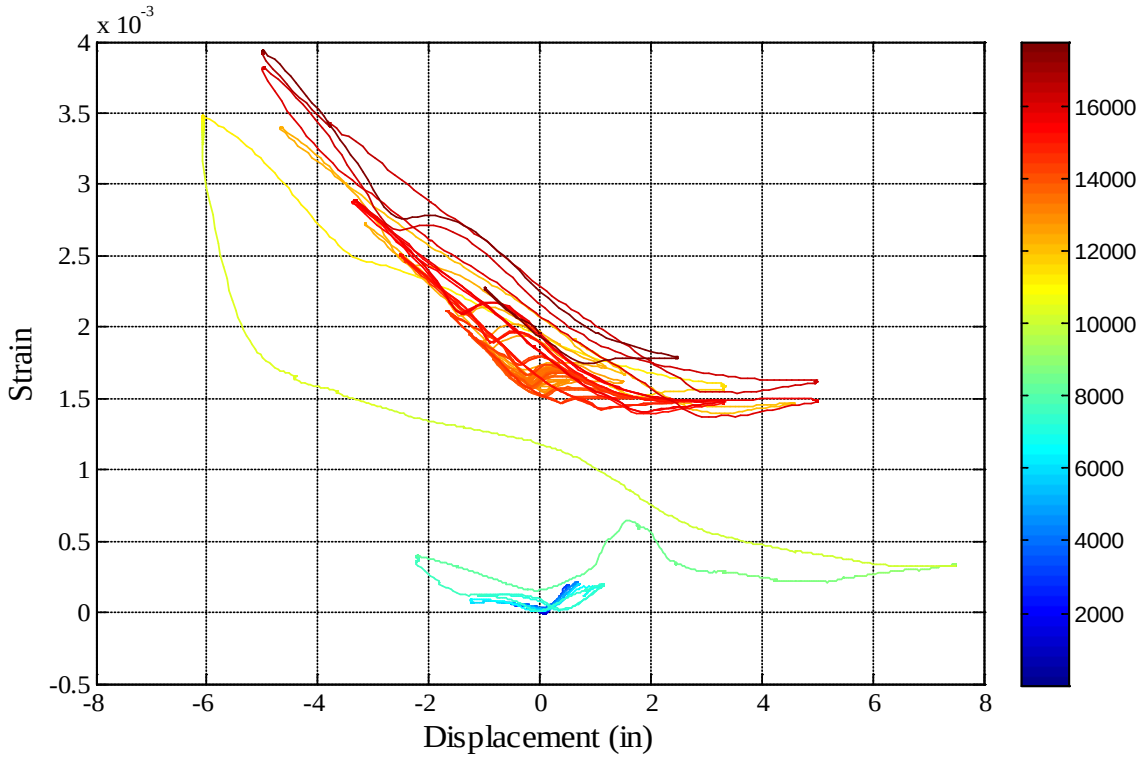

Figure 2-371. Test 18 and 18b – Transverse Steel Strain Hysteresis for the Spiral Layer overlaying Bar N3 (3.44” Above the Footing)

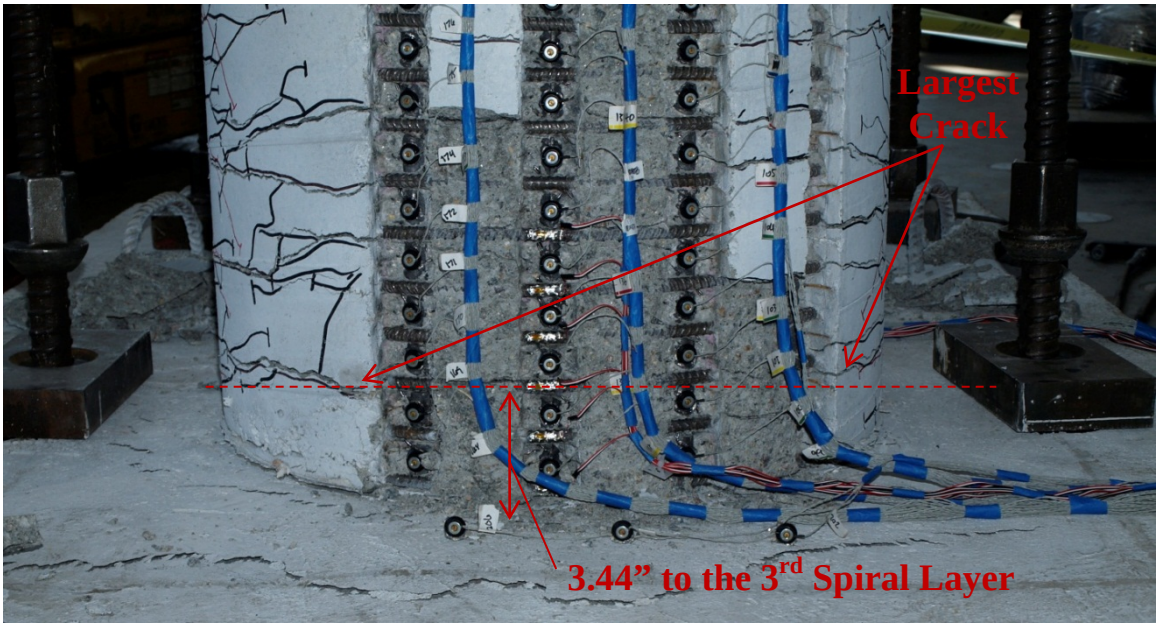

Figure 2-372. Test 18 – Crack Distribution on the North Side of the Specimen during the Peak Displacement Cycle to ($\mu_{9.0}^{24.40\,sec} = 7.46$")

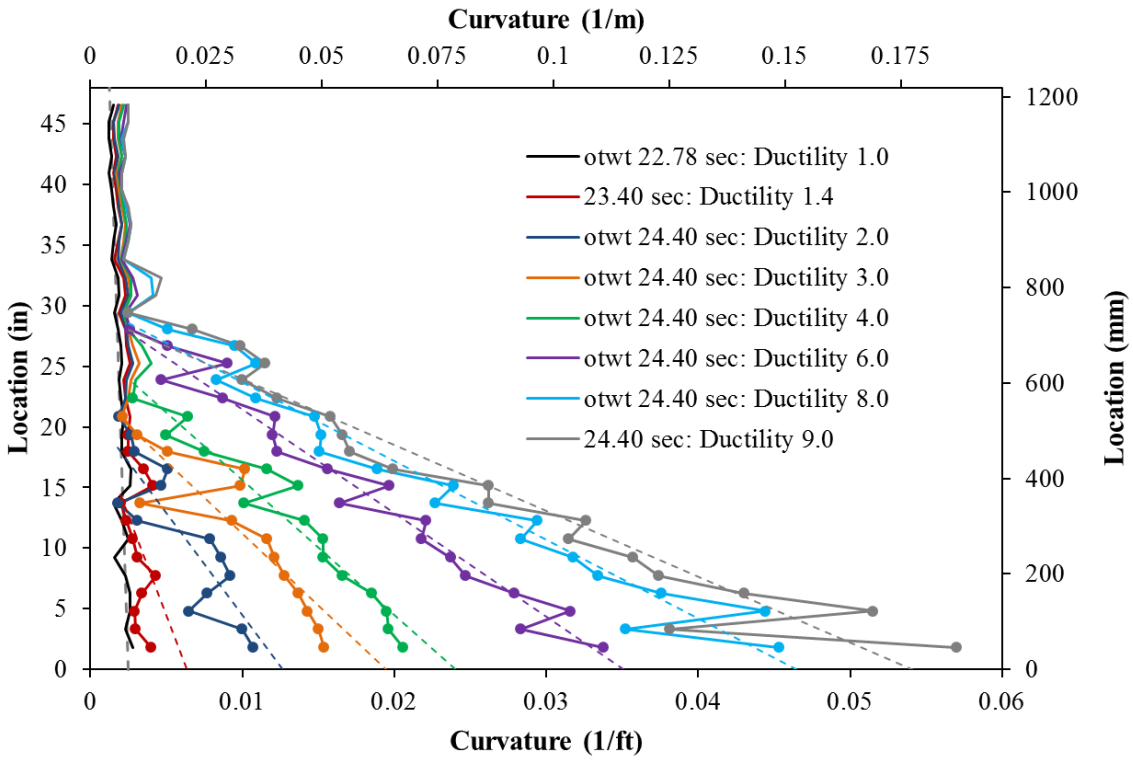

Figure 2-373. Test 18 – Vertical Curvature Profiles during Push Cycles with Linearized Plastic Curvature Least Squared Error Lines

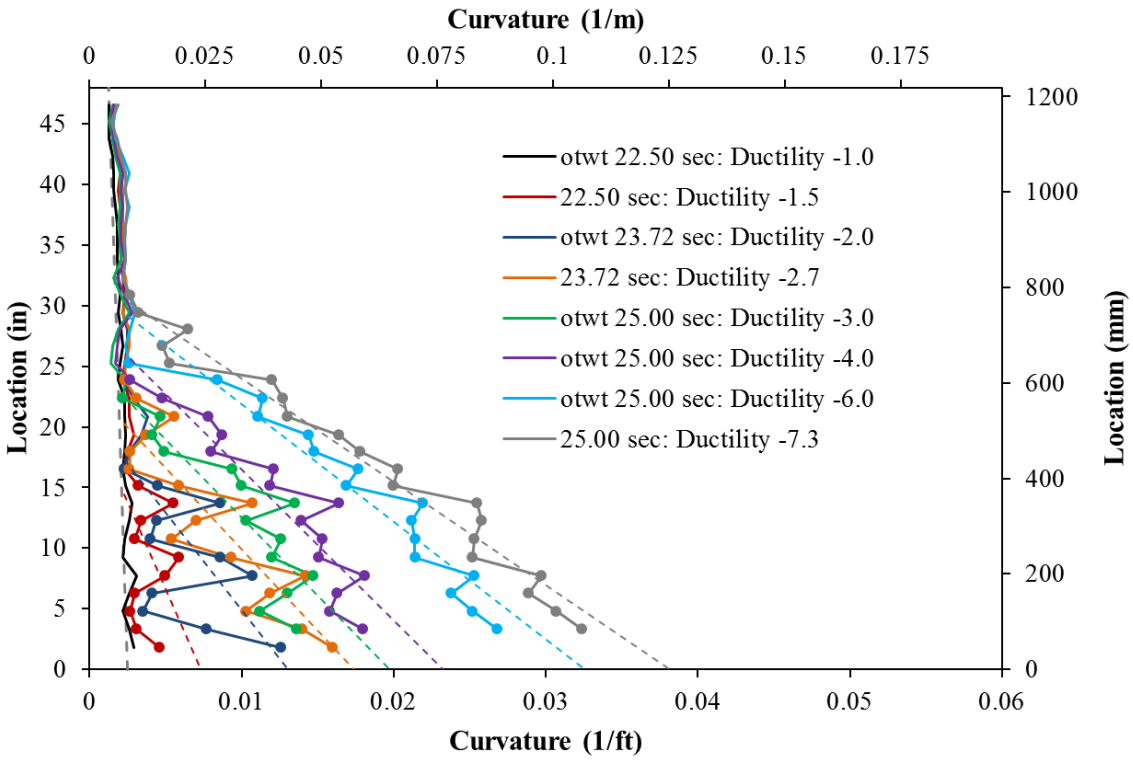

Figure 2-374. Test 18 – Vertical Curvature Profiles during Pull Cycles

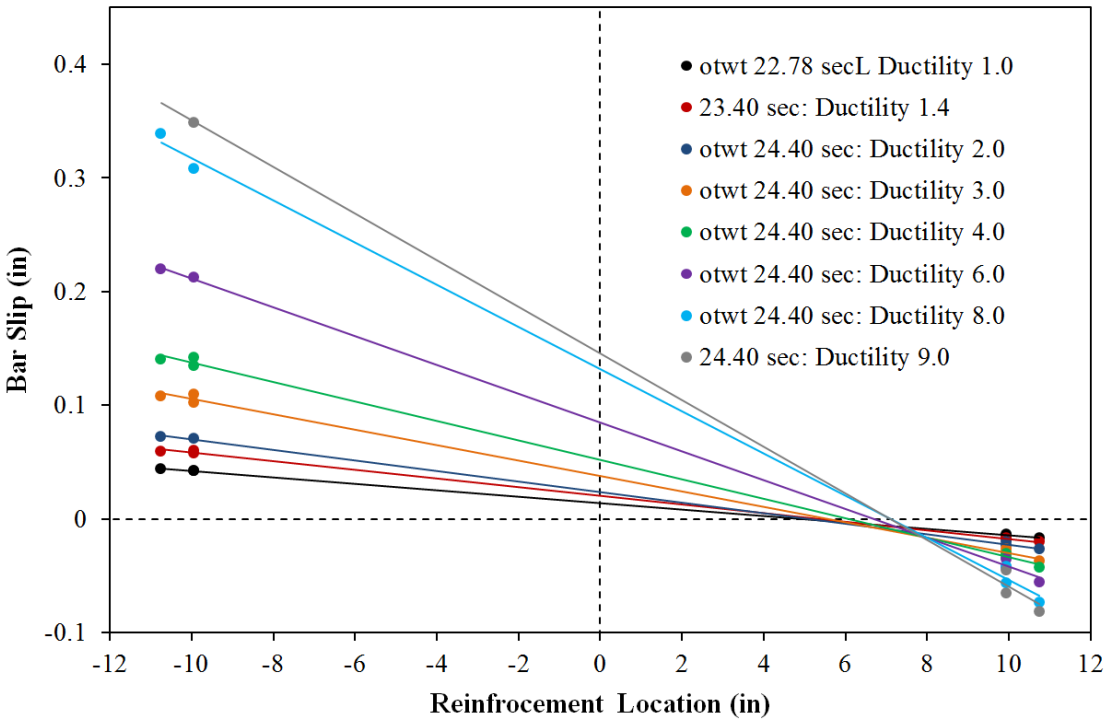

Figure 2-375. Test 18 – Base Rotation during Push Cycles due to Strain Penetration

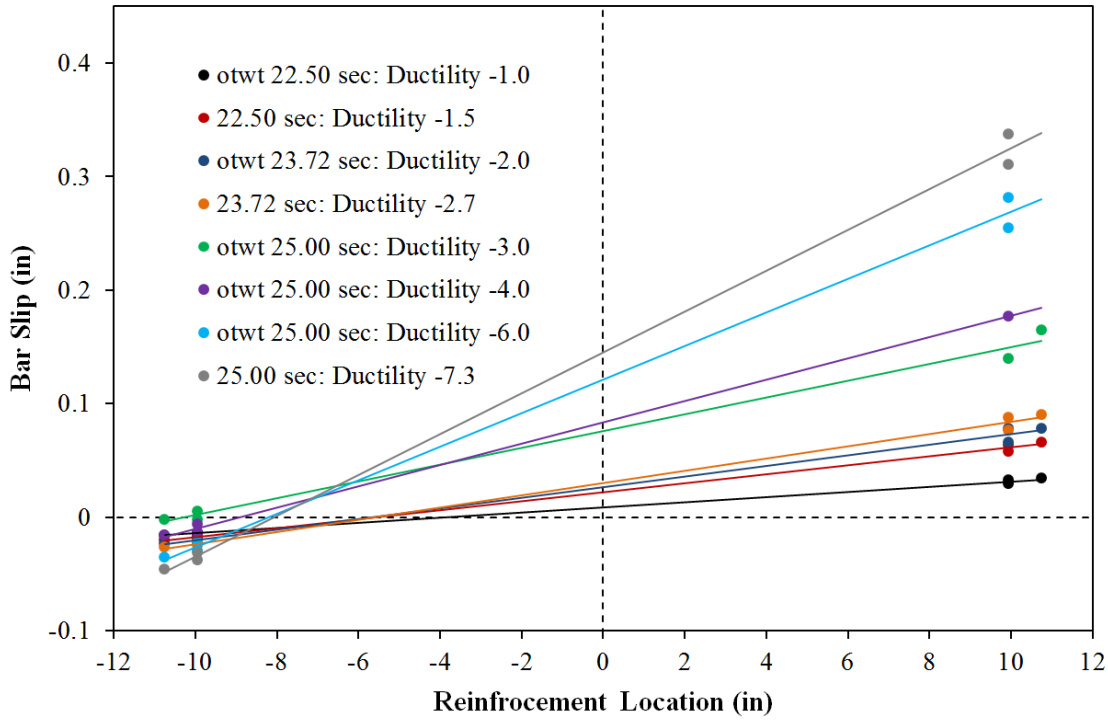

Figure 2-376. Test 18 – Base Rotation during Pull Cycles due to Strain Penetration

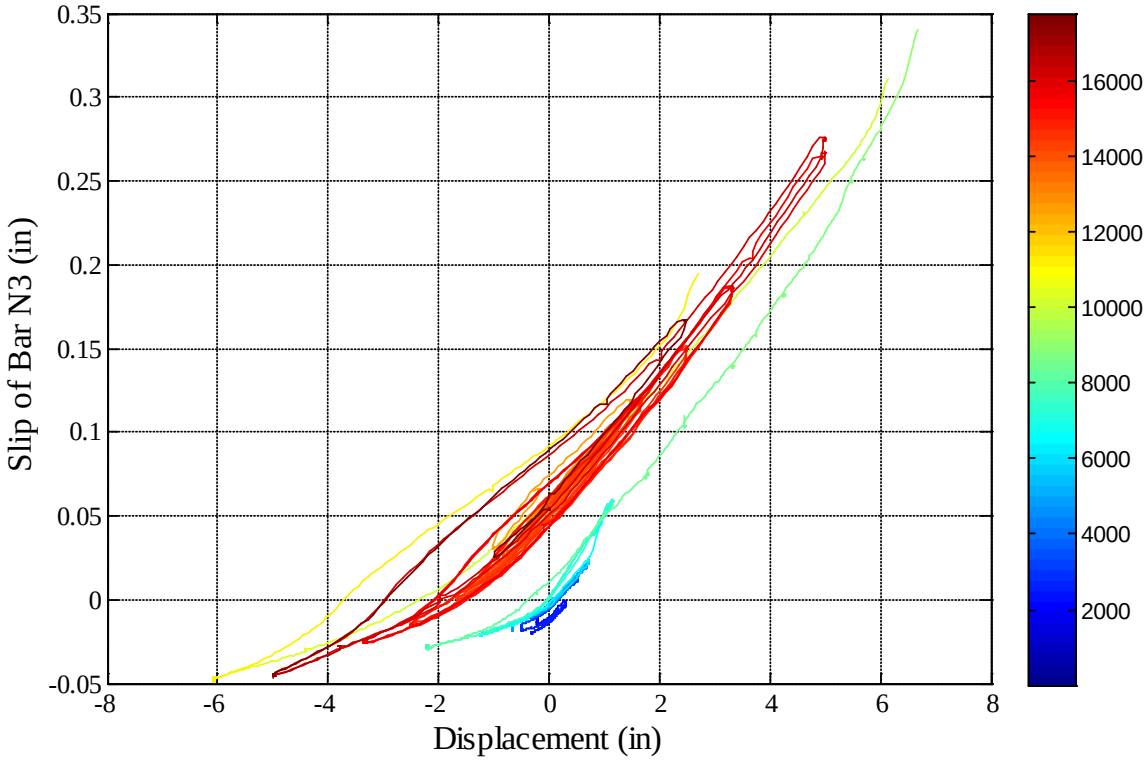

Figure 2-377. Test 18 – North Extreme Fiber Bar N3 Slip Hysteresis at the Footing-Column Interface

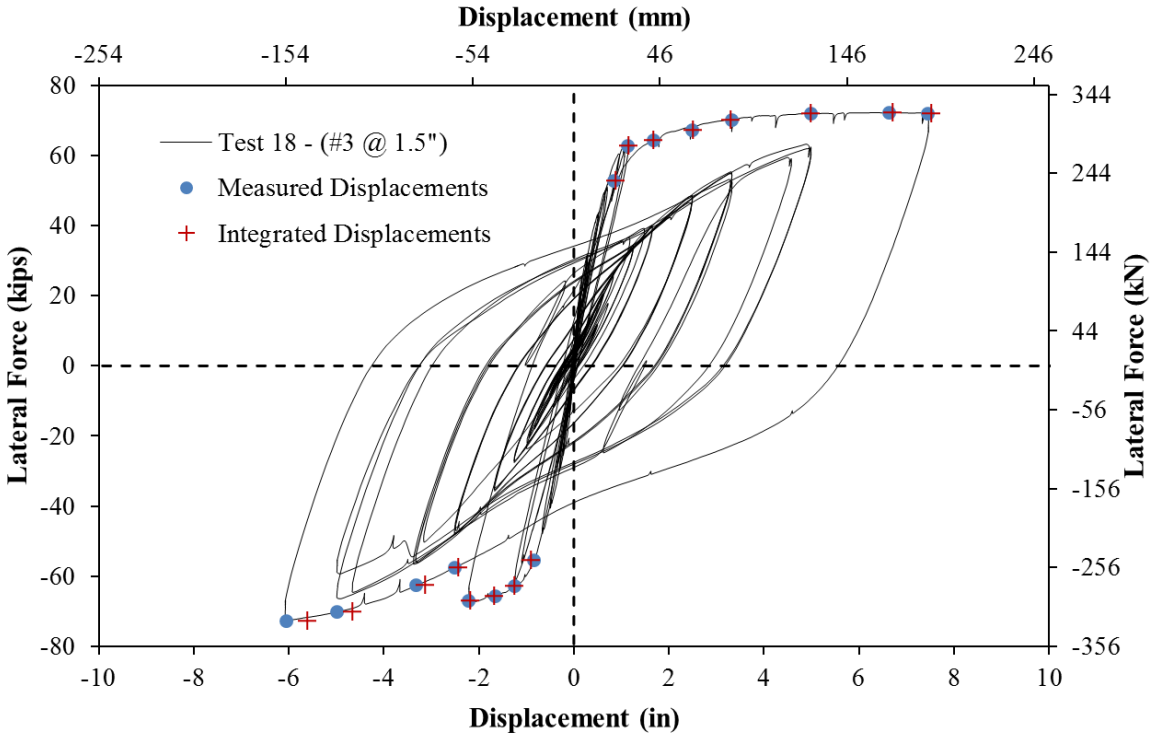

Figure 2-378. Test 18 – Comparison of Measured and Optotrak Integrated Displacements

CHAPTER 3 - Analytical Results

3.1.Development of Fiber-Based Model

Fiber-based analysis is well established for modeling of members undergoing primarily flexural deformation. The difference between fiber-based elements and frame elements lies in the method to define the global structural behavior. Frame elements are defined by their sectional properties, which include hysteretic characteristics (Figure 3-1) when conducting non-linear analysis. In the case of a fiber model, the cross section is divided into a series of fibers that follow prescribed constitutive relationships. As a consequence, the global force-deformation behavior of a fiber-based element depends on the material responses. A key advantage of fiber-models is the strain, stress and curvature information that can be obtained from them.

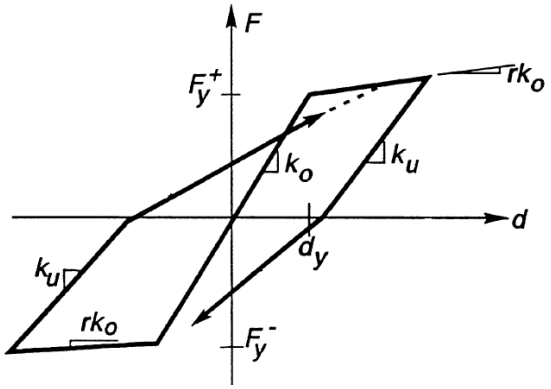

Figure 3-1. "Takeda" Force-Deformation Response for RC Beams and Columns from Appendices of Ruaumoko Manual

3.1.1.Theory of Fiber-Based Elements

In fiber-based models, materials have only uni-directional strength and stiffness. The uniaxial behavior is defined in terms of its stress-strain response. For the convenience of users, OpenSees provides a number of constitutive models for each type of material developed by various researchers. A few parameters, such as steel yield strength and concrete compressive strength, are usually required to define both monotonic and cyclic stress-strain behavior. For this research, the steel model developed by (Filippou, et al. (1983)) and the concrete model developed by (Yassin (1994)) were selected for analysis. The steel material allows the user to control the cyclic behavior by defining a pair of isotropic hardening ratios in addition to an adjustable yield strength and elastic modulus. The concrete constitutive model has an inherent cyclic behavior which depends on user defined strength parameters.

Fiber sections are assumed to remain plane throughout the analysis. In reinforced concrete structures, the fiber section is assembled with pre-defined concrete and steel materials. The section is divided into a number of concrete patches where the steel fiber will be located. Strain compatibility between reinforcement and the surrounding concrete is assumed. The sectional reactions under force and moment are in terms of axial strain at mid-section and curvature. A unique solution of this deformation combination will be obtained based on a cyclic moment-curvature analysis of the section.

To establish a fiber-based element, a number of fiber sections are spread along the length of the element. Each section is located at an integration point. A predefined interpolation function of the force or the displacement is required to distribute the global demand to sectional demands. The sectional reactions and local response are integrated to obtain the global reaction. Therefore, the accuracy of the fiber-based element depends on 1) the force or displacement interpolation function 2) and the order of exact integration of the integration scheme which relates to the number and location of integration point.

The fiber-based elements are separated into two types of elements regarding interpolation functions. The force (flexibility)-based element utilizes the force interpolation function to distribute the nodal concentrated force to each section. The sectional response is then obtained in terms of a combination of axial strain and curvature. Subsequently, the curvature is integrated to obtain the displacement. In an engineering problem, the distribution of force and moment are often known. For the case of seismic forces in bridges, the moment distribution of columns is triangular with a point load at the center of superstructure (usually, inertia weight of the columns is either ignored or a portion of it combined with the superstructure weight). The force-based element utilizes this linear load distribution to obtain the loading demand at each section. Therefore, there is no assumption on the force interpolation function and equilibrium is strictly satisfied at each section and end nodes. On the other hand, the displacement-based element applies a displacement shape function to distribute the nodal deformations. As a result, each section will be forced to accommodate the tributary deformation. Each section will react with a couple of reaction forces, including moment and axial load. The global force will be obtained by extrapolating the sectional force to the node. A shortcoming of displacement-based elements is that the displacement shape function may not reflect the real deflected shape of a structural component. As a result, a finer mesh is often required for displacement-based elements to increase the accuracy of the displacement shape. Moreover, equilibrium is only satisfied at the nodes. The distribution of moment along the column element is not required to be linear.

There are a couple variations of force-based elements. One such element (termed ‘beam with hinges’) was developed by (M. Scott and F. Fenves (2006)) to overcome the ‘loss of objective’ problem. The ‘beam with hinges’ element utilizes a plastic hinge integration method which allows defining the integration weight of the critical section with a plastic hinge length. The element involves a modified Gauss-Radau integration rule where the weight of the end integration point is adjustable, as shown in Figure 3-2 from (Scott and Fenves (2006)). Though the regular force-based element allows the user to alter the weight of the end integration point to accomplish the same goal, the length of the weight cannot be defined to the pre-calculated plastic hinge length since it depends on the number of integration points. The ‘beam with hinges’ element is more convenient for reconciling the integration weight to a plastic hinge length. To reduce the computational cost, an elastic region is defined at the interior portion of the ‘beam with hinges’ element. The elastic properties, such as elastic modulus, area and moment of inertia, are required at the interior region. It has been observed in the experimental tests that cracked regions cover most of a reinforced concrete column. As a result, a cracked section moment of inertia was used to model the elastic portion of the element.

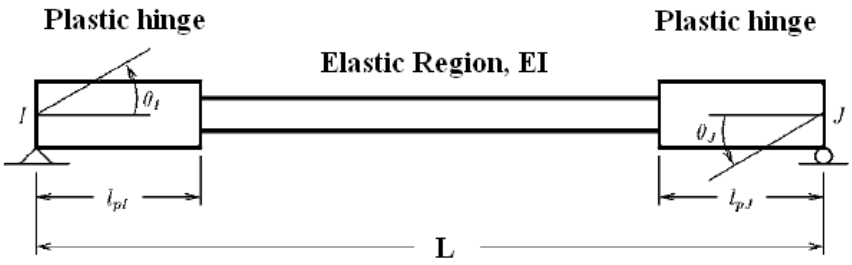

Figure 3-2. Beam with Hinges Element from (M. Scott and F. Fenves (2006))

A modified force-based element has recently been developed by (M. Scott (2011)). It has the ability to change sections and integration schemes along the length of the element. This allows the curvature distribution to be adjusted and multiple integration points in the plastic hinge region. However, the element may still suffer from strain softening behavior. The strain distribution needs to be inspected when placing multiple integration points in the plastic hinge region.

3.1.2.Selection of Fiber-Based Elements

When selecting a fiber-based element, its ability to predict the force-deformation response and material strains will be an important factor to consider. Since the parametric study (which is discussed later) will based on time history analysis, the dynamic performance of the element is also significant. Both force and displacement-based elements are utilized to simulate multiple experimental tests and results are compared in this section.

A force-based element simulates the column with only one element while a finer mesh is required with a displacement-based element to enhance accuracy of the moment distribution within the model component. Thus, the column is simulated with multiple displacement-based elements or extra integration points. Figure 3-3 compares the force-deformation responses from experimental data of a test conducted at NCSU to the analysis results from force-based and displacement-based elements. It is observed that the displacement-based element over-predicts the strength of the specimen while the force-based element provides very accurate prediction. Though the accuracy of displacement-based element might be improved by refining the mesh, the computational cost will be increased consequently. As a consequence, the force-based element is selected for the research described in this report. The Beam with Hinges Element is utilized in most cases as a result of its convenience in defining the plastic hinge length. The dynamic performance of the element will be discussed later.

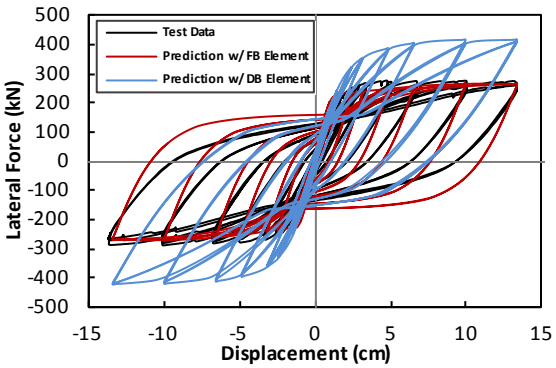

Figure 3-3. Comparison of Force-Deformation Responses

3.1.3.Strain Penetration Model

It is illustrated in Figure 3-4 that cracking was observed on the footing surface in many of the test specimens. When the column is subjected to large flexural deformation, a crack initiates near the tensile side of the column. This is due to the strain penetration of the longitudinal reinforcement into the footing. As the longitudinal reinforcement has large tensile strains in the plastic hinge region, a strain gradient is required inside the footing to allow the reinforcement strain to reduce to zero. Globally, the reinforcement will slip from the footing by a certain amount of displacement which depends on the strain gradient level in the footing. A small portion of the footing surface concrete, which is bonded to the reinforcement, cracks to accommodate this bond slip displacement.

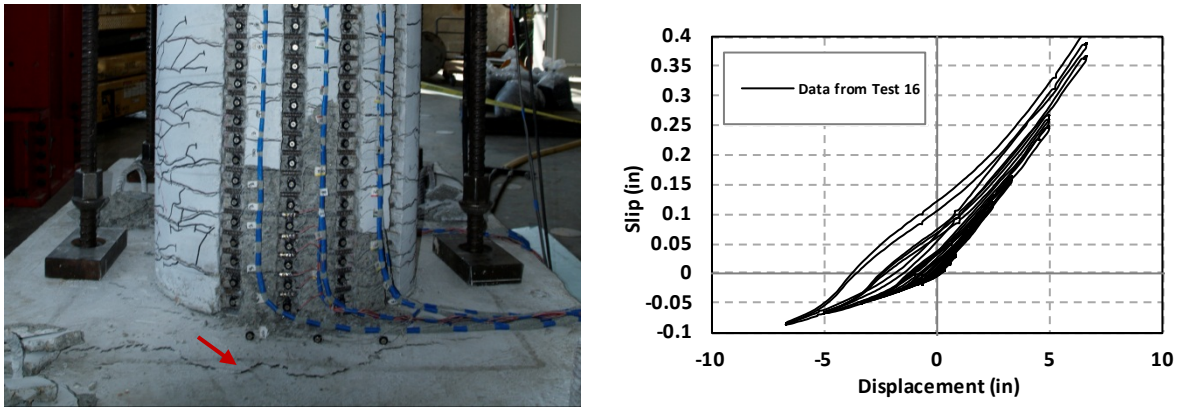

Figure 3-4. (Left) Crack on the footing near the tension side and (Right) Bond slip hysteretic response of the column

In experimental tests, the bond slip displacement of reinforcement can be obtained by monitoring the vertical movement of the LED markers. Figure 3-4 portrays the bond slip hysteretic response at the lowest marker level on the reinforcement. Since the monitored marker is located about 1.0 in (25.4mm) above the footing surface, the bond slip displacement may include a portion of plastic elongation of the reinforcement. This elongation could not be quantified precisely without the strain data at this location of reinforcement. However, Figure 3-4 still demonstrates the general behavior of bond slip.

A zero length section element is located at the base of the column element to include the bond slip behavior, as presented in Figure 3-5. The zero length element serves as a nonlinear rotational spring which accounts for the additional rotation at the base column section due to bond slip. The behavior of the zero length element depends on the associated fiber section. The zero length fiber section consists of both concrete reinforcement fibers. The steel reinforcement fiber is characterized by bond slip material model developed by (Zhao and Sritharan (2007)). The model utilizes stress-slip relationship to account for the strain penetration effect. The bond slip is represented by the slip displacement in the material which depends on the stress in the reinforcement, as shown in Figure 3-6.

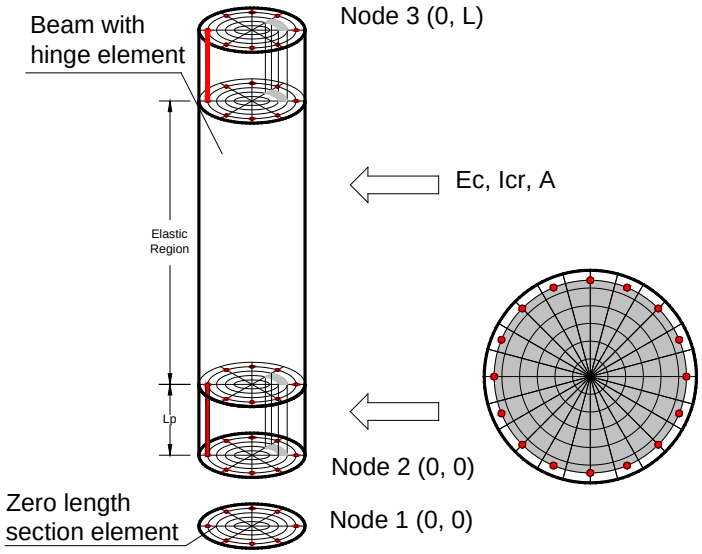

Figure 3-5. Lay-out of fiber model

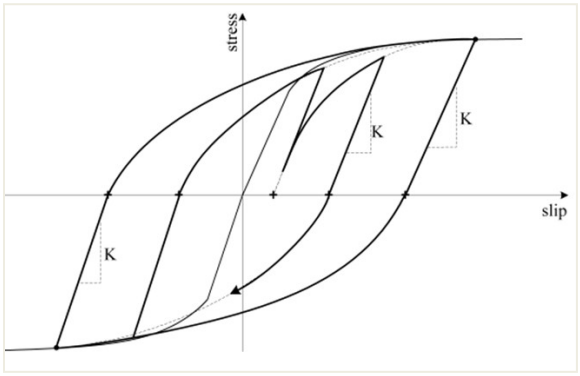

Figure 3-6. Stress-slip relationship from (Zhao and Sritharan (2007))

3.1.4.Calibration of Fiber-Based Model

A number of reinforced concrete bridge columns were tested in the Constructed Facilities Laboratory. The summary of experimental results illustrates the details and observation from test 8 to 18. The results were utilized to calibrate the fiber-based column element and support some of the modeling decisions.

3.1.4.1.Calibration of Material Constitutive Model

As previously noted, the concrete material model by (Yassin (1994)) was utilized for this research. This model was selected because of its robust cyclic response, as shown in Figure 3-7. For the analysis, the tension strength of concrete is neglected while cylinder tests provide the compression strength which is directly input to the model.

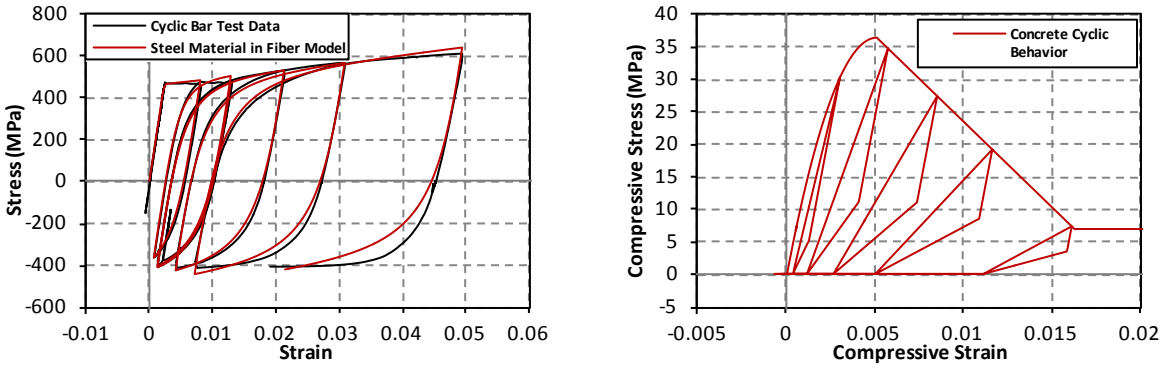

Figure 3-7. Material Constitutive Models

3.1.4.2.Calibration with Data from Static Tests

Following definition of the material models, the numerical fiber-based model was evaluated with the complete data set from the eighteen column tests where the strain information was available up to reinforcement buckling. It was observed that the behavior of the zero length section element and the numerical plastic hinge length have a large impact on the strain prediction. As a result, calibration concentrates on these two areas.

With the proposed cyclic bond slip behavior, the zero length element has relatively low moment capacity compared to the column section. It results in a strain-softening behavior where deformation concentrates in the bond slip model in terms of rotation. Consequently, the fiber model underestimated curvature and the resultant strain at the base section of the column element. The moment capacity of the bond slip model was enhanced to overcome the problem. The proposed bond slip model suggests defining the ultimate slip at maximum stress of reinforcement to be 30 to 40 times the slip at yield stress. By decreasing the ultimate slip level, the zero length section element has a higher strength which migrates a portion of the rotational deformation to the column base section.

The plastic hinge length controls the extent of plasticity in the 'beam with hinges' element. The plastic hinge length can be specified by an empirical relationship proposed by (Priestley et al. (2007)), as shown in Equation 3-1 through Equation 3-3.

$$L_{SP} = 0.022 f_y d_{bl}$$ Equation 3-1

$$k = 0.2\left(\frac{f_u}{f_y} - 1\right) \le 0.08$$ Equation 3-2

$$L_P = kL_C + L_{SP} \ge 2L_{SP}$$ Equation 3-3

where L_{SP} , L_P and L_C are the strain penetration length, the plastic hinge length, and the column length, f_y , f_u and d_{bl} are yield strength in MPa, ultimate stress in MPa and diameter of longitudinal reinforcement in millimeter respectively.

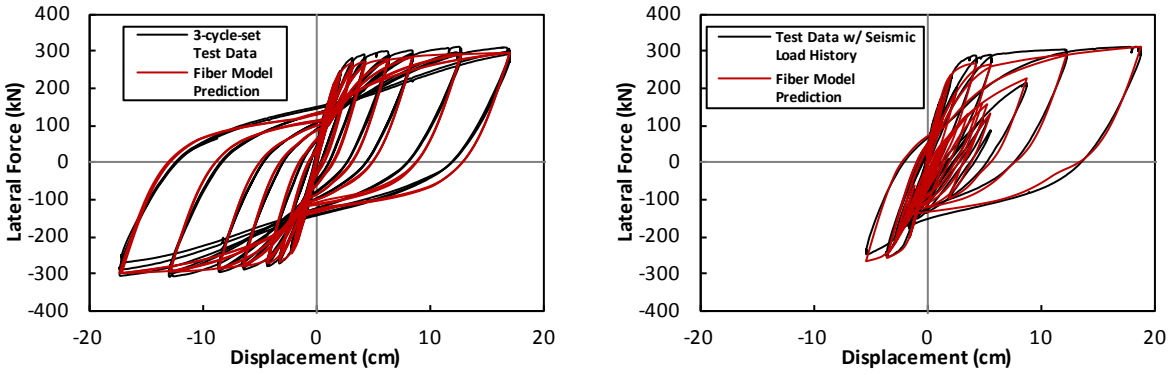

Figure 3-8. Comparison of force-deformation responses from the fiber model and test data

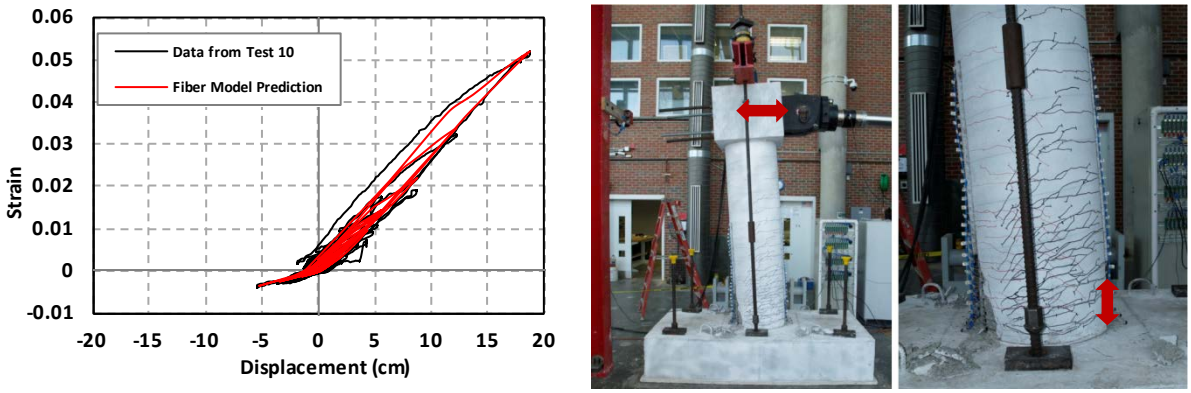

Figure 3-9. (Left) Comparison of strain hysteretic response measurement from the fiber model and test data and (Right) Locations of displacement measurement and strain measurement

Figure 3-8 demonstrates the comparison of force-deformation responses between the fiber model and test data with a 3-cycle-set load history and earthquake load history. The section-by-section-based equilibrium in the force-based element ensured an accurate prediction of response. The bond slip model contributes to the proper unloading and reloading stiffness of the model. However, the cycle to cycle strength degradation in the 3-cycle-set loading pattern is not captured because of the absence of cycle to cycle relaxation behavior in the steel constitutive model and cumulative damage in concrete. The strain hysteretic response in Figure 3-9 represents the relationship between the structural deformation and the local strain which indicates the damage in the plastic hinge region. As shown in Figure 3-9, the top column displacement is measured as the structural deformation and the strain is obtained from the plastic hinge region. The comparison shows good agreement between the model prediction and test data, especially, at the peak strain level. However, the residual strain at zero displacement level is consistently underestimated by the fiber model. Therefore, the accumulation of reinforcement strain over multiple cycles is not captured precisely. The solution to overcome this issue could be developing an advanced reinforcement material model to include the low cycle fatigue behavior of steel since most of current constitutive models are calibrated with material testing with limited cycles.

3.1.4.3.Calibration with Data from Shake Table Tests

The dynamic performance of the fiber model is important for the future parametric study which is based on nonlinear time history analysis. For the purpose of estimating the dynamic performance, the fiber model was implemented to predict the displacement response of two shake-table tests. In fiber-based time history analysis, (Petrini et al. (2008)) presented that no additional damping should be added for structural representation in a fiber model, since the hysteretic damping has been included at the material level. Therefore, there is no viscous damping applied to the fiber model.

(Petrini et al. (2008)) generated the first shake-table test at Centre of Research and Graduate Studies in Earthquake Engineering and Engineering Seismology (ROSE school) where a hollow reinforced concrete column was subjected to the Morgan Hill earthquake. The Pacific Earthquake Engineering Research Centre (PEER) and Network for Earthquake Engineering Simulation (NEES) sponsored the Concrete Column Blind Prediction Contest (2010) at University of California, San Diego (UCSD). A full scale reinforced concrete bridge column was tested under a series of six ground motions from Loma Prieta earthquake (1989) and Kobe earthquake (1995). The comparison between the displacement responses from a fiber model and those from the shake table tests are shown in Figure 3-10. The fiber model captures most of the major peaks in the displacement response, however, underestimates the residual displacement by a small amount. In the UCSD shake table test, the small amount of underestimation on residual displacement is due to lack of representation of cumulative damage in concrete. The extensive large residual displacement in the shake table test at the ROSE school is likely a result of local damage in the plastic hinge region, such as reinforcement buckling and concrete crushing or spalling. This column also ultimately suffered collapse due to a large P-Delta moment.

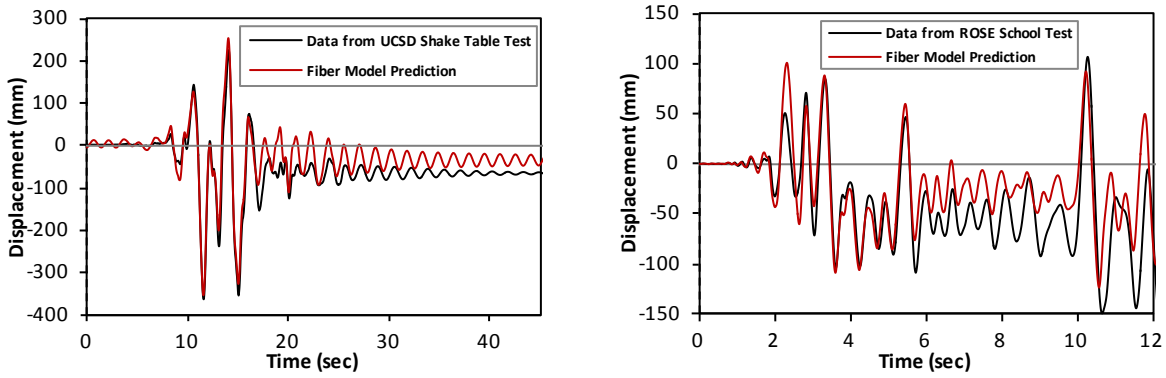

Figure 3-10. Comparisons of displacement response from fiber model and test data

It has been presented in the comparisons that the fiber-based model is able to predict accurate force-deformation response and strain hysteretic response of reinforced concrete columns. Therefore, it is felt to be for studying the load history effect on the relationship between strain and displacement. In addition, the robust dynamic performance of fiber-based model ensures the accuracy of the displacement response from time history analysis.

3.2.Parametric Study of Load History Effect on Strain-Displacement Relationship

As discussed before, load history may impact strain limit state definitions and the relationship between displacement and strain. The parametric study will focus on the strain limit defined by

buckling of reinforcement. As a multi-dimensional mechanism, buckling cannot be captured by the uniaxial material model in fiber section. However, the fiber-based model is able to capture the influence of buckling in the force-deformation response by incorporating a pre-defined buckling stress-strain behavior in the reinforcement constitutive model. With its ability to predict the strain hysteretic response, the fiber-based model can be utilized to study the effect of load history on the relationship between strain and displacement. Variables in the parametric study include the aspect ratio, the axial load ratio, the bar diameter, as well as the transverse reinforcement detailing. By altering one variable at a time, the column models were subjected to multiple earthquakes respectively, and the load history effect on the strain displacement relationship characterized.

3.2.1.Selection of Ground Motions

A large number of ground motions were collected for the parametric study. The ground motions are from large seismic events around the world. In order to generate sufficiently large displacement response and corresponding bar buckling, the ground motions were ensured to have a peak ground acceleration (PGA) larger than 0.4 g and the related earthquakes have 6 or higher magnitude. A list of all the ground motion information is shown in Table 3-1.

Table 3-1. Earthquakes for Parametric Study

Earthquake	Year	Station	PGA (g)
Chile	2010	NA	0.06
Japan	2011	TCGH	1.22
Kobe	1995	NA	0.82
Chichi	1999	NA	0.65
		No1197	0.8
		No1231	1
		No1503	0.8
		No1507	0.6
		No1517	1.2
		No2658	1
		No3474	0.8
Tabas	1978	NA	0.84
Northridge	1994	SylmarCSE	0.83
		Pacoima Dam	1.6
Darfield	2010	GDLC	0.72
Christchurch	2011	LPCC	0.88
Calexico	2010	Array11	0.6
Landers	1992	NA	0.8
Duzce	1999	Duzce	0.5
		Lamont	0.9
Erzican	1992	NA	0.5
Big Bear	1992	NA	0.5

Imperial Vally	1979	No160	0.8
		No180	0.5
		No183	0.6
Superstintion Hills	1987	No727	0.8
Managua	1972	No95	0.4
Victoria	1980	No265	0.6
Morgan Hill	1984	No451	1.2
Chalfant	1986	NA	0.45
Mammoth Lake	1980	No230	0.45
		No231	0.4
Dinar	1995	No1141	0.45
Cape Mantocino	1992	No825	1.5
		No828	0.7
Nihanni	1985	NA	1
Loma Prieta	1989	NA	0.5
San Fernando	1971	NA	1.2
Coalinga	1983	NA	0.6
N Palm Springs	1986	NA	0.7

Non-linear time history analysis is conducted with the fiber-based model under the listed ground motions. The strain hysteretic responses were compared to the monotonic response to expose the load history effect. Results from four earthquakes were selected and displayed in Figure 3-12. These four earthquakes are the 2010 Chile earthquake, 2011 Japan earthquake, 1995 Kobe (Japan) earthquake and 1999 Chichi (China) earthquake, as shown in Figure 3-11. The Chile and Japan earthquake are extremely large subduction events that are also typical of Alaskan earthquakes. These two earthquakes were selected to represent the earthquakes that may occur in Alaska area since the records of large earthquakes there are rarely available. Both ground motions have relatively long duration and a large number of reversals. However, the ground motion from Japan has one peak of peak ground acceleration of 1.22 g while the ground motion from Chile has a number of major peaks at a similar level. In contrast, the Kobe earthquake is not a subduction event and has limited number of major peaks. Time history analysis with the Kobe ground motion showed a limited number of cycles in the displacement response (Figure 3-12). The response featured a couple of large cycles of displacement at the beginning. The response of Chichi earthquake has very unique one-sided displacement response, as shown in Figure 3-12.

Note that in all of these cases, the data shown are structural responses. Changing characteristics of the structures will of course impact the resulting response. For this study, the objective was to select earthquakes which generated different response characteristics for a given column geometry.

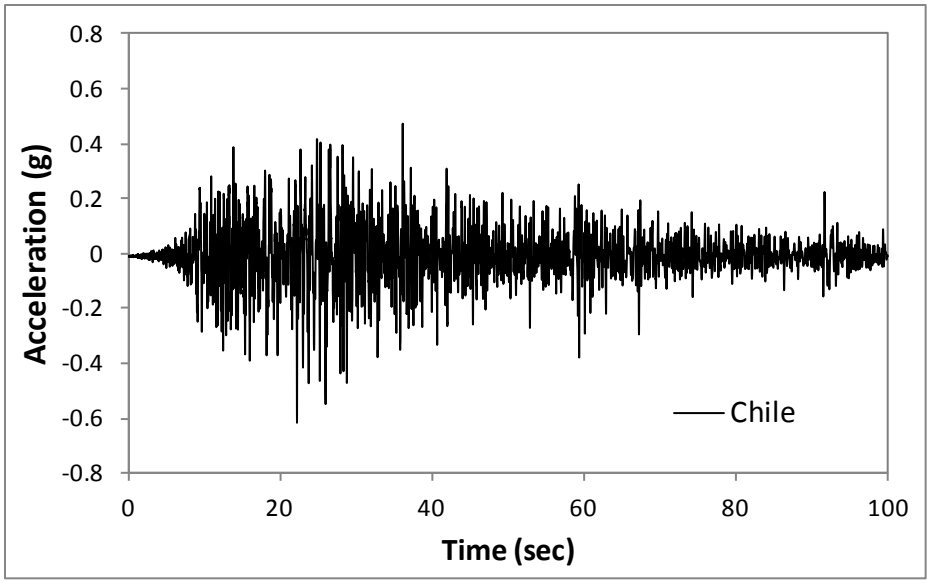

(a) Chile

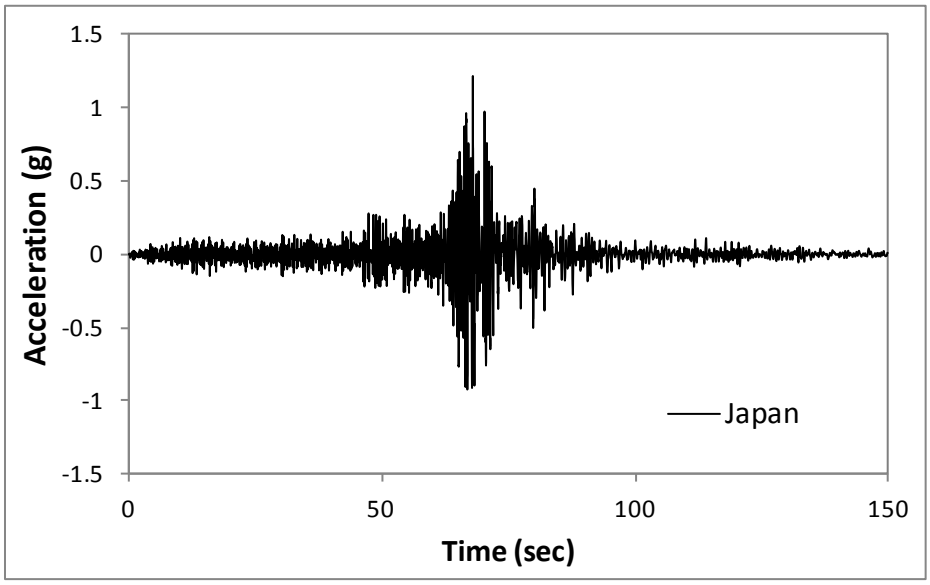

(b) Japan

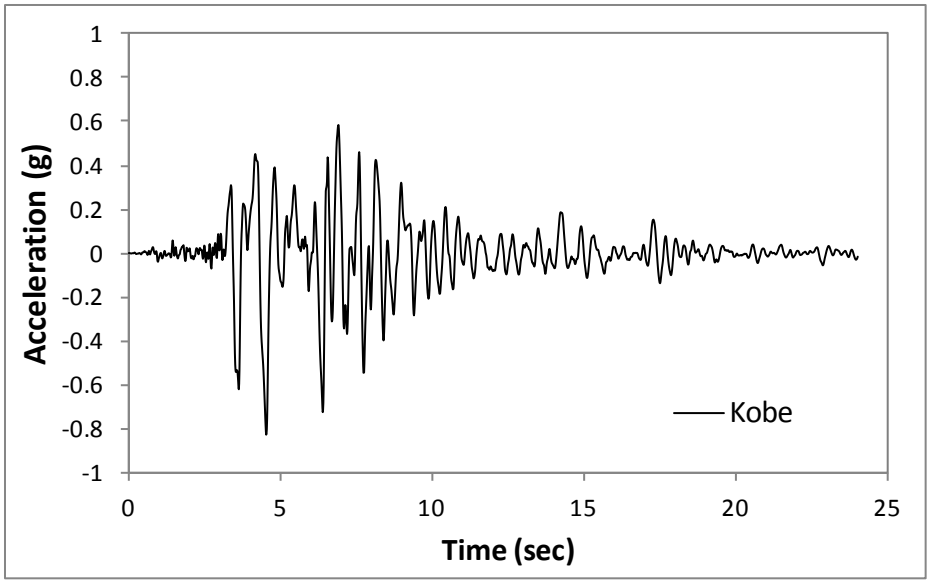

(c) Kobe

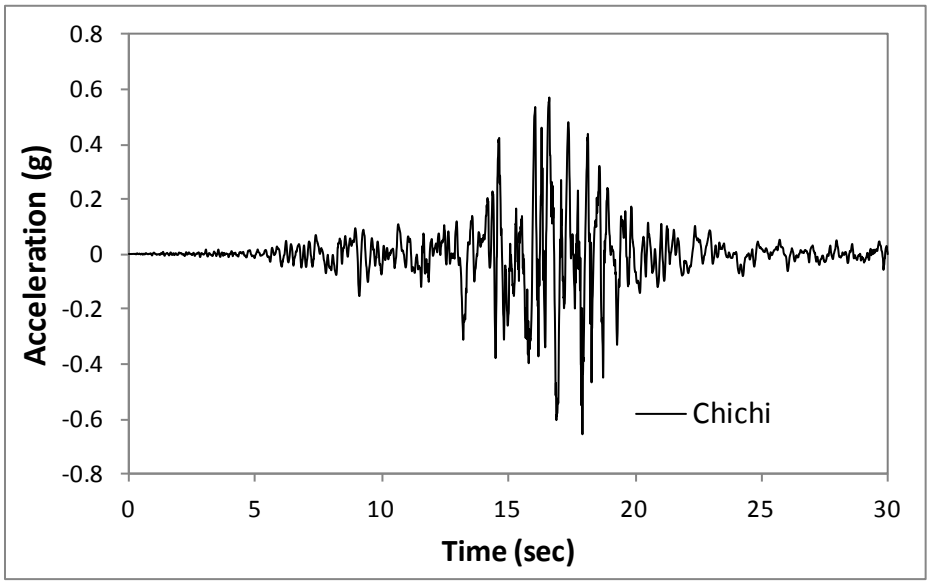

(d) Chichi

Figure 3-11. Ground Motions from Chile, Japan, Kobe and Chichi Earthquakes

3.2.2.Study of Load history effect for 8 ft Column with 2 ft diameter, #3 spiral at 2 in spacing, 16 #6 bars(ρ=1.6%) and 5.3% axial load ratio (benchmark)

This column detailing is identical to the ones from the first 12 specimens. The concrete strength may vary for these tests because of the curing time and the mix different from truck to truck when casting. In the model, an average concrete strength is assumed. The table below shows the material properties of the model.

Table 3-2. Material Properties

Material	Parameter	Value	Unit
Concrete	Compressive Strength	6100	Psi
	Elastic Modulus	4452	Ksi
Longitudinal Reinforcement	Yield Strength	68000	Psi
	Elastic Modulus	29000	Ksi
Transverse Reinforcement	Yield Strength	68000	Psi
	Elastic Modulus	29000	Ksi

The Fiber-based model previously discussed was utilized to simulate the column response. Four nonlinear time history analysis were conducted with multiple earthquakes. The displacement responses under Chile, Japan, Kobe and Chichi ground motions are displayed in Figure 3-12. It is obvious that the displacement histories for the four earthquakes are distinguishing. The displacement responses of Chile and Japan earthquakes inherit the large number of reversals from the ground motions. The Chile load history has more relatively large ductility cycles compared to the peak. The Japan load history has a large number of small displacement cycles with one major peak in the positive direction and four peaks in the negative direction. The Kobe load history has a limited number of cycles and the first large displacement cycle contains major peaks in both directions. The Chichi load history has very unique one-sided response where most of the large displacement pulses lie in the positive direction.

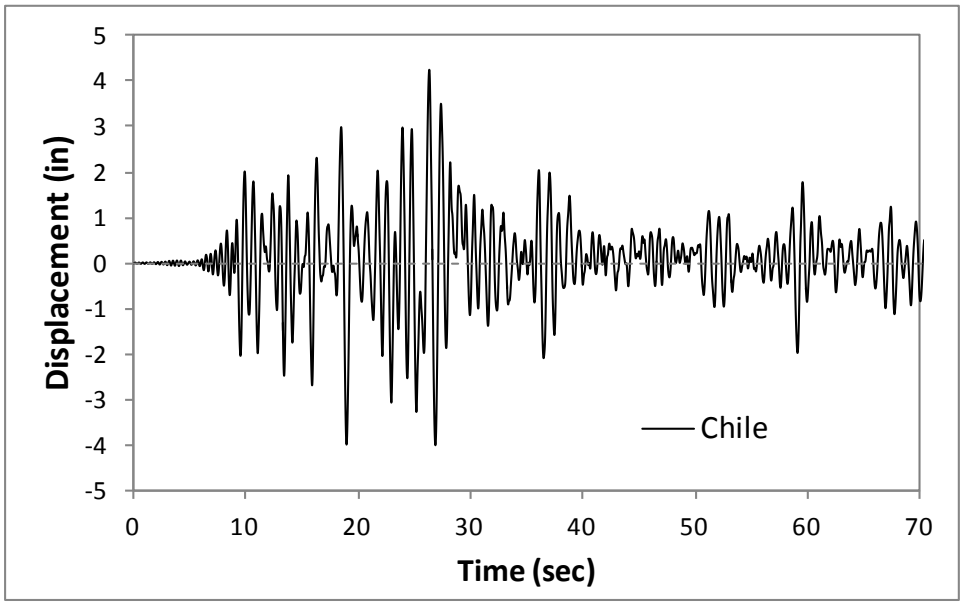

(a) Chile

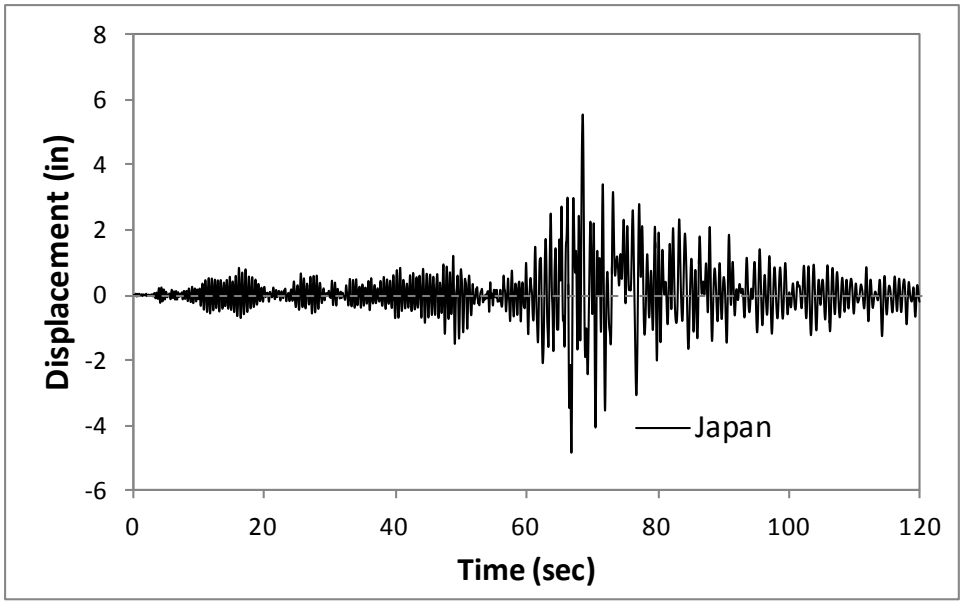

(b) Japan

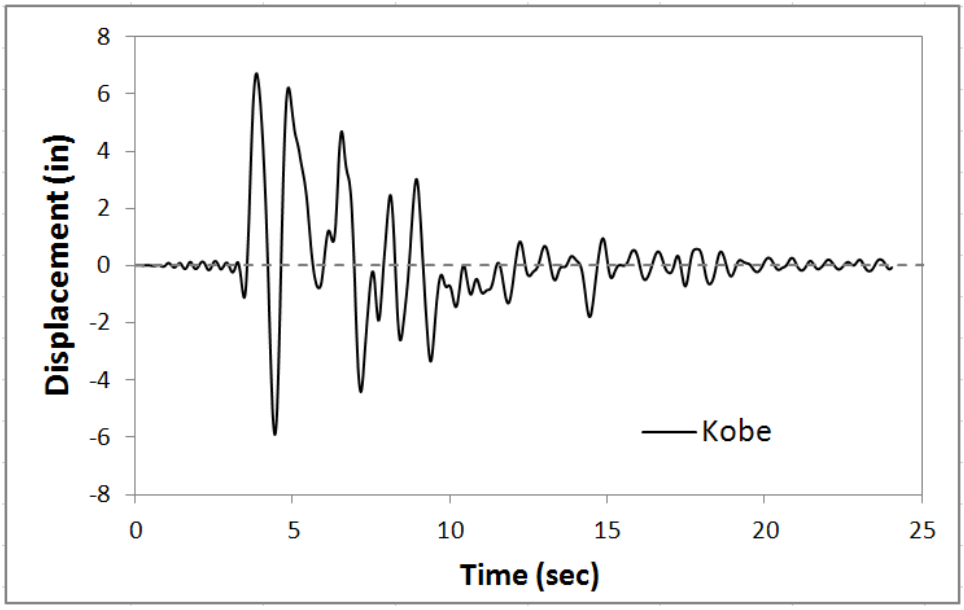

(c) Kobe

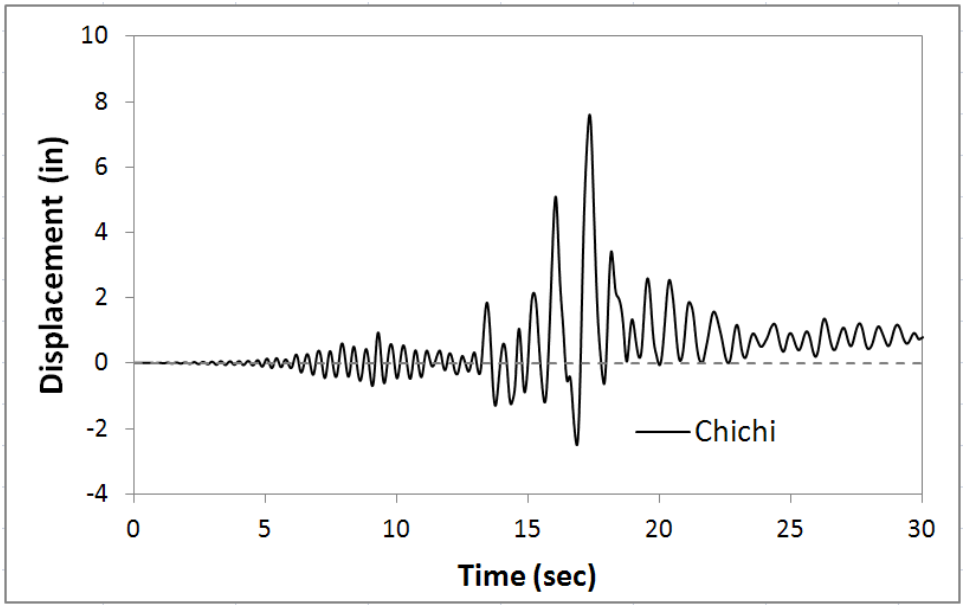

(d) Chichi

Figure 3-12. Displacement Responses of bridge columns under Four Earthquakes

The strain hysteretic responses from the four earthquakes are compared to the monotonic strain-displacement relationship in Figure 3-13. The peak compressive and tensile strains are marked with colored dots. The peak strains from all load histories are very close to the monotonic strain-displacement curve. The load history doesn't alter the strain and displacement relationship at the peak point. However, the unloading strain-displacement relationship doesn't follow the monotonic curve which causes a residual strain at zero displacement. The residual strain is smaller than observed in the experimental results since the concentration of residual strain at the cracked gauge length is not captured without including the cracking in the model.

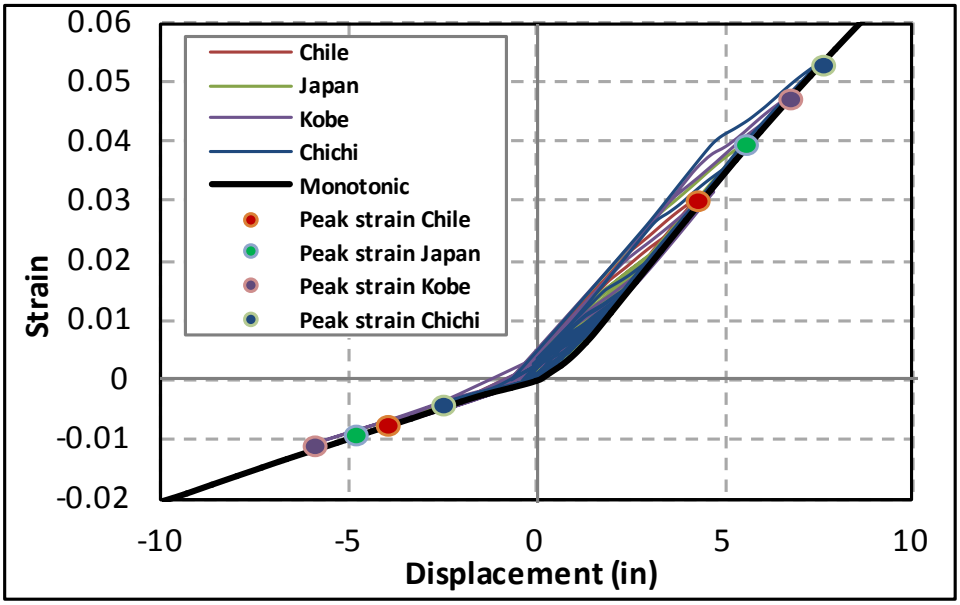

Figure 3-13. Strain Hysteretic Responses with Benchmark Column

3.2.3.Study of Load history effect with 8 ft Column with 2 ft diameter, #3 spiral at 2 in spacing, 16 #6 bars(ρ=1.6%) and 10% axial load ratio

The sectional detailing and the configuration of the column are identical to the benchmark column. However, the axial load ratio is increased to 10%. In the case of reinforced concrete bridge columns, the axial load ratio for columns is likely to lie around 10%. The associated mass at the top of concrete column which represents the superstructure is increased to the corresponding value.

Table 3-3. Material Properties

Material	Parameter	Value	Unit
Concrete	Compressive Strength	6100	Psi
	Elastic Modulus	4452	Ksi
Longitudinal Reinforcement	Yield Strength	68000	Psi
	Elastic Modulus	29000	Ksi
Transverse Reinforcement	Yield Strength	68000	Psi
	Elastic Modulus	29000	Ksi

The displacement responses of Chile, Japan and Kobe earthquake have similar characteristics as the ones with the benchmark column as shown in Figure 3-14. The increase of "superstructure" mass increases the inertia force in the time history analysis and results in a larger displacement response for most of the earthquakes. In addition, the natural frequency of the structure is reduced which impacts the dynamic reaction under the ground motions. The negative peak cycle of Kobe load history is shifted to a later cycle. The Chichi load history lost its one-sided response and the peak displacement occurred in the negative direction.

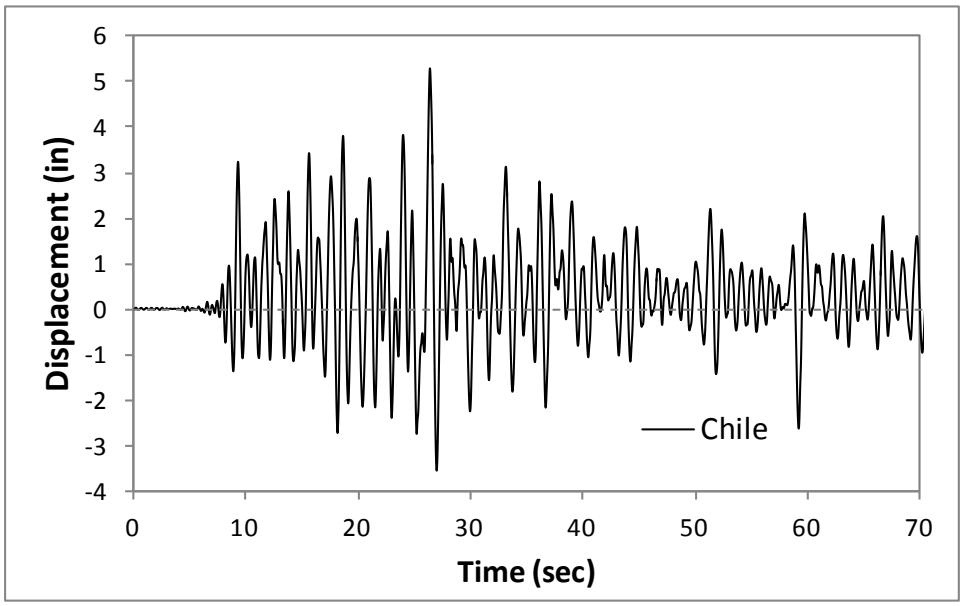

(a) Chile

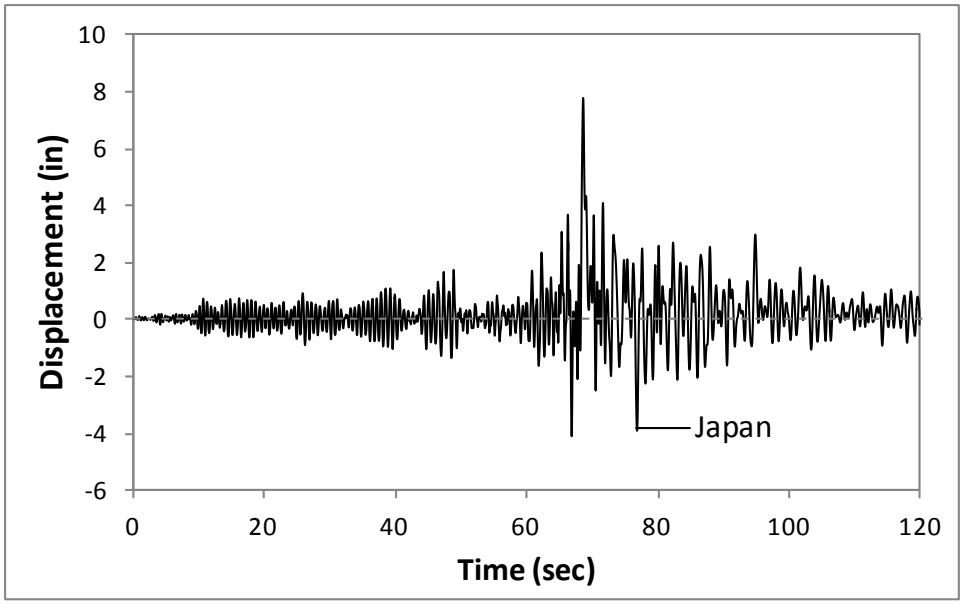

(b) Japan

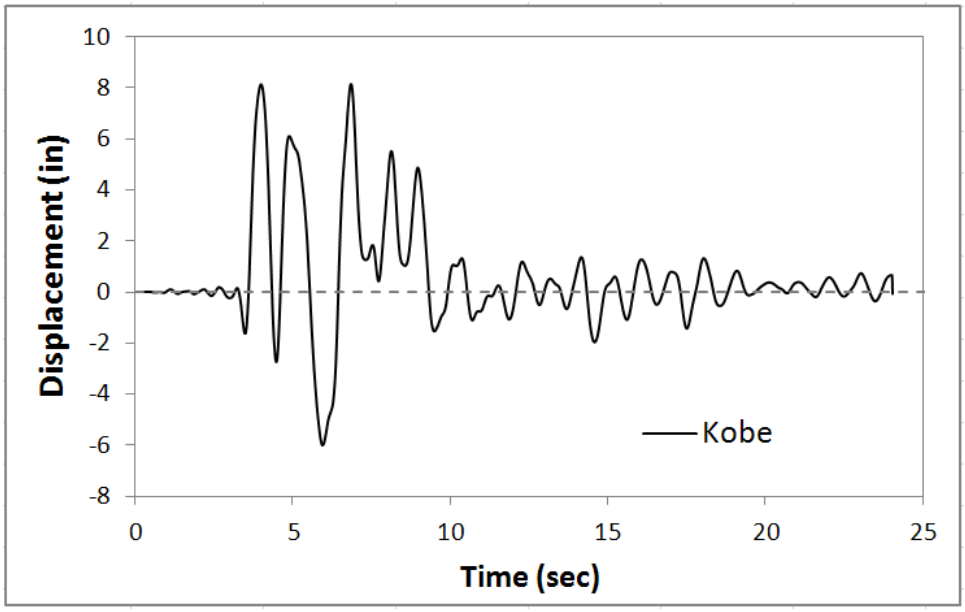

(c) Kobe

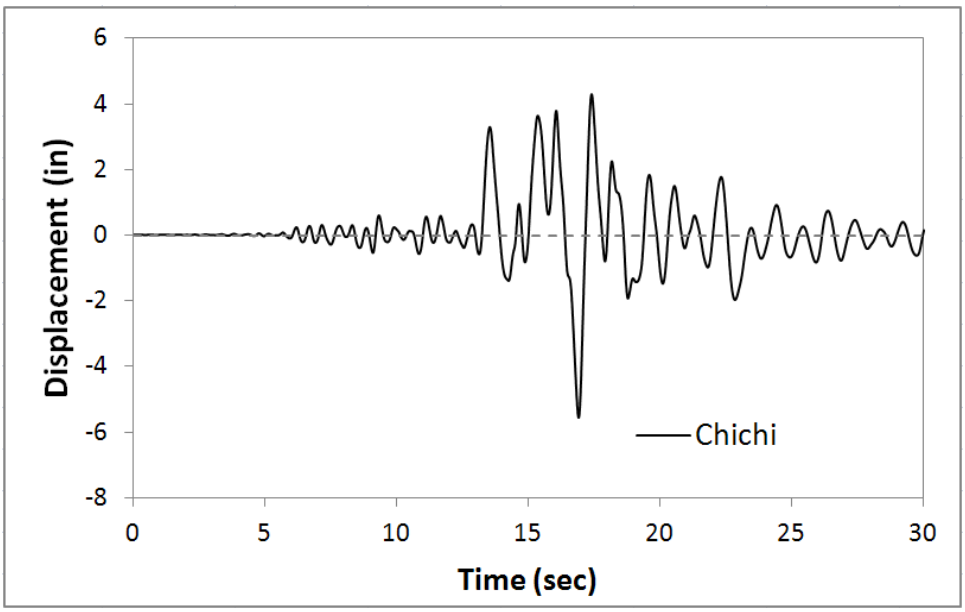

(d) Chichi

Figure 3-14. Displacement Responses under Four Earthquakes

The cyclic strain hysteretic responses follow the monotonic strain-displacement curve closely. As a result, the strain at peak displacements approaches the monotonic prediction. Again, the load histories do not alter the strain and displacement relationship. In addition, the large axial load prevents the reinforcement from having large residual strain at zero displacement.

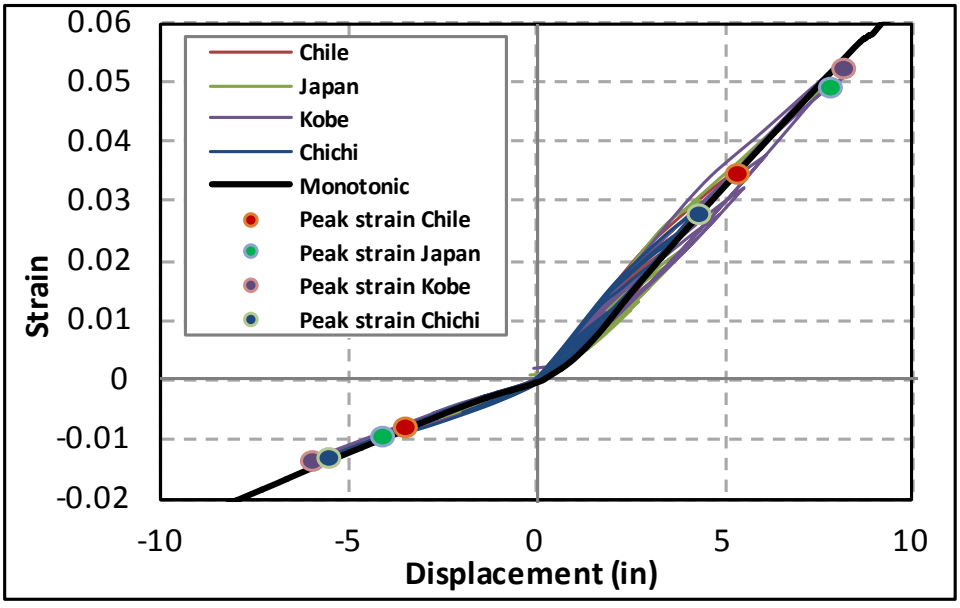

Figure 3-15. Strain Hysteretic Responses under 10% Axial Load Ratio

3.2.4.Study of Load history effect with 8 ft Column with 2 ft diameter, #3 spiral at 2 in spacing, 16 #6 bars(ρ=1.6%) and 15% axial load ratio

The geometric configuration and the sectional detailing are identical to the benchmark column for this case. The variable is the axial load ratio which is increased to 15%. The mass is also increased to the associated value. The material properties are shown in Table 3-4.

Table 3-4. Material Properties

Material	Parameter	Value	Unit
Concrete	Compressive Strength	6100	Psi
	Elastic Modulus	4452	Ksi
Longitudinal Reinforcement	Yield Strength	68000	Psi
	Elastic Modulus	29000	Ksi
Transverse Reinforcement	Yield Strength	68000	Psi
	Elastic Modulus	29000	Ksi

The fiber-based model doesn't include bar buckling, concrete crushing and shear failure of the reinforced concrete structures. The only failure mechanism which the fiber-based model includes is the collapse under large P-Delta effects. The excessive peak displacement from response of the Chile and Kobe earthquakes indicates the "collapse" of the column. The responses from Japan and Chichi earthquake also show large peak displacements however not "collapse". The strain hysteretic response will not be compared with the monotonic prediction here since the information has been lost for two of the earthquakes.

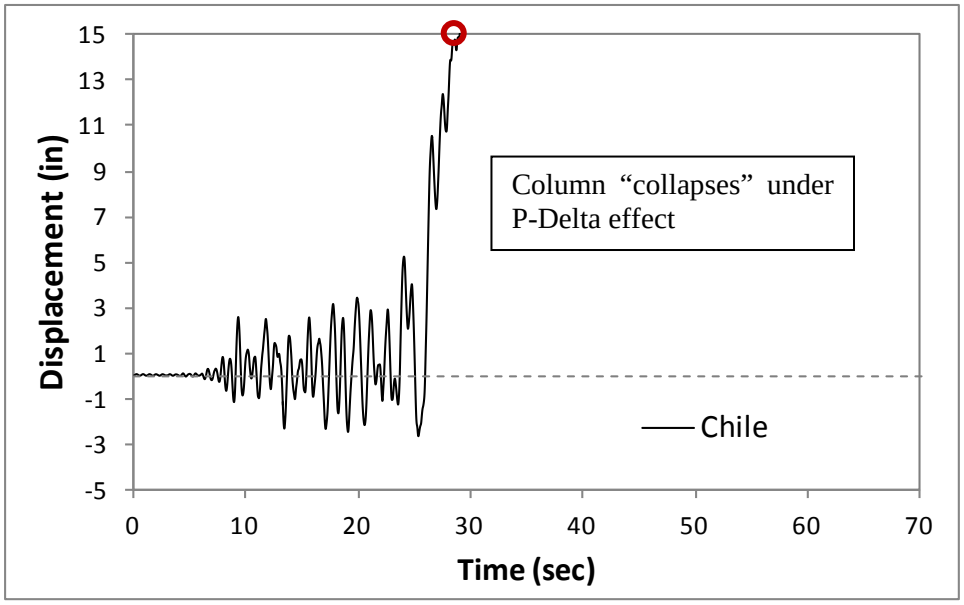

(a) Chile

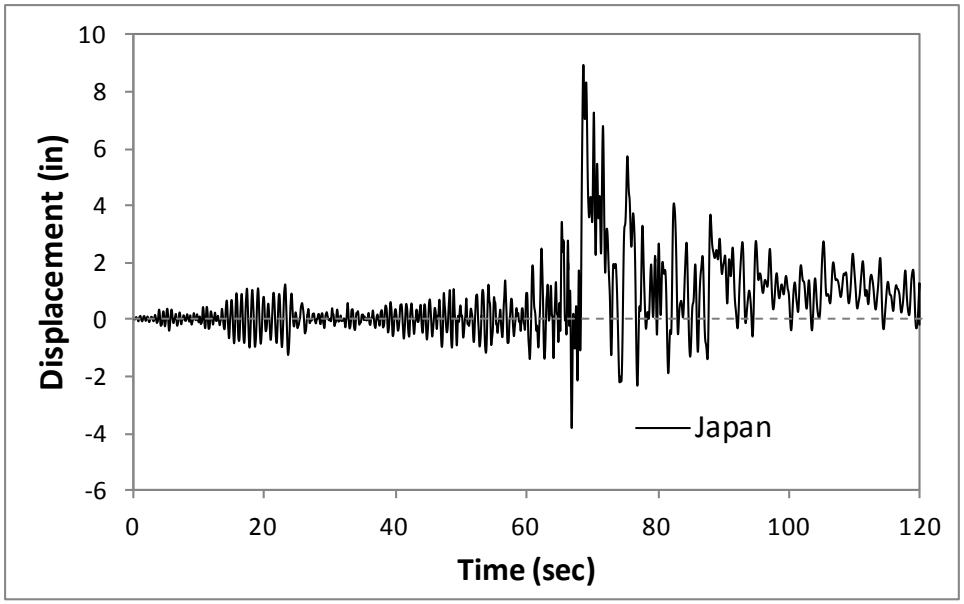

(b) Japan

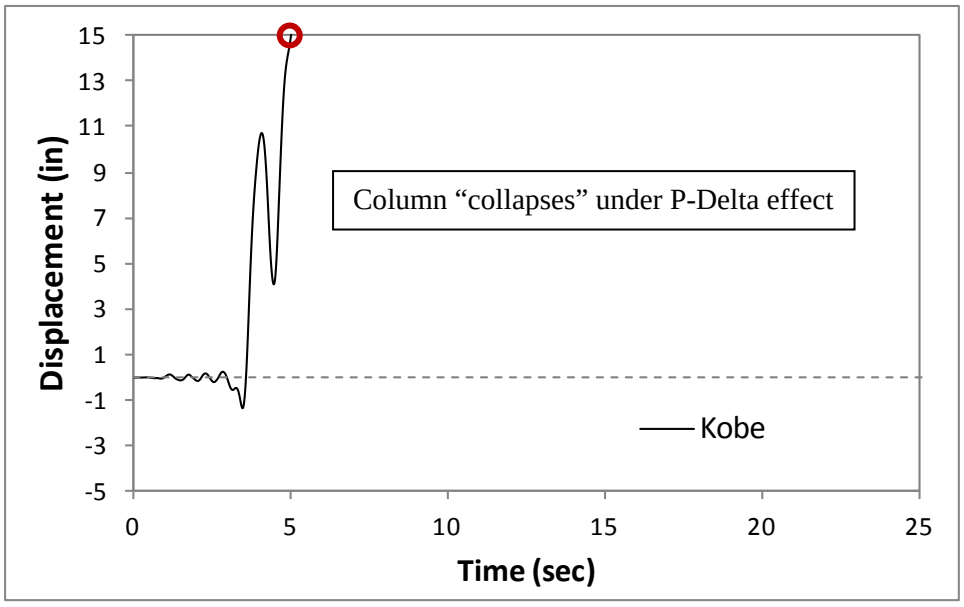

(c) Kobe

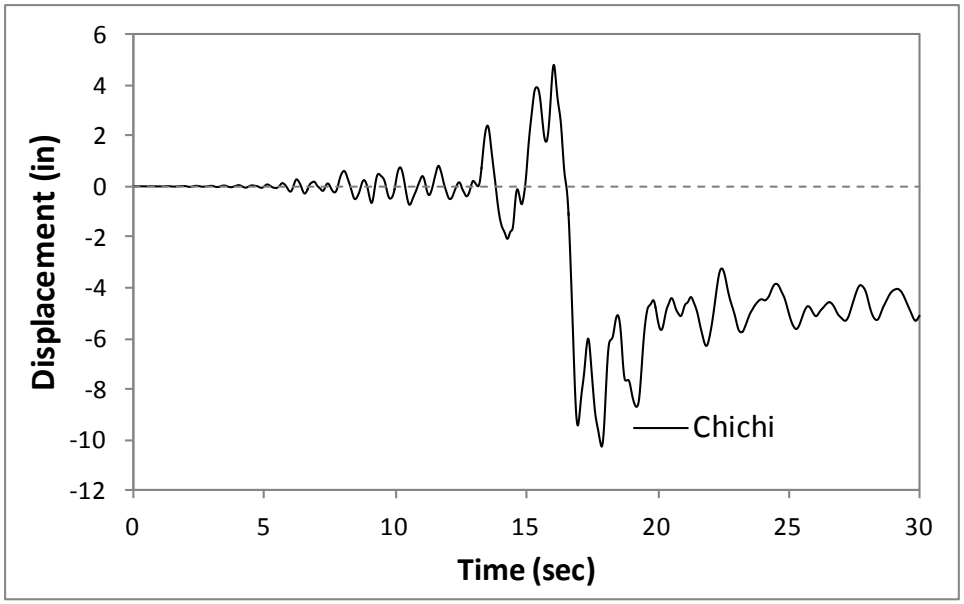

(d) Chichi

Figure 3-16. Displacement Responses under Four Earthquakes

3.2.5.Study of Load history effect with 12 ft Column with 2 ft diameter, #3 spiral at 2 in spacing, 16 #6 bars(ρ=1.6%) and 5.3% axial load ratio

The length of the column increases to 12 ft comparing to the benchmark column. The corresponding aspect ratio increases to 6. The axial load ratio remains at 5.3%. The material properties are shown in Table 3-5.

Table 3-5. Material Properties

Material	Parameter	Value	Unit
Concrete	Compressive Strength	6100	Psi
	Elastic Modulus	4452	Ksi
Longitudinal Reinforcement	Yield Strength	68000	Psi
	Elastic Modulus	29000	Ksi
Transverse Reinforcement	Yield Strength	68000	Psi
	Elastic Modulus	29000	Ksi

It is obvious that a longer column has larger flexibility and a lower natural frequency. The displacement response has generally larger amplitude compared to those from the benchmark column. The characteristics of responses from Chile, Japan and Kobe earthquakes remain. The Chichi displacement response lost the one-sided behavior again. This indicates that the one-sided displacement response is rare and unique, however, possible.

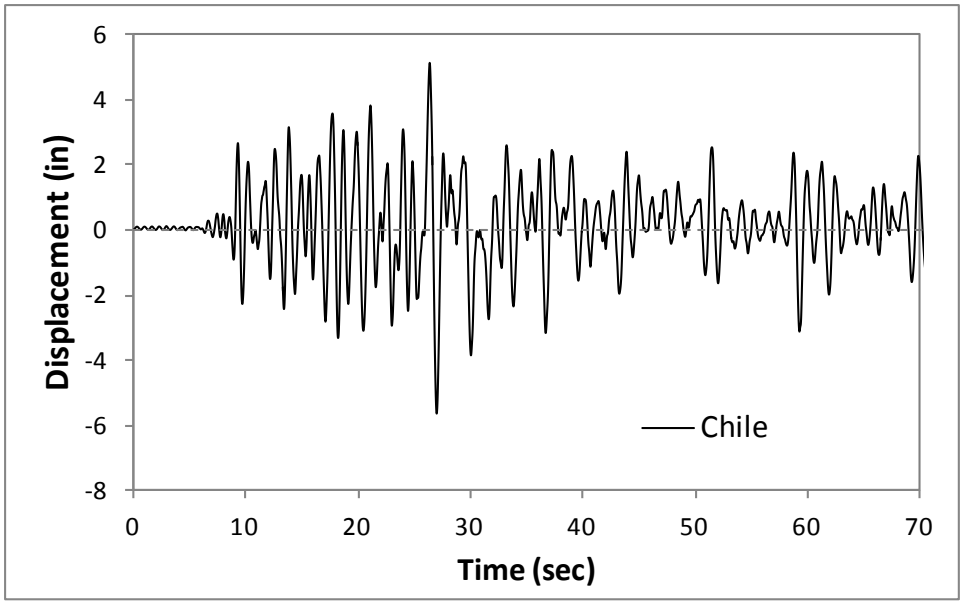

(a) Chile

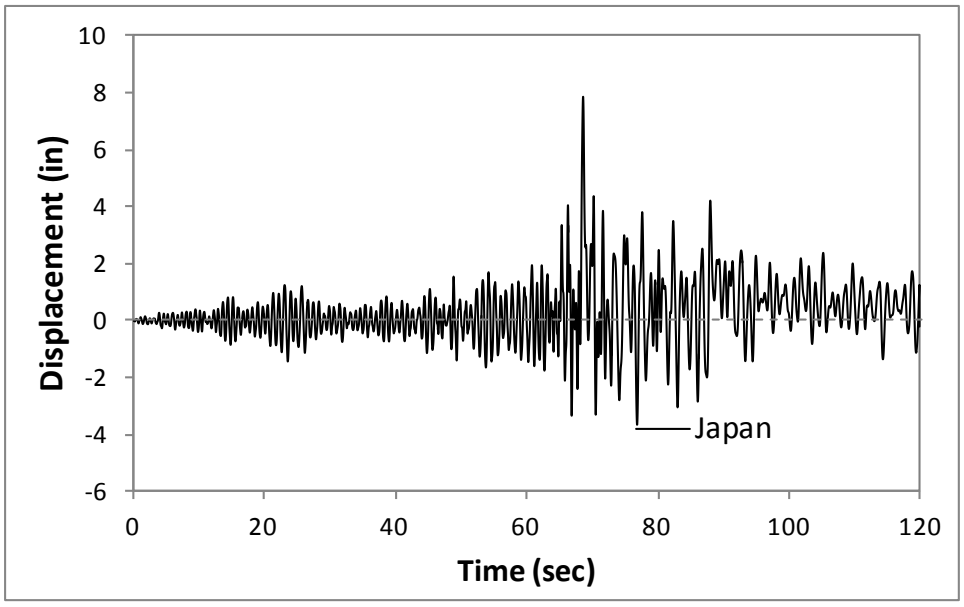

(b) Japan

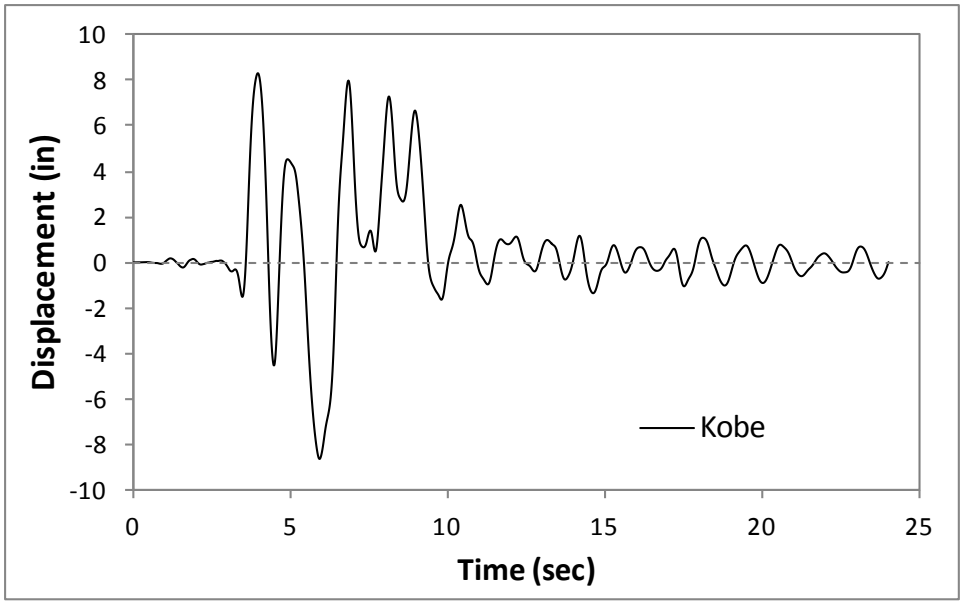

(c) Kobe

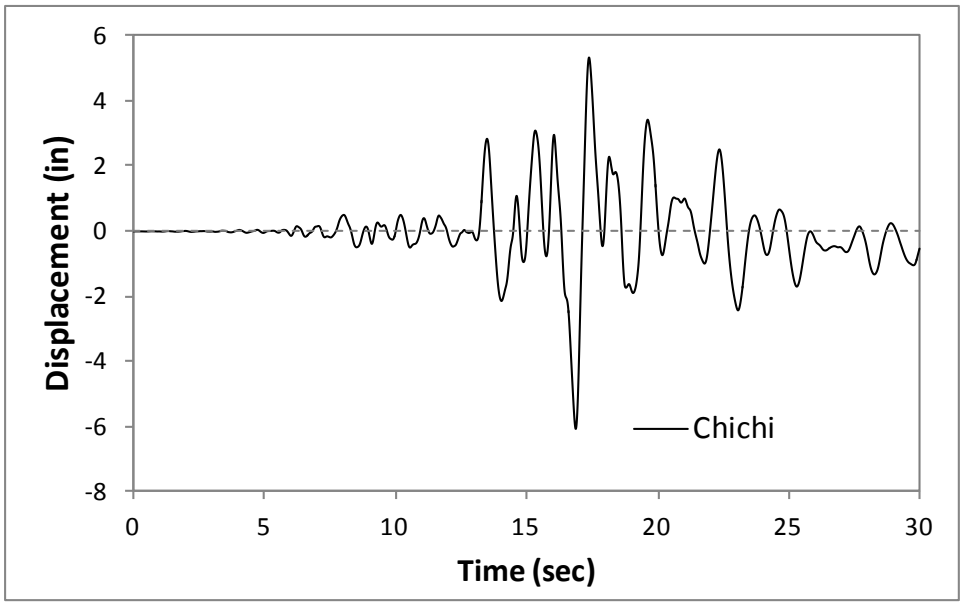

(d) Chichi

Figure 3-17. Displacement Responses under Four Earthquakes

The strain displacement relationship becomes "flatter" where strain is much lower at a specific displacement level compared to the strain from the benchmark column. A longer column has a larger plastic hinge length which results in a larger spread of plasticity. In addition, the plastic deformation at the hinge region has a larger moment arm to extrapolate the top displacement. Therefore, a longer column requires less plastic deformation at the plastic hinge region to reach a specific displacement level.

The monotonic curve again serves as an envelope of all the strain hysteretic responses. The peak points lie close to the monotonic curve.

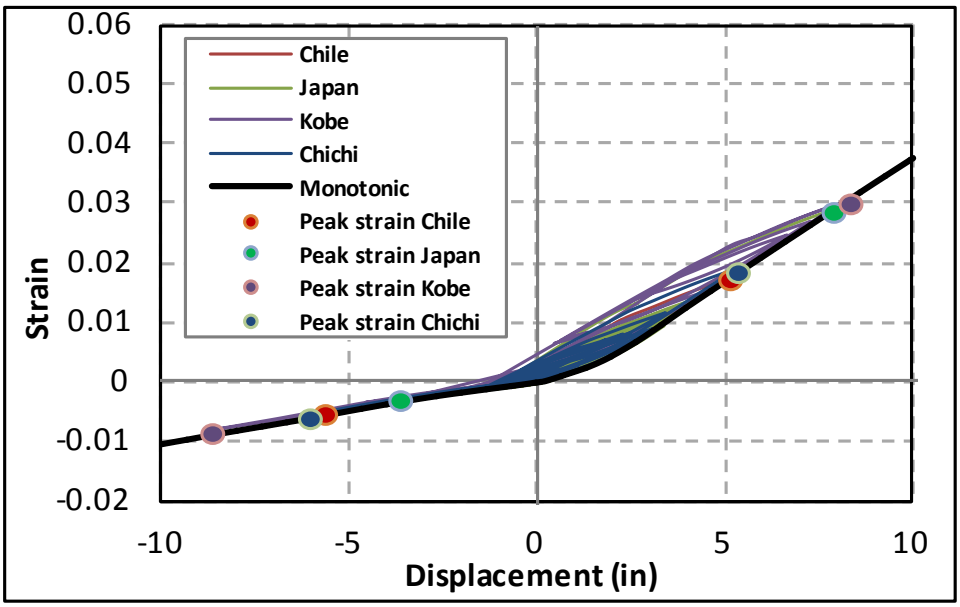

Figure 3-18. Strain Hysteretic Responses with 12 ft Column

3.2.6.Study of Load history effect with 16 ft Column with 2 ft diameter, #3 spiral at 2 in spacing, 16 #6 bars(ρ=1.6%) and 5.3% axial load ratio

The length of the column increases to 16 ft compared to the benchmark column. The corresponding aspect ratio increases to 6.The material properties are shown in Table 3-6.

Table 3-6. Material Properties

Material	Parameter	Value	Unit
Concrete	Compressive Strength	6100	Psi
	Elastic Modulus	4452	Ksi
Longitudinal Reinforcement	Yield Strength	68000	Psi
	Elastic Modulus	29000	Ksi
Transverse Reinforcement	Yield Strength	68000	Psi
	Elastic Modulus	29000	Ksi

The significant increase of flexibility of the 16 ft column led to a high amplitude response for all four earthquakes. The response from the Chile earthquake has a large residual displacement due to the large positive peak displacement. The small cycles at the beginning of Japan earthquake response were amplified significantly. The duration of most of the displacement pulses in these responses increased because of the larger natural period. Some of the displacement pulses in response of Kobe and Chichi have multi-second duration.

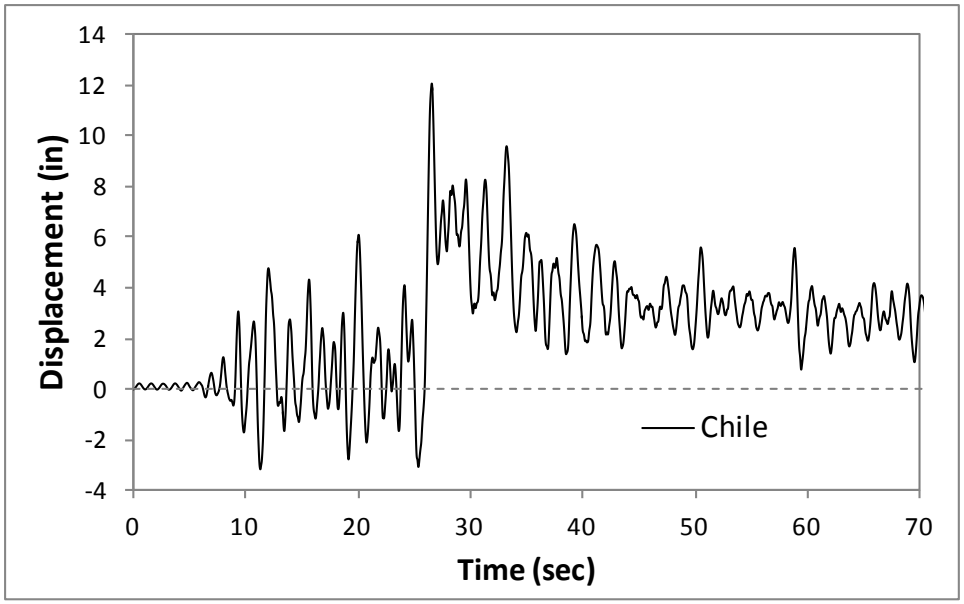

(a) Chile

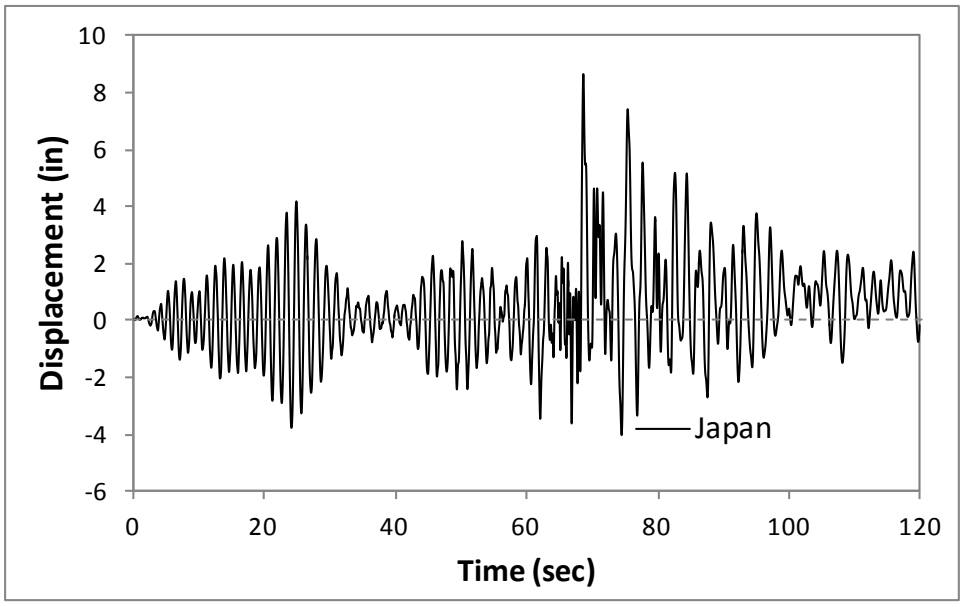

(b) Japan

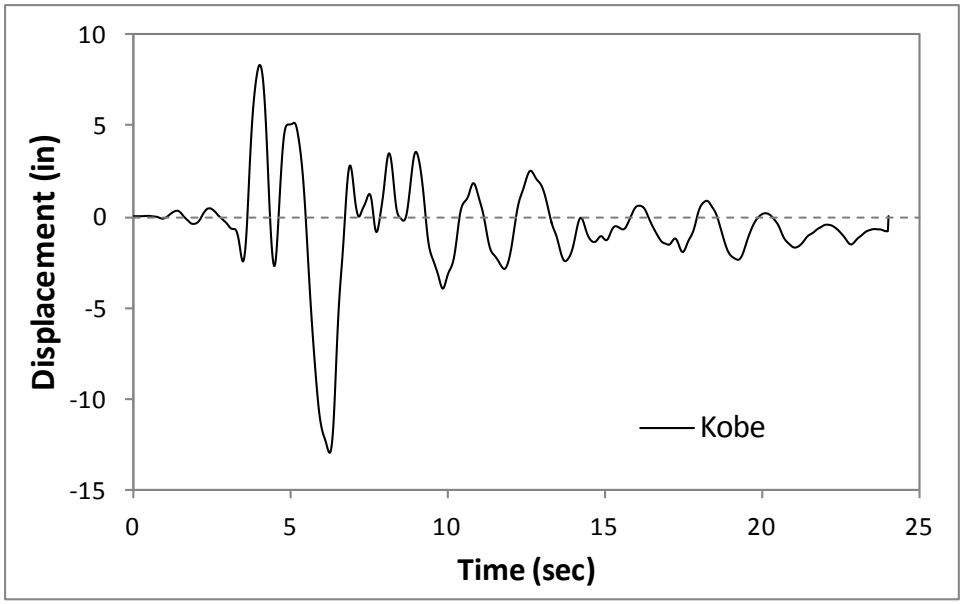

(c) Kobe

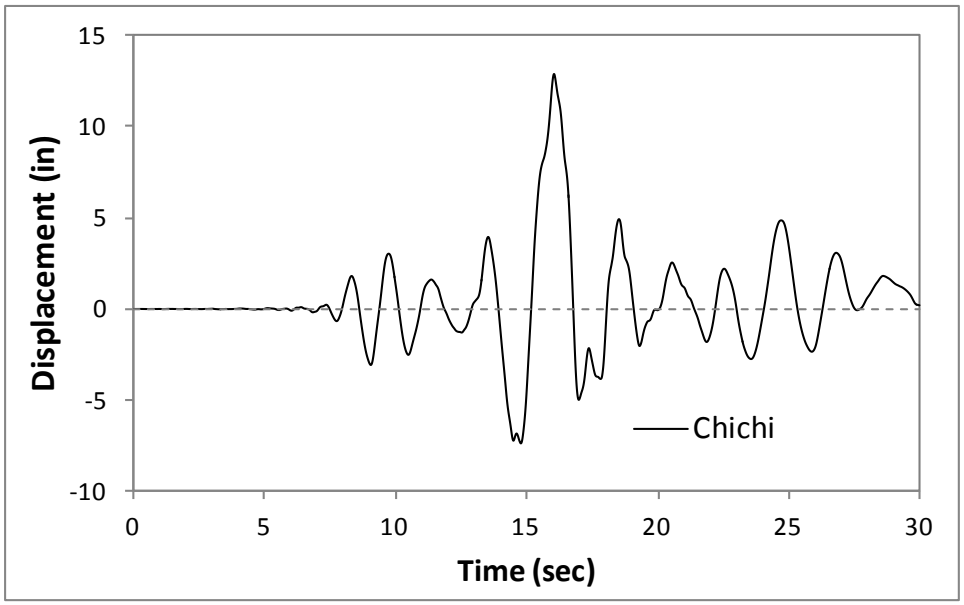

(d) Chichi

Figure 3-19. Displacement Responses under Four Earthquakes

The strain hysteretic responses predict much lower strain values compared to those with benchmark column for the same reason as discussed for the 12ft column. Again the peak points follow the monotonic curve. The load history does not impact the strain displacement relationship for the column with aspect ratio as 8.

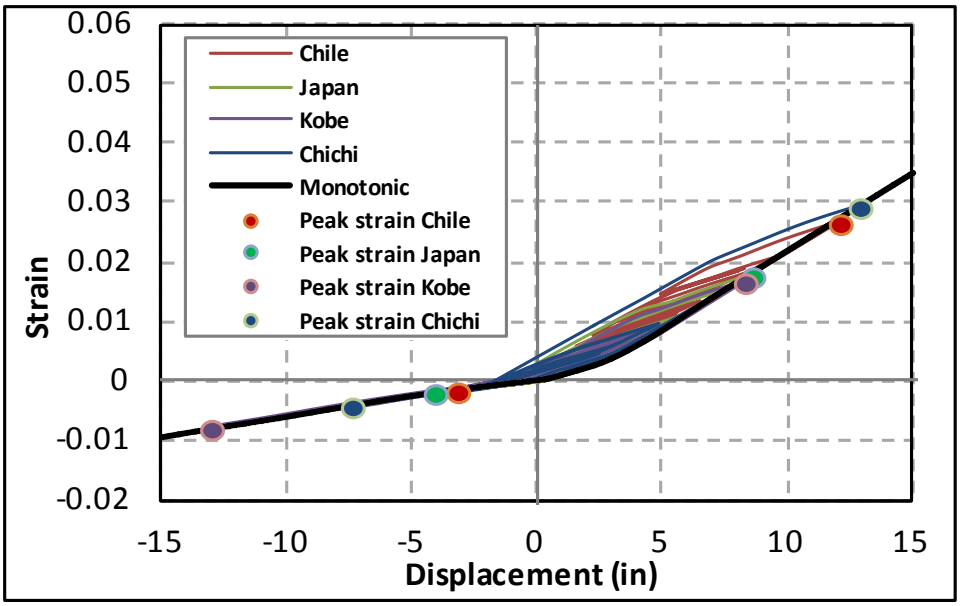

Figure 3-20. Strain Hysteretic Responses with 16 ft Column

3.3.Development of Bar Buckling Model with Finite Element Method

To capture bar buckling, a finite element model that simulates the entire specimen is established as shown in Figure 3-21. Most of the analyses with this model diverge due to high nonlinearity at the plastic hinge region.

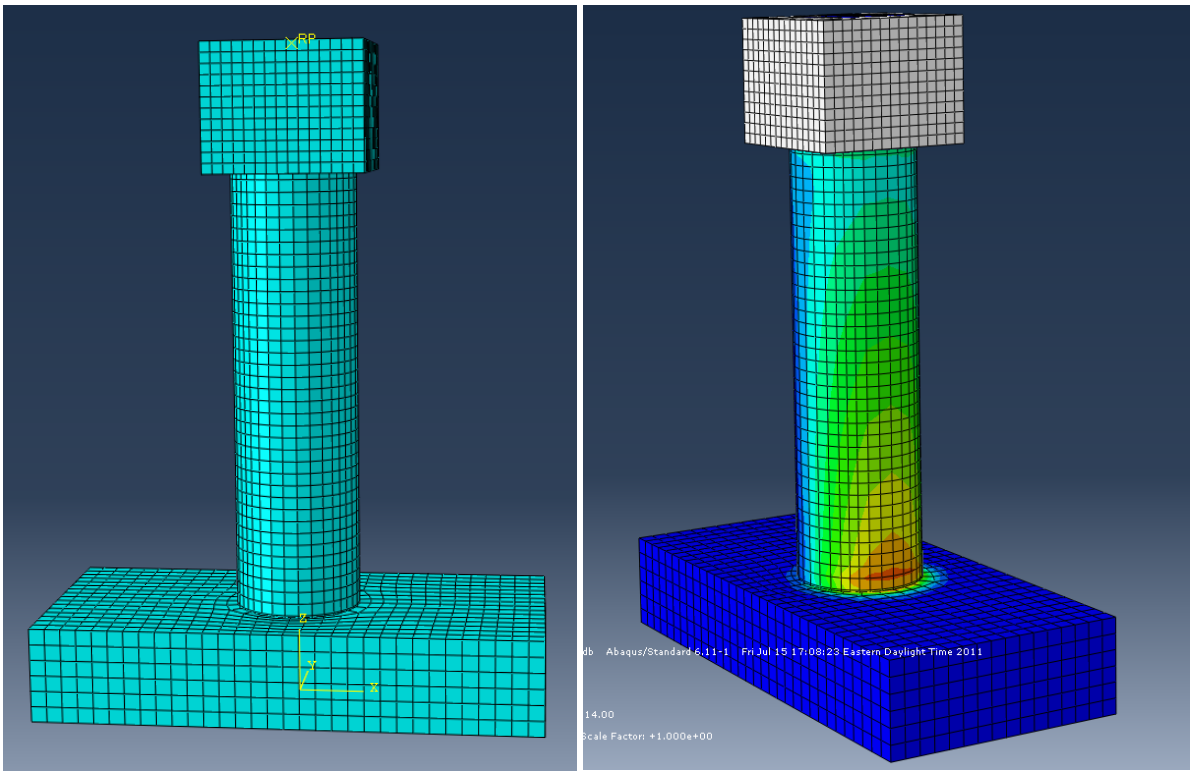

Figure 3-21. Finite Element Model of Specimen

To avoid the difficulty on convergence and the large computational cost, a bar buckling model is developed by only simulating a segment of bar and its boundary condition at the plastic hinge region. For a circular column, the extreme fiber bar will be simulated since the extreme fiber bar experiences the most severe strain history. The demand on the bar, which eventually leads to buckling, is represented by the axial strain history which is obtained by applying axial displacement to the bar segment. To predict the bar buckling in the reinforced concrete column, the strain history is first obtained with the fiber-based model. The bar behavior under the strain history is evaluated with the finite element bar buckling model. The Flowchart of bar buckling model is shown in Figure 3-23.

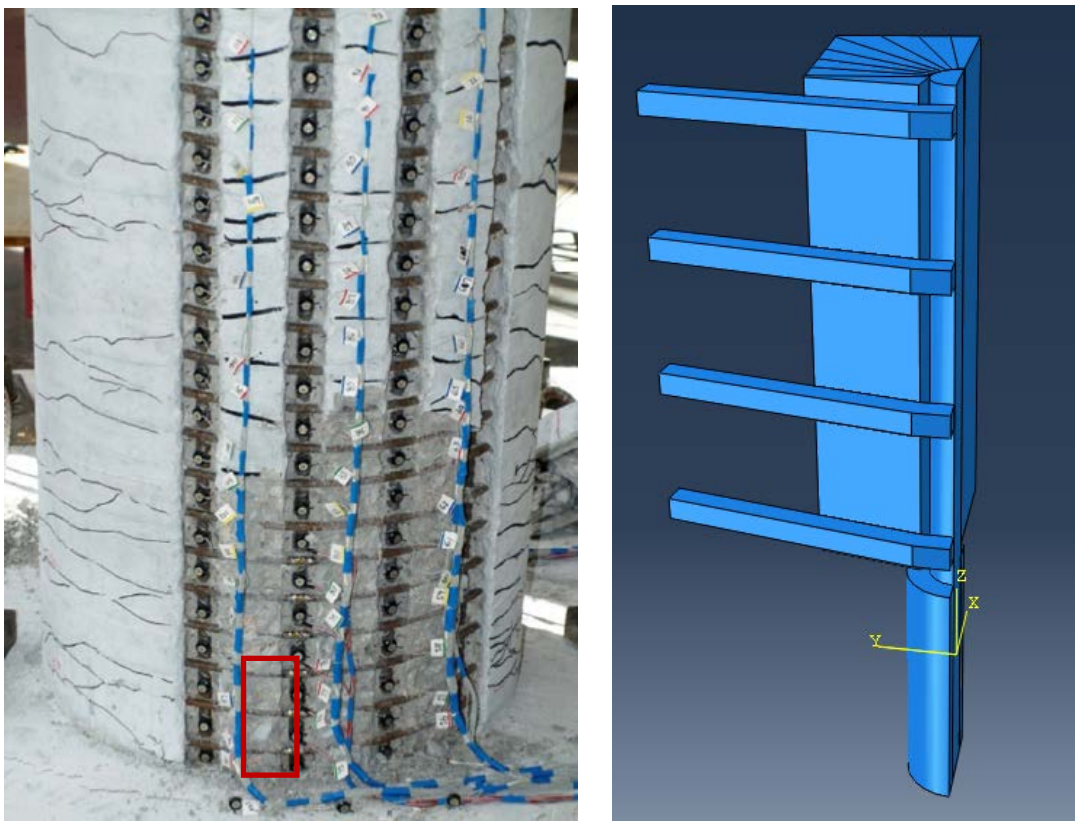

Figure 3-22. Local Modeling at Plastic Hinge Region

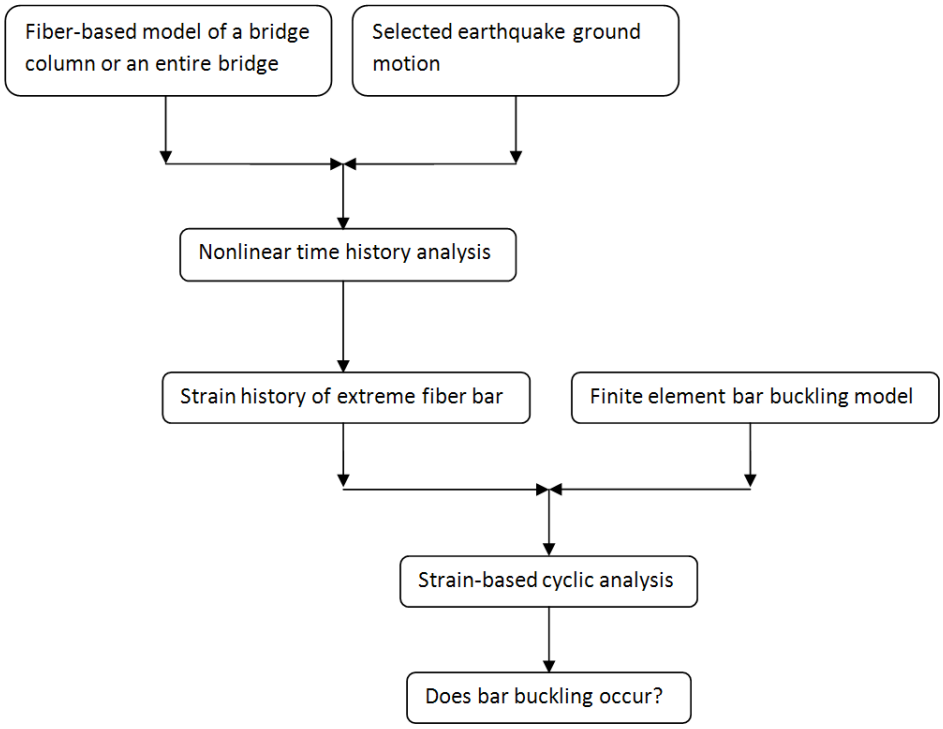

Figure 3-23. Flowchart on Predicting Bar Buckling with Finite Element Model

3.3.1.Geometrical Configuration of Bar Buckling Model

As shown in Figure 3-22, an extreme fiber bar is embedded in the core concrete. The interaction between the bar and concrete is defined. The cover concrete here is not included in the model since it will spall off during initial cycles of the seismic loadings and won't contribute to the resistance of buckling. Furthermore, the spalling of cover will cause discontinuity which is very hard to model with the finite element method (and of little value in this case).

The spiral contacts the concrete block with a friction interaction behavior between them. The contact area between the circular spiral and bar is very small where the bar may pinch into the spiral. However, if the spiral is modeled with its actual circular geometry, the contact area between the spiral and the bar will be infinitesimal which may cause stress concentration and an equilibrium problem in the finite element model. Therefore, the spiral is converted into a square section which has the same area and moment of inertia (Figure 3-24) which, as a result, ensures the axial stiffness of the spiral, the confining stress and the bending stiffness of spiral to remain the same as the actual circular cross section spiral. The bar pinches into the square spiral over a small depth to generate a small contact area. The bottom part of bar is inserted into a concrete tube which simulates the bond slip behavior in the footing. The test result in Figure 3-25 has shown that the tensile bond-slip displacement from the footing is accumulating over cycle to cycle at 3-cycle-set test. A larger bond-slip displacement will result in more severe instability at the compressive half cycle. The bottom part of the model is involved to capture the bond-slip displacement.

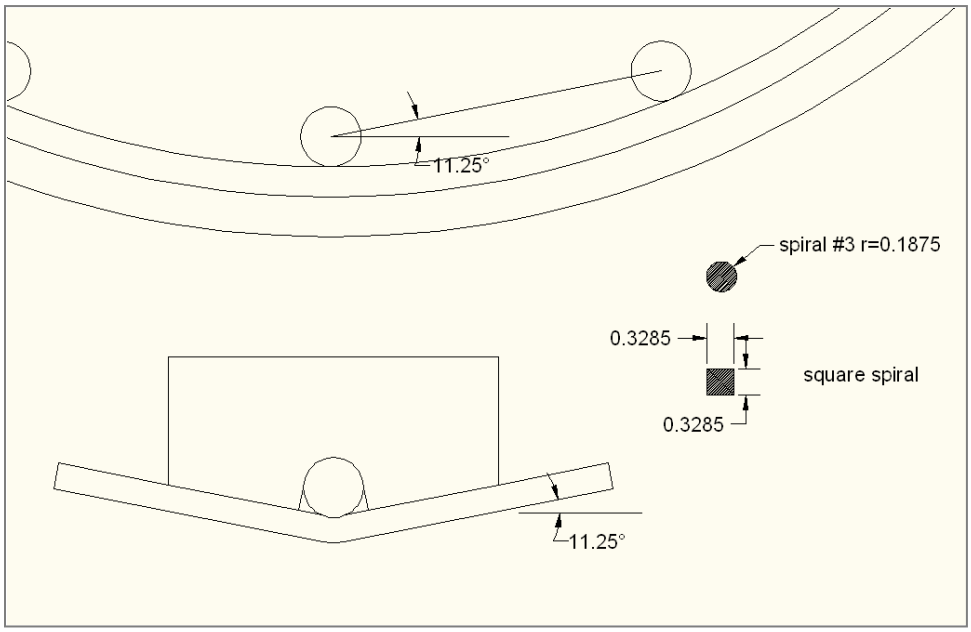

Figure 3-24. Local Modeling at Plastic Hinge Region

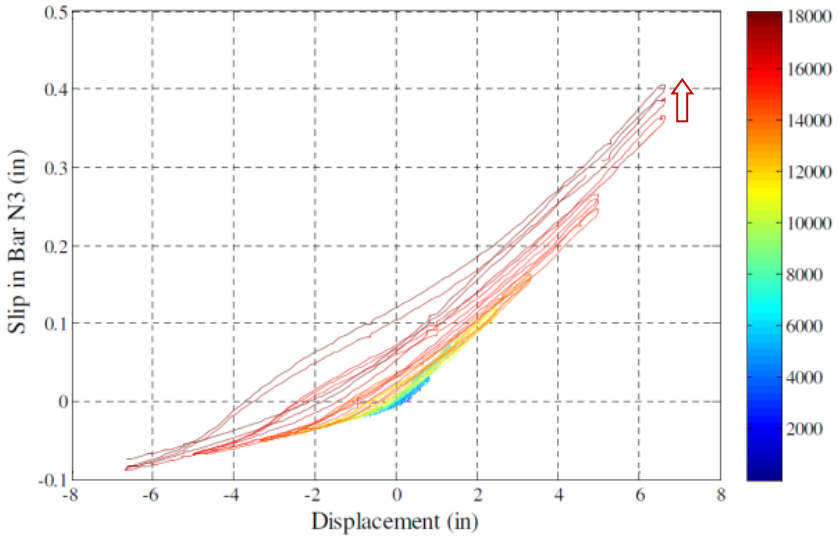

Figure 3-25. Slip Hysteretic Response from Test 9

The bar buckling model does not include the cracking of concrete and the strain gradient in the bar. The moment gradient along the column length results in a strain gradient in the reinforcement. Since the moment demand on a section has been converted to axial strain demand in the bar buckling model, the moment gradient information will be lost. However, along such a small gauge length, the change of strain due to moment gradient is relatively small which is not likely to affect bar buckling. On the other hand, the location of cracking influences the distribution of strain. The location and orientation of cracking are affected by the moment gradient, loading history, spacing of spiral and aggregate arrangement. It is extremely difficult, sometimes impossible, to capture the cracking precisely. Cracking modeling under cyclic loading will potentially cause extreme computational difficulties. As a result, the cracking is not included in the modeling.

In the tension-based buckling mechanism, bars buckle under compressive stress and tension strain where the bars form the sole source of compression zone stability before the concrete cracks close, as presented by (Moyer and Kowalsky (2003)). Cracking of concrete causes the bar to be the only compressive resistance when the bar is reversed from tension strain. To include this behavior without simulating the cracking, the bar is subjected to tension solely as shown in Figure 3-26. At subsequent compressive cycle, the bar serves as the only source of resistance for its compressive demand.

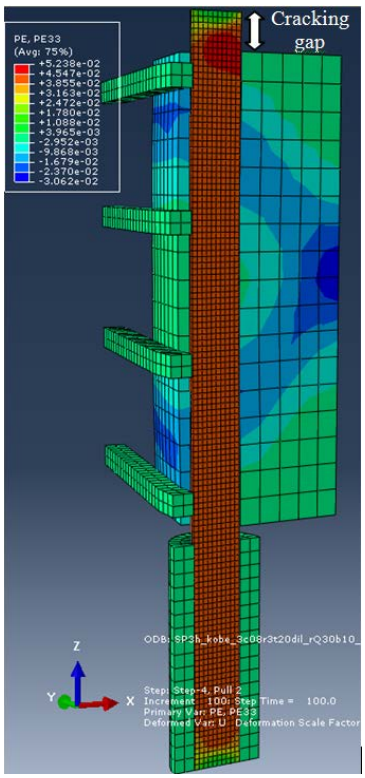

Figure 3-26. Pulling Cycle by Loading the Bar

3.3.2.Material Definition of Bar Buckling Model

The steel constitutive model is based on the work of (Lemaitre and Chaboche (1990)). The model defines the initial yield surface and its expansion as well as its translation as a function of loading history as shown in Figure 3-27. The isotropic hardening represents the expansion of yield surface. The maximum size and the rate of yield surface expansion are input variables. The kinematic hardening represents the translation of the yield surface. Similarly, the maximum translation and the translation rate of yield surface also require definition. It is important to properly define hardening of the steel model such that the impacts of load history on the steel material may be accurately captured. A cyclic bar test result is utilized to extract the hardening information for defining the steel material in the model.

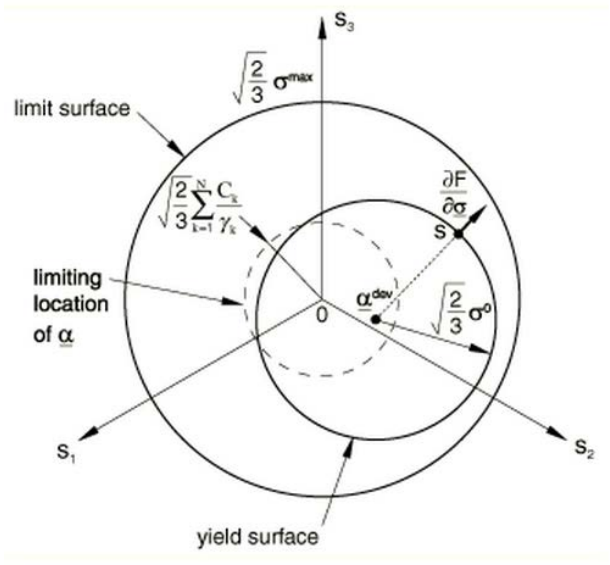

Figure 3-27. Yield Surface and Hardening Limit from Abaqus Analysis User's Manual

The concrete plasticity model is based on the work of (Lee and Fenves (1998)) and (Lubliner et al. (1989)). This model utilizes the Drucker-Prager hyperbolic function from (Druker and Prager (1952)) to generate the potential plastic flow, as shown in Figure 3-28. The 3D plastic surface is displayed in Figure 3-29. Recall that for the behavior of concrete in fiber-based model, a uniaxial stress strain curve is utilized that incorporates the effect of confinement directly. However, the concrete plasticity model in Abaqus utilizes the potential plastic flow to determine the material behavior under confining pressure. The uniaxial strength of concrete will be enhanced with a confining stress. In the case of reinforced concrete, the confinement is usually from the passive confining stress from the transverse steel.

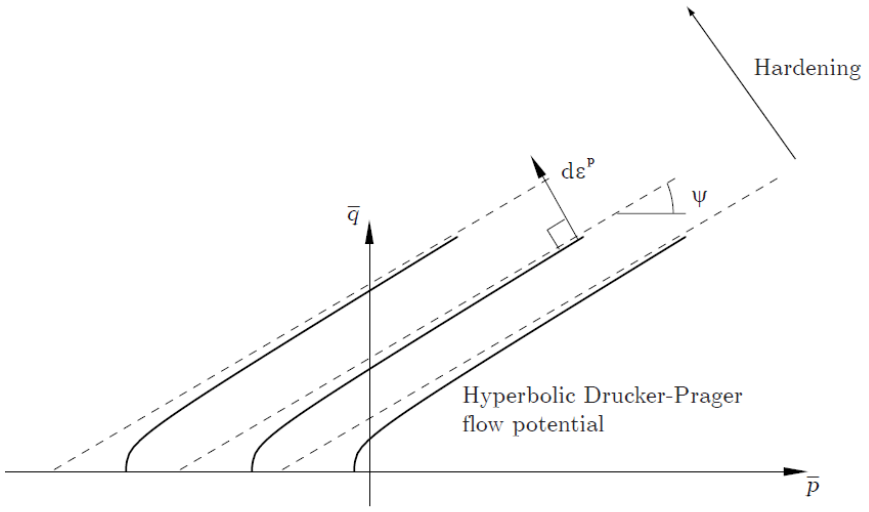

Figure 3-28. The Drucker-Prager Hyperbolic Plastic Potential Function in Meridional Plane from Abaqus Analysis User's Manual

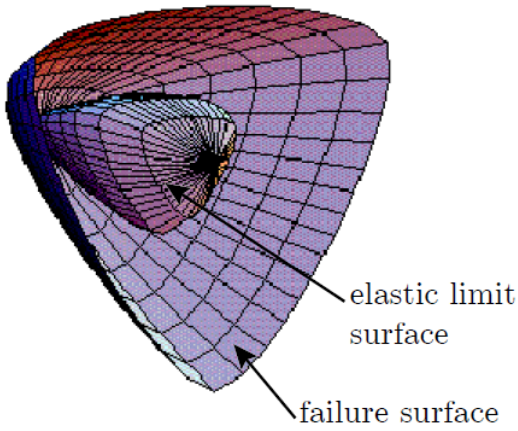

Figure 3-29. 3D Surfaces of Elastic Limit and Plastic Failure from Riedel (2000)

3.3.3.Loading Method

The model is loaded by applying axial compression and tension displacement to the top of the concrete and the bar to duplicate the strain history on the bar segment. There is no direct way to determine the required displacement to reach a prescribed strain level. The compressive displacement will depend on the target compressive strain and the length of concrete block. The tensile displacement will depend on the target tensile strain and the length of the bar segment.

3.4.Analytical Results with Finite Element Buckling Model

The finite element buckling model was utilized to replicate the bar buckling of Tests 9 and 11 which were subjected to a 3 cycle set load history and Kobe earthquake load history, respectively. The strain history of the buckled bar was applied to the model to capture the bar buckling at the same half cycle where the specimen was observed to have buckled during the test. Since the bar yield strength, spiral spacing, column dimension and concrete strength are all the same for Test 8-12, an identical bar buckling model is needed for all six tests while only applying different strain histories.

Model calibration has been conducted to ensure that the model captures different types of buckling mechanisms. Calibration was carried out by subjecting the strain history obtained from test results to the finite element buckling model, and comparing the response of the model to the experimental result. There are three major factors which determine the bar buckling behavior: (1) Impact of concrete expansion on the bar and spiral; (2) Nonlinear instability of the bar and (3) Spiral strength on resisting lateral demand from the bar and concrete. Both the demand and capacity were adjusted based on the comparison between the test results and the model response.

From experimental observations, bar buckling occurs when reinforced concrete bridge columns are subjected to cyclic loading. Bar buckling is often referred to as the visible onset of bending in the plastic hinge region. It is worth noting that elastic buckling due to axial load occurs as soon as the buckling load is reached. The inelastic buckling of the reinforcement is more complicated because of the plastic behavior of the steel and the boundary condition.

In a seismic event, columns of reinforced concrete bridges are subjected to both lateral and axial loads. As will be described in the following paragraph, this leads to the longitudinal reinforcing bars which are subjected to combined bending and axial load. Of importance here is the action of combined bending and axial compression. Of course, a reinforcing bar and surrounding concrete will experience a cyclic axial demand which depends on the location of the bar relative to the earthquake loading direction.

The core concrete under compressive load dilates laterally and results in bending of the reinforcing bars on the compression side of the column. Therefore, the strain distribution is not uniform along the bar section as shown in Figure 3-30 (left). This strain gradient in the bar reduces the required axial demand which leads to bar buckling, defined here as a marked increase in bending deformations in Figure 3-30 (right). The transverse steel resists the dilation of the core concrete and outward deformation of the bar only where the transverse steel contacts the reinforcing bars. While the bar is reversed from a given tensile strain, the lateral deformations of the longitudinal bars may increase significantly between the turns of the spiral steel, as shown in Figure 3-30 (right). This significant increase in the lateral deformations of the reinforcing bars is defined as the limit state of bar buckling.

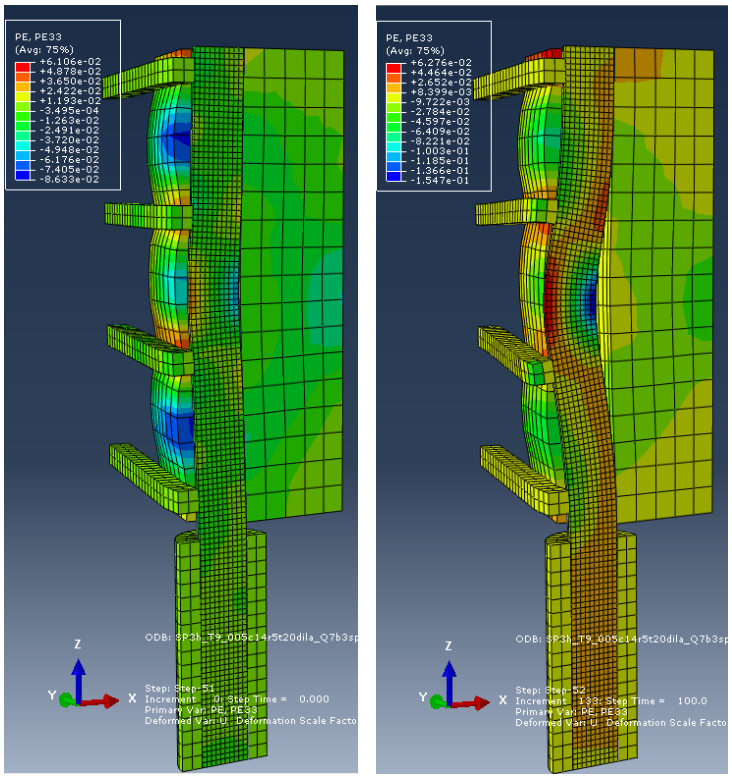

Figure 3-30. (Left) Compressive Cycle Previous to Bar Buckling; (Right) Compressive Cycle when Bar Buckled

In the absence of lateral restraint, a bar buckles when its axial load is larger than that required to maintain stability. In the presence of transverse reinforcement, lateral restraint prevents the bar from loss of axial capacity and delays buckling. It has been observed in most of the tests that the visible buckling occurs before or at the same cycle while the transverse steel yielding at the same location.

As a result, a robust model should be able to capture the complete buckling mechanism, including 1) local bending deformation of the bar after the onset of bar instability 2) transverse steel yielding 3) and the cycle bar buckles in a load history.

3.4.1.Comparison between Results from Test 11 and Buckling Model

The load history of Test 11 with the Kobe earthquake is displayed in Figure 3-31. The location of bars and the crack pattern are shown in Figure 3-32. The bar numbered N3 buckled under the tension-based mechanism when the specimen was reversed from $\mu_{9.3}^{6.56}$. (The subscript means the ductility level and the superscript refers to the time in the load history.) Therefore, there are three significant displacement ductility levels before the bar buckled, including $\mu_{10}^{3.86}$, $\mu_{-6.1}^{4.42}$ and $\mu_{9.3}^{6.56}$. The strain profile has been displayed in Figure 3-33. Since the buckling model includes three gauges of the bottom of the bar, the strain demand to apply on the buckling model is obtained by averaging the strain at the three bottom gauges, as shown in Table 3-7. A strain history demand of 0.056, -0.012, 0.048 and -0.005 was subjected to the bar buckling model, as shown in Fig. 34.

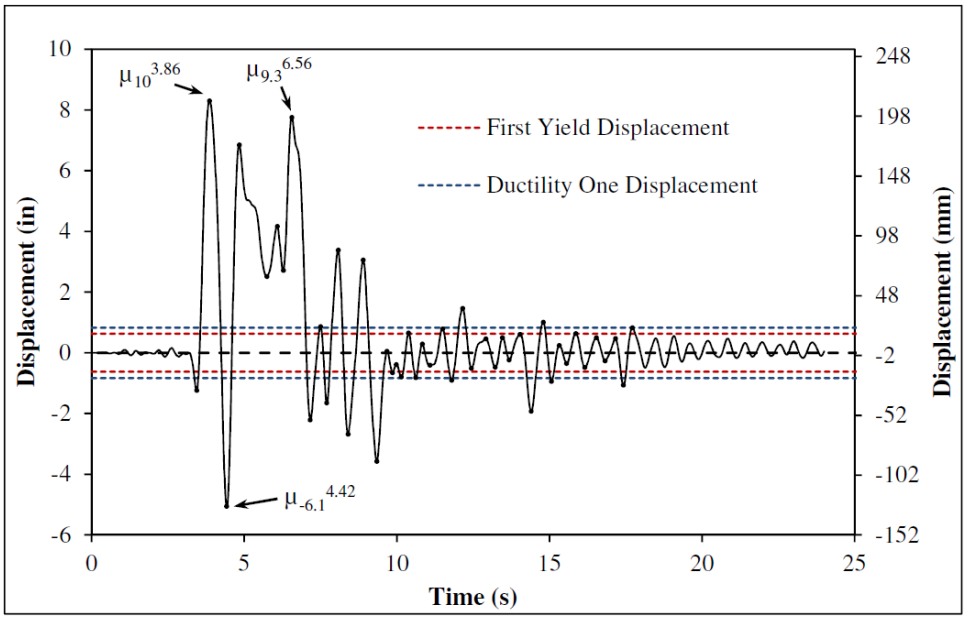

Figure 3-31. Kobe Load History

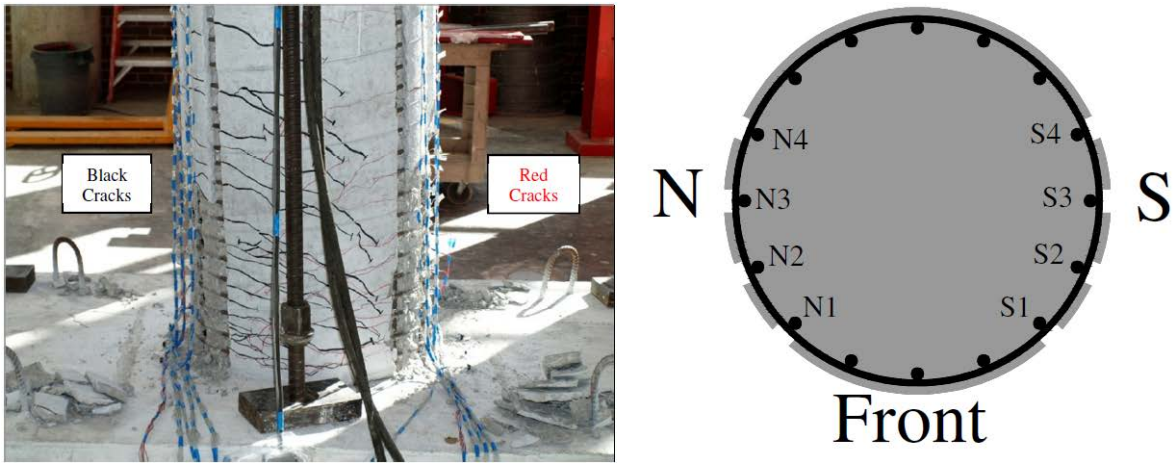

Figure 3-32. (Left) Crack Pattern on the Shear Face of the Column and (Right) Bar Designation

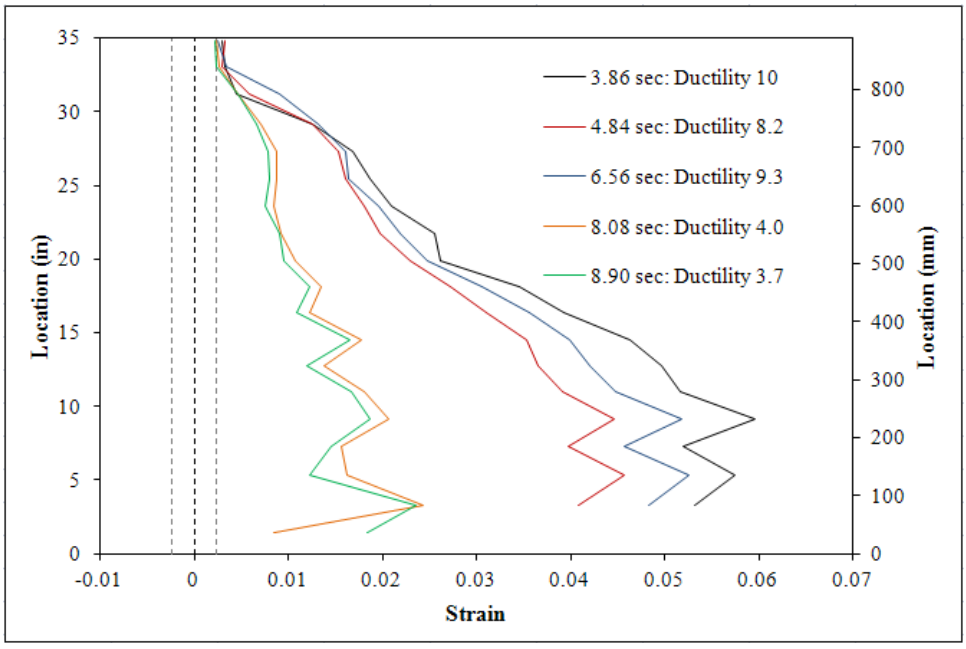

Figure 3-33. Strain Profile of Bar N3

Table 3-7. Strain Data from Experimental Test

	Compressive Strain (push in model)					Tensile Strain (pull in model)			
time	Base 1	Base 2	Base 3	AVG	time	Base 1	Base 2	Base 3	AVG
3.44	-0.0029	-0.0024	-0.0021	-0.0025	3.86	0.053	0.057		0.055
4.42	0.0015	-0.012	-0.0014	-0.0040	6.56	0.048	0.053		0.051
7.16	NA	NA	NA	-0.0018					

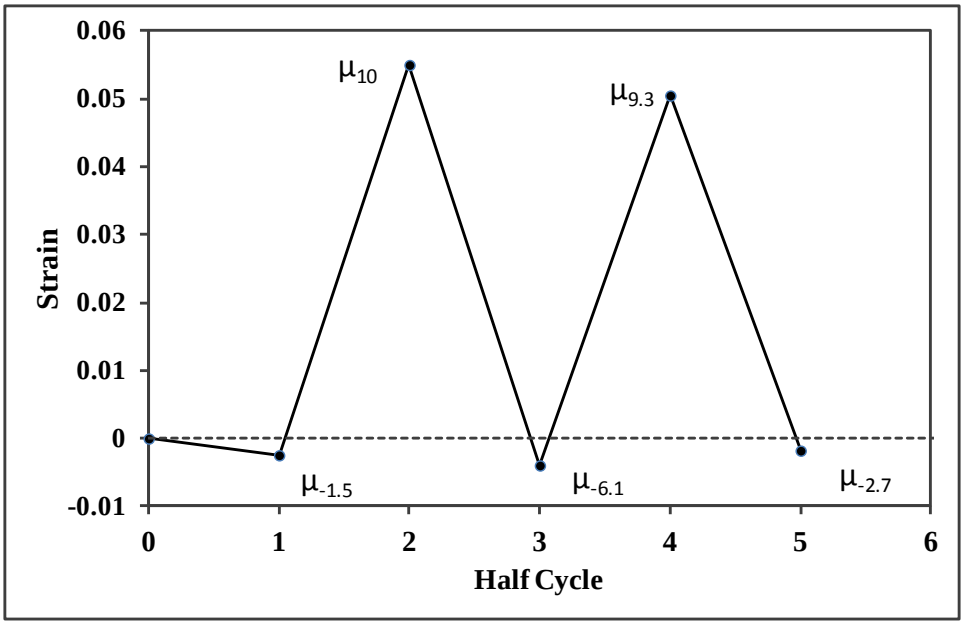

Figure 3-34. Strain History from Kobe Load history

An ideal computational result would result in the following: 1) avoidance of buckling when reversing from $\mu_{10}^{3.86}$, 2) buckling upon reversing from $\mu_{9.3}^{6.56}$ and 3) spiral yield at the time the bar buckled.

The vertical plastic strain flow graphs are shown in Figure 3-35 to show the strain distribution of the model at each peak strain point. All the graphs are marked in ductility levels corresponding to the column top displacements. The strain distribution is relatively uniform at $\mu_{-1.5}$ and μ_{10}, as shown in (b) and (c). Large plastic strain is observed at μ_{10}. The dilation of the concrete core initiates the bending behavior of the bar under axial compressive displacement. Therefore the strain distribution in the bar is not uniformly compressive. Residual tensile strain is observed at outside face of the bar under compressive axial displacement. The evolution of nonuniform strain distribution impacts the buckling of the bar, as shown in (f). The bar buckling is compared to the picture from the experimental test in Figure 3-36. The spiral yields at buckling region, as shown in Figure 3-37.

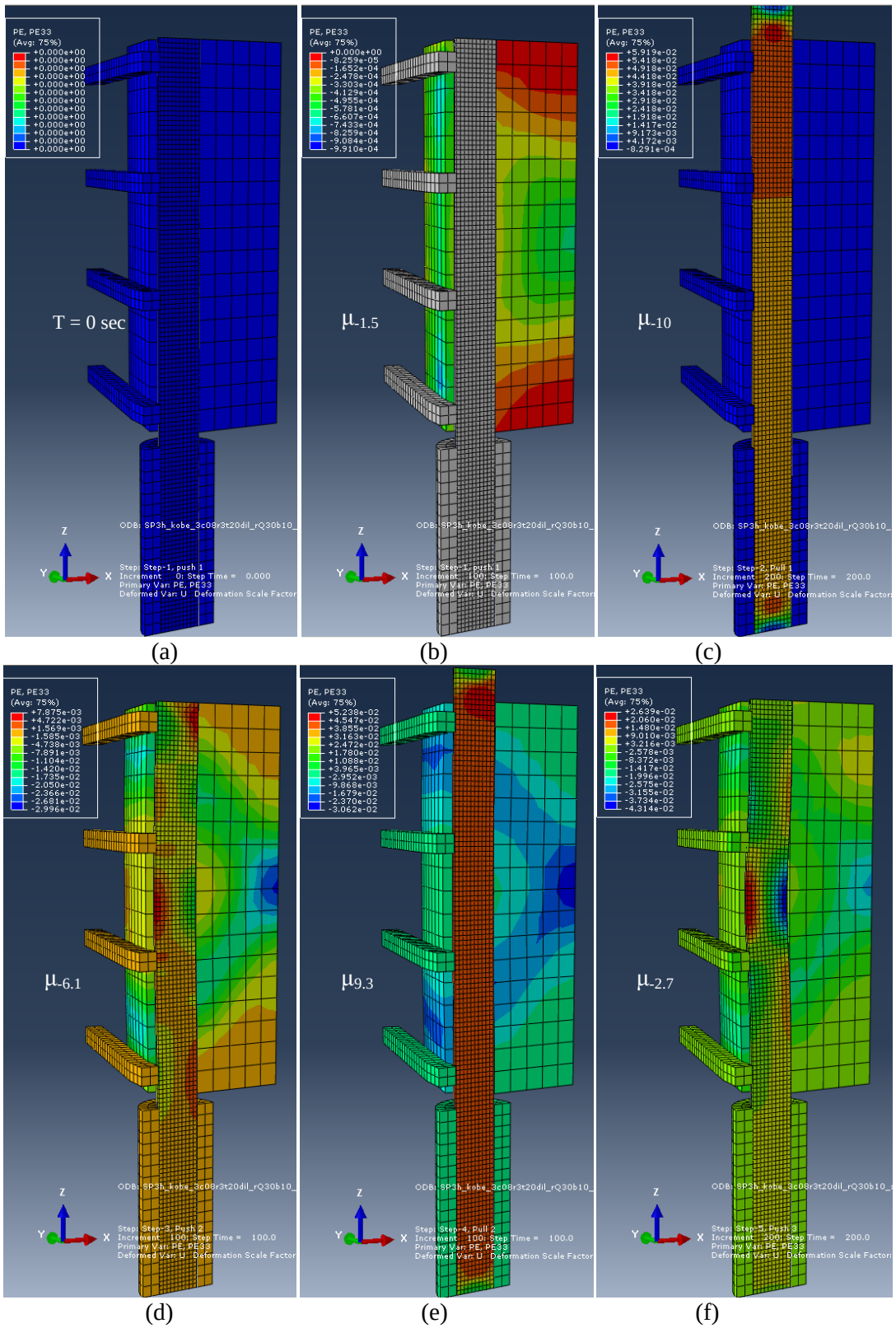

Figure 3-35. Loading Process with Strain History from Kobe Load History

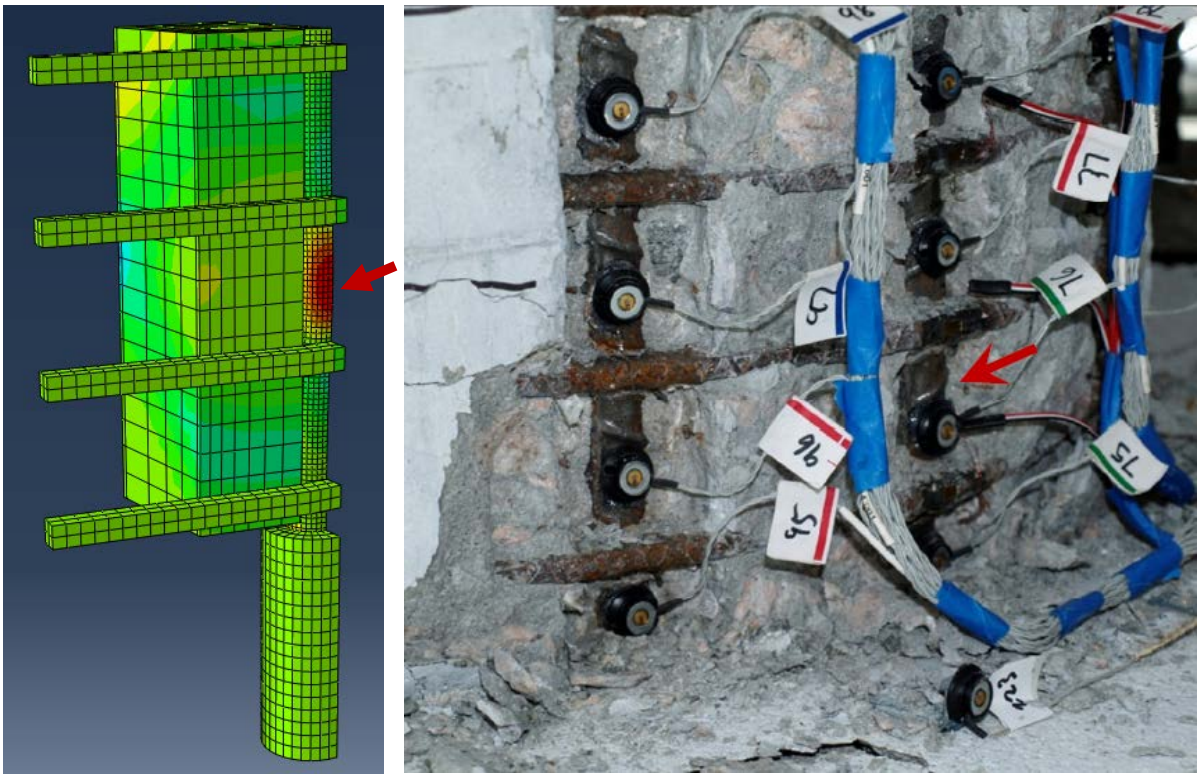

Figure 3-36. Comparison of Bar Buckling in Analysis and Experiment

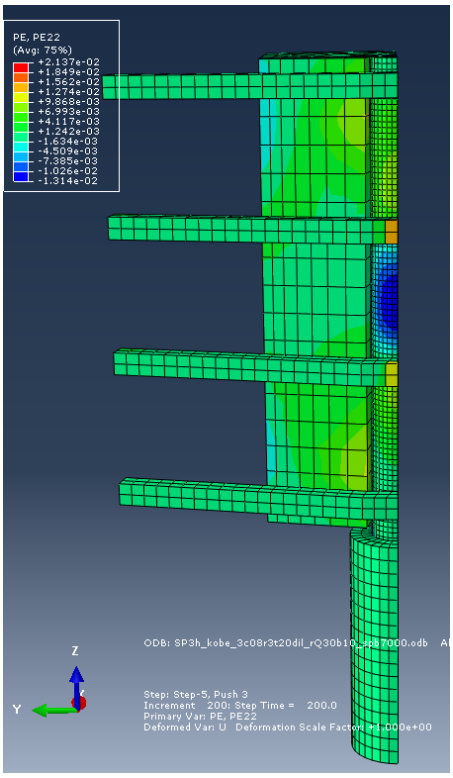

Figure 3-37. Yielding of Spiral at Buckling Area

3.4.2.Comparison between Results from Test 9 and the Buckling Model

The column specimen in Test 9 was subjected to a 3-cyclie-set loading history. Figure 3-38 showed the loading history of the top displacement of the specimen.

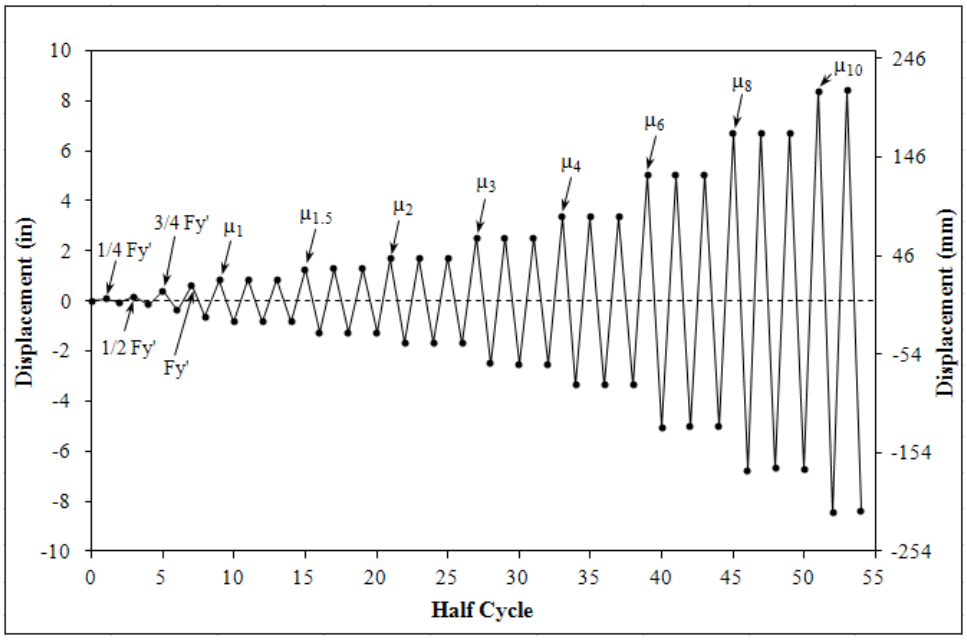

Figure 3-38. Three-Cycle-Set Load History

N3 Bar buckled at the first push cycle of ductility 8, as shown in Figure 3-39. Before bar buckling occurs, the lateral demand on the spiral is from the expansion of core concrete under compression. The initiation of bar buckling will result in a concentrated lateral push-out force on the contact point between spiral and the bar. For this analysis, the spiral yields under the lateral demand from the bar buckling. It is worth noting that spiral yields as a result of core concrete dilation. The spiral strain increase tremendously when the bar buckles, as shown in Figure 3-40.

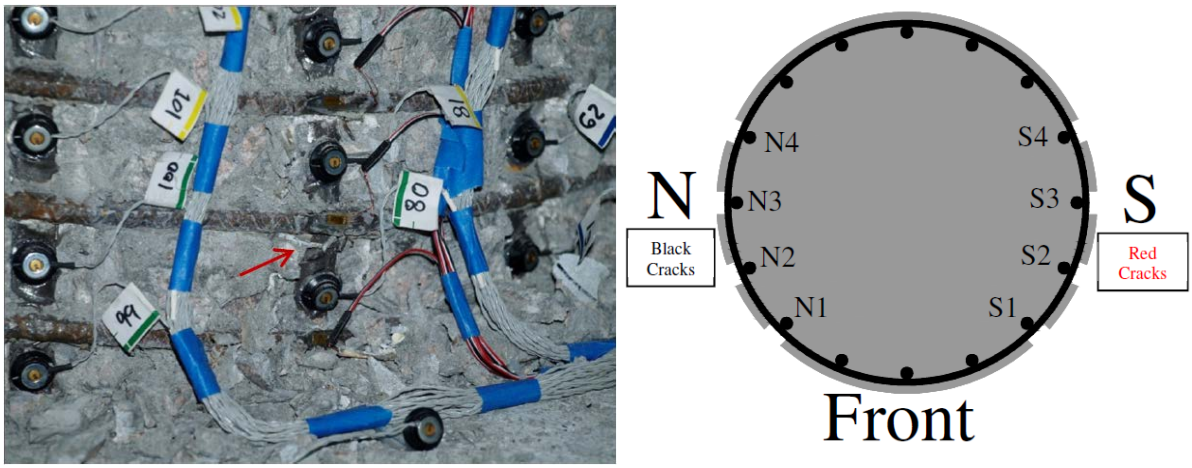

Figure 3-39. Bar Buckling at First Push Cycle of Ductility 8

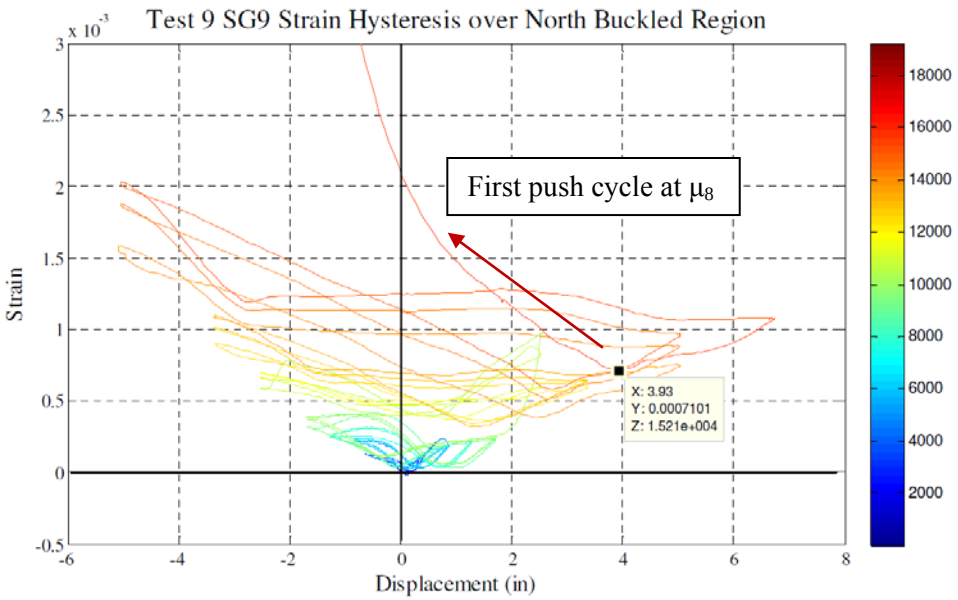

Figure 3-40. Strain Hysteretic Response of Spiral at Bar Buckling Region

The strain history to apply on the bar buckling model is not available at the cycle where bar buckled, since any strain data from LEDs after bar buckling is not reliable. Figure 3-41and Figure 3-42 portray strain profiles of extreme fiber bar at north side of the column (N3) under push and pull load respectively. The strain history which is applied to the bar buckling model is obtained from averaging the strain within six inch above the base gauge. The strain history is terminated at the cycle where buckling occurs. The target strain at this cycle is determined based on previous compression cycles where the bar has not buckled. If the column was subjected to a larger compressive displacement in a previous cycle, the compressive strain at the buckling cycle can be assumed to be similar to the one at the same displacement level of the previous cycle. If there are not any compressive cycles that have a larger displacement than that from the buckling cycle, the compressive strain can be extrapolated to get an approximation of the target strain at the buckling cycle. It is important to ensure the compressive displacement is not overestimated at the bar buckling cycle, since the bar is likely to buckle with a large enough compressive displacement demand regardless of the load history.

The strain history depends on the average strain at the three base gauges. Figure 3-41 highlights the three base gauges with red dot. Figure 3-42 shows the compressive strain profile. Strain profiles do not change significantly from cycle to cycle at the same ductility level. Therefore, the average strain is assumed to be constant at all three cycles. Some of the minor cycles were neglected since it is not likely to have a large impact. However, for the 3-cycle-set load history, the strain history needs to include most of the peak strains because every specific strain level is larger or equal to the strain at previous cycles.

Table 3-8 lists all the strain values from three base gauges of the strain profile. The target strain history is shown in Figure 3-43. As was discussed, the strain data from LEDs fail to provide the target strain at push cycle of ductility 8. As discussed, the strain at buckling cycle can be obtained by extrapolate the strain from previous cycles proportional to the displacement. The strain -0.0122 is gained by extrapolate the strain from push cycle of ductility 6.

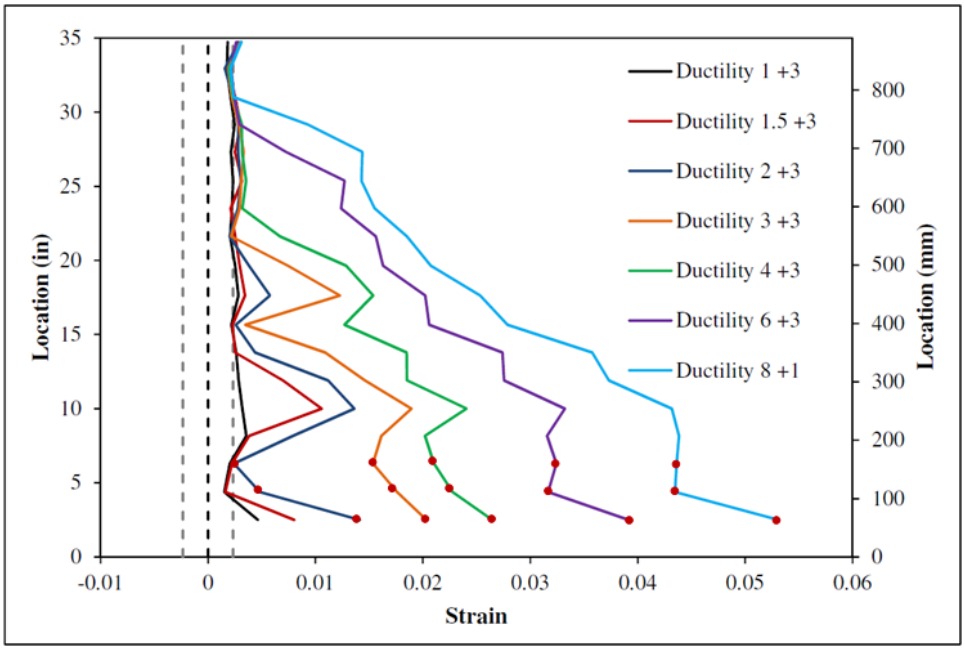

Figure 3-41. Strain Profile of Bar N3 at Tensile Cycles

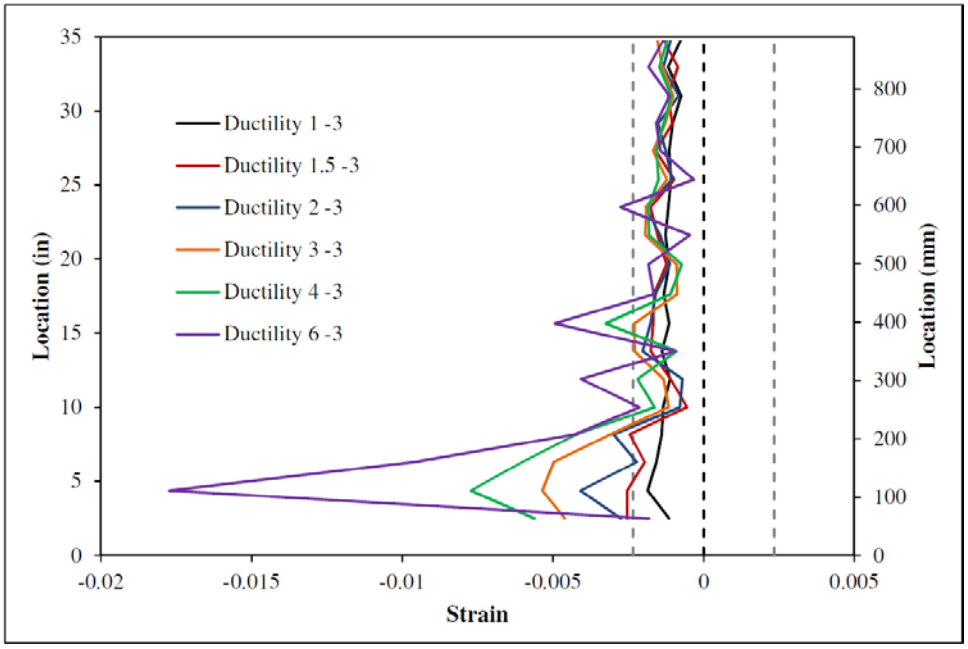

Figure 3-42. Strain Profile of Bar N3 at Compressive Cycles

Table 3-8. Strain Data from Experimental Test

	Tensile Strain (pull in model)				Compressive Strain (push in model)			
Ductility	Base 1	Base 2	Base 3	AVG	Base 1	Base 2	Base 3	AVG
2	0.014	0.005	0.012	0.010	-0.0027	-0.0041	-0.0022	-0.0030
3	0.02	0.018	0.015	0.018	-0.0046	-0.0054	-0.005	-0.0050
4	0.026	0.023	0.021	0.023	-0.0056	-0.0077	-0.006	-0.0064
6	0.039	0.032	0.032	0.034	-0.00018	-0.0177	-0.0096	-0.0092
8	0.053	0.043	0.044	0.047	NA	NA	NA	-0.0122

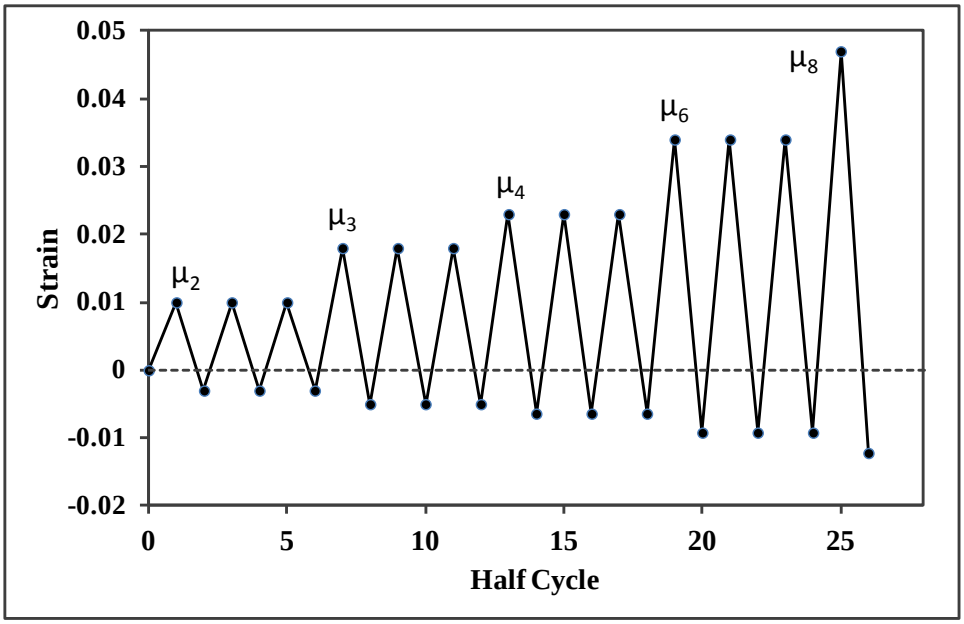

Figure 3-43. Strain History from 3-cycle-set Load History

As shown in Figure 3-44 (b), the dilation of concrete caused non uniform strain distribution in the bar early at displacement ductility level 2. It is observed that the inelastic buckling was not an instant event. The reinforcing bar was not stable under large axial demand and lateral expansion demand from concrete at low ductility levels. The transverse reinforcing steel restrained the bar from buckling at low ductility levels. As marked in red ellipse, strain around outside surface of the bar remains tension at compressive cycle. This residual tensile strain at the outer surface of the bar accumulated cycle by cycle. Similarly, the residual compressive strain accumulates around the inside surface of the bar. Residual strains in the bar lead to out of plane bending and a large lateral demand on the transverse steel. The spiral yields when the demand combination from concrete dilation and the bar out of plane deformation exceeds the spiral yield strength, as show in Figure 3-46 (k).

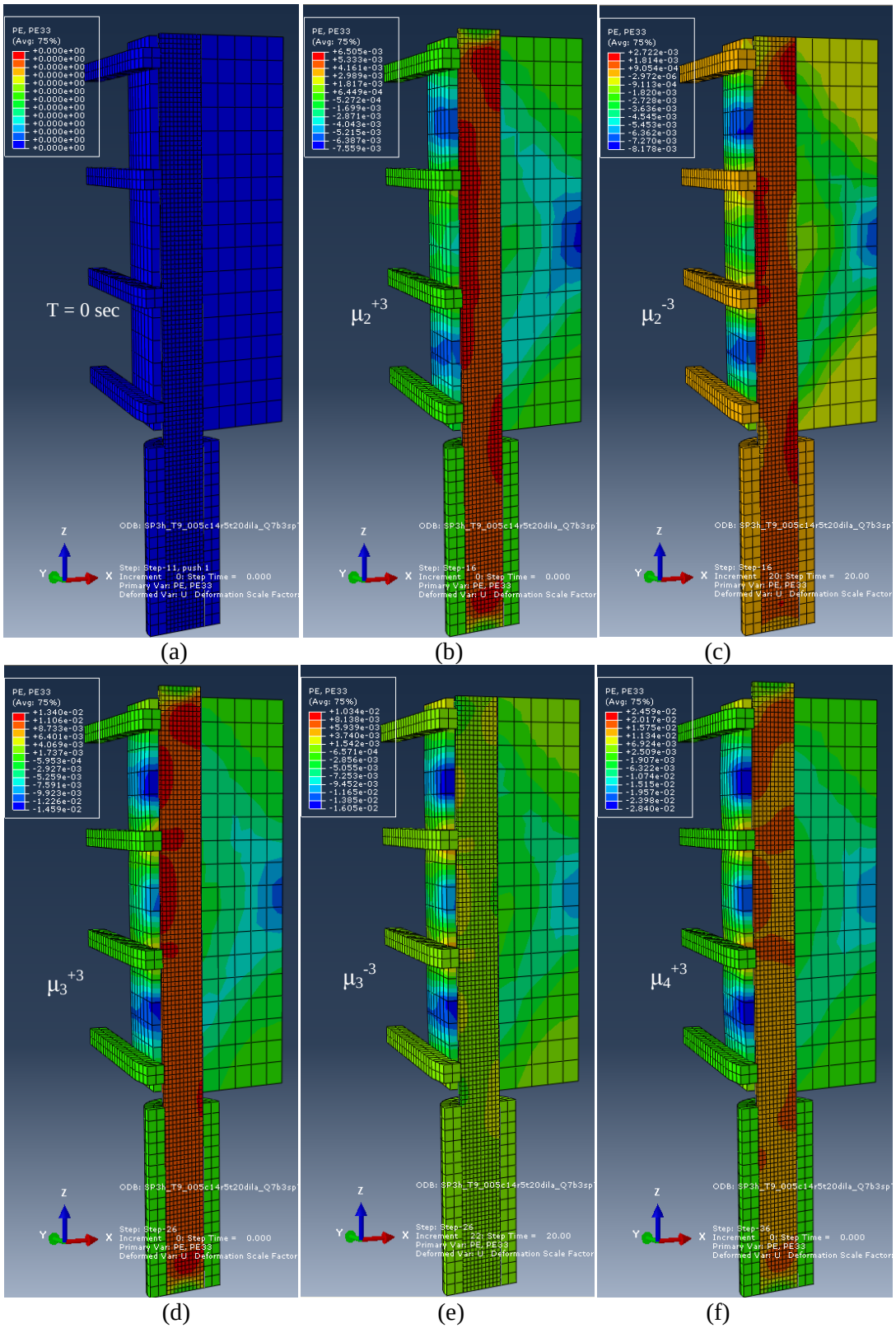

(a) (b) (c)

(d) (e) (f)

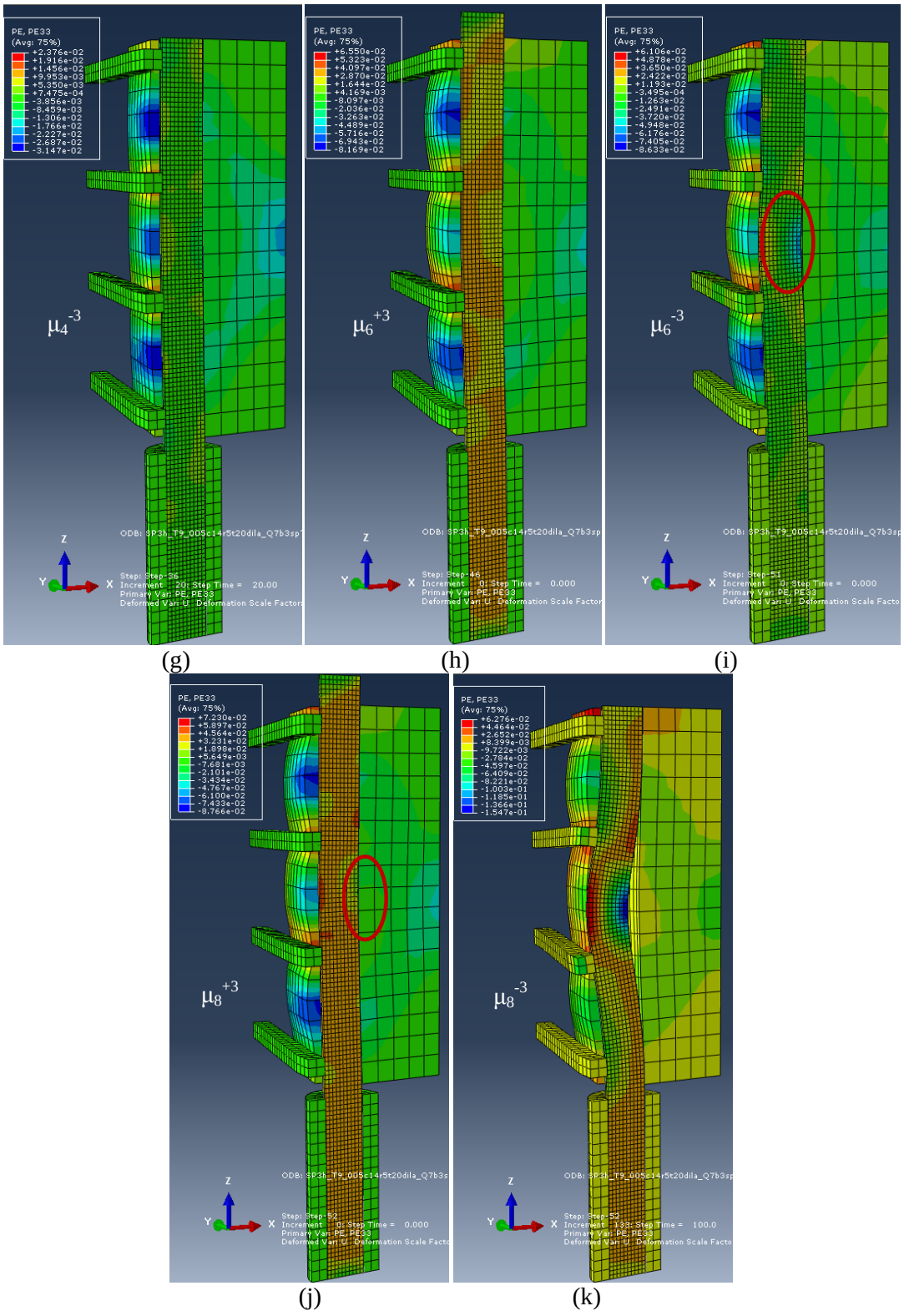

Figure 3-44. Plastic Strain Distribution at Selected Peak Strain Cycles from Loading Process

The comparison of bar buckling in the model and the experimental test is displayed in Figure 3-45. Both of them involve yielding of multiple transverse steel branches, as shown in Fig. 46.

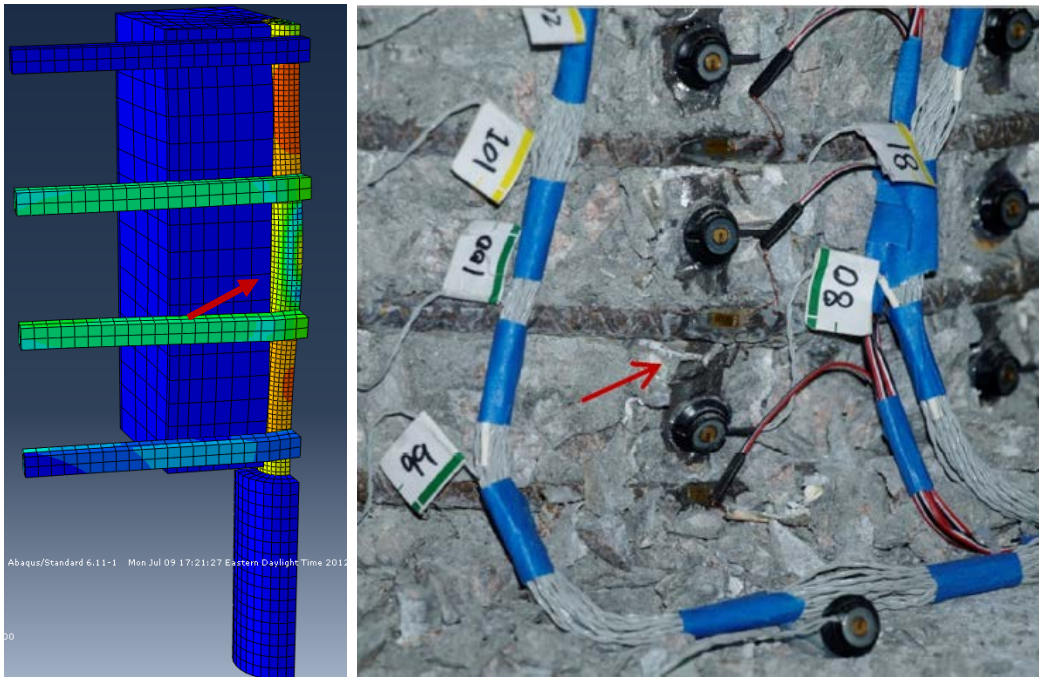

Figure 3-45. Comparison of Bar Buckling in Analysis and Experiment

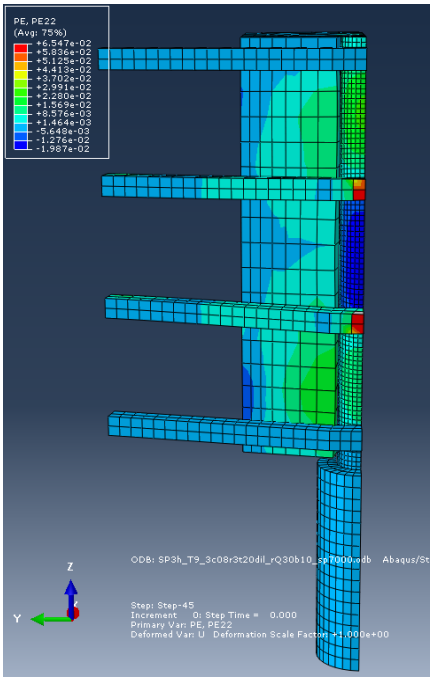

Figure 3-46. Yielding of Spiral at Bar Buckling Location

CHAPTER 4 - INTERPRETATION AND APPLICATIONS OF EXPERIMENTAL RESULTS

4.1. Interpretation of Experimental Results

4.1.1. General Damage Observations

The deformation capacity of all of the cyclically loaded specimens was limited by reinforcement bar buckling and subsequent rupture during later cycles of the load history. The following sequence of damage was observed for all of the cyclically loaded specimens: cracking, longitudinal reinforcement yield, cover concrete crushing, yielding of transverse steel, bar buckling, and then reinforcement rupture. Depending on previous compressive demands within the load history, reinforcement bar buckling either occurred with elastic transverse steel restraint, or over multiple inelastic spiral layers. In all cases the transverses steel permanently deformed over the outward buckled region which lead to a loss of core concrete confinement. This lead to cycle to cycle degradation of the core concrete. Rupture of transverse steel was never observed. The first significant loss of strength occurred when previously buckled reinforcement ruptured in tension. Out of the total of 20 buckled extreme fiber bars observed in Tests 8-18, 15 buckled at locations of previously inelastic transverse steel restraint while only 5 had previously elastic transverse steel restraint.

The symmetric three cycle set load history and resulting hysteretic response for Test 9 appear in Figure 4-1 and Figure 4-2 to illustrate the effect of each damage state on column performance. The extreme fiber bar on the North and South sides of the specimen buckled after reversal from ($\mu_8^{+1} = 6.72"$) and ($\mu_8^{-2} = -6.70"$) respectively. The first significant loss in strength occurred when the previously buckled North reinforcing bar ruptured at $5.18"$ during push to ($\mu_{10}^{+1} = 8.38"$). The first bar fracture occurred before displacement levels exceeded those required to initially produce bar buckling.

It is inconsistent to have separate performance limit states for bar buckling and bar fracture since the two damage states are linked to one another. Outward deformation during reinforcement bar buckling produces an internal strain distribution composed of curvature and direct axial components. Past research by (Restrepo-Posada et al. (1994)) suggests that the buckled deformation may lead to cracking on the compression side of the buckled bar as shown in Figure 4-3. The presence of these cracks may explain the early fracture of previously buckled bars during later cycles of the load history.

To further illustrate this point, consider the Darfield 2010 earthquake record which buckled a single reinforcing bar. The displacement ductility demands in the push and pull directions of this Darfield load history were 9.0 and -7.3 respectively. A symmetric three cycle set aftershock load history was conducted to determine the post-earthquake performance of the bridge column. Continued cycling at displacement ductility six ruptured the previously buckled reinforcing bar.

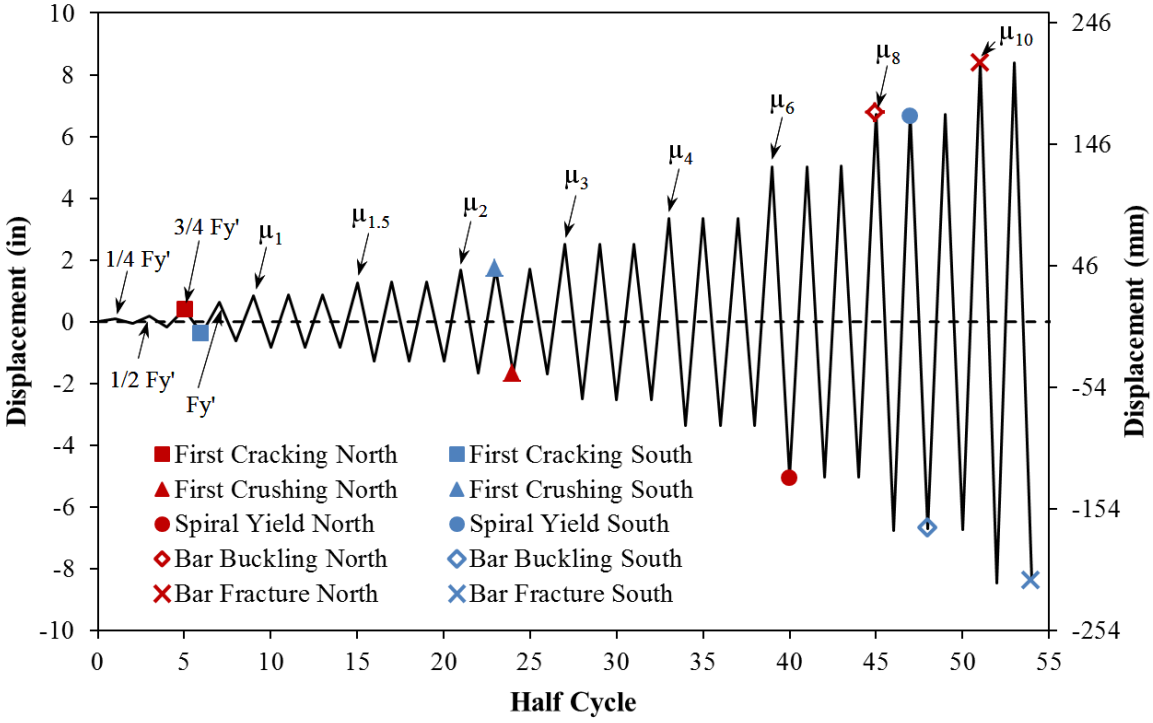

Figure 4-1. Sequence of Damage Observed in the Symmetric Three Cycle Set Load History of Test 9

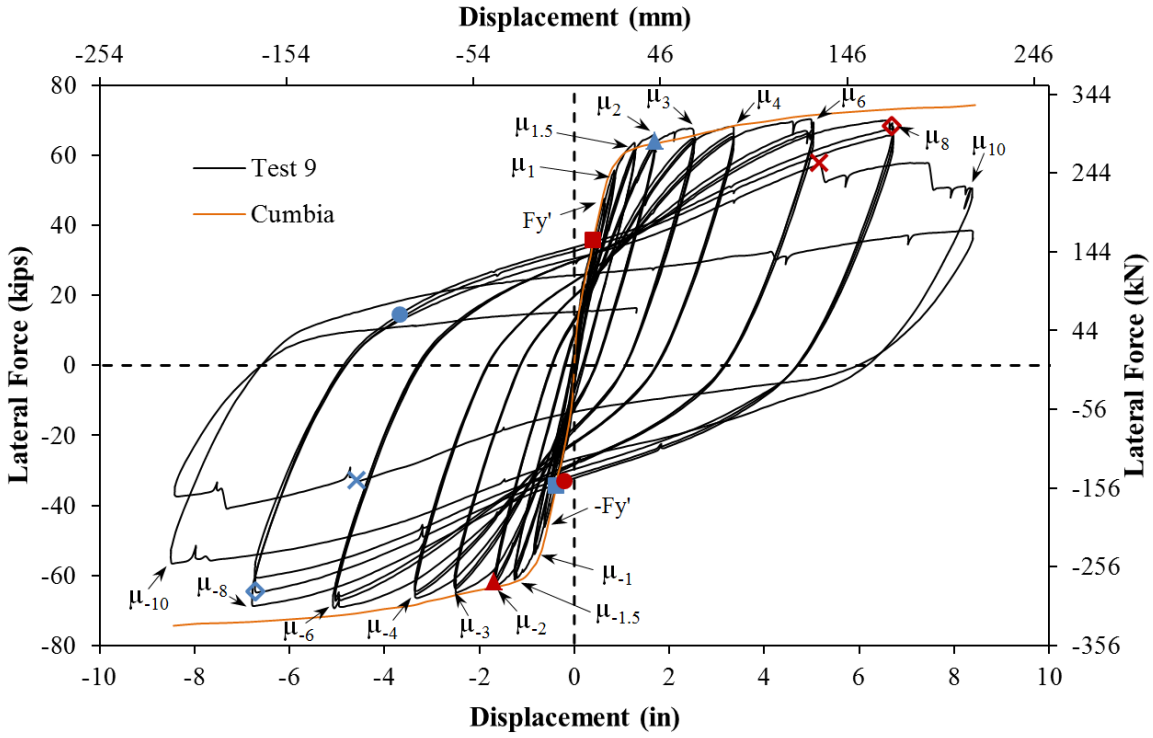

Figure 4-2. Reinforcement Bar Buckling and Subsequent Rupture during Test 9

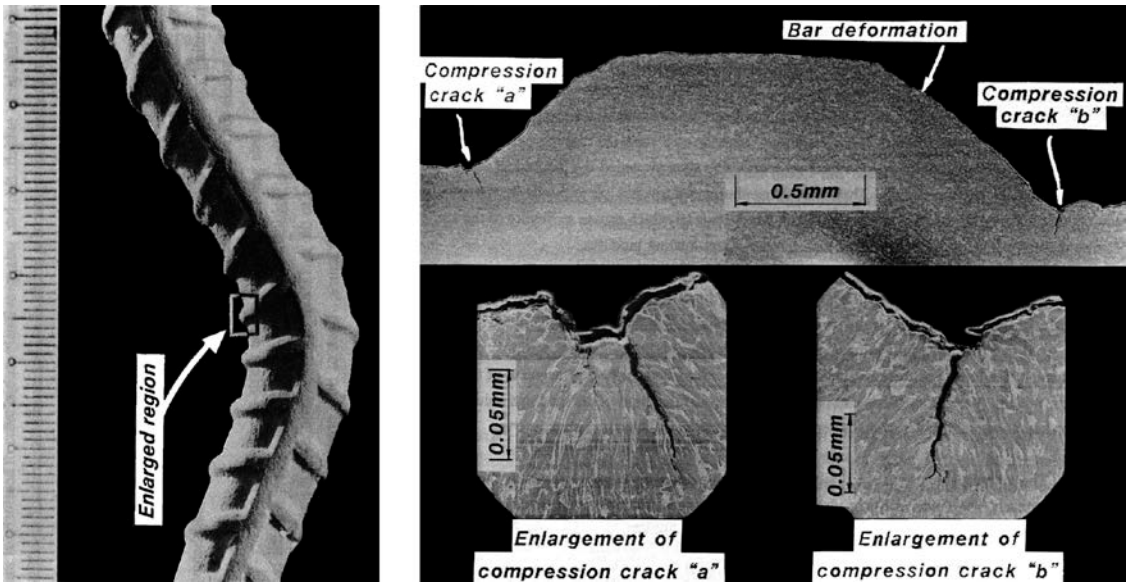

Figure 4-3. Cracks on a Buckled Bar, from (Restrepo-Posada et al. (1994))

4.1.2. Case Study on the Effects of Load History – Kobe 1995 Earthquake Record

Past research by (Moyer and Kowalsky (2003)) suggests that reinforcement buckling occurs after reversal from a peak tensile strain, while the bar is still under net elongation but compressive stress. After reversal from the peak displacement, the cracks on the tensile side begin to close, and before the column reaches zero displacement the reinforcement enters a state of compressive stress but net elongation. It is during this time, while the cracks are still open, that the reinforcement is the sole source of compression zone stability and the bars are prone to buckling. Once the cracks have closed and the concrete is reengaged, the reinforcement is unlikely to buckle. The experimental results from this series of tests further supports this hypothesis which helps to explain the influence of load history on the bar buckling limit state. The main impact of load history on column behavior is its effect on accumulated strains within the longitudinal and transverse reinforcement.

A case study for the Kobe 1995 earthquake record is presented to explain the influence of load history on accumulated strains in the longitudinal and transverse steel. The acceleration input of the Kobe record was multiplied by 1.13 to produce an analytical top column response equivalent to displacement ductility 9.9, as shown in Figure 4-4. A 24" diameter bridge column, with a #3 ASTM A706 spiral at 2" on center, was subjected to a quasi-static loading procedure which recreated the analytical Kobe displacement history and a constant axial load of 170kips equivalent to $(P/(f_c' A_g) = 6.2\%)$.

The test began with a small pull cycle followed by a near monotonic push to the peak displacement ductility of 9.9. The North longitudinal reinforcement, shown in Figure 4-6, is placed into tension during push cycles while the South side is subjected to compression, refer to Figure 4-8. The push cycle to displacement ductility 9.9 resulted in a peak tensile strain of 0.059 in the North extreme fiber bar, a peak compressive strain of -0.037 in the South extreme fiber bar, and two layers of inelastic transverse steel in the compression zone. The particular gage lengths depicted in Figure 4-6 and Figure 4-8 do not align with the peak tensile and compressive strains, but rather with the location of

outward buckling observed later in the displacement history. The peak tensile strain of 0.059 was not sufficient to buckle the North bar during the subsequent reversal to displacement ductility -6.1.

At displacement ductility -6.1, tensile strains in the South bar reached 0.033, compressive strains in the North bar measured -0.0119, and the transverse steel on the North side of the specimen remained elastic. This peak tensile strain, combined with multiple layers of inelastic transverse steel restraint, was sufficient to buckle the South extreme fiber bar after reversal of loading. At this time, the measured strains in the South bar no longer represent engineering strains due to the outward buckled deformation between target markers. As the South bar buckles outwards, the strain in the transverse steel restraint begins to rapidly increase as shown in Figure 4-9. The North extreme fiber bar buckled after reversal from the push cycle which ended at displacement ductility 9.3. The outward buckled deformation in the North bar caused measured strains in the transverse steel restraint to sharply increase as shown in Figure 4-7. Prior to buckling of the North extreme fiber bar, the transverse steel restraint remained elastic.

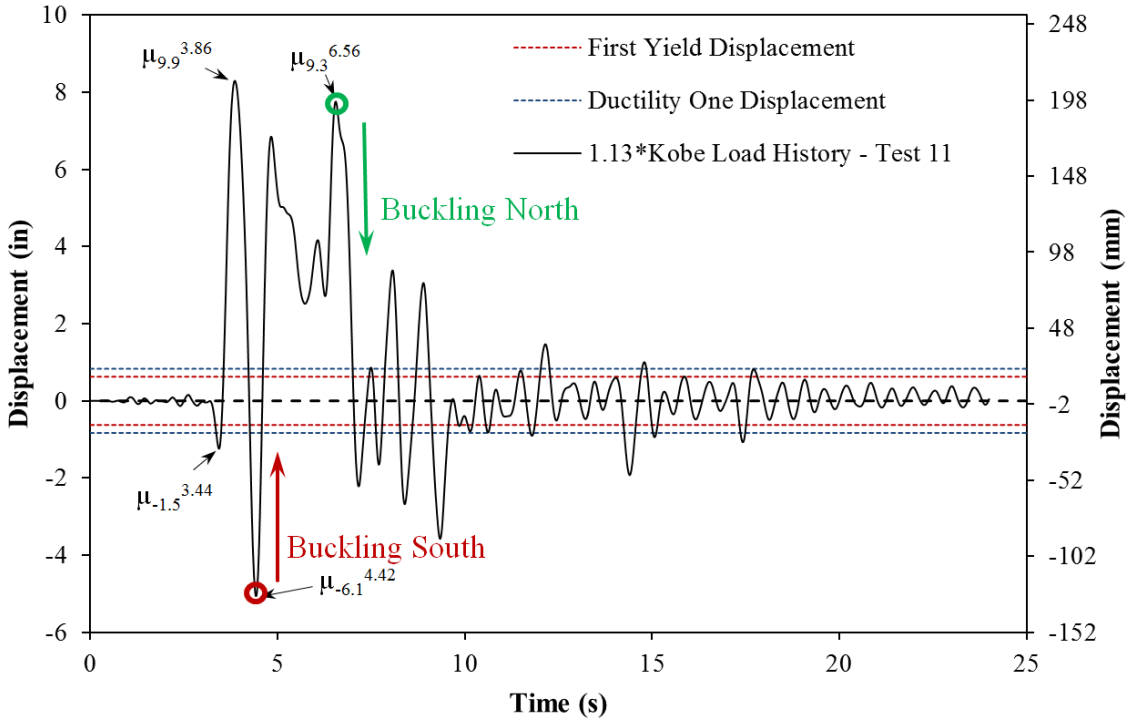

Figure 4-4. Top Column Displacement History for the Kobe 1995 Earthquake

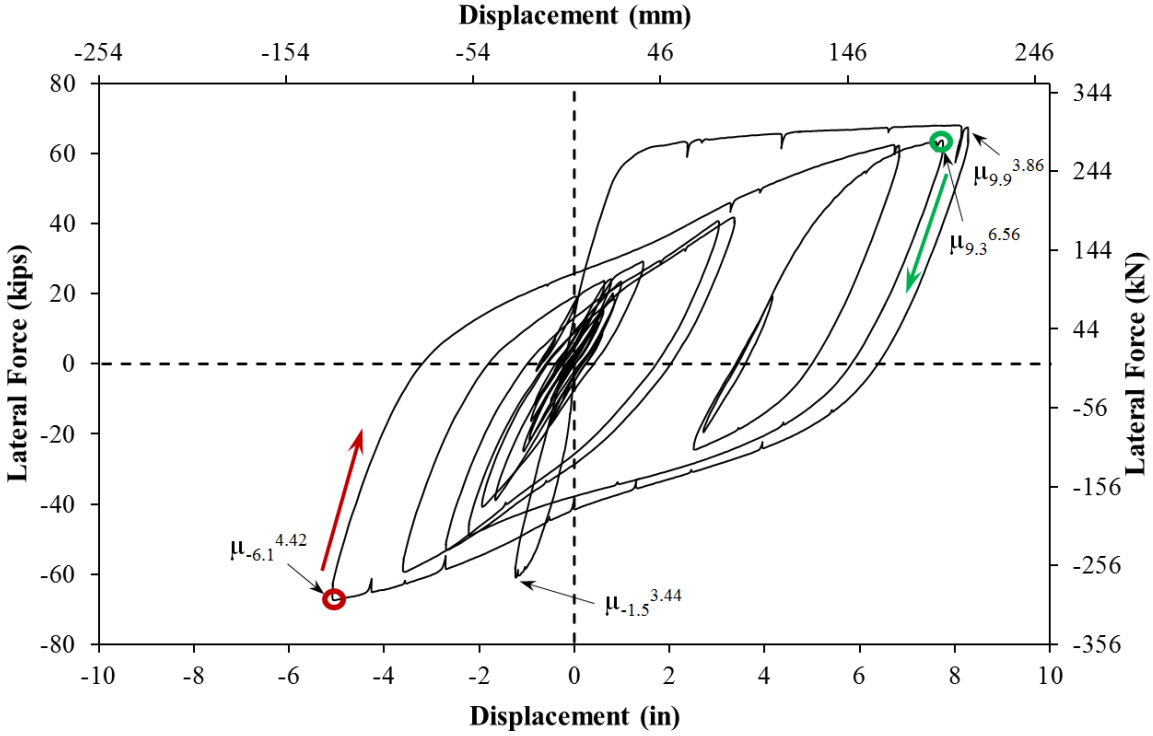

Figure 4-5. Lateral Force vs. Top Column Displacement Response for the Kobe 1995 Earthquake

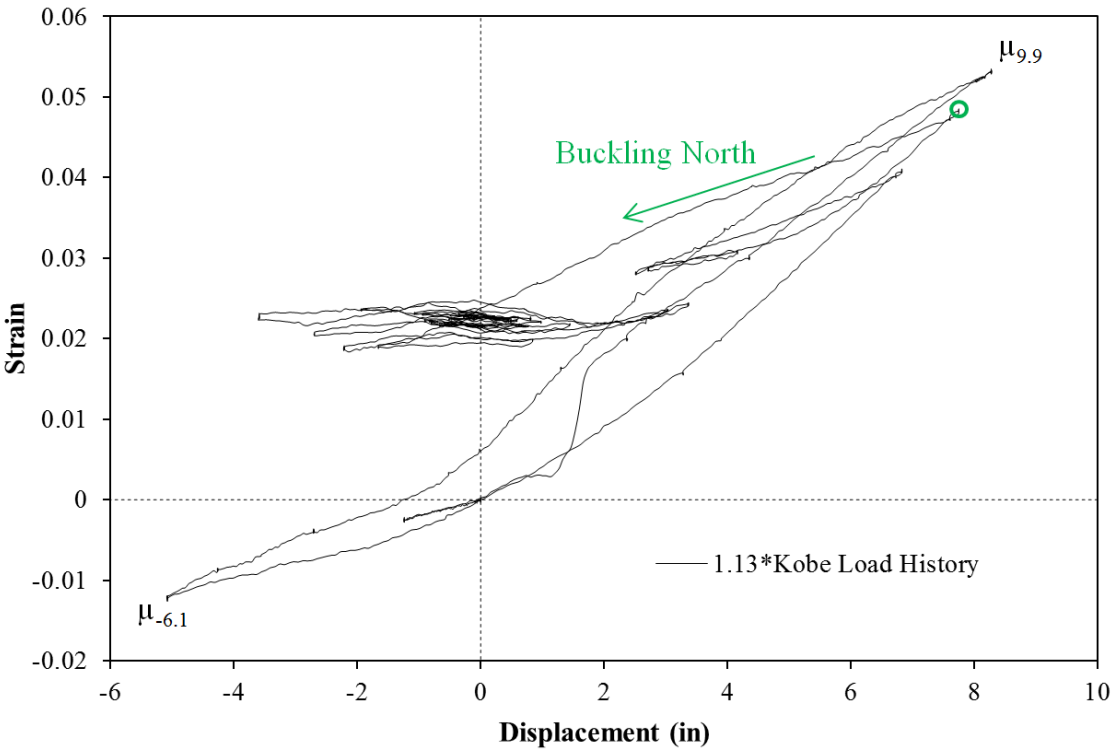

Figure 4-6. Longitudinal Steel Strain Hysteresis for the North Extreme Fiber Bar

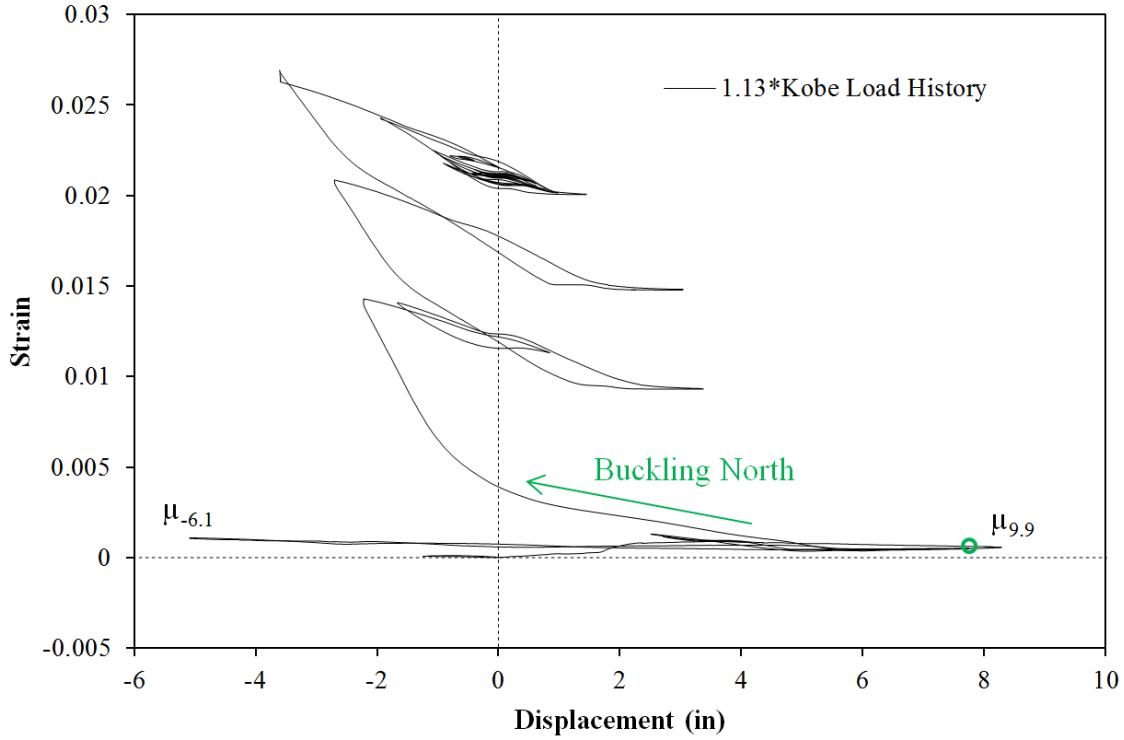

Figure 4-7. Transverse Steel Strain Hysteresis for Spiral Layer Overlaying Outward Buckled Region of North Bar

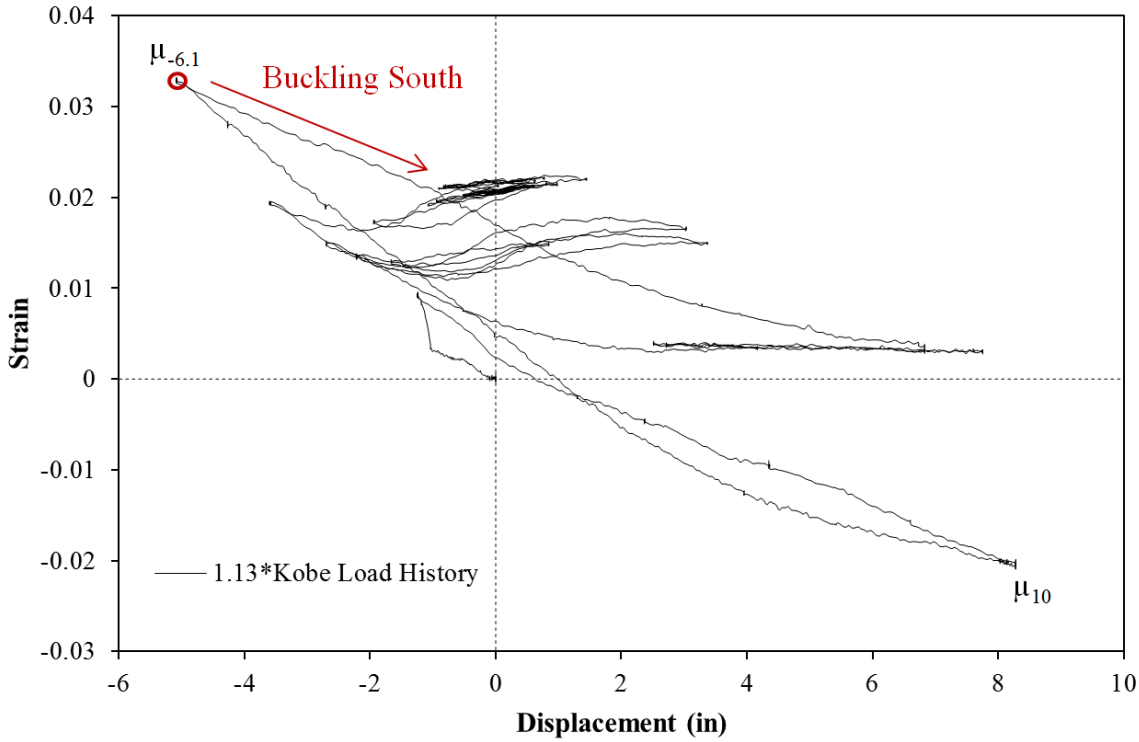

Figure 4-8. Longitudinal Steel Strain Hysteresis for the South Extreme Fiber Bar

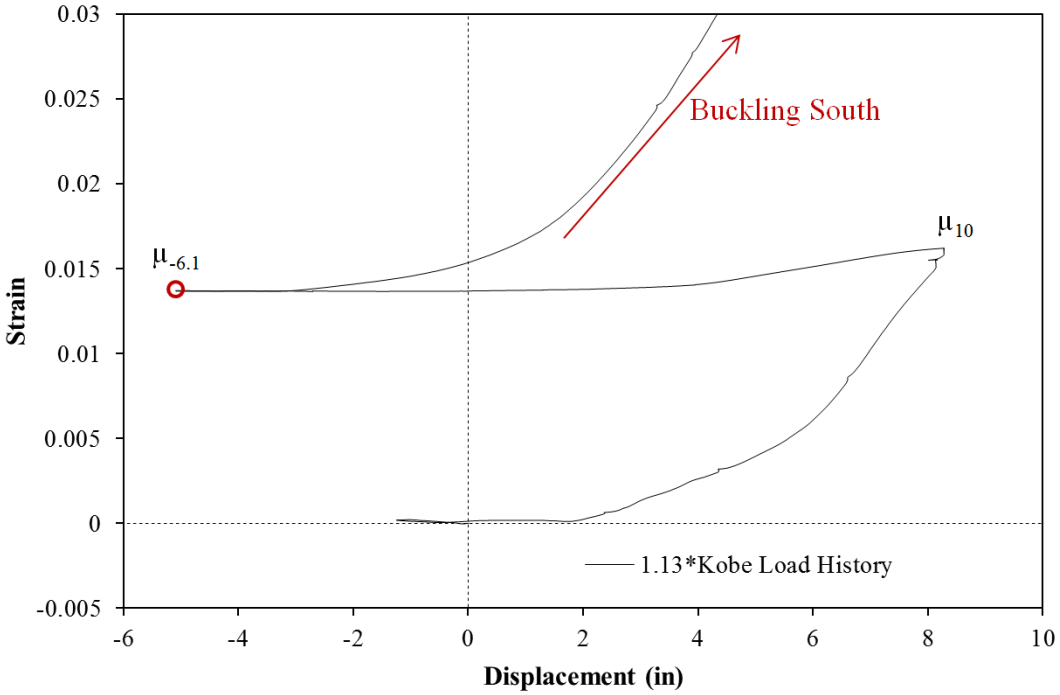

Figure 4-9. Transverse Steel Strain Hysteresis for Spiral Layer Overlaying Outward Buckled Region of South Bar

4.1.3. Effect of Load History

The effect of load history was the main variable for Tests 8-12 and 16-18. The 24" diameter bridge columns had identical longitudinal steel content, an 8ft cantilever length, and a #3 ASTM A706 spiral at either 2" (Tests 8-12) or 1.5" (Tests 16-18) on center. An overview of the column properties and top column displacement histories utilized in load history variable tests appears in Table 4-1 and Figure 4-10. Specific earthquake time-history response characteristics were evaluated including: the number and amplitude of cycles prior to the peak, degree of symmetry, and peak displacement in each direction of loading. For example, the Chichi earthquake contains a gradual ramp up to the peak displacement, but the load history is asymmetric in nature with high ductility demands in only one direction. The Kobe and Darfield load histories contain a near monotonic push cycle to the peak displacement followed by a direct reversal to the largest cycle in the opposing direction of loading. Alternatively, the Chile 2010, Japan 2011, and Llolleo 1985 load histories contain a large number of cycles both before and after the peak displacement.

The main impact of load history on column behavior is its effect on accumulated strains within the longitudinal and transverse reinforcement. Inelastic strains in the transverse steel, caused by large concrete compressive demand, can decrease its effectiveness in restraining buckling of the longitudinal bars. The majority of the extreme fiber reinforcement, 15 out of the 20 total from Tests 8-18, buckled over previously inelastic layers of transverse reinforcement. Load histories with compressive demand sufficient to produce inelastic transverse steel may require lower values of peak tensile strain to buckle reinforcing bars after reversal of load. The symmetric three cycle set load history is more severe than the load histories produced by actual earthquakes, when evaluated to the same peak displacement, due to the balanced repeated cycles at each ductility level. Multiple cycles at the same amplitude allow each side of the specimen to be subjected to the peak compressive and tensile cycles. This creates the worst situation for a given peak displacement, the possibility if

inelastic transverse steel restraint and tensile strains sufficient to buckle reinforcing bars after reversal of loading.

The relationship between tensile strain and displacement during the largest push and pull cycles of each load history variable test appears in Figure 4-11 and Figure 4-12. A summary of the peak tensile strain and displacement for North and South extreme fiber bars in each load history appears in Table 4-2 and Table 4-3 respectively. Load histories which did not produce bar buckling are labeled.

The 24" diameter bridge columns contained a #3 ASTM A706 spiral at either 2" or 1.5" on center. A specimen with each transverse steel detailing was subjected to a symmetric three cycle set load history which produced bar buckling during repeated cycles at displacement ductility eight. The following four earthquake load histories: Chichi 1999, Chile 2010, Llolleo 1985, and Darfield 2010 were scaled to produce peak response displacement ductility of 8.8, 8.7, 9.0, and 9.0 respectively. The longitudinal steel placed into tension during the peak cycle of these four load histories did not buckle during the earthquake record. For the case of the Darfield 2010 load history, the peak push displacement caused layers of transverse steel to go inelastic, and the following pull cycle to displacement ductility -7.3 had sufficient tensile strains to buckle the reinforcement after reversal. The performance of the column subjected to the Darfield 2010 earthquake closely resembled that of the Kobe 1995 earthquake. The only difference is that the tensile strains sustained during the peak displacement ductility of nine were not sufficient to buckle reinforcement after reversal of load.

The four specimens were then subjected to symmetric three cycle set aftershock load histories to determine the post-earthquake performance of the columns. Reinforcement buckling occurred during repeated cycles at displacement ductility six of the cyclic aftershock studies conducted after the Chichi 1999, Chile 2010, and Llolleo 1985 load histories. While visible bar buckling did not occur until ductility eight for the cyclic aftershock conducted after the Chile 2010 earthquake, inspection of the strain data indicated significant deformation during repeated cycles at ductility six. The cyclic aftershock conducted after the Darfield 2010 record ruptured the previously buckled reinforcement during ductility six. To produce buckling after reversal from the peak displacement response of earthquake load histories, the Kobe 1995 and Japan 2011 records were scaled to displacement ductility 9.9 and 10 respectively.

A potential problem for post-earthquake inspection arises based on the experimental observations from the Chichi 1999, Chile 2010, and Llolleo 1985 load histories. At the conclusion of the load history the specimens had crushed cover concrete and degraded stiffness, but no visible indication that the future ductility capacity could be reduced. These three specimens all produced bar buckling during repeated cycles at displacement ductility six of the symmetric three cycle set aftershock load history. Two specimens subjected to symmetric three cycle set load histories, Tests 9 and 16 without prior earthquake records, produced bar buckling during repeated cycles at displacement ductility eight.

The relationship between tensile strain and displacement during the peak cycle, see Figure 4-11 and Figure 4-12, does not appear to be affected by seismic load history. The buckling damage control steel tensile strain limit is influenced by load history, and previously inelastic layers of transverse steel are less effective at restraining bar buckling. This warrants consideration of a concrete compressive strain limit related to excessive spiral strains which render them less effective at anti-buckling restraint. At low ductility levels, the tensile strains measured during the Kobe 1995 and Darfield 2010 peak cycles are larger than the other records because these were near monotonic push cycles to the peak displacement, which occurred while the crack distribution was still forming. The relationship between compressive strain and displacement for peak push and pull cycles appears in Figure 4-13 and Figure 4-14.

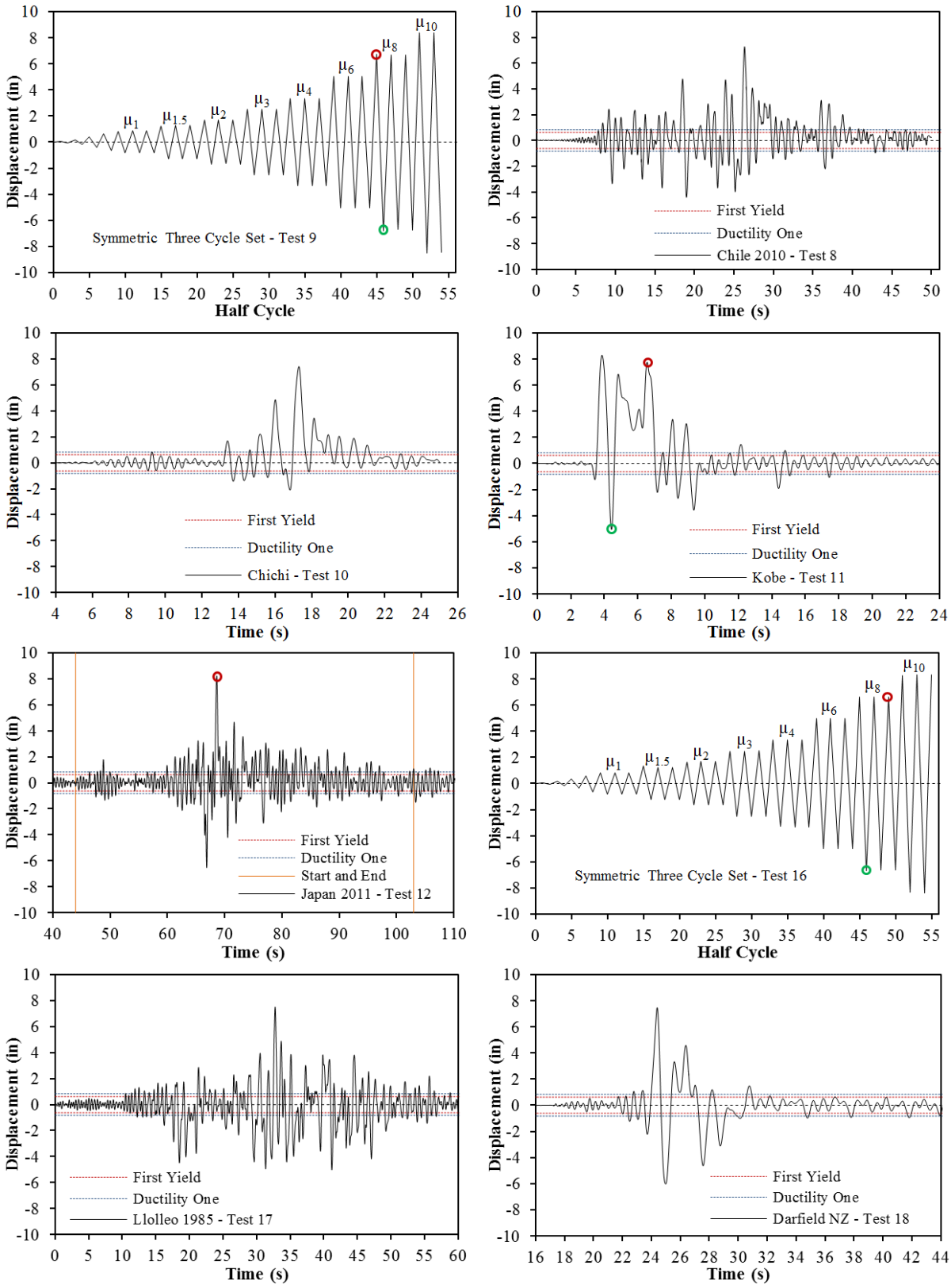

Figure 4-10. Top Column Displacement Histories for Load History Variable Tests 8-13 and 16-18

Table 4-1. Detailing Summary for Load History Based Tests

Test	Load History	D (in)	L/D	Long. Steel (ρ_l)	Spiral Detailing (ρ_s)	f'c (psi)	P/f'c*Ag
8	Chile 2010	24	4	16 #6 bars (1.6%)	#3 at 2" (1%)	6988	5.4%
8b	Cyclic Aftershock	24	4	16 #6 bars (1.6%)	#3 at 2" (1%)	6988	5.4%
9	Three Cycle Set	24	4	16 #6 bars (1.6%)	#3 at 2" (1%)	6813	5.5%
10	Chichi 1999	24	4	16 #6 bars (1.6%)	#3 at 2" (1%)	5263	7.1%
10b	Cyclic Aftershock	24	4	16 #6 bars (1.6%)	#3 at 2" (1%)	5263	7.1%
11	Kobe 1995	24	4	16 #6 bars (1.6%)	#3 at 2" (1%)	6070	6.2%
12	Japan 2011	24	4	16 #6 bars (1.6%)	#3 at 2" (1%)	6100	6.2%
16	Three Cycle Set	24	4	16 #6 bars (1.6%)	#3 at 1.5” (1.3%)	6711	5.6%
17	Llolleo 1985	24	4	16 #6 bars (1.6%)	#3 at 1.5” (1.3%)	7590	5.0%
17b	Cyclic Aftershock	24	4	16 #6 bars (1.6%)	#3 at 1.5” (1.3%)	7590	5.0%
18	Darfield 2010	24	4	16 #6 bars (1.6%)	#3 at 1.5” (1.3%)	7807	4.8%
18b	Cyclic Aftershock	24	4	16 #6 bars (1.6%)	#3 at 1.5” (1.3%)	7807	4.8%

Table 4-2. Bar Buckling Summary for North Reinforcement (Tests 8-12)

Test	Disp. (in) before Buckling North Bar	Ductility before Buckling North Bar	Peak Tensile Strain of North Bar	Inelastic Transverse Steel Before Buckling?
8	No Buckling (7.25")	No Buckling (8.7)	No Buckling (0.051)	
8b	6.64"	8 (+1)	0.043	Yes
9	6.72"	8 (+1)	0.053	No
10	7.40"	No Buckling (8.9)	No Buckling (0.052)	
10b	6.67"	No Buckling (8)	No Buckling (0.048)	
11	8.28"	10	0.059	No
12	8.22"	9.9	0.058	Yes
16	6.65”	8 (+3)	0.056	Yes
17	No Buckling (7.49”)	No Buckling (9)	No Buckling (0.055)	
17b	4.99”	6 (+2)	0.035	Yes
18	No Buckling (7.46”)	No Buckling (9)	No Buckling (0.062)	
18b	No Buckling (4.99”)	No Buckling (6 (+2))	No Buckling (0.036)	

Table 4-3. Bar Buckling Summary for South Reinforcement (Tests 8-12)

Test	Disp. (in) before Buckling South Bar	Ductility before Buckling South Bar	Peak Tensile Strain of South Bar	Inelastic Transverse Steel Before Buckling?
8	No Buckling (-4.42”)	No Buckling (-5.3)	No Buckling (0.032)	
8b	-6.65”	8 (-1)	0.048	Yes
9	-6.70”	8 (-1)	0.051	Yes
10	No Buckling (-2.11”)	No Buckling (-2.5)	No Buckling (0.016)	
10b	-5.01”	6 (-1)	0.038	Yes
11	-5.08”	-6.1	0.033	Yes
12	-6.53”	-7.9	0.044	Yes
16	-6.68”	8 (-1)	0.052	Yes
17	No Buckling (-5.02”)	No Buckling (-6)	No Buckling (0.039)	
17b	-5.00”	6 (-2)	0.036	Yes
18	-6.05”	-7.3	0.047	Yes
18b	Previously Buckled	-	-	-

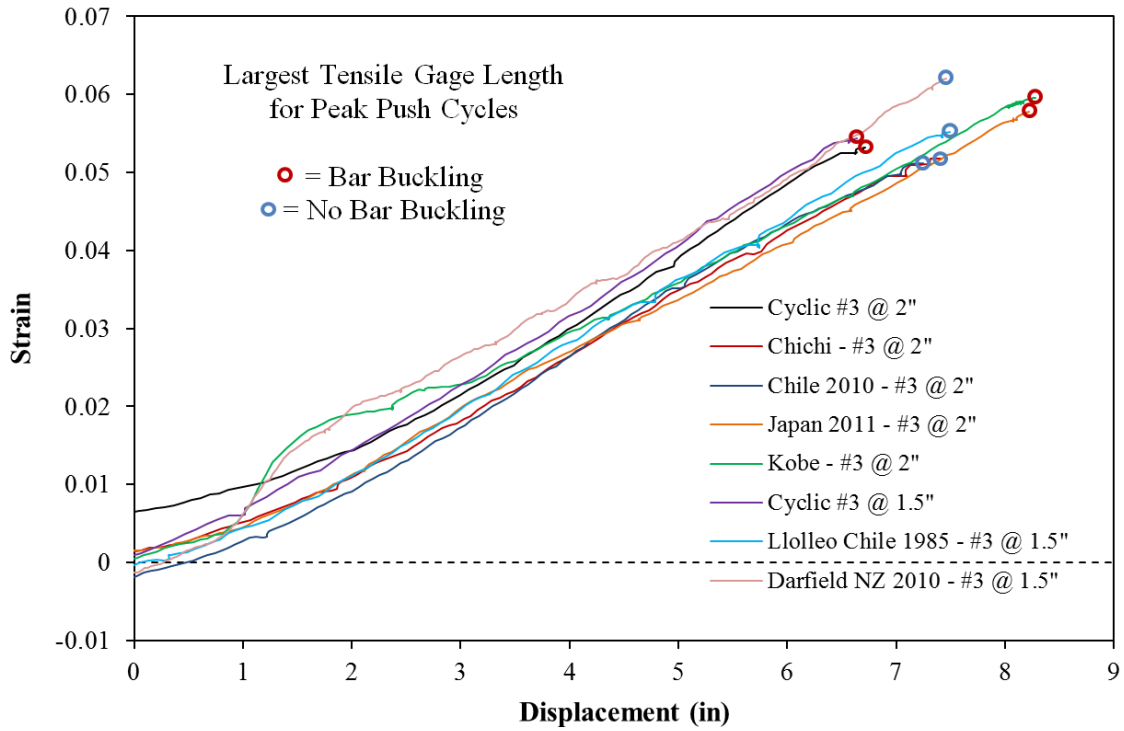

Figure 4-11. Relationship between Tensile Strain and Displacement during Peak Push Cycles of Load History Tests

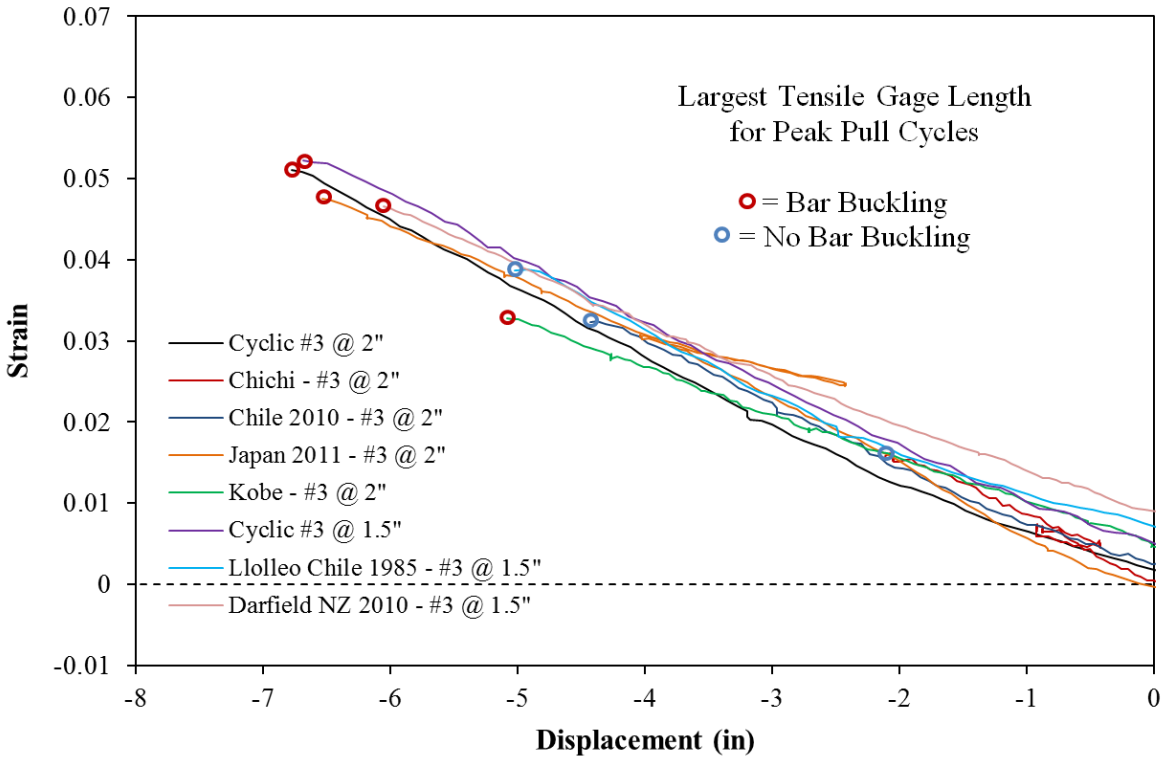

Figure 4-12. Tensile Strain and Displacement for Peak Pull Cycles of Load History Tests

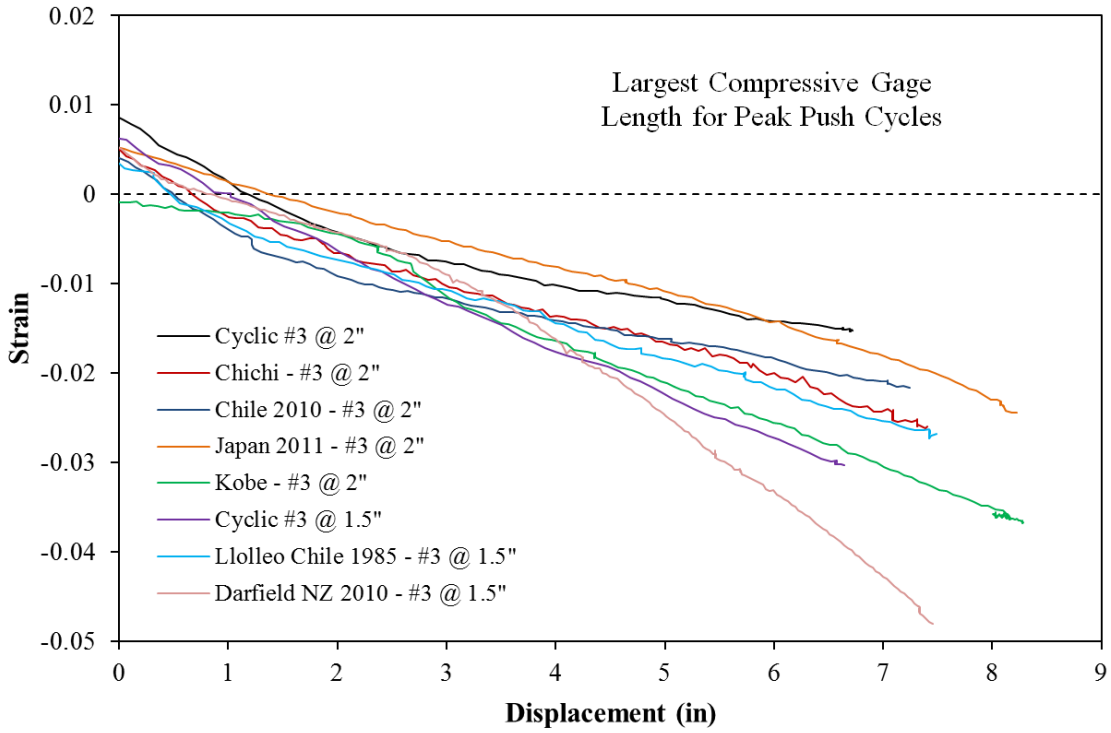

Figure 4-13. Compressive Strain and Displacement during Peak Push Cycles

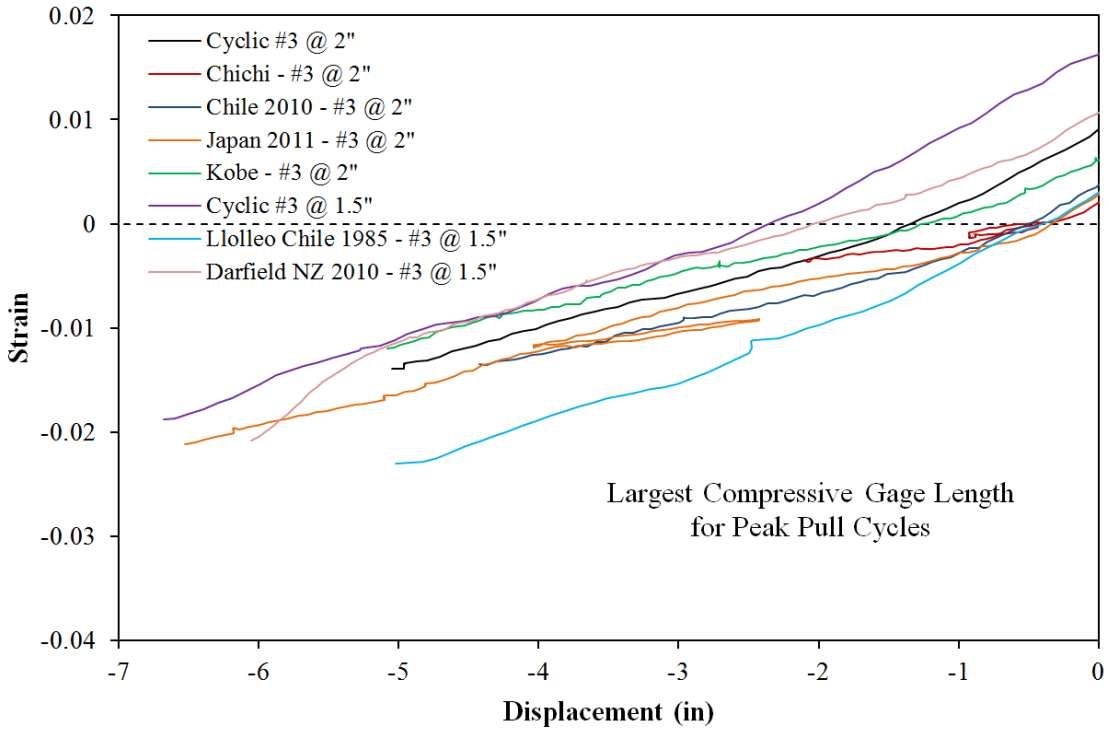

Figure 4-14. Compressive Strain and Displacement during Peak Pull Cycles

4.1.4. Effect of Transverse Steel Detailing

Five specimens with identical geometry, but varying transverse steel detailing were subjected to symmetric three cycle set load histories. The following transverse volumetric steel ratios were investigated: $(4A_{sp}/(D's)) = 0.5\%$ ($6d_{bl}$), 0.7%, 1%, and two separate detailing arrangements for 1.3%. In its current form, the symmetric three cycle set includes large increments between cycles which produced bar buckling in the experimental tests. Columns detailed with volumetric ratios 0.5% and 0.7% buckled reinforcement during displacement ductility six while columns containing 1% and 1.3% transverse steel produced bar buckling during ductility eight. An argument can be made that incremental ductility levels 5, 7, and 9 should be included in symmetric three cycle set load history. The relationship between strain and displacement does not seem to be affected by transverse steel detailing.

A summary of the peak tensile strains and displacements sustained by the North and South extreme fiber bars before they buckled after reversal of load appears in Table 4-5 and Table 4-6 respectively. The North reinforcement which buckled upon reversal from the first push cycle of a respective ductility level had elastic transverse steel restraint due to the fact that the bar buckled during the first compressive cycle of that ductility level. North reinforcement in Tests 15 and 16 buckled during the second and third push cycles of their respective ductility levels with inelastic transverse steel restraint. Since the peak tensile strain does not increase during subsequent cycles at the same ductility level, bar buckling may be attributed to inelastic transverse steel offering less restraint. For all of the transverse steel variable experiments except Test 13, the South extreme fiber bar buckled after reversal from the first pull cycle with previously inelastic transverse steel restraint which resulted due to the high compressive demand during the first push cycle of the respective ductility level.

Table 4-4. Detailing Summary for Transverse Steel Variable Tests

Test	Load History	D (in)	L/D	Long. Steel (ρ_l)	Spiral Detailing (ρ_s)	f'c (psi)	P/f'c*Ag
9	Three Cycle Set	24	4	16 #6 bars (1.6%)	#3 at 2" (1%)	6813	5.5%
13	Three Cycle Set	24	4	16 #6 bars (1.6%)	#4 at 2.75” (1.3%)	6097	6.2%
14	Three Cycle Set	24	4	16 #6 bars (1.6%)	#3 at 4” (0.5%)	6641	5.7%
15	Three Cycle Set	24	4	16 #6 bars (1.6%)	#3 at 2.75” (0.7%)	7232	5.2%
16	Three Cycle Set	24	4	16 #6 bars (1.6%)	#3 at 1.5” (1.3%)	6711	5.6%

Table 4-5. North Reinforcement Bar Buckling Summary for Transverse Steel Variable Tests

Test	Disp. (in) before Buckling North Bar	Ductility before Buckling North Bar	Peak Tensile Strain of North Bar	Inelastic Transverse Steel Before Buckling?
9	6.72"	8 (+1)	0.053	No
13	6.46”	8 (+1)	0.047	No
14	4.80”	6 (+1)	0.035	No
15	5.00”	6 (+2)	0.037	Yes
16	6.65”	8 (+3)	0.056	Yes

Table 4-6. South Reinforcement Bar Buckling Summary for Transverse Steel Variable Tests

Test	Disp. (in) before Buckling South Bar	Ductility before Buckling South Bar	Peak Tensile Strain of South Bar	Inelastic Transverse Steel Before Buckling?
9	-6.78”	8 (-1)	0.051	Yes
13	-6.50”	8 (-3)	0.047	No
14	-4.80”	6 (-1)	0.035	Yes
15	-5.00”	6 (-1)	0.038	Yes
16	-6.68”	8 (-1)	0.052	Yes

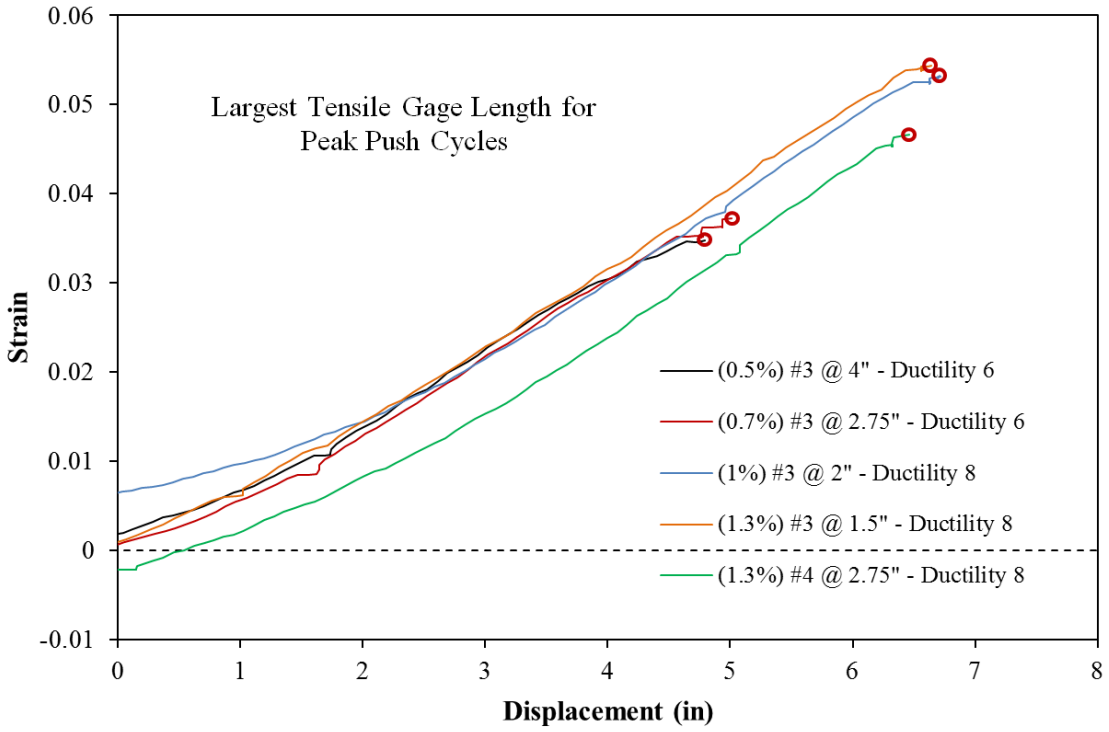

Figure 4-15. Relationship between Tensile Strain and Displacement during Peak Push Cycles of Transverse Steel Variable Tests

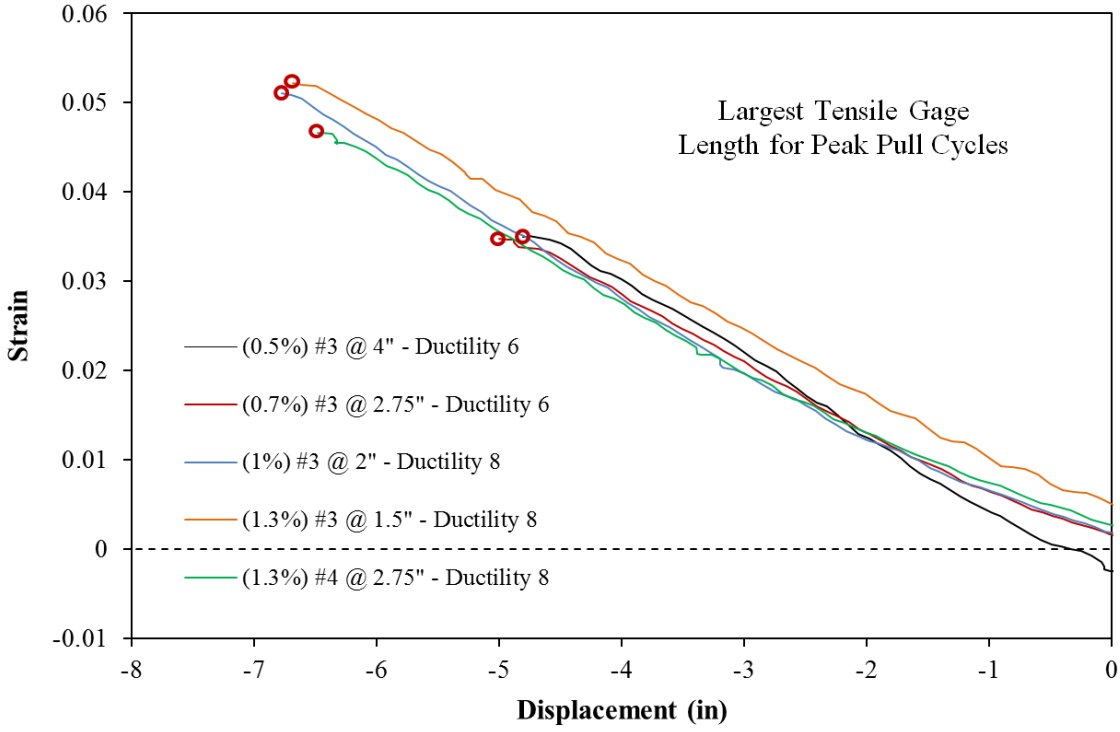

Figure 4-16. Tensile Strain and Displacement during Peak Pull Cycles

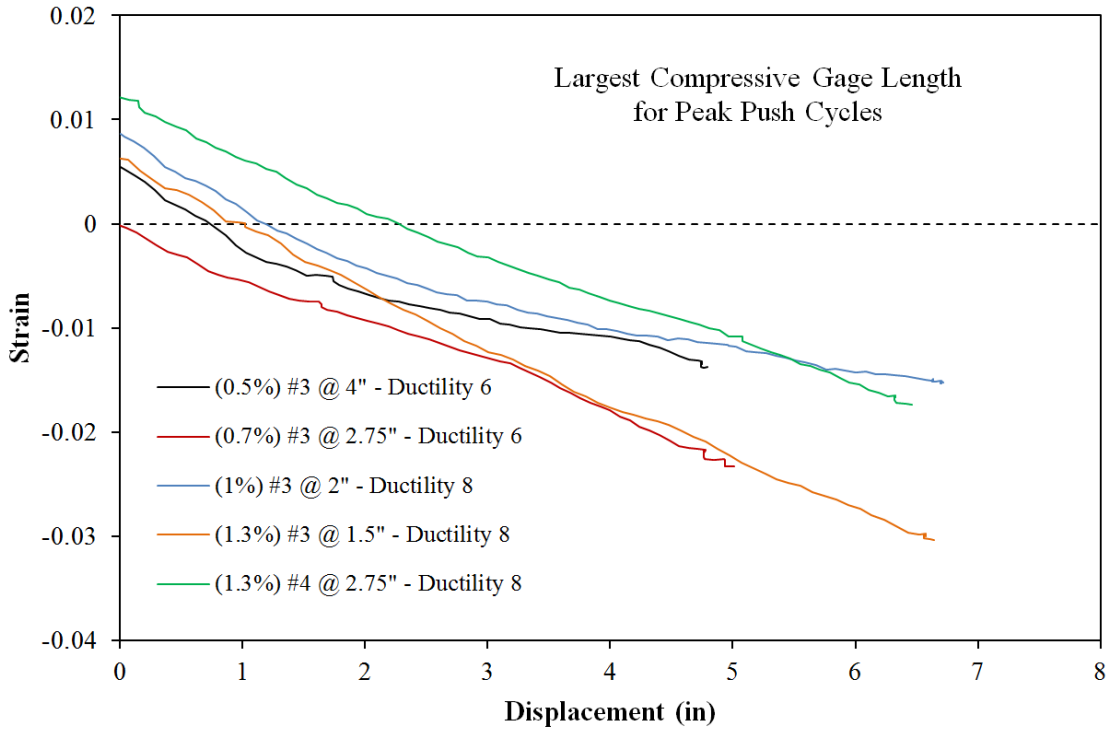

Figure 4-17. Compressive Strain and Displacement during Peak Push Cycles of Transverse Steel Variable Tests

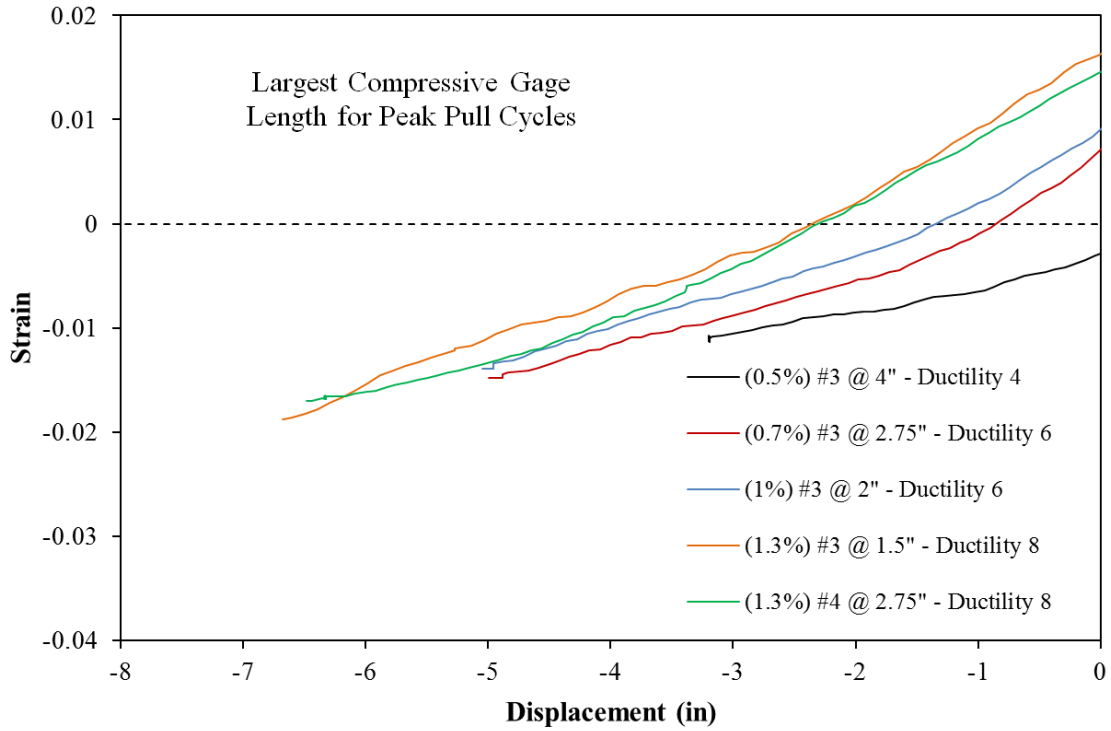

Figure 4-18. Compressive Strain and Displacement during Peak Pull Cycles

4.2. Relationship between Strain and Displacement for Tests 8-18

Accurate limit state target displacements are required to appropriately design a structural component for a specific level of damage and seismic hazard. In a design scenario, this is accomplished utilizing moment curvature analysis and an equivalent distribution of curvature. Moment curvature analysis is an accepted design tool which can be used to determine the base-section curvature at each of the performance limit states. The target displacement is calculated using an equivalent distribution of curvature for the bridge column such as the plastic hinge method. While there are many versions of the plastic hinge method, such as the one shown in Figure 4-19 from (Priestley, Calvi, and Kowalsky (2007)), they all operate by integrating an equivalent distribution of curvature with the moment area method. The elastic and plastic curvature distributions are separated into simplified shapes to facilitate design. The elastic flexural displacement is determined using a triangular curvature distribution. The plastic flexural displacement is obtained using a rectangular curvature distribution with a constant height called the plastic hinge length. The width of the rectangle is equal to the plastic curvature at the base section. To account for the additional displacement produced from the fixed-end rotation at the footing-column interface due to strain penetration of longitudinal steel, the curvature distribution extends into the footing by a depth termed the strain penetration length.

The constant plastic hinge length is not physical parameter; it is simply a numerical convenience to obtain the correct top column displacement. The plastic hinge length expression is intended only for the ultimate displacement level; therefore, its use for varying levels of response is inconsistent with the derivation of the method. The Optotrak instrumentation system allows for a closer inspection of the accuracy of moment curvature prediction. The monotonic moment curvature analysis was conducted in a script developed at NCSU called Cumbia (2007). The program utilizes the Mander (1988) confined and unconfined concrete stress strain curves and the King (1986) steel model for longitudinal reinforcement. Top column displacements are obtained using the plastic hinge method and shear displacement models presented in (Priestley, Calvi, and Kowalsky (2007)).

Monotonic moment curvature analysis is an accepted design tool that provides an accurate backbone curve prediction for cyclic response, as shown in Figure 4-20 for the symmetric three cycle set load history of Test 16. This however, does not insure an accurate local response prediction for the relationship between strain and displacement. Similar material properties utilized in Tests 8-18 allow for a direct comparison between the measured and predicted strain values. The moment curvature predictions for the relationship between strain and displacement appear in Figure 4-21, Figure 4-22, Figure 4-23, and Figure 4-24 for the largest cycles of Tests 8-18 prior to bar buckling. Load history and transverse steel detailing do not appear to have a large influence on the relationship between strain and displacement during the peak cycles. Tensile strains are over predicted by the moment curvature analysis at an increases rate at higher displacements levels. The general trend in the relationship between compressive strain and displacement is captured well even though measured strains are higher for many of the tests. The use of a constant plastic hinge length does not account for the spread of plasticity in reinforced concrete bridge columns which results due to the effects of tension shift from the inclined crack patterns.

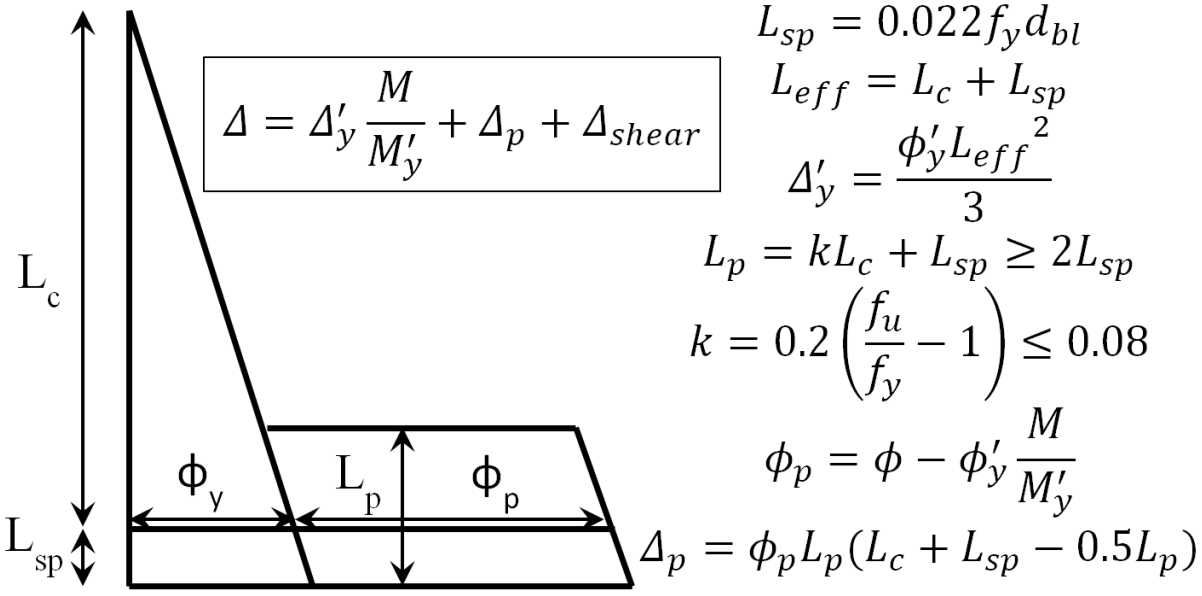

Figure 4-19. Plastic Hinge Method for Member Deformations (Priestley, Calvi, and Kowalsky (2007))

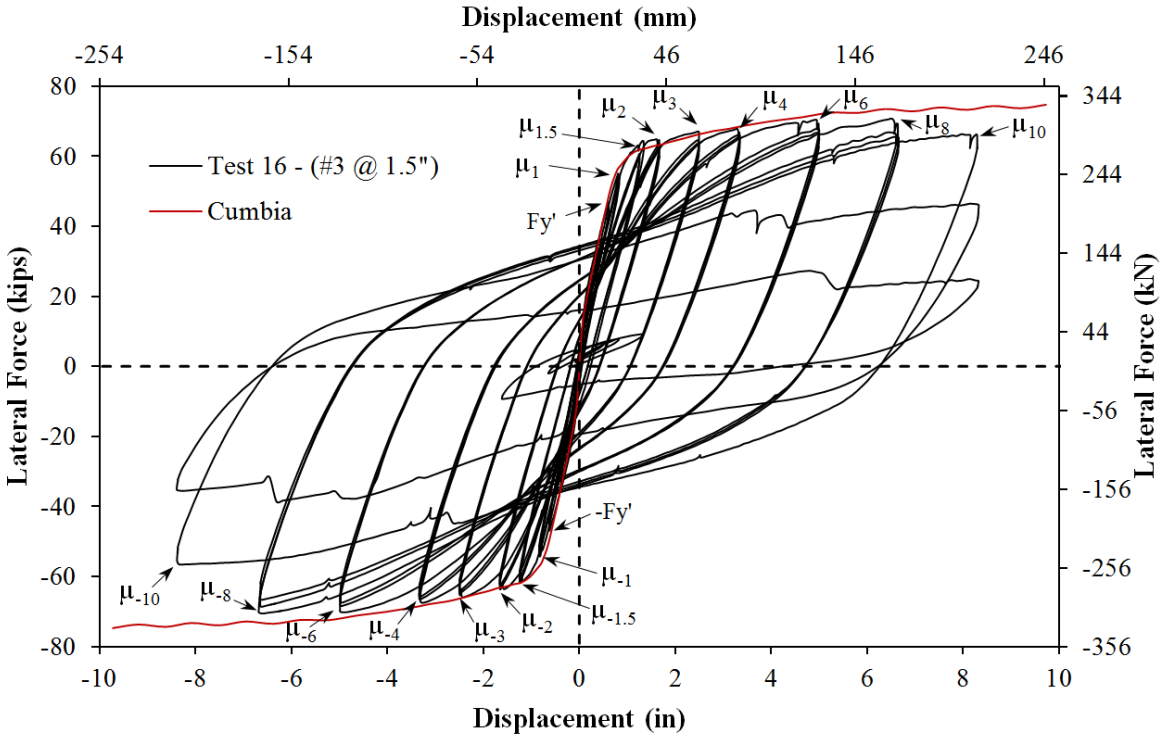

Figure 4-20. Hysteretic Response and Cumbia Moment Curvature Prediction for Test 16

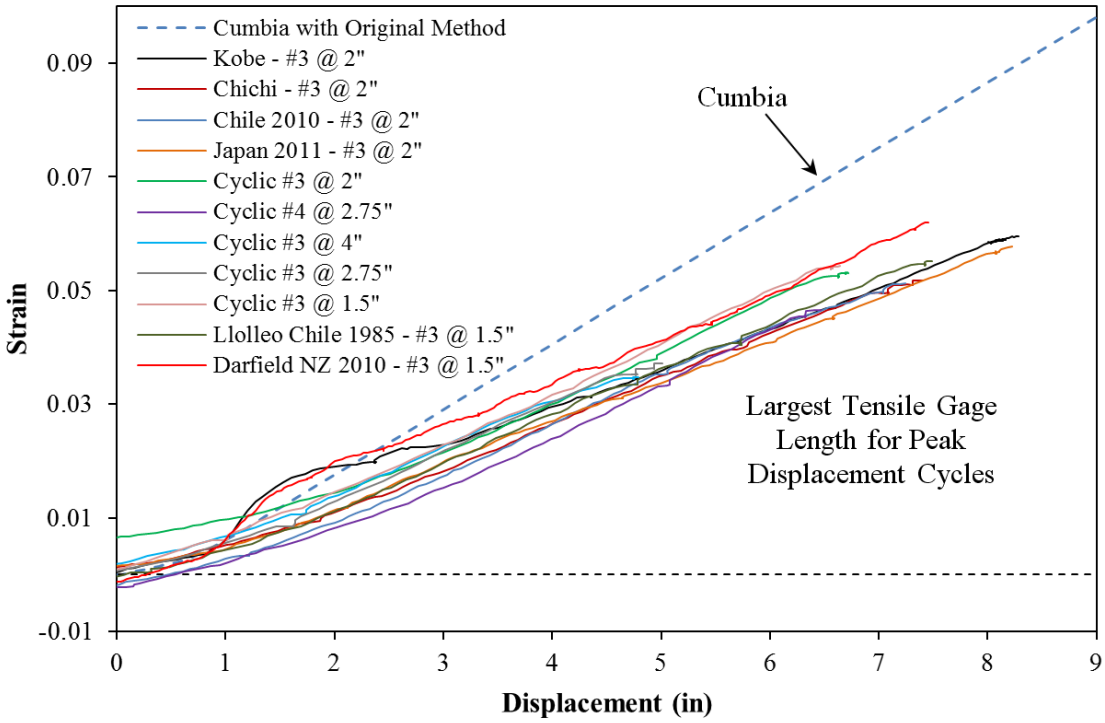

Figure 4-21. Cumbia Tensile Strain and Disp. Prediction for Tests 8-18 (Push Cycles)

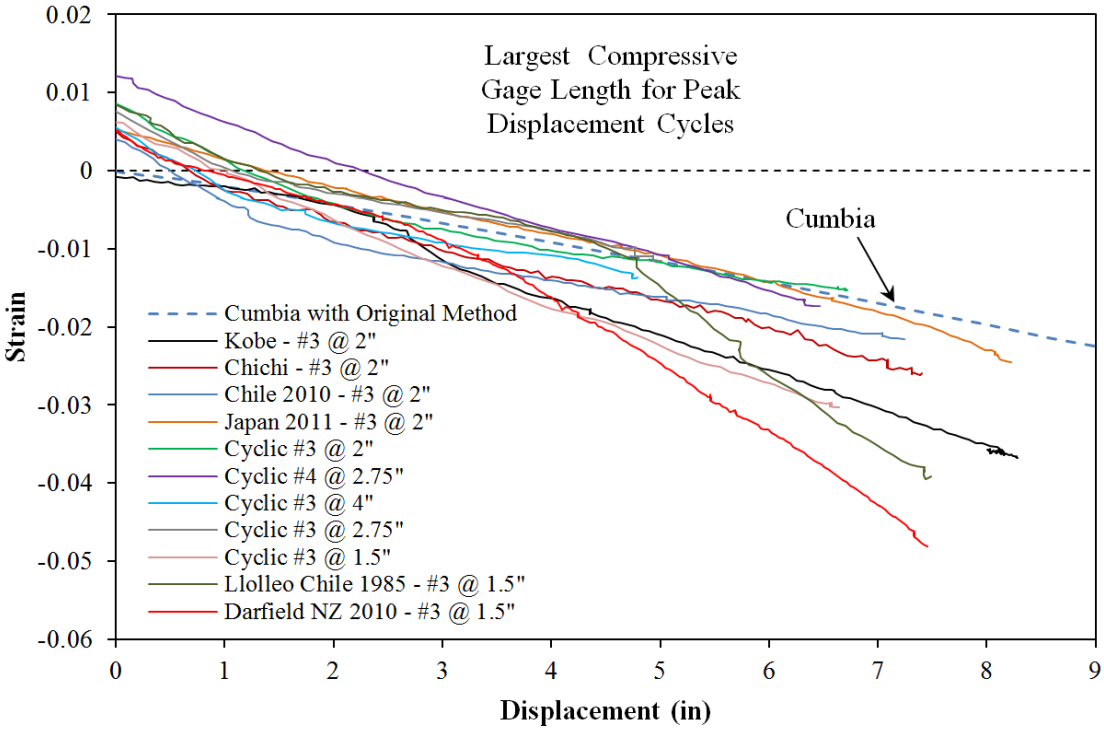

Figure 4-22. Cumbia Compressive Strain and Disp. Prediction for Tests 8-18 (Push Cycles)

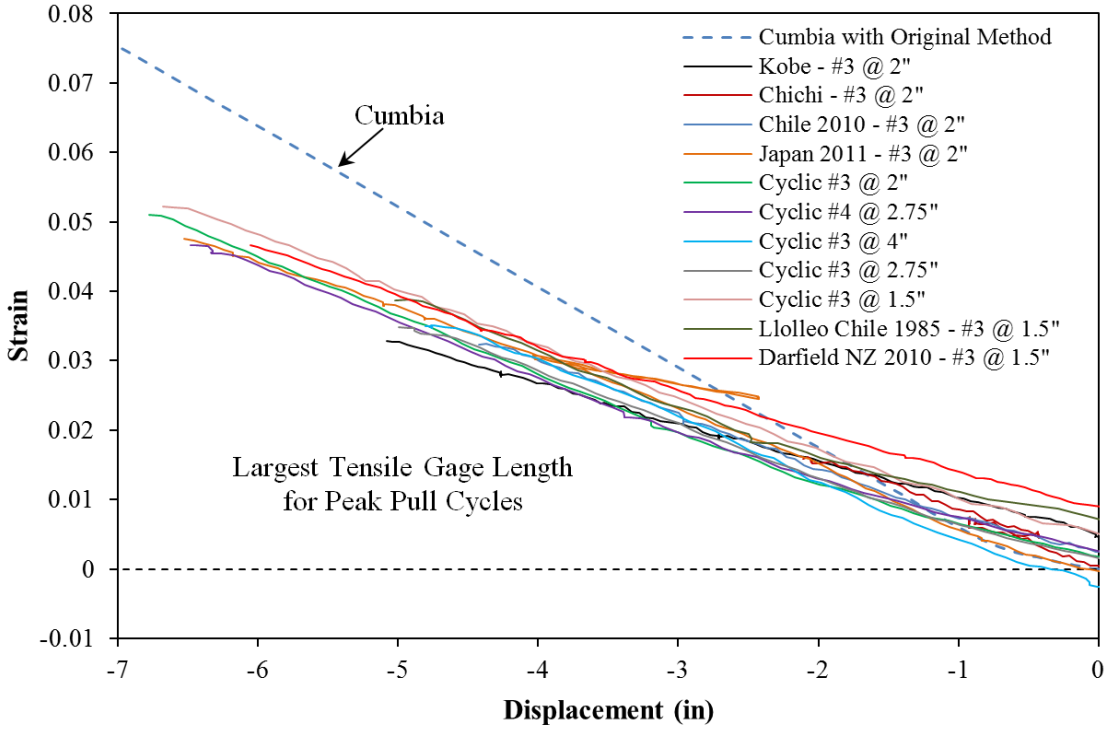

Figure 4-23. Cumbia Tensile Strain and Disp. Prediction for Tests 8-18 (Pull Cycles)

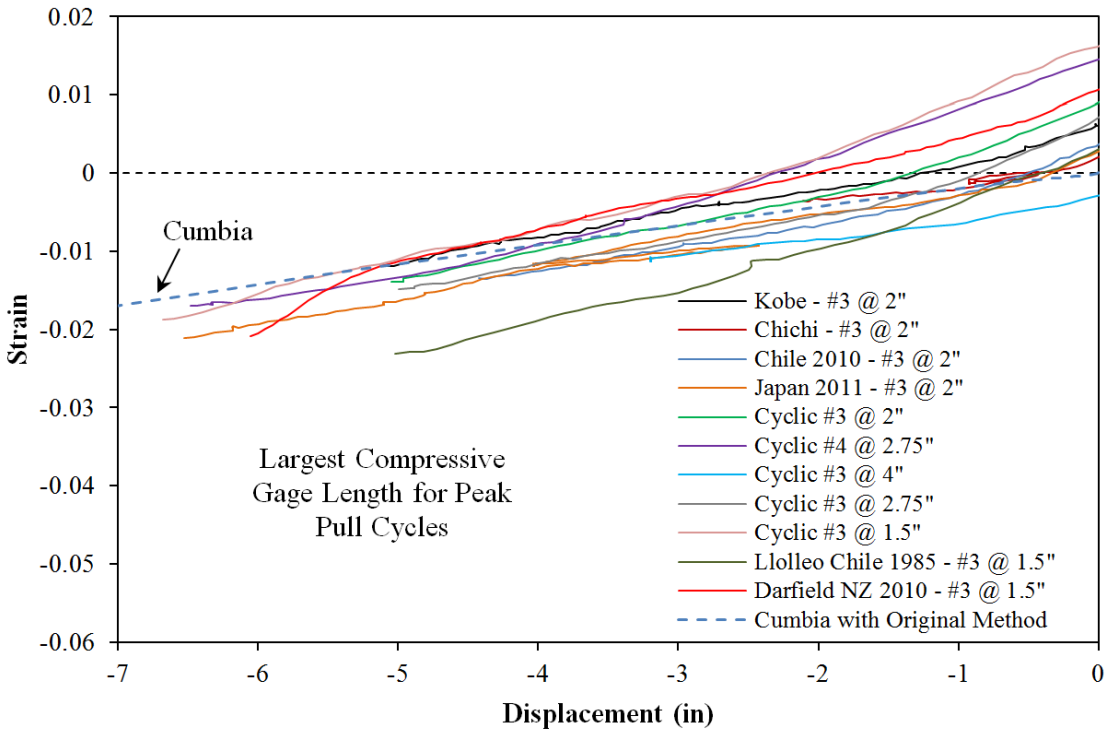

Figure 4-24. Cumbia Compressive Strain and Disp. Prediction for Tests 8-18 (Pull Cycles)

4.3. Spread of Plasticity in Reinforced Concrete Bridge Columns

4.3.1. Case Study on Deformation Components – Three Cycle Set Test with #3 Spiral at 1.5" on Center

The Optotrak instrumentation system allows a closer look at column flexure and strain penetration deformation components. To describe the process and capabilities of the system, sample test results related to the spread of plasticity in a symmetric three cycle set load history are presented. The displacement history along with data points which mark cycles where cover crushing and bar fracture occurred and cycles which produced visible bar buckling after reversal of loading appear in Figure 4-25. The measured compressive and tensile strains for South and North extreme fiber bars during push cycles appear in Figure 4-27. This figure shows strain profiles for each extreme fiber bar to illustrate the effects of tension shift. The reinforcing bars contain thirty-two separate approximate 1.5" gage lengths which appear as a single data point at its center linked to adjacent gage lengths with straight lines. Due to the effects of tension shift, compressive strains are concentrated near the column base and tensile strains are fanned out to a greater height following inclined crack distribution (Park and Paulay (1975)). Near the footing cracks remain effectively horizontal, but above this base section the flexural shear cracks are inclined as shown in Figure 4-30. The tensile strains at the beginning of an inclined flexural shear crack do not coincide with the perceived moment demand at that location based on its height above the footing and the applied lateral load.

The measured strains of six reinforcing bars are plotted along the cross section to obtain curvatures in Figure 4-28. The curvature was taken as the slope of the least squared error line. Curvature profiles obtained from thirty-two horizontal cross sections at different heights above the footing appear in Figure 4-29. The measured linear plastic curvature distribution agrees with observations presented in (Hines, Restrepo, and Seible (2004)). The dashed lines for each curvature distribution represent a least squared error linear fit to the plastic portion of the measured curvatures. The extent of plastic curvatures above the footing may be calculated by determining where the linear plastic curvature distribution intersects the triangular yield curvature distribution, shown as a grey dashed line.

The target marker on each bar placed closest to the footing-column interface can be used to measure the effects of strain penetration of longitudinal reinforcement into the footing. Development of fully anchored column longitudinal bars into the footing leads to bar slips along the partially anchored region of the bar near the footing-column interface, as summarized by (Zhao and Sritharan (2007)). This slip is not a pull-out of the entire bar embedment length resulting from poor bond between the concrete and reinforcing bar. If the measured slips of the target markers are plotted along the cross section, the fixed-end rotation attributable to strain penetration may be calculated as the slope of a least squared error line, Figure 4-31.

The hysteretic response in Figure 4-33 was obtained from a string potentiometer at the center of load which measured the deflection at the center of the applied lateral load. The total deformation is the addition of the column flexure, column shear, and strain penetration components. The flexural displacement may be determined by integrating the measured curvature distribution using the moment area method, shown in Figure 4-32, and adding the strain penetration deformation component. The curvatures above the instrumented region are assumed to follow the triangular yield curvature distribution. The strain penetration deformation component is equal to the measured fixed-end rotation multiplied by the clear column height. The integrated displacements from the Optotrak system are compared to the measured string potentiometer displacements in Figure 4-33. The good agreement suggests that the shear deformation component is small relative to the total deformation.

The Optotrak instrumentation technique may also be used to calculate the shear deformation component via diagonal measurements of shear panels, but this effort is not warranted given the accuracy of only considering flexural deformations.

The measured compression strains in the South reinforcing bar, see Figure 4-27, are larger above the base section where several layers of transverse steel entered the inelastic range as shown in Figure 4-35. The spiral layer closest to the footing-column interface remained elastic due to the additional confinement provided by the footing. Three layers of transverse steel entered the inelastic range during displacement ductility six, but bar buckling did not occur until reversal from tensile strains sustained during the first pull cycle of ductility eight. The measured compressive strains at the toe region of the fanned crack pattern begin to rapidly increase once one or more spiral layers have entered the inelastic range. The outward buckled region of the South extreme fiber bar occurred over the previously inelastic transverse steel layers, see Figure 4-35.

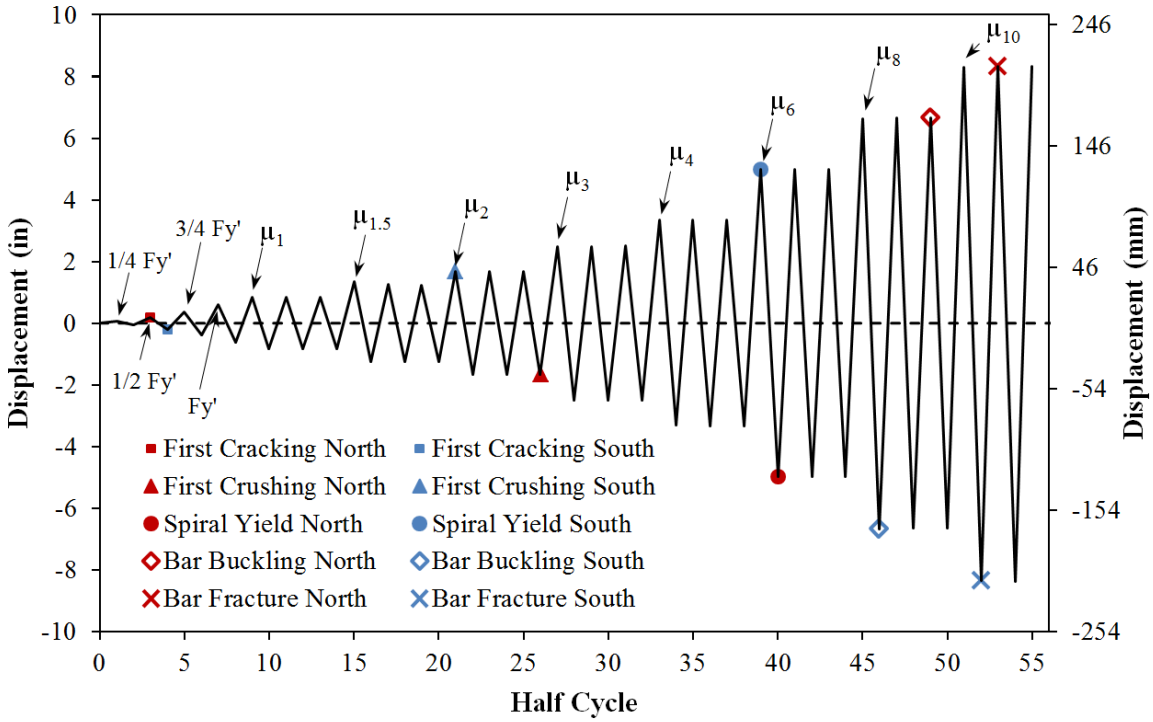

Figure 4-25. Symmetric Three Cycle Set Load History for Test 16 with a #3 Spiral at 1.5”

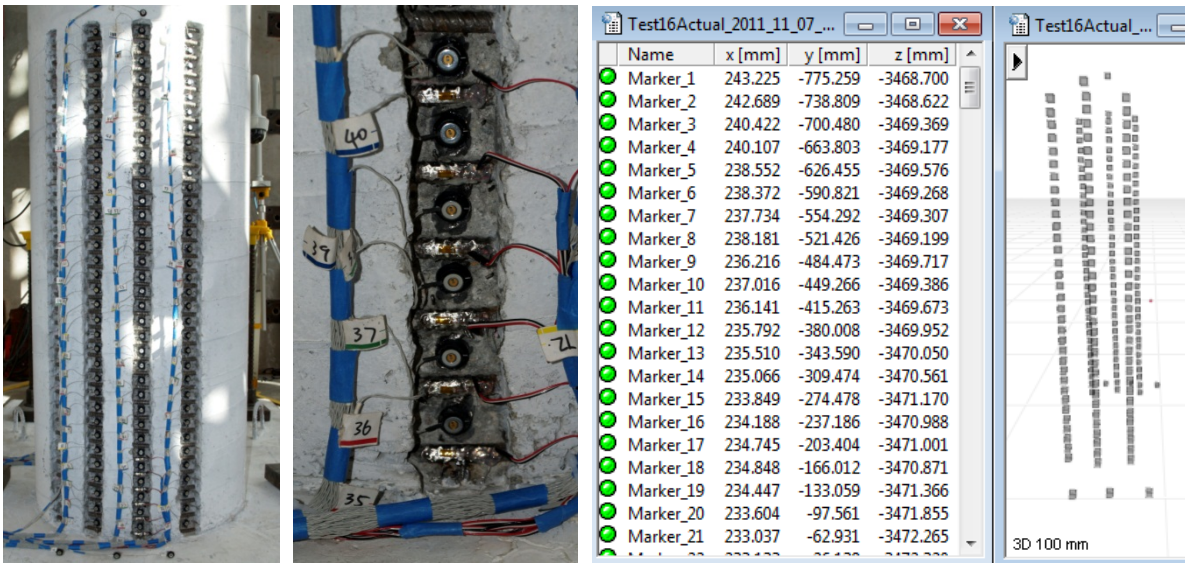

Figure 4-26. Dual Optotrak Position Monitoring System with Direct Application of Target Markers to Longitudinal Reinforcement for Test 16

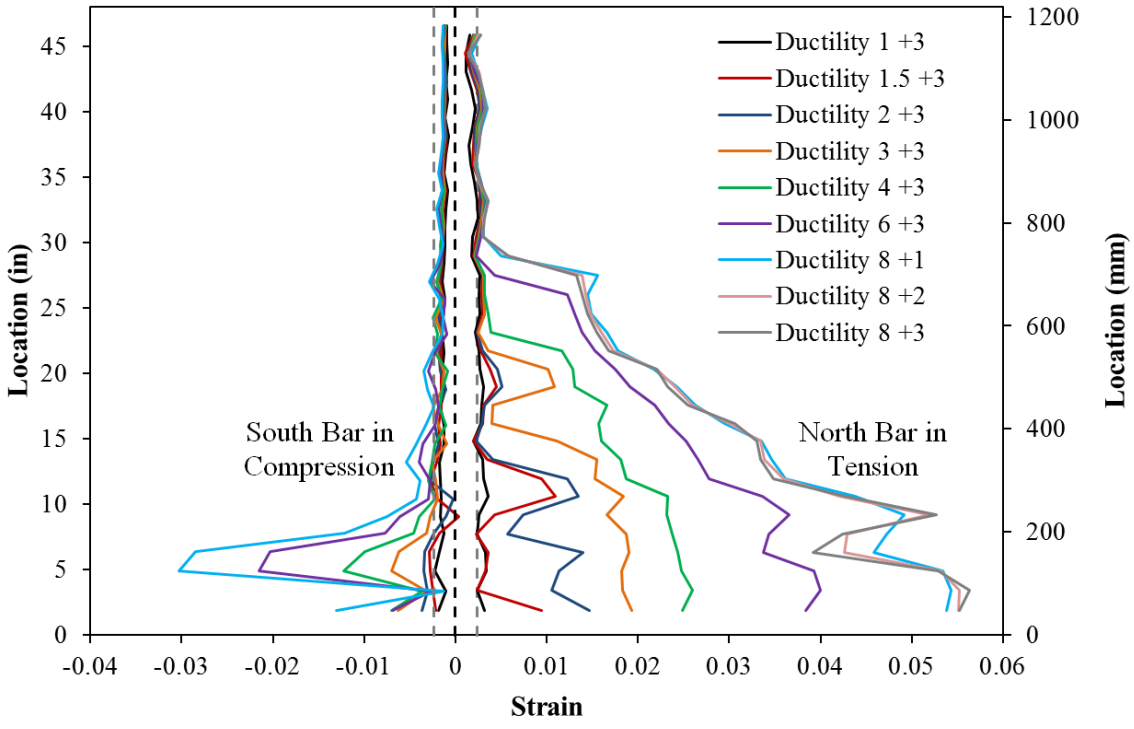

Figure 4-27. Vertical Strain Profiles for Both Extreme Fiber Bars during Push Cycles

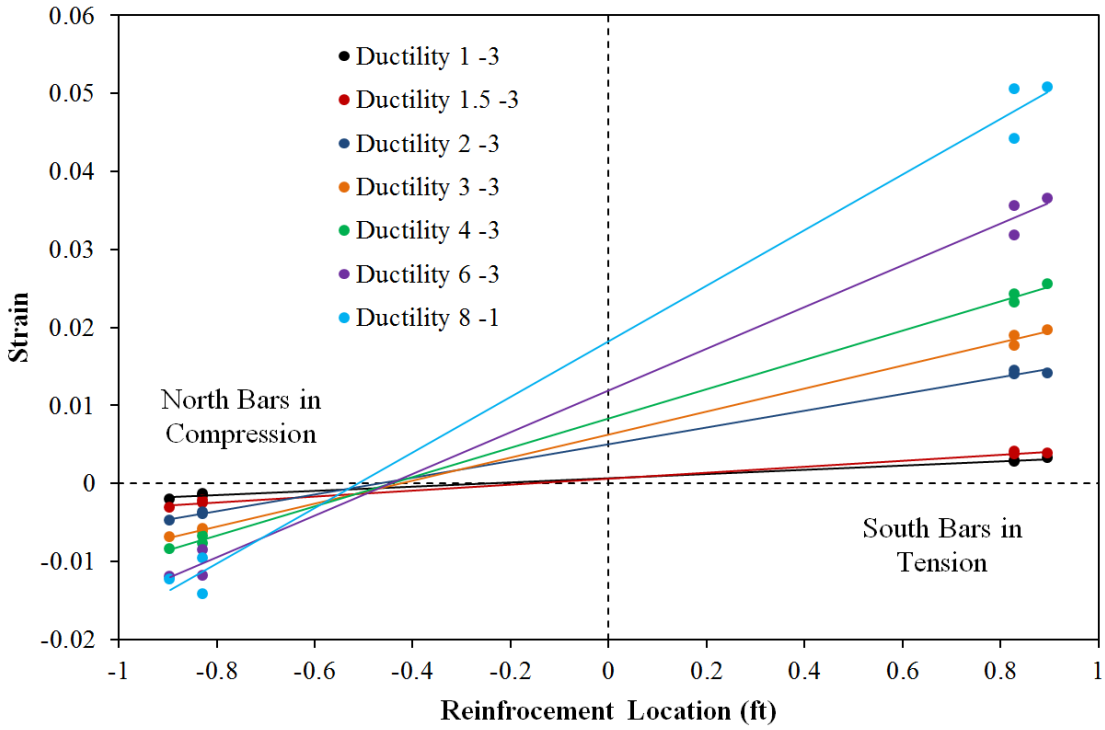

Figure 4-28. Cross Section Curvature from All Six Instrumented Bars

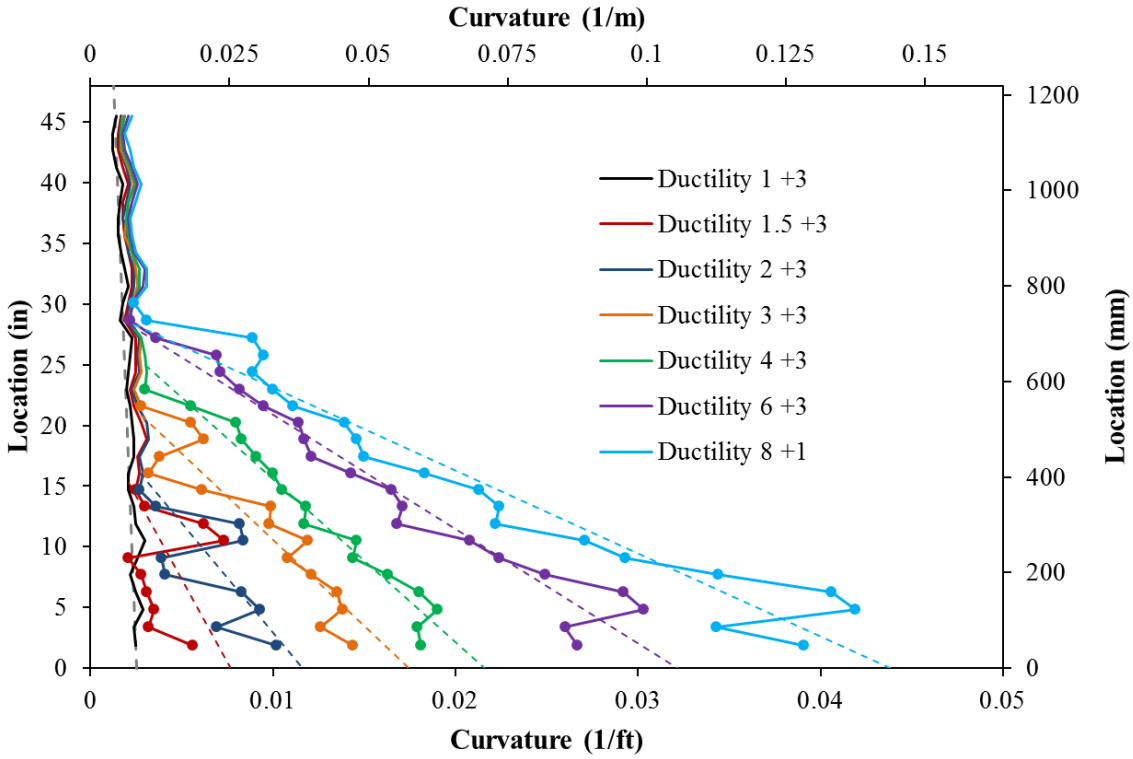

Figure 4-29. Vertical Curvature Profiles for Push Cycles of Test 16 (Linear Least Squared Error Plastic Curvature Lines)

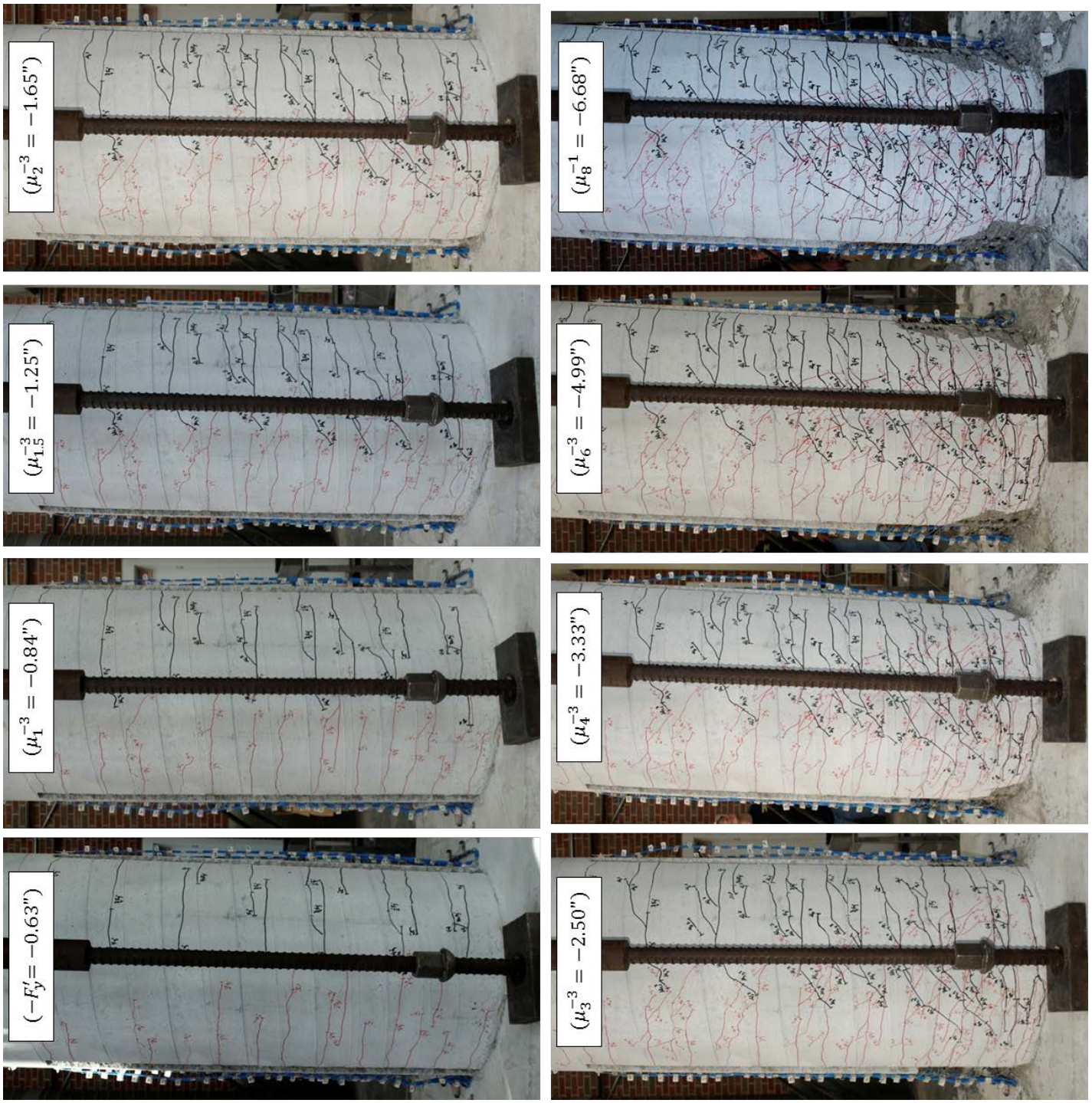

Figure 4-30. Crack Progression on the Back Side of the Specimen (North Side Tension Cracks during Push Cycles Appear as Black Lines and South Side Tension Cracks Appear as Red Lines)

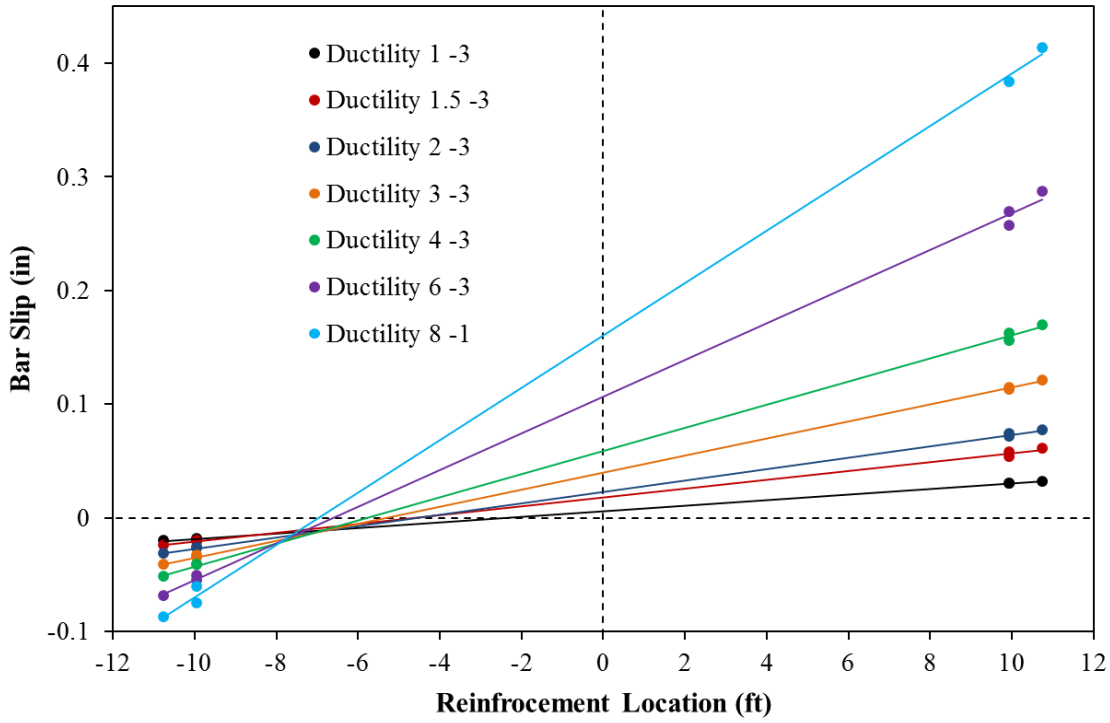

Figure 4-31. Test 16 – Base Section Rotation due to Strain Penetration during Pull Cycles

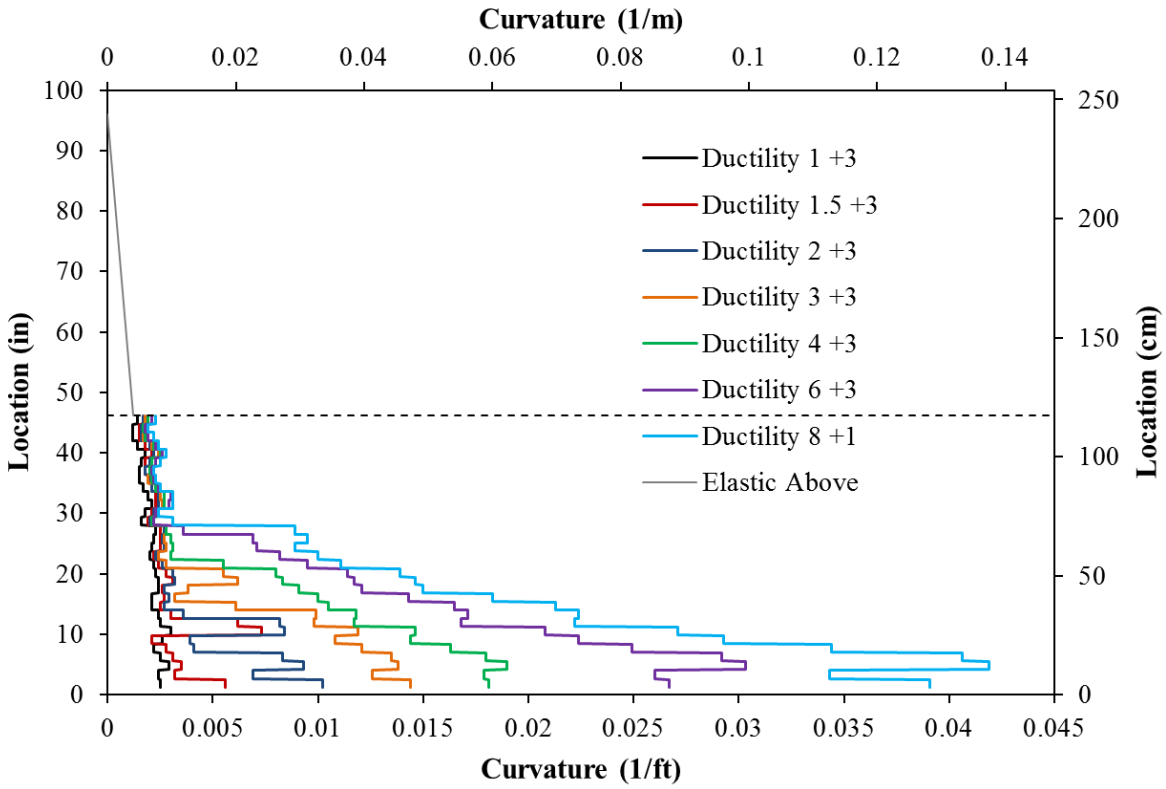

Figure 4-32. Column Curvature Profiles Used to Determine the Optotrak Integrated Flexural Displacement

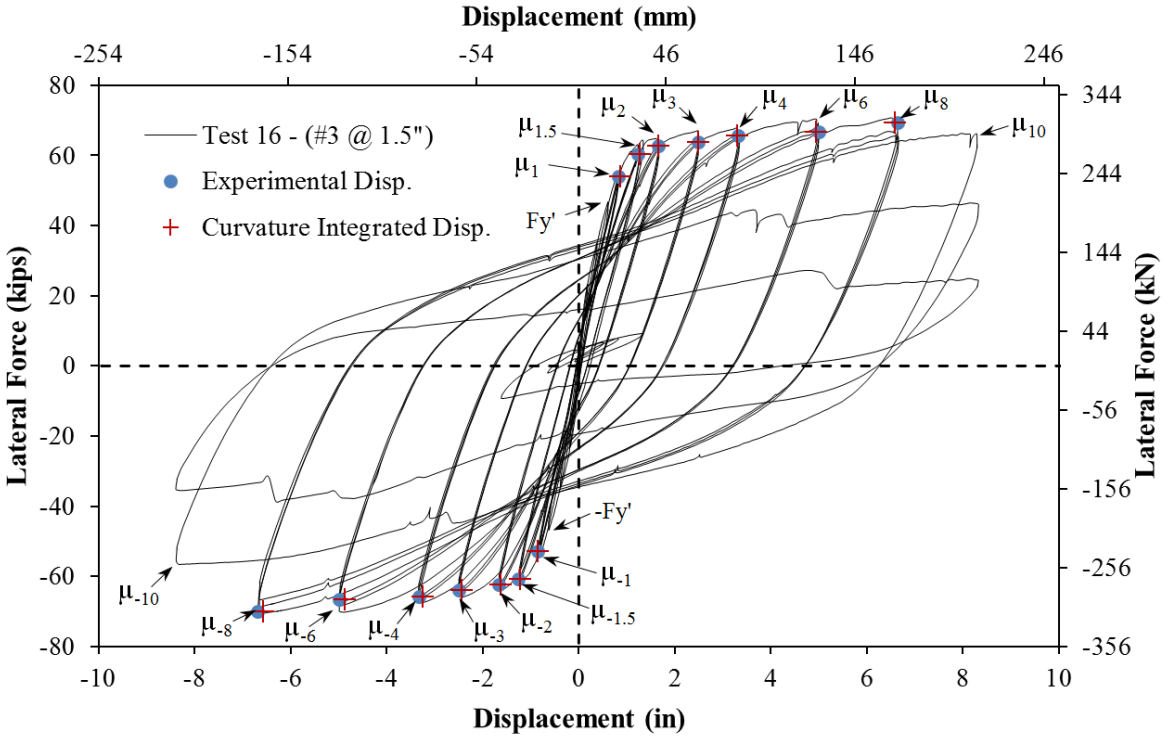

Figure 4-33. Test 16 – Comparison of Experimentally Measured and Optotrak Integrated Displacements

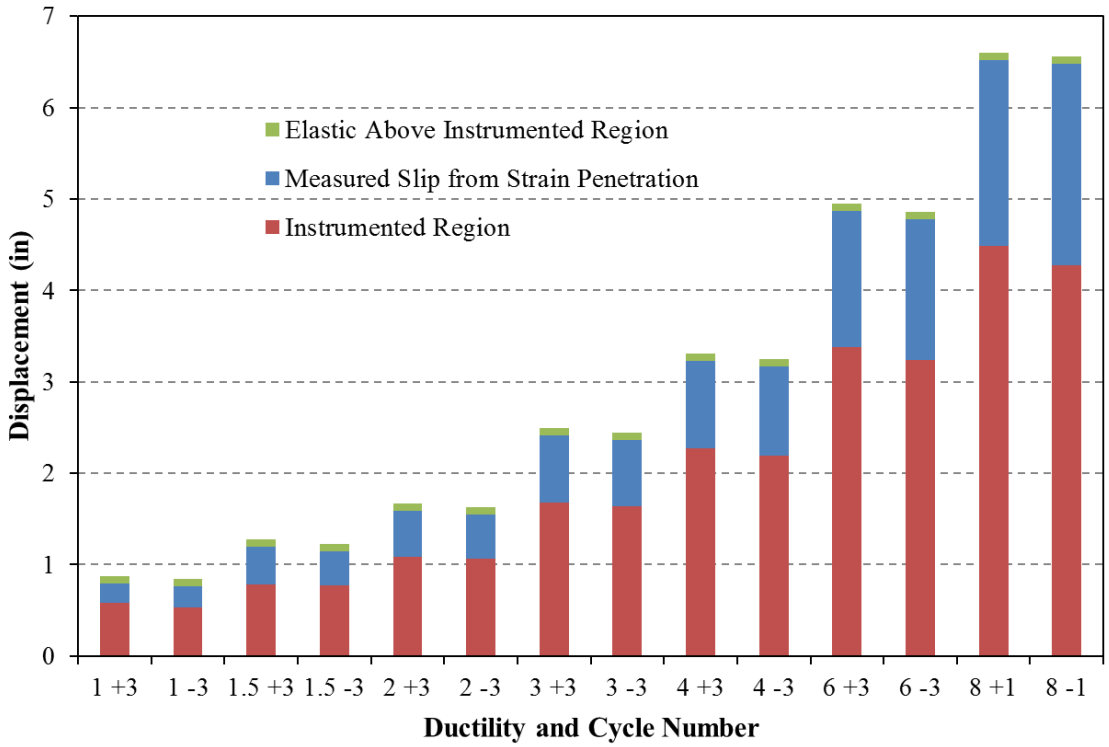

Figure 4-34. Components of Deformation Measured from the Optotrak System

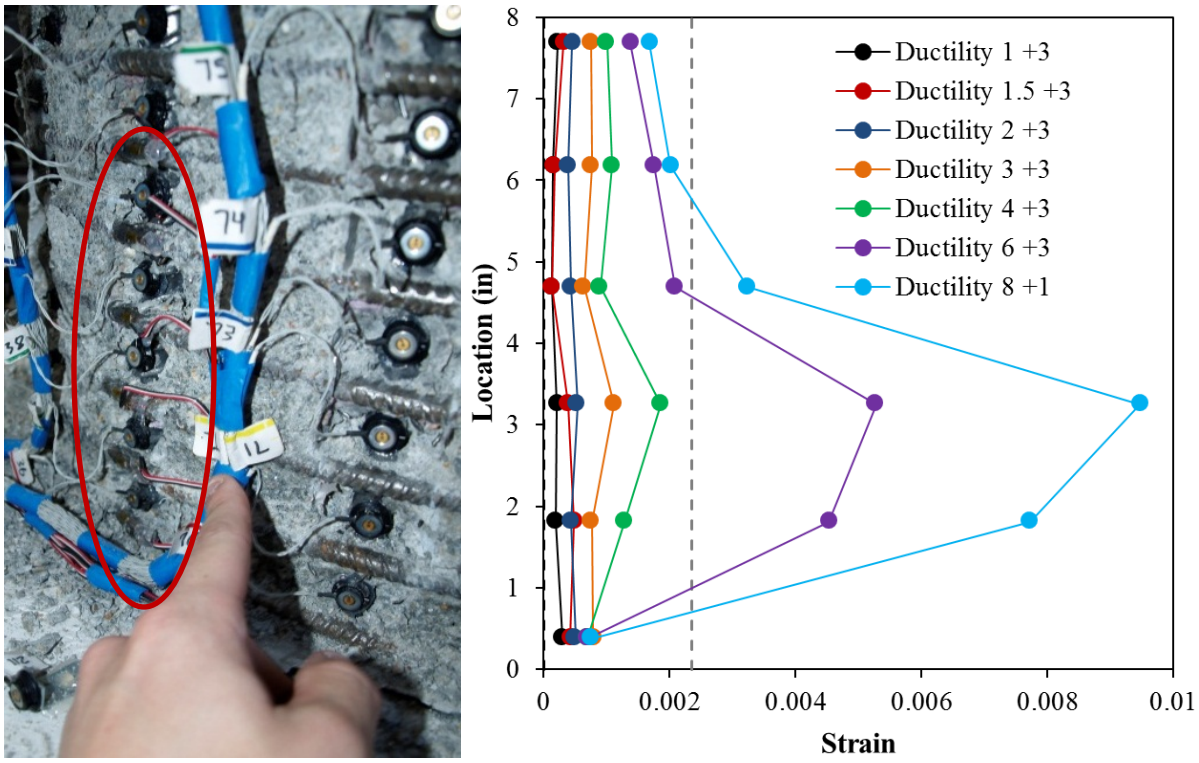

Figure 4-35. (Right) Extreme Fiber South Buckled Bar and (Left) Spiral Strains on South Side of the Specimen in Compression

4.3.2. Measured Spread of Plasticity for Tests 8-18

Plastic curvature profiles have a linear distribution which intersects the yield curvature profile at a height above the footing termed the extent of plasticity. This process is shown visually in the curvature profiles for a symmetric three cycle set load history with a #4 ASTM A706 spiral at 2.75" on center in Figure 4-36. For this test, the transverse steel remained elastic prior to bar buckling, and the measured curvatures closely follow a linear distribution. Since compression strains are concentrated at the location of inelastic transverse steel restraint, some diversion from the linear relationship was observed during high ductility cycles of other tests. The measured extent of plasticity vs. base curvature ductility appears in Figure 4-37 and Figure 4-38. The spread of plasticity for column tests with varying geometry and predictive equations for the extent of plasticity appear in (Hines, Restrepo, and Seible (2004)). The column variables, for Tests 8-18 presented in this report, include load history and transverse steel detailing. The bi-linear relationship presented is expected to change for future tests which focus on axial load ratio, aspect ratio, and longitudinal steel content. The relationship takes a bi-linear shape due to the formation of the inclined crack pattern which influences the reinforcement strains. All of the data points represent peak excursions along the backbone curve of cyclic response in their respective direction of loading.

The measured base rotation attributable to strain penetration is plotted against the base curvature ductility in Figure 4-39. Equivalent strain penetration lengths may be determined by dividing the measured fixed-end rotations by the base curvatures as shown in Figure 4-40 and Figure 4-41. The top column displacement attributable to strain penetration is equal to the base curvature multiplied by the equivalent strain penetration length multiplied by the column clear height. A constant equivalent

strain penetration length appears suitable for the range of curvature ductility levels presented in Figure 4-41. While this seems convenient for design, the relationship is expected to change in future tests focusing on longitudinal steel content.

The spread of plasticity is not largely affected by load history or transverse steel detailing. It is important to note that the data points were taken from the backbone curve of cyclic response and represented peak cycles in their respective direction of loading. Vertical curvature profiles for cycles to lower ductility levels are influenced by previous excursions to higher displacement levels. Curvature profiles measured during the cyclic aftershock load history conducted after the Chile 2010 load history of Test 8 appear in Figure 4-42. All of the profiles maintain a similar shape set in place during the peak displacement cycle of the Chile 2010 load history to displacement ductility 8.7. For these cycles the extent of plasticity is not expected to match up with the relationships presented in Figure 4-38.

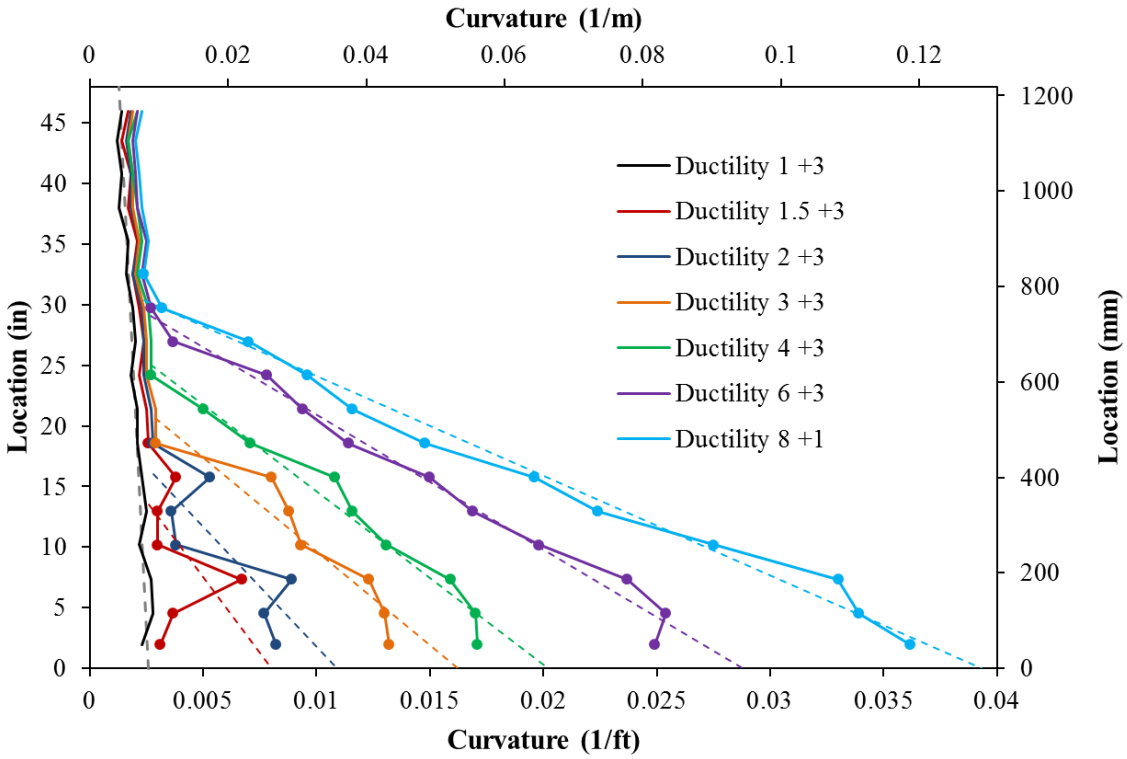

Figure 4-36. Vertical Curvature Profiles for Test 13 with Elastic Transverse Steel (The extent of plasticity is equal to the intersection of the linear plastic curvature least squared error line with the yield curvature distribution shown as a grey dashed line.)

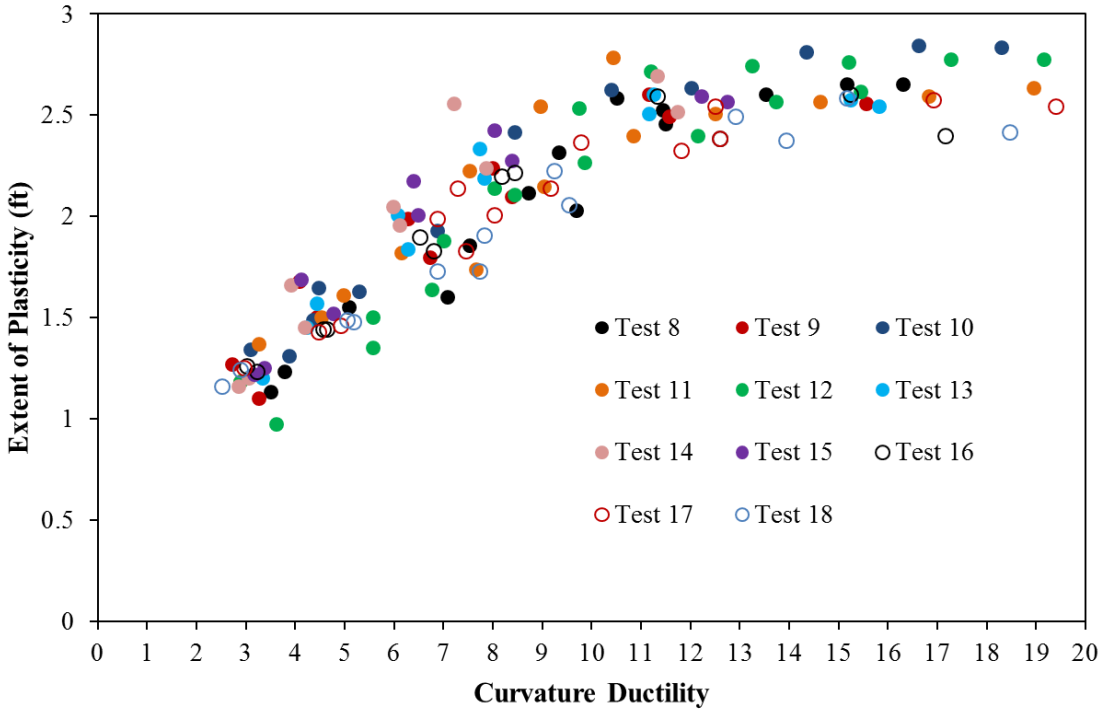

Figure 4-37. Measured Spread of Plasticity above the Footing-Column Interface (Data Points Range from Displacement Ductility 1.5 to Peak Cycle Before Bar Buckling for Tests 8-18)

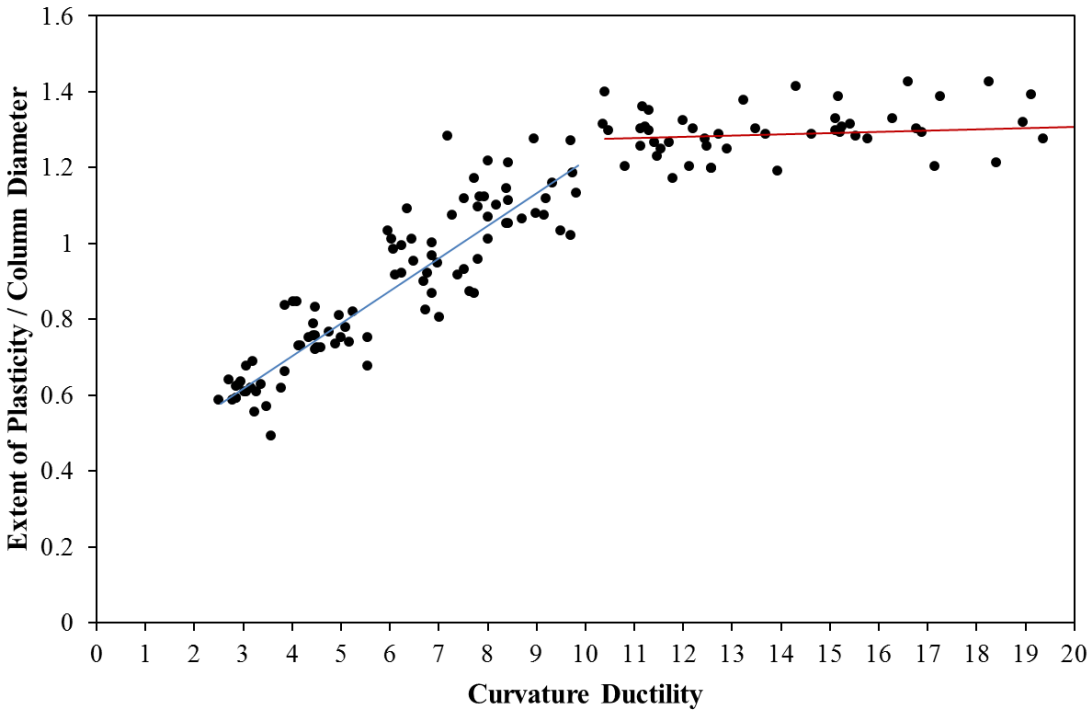

Figure 4-38. Bi-linear Relationship Depicting the Spread of Plasticity in Tests 8-18

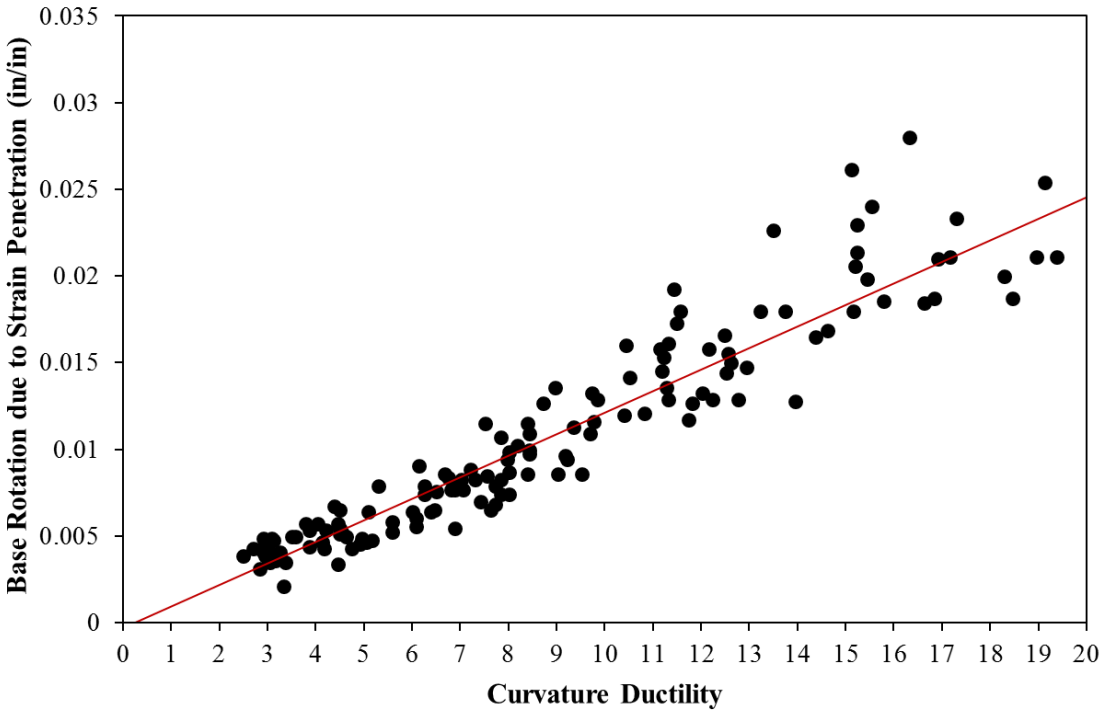

Figure 4-39. Measured Base Rotation due to Strain Penetration

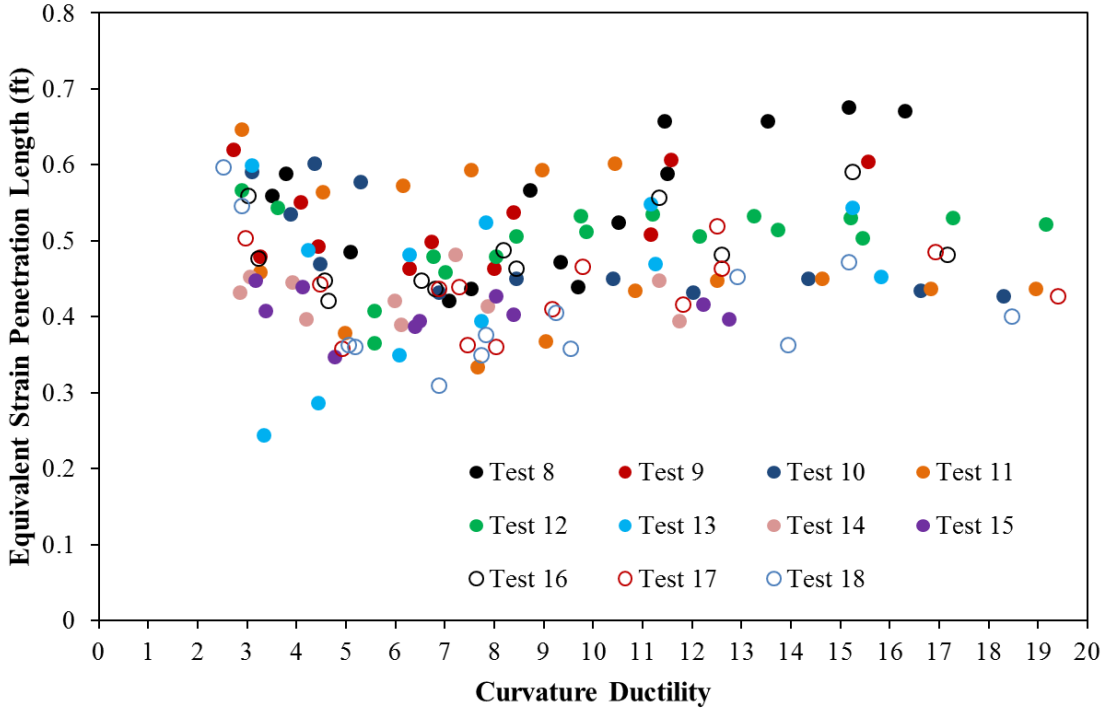

Figure 4-40. Equivalent Strain Penetration Length (Equivalent Lsp = Fixed End Rotation / Base Curvature)

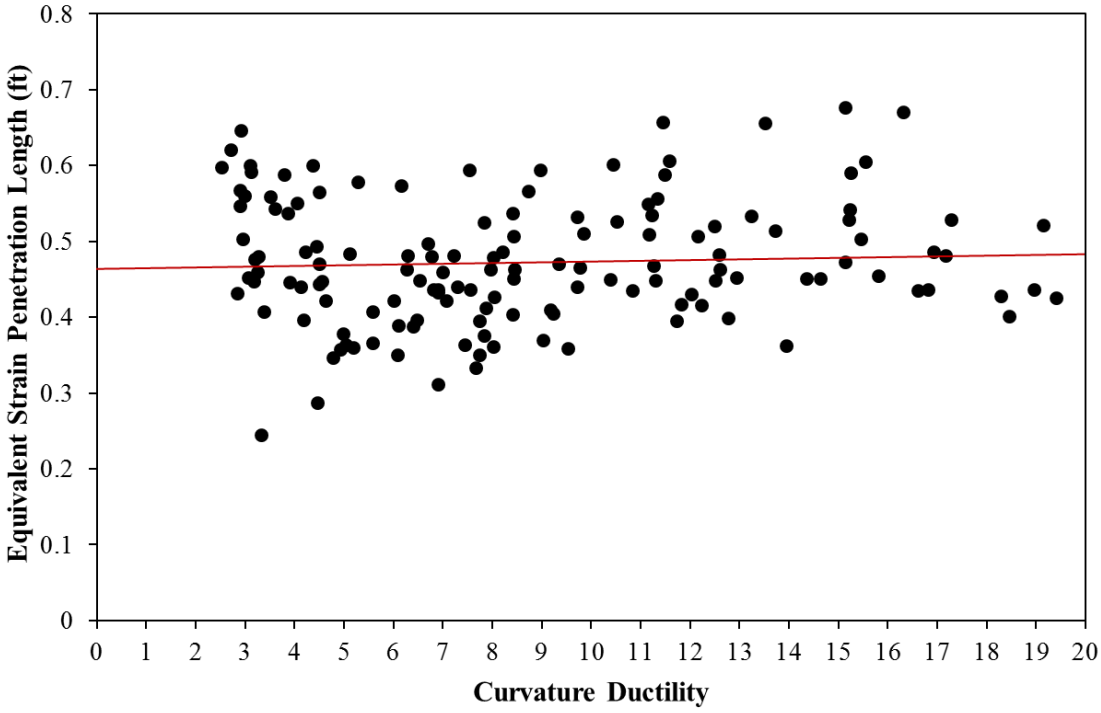

Figure 4-41. Constant Strain Penetration Length Approximation

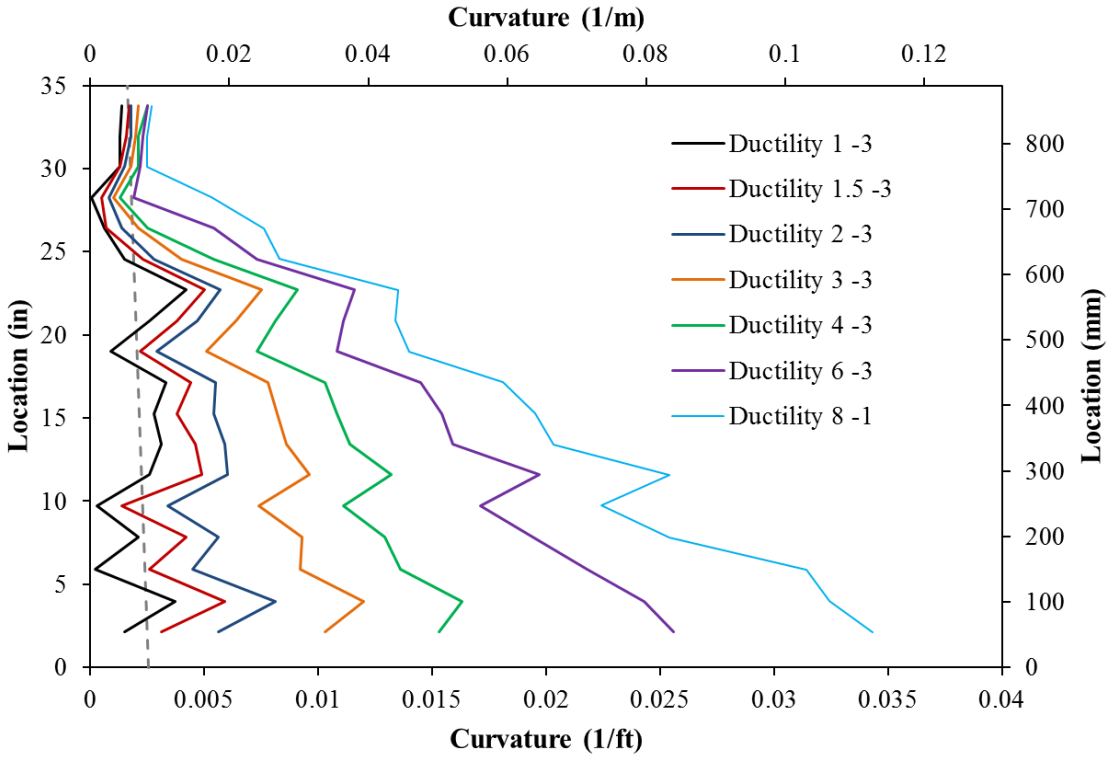

Figure 4-42. Vertical Curvature Profiles Measured during the Cyclic Aftershock Conducted after the Chile 2010 Load History in Test 8b

4.4. Improvements to the Plastic Hinge Method for Member Deformations

Improvements to the plastic hinge method for member deformation are necessary to produce accurate limit state target displacements at levels of response other than the ultimate condition which the constant plastic hinge length was intended for. As previously discussed, plastic curvatures follow a linear distribution which intersects the yield curvature distribution at a height termed the extent of plasticity, see Figure 4-36. The extent of plasticity increases as the base curvature becomes larger following a bilinear relationship with respect to curvature ductility as shown in Figure 4-38. A generalized function for the bilinear relationship must also include aspect ratio, longitudinal bar diameter, and the ratio of f_y/f_u. Variables which affect moment gradient, development of longitudinal steel, and shear crack angle are expected to influence the extent of plasticity.

An equivalent curvature distribution for the modified plastic hinge method can be devised which matches the measured spread of plasticity in flexural bridge columns, see Figure 4-43 and Figure 4-36. The deformation components incorporated into the model include: elastic column flexure, plastic column flexure, strain penetration, and shear. As previously demonstrated by the good agreement between integrated flexural displacements and total deformation, in Figure 4-33, shear displacements for slender flexural bridge columns are small compared to flexural deformations. The elastic flexure, plastic flexure, and strain penetration deformation components are calculated using the simplified curvature distribution and the moment area method resulting in the equations presented in Figure 4-43. This method is still a work in progress given that the research project still contains twelve more bridge column tests which will focus on aspect ratio, axial load ratio, and longitudinal steel content. The information presented in this section is intended to show the current progress towards the goal of improving the prediction of the relationship between strain and displacement.

A comparison of the accuracy of the original and modified plastic hinge methods applied to Tests 8-18 appears in Figure 4-44. Each method utilized the same input for the base curvature, yield curvature, first yield moment, and moment at each of the data points which are organized in ascending curvature ductility. For the purposes of this report, a simplified form of the equation for the extent of plasticity is adopted using the bi-linear relationship presented in Figure 4-38. Similar to the method of calibrating the original strain penetration equation, the constant variable “x” in Lsp was fit to minimize the error in the deformation prediction. The modified plastic hinge method does a better job of predicting the top column deformation than the original plastic hinge method. The accuracy of the lateral force vs. deformation response prediction is maintained as shown in Figure 4-45.

The goal of the modified plastic hinge method is to improve the prediction for the relationship between strain and displacement. A comparison of the relationship between tension strain and displacement for the largest tensile gage length during the peak push and pull cycles of Tests 8-18 with each plastic hinge method appears in Figure 4-46 and Figure 4-47. The solid lines represent tensile strains measured during individual cycles for tests with variable load history and transverse steel detailing. It appears that neither of these variables have a large impact on the relationship between strain and displacement. The original plastic hinge method over predicts the tension strain at a given displacement by an increasing margin as ductility demand increases. The modified plastic hinge method slightly over predicts the measured tension strains by a uniform margin over the entire range of displacements investigated. The modified plastic hinge method does not address the adequacy of the plane section hypothesis utilized in moment curvature analysis. The assumption of equal moment demand across a horizontal cross section is violated in bridge columns due to bar slips and tension shift. Therefore, insuring an accurate method of relating base section curvature to top column displacement does not insure accurate strains at that curvature. The original plastic hinge

method does a better job of predicting the relationship between compressive strain and displacement in Figure 4-48 and Figure 4-49. As the column rotates about inclined flexural shear cracks, the effects of tension shift concentrate the compressive demand at the base of the column and fan out the tensile strain demand higher above the footing. This means that at a given horizontal section near the base of the column, one would expect lower tensile strains and higher compressive strains, refer to Figure 4-27.

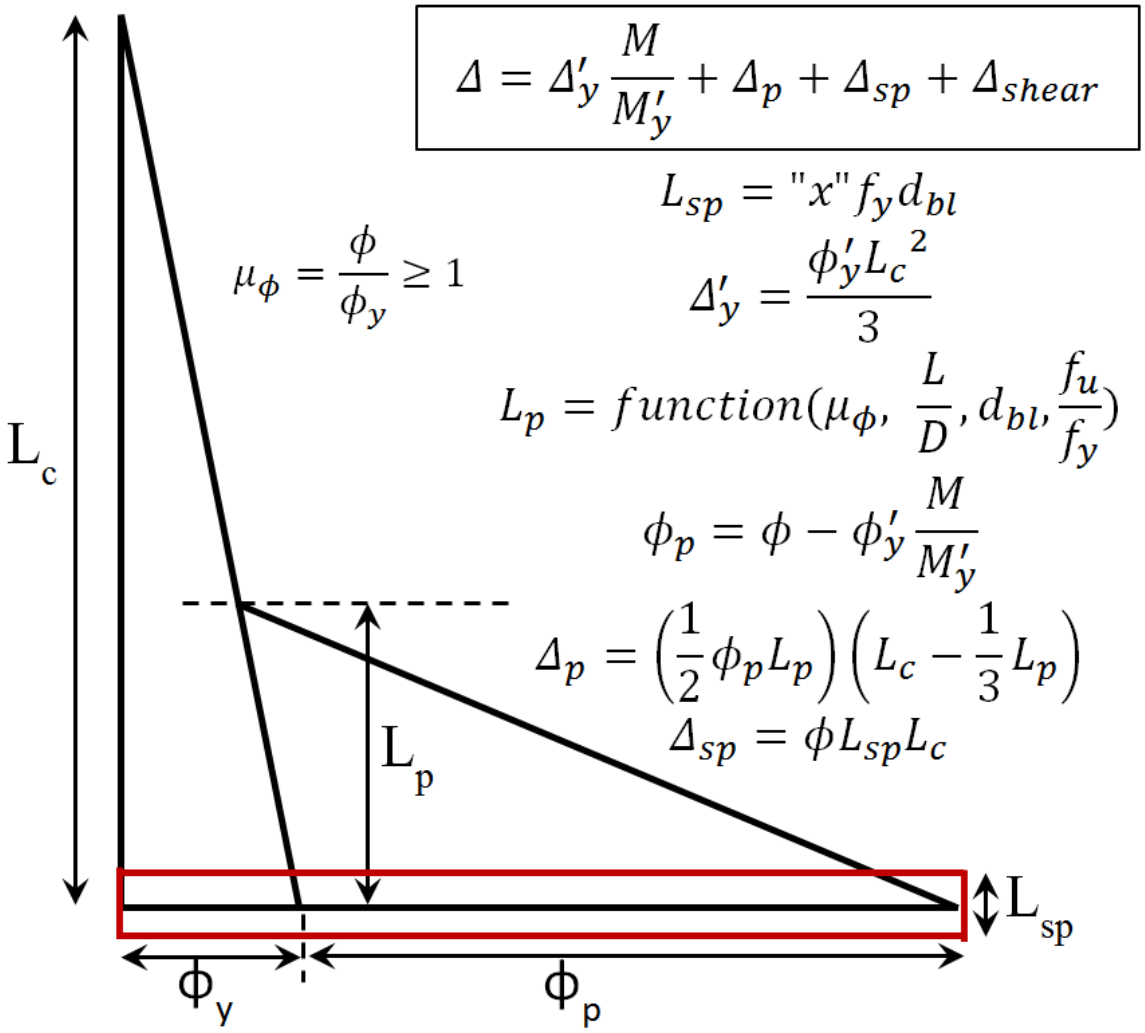

Figure 4-43. Equivalent Curvature Distribution which Utilizes the Observation of Linearly Distributed Plastic Curvatures (Formulas are placeholders since the method needs data from Tests 19-30 which are still in progress.)

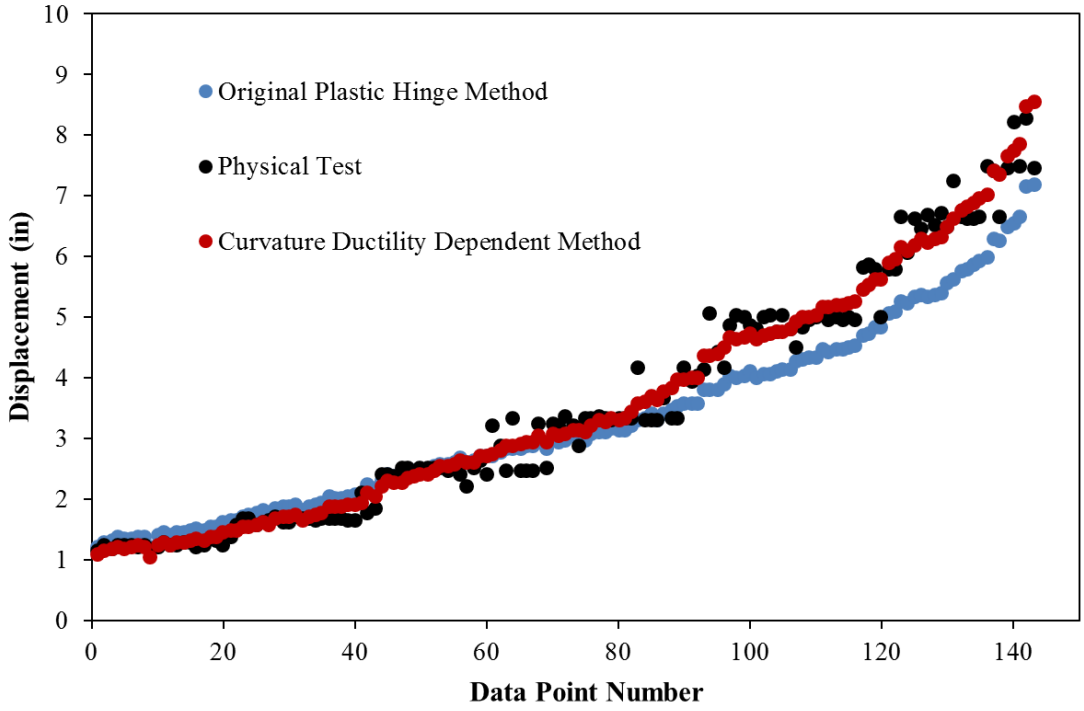

Figure 4-44. Comparison of the Displacement Prediction using the Original and Modified Plastic Hinge Methods

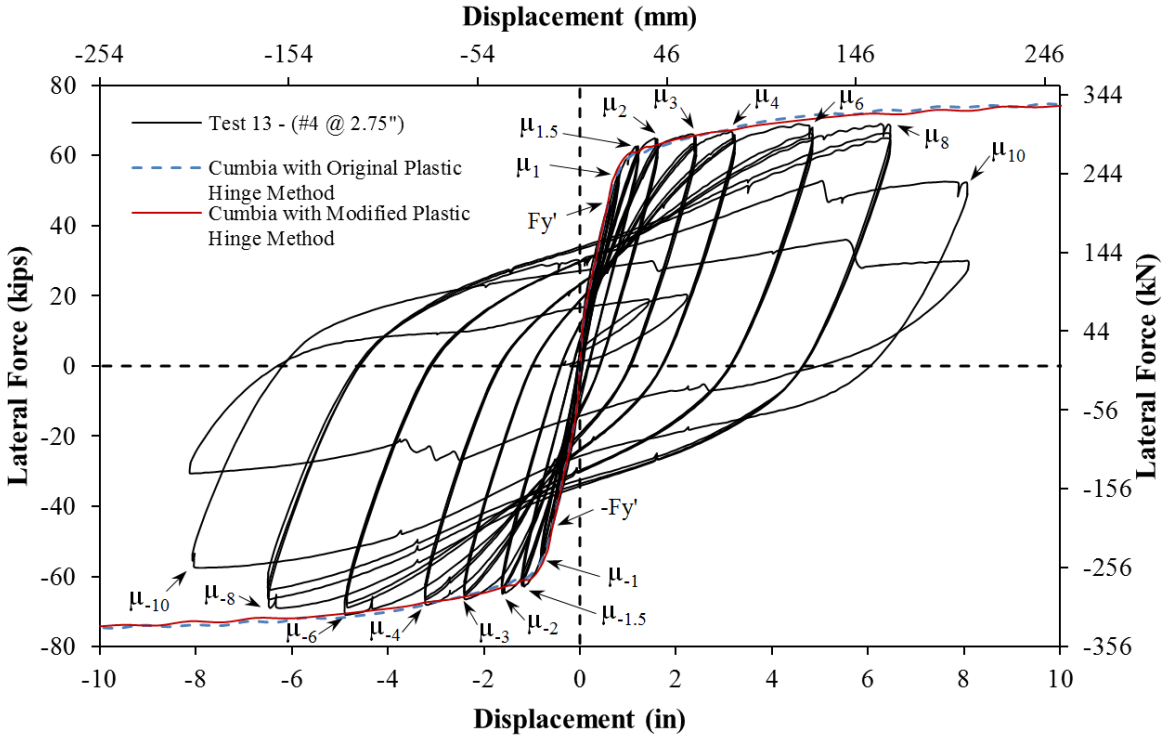

Figure 4-45. Hysteretic Comparison for the Original and Modified Plastic Hinge Methods

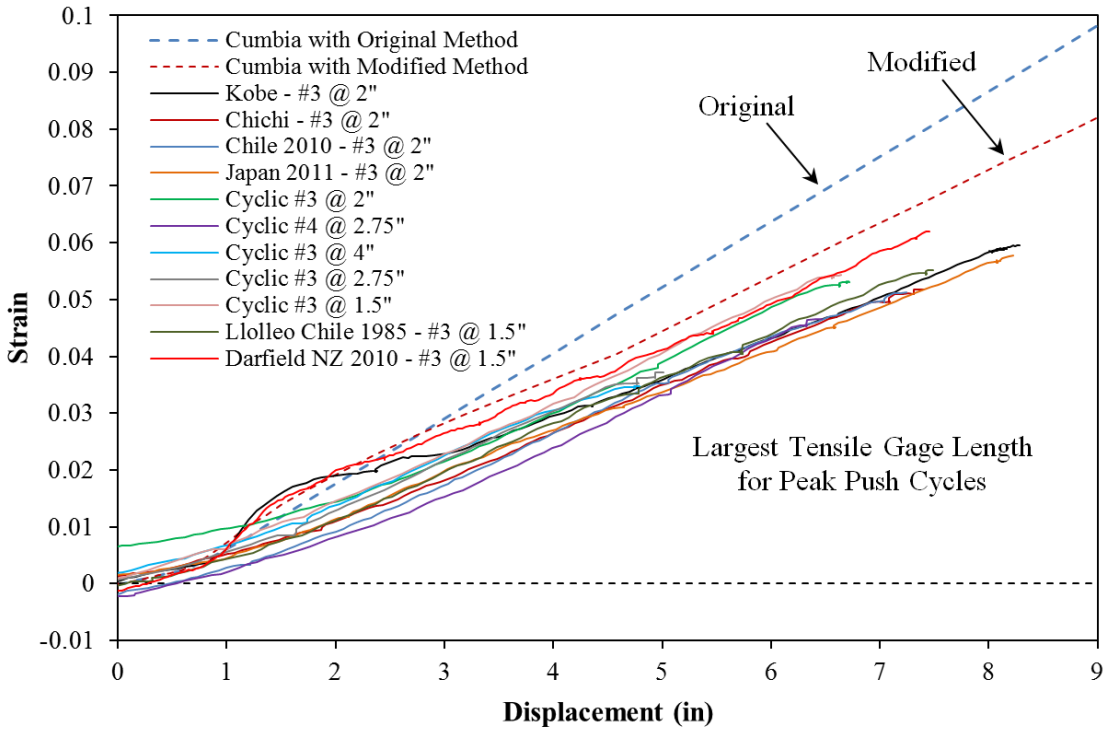

Figure 4-46. Comparison for Tensile Strain and Displacement during Push Cycles

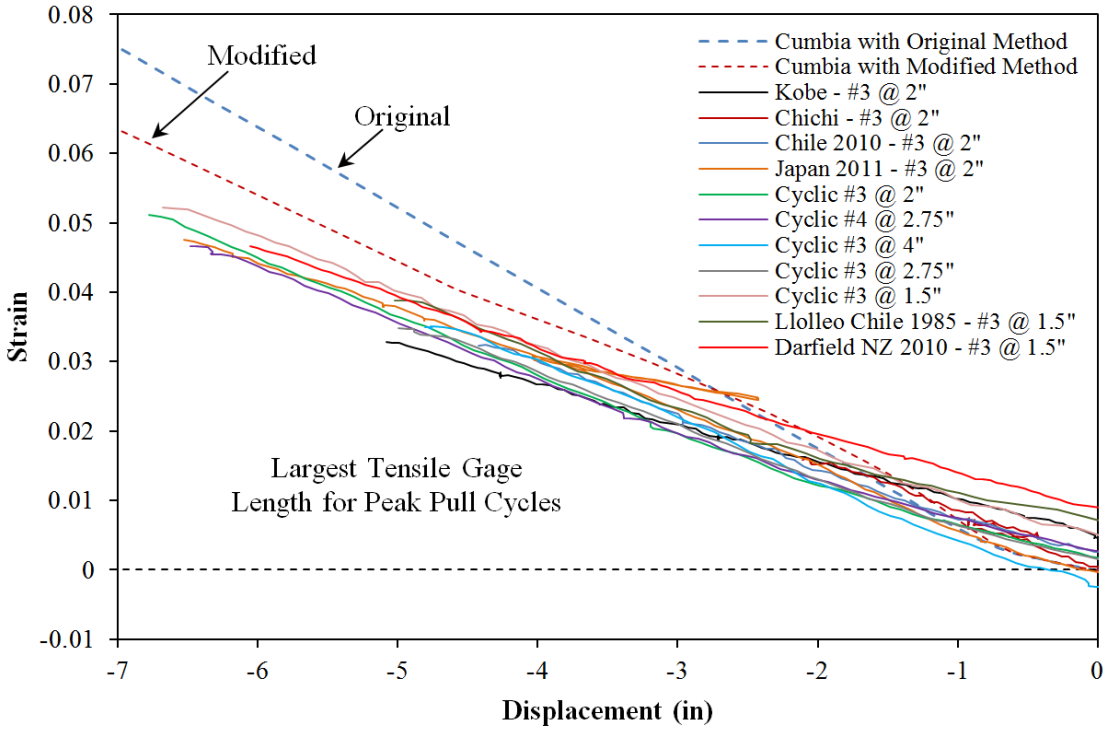

Figure 4-47. Comparison for Tensile Strain and Displacement during Pull Cycles

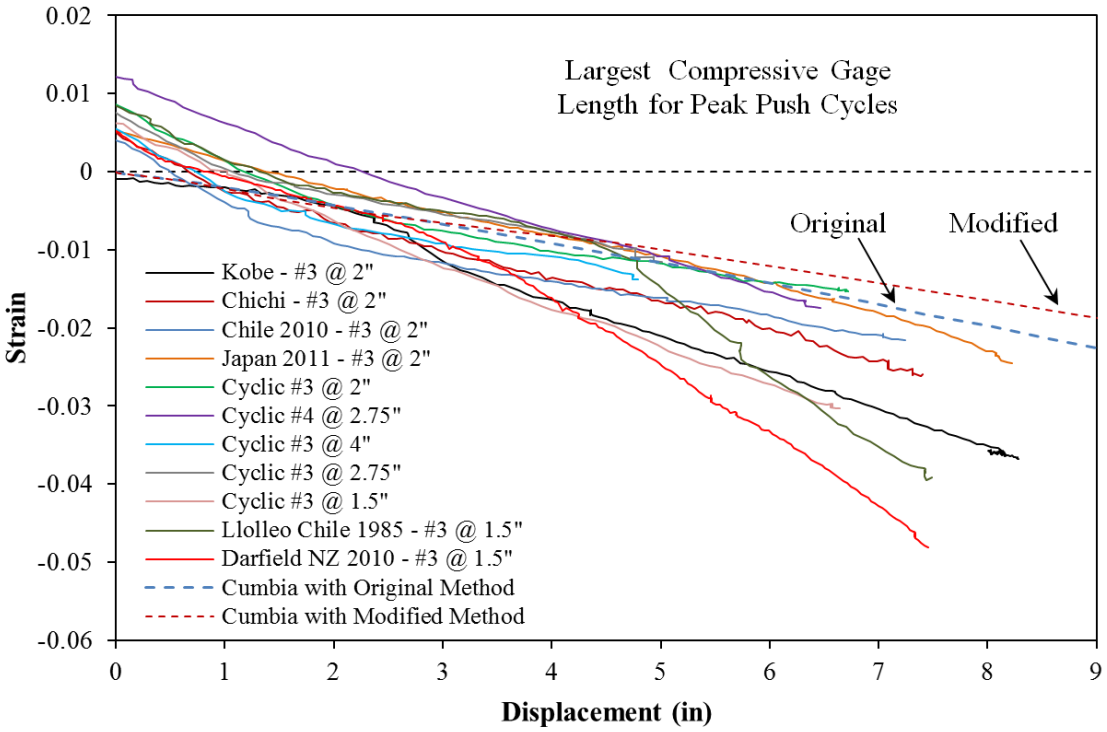

Figure 4-48. Comparison for Compressive Strain and Displacement during Push Cycles

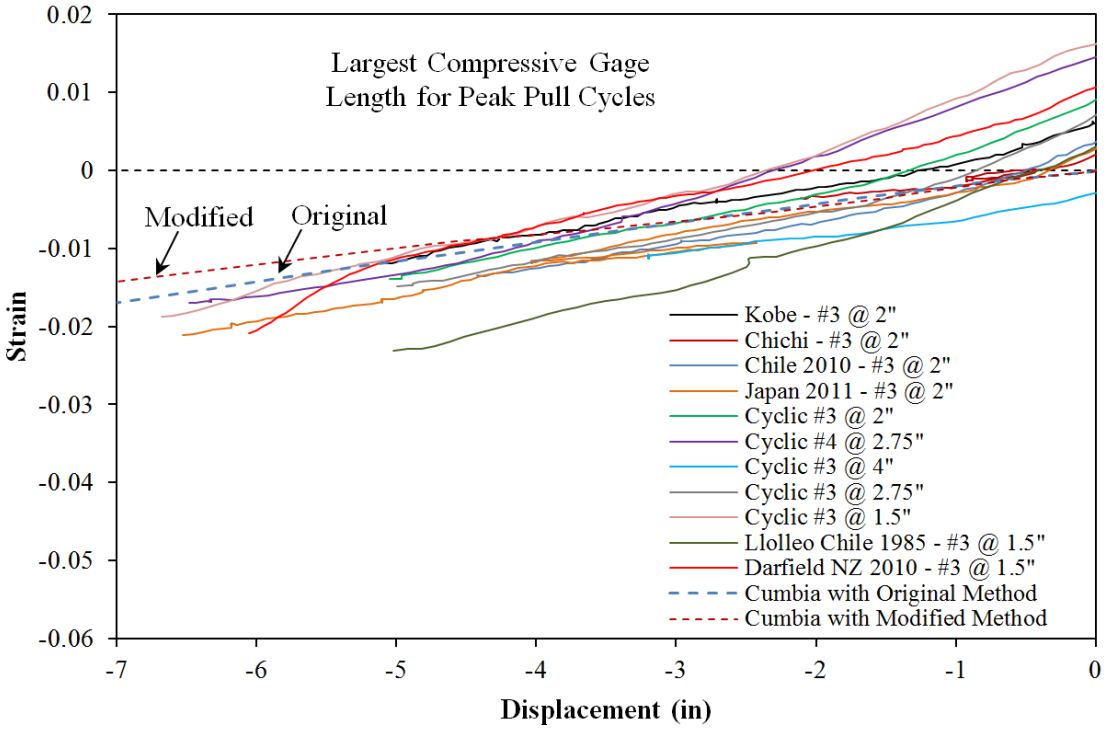

Figure 4-49. Comparison for Compressive Strain and Displacement during Pull Cycles

CHAPTER 5 - CONCLUSIONS AND SUGGESTED RESEARCH

5.1. Conclusions Based on Experimental Results

The goal of performance based seismic engineering is to design structures to achieve a specific level of performance under a specific earthquake hazard. To satisfy the aims of performance based design, levels of damage which interrupt the serviceability of the structure or require more invasive repair techniques must be related to engineering criteria. For reinforced concrete structures, concrete compressive and steel tensile strain limits are the best indicators of damage. In this paper, the importance of displacement history and its effects on performance limit states, the relationship between strain and displacement, and the spread of plasticity in reinforced concrete structures was explored. An experimental research program is currently underway to assess the performance of thirty large-scale circular, well-confined, bridge columns subjected to various unidirectional displacement histories including monotonic, reversed cyclic, and earthquake time-history response. The test variables include load history, transverse reinforcement detailing, axial load ratio, aspect ratio, and longitudinal steel content. The experimental program utilized an innovative instrumentation method to measure large strains at the level of the reinforcement with multiple Optotrak Certus HD 3D position monitors. The longitudinal reinforcement in extreme fiber regions was instrumented to obtain strain hysteresis, vertical strain profiles, cross section curvatures, curvature distributions, and fixed-end rotations attributable to strain penetration.

Results have shown that the damage control steel tensile strain limit was influenced by load history, but the relationship between strain and displacement was not. Specific earthquake time-history response characteristics were evaluated including: the number and amplitude of cycles prior to the peak, degree of symmetry, and peak displacement in each direction of loading. The symmetric three cycle set load history is more severe than the displacement history produced by real earthquakes, when evaluated to the same peak displacement, because of the high number of inelastic reversals of loading of increasing magnitude. The earthquake load histories needed to be scaled to larger displacements to produce bar buckling. Large inelastic strains, caused by large concrete compressive demand, decreased the effectiveness of the transverse steel in restraining buckling of the longitudinal bars. Plastic curvatures followed a linear distribution and as curvature ductility increased, the extent of plasticity stretched higher above the footing. Improvements to the moment curvature prediction for the relationship between strain and displacement can be made by taking into account the curvature ductility dependent linear distribution of plastic curvatures.

This report focused on specimens 8-18 which included load history and transverse steel detailing as primary variables. The remaining specimens in the research program will focus on aspect ratio, axial load ratio, and longitudinal steel content. Conclusions in the form of design recommendations for performance strain limits require inspection and comparison of the entire experimental dataset. For the purposes of this report, the influence of load history and transverse steel on column behavior was presented in the form of experimental observations. All of the variables found to be statistically significant towards describing bar buckling in a column dataset by (Berry and Eberhard (2005)) will appear in the experimental program. Upon conclusion of the research program, design recommendations for performance strain limits will be presented which apply within the bounds of the variables investigated.

Improvements to the plastic hinge method for member deformation are necessary to produce accurate limit state target displacements at levels of response other than the ultimate condition which the constant plastic hinge length was intended for. The Optotrak instrumentation system allows for measurement of cross section curvature profiles and fixed-end rotations due to strain penetration of

longitudinal reinforcement into the footing. The use of a constant plastic hinge length does not take into account the response level dependent, linear distribution of plastic curvatures within the hinge regions. As the base section curvature increase, the height at which the linear plastic curvature distribution intersects the elastic curvature profile extends further above the footing. The spread of plasticity in bridge columns is primarily due to the effects of tension shift and hardening within the hinge region. Due to the effects of tension shift, compressive strains are concentrated near the column base and tensile strains are fanned out to a greater height following inclined crack distribution. The tensile strains at the beginning of an inclined flexural shear crack do not coincide with the perceived moment demand at that location based on its height above the footing and the applied lateral load. The Optotrak data obtained during the thirty bridge column tests will be utilized to create an equivalent curvature distribution which matches the measured spread of plasticity.

5.2. Suggested Experimental Research

The logical extension of the load history research program would be to investigate the effects of bi-directional earthquake excitation on column behavior. Earthquake accelerations are recorded in two perpendicular horizontal directions and a vertical component. The goal of the load path experimental program would be to investigate the influence of bi-directional load history on performance strain limits, the relationship between strain and displacement, and the spread of plasticity in circular bridge columns. The specific issues with regards to load path are the impact of multi-directional loading on: (1) Accumulation of strain in reinforcing steel; (2) Uni-directional design (which is the normal practice); and (3) Crack formation and the plastic hinge method for member deformations. The load path study may also include the effects of variable axial load by testing a single column with controlled loading, or a multi-column bent. The goal of the research would be to determine limit state target displacements which consider the possible influences of 2D load path.

5.3.Analytical Study of Load History Effect on Strain and Displacement Relationship

Ground motions from Chile, Japan, Kobe and Chichi earthquakes represent four significant different types of load histories. As shown in the strain hysteretic graphs, the peak strain point constantly followed the monotonic strain displacement curve. The load history has a minor effect on the peak strain displacement relationship. However, the strain displacement relationship is impacted significantly by the axial load ratio and the aspect ratio of the column.

To investigate the load history effect on the strain displacement relationship, analysis considering other variables and additional earthquakes is ongoing with the fiber-based model. The structural variables includes the yield strength of longitudinal steel, yield strength of spiral and the bar diameter. All of the earthquakes in Table 1 will be involved in the parametric study. Future studies will also investigate the impact of structural variables on the relationship between strain and displacement.

5.4.Analytical Study of Load History Effect on Bar Buckling

The finite element bar buckling model has been shown to be able to capture bar buckling. Also, the load history on bar buckling has been simulated properly. Future parametric studies with the bar buckling model will focus on variables including load history, axial load ratio, aspect ratio, spiral spacing, bar diameter and steel yield strength. The strain history from test results were utilized for calibration of the bar buckling model. To predict bar buckling, the strain history prediction from fiber-based model will be utilized in the parametric study.

REFERENCES

Alemdar, B. N. and White, D. W. (2005). Displacement, Flexibility, and Mixed Beam-Column Finite Element Formulations for Distributed Plasticity Analysis. *Journal of Structural Engineering*. Vol. 131: No. 12, 1811-1819.

Berry, M. P. and Eberhard, M. O. (2005). Practical Performance Model for Bar Buckling. *Journal of Structural Engineering* 131:7, 1060-1070.

Carr, A. J. (2008). Ruaumoko Manual Appendices. Vol. 5.

Filippou, F. C., Popov, E. P. and Bertero, V. V. (1983). Effects of Bond Deterioration on Hysteretic Behavior of Reinforced Concrete Joints. *Report EERC 83-19, Earthquake Engineering Research Center, University of California, Berkeley.*

Freytag, D. (2006). Bar buckling in reinforced concrete bridge columns. Master's thesis, University of Washington.

Hines, E. M., Restrepo, J. I., and Seible, F. (2004). Force-Displacement Characterization of Well Confined Bridge Piers. *ACI Structural Journal* 101:4, 537-548.

King D. J, Priestley M. J. N., and Park R. (1986). Computer Programs for Concrete Column Design, Research Report 86/12, Department of Civil Engineering, University of Canterbury, New Zealand

Kunnath, S., El-Bahy, A., Taylor, A., and Stone, W. (1997). Cumulative Seismic Damage of Reinforced Cocnrete Bridge Piers. Technical Rep. NCEER-97-0006, National Center of Earthquake Engineering Research, Buffalo, N.Y.

Mander J. B., Priestley M. J. N., and Park R. (1988). Theoretical Stress-Strain Model for Confined Concrete. *ASCE Journal of Structural Engineering* 114:8.

Montejo L. A. and Kowalsky M. J. (2007). CUMBIA – Set of Codes for the Analysis of Reinforced Concrete Members, Technical Report No. IS-07-01, North Carolina State University

Moyer, M. J. and Kowalsky, M. J. (2003). Infulence of Tension Strain on Buckling of Reinforcement in Concrete Columns. *ACI Structural Journal* 100:1, 75-85.

Neuenhofer, A. and Filippou, F. C. (1998). Geometrically Nonlinear Flexibility-Based Frame Finite Element. *Journal of Structural Eingeering*. Vol. 124: No. 6, 704-711.

Park, R. and Paulay, T., (1975). Reinforced Concrete Structures. Wiley, New York.

Paulay, T. and Priestley, M. J. N. (1992). Seismic Design of Reinforced Concrete and Masonry Buildings, Wiley, New York.

Priestley, M. J. N., Seible, F., and Calvi, G. M. (1996). Seismic Design and Retrofit of Bridges. John Wiley & Sons, New York.

Priestley, M. J. N., Calvi, G. M., and Kowalsky, M. J. (2007). Displacement-Based Seismic Design of Structures. IUSS Press, Pavia, Italy.

SEAOC (1999). Recommended Lateral Force Requirements and Commentary (7th Edition). Structural Engineers Association of California, Seismology Committee: Sacremento, CA.

Scott, M. H. (2011). Numerical Integration Options for the Force-Based Beam-Column Element in OpenSees. *Command Manual of OpenSees.*

Scott, M. H. and Fenves, G. L. (2006). Plastic Hinge Integration Method for Force-Based Beam-Column Elements. *Journal of Structural Engineering* 132:2, 244-252.

Syntzirma, D. V., Pantazopoulou, S. J., Aschheim, M. (2010). Load-History Effects on Deformation Capacity of Flexural Members Limited by Bar Buckling. *Journal of Structural Enginering* 136:1, 1-11.

Yassin, M. H. M. (1994). Nonlinear Analysis of Prestressed Concrete Structures under Monotonic and Cycling Loads. *PhD dissertation, University of California, Berkeley.*

Zhao, J. and Sritharan, S. (2007). Modeling of Strain Penetration Effects in Fiber-Based Analysis of Reinforced Concrete Structures. *ACI Structural Journal.* 104:2, 133-141.

APPENDIXES